Thèse de Doctorat de l'Université Paris 6

Spécialité: Sciences de la Terre

préparée au

Laboratoire de Météorologie Dynamique

présentée par

Camille Risi

pour obtenir le grade de Docteur de l'université Paris 6

Les isotopes stables de l'eau: applications à l'étude du cycle de l'eau et des variations du climat

soutenue le 7 Décembre 2009 devant le jury composé de:

Présidente	Mme Katia Laval
Rapporteurs	M. Jean-Philippe Lafore M. Gavin Schmidt
Examinateurs	Mme Cathy Clerbaux M. Gilles Delaygue M. Christophe Sturm
Directeurs de thèse	Mme Sandrine Bony M. Jean Jouzel

Remerciements

Je remercie avant tout Sandrine Bony de m'avoir encadré pendant mon stage de Master puis pendant ces trois ans de thèse. J'ai beaucoup apprécié ses qualités à la fois scientifiques et humaines. Je la remercie tout particulièrement pour les nombreuses discussions scientifiques qu'on a eu, et pour m'avoir transmise sa passion de la recherche. Je la remercie aussi pour ses conseils précieux sur la préparation de mon après-thèse. Les séjours ensemble à Niamey et à Hawaii constituent parmis mes meilleurs souvenirs de thèse.

Je remercie aussi Françoise Vimeux pour les nombreuses discussions au cours de ma thèse. Son expertise concernant les données isotopiques a été précieuse, et m'a apporté des choses complémentaires à ce que j'ai appris au LMD. Je la remercie de m'avoir permis de co-encadrer avec elle Guillaume Trémoy, stagiaire de Master.

Merci aussi à Amaelle Landais pour m'avoir fait découvrir un nouvel isotope: l'oxygène 17. Bien que pas prévu initiallement dans ma thèse, j'ai été très heureuse de travailler sur la compréhension de ce nouveau traceur qui semble prometteur.

Je remercie Jean Jouzel pour avoir co-encadré cette thèse, pour les discussions que nous avons eu, et pour la relecture du manuscrit de thèse.

Je remercie aussi les différentes personnes avec qui j'ai eu l'occasion de discuter au cours de ma thèse, en particulier (dans le désordre et liste non exhaustive) Jean-Philippe Lafore, Jean-Yves Grandpeix, Frédéric Hourdin, Valérie Masson-Delmotte, Masa Kageyama, Philippe Peylin, Jérome Ogée, Thierry Bariac, Aaron Boone, Françoise Guichard, Katia Laval, Jan Polcher, Gerhard Krinner, Gilles Delaygue, Matthias Cuntz.

Je serais ravie de pouvoir à l'avenir continuer à collaborer avec les différentes personnes avec qui j'ai travaillé pendant cette thèse.

Je remercie aussi les membres du jury d'avoir accepté d'évaluer cette thèse et pour leurs suggestions pour améliorer ce manuscrit.

Je remercie Hervé Le Treut, en tant que directeur du LMD à l'époque, de m'avoir accueilie dans son laboratoire.

Merci aussi à tous les membres du LMD-Jussieu d'avoir fait de ma thèse un moment si agréable. Je remercie en particulier Martine Maherou pour son aide lors du traitement des missions ou des problèmes administratifs; Véronique Fabart, Robert Franchisseur et Laurent Fairhead pour leur aide technique sur des problèmes informatiques; Ionéla Musat et Joséphine Gatthas pour leur aide sur des problèmes en lien avec LMDZ.

Merci aussi aux nombreux thésards, stagiaires et post-docs du LMD-Jussieu pour avoir contribué à l'ambiance de travail agréable. Les repas tous ensemble à la cantine vont surement me manquer.

Je remercie les équipes enseignantes dans lesquelles je me suis intégrée dans le cadre de mon monitorat à Paris 6. Je remercie en particulier Christian Hontaas (Sciences de la Terre), Annick Deguardin (Physique), Marc Fournier, Michael Jentzer et Loic Labrousse (CAPES/Agreg de SVT), qui ont contribué à faire de mon monitorat une partie agréable de mon travail de thèse et une expérience d'enseignement enrichissante.

Enfin, merci à mes parents, pour m'avoir donné le gout et l'ambition de faire des études, ainsi qu'à tous les professeurs qui, au cours de ma scolarité de la primaire au Master, m'ont fait aimé les Sciences et plus particulièrement celles de l'atmosphère et du climat.

Résumé

La composition isotopique de l'eau ($H_2^{16}O$, HDO, $H_2^{18}O$, $H_2^{17}O$) est de plus en plus utilisée pour étudier le cycle de l'eau actuel et ses variations passées. Mais tandis que la composition isotopique enregistrée dans les glaces polaires est depuis longtemps à la base des reconstitutions des variations passées des températures polaires, beaucoup de questions subsistent concernant les facteurs contrôlant la composition isotopique dans les tropiques. Le but de cette thèse est donc de mieux comprendre les processus affectant la composition isotopique de l'eau (précipitation, eau atmosphérique), en particulier dans les tropiques. Comme la majeure partie des précipitations tropicales a une origine convective, et que la plupart des archives isotopiques se trouvent sur le continent, nous portons une attention plus particulière à la convection atmosphérique d'une part et à l'hydrologie de surface continentale d'autre part. En retour, que peut apporter la composition isotopique sur les processus convectifs et l'hydrologie de surface? Peut-elle aider à mieux contraindre la représentation de ces processus dans les modèles? A l'échelle inter-annuelle ou des changements climatiques, quelles informations apportent les archives isotopiques sur la variabilité du climat tropical? Ce sont autant de questions auxquelles nous essayons de répondre dans cette thèse.

Tout d'abord, nous analysons l'influence de la convection atmosphérique sur la composition isotopique de l'eau tropicale. Nous combinons pour cela deux approches: (1) la modélisation numérique, avec une hiérarchie de modèles (modèle uni-colonne, modèle 2D de ligne de grains, modèle de circulation générale LMDZ dans lequel nous avons introduit les isotopes), et (2) de l'analyse de données isotopiques de pluies collectées au Niger au cours de la campagne de terrain AMMA (Analyse Multi-disciplinaire de la Mousson Africaine), aux échelles de l'événement et de l'intra-événement. Ces études montrent un impact fort de la convection sur la composition isotopique des précipitations, ainsi que l'importance de la réévaporation de la pluie et des subsidences convectives ou méso-échelles pour contrôler cette composition. La convection joue aussi un rôle important sur les profils isotopiques dans la haute troposphère-basse stratosphère.

Ensuite, nous étudions quelles informations sur la variabilité climatique passée la composition isotopique des précipitations enregistrent. Nous analysons des simulations LMDZ du climat actuel et des climats passés, et evaluons dans quelle mesure les archives isotopiques de précipitation tropicale peuvent être utilisées pour reconstituer les changements de précipitation passés. Nous explorons aussi la valeur ajoutée apportée par un nouveau traceur isotopique encore peu utilisé: l' $H_2^{17}O$.

Enfin, nous analysons l'influence des processus de surface continentale sur la composition isotopique des precipitations ou des réservoirs d'eau continentaux, grâce à des simulations avec le modèle d'hydrologie continentale ORCHIDEE, dans lequel nous avons aussi introduit les isotopes. Les compositions isotopiques de différents réservoirs d'eau du système surfaces continentales-atmosphère contiennent des informations sur le partitionnement de la précipitation en ruissellement, drainage, transpiration par la végétation ou évaporation du sol nu.

Summary

The stable isotopic composition of water ($H_2^{16}O$, HDO, $H_2^{18}O$, $H_2^{17}O$) is a promising tracer of the present day water cycle and past climates. While the isotopic composition recorded in polar ice core have long been used to reconstruct past temperatures, however, what controls the isotopic composition of the tropical precipitation is more complex. The goal of this thesis is thus to better understand the processes that affect the isotopic composition of tropical precipitation and atmospheric water, more particularly in the tropics. Since most of the tropical precipitation arises from atmospheric convection, and most isotopic archives are on land, we focus more particularly on the impact of convective and land surface processes. In turn, what can be learned about convection and land surface processes using isotopic measurements? Can they help constrain their representation in models? At the inter-annual to climate change scale, what information about the tropical climate variability is recorded in isotopic signals observed in archives?

First, we investigate the influence of convection on water stable isotopes. We use both (1) numerical modeling, with a hierarchy of models (single column model, two-dimensional model of squall lines, general circulation model) and (2) data analysis, using isotopic data from rain collected in the Sahel during the African Monsoon Multidisciplinary Analysis campaign, at the event and intra-event scales. These studies highlight the strong impact of convection on the precipitation composition, and stress the importance of rain evaporation and convective or meso-scale subsidence in controlling the rain isotopic composition. Convection also plays an important role on isotopic profiles in the upper troposphere-lower stratosphere.

Second, we study what information about climatic variability is recorded by water stable isotopes in precipitation. We analyze simulations of present day and past climates with LMDZ, and evaluate to what extent isotopic archives of tropical precipitation can be used to reconstitute past precipitation changes. We also explore the added value of a new but promising isotopic tracer: $H_2^{17}O$.

Third, we analyze the influence of land surface processes on the isotopic composition of precipitation and land surface waters, using simulations with the land surface model ORCHIDEE in which we also introduced the isotopes. The isotopic composition of the different water pools of the land-atmosphere system may inform about the partitioning of precipitation into runoff, drainage, transpiration and bare soil evaporation.

Table des matières

Chapitre 1

Introduction générale

Dans ce chapitre d'introduction, nous définissons la composition isotopique de l'eau, et présentons les principales propriétés de sa distribution spatiale actuelle dans la précipitation (section 1.1). Ceci est l'occasion d'introduire les principaux processus contrôlant la composition isotopique de l'eau à l'échelle globale. Puis nous introduisons les différentes applications de l'étude de la composition isotopique de l'eau, aussi bien pour la paléo-climatologie que pour l'étude du cycle de l'eau dans le climat actuel (section 1.2). Pour mieux comprendre et interpréter les données observées, on a souvent recours à de la modélisation isotopique, dont nous décrirons les principaux degrés de complexité (section 1.3). Enfin, nous introduirons les grandes problématiques auquelles nous nous sommes intéressés au cours de cette thèse (section 1.4).

1.1 Les isotopes stables de l'eau: définition et distribution spatiale actuelle

1.1.1 Définition et fractionnements isotopiques

Définition et notations

Dans cette section, nous définissons la composition isotopique de l'eau et présentons les principales caractéristiques de sa distribution spatiale actuelle dans la précipitation.

Deux *isotopes* sont des atomes ayant le même nombre de protons et d'électrons, mais un nombre de neutrons différent. Ainsi, ils réagissent chimiquement de la même façon, mais ont un nombre de masse différent. Par exemple, l'atome d'hydrogène peut se présenter sous la forme ^1H (aucun neutron), ^2H (aussi appelé deutérium D, avec un neutron) ou ^3H (aussi appelé tritium T, avec deux neutrons). L'atome d'oxygène peut se présenter sous la forme ^{16}O, ^{17}O ou ^{18}O.

L'eau est composée en majorité de molécules d'$H_2^{16}O$, mais contient aussi quelques molécules plus lourdes d'$H_2^{17}O$ (0.004%), d'$H_2^{18}O$ (0.2005%), d'HDO (0.0155%,) et d'HTO (en quantité très faible actuellement). Ces différentes molécules sont appelées *isotopologues*, ou, par abus de language, simplement "*isotopes de l'eau*". Dans cette thèse, nous nous concentrons sur les trois isotopes lourds $H_2^{17}O$, $H_2^{18}O$ et HDO, qui sont *stables*, au contraire du HTO qui est radioactif.

La proportion relative de ces différentes molécules s'appelle la *composition isotopique* et est quantifiée par la notation δ:

$$\delta = \left(\frac{R_{sample}}{R_{SMOW}} - 1\right) \cdot 1000$$

avec R_{sample} le rapport du nombre de molécules lourdes sur le nombre de molécules totales dans l'échantillon et R_{SMOW} ce même rapport dans une référence internationale correspondant à une eau de surface océanique moyenne: Standard Mean Ocean Water (SMOW). Le δ s'exprime en ‰. On définit ainsi le $\delta^{17}O$, $\delta^{18}O$ et δD pour quantifier la richesse en $H_2^{17}O$, $H_2^{18}O$ et HDO respectivement.

Dans le langage courant, on dit qu'une eau est plus "riche" ou "enrichie" lorsqu'elle possède une plus grande concentration en isotopes lourds. Inversement, une eau est plus "pauvre" ou "appauvrie" quand la concentration en isotopes lourds est plus faible.

Fractionnements isotopiques

Les différentes espèces isotopiques de la molécule d'eau ont des masses et des symétries différentes. En conséquence, au cours de la plupart des changements de phase, elles sont redistribuées entre les phases: c'est ce qu'on appelle un *fractionnement isotopique*. Les raisons physiques à la base des fractionnements isotopiques dépassent largement le cadre de cette thèse (voir [Criss, 1999] pour un aperçu de la théorie des fractionnements isotopiques). En résumé, le fractionnement isotopique a deux causes: *thermodynamique* et *cinétique*.

- D'une part, les différences de *masse* induisent un fractionnement dit *thermodynamique* ou *à l'équilibre*: les molécules les plus lourdes se concentrent dans la phase la plus condensée (liquide ou glace). Ceci est dû à une pression de vapeur saturante plus faible pour les isotopes lourds. Par exemple, lors de la condensation à 20°C d'une vapeur, le condensat a un $\delta^{18}O$ environ 9.5‰ plus fort que la vapeur. Ce fractionnement dépend de la température (annexe B.1). Par exemple, à 10°C et -10°C, le condensat est respectivement 10.5‰ et 16.5‰ plus riche que la vapeur.

- D'autre part, la différence de *diffusivité moléculaire* entre ces espèces isotopiques (liée à la masse et à la symétrie des molécules) induit un fractionnement *cinétique*. Les molécules lourdes ont une diffusivité plus faible. Ainsi, lors de l'évaporation, la composition du flux d'évaporation est plus pauvre dans un cas hors équilibre qu'à l'équilibre thermodynamique. Le fractionnement cinétique dépend notamment de l'humidité relative de l'air ainsi que des diffusivités turbulentes et moléculaires des isotopes dans l'air (annexe B.3).

Le $\delta^{18}O$ et le δD ont été mesurés dans les eaux météoriques depuis longtemps ([Dansgaard, 1953, Dansgaard, 1964]). La mesure du $\delta^{17}O$ est en revanche beaucoup plus récente ([Barkan and Luz, 2005]), et sa distribution spatiale et ses contrôles commencent tout juste à être étudiés. Nous traiterons donc du $\delta^{17}O$ dans un chapitre à part (chapitre 7), et introduisons ici uniquement les principales propriétés et applications des $\delta^{18}O$ et δD.

1.1.2 Distribution spatiale actuelle de la composition isotopique de l'eau

Distribution spatiale du $\delta^{18}O$

Au premier ordre, le $\delta^{18}O$ et le δD montrent les mêmes distributions spatiales, mais les amplitudes de variations du δD sont 8 fois supérieures à celles du $\delta^{18}O$. La richesse en isotopes lourds peut donc se mesurer au premier ordre indifféremment par le $\delta^{18}O$ ou le δD. La figure 1.1 montre la distribution spatiale de la composition isotopique de la précipitation, en moyenne annuelle, collectée sur les stations du réseau GNIP (Global Network for Isotopes in Precipitation, un réseau mondial de collecte de précipitation et de mesure des compositions isotopiques sous l'égide de l'IAEA et du WMO). La distribution spatiale de la composition isotopique a été décrite en détail par [Dansgaard, 1964, Rozanski et al., 1993], et est résumée ici.

L'effet de température ("temperature effect") Le $\delta^{18}O$ montre principalement une distribution zonale, avec une composition de plus en plus pauvre quand la latitude augmente. Ceci est lié à l'effet de température (*temperature effect*): plus la température est faible, plus la précipitation est pauvre. En effet, imaginons une masse d'air se dirigeant des basses latitudes vers les pôles (figure 1.2a). Au fur et à mesure que la température diminue, l'humidité spécifique à saturation diminue et donc une partie de la vapeur condense et précipite. Comme les isotopes lourds se concentrent dans la phase la plus condensée, la vapeur perd alors par condensation une partie de ses isotopes lourds. Les événements successifs de condensation et précipitation résultent donc en un appauvrissement progressif de la masse d'air au cours de son transport vers les pôles. En conséquence, la précipitation produite par cette masse d'air est aussi de plus en plus pauvre quand on va vers les pôles. Cet appauvrissement au cours de la condensation se modélise par une

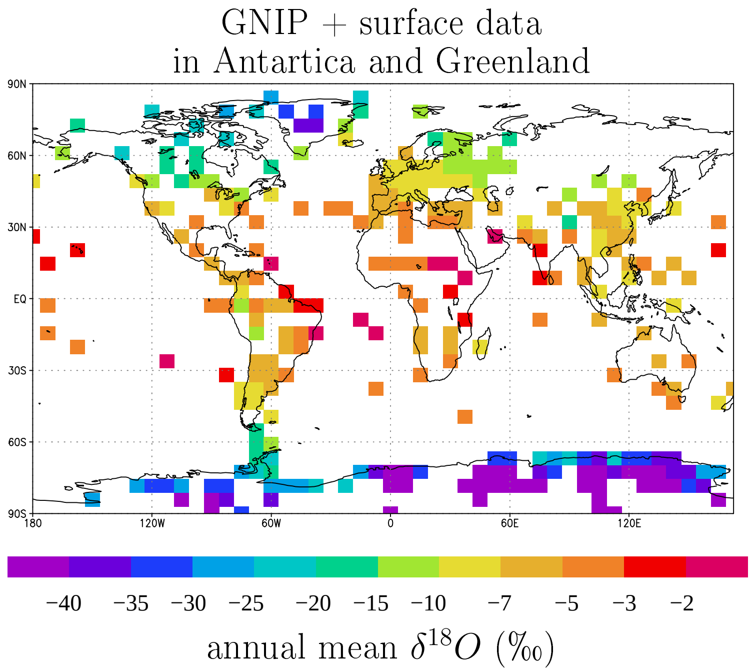

FIG. 1.1 – Distribution spatiale en moyenne annuelle et sur toutes les années disponibles du $\delta^{18}O$ dans les précipitations collectées par le réseau GNIP. Les données de neige de surface compilées par [Masson-Delmotte et al., 2008] pour l'Antarctique et [Masson-Delmotte et al., 2005] pour le Groenland ont aussi été rajoutées.

distillation de Rayleigh (figure 1.2b). Comme démontré en annexe C.1.1, si une vapeur initiale de rapport isotopique R_{v0} perd une fraction $1 - f$ de son eau par condensation et en retient une fraction f, son rapport isotopique R_v est donné par:

$$R_v = R_{v0} \cdot f^{\alpha - 1} \tag{1.1}$$

avec α le coefficient de fractionnement liquide/vapeur ou glace/vapeur (annexe B.1). Le facteur principal contrôlant la composition isotopique à l'échelle globale est donc f, qui est contrôlé par la température d'après la relation de Clausius-Clapeyron. Ceci explique la distribution zonale de la composition isotopique, mais aussi les précipitations plus pauvres observées en haute altitude (*altitude effect*).

L'effet de continentalité ("continental effect") Mis à part la distribution zonale des δ, on observe un appauvrissement des précipitations le long des trajectoires des masses d'air sur les continents. Par exemple, les précipitations sont de plus en plus pauvres lorsqu'on va vers l'Est sur le continent eurasiatique. C'est l'effet de continentalité (*continental effect*). En effet, au fur et à mesure du transport des masses d'air sur le continent, une partie de la vapeur précipite, appauvrissant la vapeur par distillation de Rayleigh. Sur l'océan, l'évaporation forte en surface permet de compenser cet appauvrissement, en réinjectant de l'eau relativement riche. Mais sur le continent, une partie de la précipitation est définitivement perdue sous forme de ruissellement. Le continental effect est ainsi moins marqué sur l'Amazonie, où le recyclage des précipitations par évaporation de surface est plus fort ([Rozanski et al., 1993]). Aux moyennes et hautes latitudes se surimpose à l'effet de continentalité un effet de température, avec des températures plus froides en hiver à l'intérieur des continents.

L'"amount effect" Enfin, un troisième facteur important contrôlant le composition isotopique est la quantité de précipitation. Ceci joue surtout dans les tropiques. L'amount effect explique par exemple les précipitations plus pauvres sur l'Indonésie où la convection est plus forte. Des causes possibles de cet amount effect sont ([Dansgaard, 1964]):

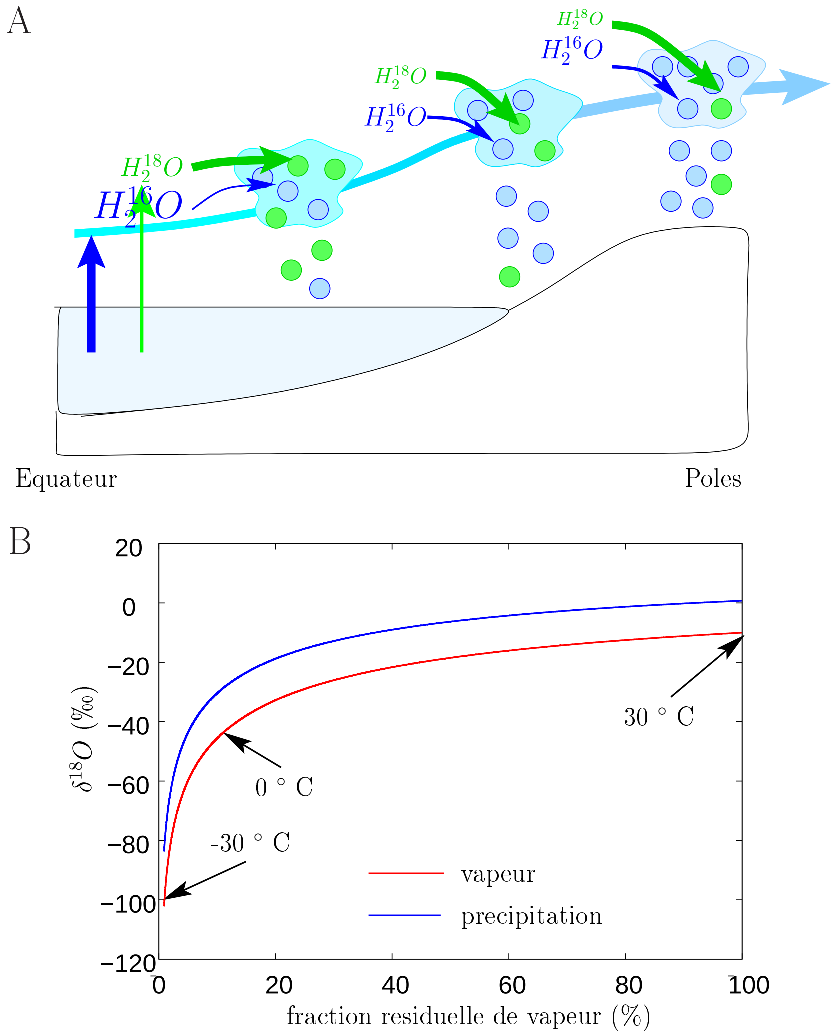

Fig. 1.2 – a) Schéma illustrant l'appauvrissement de la vapeur et des précipitaton quand une masse d'air se dirige vers les pôles.
b) Evolution du $\delta^{18}O$ de la vapeur et des précipitations d'une masse d'air lors de la Rayleigh de 30°C à -30°C.

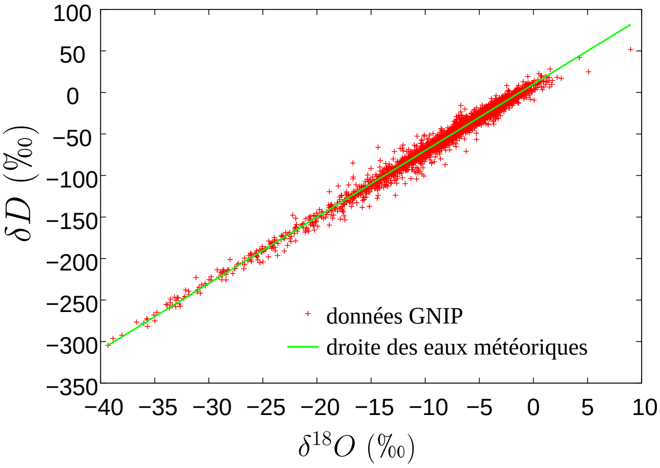

FIG. 1.3 – La droite des eaux météoriques, superposée aux données GNIP (moyennes annuelles sur toutes les années disponibles) sur chaque station.

- quand la convection est plus intense, la vapeur condense plus haut et le condensat se forme donc à partir d'une vapeur plus appauvrie,
- quand la convection est plus forte, les gouttes se réévaporent moins, donc se concentrent moins en isotopes lourds par évaporation lors de leur chute,

Les causes de l'amount effect seront étudiées plus en détail et quantifiées dans le chapitre 2.6.3.

L'amount effect est plus particulièrement visible sur les océans ([Rozanski et al., 1993]). Sur les continents, l'amount effect est aussi visible mais pas nécessairement à l'échelle locale: par exemple, la composition au pied des Andes est d'autant plus pauvre que la précipitation le long des trajectoires (sur l'Amazonie) a été intense ([Vimeux et al., 2005]).

Distribution spatiale du deuterium excess

Définition du deuterium excess On a vu qu'au premier ordre, le δD varie 8 fois plus que le $\delta^{18}O$. La figure 1.3 montre le δD en fonction du $\delta^{18}O$ dans les précipitations collectées par le réseau GNIP. Les données se rassemblent le long d'une droite de pente 8 et d'ordonnée à l'origine 10, que l'on appelle la *droite des eaux météoriques* (MWL, Meteoric Water Line). La déviation par rapport à cette droite est quantifiée par un paramètre de deuxième ordre appelé *excès en deutérium*, ou deutérium excess, ou d-excess, souvent noté d ([Craig, 1961, Dansgaard, 1964]):

$$d = \delta D - 8 \cdot \delta^{18}O$$

Le pente de 8 dans le diagramme $\delta^{18}O$ -δD correspond approximativement à des variations de δ liées à des processus de fractionnement à l'équilibre. En effet, la pente suivie lors d'une distillation de Rayleigh est donnée approximativement par le produit suivant (équation C.3 de l'annexe C.1.3):

$$\frac{d\delta D}{d\delta^{18}O} = \frac{\delta D + 1000}{\delta^{18}O + 1000} \cdot \frac{\alpha_{eq}^{D} - 1}{\alpha_{eq}^{18} - 1}$$

Ce produit reste relativement proche de 8, les variations de chacun de ses deux facteurs avec la température se compensant (annexe C.1.3). Comme ce produit varie relativement peu lors d'une distillation de Rayleigh, les déviations des précipitations par rapport à la droite des eaux météoriques sont souvent interprétées comme l'effet de processus de fractionnement cinétique. Par exemple, lors de l'évaporation, la diffusivité plus forte de l'HDO par rapport à l'$H_2^{18}O$ induit un excés en deutérium plus fort dans le flux d'évaporation que dans le liquide initial. La figure 1.4 illustre l'évolution du d-excess lors de quelques changements de phases au cours du cycle de l'eau. Le fractionnement cinétique lors de l'évaporation à la surface de l'océan explique que la vapeur, et les précipitations qui en découlent, ont généralement des d-excess positifs (autour de 10‰), expliquant l'ordonnée à l'origine de 10‰ de la droite des eaux météoriques.

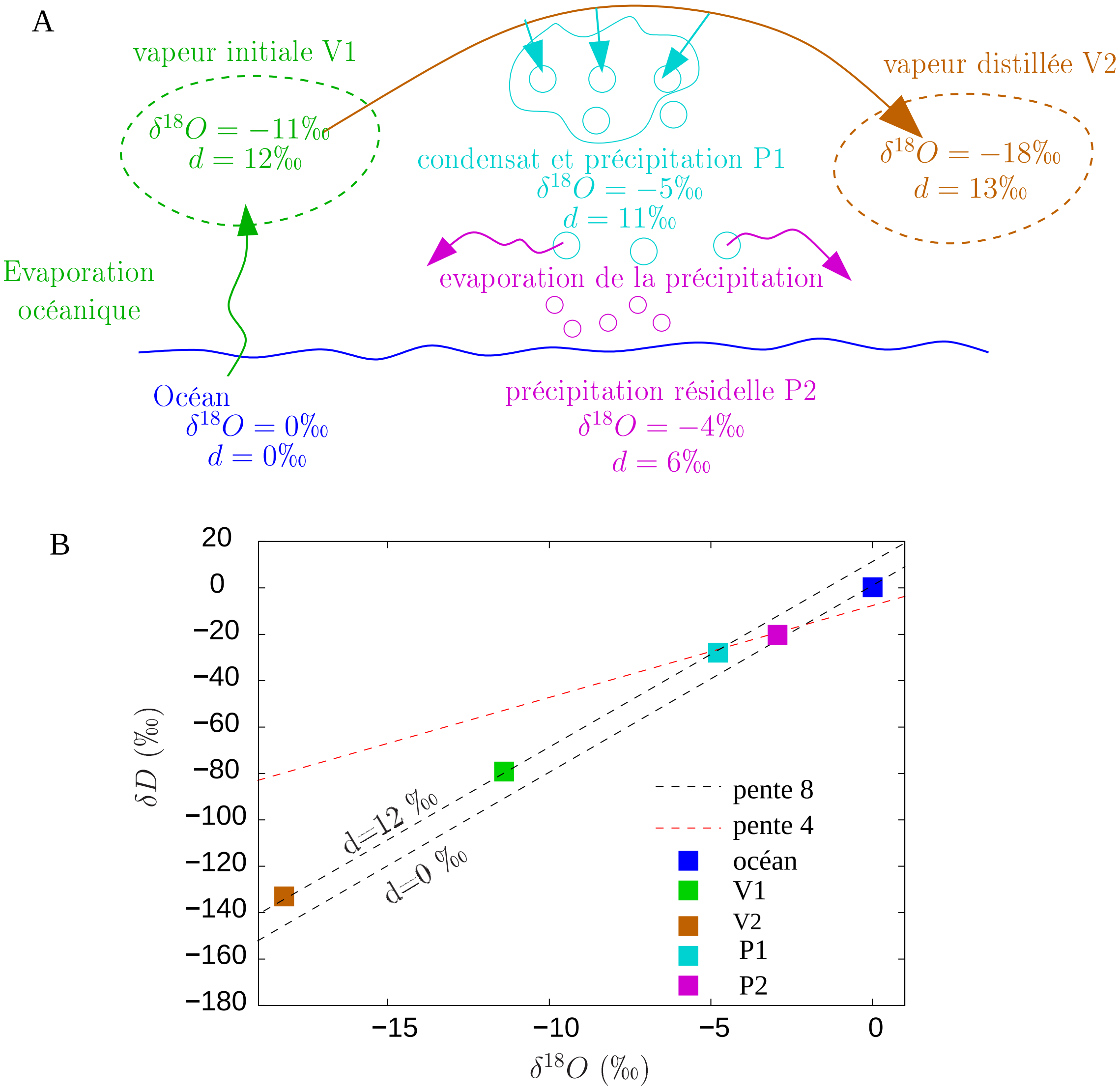

FIG. 1.4 – A: Illustration des variations du d-excess lors de quelques changements de phase au cours du cycle de l'eau, dans un exemple idéalisé. B: illustration de ces variations dans le diagramme $\delta^{18}O$-δD. Dans cet exemple, l'océan s'évapore dans une humidité relative de 70% à 20°C. Cette vapeur accumulée au dessus de l'océan, V1, a un d-excess plus fort que l'océan à cause du fractionnement cinétique lors de l'évaporation. Cette vapeur est ensuite distillée à 50% à 20°C, et donne une vapeur résiduelle V2 et un condensat P1. Cette distillation se fait sans grand changement de d-excess, le long d'une droite de pente environ 8. Le condensat précipite et se réévapore à 5% dans la vapeur V2 avec une humidité relative de 70%. La réévaporation suit une droite de pente environ 4 et donne une précipitation résiduelle de faible d-excess.

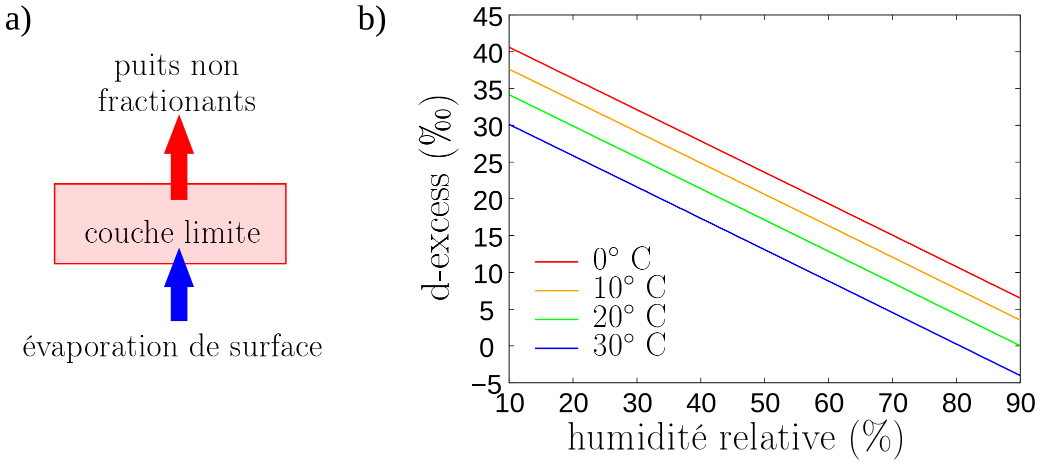

FIG. 1.5 – a) Schéma illustrant les hypothèses faites pour l'équation de fermeture.
b) Le d-excess de la couche limite océanique prédit par l'équation de fermeture, en fonction de l'humidité relative à la surface et pour différentes températures de surface.

Equation de fermeture L'effet du fractionnement cinétique sur la composition isotopique de la vapeur au dessus de l'océan peut être modélisé très simplement par l'équation de fermeture ([Merlivat and Jouzel, 1979]).

On considère une couche limite océanique de composition R_{BL} dans laquelle la seule source de vapeur est l'évaporation de surface, et les puits de vapeurs sont non fractionnants: ex: flux de masse vers le haut (figure 1.5a). A l'état stationnaire, le flux de vapeur entrant par évaporation est égal au flux sortant. De même, la composition du flux entrant par évaporation, R_E est égale à celle du flux sortant non fractionnant, donc de composition R_{BL}. On a donc:

$$R_E = R_{BL}$$

Or la composition du flux d'évaporation de surface est donnée par l'équation de [Craig and Gordon, 1965] (annexe B.3.1):

$$R_E = \frac{1}{\alpha_K} \cdot \frac{R_{oce}/\alpha_{eq} - rh_s \cdot R_{BL}}{1 - rh_s}$$

On a donc:

$$R_{BL} = \frac{R_{oce}}{\alpha_{eq} \cdot (\alpha_K + rh_s \cdot (1 - \alpha_K))} \tag{1.2}$$

L'application de cette formule montre que le d-excess de la couche limite diminue quand l'humidité relative augmente, avec une pente de 0.43‰/%, et augmente avec la température, avec une pente de $0.38‰/K$ (figure 1.5b)

Distribution spatiale annuelle La figure 1.6 montre la distribution spatiale du d-excess dans les précipitations GNIP en moyenne annuelle.

On observe une diminution du d-excess avec la latitude, avec un minimum de d-excess autour de l'océan austral. Ceci est en grande partie lié aux conditions d'évaporation (figure 1.5b), qui sont plus froides et humides dans cette région.

On observe aussi un maximum de d-excess en Méditerranée orientale. Ceci est interprété de nouveau comme l'effet des conditions d'évaporation, dans un air sec et sur une mer chaude.

Enfin, le d-excess augmente à l'intérieur des continents polaires. Le d-excess augmente en effet au cours d'une distillation de Rayleigh, pour deux raisons (annexe C.12):

- variations des coefficients de fractionnement à l'équilibre avec la température. Aux températures plus basses, le rapport $\frac{\alpha_{HDO}-1}{\alpha_{H_2^{18}O}-1}$ devient plus fort.

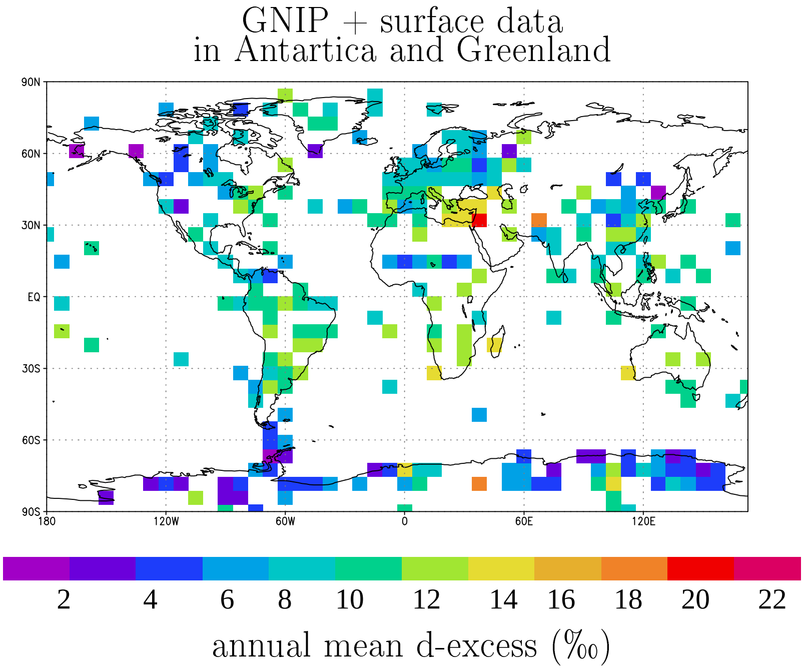

FIG. 1.6 – Distribution spatiale en moyenne annuelle et sur toutes les années disponibles du d-excess dans les précipitations collectées par le réseau GNIP. Les données de neige de surface compilées par [Masson-Delmotte et al., 2008] pour l'Antarctique et [Masson-Delmotte et al., 2005] pour le Groenland ont aussi été rajoutées.

- définition linéaire du d-excess: dans le cas limite où la distillation de Rayleigh épuise totalement les isotopes lourds, $\delta D = \delta^{18}O = -1000$‰, donc $d = 7000$‰. Le d-excess augmente donc mathématiquement quand les δ diminuent.

Pour conclure, la distribution spatiale des δD et des $\delta^{18}O$ est contrôlée au premier ordre par les effets de distillation des masses d'air (temperature, continental, altitude effects), ainsi que l'effet des processus nuageux, en particulier dans les tropiques (amount effect). L'effet de ces processus nuageux sera analysé en détail dans le chapitre I de cette thèse. Le contrôle du d-excess, paramètre de second ordre, est quant à lui plus complexe. En plus d'effets de distillation, il est sensible aux effets cinétiques, notamment lors de l'évaporation de l'eau en surface et de la réévaporation des gouttes de pluies, ainsi que la formation des cristaux de glace.

1.2 Les applications des isotopes stables de l'eau

Nous venons de présenter la distribution spatiale actuelle de la composition isotopique de l'eau, et introduit les principaux processus la contrôlant. Nous présentons maintenant les principaux domaines d'application de la composition isotopique de l'eau.

1.2.1 Applications paléoclimatiques

Aux hautes latitudes

Depuis plus de 50 ans, la composition isotopique des glaces polaires mesurée le long des carottes est utilisée pour reconstituer les variations passées de la température polaire. La figure 1.7a montre la composition isotopique des glaces au cours de 400 derniers milliers d'années à Vostok. Elle montre de fortes variations, avec des cycles glaciaires inter-glaciaires d'amplitudes de l'ordre de 6‰. Nous avons vu que l'appauvrissement des δ quand la latitude augmente est expliqué au premier ordre par la distillation de Rayleigh. Réciproquement, en un endroit donné, plus la température est

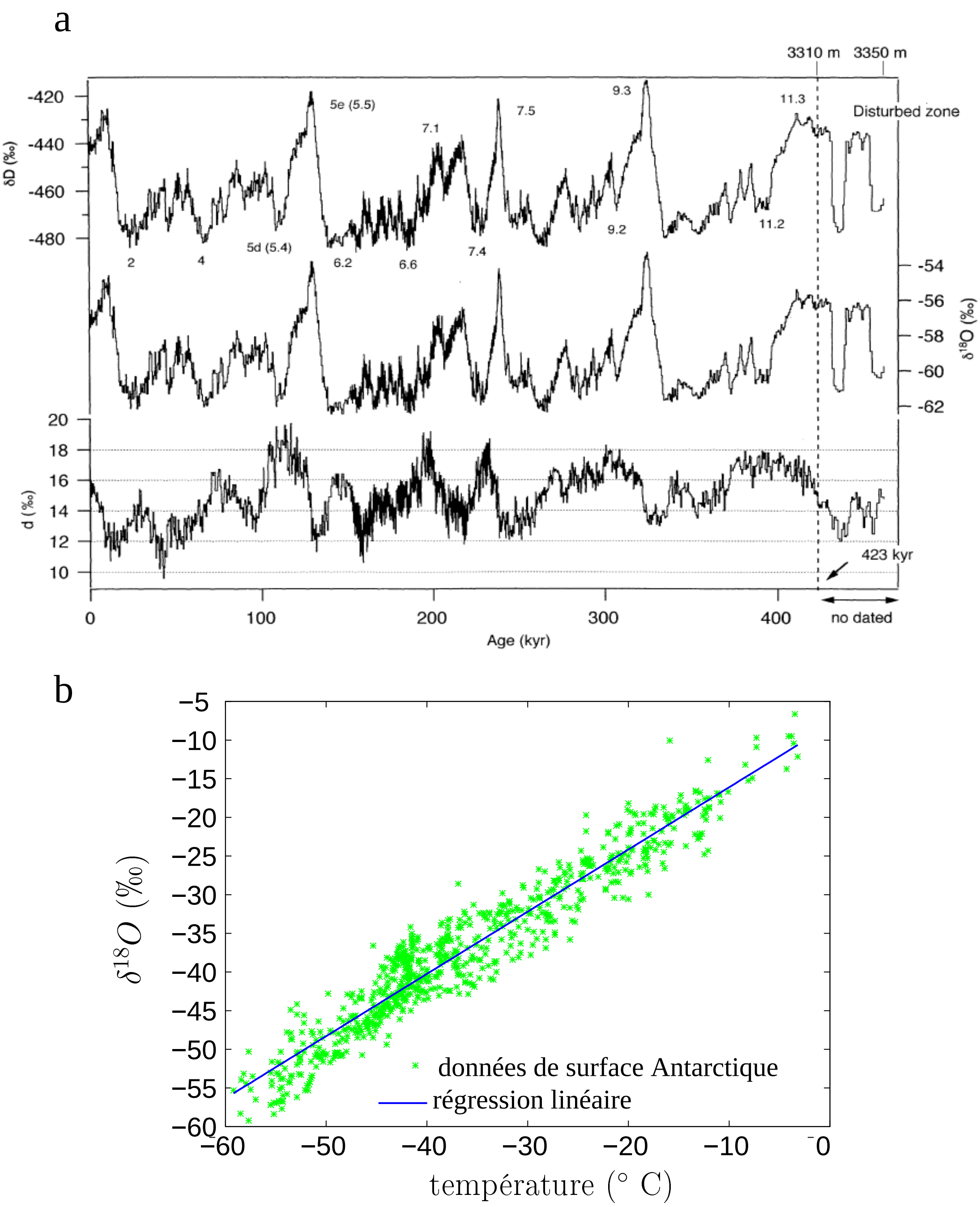

FIG. 1.7 – a) L'évolution du δD, $\delta^{18}O$ et d-excess dans la carotte de Vostok au cours des 400 derniers milliers d'années (figure extraite de [Vimeux et al., 2001]).
b) La pente spatiale δ-température actuelle, d'après les données de neige de surface antarctiques de [Masson-Delmotte et al., 2008]

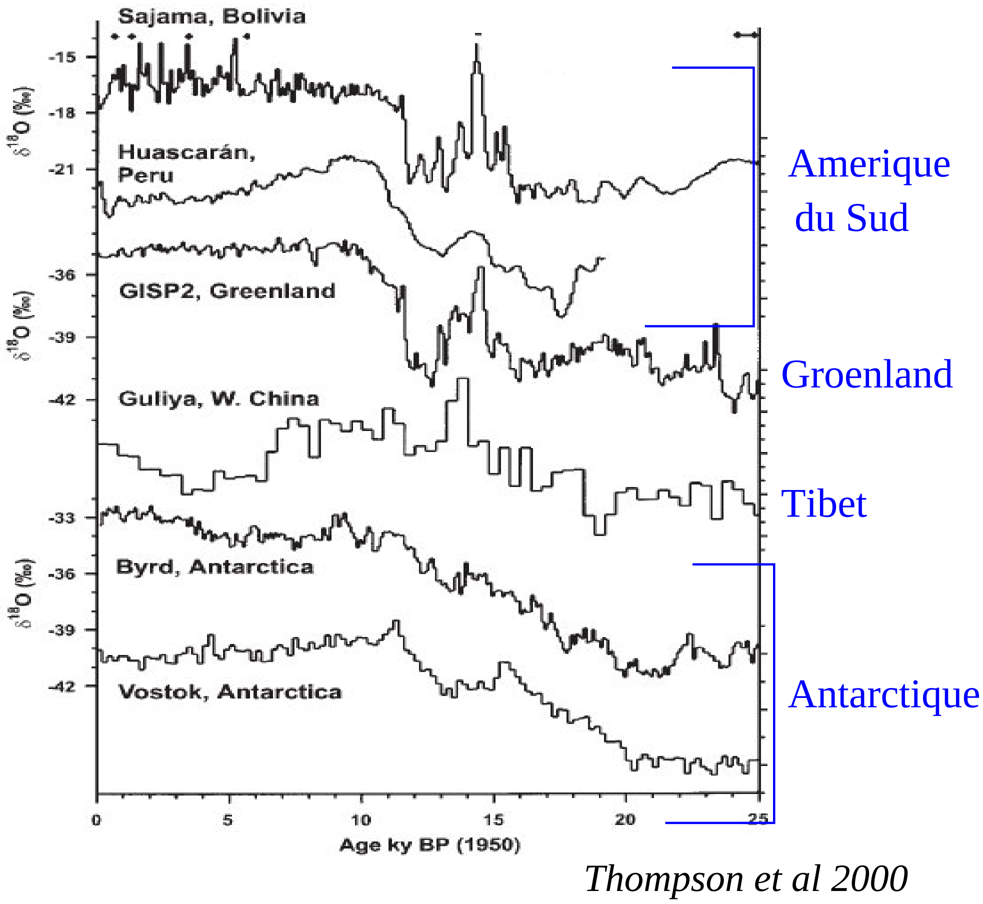

FIG. 1.8 – Evolution du $\delta^{18}O$ des carottes de glaces dans différentes régions du globe au cours des 30 derniers milliers d'années (figure extraite de [Thompson et al., 2000]).

faible, plus la distillation de Rayleigh est aboutie, et donc plus la composition est pauvre. Dans les premières applications paléoclimatiques de la composition isotopique des glaces polaires, la pente temporelle δ-température en un endroit donné est approximée par la pente spatiale observée aux hautes latitudes à l'actuel ([Dansgaard, 1964]), d'environ 0.67‰/K (figure 1.7b). On obtient alors des variations de température glaciaires-interglaciaires de l'ordre de 12K.

Depuis, il a été montré que la pente temporelle δ-température à l'échelle climatique n'était pas tout à fait égale à la pente spatiale observée sur l'actuel. Par exemple, au Groenland, la méthode isotopique sous-estime les variations de températures glaciaire-inter-glaciaires mesurées directement dans les trous de forages d'un facteur 2 ([Jouzel, 1999, Jouzel et al., 2003]). La composition isotopique de la neige n'est en effet pas seulement fonction de la température de la station de forage. Elle dépend aussi de la température de la source de la vapeur ([Boyle, 1997]) ou de la saisonalité des précipitations ([Krinner et al., 1997b]). La pente spatiale en Antarctique semble en revanche plus robuste ([Jouzel, 1999]).

Aux basses latitudes

Plus récemment, la composition isotopique des glaces a aussi été mesurée dans des glaciers tropicaux: Andes ([Thompson et al., 2000, Ramirez et al., 2003]), Tibet ([Thompson et al., 1989]). Les enregistrements isotopiques dans les glaciers tropicaux montrent des variations sur les dernières dizaines de milliers d'années très similaires à celles enregistrées dans les glaces polaires, avec en particulier un enrichissement au cours de la dernière déglaciation (figure 1.8). Ces similitudes avec les hautes latitudes ont conduit [Thompson et al., 2000] à interpréter les variations isotopiques tropicales en terme de température. L'application de la pente δ-température des hautes latitudes aux glaciers tropicaux donnent des températures plus basses d'environ 12°C au dernier maximum glaciaire.

Toutefois, cette interprétation en température a depuis été remise en cause. En effet, nous avons vu que le principal contrôle actuel du δ des précipitations dans les tropiques est la quantité de précipitation (amount effect). Les δ plus faibles au LGM dans les glaciers andins ont ainsi été interprétés comme un climat plus pluvieux le long des trajectoires des masses d'air vers les Andes ([Hoffmann, 2003, Ramirez et al., 2003]). De même, la composition des spéléothèmes (concrétions carbonatées dont la composition est souvent révélatrice de la composition de la précipitation) en région de mousson (Amérique du Sud, Oman, Chine) est interprétée comme des variations d'intensité de la mousson ([Cruz et al., 2005b, Fleitmann et al., 2007, Wang et al., 2008]). Comme la majeure partie des précipitations tropicales provient de la convection atmosphérique (orages), comprendre l'impact de la convection sur la composition isotopiques est une étape importante dans l'interprétation quantitative de telles archives. Ceci fera l'ojet de la partie I de cette thèse.

1.2.2 Applications pour la compréhension du cycle de l'eau actuel

En plus des applications paléo-climatiques, de nombreux travaux ont été faits pour essayer d'utiliser les isotopes pour l'étude du cycle de l'eau actuel. En effet, la composition isotopique d'une eau collectée à un endroit donné dépend de toute l'histoire des changements de phase subie par la masse d'air depuis son lieu d'évaporation jusqu'à son lieu de collection. La composition isotopique de cette eau est donc susceptible d'apporter une information sur les sources et puits d'eau au cours du transport des masses d'air, à condition de bien comprendre les différents contrôles de la composition isotopique. Nous donnons ici quelques exemples de ce type d'applications: quantification du recyclage continental et de ses contributions, hydrologie de surface, transport d'eau dans la tropopause tropicale. Ces applications seront détaillées dans les introductions de chapitres spécifiques de cette thèse.

Quantification du recyclage continental et de ses composantes

Nous avons vu que la composition s'appauvrit le long des trajectoires des masses d'air au-dessus des continents (continental effect), et que cet appauvrissement est d'autant plus faible que le recyclage continental est intense ([Rozanski et al., 1993]). La composition isotopique est donc susceptible de donner des informations sur le taux de recyclage continental. De plus, les isotopes sont susceptibles de donner une information sur la façon dont l'eau est recyclée: évaporation physique du sol nu ou des lacs, ou transpiration par la végétation. En effet, tandis que l'évaporation du sol nu ou des lacs donnent lieu à un fractionnement par rapport à l'eau du sol, ce n'est pas le cas de la transpiration, d'où la possibilité d'évaluer la contribution de ces deux types d'évaporation au recyclage total ([Salati et al., 1979, Gat and Matsui, 1991]). Nous détaillerons ce type d'application dans la partie 8.

Notons de plus que la composition isotopique de l'eau du sol et des feuilles est un contrôle majeur de la composition isotopique du CO_2 émis par la respiration. Les signatures isotopiques contrastées des différents flux de CO_2 à la surface des continents peuvent être utilisée pour quantifier la contributions de la respiration des plantes et du sol au cycle du carbone ([Ciais et al., 1996, Yakir et al., 2000]). La composition isotopique des feuilles est aussi un contrôle majeur de la composition isotopique de l'O_2 émis par photosynthèse. La composition isotopique de l'O_2 dans l'air peut ensuite être utilisée pour estimer la productivité globale d'O_2 par photosynthèse (e.g. [Blunier et al., 2002]) et quantifier la contribution relative des écosystèmes continentaux ou océaniques (e.g. [Bender et al., 1994]). Mais ces domaines ne seront pas abordés au cours de cette thèse et nous nous restreindrons aux formes isotopiques de l'eau.

Hydrologie de surface

Comme l'évaporation directe du sol induit un fractionnement, l'eau du sol est souvent enrichie par rapport à la précipitation. Ce contraste isotopique peut permettre d'évaluer la proportion de l'eau d'une crue d'une rivière venant directement de l'eau du sol et venant de la précipitation nouvelle ([Wels et al., 1991, Millet et al., 1997]).

L'enrichissement du sol par évaporation est surtout fort en surface ([Barnes and Allison, 1988]). Ces différentes compositions isotopiques selon la profondeur peuvent permettre de mieux comprendre les transferts verticaux d'eau dans le sol ([Gazis and Geng, 2004]) et d'estimer la profondeur d'extraction de l'eau par les racines ([Brunel et al., 1997]). Ce type d'application sera aussi discuté dans la partie 8 de cette thèse.

Transport d'eau au travers de la tropopause tropicale

L'humidité dans la basse stratosphère joue un rôle important dans le bilan radiatif terrestre et dans la chimie stratosphérique. Les facteurs contrôlant cette humidité ainsi que ses variations à l'échelle inter-annuelle, ou sa tendance récente à la hausse, sont encore débattus. Il semble que la convection atmosphérique (orages) puisse contribuer au transport d'eau vers la stratosphère en apportant des cristaux de glace dans la haute troposphère. Toutefois, le rôle de la convection dans l'humidification de la basse stratosphère est difficile à quantifier à grande échelle ([Folkins et al., 1999, Gettelman et al., 2002, Khaykin et al., 2009]).

Dans ce contexte, la composition isotopique de l'eau dans la haute troposhère et basse stratotosphère (UT-LS) est susceptible d'apporter une information. En effet, le condensat apporté directement par la convection est plus riche, car il a condensé majoritairement à basse altitude dans les panaches convectifs. Les données isotopiques collectées in situ ([Webster and Heymsfield, 2003]) ou mesurées par satellite ([Moyer et al., 1996, Kuang et al., 2003, Nassar et al., 2007]) dans l'UT-LS montrent des valeurs plus enrichies qu'une distillation de Rayleigh, suggérant un apport de condensat détrainé par la convection. Mais l'interprétation de ces données isotopiques en terme de bilan d'eau est encore loin d'être quantitative.

Cette application des isotopes de l'eau fera l'objet du chapitre 5.

1.3 La modélisation isotopique

Dans la section précédente, nous avons vu que la composition isotopique de l'eau avait de nombreuses applications aussi bien pour l'étude du cycle de l'eau actuel qu'en paléoclimatologie. Toutefois, nous avons aussi vu que de nombreux processus contrôlent la composition isotopique. Déduire une information à partir de la composition isotopique de l'eau nécessite donc tout d'abord de bien comprendre l'effet des différents processus et d'identifier les processus dominants. Pour cela, on a recours à la *modélisation isotopique*, à différents degrés de complexité. La modélisation isotopique permet de calculer la composition isotopique d'une eau en fonction de conditions climatiques ou météorologiques données, et d'évaluer la sensibilité de la composition à des perturbations de ces conditions.

Nous présentons ici différents degrés de complexité dans la modélisation isotopique. Comme une grande partie des variations isotopiques spatiales et temporelles peut être expliquée par la distillation de Rayleigh, la plupart des travaux de modélisation isotopique "simples" reposent sur la distillation de Rayleigh (section 1.3.1). La combinaison complexe des nombreux processus pouvant contrôler la composition isotopique, au contraire, est modélisée par l'implémentation des isotopes dans des modèles de climat (section 1.3.2).

1.3.1 Les modèles de distillation de Rayleigh

Les modèles de distillations de Rayleigh (équation 1.1) sont abondamment utilisés pour interpréter la composition isotopique des glaces polaires. Ils simulent l'évolution de la composition de la vapeur et de la précipitation le long de la trajectoire d'une parcelle vers les pôles. Ils nécessitent en entrée:

- La composition isotopique initiale de la vapeur à la source,
- La température, la pression et l'humidité de la masse d'air à la source et à l'arrivée, ou l'évolution de ces variables au cours de la trajectoire

Composition initiale de la vapeur Dans les premières applications des modèles de distillation de Rayleigh, la composition initiale était prédite par l'équation de fermeture ([Merlivat and Jouzel, 1979], equation 1.2). Toutefois, l'équation de fermeture suppose une couche limite océanique très simple, dans laquelle la seule source de vapeur est l'évaporation de surface. Dans la nature, la couche limite reçoit aussi de la vapeur par advection verticale, latérale, mélange vertical convectif. La composition isotopique peut ainsi être très différente de celle prédite par l'équation de fermeture en cas de forte convection tropicale ([Jouzel and Koster, 1996, Lawrence et al., 2004]). Des travaux plus récents ont donc initialisé leurs distillation par les champs isotopiques simulés par des modèles plus complexes ([Delmotte et al., 2000, Helsen et al., 2006]).

Complexifications de la distillation de Rayleigh Le modèle de distillation de Rayleigh peut être complexifié pour prendre en compte:

- un effet cinétique lors de la formation des cristaux de glace ([Jouzel and Merlivat, 1984])
- la rétention d'une partie du condensat avant de précipiter, la cohabitation de phase liquide et solide dans certains nuages ([Ciais and Jouzel, 1994]: Mixed Cloud Isotopic Model, MCIM),
- une évolution réaliste de la température, pression et humidité de la masse d'air le long de sa trajectoire, diagnostiquée des réanalyses météorologiques ([Helsen et al., 2007]),
- la recharge de la parcelle d'air par évaporation sur les océans le long de sa trajectoire ([Helsen et al., 2007]).
- A l'origine uni-dimensionel, le modèle de distillation de Rayleigh a été introduit dans un modèle global 2D (latitude-longitude) dont la dynamique est dérivée de réanalyses météorologiques ([Yoshimura et al., 2003]).

1.3.2 Les isotopes dans des modèles de climat

Les modèles de climat sont des modèles globaux permettant de simuler les climats actuel ou passés et de prédire le climat futur. Ils sont composés de modèles de différentes composantes du système climatique, couplés: modèles d'atmosphère (modèle de circulation générale atmosphérique, appelé ci-après GCM), d'océan, de surface continentale, de glace de mer. Comme un grand nombre de processus physiques y sont représentés, la simulation des isotopes de l'eau dans ces modèles (ou certaines de leur composantes) est un outil idéal pour étudier les contrôles de la composition isotopique de l'eau. Toutefois, la simulation de la composition isotopique dans ces modèles est parfois limitée par la simulation du climat et du cycle hydrologique par ces modèles. La validation de la représentation du climat et des isotopes permet de définir les régions et les échelles de temps pour lesquelles le GCM isotopique est applicable.

La première implémentation des isotopes de l'eau dans un tel modèle a été effectuée par [Joussaume et al., 1984] dans le GCM du Laboratoire de Météorologie Dynamique (LMD). Puis ont suivi l'implémentation des isotopes dans les GCM GISS ([Jouzel et al., 1987, Schmidt et al., 2007]), ECHAM ([Hoffmann et al., 1998]), MUGCM ([Noone and Simmonds, 2002b]), GENESIS ([Mathieu et al., 2002]), CAM ([Lee et al., 2007]), GSM ([Yoshimura et al., 2008]), HadCM3 ([Tindall et al., 2009]) ainsi que dans le modèle régional REMO: [Sturm et al., 2005]).

Ces études ont permis de mieux comprendre ce qui contrôle la composition isotopique, aussi bien dans le climat actuel aux échelles saisonnières et inter-annuelles que lors de changements climatiques (LGM, Mid-Holocène, changement futurs: [Joussaume and Jouzel, 1993, Jouzel et al., 1994, Jouzel et al., 2000]).

Dans cette thèse nous présentons l'implémentation des isotopes dans le GCM LMDZ4, ainsi que des applications paléo-climatiques en région tropicales (chapitre 6).

1.3.3 Les isotopes dans les modèles hautes résolution

Dans les modèles de climats, les processus d'échelles inférieures au maillage (typiquement quelques centaines de km) sont représentés de manière statistique par le biais de paramétrisations (représentation uni-dimensionelle d'un processus tri-dimensionel). C'est le cas par exemple de la convection atmoshérique. Pour étudier l'effet de processus de fine échelle sur la composition isotopique de l'eau de manière explicite, les isotopes stables de l'eau ont été introduits dans un modèle résolvant les gros tourbillons (Large Eddy Simulations LES). Des simulations haute résolution (375m) ont permis d'étudier le rôle de la convection sur les profils isotopiques dans la tropopause tropicale ([Smith et al., 2006]). Une implémentation des isotopes stables de l'eau dans un modèle résolvant les nuages (Cloud Resolving Model CRM) est aussi en cours (P. Blossey, communication personnelle).

1.4 Objectifs généraux de la thèse

Le principal but de cette thèse est de mieux déterminer les informations que les isotopes de l'eau peuvent apporter sur le cycle de l'eau actuel et sur les climats passés. En particulier:

- Que nous apportent les isotopes sur le fonctionnement des sytèmes convectifs? L'effet de la convection sur l'humidification de la haute troposphère-basse stratosphère? Quelles informations apportent-ils sur les processus hydrologiques sur les surfaces continentales?
- Peuvent-ils aider à mieux contraindre la représentation des processus convectifs et hydrologiques de surface dans les modèles?
- Comment interpréter les variations isotopiques enregistrées dans les archives paléoclimatiques, en particulier tropicales (carottes de glace, spéléothèmes)?

Pour cela, il s'agit tout d'abord de mieux comprendre ce qui contrôle la composition isotopique de l'eau (atmosphérique et précipitation) et ses variations, avec ici une attention plus particulière sur les tropiques.

Pour cela, deux types d'approche sont utilisées au cours de ma thèse: l'analyse de données et la modélisation.

- Analyse de données isotopiques:
  - analyse des données isotopique de pluies collectées au Niger pendant la campagne AMMA, aux échelles intra-saisonnières et saisonnières (chapitre 3) et à l'intérieur des systèmes convectifs (chapitre 4).
  - analyse des données isotopiques dans les précipitations, la vapeur, les rivières, les sols, tiges et feuilles issues de réseaux mondiaux, principalement à des fins de validation des modèles isotopiques: GNIP (Global Network for Isotopes in Precipitation, [Rozanski et al., 1993]), GNIR (Global Network for Isotopes in River, [Vitvar et al., 2007]) et MIBA (Moisture Isotopes in the Biosphere and Atmosphere, [Twining et al., 2006]).
- Modélisation
  - Etude de l'influence de la convection sur la composition isotopique de l'eau à partir de simulations avec un modèle uni-colonne (chapitres 2 et 5).
  - Interprétation des données intra-événement à partir d'un modèle 2D de transport et de microphysique dans une ligne de grains (chapitre 4)
  - Implémentation des isotopes stables de l'eau dans LMDZ (chapitre 6), pour mieux comprendre l'effet des processus grande échelle sur la composition isotopique et déduire des conclusions paléoclimatiques (chapitre 6.4). LMDZ est le modèle de circulation générale (GCM) développé au LMD et la composante atmosphérique du modèle couplé de l'IPSL. Un avantage important de ce modèle est de permettre de zoomer sur certaines régions, ce qui permet de réaliser des simulations régionales jusqu'à 50km de résolution (exemple sur l'Amérique du Sud en annexe G).
  - Implémentation des isotopes stables de l'eau ORCHIDEE (chapitre 8), pour explorer le potentiel des isotopes à étudier des problématiques liées aux surfaces continentales et pour mieux en contraindre la représentation des processus dans les modèles de climat. ORCHIDEE est la composante de surface continentale du modèle couplé de l'IPSL.

Première partie

Les isotopes stables de l'eau et la convection atmosphérique

Introduction de la partie

La composition isotopique des archives tropicales telles que les glaces andines montre des variations importantes à l'échelle décennale et de plusieurs milliers d'années. Mais tandis que le principal contrôle de la composition isotopique dans les tropiques semble la quantité de la précipitation (amount effect) à l'échelle spatiale et saisonnière, l'interprétation paléo-climatique de ces enregistrements isotopiques n'est pas évidente. Nous avons vu que ces enregistrements ont été successivement interprétés en terme de température ([Thompson et al., 2000]) puis en terme de précipitation ([Ramirez et al., 2003, Hoffmann, 2003, Vimeux et al., 2004]). Une bonne compréhension des processus contrôlant la composition isotopique des précipitations dans les tropiques est pour cela nécessaire.

Dans les tropiques, la majeure partie de la précipitation est liée à des processus convectifs. La convection est un ensemble de mécanismes permettant de brasser l'air verticalement, et se matérialise dans l'atmosphère tropicale par des orages, appelés systèmes convectifs (figure .9). Des mouvements verticaux importants y ont lieu:

- ascendances adiabatiques (air de la couche limite montant sans dilution),
- ascendances ou subsidences de mélanges entre les ascendances adiabatiques et l'environnement,
- descentes insaturées, provoquées par le refroidissement de l'air par évaporation des gouttes dans un environnement sous-saturé ([Zipser, 1977, Houze, 1977]).

La convection est associée à de nombreux changements de phases: condensation dans les ascendances, réévaporation de l'eau lors de son détrainement vers l'environnement, réévaporation des gouttes lors de leur chute dans un environnement sous-saturé. On s'attend donc à une forte influence de la convection sur la composition isotopique de l'eau. Le but de ce chapitre est de *mieux comprendre comment ces processus convectifs affectent la composition isotopique de l'eau.*

En retour, si la composition isotopique de l'eau est sensible aux processus convectifs, alors quelle information supplémentaire par rapport aux mesures classiques les isotopes de l'eau peuvent-ils apporter sur la compréhension de ces processus? En particulier, peuvent-ils apporter une information sur les bilans d'eau des systèmes convectifs? Peuvent-ils aider à mieux contraindre la représentation de la convection dans les modèles? Dans les modèles de climat, la convection est représentée sous forme uni-colonne par des *paramétrisations.* Les isotopes peuvent-ils constituer un *test observationnel* additionnel de ces paramétrisations?

Dans les trois premiers chapitres de cette partie, nous nous concentrerons sur les contrôles de la composition isotopique de la précipitation. Pour cela, deux approches complémentaires ont été utilisées:

- modélisation numérique, avec un modèle uni-colonne d'atmosphère tropicale utilisant le schéma de convection d'Emanuel. Ce travail est décrit dans le chapitre 2, basé sur deux articles compagnons: [Bony et al., 2008] et [Risi et al., 2008a].
- analyse de données isotopiques collectées dans les pluies au Niger, à Niamey, en été 2006, pendant la campagne AMMA (Analyse Multi-disciplinaire de la Mousson Africaine). Deux types de données ont été collectés:
  - données à l'événement (chaque échantillon représente la moyenne sur un événement pluvieux) pendant la saison de mousson 2006, pour étudier l'effet de la convection à l'échelle saisonnière, intra-saisonnière et à l'échelle des systèmes individuels. Ce travail est décrit dans le chapitre 3, basé sur l'article [Risi et al., 2008b]

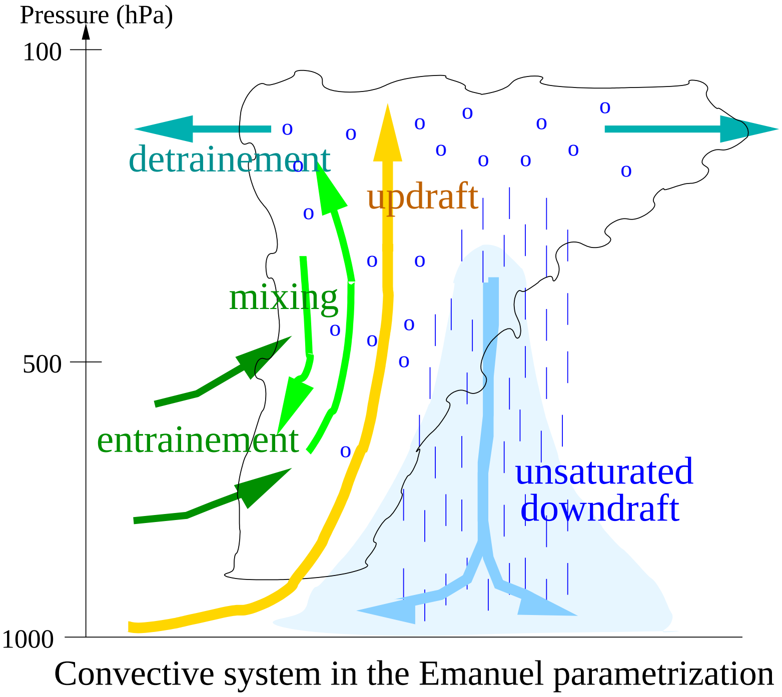

FIG. .9 – Les principales composantes d'un système convectif.

- données intra-événement (échantillons toutes les 5 à 10 minutes pendant les événements), pour étudier l'effet des processus convectifs dans les différentes parties d'un système convectif, et ainsi mieux décortiquer l'effet de la convection. Ce travail est décrit dans le chapitre 4, basé sur l'article [Risi et al., 2010a].

En outre, mieux comprendre l'effet de la convection sur la composition isotopique des précipitations est utile pour la paléoclimatologie, pour mieux comprendre ce que signifient les enregistrements isotopiques tropicaux ([Vimeux et al., 2005]).

D'autre part, mieux comprendre l'effet de la convection sur la composition isotopique de l'eau au niveau de la haute-troposphère-basse stratosphère a des implications pour l'étude des échanges d'eau entre la troposphère et la stratosphère ([Moyer et al., 1996, Webster and Heymsfield, 2003]). Le chapitre 5 est consacré à l'influence de la convection sur les profils isotopiques dans la troposphère et plus particulièrement au niveau de la tropopause. Ce travail s'appuie sur des travaux de modélisation utilisant le schéma de convection d'Emanuel, dans un cadre aussi bien 1D (modèle uni-colonne) que 3D (GCM LMDZ). Une partie de ce travail a été publiée dans [Bony et al., 2008].

Chapitre 2

Etude avec un modèle uni-colonne

Ce chapitre a fait l'objet de deux articles compagnons: [Bony et al., 2008] et [Risi et al., 2008a]. Leur forme publiée est substantiellement différente de leur forme ci-dessous, en particulier l'article [Bony et al., 2008].

2.1 Introduction

2.1.1 Context and questions

Due to differences in mass and symetry, the stable forms of the water molecule ($H_2^{16}O$, HDO, $H_2^{16}O$) undergo an isotopic fractionation during different phases depending on physical conditions. The isotopic composition of water is thus a valuable tracer of the water cycle and past climates. While isotopic records in polar ice cores are widely used for paleotemperature reconstructions in high latitudes ([Jouzel, 2003]), interpretation of isotopic records in tropical ice cores (such as Andean ice cores) is more complex. Tropical ice cores have been interpreted for example in terms of relative humidity ([Broecker, 1997]), local temperature ([Thompson et al., 2000]) or precipitation amount ([Ramirez et al., 2003, Hoffmann et al., 2003]). Studies have revealed a large variety of factors controlling the isotopic composition of tropical precipitation. Local precipitation amount ([Dansgaard, 1964, Rozanski et al., 1993]) and precipitation amount along the air parcels' trajectories ([Vimeux et al., 2005, Vuille et al., 2003]) seem to be major factors controlling the isotopic composition of precipitation. An impact of the storm activity and the degree of organization of convective systems have been suggested by ([Lawrence and Gedzelman, 1996, Gedzelman et al., 2003, Lawrence and Gedzelman, 2003, Lawrence et al., 2004]). [Cole et al., 1999, Vuille et al., 2003] pointed to the importance of the moisture source of the precipitation. Water recycling through land-surface evaporation or vegetation transpiration ([Pierrehumbert, 1999, Gat and Matsui, 1991, McGuffie and Henderson-Sellers, 2004]) or reevaporation of falling precipitation ([Worden et al., 2007]) have also been cited as potentially controlling the composition of precipitation.

In the tropics, most of the precipitation arises from atmospheric convection. Understanding its impact on the isotopic composition of precipitation is thus crucial. The goal of this paper is thus to investigate the influence of convection on the isotopic composition of the precipitation, together with the underlying physical processes.

2.1.2 Approach

Many modeling studies have been carried out to study the processes that control the isotopic distribution and its response to climate. Some have been using simple conceptual or analytic models to focus on some individual process (e.g., [Pierrehumbert, 1999]), while others have been using complex general circulation models (GCMs) to take into account most of the dynamical and physical mechanisms potentially in- volved in the global isotope cycle ([Hoffmann et al., 1998, Noone and Simmonds, 2002b, Mathieu et al., 2002, Schmidt et al., 2005, Tindall et al., 2009]).

In this study, we introduced water stable isotopes into a Single Column Model (SCM) whose physical package has been carefully evaluated against tropical data ([Bony and Emanuel, 2001]).

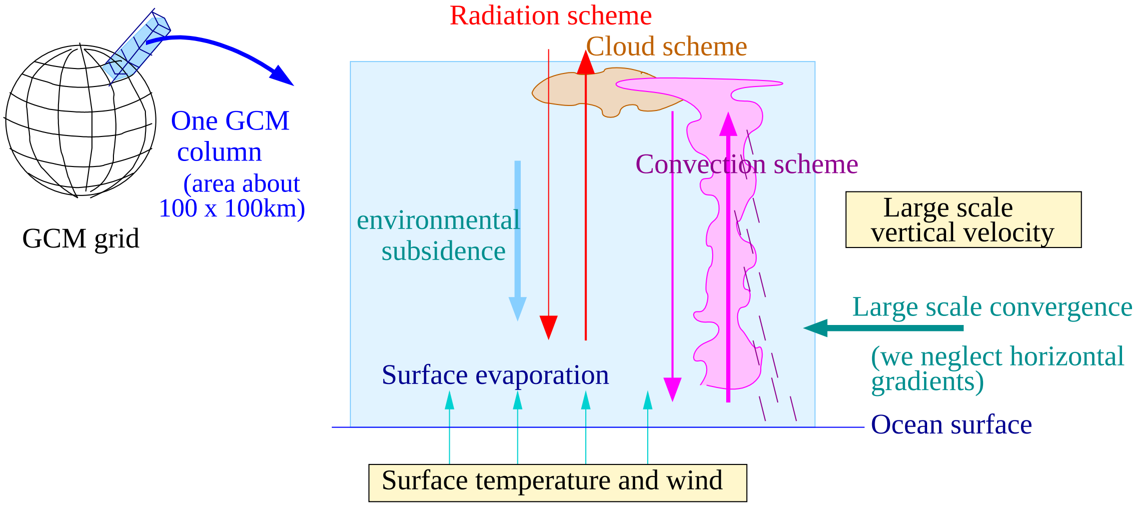

Figure 2.1 – Le modèle uni-colonne: ses composantes, ses conditions aux limites (encadrées en jaune).

The SCM is run to radiative-convective equilibrium ([Xu and Emanuel, 1989]) over ocean. We use a deliberately simple and idealized framework to better isolate and understand key convective processes affecting the isotopic composition of the precipitation.

The SCM includes the Emanuel convection parametrization ([Emanuel, 1991, Emanuel and Zivkovic-Rothman, 1999]), whose advantage is to represent an unsaturated downdraft (downdraft generated by the cooling of air due to the reevaporation of falling precipitation), in which precipitation reevaporation is thought to have a strong impact on the precipitation isotopic composition ([Liebminger et al., 2006]). In section 2.2, we describe the model physics and the representation of isotopic processes. We evaluate the isotopic representation against monthly tropical data in section 2.3. We then present the sensitivity of the isotopic composition of the precipitation to boundary conditions (SST and large-scale circulation, section 2.4) and to model parameters (section 2.5). Section 2.6 focuses on understanding the sensitivity of the isotopic composition of the precipitation to precipitation rate, and explore its time scales in section 2.7. Section 2.8 summarizes and present some perspectives.

2.2 Model description

2.2.1 The single column model framework

The single column model used is the same as described in [Bony and Emanuel, 2001]. It includes bulk formulas for sea surface evaporation, a radiation parametrization ([Fouquart and Bonnel, 1980] and [Morcrette, 1991]), the Emanuel convective parametrization and a statistical cloud scheme coupled to the convection scheme ([Bony and Emanuel, 2001]) (figure 2.1).

Boundary conditions of this model are sea surface temperature (SST), surface wind speed and insolation. In some cases, we also prescribe a large-scale dynamical forcing: large scale convergence or divergence of mass. This large scale circulation is represented by a large scale vertical velocity profile. For example, a large scale ascent is associated with large scale convergence of mass which provides humidity to convection. When advecting air by large scale circulation, horizontal gradients of temperature, humidity and isotopes are neglected. While neglecting temperature gradients is well justified in the tropical atmosphere, neglecting humidity and isotopes gradients is a stronger assumption that will be discussed in section 2.3.2.

Single column simulations are initialized with standard tropical temperature and water vapor profiles, but with no isotopes in the atmosphere. Surface fluxes progressively fill the atmosphere with water and isotopes until steady state is achieved. In the absence of large-scale flow, steady

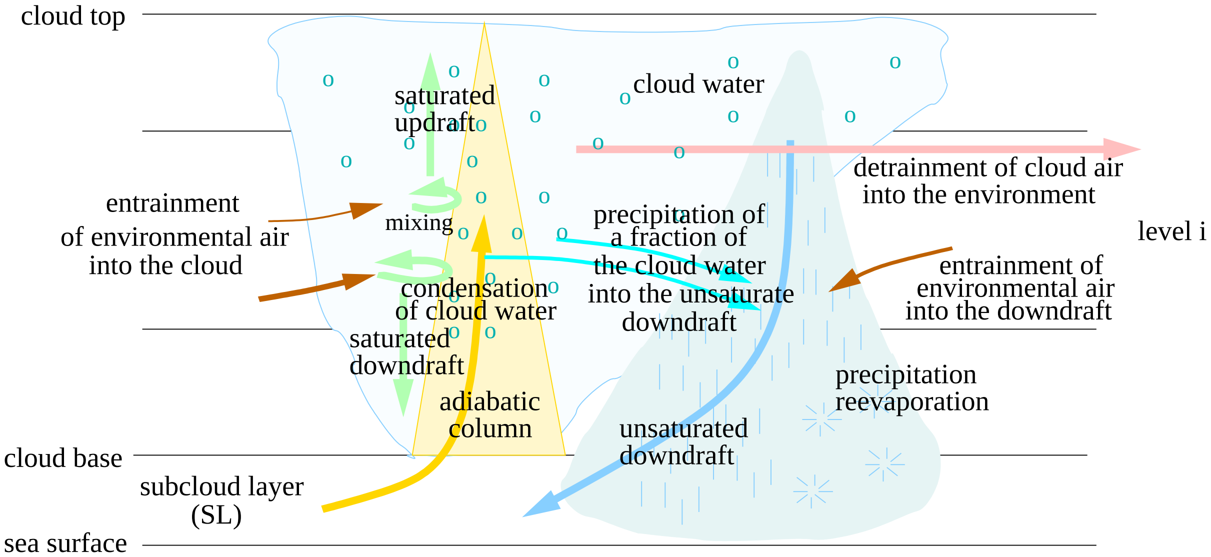

Figure 2.2 – Schematic picture illustrating the representation of convection in the Emanuel scheme.

state is achieved when input of water and isotope from surface evaporation balances output by precipitation, after about 20 days.

2.2.2 Parametrized physics

The Emanuel scheme is a convection parametrization for use in large scale models. The parametrization physics are extensively described in [Emanuel, 1991] and [Emanuel and Zivkovic-Rothman, 1999] and are only briefly summarized here (figure 2.2).

Air parcels from the subcloud layer, called SL, are adiabatically lifted to any level i between cloud base and the level of neutral buoyancy. A fraction $\epsilon_p(i)$ of the total condensate formed between cloud base and level i is converted to precipitation. The remaining adiabatic air is mixed with the environnement (we call “environment” the air outside the convective drafts) in various proportions, forming a spectrum of mixtures. These mixtures ascend or descend according to their buoyancy and may condense and subsequently precipitate more water. The falling precipitation partially or totally reevaporates as it falls through unsaturated atmospheric layers, driving an unsaturated downdraft.

2.2.3 Implementation of water stable isotopes

The implementation of water isotopes in the convective scheme is described in appendix D.1.

2.3 Model evaluation

2.3.1 Methodology

The goal in this section is to ensure that our results concerning the isotopic composition of precipitation are in sufficient agreement with data to be used to investigate the climatic controls on the composition of precipitation. In particular, we focus on the simulation of the amount effect, which is a major feature in the tropics ([Dansgaard, 1964, Rozanski et al., 1993]). A more careful evaluation of water stable isotopes in the convective parametrization will be carried out in a more realistic (3D) framework (section 6.3).

The unidimensional model was run on nine selected tropical maritime GNIP (Global Network for Isotopes in Precipitation) stations (table 2.1). Boundary conditions for the model are monthly observed sea surface temperature (SST) ([Reynolds et al., 2002]), a constant background surface wind speed of 6m/s and a 6-hourly large-scale vertical velocity derived from ERA40 reanalysis

Name	active years	ocean basin	latitude (°)	longitude(°)
Apia	1962-77	Pacific	-13.8	-171.8
Barbados	1961-92	Atlantic	13.0	-59.3
Canton Island	1962-66	Pacific	-2.77	-171.8
Diego Garcia	1962-69	Atlantic	-7.3	72.4
Madang	1968-82	Pacific	-5.2	139.1
Taguac	1962-77	Pacific	13.6	144.8
Truk	1968-77	Pacific	7.5	155.9
Wake Island	1962-76	Pacific	19.3	166.7
Yap	1968-76	Pacific	9.5	138.1

Table 2.1 – Name, location and active years for the different IAEA stations used in this study.

data ([Uppala et al., 2005]). We advect temperature, moisture and isotopes consistently with the vertical velocity profile with the assumption that there are no horizontal gradients. For each station, the SST and large-scale circulation forcings are averaged over a grid box including the station. To ensure the consistency between the local precipitation collected by the GNIP station and the large-scale forcing, only stations whose GNIP seasonal cycle of precipitation amount was representative of that at larger scale were selected.

2.3.2 Results

The model reproduces well the main features of the relationships between precipitation rate and δD or $\delta^{18}O$ in precipitation (hereafter noted δD_p or $\delta^{18}O_p$) (figure 2.3 A). The mean simulated amount effect ($-4.4‰/mm.day$ for δD_p and $-0.6‰/mm.day$ for $\delta^{18}O_p$) compares well with the observations on our 9 tropical stations ($-4.1‰/mm.day$ for δD_p and $-0.55‰/mm.day$ for $\delta^{18}O_p$). Both model and data show similar dispersion (correlation coefficients of -0.80 and -0.87 respectively for the δD-precipitation rate relationship).

The model also captures the observed non-linearity of the amount effect (figure 2.3B). The observed δD_p is more sensitive to precipitation rates in regimes of low precipitation than in regimes of strong precipitation (-7.5$‰ \cdot mm^{-1}$.day around precipitation rates of 2 mm/day and -4 $‰ \cdot mm^{-1}$.day around precipitation rates of 10 mm/day). However, the non-linearity is exagerated in the model: the simulated slopes are slightly overestimated for low precipitation rates (below 3-4 mm/day). Here are some possible explanations for this overestimation:

1. We assume that all raindrops have the same size. At low precipitation rates, however, rain drops are expected to be smaller and some may reevaporate totally without fractionation. In an idealized example, totally evaporating half of the droplets for P=0.8 mm/day leads to a decrease of δD_p by about 10 ‰. If no drops reevaporate totally for $P >$4 mm/day, then the amount effect below 4 mm/day is reduced by about 2.5 ‰/mm.day. Neglecting the spectrum of droplets' size is thus a plausible contributor to our overestimation of the amount effect.

2. In the Emanuel scheme, the fractional area of the unsaturated downdraft σ_d is assumed constant at σ_d=0.05. As another idealized example, if σ_d increased with convective intensity through $\sigma_d = 0.01 \cdot P$, then the amount effect would be reduced by about 1 ‰/mm.day for $P <$4 mm/day. The representation of the unsaturated downdraft is thus another plausible contributor to the bias.

3. Finally, the overestimation of the amount effect for low precipitation rates might also result from the single column framework and neglecting horizontal advections of water isotopes from the surrounding vapor. In a 3D model, regions with high precipitation rates would receive inflow of less depleted water vapor coming from surrounding regions with less intense convection. This hypothesis will be confirmed by 3D simulations in chapter 6.

The model reproduces well the mean d_p values (figure 2.3C) and captures the slight increase in d_p when precipitation rate increases ($0.4‰/mm.day$ for data, $0.5‰/mm.day$ for the model). However, the model partly underestimates the dispersion: correlation between d_p and precipitation rate is 0.39 for the data and 0.55 for the model.

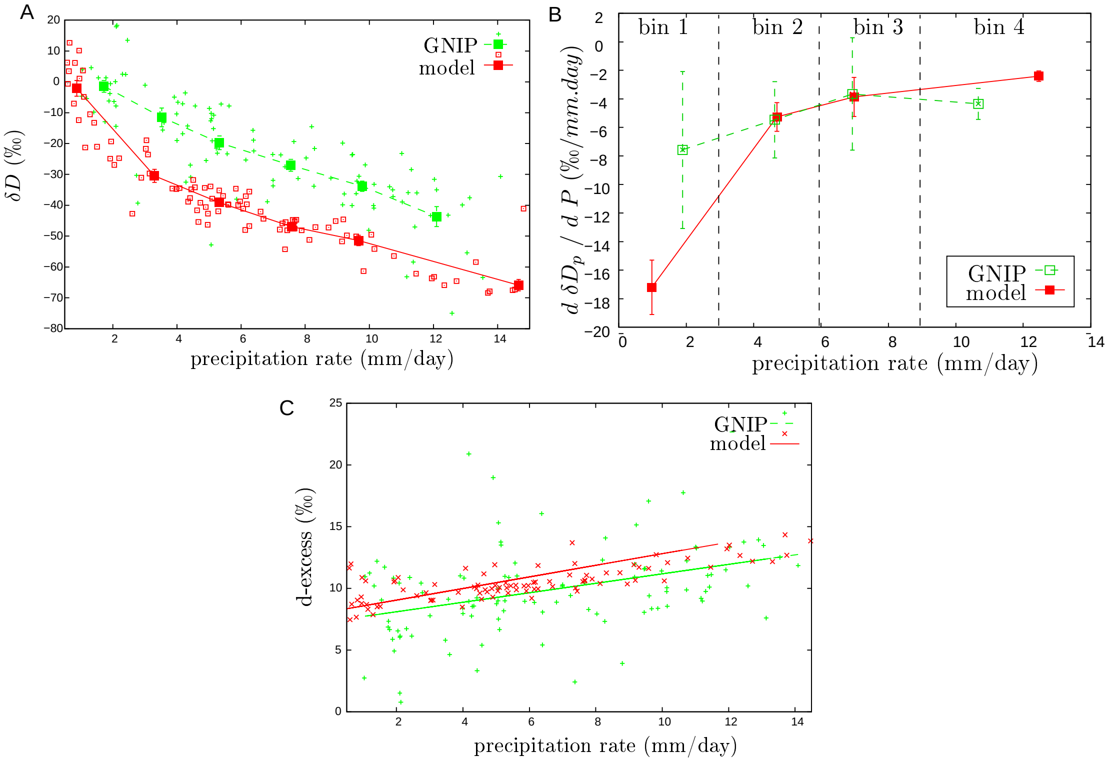

Figure 2.3 – A. Relationship between δD_p and precipitation rate (P) on 9 tropical maritime IAEA stations the GNIP data base (green) and for the single column model (red). Each dot represent one month on each station, while the lines represent an average relationship calculated by averaging these data or results within each of 6 bins. Errorbars represent the δD_p standard deviation in each bin.

B. Slope in the δD_p versus P diagram, $\frac{d\,\delta D_p}{d\,P}$, as a function of P, for model results (red solid line) and GNIP data (green dashed line) from 9 tropical islands. The slope is calculated for each bin of 3mm/day, by performing a linear regression on the points within each bin. The error bars represent the standard deviation of the slope.

C: Relationship between d_p and precipitation rate. The lines represent linear regressions on all data points or model points.

2.4 Sensitivity to boundary conditions

2.4.1 Relative sensitivity to SST versus large-scale circulation

Radiative convective equilibrium simulations were performed up to steady state for various pairs of (SST, ω) values. The SST was varied from 25°C to 30°C and the large-scale vertical velocity from -90hPa/day to 10hPa/day, which are typical variation ranges in the tropics. SST and large-scale vertical velocity, which in nature vary in concert, can thus be studied independantly and their effect on the precipitation composition can be disentangled. An increase in SST increases the surface evaporation flux and therefore the equilibrium precipitation amount (figure 2.4a). A decrease of the large scale vertical velocity ω (expressed in hPa/day) causes an increase of convective fluxes, and therefore of convective activity and precipitation rate (figure 2.4a).

The sensitivity of δD_p to SST is approximately $3‰/K$ ($0.3‰/K$ for $\delta^{18}O_p$) for strong precipitation and lower for lighter precipitation, and cannot explain most of the variability of δD_p in the tropics. The increase in δD_p when the SST increases, for a fixed ω, is explained mostly by 2 reasons:

1. when the SST increases, the evaporation flux from the ocean (and thus the precipitation) is more enriched.
2. when SST increases, the temperature lapse rate decreases, and the fraction of vapor that condensates in updrafts decreases, leading to a reduced depletion of the atmosphere.

The amplitude of δD_p variations when precipitation amount varies are much higher than those when SST varies (figure 2.4b). The sensitivity of δD_p to precipitation rate is between -4‰/mm.day for a precipitation rate of 14mm/day and -8‰/mm.day for a precipitation rate of 4mm/day (respectively -0.5 to -1$‰/mm.day$ for $\delta^{18}O_p$). Hence, at steady state over ocean, the main control on δD_p is precipitation amount, as was already pointed by [Dansgaard, 1964, Rozanski et al., 1993]. The physical processes underlying the amount effect are extensively discussed in section 2.6.3.

Whereas these simulations showed the results of δD_p when SST and ω were varied independently, in nature, those variables vary in concert (black dots over figure 2.4a). On tropical oceans, precipitation amount is mainly controled by large scale atmospheric circulation, which is itself largely controled by the spatial SST distribution. For example, deep convection occurs predominently on warmer waters. Since δD_p is mainly controlled by precipitation amount and precipitation amount increases with regional SST, δD_p is anticorrelated with SST at the spatial scale (black dots on figure 2.4b) as was already noted by [Rozanski et al., 1993]).

2.4.2 Sensitivity to dynamic and thermodynamic changes of precipitation

To better understand the relative influence of SST and large scale circualtion on the isotopic composition of precipitation, we compare the amount effect between simulations in which either only SST, or only large-scale vertical velocity is varied, or in which the large-scale vertical velocity and the sea surface temperature are varied correlatively following a mean relationship ([Bony et al., 2004]). The amount effect simulated by the model when ω only varies (figure 2.5, blue curve) is very close to the one simulated when both the SST and ω vary (figure 2.5, red curve): the mean slope when ω only varies is $-6.3‰ \cdot mm^{-1} \cdot day$, while the mean slope when both SST and ω vary is $-5.3‰ \cdot mm^{-1} \cdot day$. The amount effect is therefore largely explained by ω variations only: assuming that the amount effect is due to ω variations only leads to an error of less than 15% in the mean amount effect.

On the contrary, δD_p increases with increasing precipitation when precipitation variations are caused by SST variations only (figure 2.5, magenta curve): this seems in contradiction with the amount effect. The effect of SST on δD_p overwhelms the impact of the increased precipitation. Note that the temperature dependance of the fractionation coefficients during condensation have very little impact.

This suggests that the amount effect in nature is only observable if precipitation rate variations are associated with ω variations, that is, with variations of large-scale circulation.

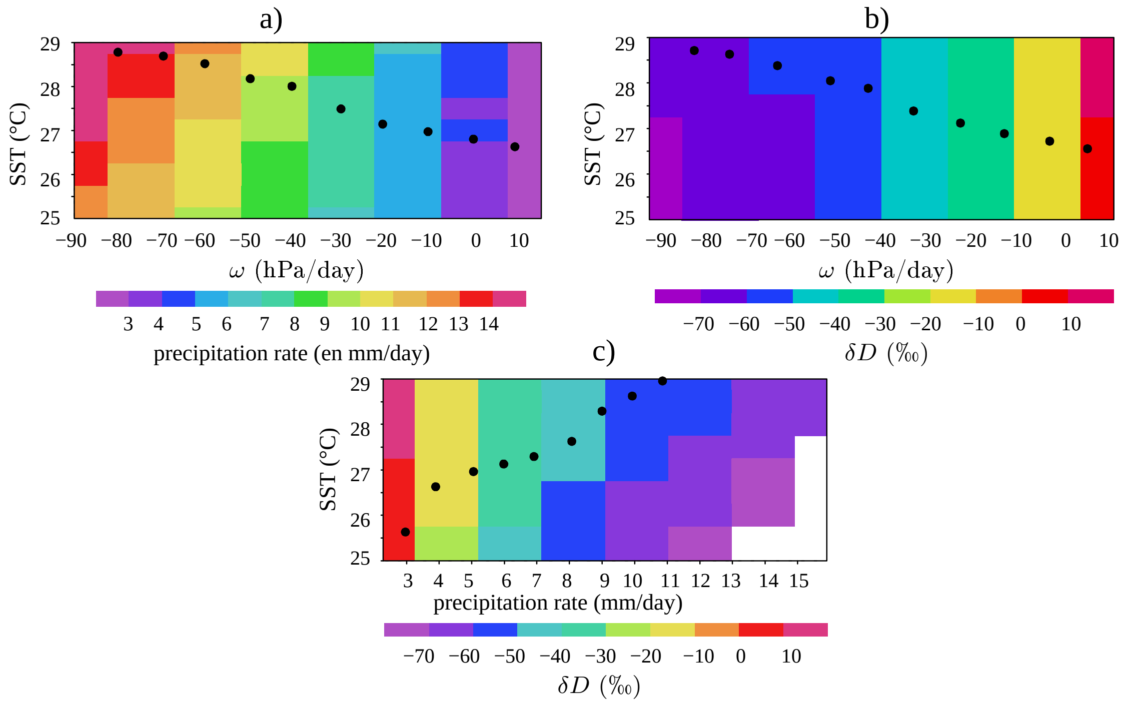

Figure 2.4 – a) precipitation as a function of SST and ω. The black dots show a mean statistical relationship between SST and ω calculated from reanalysis data as in [Bony et al., 2004]. b) Sensitivity of δD_p in a SST-precipitation amount diagram, when SST and ω are varied independently. The black dots show the mean statistical observed relationship between SST and precipitation rate derived from the relationship between SST and ω shown on a) and from the simulated precipitation rates.

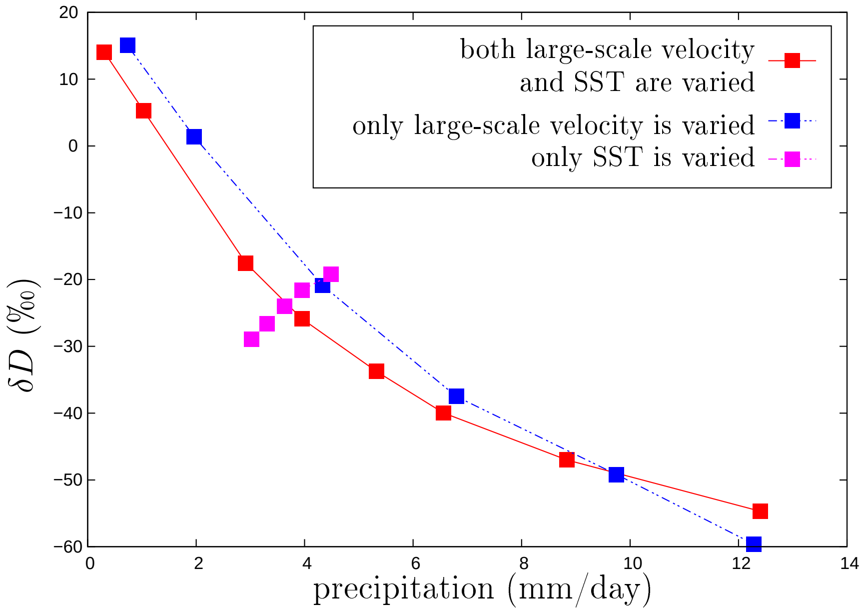

Figure 2.5 – δD_p as a function of precipitation rate in equilibrium simulations in which: (1) both SST and large scale vertical velocity were varied correlatively, following a mean statistical relationship derived from from reanalysis data as in [Bony et al., 2004] (red); (2) only the large scale vertical velocity was varied, and SST was set to 29°C (blue); 3) only SST was varied, and large scale vertical velocity was set to 0hPa/day; The range considered for SST and ω variations are from 20°C to 30°C and -60hPa/day to 30hPa/day respectively.

2.4.3 Sensitivity of d-excess

The same work was performed for precipitation deuterium excess d_p (not shown). d_p also shows little sensitivity to SST (a very slight decrease with SST) but increases as precipitation amount increases by about 0.7‰ per mm/day of rain. The increase of d_p when precipitation increases has two main reasons. First, when precipitation increases, rainfall reevaporation decreases. Since rainfall reevaporation lowers the d_p, d_p is higher in regimes of high precipitation. Secondly, when convective updrafts mass fluxes are greater, the recycling of the subcloud layer vapor by the unsaturated downdraft is higher. Since the vapor at higher altitudes have higher values of d (profiles on figure 5.3b), this recycling increases the d of the subcloud layer feeding the convective system, and thus the whole convective system and the precipitation.

Note that observed d_p decreases when precipitation increases on some tropical continents such as tropical South America (Françoise Vimeux, personnal communication). This observation cannot be explained by our radiative-convective equilibrium model over ocean. Reproducing this observation may require a representation of advection of air masses and/or land surface processes.

2.5 Sensitivity to model parameters

We now examine the sensitivity of the simulated isotopic composition of the precipitation to key model parameters. For this purpose, we perform systematic tests of the radiative-convective equilibrium by perturbing individually the parameters by ±20%. These parameters are mainly related to the representation of cloud physics and microphysics in the convection scheme (table 2.2). These parameters have been calibrated using tropical data from the TOGA-COARE (Tropical Ocean--Global Atmosphere-Coupled Ocean-Atmosphere Response Experiment) campaign ([Emanuel and Zivkovic-Rothman, 1999, Bony and Emanuel, 2001]). Two other parameters, λ and ϕ, are involved in the representation (and the tuning) of kinetic effects associated with kinetic fractionation processes during ice condensation and rain reevaporation, respectively (appendix B.2 and D.2). We vary ϕ between 0 and 0.9, given that it is an extremely empirical parameter.

δD_p is significantly sensitive (compared to measurement accuracy of approximately 0.5‰) to parameters related to unsaturated downdrafts (figure 2.6). In particular, it is sensitive to parameters controlling the reevaporation of raindrops. This highlights the importance of a detailed representation of convective processes for an accurate simulation of water isotopic composition. Conversely, it points to the potential use of isotopes to better understand some convective processes and better constrain their representation in large scale models, as was already discussed in [Schmidt et al., 2005].

The high sensitivity to isotopic parameter ϕ shows that kinetic effects during rain reevaporation are crucial to accurately simulate the isotopic composition of tropical precipitation, in particular in regimes of low precipitation and where the air is dry. Simultaneous measurements of precipitation and vapor compositions would be necessary to better constrain these kinetic effects.

On the other hand, the composition of the precipitation is not very sensitive to parameters controlling the precipitation efficiency, in spite of variations of more than 100‰ in the δD of the environment around 150hPa. This is because the precipitation mainly (more than 90%) originates from condensed water in the adiabatic column, whose composition is bounded between the composition of the subcloud layer vapor (this composition is achieved when all water is condensed) and the composition of the condensate at equilibrium with this subcloud layer vapor (this is the composition of the first drop). Therefore, the composition of the condensate in the adiabatic column is stronly constrained and cannot vary much (red curve on figure 5.4a), whatever happens above the subcloud layer.

2.6 Understanding the amount effect

2.6.1 Context, goals and approach

In the tropics, a major feature of the isotopic composition of precipitation is the observed anticorrelation at the surface between the amount of precipitation and the proportion of heavier isotopes in the precipitation, called the "*amount effect*" ([Dansgaard, 1964]). This robust effect is

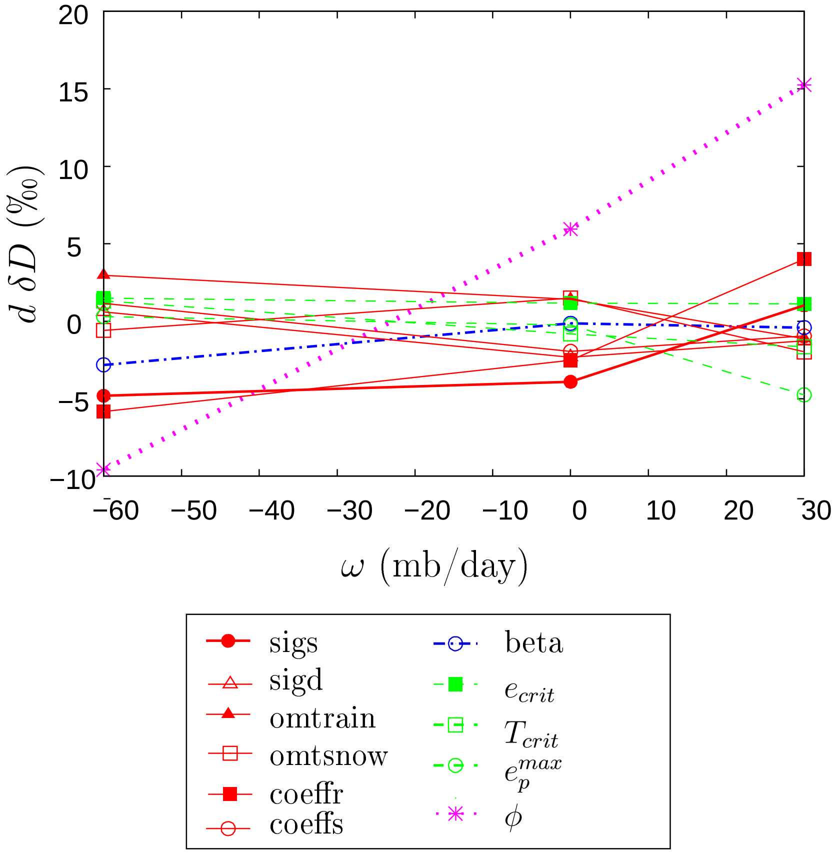

Figure 2.6 – Difference of δD_p between simulations where the convective model parameters (summurized in table 2.2) are changed by ±20%. For parameter ϕ, we show the difference between simulations with $\phi = 0$ and $\phi = 0.9$. Three values of ω are tested (markers): $\omega = -60hPa/day$, $\omega = 0hPa/day$ and $\omega = 30hPa/day$, corresponding respectively to precipitation rates of 12mm/d, 4mm/d and 0.7 mm/d. Results are shown as a function of large scale vertical velocity ω. Simulations were performed with SST=29°C.

parameter name	Physical signification	default value
sigs	fraction of the precipitation falling in unsaturated layers	0.12
omtrain	involved in the calculation of the evaporation rate of falling rain	$50Pa/s$
coeffr	involved in the calculation of the evaporation rate of falling rain	1
omtsnow	involved in the calculation of the evaporation rate of falling snow	$5.5P/s$
coeffs	involved in the calculation of the evaporation rate of falling snow	0.8
sigd	area covered by the unsaturated downdraft (assumed constant)	0.05
beta	impact of the gust wind generated by unsaturated downdrafts on surface fluxes	10
e_{crit}	involved in the calculation of the precipitation efficiency	$0.0011g/kg$
T_{crit}	involved in the calculation of the precipitation efficiency	-55°C
e_p^{max}	maximum value possible for the precipitation efficiency	0.999
λ	tuning kinetic effects during ice condensation	0.002
ϕ	tuning kinetic effects during rain reevaporation	0.9

Table 2.2 – Physical signification of the model parameters used in sensitivity tests.

observed at monthly and annual scales, especially on oceanic conditions such as on tropical islands ([Dansgaard, 1964, Rozanski et al., 1993]).

While work as been done to calibrate the relationship between precipitation amount and the isotopic composition of the precipitation ([Vimeux et al., 2005]) and to interpret the Andean ice cores as informing about past precipitation amounts ([Hoffmann et al., 2003, Ramirez et al., 2003]), the physical processes explaining this observed "amount effect" are still poorly understood and quantified. This is partly because most of the precipitation in the tropics is related to convective processes, whose influence on the isotopic composition is complex. As stated by [Dansgaard, 1964], "*When looking for reasons for the amount effect we are confronted with difficulties, mainly because of the extreme complexity of the isotopic turnover in the processes forming the convective rain*". Little has been done since then to better understand physically and quantitatively how convective processes contribute to the amount effect. The amount effect is often interpreted by the depletion of air parcels by condensation and precipitation. For example, [Vuille et al., 2003] explains: "*As condensation proceeds, the isotopically enriched molecules are preferentially removed, leaving the isotopic composition of the remaining vapor increasingly lighter. The stronger the convective nature of a particular rainfall event, the higher the total amount of precipitation and thus the more depleted the isotopic composition of this rainwater*"). However, [Dansgaard, 1964] cited several other possible reasons for the amount effect: the falling rain gets less reenriched as rainfall gets stronger, through either a lowest reevaporation rate or more efficient diffusive exchanges with the water vapor.

The goal of this section is thus to better understand the physical processes underlying the amount effect, and to quantify their relative importance. To this aim, we perform different radiative-convective equilibrium simulations, differing by their precipitation rates at equilibrium. The precipitation rates are varied between the different simulations by changing the large scale dynamical forcing. We showed that variations of the large-scale dynamical forcing only, with SST variations neglected, leads to an amount effect that is close (within 15%) to the one simulated when both the large scale dynamical forcing and SST variations are considered. For this reason, and for the sake of simplicity of the analysis, we vary the precipitation rate through variations of the large scale dynamical forcing only.

We showed in section 2.3.2 that the simulated amount effect simulated in these idealized simulations (red curve on figure 2.8) is close to the amount effect observed in the GNIP data (green curve on 2.3), with an amount effect of -9 $‰ \cdot mm^{-1} \cdot day$ and -4 $‰ \cdot mm^{-1} \cdot day$ for precipitation rates around 2 mm/day and 7 mm/day respectively.

2.6.2 Methodology to quantify the different contributions to the amount effect

The isotopic composition of the precipitation depends first on the composition of the subcloud layer (hereafter name SL), from which ascending drafts of the convective system originate. The SL represents the first 50hPa (roughly the first 400m) of the model. The composition of the SL depends on the composition of its sources (surface evaporation, vapor from the unsaturated downdraft injected into the SL, subsiding environment, rain reevaporation), and on the relative proportion of these different sources. Then, the composition of the rain depends on the composition of the environment entrained into the convective system, on the fractionation during the condensation in updrafts, and on the fractionation as the rain falls, partially reevaporates and reequilibrates with the surrounding vapor through diffusive exchanges.

To explain the amount effect, we thus quantify the contributions from these different processes. For this purpose, using a methodology detailed in appendix H.1, we split the amount effect (ie the sensitivity of the δD_p to precipitation rate, $\frac{d\,\delta D_p}{d\,P}$) into a sum of contribution from 5 different types of processes, whose physical meanings are illustrated on figure 2.7 and detailed below:

$$\frac{d\,\delta D_p}{d\,P} = \frac{d\,\delta D_{surf}}{d\,P} + c_{ascend} + c_{unsat} + c_{recycling} + c_{env}$$

where:

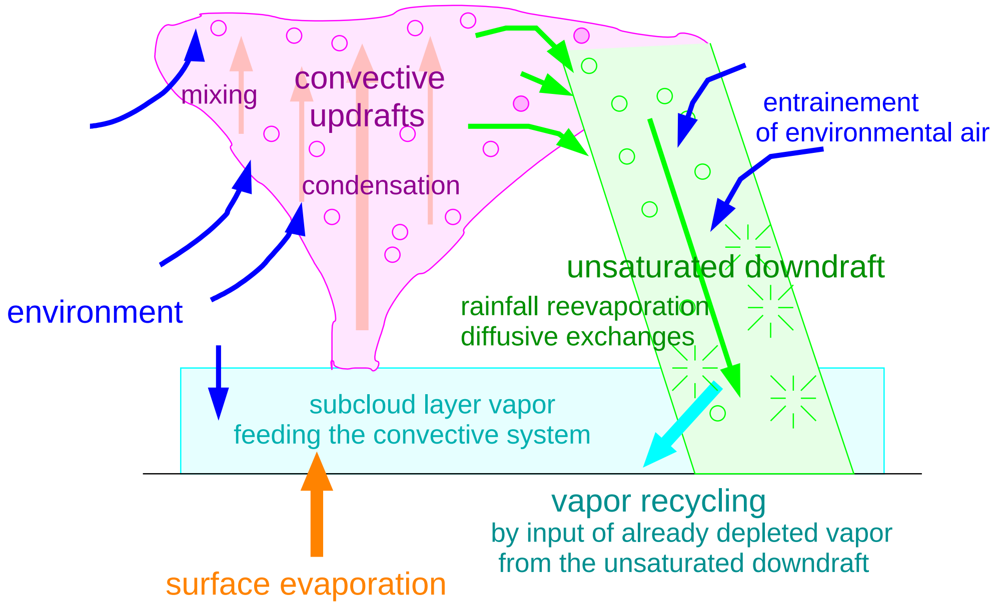

Figure 2.7 – Scheme illustrating how the amount effect is decomposed into a sum of different contributions, each corresponding to one or to an ensemble of physical processes. Each color in the scheme represents a contribution.

1. $\frac{d\,\delta D_{surf}}{d\,P}$ (orange on figure 2.7) represents the effect of the composition of the evaporated water from the ocean surface. This composition directly affects the composition of the SL vapor feeding the convective system and therefore the whole system.

2. c_{ascend} (pink on figure 2.7) represents the effect of processes in convective updrafts affecting the composition of the condensate relatively to the composition of the SL vapor. This depends on the altitude at which the precipitating condensate has formed.

3. c_{unsat} (green on figure 2.7) represents the effect of processes in the unsaturated downdraft. This includes on the one hand a direct effect on the falling precipitation by reevaporation and diffusive exchange with the surrounding vapor. It also includes a more indirect effect on the composition of the SL vapor, through the composition of the unsaturated downdraft vapor that is injected into the SL.

4. $c_{recycling}$ (cyan on figure 2.7) represents the effect of the origin of the SL vapor. More specifically, it represents the effect of the relative fraction of the SL vapor coming from surface evaporation or from already depleted vapor recycled into the SL through the unsaturated downdraft or through environmental subsidence.

5. c_{env} (dark blue on figure 2.7) represents the effect of the composition of the environment entrained into the convective system (into convective updrafts, into unsaturated downdrafts or into the SL by environmental subsidence). The composition of the environment is taken relatively to the composition of the SL vapor. Therefore, this contribution represents the effect of the vertical gradient of isotopic composition in the atmosphere.

2.6.3 Results: interpretation of the amount effect

Figure 2.8 shows $\frac{d\,\delta D_p}{d\,P}$ and its five contributions as a function of the precipitation rate.

- The contribution of condensation and precipitation processes in updrafts (pink on figure 2.8) is approximately constant for all precipitation amounts and contribute for an amount effect of -1 to -2‰ $\cdot\, mm^{-1} \cdot day$. They explain no more than 30% of the amount effect (maximum for highly convective regimes). When convective activity is stronger, the condensate that precipitates forms on average at slightly higher altitude, and is thus more depleted.

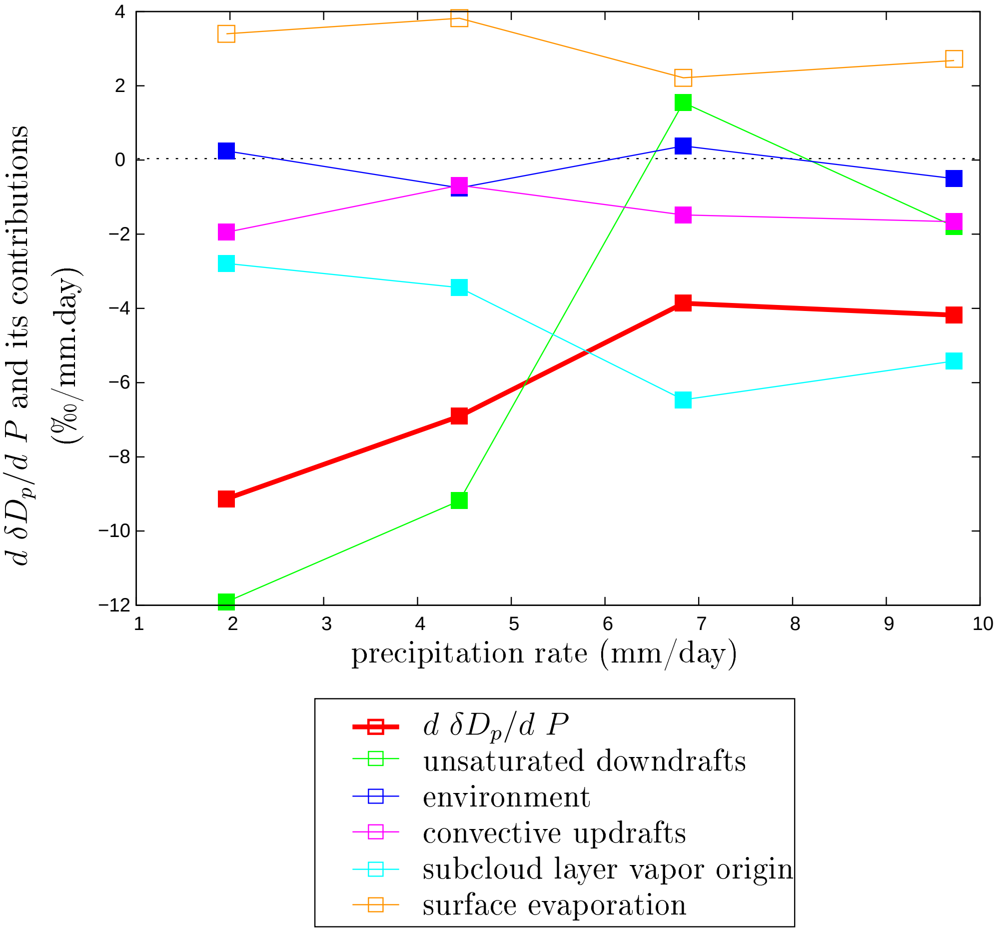

Figure 2.8 – Sensitivity of the δD_p to precipitation rate ($\frac{d\,\delta D_p}{d\,P}$) and its contributions from different processes as a function of precipitation rate. The contributions are the processes in unsaturated downdrafts (green), the isotopic composition of the environment (blue), processes in ascending drafts (magenta), origin of the low-level vapor (cyan) and composition of the surface evaporation flux (orange). The meanings of these contributions are illustrated on figure 2.7 using the same color code and explained in the text.

- The origin of the SL vapor (cyan on figure 2.8) represents an important component of the amount effect, especially for large precipitation rates ($-4‰ \cdot mm^{-1} \cdot day$). Indeed, when convection is more intense, the convective mass fluxes are larger, and unsaturated downdrafts are stronger. Therefore, the contribution of the downdraft mass flux to the balance of the SL vapor increases. The proportion of the SL vapor originating from the unsaturated downdraft is 45% for the strongly convective regime, but only 34% for the light precipitation regime, despite a more efficient reevaporation in the weakly convective regime case (figure 2.9). Since the composition of the unsaturated downdraft vapor is always more depleted than the SL vapor (figure 2.9), the stronger the downdraft mass flux, the more depleted the SL vapor feeding the system. This process is summarized on the left part of figure 2.10. We call this contribution "downdraft recycling" because the downdraft recycles already depleted water into the subcloud layer and therefore into the whole system. The more efficient this recycling, the more depleted the SL vapor and therefore the rain, as pointed by [Lawrence and Gedzelman, 1996] and [Lawrence et al., 2004] to explain highly depleted rains and vapor in organized convective systems.

- Processes in unsaturated downdrafts (green on figure 2.8) provide a major contribution to the amount effect in regimes of low precipitation rates (figure 2.8). Furthermore, they explain the non-linearity of the amount effect. The contribution of the unsaturated downdraft is explained by two effects (figure 2.10), each accounting for about one half of the downdraft contribution:

- First, a direct effect on precipitation. If the precipitation rate increases, the fraction of reevaporated rain (ie the ratio of the precipitation rate on the ground surface to the vertically integrated flux of condensate that precipitates) is decreased, both due to a stronger precipitation rate and a higher relative humidity: the reevaporated fraction is 38% for a rain rate of 9.7mm/day and 73% for a rain rate of 2mm/day. Consequently, the falling precipitation gets less enriched by reevaporation. This evaporative effect was already cited by [Dansgaard, 1964] as a possible reason for the amount effect. The evaporative enrichment is further reduced at higher precipitation rates by the fact that the fractionation during reevaporation is less efficient for high relative humidity (appendix C.3): reevaporation acts as a reverse distillation process (highly fractionating) for low relative humidity and as a diffusive reequilibration for high relative humidity (less fractionating). Note that diffusive exchanges tend to reequilibrate the falling rain with the vapor, so that they enrich the precipitation and deplete the vapor. In regimes of very high precipitation rates, diffusive exchanges dominate. When precipitation rate increases, relative humidity increases, and diffusive exchanges are more effective to reenrich the rain. This explains the slightly positive contribution of the unsaturated downdrafts at high precipitation rates.

- Second, an indirect effect on the SL vapor. When the precipitation rate increases, the fraction of the reevaporated rain f_{revap} decreases, because the relative humidity increases. Because f_{revap} decreases, the composition of the vapor evaporating from the rain is more depleted (indeed, the composition of the vapor evaporating from the rain is generally more depleted than the rain, but tends toward that of the rain as f_{revap} tends toward 1; the evaporating vapor is thus richer when f_{revap} increases, and more depleted when f_{revap} decreases). The vapor in the unsaturated downdraft, which originates partly from the rain reevaporation, is thus more depleted for higher precipitation rates (figure 2.9). Besides, as the relative humidity increases, diffusive exchanges become more efficient. As already pointed by [Dansgaard, 1964] and [Lawrence and Gedzelman, 1996] and explained above, diffusive exchanges deplete the vapor. The vapor thus gets more depleted when the relative humidity is higher. This diffusive effect was already cited by [Dansgaard, 1964] as another possible reason for the amount effect.

Note that for precipitation rates lower than 4mm/day, the model overestimates the amount effect (as was shown in section 2.3.1). Downdrafts processes in the model might be responsible for this overestimation, so that their contribution for very low precipitation rates might be overestimated and shoud be taken with caution.

- the contribution of the isotopic vertical gradient in the environment (dark blue on figure 2.8) is small. This is because in equilibrium simulations, variations in the large-scale dynamical forcing do not modify much the isotopic gradient in the environment.
- The contribution of ocean evaporation (orange on figure 2.8) has a sign opposite to the amount effect: the larger the precipitation amount, the more depleted the vapor at low levels, and the more enriched the evaporation flux. For example, for a strongly convective regime (precipitation rate of about 9.7mm/day), δD_{surf} is 5 ‰ while for a light rain regime (2mm/day), δD_{surf} is of -53 ‰ (figure 2.9). Ocean evaporation thus acts to reduce the amount effect.

To summarize, this quantitative analysis of the amount effect shows that the amount effect is not a simple effect interpretable only by the depletion of an air mass as condensation proceeds. It is rather a sum of contributions from different processes. The two main processes are (1) the recycling of the SL vapor by injection of depleted vapor through convective fluxes into the SL, and (2) the reevaporation and diffusive processes affecting the rain and its surrounding vapor as the rain falls. The first process contributes the most to the amount effect in regimes of weak precipitation, while the second is predominant in regimes of strong precipitation. The importance of the reevaporative processes highlights the importance of a detailed representation of such convective processes for an accurate simulation of the precipitation isotopic composition.

The robustness of the observed amount effect at monthly scale might be explained by the fact that the main processes involved (SL recycling and reevaporative processes) all act together to contribute to the amount effect.

Surprisingly, condensation processes, often believed to be the main reason for the amount effect, have a relatively small contribution. Such a little impact might be dependent on the representation of convective updrafts in the parametrization. In the model, precipitation comes mainly from adiabatic updrafts that originate from the SL and ascend sufficiently rapidly to conserve all the condensate during their ascent. The condensation in adiabatic updrafts thus occurs as in a closed system. Therefore, the composition of the condensate is strongly constrained between (1) at the upper bound, the composition of a condensate in equilibrium with the SL vapor, and (2) at the lower bound, the composition of the SL vapor. Besides, the altitude of the cloud top in the Emanuel scheme does not vary much with convective activity, hence small variations in the altitude of condensation. Although the quantitative value of the condensation contribution is linked to the representation of convective updrafts in the Emanuel scheme, our results suggest that such processes are not required to explain the largest part of the amount effect.

The recycling of the SL vapor, which is one of the main contributions, includes the proportion of vapor originating from surface evaporation, environmental subsidence or unsaturated downdrafts. In our single column framework, this does not include horizontal advection of air masses of different origins, which could also modulate the isotopic composition. [Yoshimura et al., 2003], [Cole et al., 1999] and [Vuille et al., 2003] underlined the importance of the advection of moisture of different isotopic signatures in controlling the isotopic composition of the rain. Neglecting large scale horizontal advections in our model might explain why we predict over-depleted precipitation compared to observations in regimes of strong precipitation. However, our study suggests that the horizontal advection of air masses of different isotopic compositions is not required to explain the amount effect, which appears as a robust feature of convective atmospheres.

2.6.4 Additional note

Note that in this study, the effect of condensation process has been over-estimated. We have assumed that δD_p is the results of contributions that can be summed up linearly. However, the isotopic composition of the condensate δD_{dtr} is at least partly forgotten as the rain reequilibrates with the vapor as it falls (chapter 4, [Risi et al., 2010a]). For example, if the condensate forms higher in altitude, the condensate is more depleted: $\delta D_{dtr} - \delta D_{SL}$ is lower (with δD_{SL} the composition of the sub-cloud layer, H.1.1), but as the rain reequilibrates with the vapor, δD_p of the final rain becomes similar to the case in which the condensate had formed lower in altitude. Quantifying the contribution of condensation effects by $\delta D_{dtr} - \delta D_{vSL}$ thus yields an upper bound of the condensation effect, corresponding to a case without rain drop equilibration.

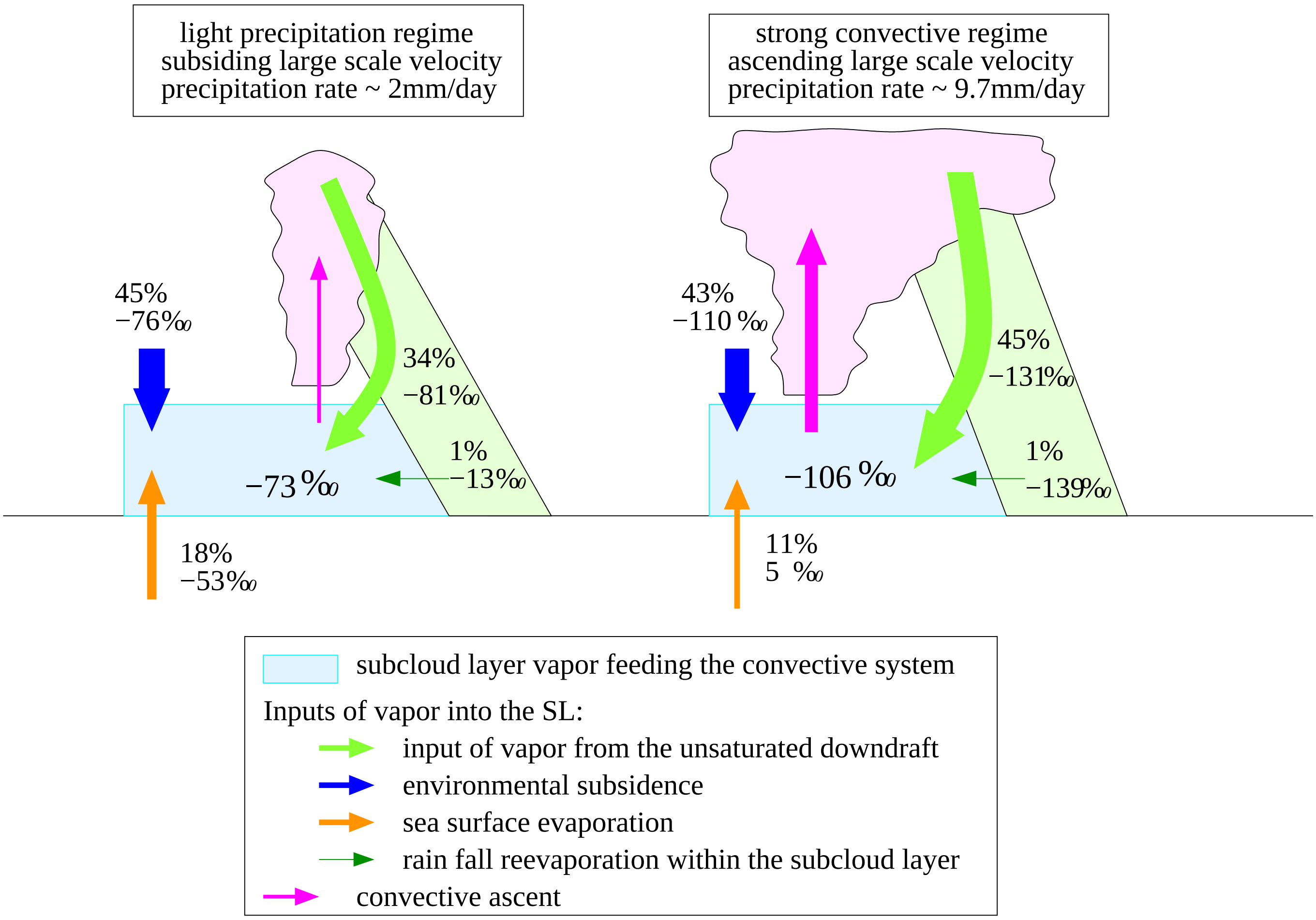

Figure 2.9 – Illustration of what controls the isotopic composition of the water vapor in the subcloud layer. The water mass fluxes from different sources are illustrated as colored arrows: sea surface evaporation (orange), unsaturated downdraft (light green), subsiding environment (dark blue) and reevaporation of rain (dark green). The proportion of the total water input from each flux into the subcloud layer (in %), as well as the δD composition of the incoming vapor (in ‰), are indicated as numbers next to each arrows, for two different regimes: on the left, a subsiding regime with light precipitation (simulated with $\omega = 20 hPa/day$); on the right, a convective regime with strong precipitation (simulated with $\omega = -60 hPa/day$). We omit the input of vapor from large-scale ascent because it does not change the isotopic composition of the SL vapor since we neglect horizontal isotopic gradients.

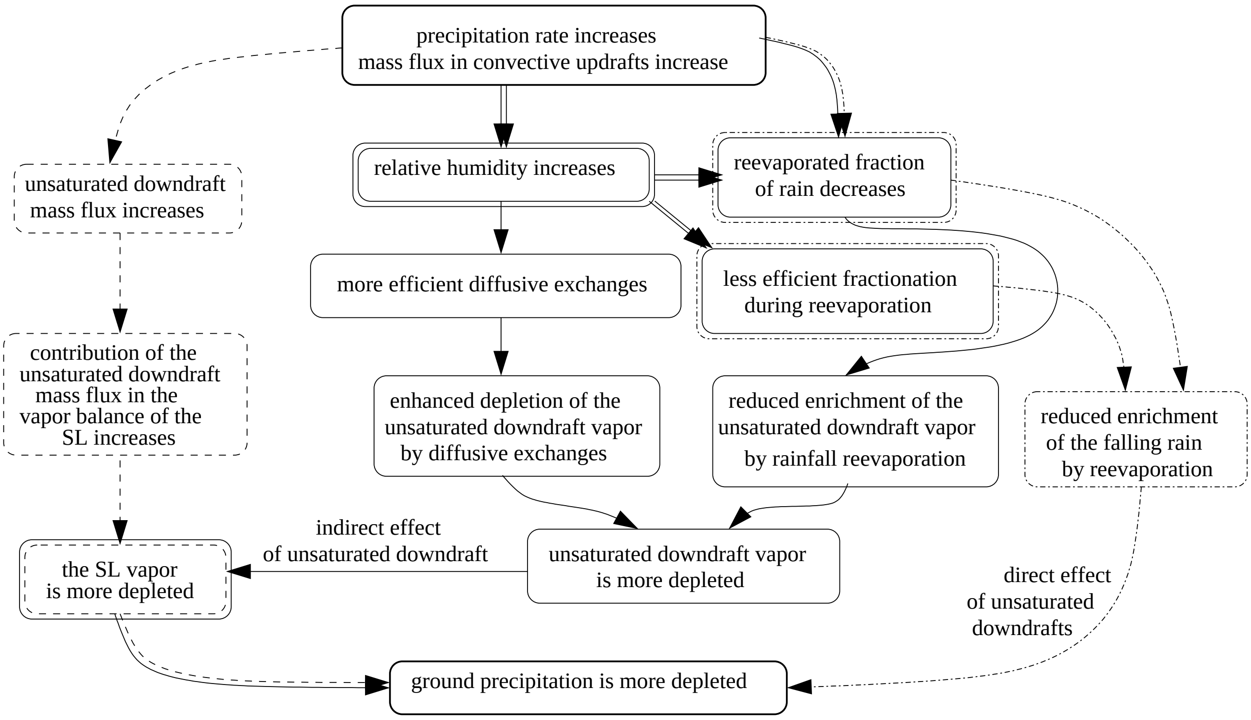

Figure 2.10 – Summary of the main processes that explain the amount effect: subcloud layer vapor recycling (dashed, left part of the figure) and processes during the reevaporation of the rain: (1) direct effect on the precipitation composition (dashed-dotted, right part of the figure), and (2) effect on the composition of the vapor in the unsaturated downdraft (solid, middle part of the figure).

The conclusion of the article is unchanged, except that the condensation has in reality an even smaller effect.

2.7 The time scales of the amount effect

2.7.1 Goals and approach

So far, we have studied the amount effect through equilibrium simulations. This represents large spatial (the scale of a GCM grid) and temporal scales (monthly scales or longer). Although the amount effect seems to be a robust feature of the tropical atmosphere at these scales, some studies showed no amount effect at the event scale ([Vimeux et al., 2005]). The question thus arises as to what are the characteristic time scales of the amount effect, and to what extent the above interpretation of the amount effect applies to shorter time scales.

To answer these questions, we performed a simulation of the TOGA COARE campaign. The TOGA-COARE campaign was conducted from November 1992 to February 1993 over the western Pacific warm pool. This region of high SST (29.4°C on average during the 4 months) is characterized by a strong convective activity. This simulation is chosen because (1) the single column model and its physical package have been carefully evaluated and optimized on their water vapor prediction for this simulation ([Emanuel and Zivkovic-Rothman, 1999, Bony and Emanuel, 2001]), and (2) convective activity during this campaign featured a pronounced intra-seasonnal variability ([Bony and Emanuel, 2001]). The SCM was forced by observed SST and 6-hourly large scale advections of heat and moisture ([Bony and Emanuel, 2001, Bony et al., 2008]).

2.7.2 Factors controlling δD_p depending on time scale

The evolution of the precipitation rate and the δD_p are shown in figure 2.11. The precipitation rate exhibits two prominent time scales of variability (figure 2.12, black dashed lines): 10-15 days (related to Kelvin waves) and 30-40 days (related to tropical intra-seasonnal oscillations). δD_p exhibits similar time scales of variability, except that variability at scales smaller than a few days is reduced (figure 2.12, red lines).

To analyze what explains the amount effect at different time scales, the decomposition of δD_p presented in section 2.6.3 is applied at each time step to the TOGA COARE simulation (appendix H.1.4). We check that the sum of all our contributions closely matches the original δD_p signal (figure 2.11): the mean difference between the sum of all our contributions (green curve on figure 2.11) and the simulated δD (black curve on figure 2.11) is approximately 1.5‰, which is small compared to the standard deviation of the δD signal of more than 100‰. The spectral analysis of the different contributions to δD_p is shown by colored lines on figure 2.12. The relative importance of the different processes to δD_p variations at different time scales are quite similar to the one predicted at equilibrium. At all time scales, the δD_p variations are largely due to reevaporation processes, and, to a lesser extent, to surface evaporation and SL recycling. The contribution of processes in ascending drafts is small. The effect of the composition of the environment is small, but higher than predicted at steady state. This might be because the composition of the free troposphere in this simulation shows larger and less vertically uniform variations than at equilibrium ([Bony et al., 2008])

In brief, over tropical ocean at time scales ranging from a few days to a month, the modulation of δD_p with time is likely to reveal mostly the effect of the modulation of rain reevaporation and of the unsaturated downdraft mass flux. The effect the advection of air masses with different isotopic composition could also be significant ([Yoshimura et al., 2003]) and would reduce the amplitude of δD_p variations.

2.7.3 At which time scale is the amount effect observable?

At which periodicity of isotopic sampling is the amount effect observable? Figure 2.13a shows the correlation between the average of precipitation $\bar{P}$ over the τ_m previous days ($\bar{P} = \int_{t-\tau_m}^{t} P(t) \cdot dt$) and the precipitation-weighted average of δD_p over the τ_m previous days ($\delta \bar{D}_p = \frac{\int_{t-\tau_m}^{t} \delta D_p(t) \cdot P(t) \cdot dt}{\int_{t-\tau_m}^{t} P(t) \cdot dt}$), as a function of the sampling period τ_m. The amount effect becomes optimally observable at time scales higher than about 10 days. At the daily scale, the precipitation amount explains less than half of the isotopic variance (r<0.7). This is consistent with studies observing the amount effect at interannual ([Rozanski et al., 1993]), monthly ([Dansgaard, 1964, Rozanski et al., 1993]) and intra-seasonal ([Sturm et al., 2007b]) time scales, but seldom at the event time scale ([Vimeux et al., 2005]). $\delta \bar{D}_p$ is therefore an indicator of low frequency variations in convective activity.

2.7.4 Characteristic time scale of the amount effect

To investigate the time scales of the amount effect, we calculate the correlation between $\delta D_p(t)$ (each time t corresponds to a 6-hourly average) and the average of the precipitation over the τ_m previous days ($\bar{P}$). The anticorrelation is maximum at a time scale of τ_m^{max}=4 days (red curve on figure 2.13 b). This means that event-scale δD_p (which is roughly represented by the 6-hourly averages) does not depend on the event precipitation rate, in agreement with event-scale isotopic observations ([Vimeux et al., 2005]). Event-scale δD_p appears more related to the convective activity (here measured by precipitation rate P) that occured during the τ_m^{max} previous days (here 4 days) than to the instantaneaous convective activity. The isotopic composition of precipitation is thus an integrator of past convective activity. One reason for this is that δD_p strongly depends on the isotopic composition of the SL vapor, whose reaction to convection is slower than convective activity owing to its dependence on large scale subsidence and surface evaporation.

The "memory" in the response of δD_p to convective activity can be understood through a simple relaxation equation of the form:

$$\frac{d\delta D_p}{dt}(t) = S \cdot P(t) - \frac{\delta D_p}{T} \tag{2.1}$$

where the first term represents the cumulative effect of convection on δD_p and the second term is a relaxation with a time constant T. Note that this equation is unchanged if several (n) time scales of relaxation (T_i) are involved (for example, in nature, reevaporation in convective downdrafts varies very quickly at the convective time scale, whereas the isotopic composition of the SL evolves more slowly): in this case, $\frac{1}{T} = \sum_{i=1}^{n} \frac{1}{T_i}$. The maximum anticorrelation in the TOGA COARE simulation, τ_m^{max}, is best predicted for T=3days (green curve on figure 2.13 b). The time constant τ_m^{max} depends not only on T, but also on the time scales of convective variability. As an idealized example, for sinusoidal variations of precipitation rate of period τ_p, the anticorrelation between δD_p and the average precipitation would be maximum for $\tau_m^{max} = \frac{\tau_P}{\pi} \cdot atan(\frac{2\pi T}{\tau_P})$ (appendix H.2). Therefore, δD_p integrates temporally past convective activity all the more as convection varies at lower frequency.

T represents the residence time of the water reservoir whose composition affects the composition of the precipitation. In the model, T is a combination of the residence time of water in the subcloud layer (<1 day) and that of the whole troposphere (of the order of 10 days), both reservoirs influencing the isotopic composition of the precipitation. Over the continents, T could in addition be related to the residence time in continental reservoirs such as soil moisture. The time constant T, which could be inferred from event-scale isotopic measurements (by optimizing the prediction of τ_m^{max} through equation 2.1 for example), could thus yield some information about the time constant of the water recycling within atmospheric or continental water reservoirs.

Note that in this study, we considered the local correlation between the isotopic composition of precipitation and the precipitation rate. Cases in which the isotopic composition is sensitive to convection upstream of air mass trajectories (e.g. in the Andes: [Vimeux et al., 2005]) are beyond the scope of this paper. However, we anticipate that the property of the isotopic composition to integrate convective activity over the previous days still hold in these cases ([Sturm et al., 2007b]).

2.8 Summary and perspectives

2.8.1 Summary

Water stable isotopes have been implemented in the Emanuel convection parametrization. This parametrization was included in a single column model (SCM) optimized in its prediction of humid-

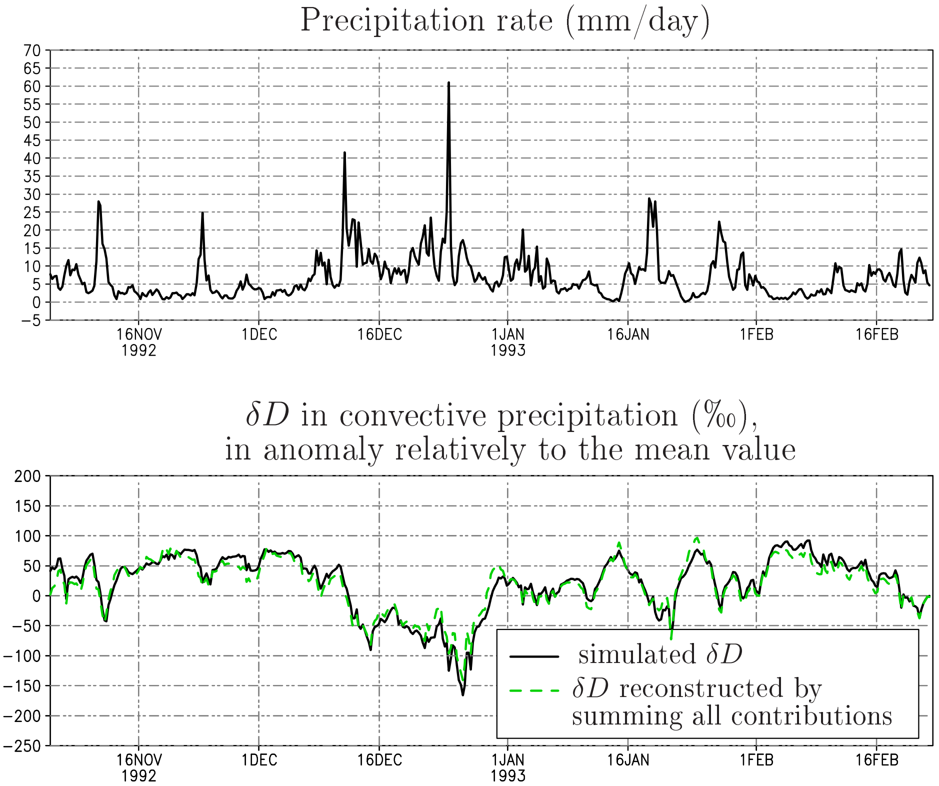

Figure 2.11 – Temporal evolution of the precipitation rate and the δD in the convective precipitation during the TOGA-COARE simulation (black solid curves). δD values are given relatively to the mean δD values. The green dashed line is the evolution of δD in precipitation as reconstructed by summing up all the contributions from the different processes.

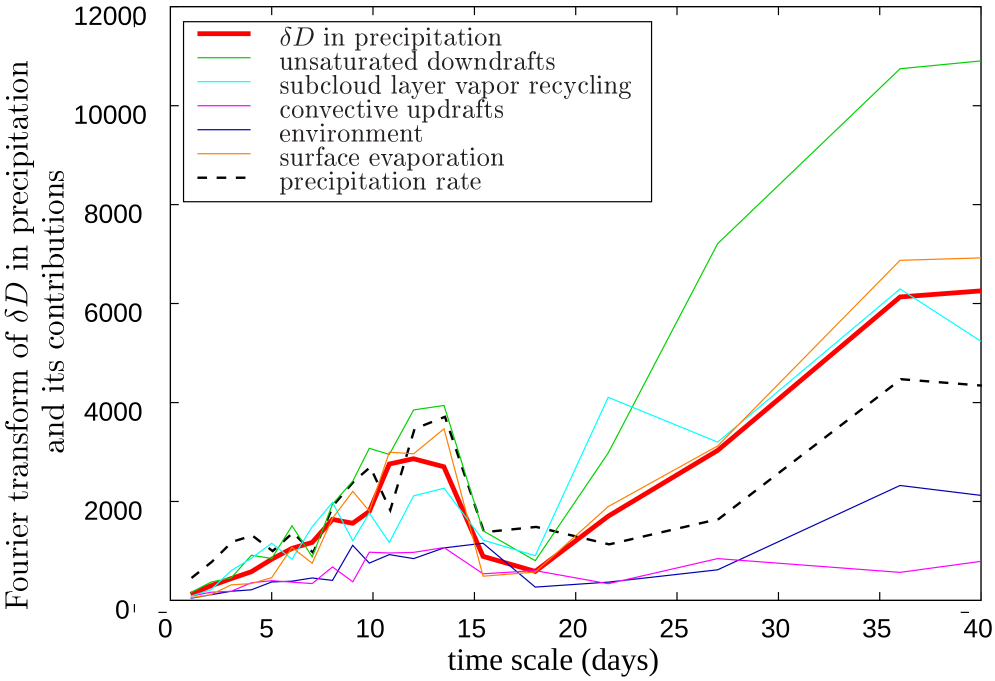

Figure 2.12 – Spectral analysis of the δD signal in precipitation during the TOGA-COARE simulation (red), and of its different contribution (colours defined on figure 2.7). The spectral analysis of the precipitation rate is also shown (black dashed line; its Fourier transform was multiplied by a factor of 8 to facilitate comparison with the Fourier transform of the δD in precipitation).

ity in convective oceanic cases. Radiative-convective equilibrium simulations have been performed for different boundary conditions. These simulations were analysed to better understand the influence of convective processes on the isotopic composition of the atmospheric water and precipitation composition in the tropics.

SCM simulations shwo that precipitation amount is the main factor controlling the composition of precipitation on tropical oceans and that SST has little impact. Besides, the amount effect is observable only if precipitation variations are mainly related to variations in the large-scale circulation. An increase in precipitation induced by an increase of surface temperature not associated with a change in large-scale vertical motion leads on the contrary to an “anti–amount effect” (i.e., a higher δD_p for a larger precipitation).

Our results underline the importance of some microphysical processes, in particular those occurring during the fall of the rain. Besides, we showed that the simulated amount effect was sensitive to some model parameters related to rain reevaporation. This highlights the importance of a detailed representation of such processes to accurately simulate the isotopic composition of precipitation. In turn, the isotopic composition of the precipitation may be used to evaluate the representation of rain reevaporation in convective parametrization.

We then analyse quantitatively the observed relationship between precipitation amount and δD in precipitation, called the amount effect, and interpret it in terms of physical processes. The fractionation occurring during the rain fall (associated with rain reevaporation and diffusive exchanges with the surrounding vapor) and the injection of vapor from the unsaturated downdraft (driven by rain reevaporation) into the subcloud layer constitute the two main contributions of the amount effect. The first process contributes the most to the amount effect in regimes of weak precipitation, while the second is predominant in regimes of strong precipitation. While these processes were already hypothesized in [Dansgaard, 1964] to possibly contribute to the amount effect, this study rigourously and explicitely quantifies these contributions.

The results yields a new interpretation of the amount effect. The amount effect is often interpreted in terms of depletion of an air mass through rainout (e.g. [Vuille et al., 2003]: the more intense the convection, the more intense the condensation during the ascent of the air parcels,

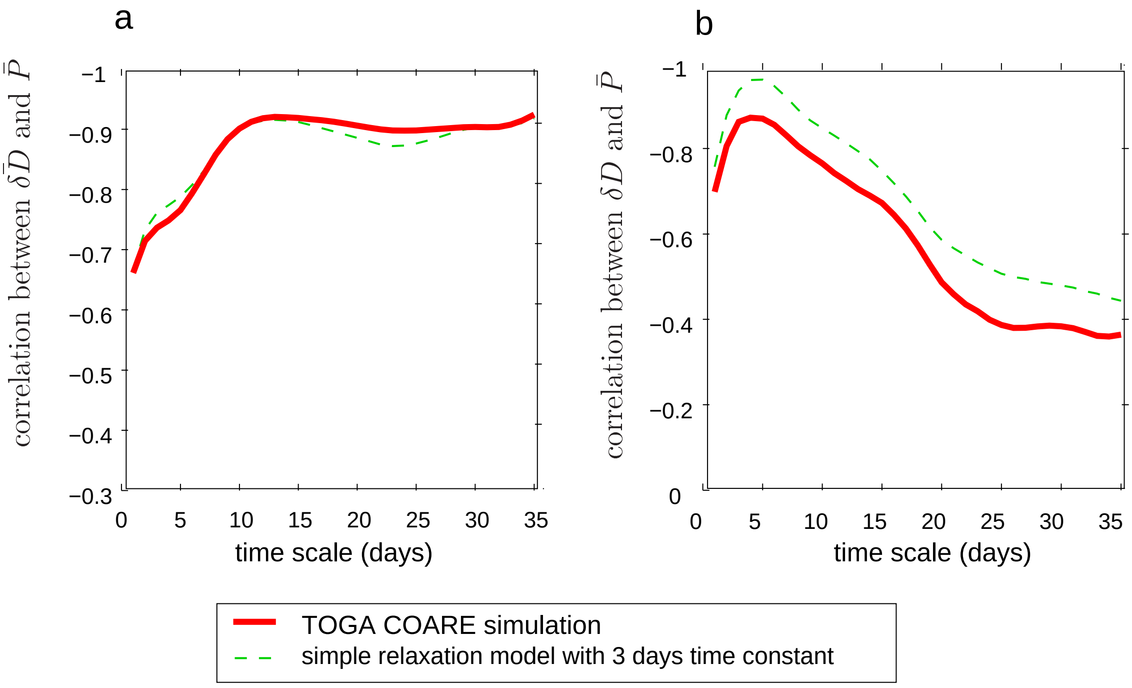

Figure 2.13 – (a) Temporal correlation between the precipitation-weighted average of δD_p over the τ_m previous days ($\delta\bar{D}_p(t) = \frac{\int_{t-\tau_m}^{t} \delta D_p(t)\cdot P(t)\cdot dt}{\bar{P}}$) and the precipitation rate averaged over the τ_m previous days ($\bar{P}(t) = \int_{t-\tau_m}^{t} P(t)\cdot dt$), as a function of time constant τ_m. The red solid curve corresponds to TOGA COARE simulation results. The green dashed curve corresponds to what predicts the simple equation $\frac{d\delta D_p}{dP}(t) = S\cdot(P(t) - \frac{\delta D(t)}{T})$ with $T = 3$ days (the precipitation rate is taken from the TOGA COARE simulation). (b) Same as a, but correlations are between the instantaneous $\delta D_p(t)$ and the average precipitation ($\bar{P}$) over the time constant τ_m. The dashed black line shows the critical correlation significant at the 99% level. All correlations in both (a) and (b) are significant at this level.

and the more depleted the following vapor and precipitation). On the contrary, we show that the predominant processes are related to the fall and reevaporation of the precipitation, rather than processes occurring during the ascent of air parcels. More generally, we show that the amount effect is associated with an ensemble of physical and microphysical processes in the convective system, whose sum yields an observable and robust signal on the ground between precipitation amount and precipitation composition.

Does the quantification of the contributions to the amount effect depend on the convective parametrization used? Particular features of the Emanuel parametrization that might affect the relative contributions are for instance:

1. the assumption that condensate is lofted up to the cloud top altitude before precipitation processes start to operate,
2. the small sensitivity of the cloud top altitude to convective regime.

Besides, since the explicit representation of an unsaturated downdraft is a particularity of the Emanuel scheme, the rain reevaporation and the recycling of the low-level vapor by convective fluxes might affect the isotopic composition of the precipitation differently in other models. However, an explicit representation of an unsaturated downdraft might not be necessary to represent at least qualitatively the two major effects, which are likely to be robust features:

1. reduced reevaporation of the rain and
2. stronger vertical mixing (here taking the form of unsaturated downdrafts) when convective activity is stronger.

Our analysis method provides a general framework to quantify the relative importance of different convective processes in the control of the isotopic composition of precipitation. This method could be applied to other models to test the sensitivity of our results to the representation of microphysical processes in different convective parametrizations.

Because of a delay in the response of the atmospheric water vapor to convection, the amount effect is best observable at intra-seasonnal or longer time scales. The period of time over which convective activity significantly affects the isotopic composition of precipitation might give some additional information about the residence time of water.

2.8.2 Perspectives

Our physical interpretation of the amount effect underlines the importance of the origin of the low level vapor feeding the convective system. Although not required to explain the amount effect, low level horizontal advection of air masses of various isotopic compositions, neglected in this single column approach, might affect the amount effect. Besides, our study was restricted to maritime conditions. In order to more rigourously evaluate our model and better understand what controls the isotopic composition of precipitation in a broader range of conditions, including in tropical ice cores, taking into account horizontal advection of air masses and land surface processes would be necessary. For this purpose, we have implemented water isotopes in the general circulation model LMDZ4 developped at the LMD ([Hourdin et al., 2006]), which uses the Emanuel scheme as the convective parameterization. 3D simulations allow us to make a more rigourous model evaluation with comparison with GNIP data (chapter 6).

Chapitre 3

Variabilité saisonnière et intra-saisonnière pendant la campagne AMMA

Dans le chapitre précédent, à partir de simulations uni-colonnes de l'atmosphère tropicale dans un cadre très idéalisé, nous avons analysé les processus physiques à l'origine de l'impact de la convection sur la composition isotopique des précipitations, ainsi que les constantes de temps associées. Pour évaluer la réponse de la composition isotopique des précipitations à la convection dans un cas réel, et analyser les constantes de temps de cette réponse, nous avons collecté la précipitation dans la région de Niamey (Niger) au cours de la saison mousson 2006, dans le cadre de la campagne AMMA.

Les quatre premières sections de ce chapitre présentent la variabilité saisonnière et intra-saisonnières observées dans ces prélèvements isotopiques. Ce travail a été publié dans l'article [Risi et al., 2008b], sur lequel sont basées les quatres premières sections de ce chapitre.

Pour mieux interpréter ces données, nous avons utilisé la version isotopique du modèle de circulation générale LMDZ (décrite dans le chapitre 6). Ce travail plus récent, toujours en cours, est décrit dans la section 3.5.

3.1 Introduction

The goal of this study is thus to better understand what controls the isotopic composition of tropical precipitation. The African Monsoon Multidisciplinary Analysis (AMMA) campaign ([Redelsperger et al., 2006]) that took place in West Africa in 2006 was an opportunity to investigate this question. We analyze the event-based isotopic composition (δD and $\delta^{18}O$) of precipitation collected in the Niamey area (Niger) during the 2006 intensive observation period of the campaign. For this period, a large amount of atmospheric data is available and the synoptic, intra-seasonal and seasonal variability of convection has been thoroughly monitored and analyzed.

Since the isotopic data are available only for the year 2006 so far, we focus on the intra-seasonal and seasonal time scales of variation. The total precipitation of the 2006 monsoon season is similar to previous years, despite a 10-day late onset of the monsoon in the Sahel compared to the climatology ([Janicot et al., 2008]). The large scale context of Niamey at the middle of the monsoon season (August) is illustrated in fig 3.1a. At low levels, moisture is supplied mostly by the monsoon flow, and at mid-levels, by the African Easterly Jet (AEJ).

3.2 Data

From June 9th to September 24th 2006, precipitation was collected on an event-based resolution at Wankama (13.65N, 2.65E) and Banizoumbou (13.53N, 2.66E). Precipitation was collected right after the end of each event (except on June 28th at Wankama and on June 17th and August 25th

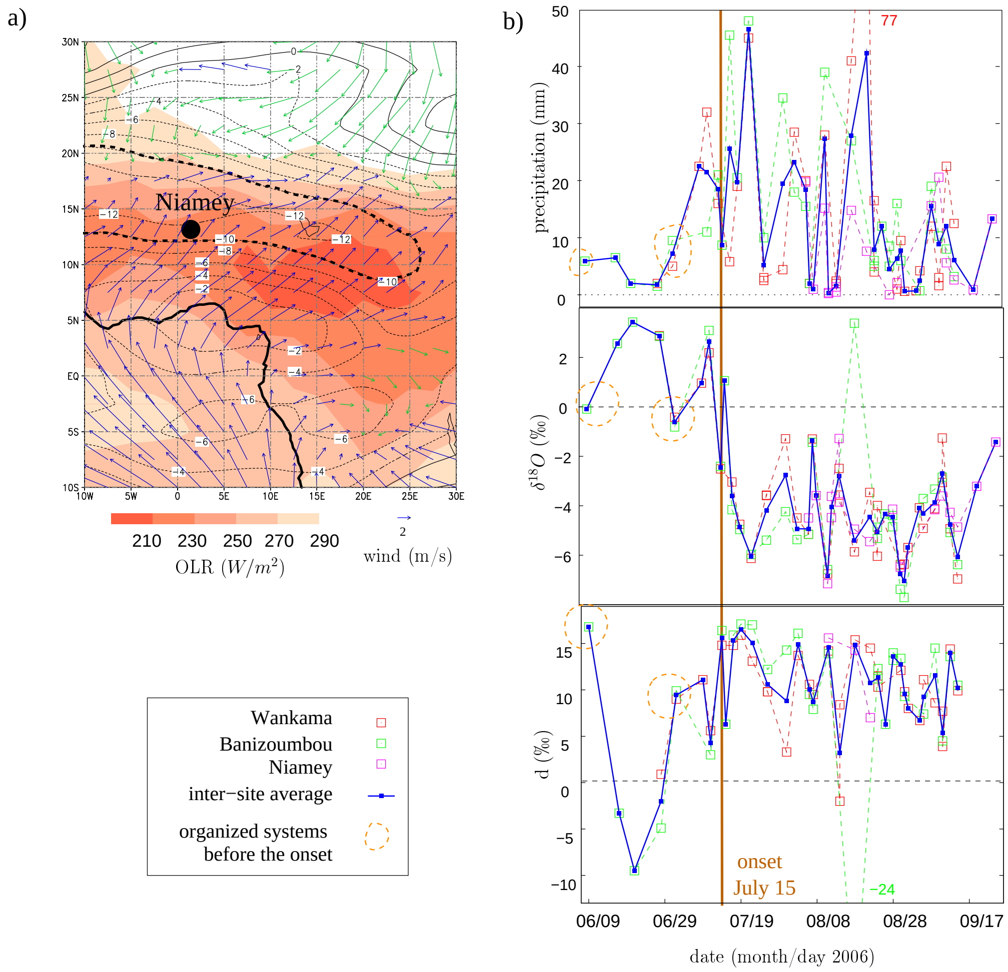

Figure 3.1: (a) August 2006 monthly mean OLR (shading) showing convective activity; 950 hPa wind vectors, indicating the monsoon flow; 600 hPa zonal wind (dashed contours), with the heavier isoline highlighting the AEJ. (b) Evolution of the cumulated precipitation, $\delta^{18}O$ and d-excess for events collected at each site (squares) and on average over the 3 sites (thick line).

at Banizoumbou, when the collection was delayed), ensuring the quality of observations. We also collected precipitation at high frequency during the passage of convective systems over Niamey (13.53N, 2.1E) ([Risi et al., 2010a]) but present here the average composition over each event. In total, 30, 31 and 14 events were sampled at Banizoumbou, Wankama and Niamey respectively. All $\delta^{18}O$ and δD measurements are performed with an accuracy of ±0.05‰ and ±0.5‰ respectively leading to an accuracy of about ±0.7‰ on deuterium excess ($d = \delta D - 8 \cdot \delta^{18}O$, [Dansgaard, 1964]).

Some of the measurements show small or negative d, especially before the monsoon onset (fig 3.1b). Given our efforts to reliably collect precipitation, this probably arises from reevaporation of the precipitation in a dry atmosphere.

Hereafter, we note $\delta^{18}O_p$ and d_p the $\delta^{18}O$ and d in the precipitation.

3.3 Relationship between isotopic composition and convection

The coherent features between the 3 sites (fig 3.1b) can be explained by the proximity of the 3 stations (within 60 km), which often receive precipitation from the same large convective systems. This suggests that processes at the large-scale dominate over processes at the scale of convective systems in the control of the composition of the event-based precipitation. To highlight even better the influence of large-scale processes, we average the isotopic composition measured at the 3 sites to produce a single time series (blue lines on fig 3.1b), analyzed below.

The isotopic composition does not exhibit any clear correlation with winds, air masses trajectories and relative humidity at different levels derived from the NCEP reanalysis ([Kalnay et al., 1996]). On the other hand, they are well correlated with proxies of convective activity, both local and large-scale: in-situ precipitation (data from fig 3.1); large-scale (1x1°) precipitation estimates from the Global Precipitation Climatology Project (GPCP, [Huffman et al., 1997]) or from the AMMA rain gauge network; 2.5x2.5° Outgoing Longwave Radiation (OLR, [Liebmann and Smith, 1996]). This suggests that the convective activity is the main control of the isotopic composition of precipitation in this region, in agreement with the amount effect. The main reasons for the amount effect are the following. (1) When rainfall is more intense, the atmosphere gets moister and the reevaporation of the falling rain decreases, which leads to a lower $\delta^{18}O_p$ in the rain ([Dansgaard, 1964, Risi et al., 2008a]) and a higher d_p ([Bony et al., 2008]). (2) More frequent and more intense convective events deplete more efficiently the vapor at low-levels ([Lawrence et al., 2004, Risi et al., 2008a]) which then feeds the subsequent convective systems with lower $\delta^{18}O_p$. Hereafter, we will focus on the relationship between isotopic composition and convection and investigate at which time scales the amount effect operates.

3.3.1 Water isotopes record the monsoon onset

The isotopic composition abruptly changes on July 15th: $\delta^{18}O_p$ drops by about 6‰ and d_p increases by about 7 ‰ on average (fig 3.1b). This date coincides with the end of the monsoon transition period and the arrival of the Inter Tropical Convergence Zone in the Sahel ([Sultan and Janicot, 2003, Janicot et al., 2008]). The average precipitation rate increases from 1.7 to 5.3 mm/day. The abrupt drop of $\delta^{18}O_p$ is thus the signature of the amount effect at the seasonal scale. The data collected by [Taupin et al., 1997] also featured such an amount effect at the seasonal scale (though the shift was smoother). The difference between the average $\delta^{18}O_p$ before and after the onset yields an amount effect of about -1.7‰/mm.day, more than twice that for the GNIP (Global Network for Isotopes in precipitation) tropical island stations (-0.6‰/mm.day: [Rozanski et al., 1993]). This likely results from the strong effect of rain reevaporation in dry conditions ([Risi et al., 2008a]) as is the case before the onset.

The intensity of individual convective systems does not explain the shift in $\delta^{18}O_p$: the rain before the onset is systematically more enriched than after the onset, even for systems having higher precipitation amounts before the onset. The abrupt isotopic shift is thus the signature of the increase of convection on average at the regional scale, or a change in large scale environmental conditions.

3.3.2 Before the onset: the intensity and organization of individual events

Over tropical oceans, [Lawrence et al., 2004] have shown an effect of the degree of organization of convective systems on the $\delta^{18}O$ of precipitation. Here, we use Meteosat infrared images to classify convective events into two classes: isolated (small events triggered in the Niamey area) or organized (large systems initiated over East Africa and propagating westward). Before the onset, the rain from organized systems is systematically more depleted (and has a higher d) than that from isolated systems, even for a similar cumulated precipitation, in agreement with [Lawrence et al., 2004]: the 6 isolated systems have a positive $\delta^{18}O$ whereas the 2 organized systems have a negative $\delta^{18}O_p$ (fig 3.1b).

For the 5 isolated systems before the onset, $\delta^{18}O_p$ is lower and d_p higher for more intense systems: the correlation between $\delta^{18}O_p$ and daily OLR in the 2.5x2.5 Niamey grid box is r=0.9 (-0.6 for d_p). OLR and 1000hPa relative humidity being strongly anti-correlated (r=-0.95), the correlations of $\delta^{18}O_p$ and d_p with relative humidity are the same as with OLR. For isolated systems occurring before the onset, the local convective intensity, and the associated relative humidity variations, thus control the isotopic composition of precipitation.

3.3.3 After the onset: intra-seasonal variability

After the onset, the isotopic record exhibits a strong intra-seasonal variability, with $\delta^{18}O_p$ ranging from -1 to -8 ‰. The data from [Taupin et al., 1997] also featured such large variations, with amplitudes up to 6‰. Contrary to the period before the onset, we find no significant correlation between convection and the isotopic composition at the scale of individual events. On the other hand, a good correlation between $\delta^{18}O_p$ and the OLR over Niamey is found after the onset when the OLR is averaged over the τ_m days preceding the events, with a maximum correlation for τ_m=9 days (fig 3.2a): the precipitation is more depleted when convective activity has been more intense over the 9 previous days. Thus, after the onset, $\delta^{18}O_p$ does not respond instantaneously to convection, but rather integrates convective activity over the previous days. This is in agreement with modeling studies by [Sturm et al., 2007b] and [Risi et al., 2008a]. Spatially, the correlation between $\delta^{18}O_p$ and the OLR averaged over the 9 previous days is maximum North and East of Niamey (fig 3.2 b), suggesting that the $\delta^{18}O_p$ records a regional signal of convective variability.

The property of $\delta^{18}O_p$ to integrate convection may be explained by each convective system depleting a little more the low-level vapor; the isotopic composition of the vapor feeding a convective system is thus influenced by the cumulative effect of the previous convective systems. In addition, the soil moisture may contribute to integrate convective activity on longer time scales, by storing the precipitation of convective events and reevaporating it later. If the integrative property of $\delta^{18}O_p$ is due to the accumulation of the convective effect in water reservoirs (low-level vapor or soil moisture), then the time constant over which $\delta^{18}O_p$ integrates convection could yield some information about the residence time of water in these reservoirs.

$\delta^{18}O_p$ really integrates convection rather than just responding to it with delay, since correlations between $\delta^{18}O_p$ and averaged OLR are stronger than lag correlations: averaging allows use to select the low-frequency variability of OLR and discard the higher frequency variability to which water isotopes respond more weakly. Consistently, other proxies of convection feature a similar maximum of the correlation with $\delta^{18}O_p$ at 9 days, but faster varying proxies (e.g. precipitation from GPCP and pluviometers) need a longer averaging time or larger averaging domain to reach the maximum correlation (fig 3.2a). This highlights the property of $\delta^{18}O_p$ to integrate temporally and spatially convection.

To characterize the time scales of variability recorded by $\delta^{18}O_p$, we perform correlations between $\delta^{18}O_p$ and averaged OLR for OLR filtered at different frequencies. Filtering between 6 and 18 days (fig 3.2c) preserves the correlation pattern, whereas other filters erase it. $\delta^{18}O_p$ thus records intra-seasonal time scales. In the Sahel, modes of variability at such time scales have been documented: the Sahelian ([Sultan et al., 2003, Mounier and Janicot, 2004]) and Guinean ([Mounier and Janicot, 2004]) modes operate at the 15-20 days time scale. We calculated correlations between $\delta^{18}O_p$ and the time series of the 10-60 days filtered OLR projected on the Sahelian and Guinean modes ([Mounier and Janicot, 2004], fig 3.2c): they reach maxima of 0.35 and 0.5 when averaged over 10 and 15 days respectively. $\delta^{18}O_p$ is thus a good recorder of these two modes of intra-seasonal variability, even better than the raw local OLR itself: the correlation between these modes and the daily OLR over Niamey reach maxima of 0.33 and 0.28 respectively.

To further characterize the variability recorded by $\delta^{18}O_p$ after the onset, OLR and winds are composited as a function of $\delta^{18}O_p$. The difference between the composites of low and high $\delta^{18}O_p$ (fig 3.2d) shows that the most depleted events coincide with an increased convective activity East and North of Niamey, consistent with fig 3.2b. This is compatible with the $\delta^{18}O_p$ response to a westward propagating disturbance of convective activity over the Sahel. During the same time, the AEJ is located northward and the monsoon flow is enhanced (fig 3.2d). These features are consistent with the Sahelian mode of variability ([Sultan et al., 2003]).

Lower d_p correlates with higher convective activity integrated over the previous days: this is opposite to the relationship found at the seasonal scale or before the onset, and to the expected effect of convection on d_p (higher convective activity is expected to be associated with less rain reevaporation and thus higher d: [Bony et al., 2008, Risi et al., 2010a]). Such a “reverse” relationship is also observed in South America. During this period, surface processes (e.g. the partition of evapo-transpiration into transpiration and evaporation) may exert a control on d_p ([Taupin et al., 2000]) strong enough to offset the effect of convection.

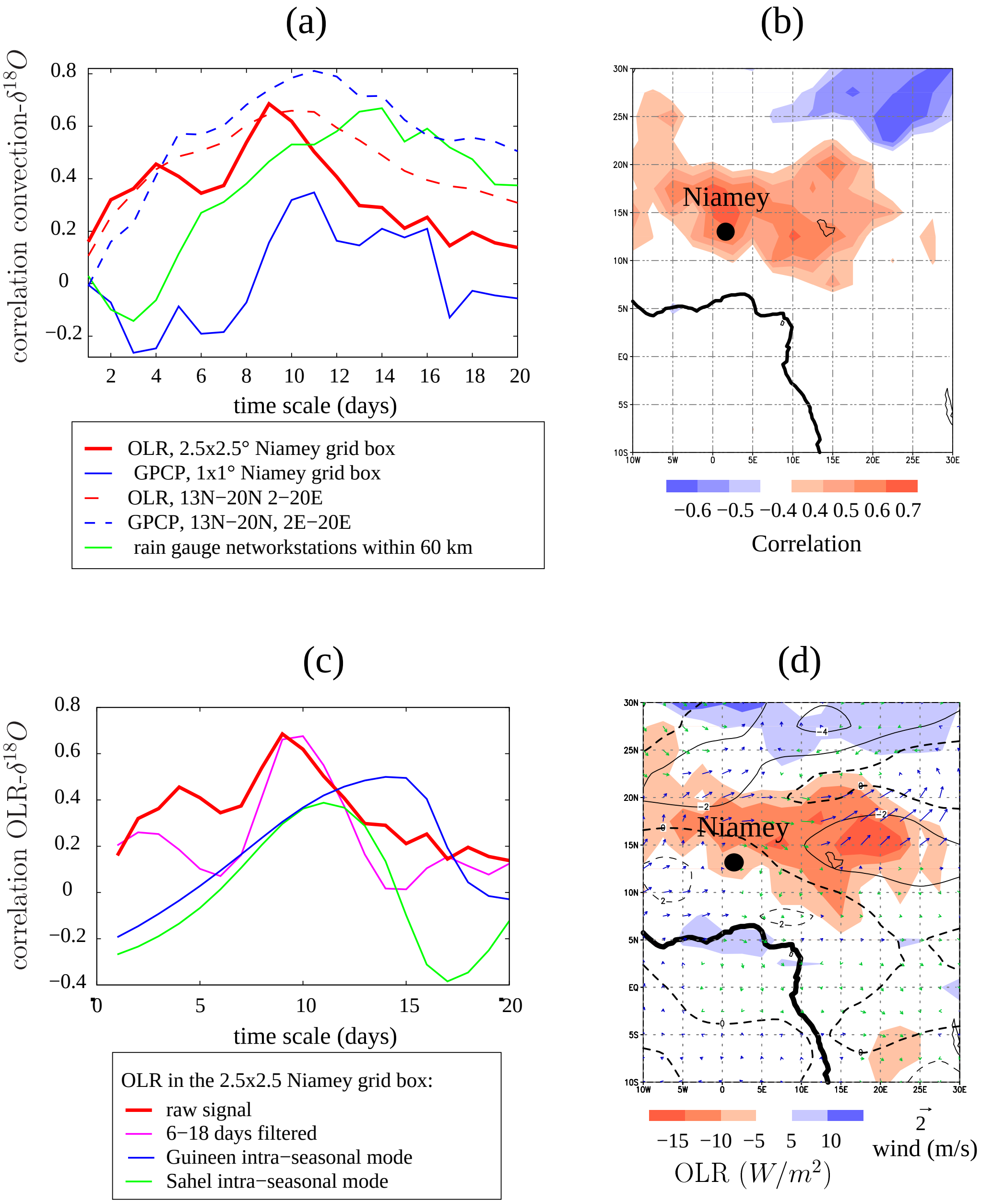

Figure 3.2: (a) Correlation between $\delta^{18}O_p$ of organized events after the onset and different proxies of convective activity averaged over the τ_m days preceding each rainy event, as a function of τ_m: OLR in the 2.5x2.5 Niamey grid box (solid red), GPCP precipitation in the 1x1 Niamey grid box (solid blue), OLR (dashed red) and GPCP precipitation (dashed blue) both averaged over the 13N-20N-2E-20E domain, precipitation averaged over the AMMA rain gauge network stations within 60 km of the 3 sites barycenter (green). (b) Correlation between the $\delta^{18}O_p$ of the events and the OLR averaged over the 9 days preceding each event. (c) Red: same as heavy red line in (a); magenta: same for 6-18 days filtered OLR ; blue and green: same for time series of 10-60 days filtered OLR projected on the Sahelian and Guinean modes of OLR variability ([Mounier and Janicot, 2004]. (d) Difference between low $\delta^{18}O_p$ and high $\delta^{18}O_p$ composites, for organized events after the onset: difference of the composites of OLR averaged over the 9 previous days (shading), of 600hPa zonal winds (contours, zero, positive and negative isolines in thick dashed, thin solid and thin dashed respectively) and of 950hPa winds (vectors).

3.4 Conclusion and perspectives (based on this data)

At the seasonal scale, the increase in convective activity after the monsoon onset induces a strong drop in $\delta^{18}O_p$ (in agreement with the amount effect) and an increase in d. Before the onset, when the average convective activity is weak, the amount effect is observed at the scale of individual event: organized systems are systematically more depleted than isolated systems, and for the latter the intensity of convection is the major control on the isotopic composition. On the contrary, after the onset, $\delta^{18}O_p$ integrates convective activity over time and records the intra-seasonal variability of convection over the Sahel.

The integrative property of $\delta^{18}O_p$ was also found in South America ([Sturm et al., 2007b]). However, the isotopic composition collected in the Andes was found to be related to convection upstream of low-level trajectories ([Vimeux et al., 2005]). In Niger, no relationship is found with proxies of convection along the southerly monsoon flow trajectories, but rather North and East of Niamey. This feature may be tentatively explained by two elements: first, it is consistent with the westward propagation of intra-seasonal convective disturbances. Second, over the Sahel, a substantial part of the moisture (up to half, J.-Y. Grandpeix, pers. comm.) converging into convective systems comes from the AEJ that blows westward. This, combined with the fact that in convective atmospheres, water vapor $\delta^{18}O_p$ varies more in the mid-troposphere than at low levels ([Bony et al., 2008]), may explain that convection occurring eastward of Niamey affects more the $\delta^{18}O_p$ over Niamey than the convection occurring along the monsoon flow.

Although few paleoclimatic isotopic archives have been exploited so far in West Africa, we show that the $\delta^{18}O_p$ in this monsoon region records the monsoon onset and large-scale convective variability. However, what controls the inter-annual variability of the isotopic composition will be explored in the future when other years of data will be available. We show that the isotopic composition of precipitation constitutes a tracer of several characteristics of the African monsoon. A long-term and extended network of isotopic data over Western Africa would thus be useful for a better understanding of tropical monsoons, African water cycle and paleoclimates.

3.5 Interpretation of this data using LMDZ simulations

Based on the data presented above, we showed that the isotopic composition of the precipitation records variations in convective activity, notably the monsoon onset. Before the monsoon onset, the isotopic composition of the precipitation responds immediately and locally to the properties of individual convective systems (intensity, organization). On the other hand, after the onset, the $\delta^{18}O_p$ integrates convection over the previous days, recording a large-scale signal of convective activity.

What are the mechanisms for the isotopic reponse to convection? In chapter 2, we suggested rain reevaporation and convective subsidence (through unsaturated downdrafts) were the main processes. What are the relative contributions of these processes? What is the mechanism for the temporal integration of convection by $\delta^{18}O_p$ after the onset? Is the memory due to water storage in the atmosphere, or in the soil?

To better understand these processes, and in turn have a better idea of what can be learned from isotopes about the water cycle in this monsoon region, we use simulations with the General Circulation Model (GCM) LMDZ ([Hourdin et al., 2006]), in which water isotopes were introduced (LMDZ-iso, [Risi et al., 2010b], chapter 6). From model simulations, a number of diagnostics can be analyzed, including the isotopic composition of the vapor. Such observations were critically lacking for the interpretation of our precipitation data. In addition, we added diagnostics of the origin of water vapor to LMDZ (water tagging, appendix E). This is a work in progress.

3.5.1 Simulations

LMDZ configuration and nudging

We present here a simulation with LMDZ4 using the AR4 physical package, 19 vertical levels and a 2.5×3.75° horizontal resolution. The 3D field of horizontal winds is nudged by the NCEP1 reanalyses ([Kalnay et al., 1996]). The simulation is the same as the nudged simulation described in [Risi et al., 2010b], except that we use the NCEP rather than the ECMWF ERA-40 reanalyses ([Uppala et al., 2005]) due to a southward shift of the ITCZ in West Africa in the ECMWF model (with ECMWF nudging, LMDZ simulates a total monsoon precipitation over Niamey from June to September 4 times smaller than in the GPCP data). The simulation runs from January 2005 to December 2006. The water, isotopes and their tags are all already at stationary state during the monsoon 2006 that we analyse.

Precipitation simulated by LMDZ

The annual and June-July-August (JJA) precipitation spatial distribution simulated by LMDZ over West Africa are satisfyingly simulated (not shown).

Despite the nudging, LMDZ is not able to reproduce the exact phasing of the intra-seasonal variability in precipitation (figure 3.3a). In LMDZ, the monsoon onset occurs approximately early August, compared to mid-July in the data. However, the total cumulated precipitation from June 1 to September 30 is similar (480mm in GPCP and 400 in LMDZ) and the order of magnitude of the amplitude and frequency of the intra-seasonal variability is correctly simulated.

Water tagging experiments

To better understand the processes controlling the isotopic composition of precipitation in the Sahel and the potential of isotopes to study the origin of air masses, we devised several water tagging experiments:

- tag evaporation from ocean versus evaporation from continent (appendix E.2.1)
- tag evaporation from the different oceanic basins and from the continent (similar to experiments by e.g. [Koster et al., 1986, Delaygue et al., 2000, Werner et al., 2001, Noone and Simmonds, 2002a]): (appendix E.2.1)
- tag water molecules that go through some 3D domains (appendix E.2.4). Three such domains are defined (table 3.1, figure 3.5), corresponding to the three main flows of air in the Sahel: the monsoon flow, advecting at low-levels moist and cool air from the South-West; the Harmattan, advecting at low and mid-levels dry and warm air from the Sahara, and the African Easterly Jet (AEJ), advecting moist air at mid-levels from the East. As soon as a molecule enters this domain, it gets the tag of this domain. This tag is lost when water molecules enter another domain or precipitate. Evaporation from the surface is tagged with a fourth tag.
- tag molecules that go through unsaturated downdrafts in the convective parametrization (appendix E.2.5)

3.5.2 Isotopic reponse to convection in LMDZ-iso

The $\delta^{18}O_p$ simulated by LMDZ-iso decreases from 0 to 2‰ in July to -4 to -6‰ in September (figure 3.3 b), very similar to the observed decrease from 0 to 4‰ in June to -4 to -6‰. The increase of d_p observed concomitantly to the decrease of $\delta^{18}O_p$ during the monsoon onset is well simulated by LMDZ-iso (figure 3.3c). LMDZ thus reproduces the isotopic signature of the monsoon onset, though slightly smoother than in observations.

LMDZ-iso has more difficulties to simulate the average values of d_p than $\delta^{18}O_p$: LMDZ-iso is not able to simulate d-excess lower than 10‰ before the onset, while the observations can be as low -15‰. After the onset, d_p is overestimated by LMDZ by about 10‰. Before the onset, when the air is very dry, d_p can be improved by tuning parameter ϕ, controlling kinetics effects during rain reevaporation (appendix D.2). When $\phi = 0.7$ instead of $\phi = 0.9$ for example, d_p before the onset is reduced by 25‰, thus in better agreement with observations (not shown).

Before the onset, the isotopic composition in LMDZ responds instantaneously to variations in convective activity, as in observations: $\delta^{18}O$ increases and d-excess decreases as the daily rainfall increases (vertical dashed blue lines on figure 3.3 a, b).

After the onset on the other hand, $\delta^{18}O_p$ integrates convection in LMDZ as in the observations: the $\delta^{18}O_p$ best correlates with precipitation when precipitation is averaged over the 15 to 20

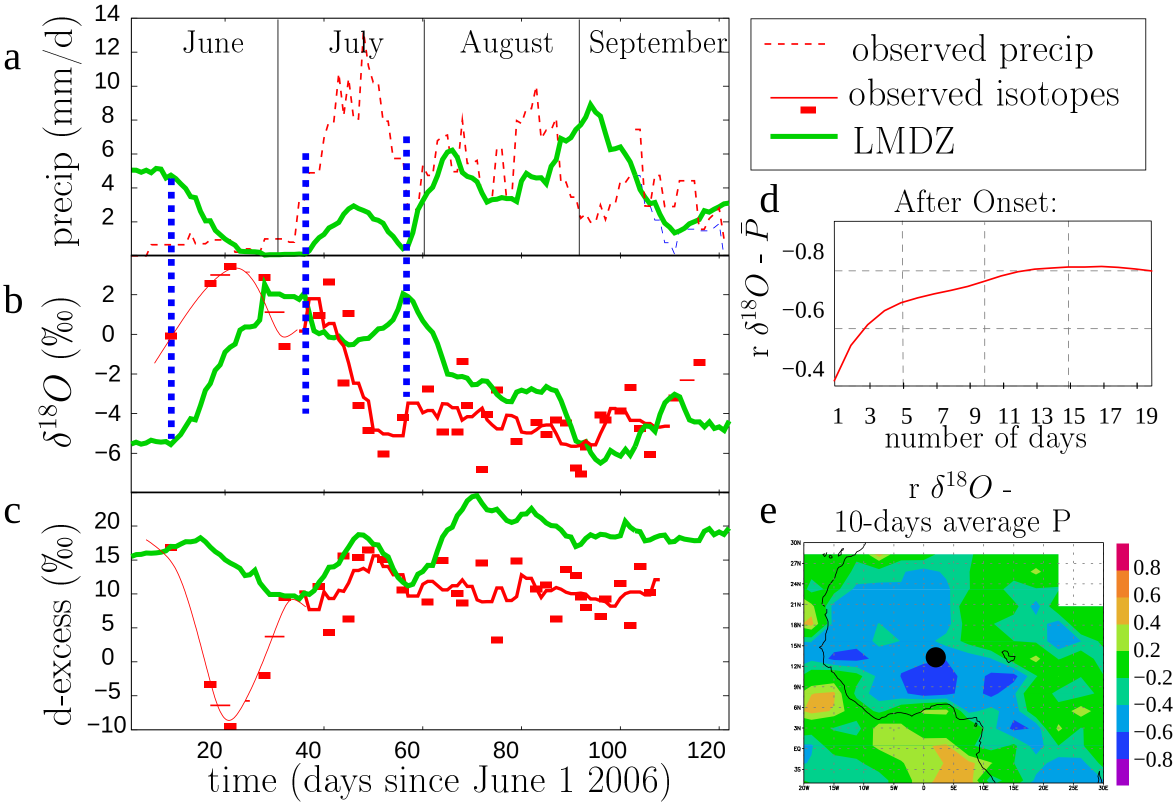

Figure 3.3: a) Precipitation simulated over Niamey (green) and observed by GPCP (dashed red) from June to September 2006. A 5-day running mean has been applied. b) $\delta^{18}O_p$ simulated over Niamey (green) and observed (red). c) Same for d-excess. d) correlation between daily $\delta^{18}O_p$ and precipitation, from July 15 to September 30, as a function of the number of previous days over which precipitation rate is averaged. e) Correlation between daily $\delta^{18}O_p$ and precipitation averaged over the 10 previous days, from July 15 to September 30.

previous days (figure 3.3d, to be compared with figure 3.3.3). Spatially, the correlation between $\delta^{18}O_p$ and precipitation averaged over the 10 previous days is high over a broad Sahelian region (figure 3.3e). The spatial extent of this correlation is similar to that in the data, although the correlations in LMDZ are stronger in the model southward and westward of Niamey. The evolution of $\delta^{18}O_p$ simulated by LMDZ is very similar to what would predict the simple relaxation equation (equation 2.1) introduced in section 2.7 ([Risi et al., 2008a]):

$$\frac{d\delta^{18}O_p}{dt}(t) = P(t) - \frac{\delta^{18}O_p}{T}$$

with a time constant T of 10 days. LMDZ-iso is thus able to reproduce the different time and space scales of the observed $\delta^{18}O_p$ response to convection before and after the monsoon onset.

3.5.3 Mechanisms for the isotopic reponse to convection

To better understand what controls $\delta^{18}O_p$, we decompose $\delta^{18}O_p$ as:

$$\delta^{18}O_v + \left(\delta^{18}O_p - \delta^{18}O_v\right)$$

where $\delta^{18}O_v$ is the $\delta^{18}O$ of the lowest level vapor (about 130m). The first term includes the effect of convective subsidence and large-scale processes affecting the vapor (blue on figure 3.4a). The second represents the effect of rain reevaporation and its consequence on rain-vapor disequilibrium (green on figure 3.4a). The underlying hypothesis is that $\delta^{18}O_p$ is mainly controlled by the $\delta^{18}O$ of

	AEJ	Monsoon flow	Saharian boundary layer
latitude extention	8°N−20°N	5°S−8°N	20°N−30°N
longitude extention	10°E−30°E	40°W−15°E	10°W−40°E
altitude extention	700−400hPa	1000−850hPa	1000−700hPa

Table 3.1: Vertical and horizontal extension of the three tagged domains.

the vapor with which it reequilibrates on the one hand, and by the degree of reequilibration with this vapor on the other hand.

Before the onset, almost all the variability in $\delta^{18}O_p$ is explained by variations in rain reevaporation. This is consistent with the instantaneous response of $\delta^{18}O_p$ to convection: when a convective system is more intense, there is less reevaporation and in a wetter air, therefore the precipitation is immediately more depleted (figure 3.4 b and c).

After the onset on the other hand, both the rain reevaporation (70%) and the processes affecting the vapor (30%) affect $\delta^{18}O_p$ (figure 3.4). To understand what processes affect $\delta^{18}O_v$ after the onset, we compare $\delta^{18}O_v$ with the $\delta^{18}O$ of the vapor from different origins in the water tagging simulations (figure 3.4 d). $\delta^{18}O_v$ after the onset is significantly correlated with the $\delta^{18}O$ originating from ocean evaporation ($\delta^{18}O_{oce}$). In particular, the depleted event during the first week of september is mainly due to the depletion in $\delta^{18}O_{oce}$. This suggests that $\delta^{18}O_v$ over Niamey in LMDZ is modulated by convection along monsoon trajectories affecting $\delta^{18}O_{oce}$. $\delta^{18}O_v$ is also correlated with the $\delta^{18}O$ of the vapor having been through unsaturated downdrafts ($\delta^{18}O_{ddft}$). This suggests the depletion of the vapor along monsoon trajectories is through the input of depleted downdraft vapor. Both $\delta^{18}O_{oce}$ and $\delta^{18}O_{ddft}$ over Niamey correlates well with precipitation averaged over the 10 to 20 previous days over a wide Sahelian area and along the monsoon trajectories (not shown). $\delta^{18}O_{ddft}$ is all the more depleted compared to $\delta^{18}O_v$ as convection is stronger. This effect of unsaturated downdrafts is in agreement with results from the single column modelling approach (section 2.6.3, [Risi et al., 2008a]).

$\delta^{18}O_v$ shows no relationship with $\delta^{18}O$ of the vapor originating from continental evaporation ($\delta^{18}O_{con}$). In addition, in an additional experiment in which the soil moisture composition was held constant, the $\delta^{18}O_v$ variability was almost unchanged. This suggests that contrary to the hypothesis formulated in section 3.3.3 ([Risi et al., 2008b]), the soil moisture has no impact on $\delta^{18}O_p$ variations at the intra-seasonal scale and is not responsible for the temporal integration of the convective signal.

D-excess, all along the monsoon, is mainly controled by local rain reevaporation (figure 3.4c).

3.5.4 Origin of vapor and its relationship with the isotopic composition

The contributions of the different evaporative regions and flows to the low level vapor in Niamey are given in table 3.2 and 3.3 respectively. Moisture over Niamey originates from the northerly Harmattan in winter and from the monsoon flow and the AEJ in summer, as expected from [Hall and Peyrillé, 2006]. Moisture originates from the AEJ as much as from the monsoon flow, confirming the important role of the AEJ in the moisture budget (J-Y Grandpeix, pers. comm., 2006). The continental recycling is high during the monsoon summer: 60% of the lowest level vapor has evaporated over the continent. This continental vapor is more enriched by 20‰ in average than the oceanic vapor, and its d-excess is 12‰ higher (not shown). This confirms the potential of water isotopes to better constrain continental recycling.

3.5.5 Conclusion and perspectives

Conclusion

Both the data and the LMDZ model show a consistent isotopic response to convection. The isotopic composition records mainly variations in convective activity, in particular the monsoon

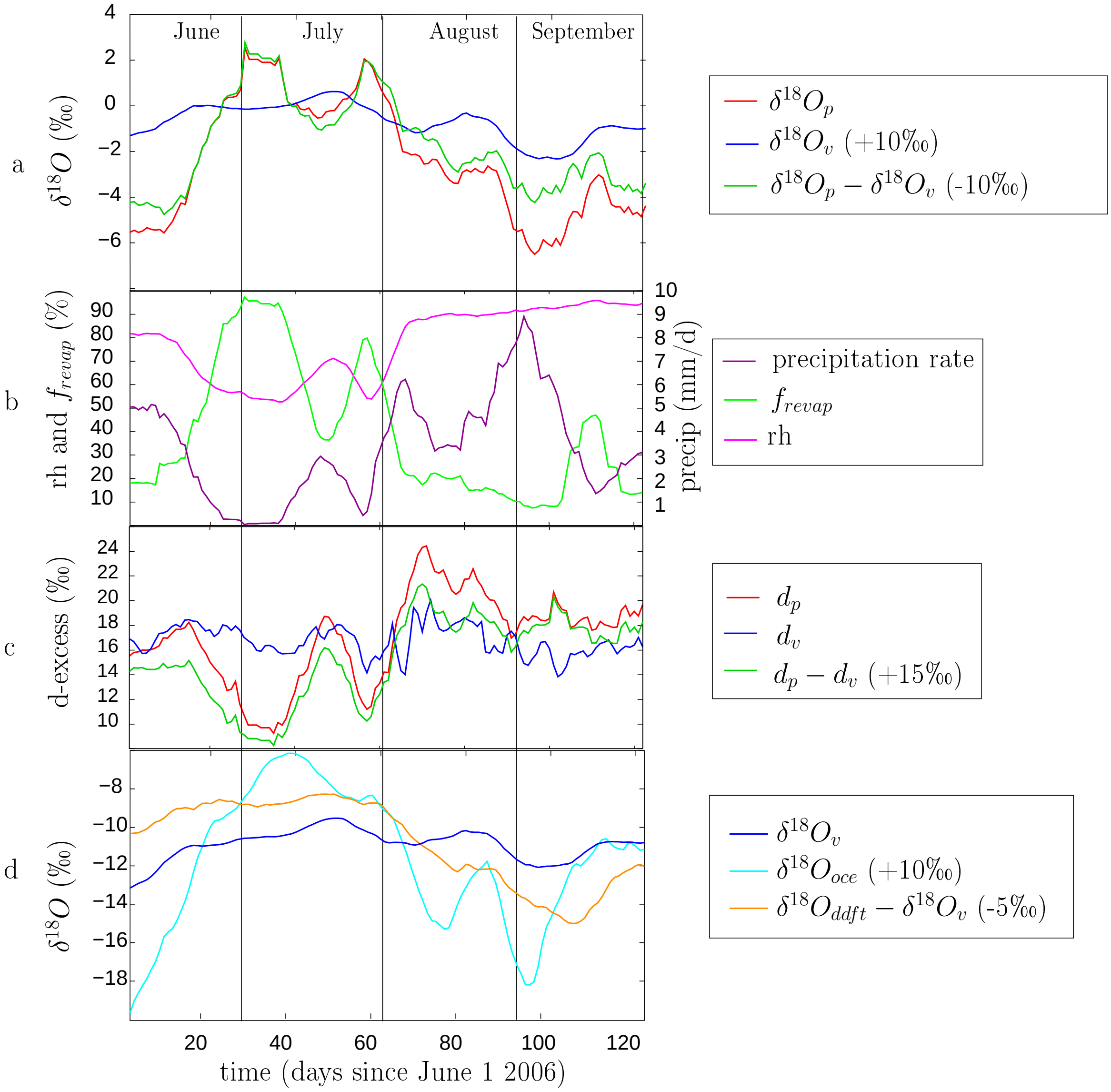

Figure 3.4: a) Daily $\delta^{18}O$ in the precipitation ($\delta^{18}O_p$) and in the lowest level vapor ($\delta^{18}O_v$), and the difference $\delta^{18}O_p - \delta^{18}O_v$, simulated by LMDZ-iso. b) Precipitation rate, relative humidity of the lowest level air, and reevaporated fraction of the rain, simulated by LMDZ-iso. c) Same as a but for d-excess. d) $\delta^{18}O$ in the total vapor ($\delta^{18}O_v$) at the lowest level, in the oceanic tagged vapor ($\delta^{18}O_{oce}$) and difference between the downdraft tagged vapor ($\delta^{18}O_{ddft}$)and the total vapor. All time series have been applied a 5-day running mean.

	summer	winter
continent	60%	30%
Atlantic	30%	45%
Mediterranean	2%	10%
Indian Ocean	10%	15%

Table 3.2: Percentage of the lowest level vapor having evaporated over different areas during summer (July-August) and winter (January-February), as diagnosed from water tagging simulations.

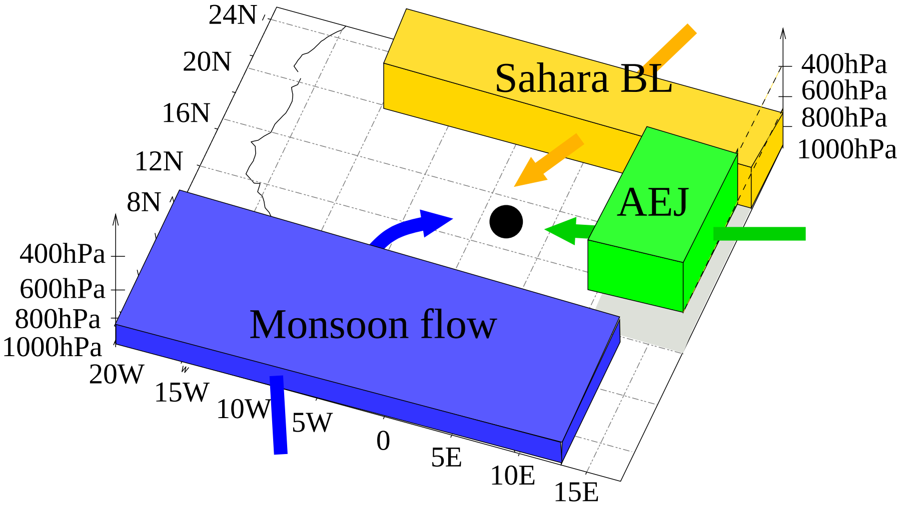

Figure 3.5: Illustration of the 3 tagged domains.

	summer	winter
Monsoon flow	32%	20%
AEJ	32%	10%
Sahara BL	8%	60%
unsat. downdraft	70%	50%

Table 3.3: Percentage of the lowest level vapor having been through one of the 3 boxes defined in table 3.1 and figure 3.5. Last line: Percentage of vapor having been through an unsaturated downdraft.

onset. Before the onset, the isotopic composition of the precipitation responds instantaneously and locally to variations in convection, through variations in drop reevaporation rate. After the onset, both the observations and the model show a temporal integration of convective activity during the one or two previous weeks. In the model, this integration can be explained by the progressive depletion of $\delta^{18}O$ of the vapor from the ocean to Niamey along the monsoon flow by convective downdrafts.

Perspectives

To what extent are processes evidenced in LMDZ the same as those at play in nature? To check the validity of the isotopic processes suggested by LMDZ, it would be valuable to be able to evaluate the simulated isotopic composition of the low-level vapor. Water vapor measurements were lacking during the AMMA campaign. Having such measurements would help evaluate the simulated vapor composition as well as the representation of the isotopic exchanges between rain and vapor (which is the main uncertainty of LMDZ-iso in the tropics, chapter 6). The effect of large-scale processes, such as the origin of air masses would appear clearer than in the precipitation. Also, such measurements would be available all year long and for all days, allowing a more continuous record of the effect of convection on the water vapor.

In the future, we thus plan to make use of new and promising methods of isotopic measurements in the low level vapor:

- satellite measurements of the vertically integrated δD (with the strongest weight in low levels) by SCIAMACHY ([Frankenberg et al., 2009]), whose retrievals are particularly successfull over the Sahara and Sahel,
- in-situ measurements of the vapor isotopic composition by the new Picarro instrument. An installation of this instrument in Niamey is planned as part of Guillaume Tremoy's PhD thesis (2009-2012).

Chapitre 4

Données intra-événement pendant la campagne AMMA

Le chapitre précédent a illustré la forte influence de la convection sur la composition isotopique de la précipitation sahélienne aux échelles intra-saisonnières à saisonnières. Le chapitre 2, basé sur une modélisation uni-colonne de l'atmosphère tropicale, avait suggéré des processus physiques expliquant cette influence et leurs contributions avaient été quantifiées. Le but de ce chapitre est de poursuivre la compréhension de l'effet des processus convectifs sur la composition isotopique de la précipitation, en utilisant des données collectées à l'échelle intra-événement au cours du passage de lignes de grains au dessus de Niamey, pendant la campagne AMMA.

Ce chapitre est basé sur l'article [Risi et al., 2010a] (sous presse).

4.1 Introduction

Owing to mass and symmetry differences, water stable isotopes ($H_2^{16}O$, HDO, $H_2^{18}O$) are sensitive to phase changes and diffusive processes. Water stable isotopes have long been used in polar studies as proxies for climate and especially temperature changes. In the tropics, however, the primary control of the isotopic composition of the precipitation is not temperature but precipitation ([Dansgaard, 1964]). A recent analysis using a single column model including the Emanuel convective parametrization ([Emanuel, 1991]) suggests that the relationship between the enrichment in heavier isotopes and the precipitation rate, known at the monthly scale as the "amount effect", is primarily controlled by rain reevaporation (raindrops get more enriched as they reevaporate), diffusive exchanges, and the recycling of the boundary layer vapor by depleted vapor from convective downdrafts generated by the rain reevaporation ([Risi et al., 2008a]).

The intensity of convection and rain reevaporation are known to exhibit a systematic evolution along the life cycle of individual convective systems ([Zipser, 1977, Houze, 1977, Sherwood and Wahrlich, 1999]). The temporal evolution of the rain isotopic composition in well organized convective systems is therefore likely to reveal the effect of these processes on the precipitation isotopic composition. To test this hypothesis, measuring the rain isotopic composition along squall lines in the Sahel is appealing: the Sahel is associated with both intense convective systems and strong reevaporation ([Chong and Hauser, 1990, Zahiri, 2007]), because of the dryness of the air in the vicinity of the Sahara. [Taupin and Gallaire, 1998] noted a systematic evolution of the isotopic composition along squall lines in Niamey, Niger. A systematic evolution was also observed along convective systems in other regions (e.g. [Celle-Jeanton et al., 2004, Barras and Simmonds, 2009]) or along radial transects in tropical cyclones ([Gedzelman et al., 2003, Fudeyasu et al., 2008]. These studies identified a variety of processes controlling the observed isotopic evolution of the precipitation, such as (1) the origin of air masses ([Taupin and Gallaire, 1998]), (2) rain reevaporation ([Taupin and Gallaire, 1998, Barras and Simmonds, 2009]), (3) condensation altitude (at higher condensation altitude, the vapor is more depleted due to previous condensation, and thus the condensate forming the precipitation is more depleted: [Celle-Jeanton et al., 2004]) and (4) diffusive exchanges between the low-level vapor and the raindrops that deplete the vapor (particularly efficient when the relative humidity is high: [Gedzelman et al., 2003, Fudeyasu et al., 2008]). However, the large number of processes potentially involved makes the detail of the observed evolution difficult to interpret.

In this study, we take advantage of the second special observation period (15 July to 15 September: SOP-2) of the AMMA (African Monsoon Multidisciplinary Analysis) campaign ([Redelsperger et al., 2006, Janicot et al., 2008]) to analyze the evolution of the isotopic composition of precipitation sampled along four squall lines in Niamey, Niger, in August 2006. The campaign offers a huge amount of data documenting each system (radars, mobile facility from the Atmospheric Radiation Measurement (ARM) program, in situ measurements, satellites), allowing a more detailed interpretation of isotopic data. In addition, 3D winds have been retrieved from the MIT (Massachusetts Institute of Technology) radar data ([Chong, 2009], this issue) for one of the squall lines sampled, on 11 August.

The main goal of this study is thus to better understand the role of convective processes in controlling the precipitation isotopic composition, and more generally to explore what information may be learned from water isotopes regarding cumulus convection and atmospheric processes.

In section 4.2, we present and compare the evolution of the isotopic composition of the precipitation along four squall lines and suggest some processes to explain the isotopic evolutions. In section 4.3, we focus on the 11 August squall line, on which a simple 2D model of transport and microphysics is run: we first describe this model, and then use it to investigate what controls the isotopic composition along squall lines. A discussion and concluding remarks are given in section 4.4.

4.2 Data

4.2.1 Rainwater collection and isotopic analysis

Rain from squall lines systems on 6, 11, 18 and 22 August 2006 were sampled on the roof of the IRD (Institut de Recherche pour le Développement) building in Niamey (13.53°N, 2.1°E), at about 3m above the ground and with no nearby obstacles or vegetation. Rain reevaporation in the pluviometer is strongly limited: the pluviometer is devised with this aim, the relative humidity of the surface air is always above 90% during rain fall, and the precipitation never spends more than 30 minutes in the pluviometer. Every five minutes, we read the precipitation amount and collect precipitation samples from the pluviometer into 15 ml bottles. When precipitation was weak, we waited until there is enough precipitation in the pluviometer to fill the bottle, increasing the time step up to 30 minutes at maximum.

The isotopic composition is expressed as an enrichment in heavier isotopes HDO or $H_2^{18}O$ relatively to the SMOW (Standard Mean Ocean Water), noted respectively δD and $\delta^{18}O$:

$$\delta = \left(\frac{R_{sample}}{R_{SMOW}} - 1 \right) \cdot 1000$$

The R notation denotes the ratio of the HDO or $H_2^{18}O$ mixing ratio over that of $H_2^{16}O$; R_{sample} and R_{SMOW} are the ratio in the sample and the SMOW respectively. At first order, variations in δD are 8 times those of $\delta^{18}O$. The deviation to this behavior is measured by the deuterium excess: $d = \delta D - 8 \cdot \delta^{18}O$ ([Dansgaard, 1964]). Hereafter, we note $\delta^{18}O_p$ and d_p the $\delta^{18}O$ and d of the precipitation.

All $\delta^{18}O$ and δD measurements are performed with an accuracy of ±0.05‰ and ±0.5‰ respectively, leading to an accuracy of about ±0.7‰ on d.

4.2.2 Variability and robust features among squall lines

Snapshots of radar reflectivity from the MIT ([Williams et al., 1992]) and ARM mobile facility radars in the Niamey airport (about 10km from IRD), thermodynamical profiles from radiosoundings and the corresponding evolution of the observed precipitation rate, $\delta^{18}O_p$ and d_p for the four squall lines are plotted on Figures 4.1 and 4.2. West African squall lines are convective systems aligned roughly in the North-South direction (Figure 4.1a) and propagating westwards. Therefore, assuming that the squall line is stationary, the temporal evolution at the sampling site corresponds to the spatial evolution along a East-West transect of the squall line. In agreement with previous squall line studies (e.g. [Houze, 1977]), the precipitation rate features two maxima corresponding to the convective zone at the front and the stratiform zone at the rear, with a transition zone between these two maxima (Figure 4.2). Only for the 22 August are the convective and stratiform zone not clearly defined.

The amplitude of isotopic variations along each squall line is of the order of 2 to 4 ‰ for $\delta^{18}O_p$ and 10 to 30 ‰ for d_p, demonstrating the strong influence of the different phases of convection on the isotopic composition. At first sight, the isotopic composition exhibits a large variability from one line to another, which is not surprising given the differences in the squall line structures and dynamics, as illustrated by the radar reflectivity patterns (Figure 4.1b). However, squall lines show some consistent features, confirming the robust effect of some convective processes on the isotopic composition. In particular, $\delta^{18}O_p$ exhibits a "W" shape: $\delta^{18}O_p$ decreases at the beginning of the squall line (the range of this decrease is between 0.8 and 3.5 ‰ depending on the squall line), reaching a local minimum at the core of the convective zone. It increases then (between 0.2 and 1.5‰) to reach a local maximum during the transition zone (or just after for 18 August). $\delta^{18}O_p$ decreases along the stratiform zone (between 0.5 and 1.5‰), before increasing again at the end of the squall line (between 0.2 and 1‰). Such a "W" shape was also observed by [Rindsberger et al., 1990] and by [Taupin and Gallaire, 1998] in a Niamey squall line.

The d_p shows different evolutions in the convective zones (increase for the 6 and 18 August, decrease for the 22 August and stable for the 11 August) but some robust features appear in the stratiform zone. It follows a similar pattern as $\delta^{18}O_p$, especially for the 11 and 22 August: it decreases in the first portion of the transition zone (by 7 to 23‰ depending on the squall line), and then increases at the end of the squall line (by 5 to 15‰, except for the 6 August squall line). These features were also observed by [Taupin and Gallaire, 1998].

4.2.3 Preliminary hypotheses

In this section, we present different preliminary hypotheses that may explain the observed evolution of $\delta^{18}O_p$ and d_p along squall lines (Figure 4.4).

Rain reevaporation

In previous studies, evolutions of $\delta^{18}O_p$ and d_p during storms have often been interpreted as the signature of rain reevaporation ([Taupin and Gallaire, 1998]): as rain reevaporates, $\delta^{18}O_p$ increases (since the heavier isotopes concentrate in the condensed phase) and d_p decreases (since HDO diffuses faster than $H_2^{18}O$ out of the drop boundary layer). Reevaporation is stronger where rainfall is weaker and the relative humidity (RH) is lower: at the start, in the transition zone and at the end of the rainfall. This could explain the W shape of $\delta^{18}O_p$. Reevaporation is also higher in the stratiform than in the convective zone ([Zahiri, 2007]), which could explain the decrease of d in the stratiform zone. At the start and at the end of the 6 August squall line, the opposite evolution of $\delta^{18}O_p$ and d_p further supports the role of rain reevaporation. However, reevaporation alone would make $\delta^{18}O_p$ and d_p vary in the opposite direction all along the squall line, in contradiction with the common evolution of $\delta^{18}O_p$ and d_p observed on 11, 18 and 22 August (Figure 4.2). Moreover, the evolution of δD_p and $\delta^{18}O_p$ in the δD vs $\delta^{18}O$ diagram (Figure 4.3) does not follow the classical evaporation line of slope of the order of 4 or 5 expected from the effect of evaporation ([Dansgaard, 1964]). Therefore, this suggests that in addition to rain reevaporation other processes are likely to be involved. We hypothesize in the following a series of processes that might explain the observed evolutions (Figure 4.4).

Condensation height

The evolution of the precipitation composition might be related to that of the condensate that forms the precipitation. The condensate is all the more depleted as it condenses higher in altitude, since the vapor is more strongly depleted by previous condensation at higher altitude due to the lower temperature ([Celle-Jeanton et al., 2004, Gonfiantini et al., 2001]). We expect the condensate to form higher in altitude in the stratiform zone than in the convective zone, since the meso-scale updraft in the stratiform zone is restricted to above the 0°C isotherm approximately ([Houze,

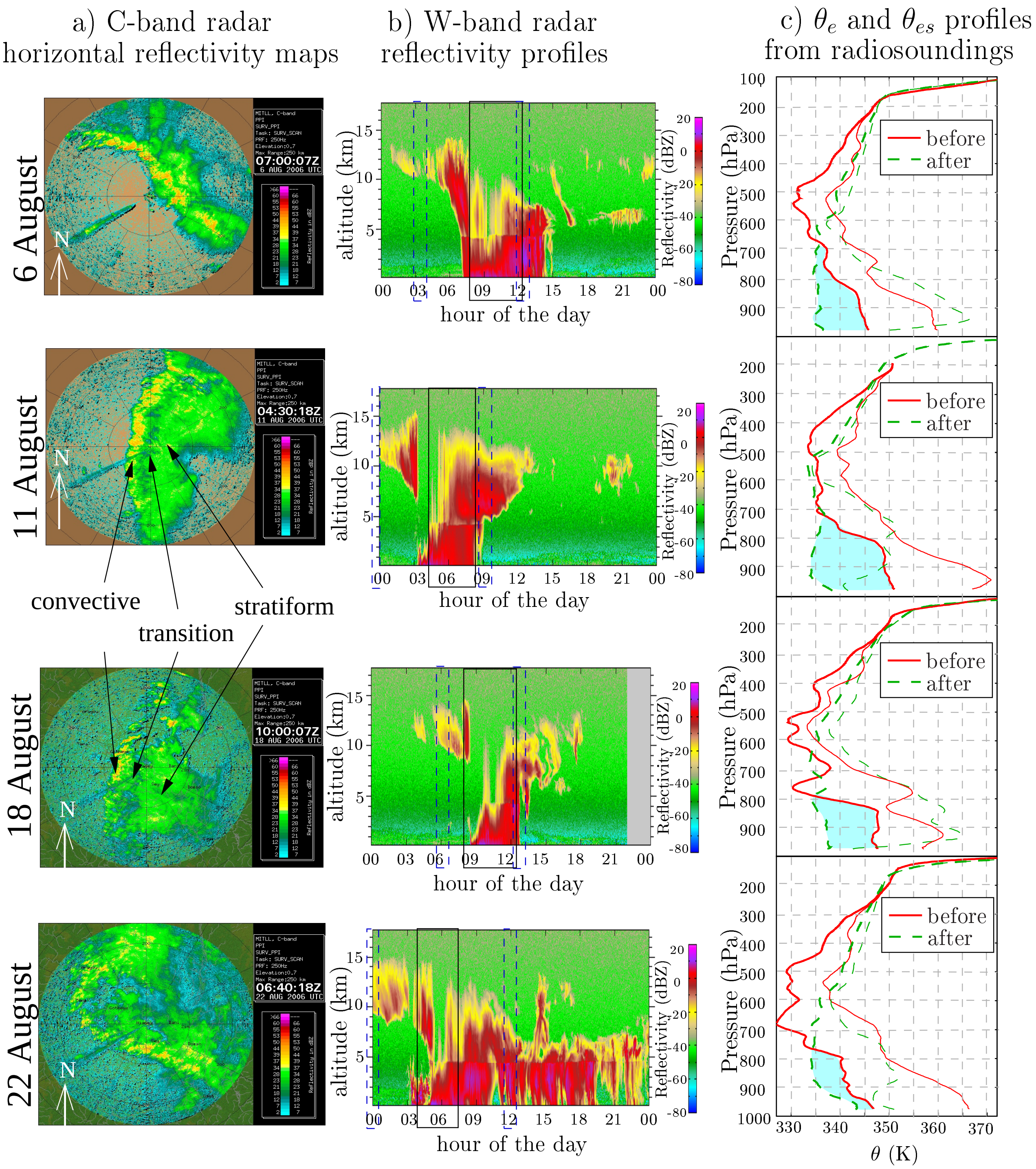

Figure 4.1: (a) snapshots of C-band radar reflectivity maps for the 4 squall lines sampled, obtained by the MIT radar. (b) W-band reflectivity profiles obtained by the ARM radar. (c) Profiles of equivalent potential temperature (θ_e) and equivalent potential temperature at saturation (θ_{es}) from available radiosoundings before (red) and after (green) the systems, giving information about the stabilisation of the atmosphere by the system, notably through unsaturated downdrafts and mesoscale subsidence. The time of the roundiosoundings are indicated in (b) by dotted blue rectangles. A 20 hPa smoothing filter was applied for an easier visualisation. Radiosoundings performed with RS80-A sondes (6 August 03 UTC and 11 August 09 UTC) were corrected following [Nuret et al., 2008]. In (b), the time period over which the rain was sampled is indicated by black solid rectangles.

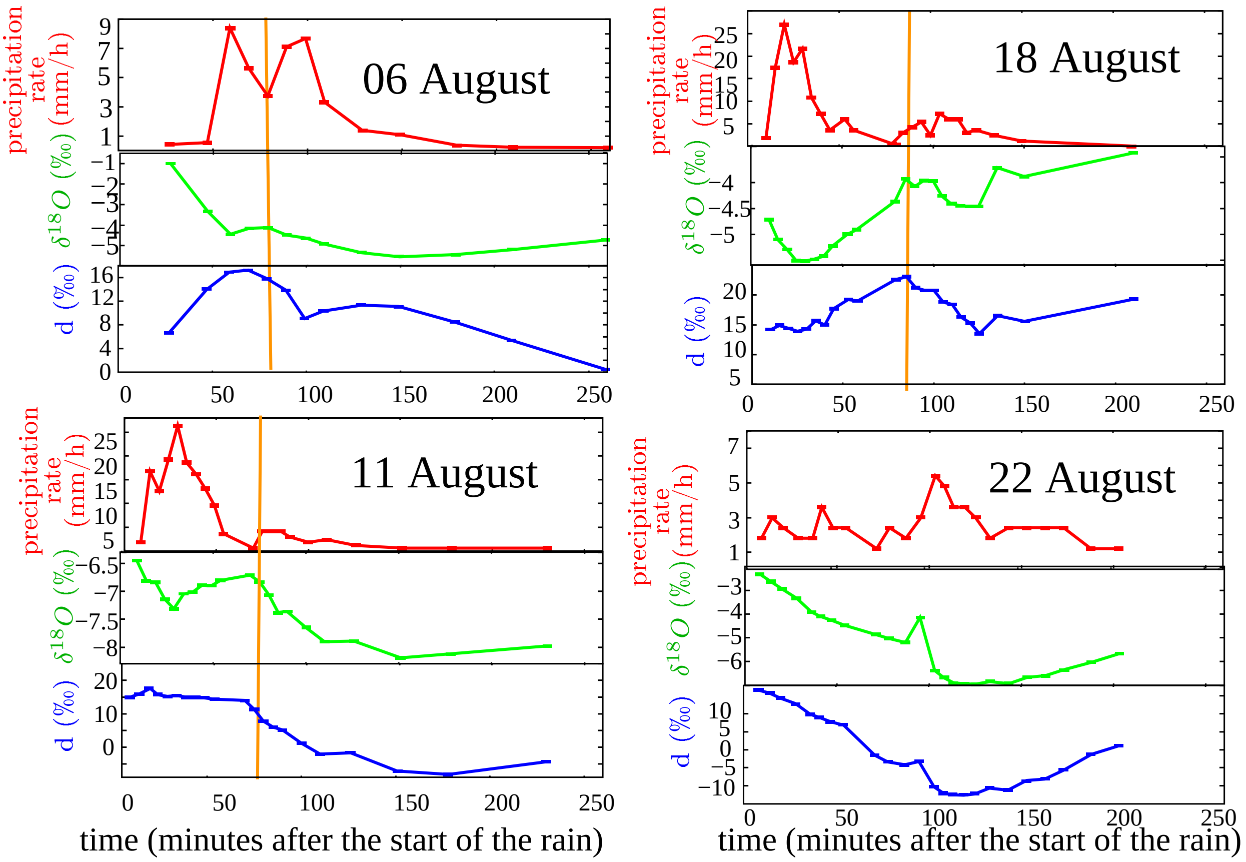

Figure 4.2: Evolution of precipitation rate, $\delta^{18}O$ and d-excess along the 4 squall lines. The orange line indicates the transition zone (defined as the local precipitation minimum between the convective and stratiform precipitation maxim), except for the 22 August squall line for which the transition zone is note obvious.

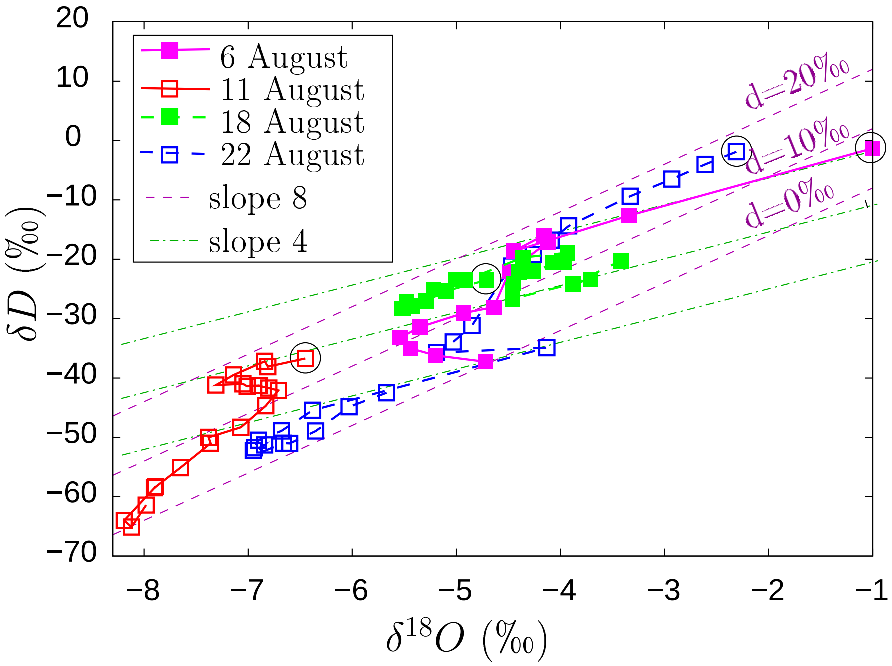

Figure 4.3: Evolution of δD versus $\delta^{18}O$ of the precipitation for the four squall lines sampled. The Meteoric Water line is the lines of slope 8 with d-excess. Traditionally, condensation processes at equilibrium are assumed to follow a line of slope 8 and evaporation processes with kinetic factionation a line of slope 4 ([Dansgaard, 1964]).

1977, Caniaux et al., 1994], whereas the convective updrafts extend throughout the troposphere. This could explain why $\delta^{18}O_p$ is usually lower in the stratiform zone than in the convective zone.

Reequilibration of raindrops with the vapor

As rain falls, it partially reequilibrates isotopically with the surrounding vapor through diffusive exchanges. This process is all the more efficient as RH is high ([Stewart, 1975]). Through this process, variations in the composition of the low-level vapor can be transmitted to the precipitation. The following two points are possible reasons for such variations in the low-level vapor composition.

Meso-scale subsidence

Owing to fractionation during condensation, vapor is all the more depleted as altitude increases. Therefore, a subsiding vapor is all the more depleted as it originates from higher in in altitude. In squall lines, the mesoscale downdraft, combined with the rear-to-front flow, advects depleted vapor down to low-levels under the stratiform zone. Reequilibration of the rain with a more depleted vapor might explain the lower $\delta^{18}O_p$ in the stratiform zone observed in most squall lines.

Through this process, the $\delta^{18}O_p$ should decrease more strongly after the transition zone in squall lines for which the mesoscale subsidence at the rear is the strongest. To test this hypothesis, we estimate qualitatively the strength of the subsidence by analyzing profiles of equivalent potential temperature (θ_e) before and after the systems (Figure 4.1c): since θ_e is minimum in the mid-troposphere before the arrival of the systems, a strong decrease of θ_e in the lower troposphere suggests a strong subsidence ([Zipser, 1977, Chalon et al., 1988]). The 11 August squall line, which features a strong $\delta^{18}O_p$ decrease by 1.5‰ from the transition zone to the minimum in the stratiform zone, also exhibits a strong θ_e decrease extending up to 700 hPa. Conversely, the 18 August squall line, featuring a weak $\delta^{18}O_p$ decrease of only 0.4‰, exhibits a weaker θ_e decrease restricted to below 800 hPa. The 6 August squall line is intermediate, with a $\delta^{18}O_p$ decrease by 1.4‰ and a θ_e decrease extending up to 700 hPa but weaker than for the 11 August. This comparison between the squall lines suggests that the subsidence effect on $\delta^{18}O_p$ could be substantial.

Besides, low RH at low-levels associated with subsidence, leads to lower d_p through rain reevaporation. This could explain the parallel decrease of $\delta^{18}O_p$ and d_p observed after the transition zones.

Vapor modification through interaction with the rain

As raindrops reevaporate or reequilibrate isotopically with the vapor, the composition of the latter is modified. In squall lines, as low-level air flows from rear to front, it is exposed to rain reevaporation and gets more and more affected by diffusive exchanges and rain reevaporation.

For strong rates of rain reevaporation, the vapor resulting from rain reevaporation is richer than the vapor at low-level, since its composition tends towards that of the rain when the reevaporation is close to total. As an idealized example, using the module of isotopic fractionation during rain reevaporation of [Bony et al., 2008], we calculate that at 70% relative humidity, the reevaporation of a droplet of $\delta^{18}O = -15‰$ into a vapor of $\delta^{18}O = -20‰$ (respectively $-25‰$) enriches the vapor if the reevaporated fraction exceeds 70% (respectively 40%). The reevaporated fraction above which the vapor gets enriched by evaporation is all the lower as the relative humidity is high and as the vapor is more depleted compared to the rain.

For low evaporation rates, on the contrary, diffusive exchanges dominate over rain reevaporation. In these conditions, the vapor might get more and more depleted by the interaction with the rain ([Gedzelman et al., 2003, Lee and Fung, 2008]).

[Zahiri, 2007] calculated reevaporation rates of 40 to 70% in the stratiform regions of Sahelian squall lines, suggesting the rain reevaporation rather enriches the vapor in squall lines, in particular in stratiform zones.

In addition, the vapor from the rain reevaporation has a higher d, since HDO diffuses faster than $H_2^{18}O$. Therefore, $\delta^{18}O$ and d in the vapor both increase as the air moves frontwards and is humidified by rain reevaporation. In turn, the composition of the vapor affects the composition of the subsequent rain by isotopic equilibration (section 4.2.3). This would explain the simultaneous decrease of $\delta^{18}O_p$ and d_p rearwards along the stratiform zone after the transition zone, which is particularly visible on 11 and 22 August.

In the next section, we evaluate the relative contributions of these different processes in two-dimensional simulations of the 11 August squall line.

4.3 Detailed analysis of the 11 August 2006 squall line using a 2D model

The restitution of the 3D wind field by [Chong, 2009] for the 11 August 2006 squall line, combined with a simple 2D model, offers a unique opportunity to evaluate the contribution of the aforementioned hypotheses. The 2D model allows us to simulate both the microphysical and isotopic properties of the squall line. Although this model does not accurately simulate the observed isotopic evolution given its simplicity (incorporating isotopes in a Cloud Resolving Model CRM might be necessary for a more accurate prediction), we use it to investigate the processes controlling the isotopic composition of precipitation.

4.3.1 Model description

Model physics, boundary conditions and numerical solution

The model represents the transport and microphysics in a 2D (altitude-longitude) framework and we assume that the squall line is stationary. The model is inspired by the microphysical retrieval technique of [Hauser et al., 1988], though simplified. The water vapor, cloud water and rain are advected in the 2D domain by 2D winds using an upstream advection scheme. Vapor condenses as soon as it reaches saturation. Microphysical processes are parametrized by the Kessler scheme ([Kessler, 1969]) using the same parameters as [Hauser et al., 1988]. The model also includes a representation of diffusion to ensure numerical stability.

West and East boundary conditions for RH are the 30 minutes-averaged ARM profiles before and after the squall line (01 UTC and 09 UTC respectively) below 10km and NCEP profiles at 06

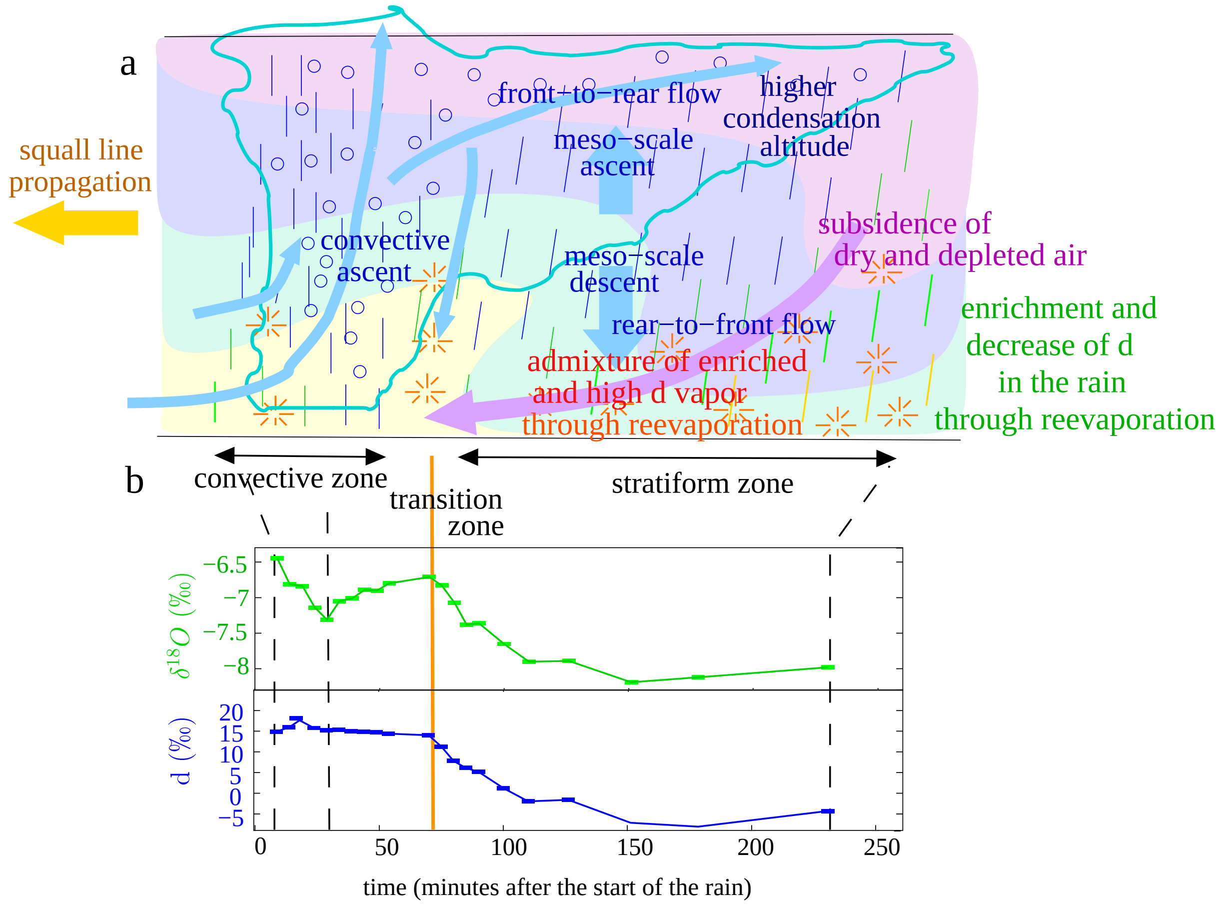

Figure 4.4: (a) Conceptual scheme illustrating the different mechanisms controlling the isotopic evolution along squall lines: condensation altitude, modification of the rain and low-level vapor by rain reevaporation and diffusive exchanges and subsidence of depleted air. See section 4.2.3 for more details. (b) evolution of $\delta^{18}O$ and d-excess for the 11 August squall line.

UTC above this altitude. Temperature and pressure are assumed to be horizontally homogeneous and are taken from the ARM profiles at 01 UTC below 10km and from the reanalyses at 06 UTC above 10km. Our results are not significantly sensitive to the representation of horizontal temperature perturbations (section 4.3.4). We neglect air and water fluxes throughout the bottom and top boundaries, but a sensitivity test to the addition of surface evaporation is presented in section 4.3.4.

Contrary to [Hauser et al., 1988], we calculate here the stationary solution by a temporal integration, because it facilitates the subsequent implementation of water isotopes. The advection, diffusion and microphysical processes are evaluated every 30s until reaching a steady state, after about 15 hours. The model is initialized with the profiles of the West boundary conditions.

Wind fields

The 3D wind were retrieved following the procedure described in [Chong, 2009], using a squall line propagation speed of 13.7 m/s. The wind field is highly variable in the along-line dimension, consistently with the high spatial and temporal variability pointed out by [Lafore et al., 1988]). We force the advection scheme with 2D winds obtained by averaging the 3D winds in the along line (South-North) direction over different domains (Figure 4.5). Missing values are filled using a Cressman interpolation scheme as in [Hauser et al., 1988]. Winds are slightly modified so that they respect the conservation of air mass given the 2D framework and the prescribed temperature and pressure profiles. The along-line wind component is neglected. Such 2D winds are represented on Figure 4.6a and b. Note that the domain is 122 km in the across line direction and does not capture completely the rear of the squall line. However, extending the domain by 100 km using additional wind profiles in the rear of the squall line has no influence on our results.

Representation of isotopic processes

Isotopic species are transported passively by advection and diffusion, but a fractionation is introduced at each phase change. The implementation of fractionation during condensation, evaporation and diffusive exchanges are detailed in [Bony et al., 2008]. It is similar to that used in most isotopic General Circulation Models (e.g. [Jouzel et al., 1991, Hoffmann et al., 1998, Noone and Simmonds, 2002b, Lee et al., 2007, Tindall et al., 2009]) except for rain reevaporation: we calculate explicitly the degree of equilibration between rain and vapor and take into account the concomitant evolution of both rain and vapor compositions throughout the evaporation process ([Bony et al., 2008], appendix D.2).

The isotopic boundary and initial conditions are Rayleigh distillation profiles, which represent the effect of previous condensation and precipitation:

$$R_v(z) \sim R_{v0} \cdot \left(\frac{q_{sat}\,(z)}{q_{v0}} \right)^{\alpha - 1}$$

where $R_v(z)$ is the profile of isotopic ratio in the vapor, R_{v0} and q_{v0} are the isotopic ratio and the specific humidity at the lowest level (0-500 m), $q_{sat}(z)$ is the saturation specific humidity at the temperature of level z and α is the effective fractionation (including kinetic fractionation) at the same temperature. We take $\delta^{18}O_{v0} = -15‰$ and $d_{v0} = 10‰$ to yield $\delta^{18}O_p$ and d_p of the same order of magnitude as those observed (the evolution of $\delta^{18}O_p$ and d_p is insensitive to these values). Sensitivity to the Rayleigh assumption will be discussed in section 4.3.4.

4.3.2 Model results

Given the strong along line variability in the wind field, we consider various cross-line transects of the squall line (Figure 4.5). Rather than trying to reproduce exactly the observed isotopic evolution, we explore the different dynamics based on a single squall line, as a “proxy” for different squall lines. Figure 4.6 shows five of these simulations, representative of the variability range of the results. The goal is to extract the robust and consistent features among the different simulations, as well as exploring the along-line variability.

The simulated precipitation (Figure 4.6e) is of the same order of magnitude as in observations (Figure 4.2), and with similar evolutions: the model simulates a maximum corresponding to the convective zone and a secondary maximum corresponding to the stratiform zones. The simulated 2D fields of relative humidity (Figure 4.6c), cloud water content (Figure 4.6d), condensation, precipitation and evaporation rates (not shown) are consistent with fields retrieved by the unidimensional method of [Chong, 2009] for this same squall line. More generally, these fields are consistent in patterns and in magnitude with fields for other squall lines retrieved by the more sophisticated method of [Hauser et al., 1988] or simulated by 3D models ([Caniaux et al., 1994, Lafore et al., 1988]). The physics of the squall line are thus reasonably well captured by the 2D model, and can thus be used to investigate isotopic controls.

The isotopic evolution of the precipitation is very sensitive to the squall line dynamics: for the same microphysical model and the same squall line, along-line wind variations induce a strong variability in the shape of the isotopic evolution, especially in $\delta^{18}O_p$ (Figure 4.6f). However, all simulations share the same robust features observed for the different squall lines (section 4.2.2), i.e. the W shape of the $\delta^{18}O_p$ evolution and the decrease of d_p.

The different simulations also span the variability observed for the different squall lines samples: the domain 2, for example, features in addition to the W shape an increasing trend of $\delta^{18}O$ of about 1‰ from the convective precipitation maximum to the stratiform precipitation maximum, as observed for the 18 August squall line. On the other hand, the other domains feature decreasing trends spanning from 1 to 4 ‰, in the range of the other observed squall lines. The d_p decrease in the first part of the stratiform zone is well reproduced in all simulations (Figure 4.6g). However, the re-increase of d_p at the end of the squall line is never simulated. Besides, none of the simulations were able to reproduce the particular d_p pattern of August 18, suggesting that the dynamics or microphysics of this line were particular.

4.3.3 Processes controlling the isotopic composition in the model

Although the exact isotopic evolution of the 11 August squall line was not reproduced, the simulated isotopic features are consistent with the observations, and the simulated along-line isotopic variability is comparable to the variability observed among squall lines. We now use the model to explore what processes, among the ones described in section 4.2.3, control these isotopic evolutions.

Control on precipitation $\delta^{18}O$

The evolution of $\delta^{18}O_p$ (Figure 4.7c) has no similarities with the evolution of the $\delta^{18}O$ of the condensate from which the precipitation originates ($\delta^{18}O_c$, i.e. vertically-averaged $\delta^{18}O$ of the condensate weighted by the rate of conversion to precipitation, Figure 4.7b). Variations in $\delta^{18}O_c$ thus do not yield any visible variations in $\delta^{18}O_p$, suggesting that processes controlling $\delta^{18}O_c$ (such as condensation height) have little influence on $\delta^{18}O_p$. On the contrary, $\delta^{18}O_p$ tightly follows the $\delta^{18}O$ of the low-level vapor (between 0 and 500m, hereafter $\delta^{18}O_v$, 4.7d), suggesting that the precipitation reequilibrates isotopically as it falls, “forgetting” its condensation history.

To check this hypothesis and to interpret the isotopic ratio in the precipitation, R_p, simulated by the 2D model, we use a deliberately simple equation ([Stewart, 1975], appendix C.3):

$$R_p = R_{l0} \cdot f_r^{\beta} + \gamma \cdot R_v \cdot \left(1 - f_r^{\beta}\right) \tag{4.1}$$

where R_v is the simulated isotopic ratio in the lowest-level vapor, f_r the simulated vertically-integrated fraction of the rain that remains after reevaporation (Figure 4.7e), R_{l0} the composition of the condensate that forms the precipitation and β and γ coefficients depending on low level RH (defined by [Stewart, 1975] and recalled in appendix A of [Bony et al., 2008]). This equation 4.1 is a strong simplification of processes represented in the 2D model: the goal here is to reproduce the modeled results with as simple an equation as possible, to identify the dominant processes. First, we assume that R_v varies little as evaporation proceeds, neglecting feedbacks of reevaporation on R_v ([Stewart, 1975]). Second, we assume that the composition of the condensate forming the precipitation is constant ($\delta^{18}O_c = -15$‰, corresponding to the average values in the simulations), so as to check that variations in $\delta^{18}O_c$ are not a dominant control on $\delta^{18}O_p$. Third, we consider only the vertically-integrated f_r and take R_v and RH at the lowest level only, whereas reevaporation is treated at all vertical levels in the 2D model.

This equation is able to reproduce well the $\delta^{18}O_p$ evolution simulated by the 2D model (Figure 4.7c), showing that variations in the condensate composition has little influence on $\delta^{18}O_p$. Rather, rain reevaporation and isotopic equilibration with the vapor are key controls of $\delta^{18}O_p$. $\delta^{18}O_p$ is actually very close to isotopic equilibrium with the vapor (Figure 4.7c), in agreement with [Lee and Fung, 2008] who simulated a degree of rain-vapor equilibration above 70% over the tropics. Therefore, the understanding of the $\delta^{18}O_p$ requires the understanding of what controls $\delta^{18}O_v$. This is discussed below.

Control on vapor $\delta^{18}O$

The vapor at low-levels in the 2D model is a mixture of vapor originating from rain reevaporation and vapor advected from different levels. In section 4.2.3, we hypothesized that rain reevaporation and subsidence could influence the low-level vapor composition. To evaluate these two hypotheses, we implemented a method to track the vapor origin in the 2D model, as detailed in appendix H.3. This method allows us to estimate: (1) the fraction of the vapor that originates from rain reevaporation or advection from different levels, and (2) the isotopic composition of air parcels originating from rain reevaporation ($\delta^{18}O_e$) or advection by the dynamics ($\delta^{18}O_{dyn}$).

Since the two sources of vapor are rain evaporation and advection by the dynamics (and more particularly by subsidence), the evolution of $\delta^{18}O_v$ is intermediate between the evolutions of $\delta^{18}O_e$ and $\delta^{18}O_{dyn}$(Figure 4.7d). For domain 4, the 11‰ decrease in $\delta^{18}O_v$ along the line is driven by the 16‰ decrease of $\delta^{18}O_{dyn}$. Since any departure of $\delta^{18}O_{dyn}$ from the boundary value of −15‰ is entirely due to the subsidence, this demonstrates the impact of subsidence on $\delta^{18}O_v$. More generally, the role of the dynamics is dominant in all the domains in which the $\delta^{18}O_p$ features a strong depletion (more than 5‰) from the convective to stratiform zone (not shown). For the other domains, the evolution of $\delta^{18}O_v$ follows more closely the evolution of $\delta^{18}O_e$ and is thus primarily affected by rain reevaporation. For example, in domain 1 the 2‰ variations in $\delta^{18}O_v$ around the transition zone is due to the 3‰ variation in $\delta^{18}O_e$.

In the following paragraphs, we detail what controls the evolution of $\delta^{18}O_{dyn}$ and $\delta^{18}O_e$.

The method to track the vapor origin in the 2D-model allows us to estimate the average maximum altitude reached by low-level parcels during their transport through the squall line (appendix H.3). The maximum altitude $\overline{z_{max}}$ that parcels have undergone is equivalent to the minimum temperature encountered (since we neglect horizontal temperature perturbations) and thus represents the maximum depletion undergone by the parcels as they condense during their ascent. The $\overline{z_{max}}$ altitude thus controls, at first order, the composition of the subsiding vapor, in an analogous way as the minimum saturation temperature encountered controls the relative humidity of subsiding vapor ([Pierrhumbert and Roca, 1998]). Indeed, as shown in Figure 4.7d (dashed), a simple Rayleigh distillation predicts well the composition of the vapor advected by the dynamics $\delta^{18}O_{dyn}$:

$$R_{dyn} \sim R_{v0} \cdot \left(\frac{q_{sat}\left(\overline{z_{max}}\right)}{q_{v0}} \right)^{\alpha - 1}$$

where R_{v0} and q_{v0} are the composition and the specific humidity of the boundary vapor at low levels, and α the effective isotopic fractionation. Note that this equation neglects the effect of cloud and rain reevaporation on the vertical isotopic profiles.

Due to the squall line dynamics (meso-scale downdraft and rear-to-front flow), $\overline{z_{max}}$ increases from the convective to the stratiform zone. For domain 4, $\overline{z_{max}}$ increases from 0 km at the beginning of the line (no subsidence) to 2.5km in the stratiform zone, leading to the strong decrease of $\delta^{18}O_{dyn}$ (from −15 to −31‰) and thus that of $\delta^{18}O_v$ (−15 to −22‰) and $\delta^{18}O_p$ (−4 to −12‰). This confirms the importance of meso-scale subsidence in the control of the isotopic composition of the vapor and precipitation along squall lines.

On the other hand, the composition of the reevaporated vapor ($\delta^{18}O_e$) follows the evolution of the reevaporated fraction f_{revap}. Indeed, the higher f_{revap}, the more enriched the vapor from the rain reevaporation. As expected from section 4.2.3, the rain reevaporation is generally more enriched than the vapor, by 1 to 4‰. In addition to the effect of f_{revap}, the evolution of $\delta^{18}O_e$ is modulated by how the squall line dynamics transports the reevaporated vapor.

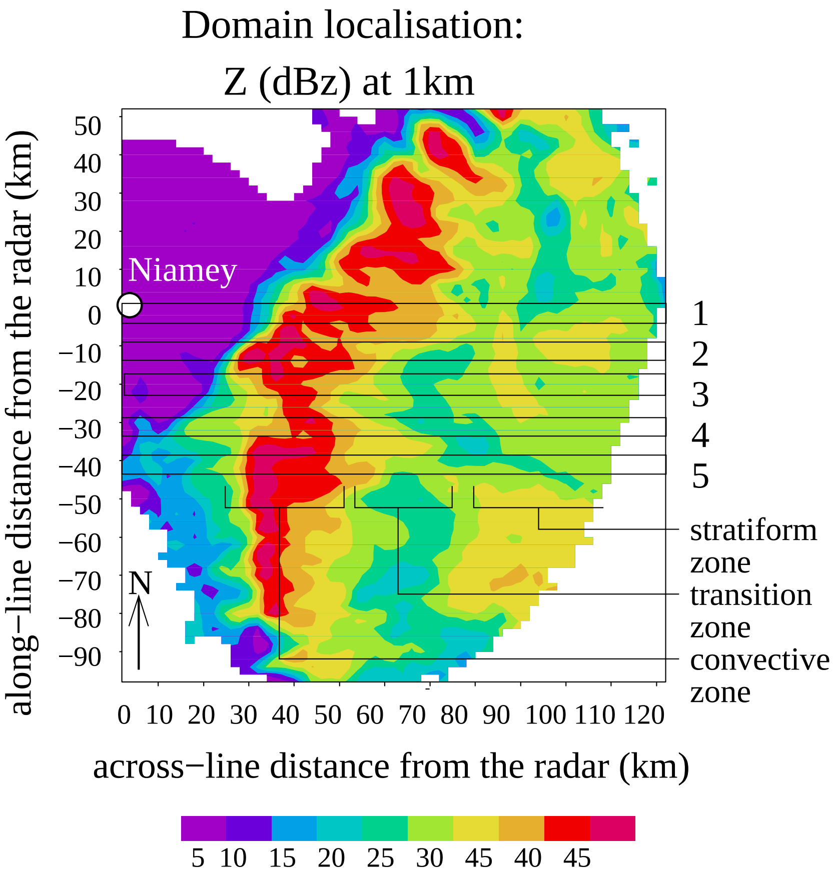

Figure 4.5: Horizontal reflectivity map from the MIT radar at 1km on 11 August 2006 between 0241 and 0311 UTC, in the domain of the 3D wind retrieval extending over 120 and 150 km in the west-east and south-north directions, respectively. The 5 domains selected for out analyse in figures 4.6 and 4.7. are indicated. The position of Niamey (x=0 km, y=0 km) is indicated by a white dot.

To conclude on the control of $\delta^{18}O_p$ in the 2D model, $\delta^{18}O$ in vapor and thus in precipitation are controlled by two processes: (1) meso-scale subsidence of depleted air and (2) admixture of vapor arising from the reevaporation of the falling rain and transported by the squall line dynamics. Note that the controls on low-level RH are very similar: subsidence brings dry air downwards, while evaporation moistens this air as it moves frontwards under the stratiform region.

Control on precipitation deuterium excess

The evolution of deuterium excess in precipitation (d_p) follows very tightly that of low-level (0-500m) RH (Figure 4.7f and g). d_p thus seems to be mainly controlled by RH during rain reevaporation: the lower the RH, the more dominant kinetic fractionation is relatively to equilibrium fractionation, thus the lower the d_p. The good prediction of the d_p evolution by equation 4.1 (4.7g dashed), which includes the effect of low-level RH, confirms that reevaporation is the key control on d_p.

The linear correlation coefficient between the evolution of d_p and low-level RH (where the precipitation is significant: >0.5mm/h) varies from 0.90 to 0.97 for the different domains (not shown). The relationship d_p-RH is robust, with a slope ranging from 0.30 to 0.37 ‰/%. In our model, d_p is thus an excellent indicator of the RH. However, this d_p-RH relationship cannot be checked with observations, because although we do have RH measurements at the surface along the squall line sampled, the RH at the surface does not accurately reflect the low-level RH that affects the isotopic composition of the rain.

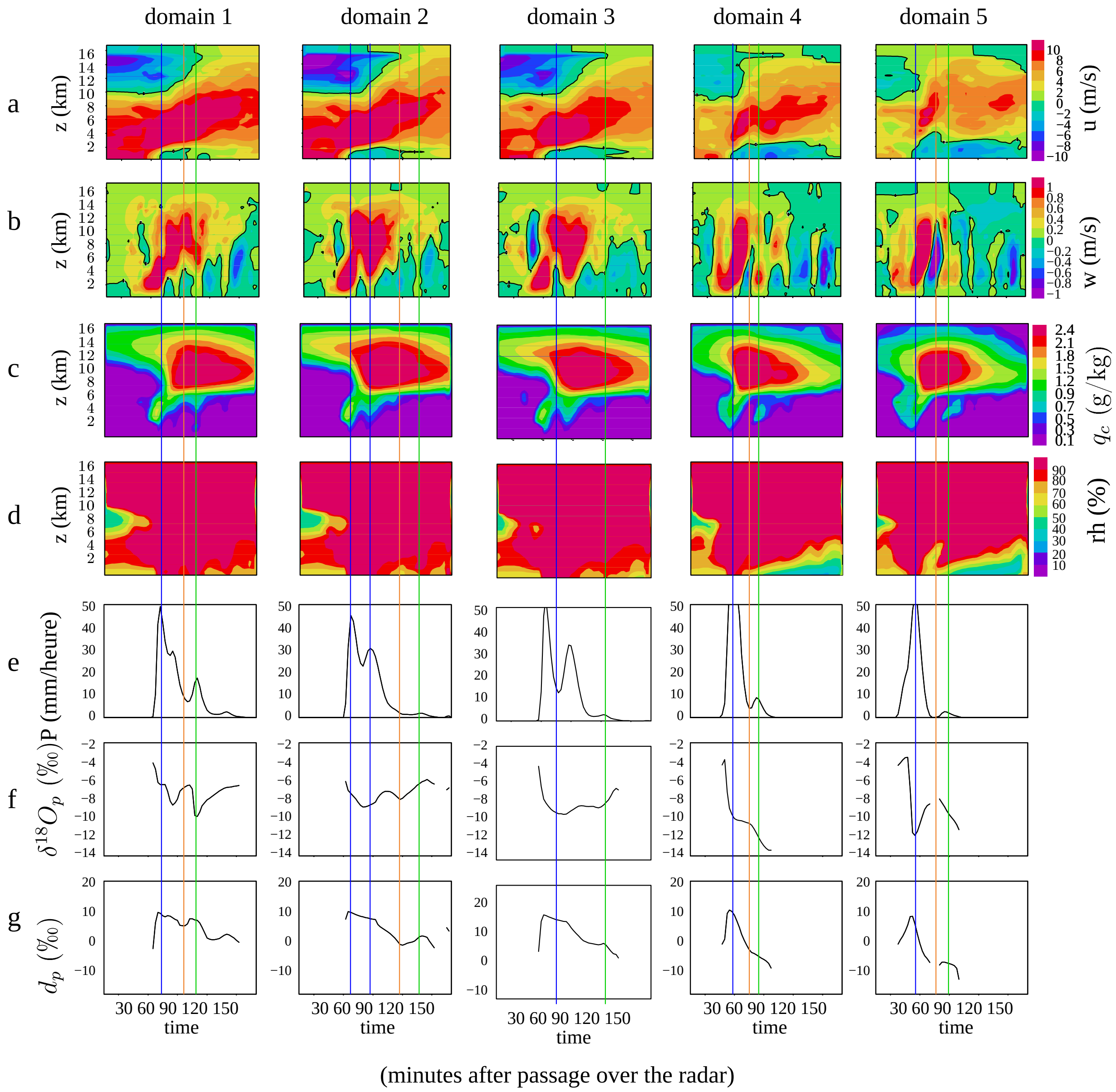

Figure 4.6: Five examples of simulations along different across-line transects of the 11 August 2006 squall line. (a) and (b): across-line and vertical wind components of the 2D wind field used to force the model; the zero isoline is highlighted. (c) simulated condensate water content (both liquid and ice). (d) Simulated relative humidity. (e), (f) and (g): simulated evolution of the precipitation rate, $\delta^{18}O$ and d-excess. The different domains are shown in figure 4.5. The vertical lines indicate the position of the convective cores (blue), transition zones (orange) and stratiform precipitation maxima (green).

4.3.4 Sensitivity tests to dynamics, microphysics and isotopes

We discuss below the sensitivity of our results to different assumptions done in our model.

Horizontal temperature perturbations

We neglect horizontal perturbation in the 2D model, whereas [Hauser et al., 1988] evaluated temperature perturbations of the order of -4K in the rear-to-front flow. Decreasing the temperature by about 4K in the rear-to-front flow slightly increases locally the relative humidity by 10%, increases $\delta^{18}O_p$ by 2‰ and the d_p by about 5 ‰. However, it does not change qualitatively the isotopic evolution.

Rayleigh assumption

In nature, isotopic profiles in the upper troposphere are usually more enriched than predicted by a Rayleigh distillation due to convective detrainment (e.g. [Moyer et al., 1996, Dessler and Sherwood, 2003, Webster and Heymsfield, 2003, Bony et al., 2008]). Here we consider Rayleigh distillation as West and East boundary conditions. However, modifying the isotopic profile at upper levels does not affect much our results: when assuming that 50% of the condensate formed during the Rayleigh distillation is detrained rather than instantaneously precipitated (leading to an enrichment of up to 70‰ at 16km), $\delta^{18}O$ only increases by 1 to 2 ‰ in the stratiform zone.

Microphysics

We also performed sensitivity tests to microphysics (not shown). Little isotopic sensitivity was found to Kessler parameter variations, even though the precipitation evolution was sometimes deeply distorted. This confirms that the dynamic control dominates. The isotopic parameter ϕ (controlling the intensity of kinetic effects during evaporation, [Bony et al., 2008], appendix D.2) was the only isotopic parameter to have a significant sensitivity. When $\phi = 0$ (strong kinetic effects), $\delta^{18}O_p$ is increased by 3 ‰ and d_p is decreased by 10 ‰ at the start and the rear of the squall line, where evaporation is the strongest and the atmosphere the driest. This confirms that the details of the parametrization of the isotopic behavior during reevaporation is crucial in dry conditions. However, this parameter had little influence on the evolution in the convective and stratiform zones.

The drop size distribution has been shown to influence the isotopic evolution of the rain as it reevaporates ([Lee and Fung, 2008]). However, taking into account explicitly the effect of the drop size distribution, rather than assuming homogeneous drop sizes, has little influence on our 2D model results. In our model, the rain drop size distribution influences the reevaporated fraction f_{revap}, since smallest drops would reevaporate totally whereas the largest drops conserve most of their mass. In a sensitivity experiment, the drop size distribution was determined by the Kessler microphysics scheme ([Kessler, 1969]) and isotopic calculations were performed in each of 40 size bins. The results were virtually unchanged, except in extremely dry reevaporation conditions. For example, for $f_{revap} = 80\%$ and $h = 50\%$, $\delta^{18}O_p$ was decreased by 2‰ and d_p was increased by 1‰ when taking into account the drop size distribution.

Surface evaporation

None of our simulations is able to reproduce the d_p increase observed at the end of most squall lines. A possible interpretation might be the reevaporation of the water accumulated on the soil, neglected in our model, which would increase d_v and thus d_p by reequilibration of raindrops with the vapor. To check this hypothesis, we performed simulations in which we added surface evaporation, calculated by a simple Penman-like equation (appendix H.4). A large uncertainty in this calculation is the net radiation minus soil heat flux, $R_n - G$, under the heavy cloud cover of a squall line. Therefore, we performed tests with different values for $R_n - G$. As justified in appendix H.4, we take $R_n - G = 150W/m^2$ as an upper bound for a midday squall line, and $R_n - G = 0W/m^2$ for a night time squall line.

For $R_n - G = 150W/m^2$ (midday), the resulting evaporation reaches maxima of 6 mm/day in the stratiform zone for domains with very dry air in the stratiform zone (domains 4, 5), and 3 mm/day for domains with wetter air (domains 1, 2). For $R_n - G = 0W/m^2$ (night), the evaporation peaks at 2 mm/day. The moistening effect of surface evaporation is very small. It is maximum for squall lines with dry stratiform regions (domains 4 and 5) at midday, but the relative humidity is increased only 4 to 6%. This is because the surface evaporation flux under the squall line is much smaller than the vapor flux from advection, due to the small spatial scale of the squall line.

The effect on $\delta^{18}O_p$ is negligible (always lower than 1‰). The d of the evaporation flux, d_{sfc}, is highly sensitive to kinetic fractionation formulation. Taking [Mathieu and Bariac, 1996]'s formulation for a saturated soil, d_{sfc} is 140‰ higher than d_v. The d_v is increased by 7‰ at midday in dry stratiform zones, but only by 2-3‰ in wetter stratiform zones at midday and by less than 1‰ during the night. This effect of surface evaporation on d_v is almost totally transmitted to d_p. The transmission of the d_v anomaly to d_p is by rain reequilibration with the vapor, since the vapor from surface evaporation is only confined to low-levels due to the subsidence in the stratiform zone.

Therefore, the effect of surface evaporation on d_p may be significant for dry stratiform zones at midday. However, the increase of d_p at the end of the 22 August stratiform zone by 15‰ presumably does not result from surface evaporation only. Since the 11 August squall line occurred mainly during night time, the 5‰ increase in d_p is not attributable either to surface evaporation only.

4.4 Summary and conclusion

4.4.1 Summary

This paper presents the evolution of precipitation $\delta^{18}O$ and d along different squall lines observed in the Sahel during the AMMA campaign. Despite a large variability in the isotopic evolution among the different squall lines, some robust features appear, such as the W shape of the $\delta^{18}O_p$ and the decrease of d_p in the stratiform region. Several processes may a priori contribute to such evolutions, such as the condensation altitude, modifications of the rain composition as it reevaporates during its fall, and variations of the composition of the vapor with which the rain reequilibrates, due either to subsidence or to the interaction with the falling rain.

To test these hypotheses and explore the relative contributions of the dynamics and the microphysics of the squall line to the evolution of the isotopic composition of the rain, a simple 2D model of transport and microphysics forced by observed wind fields was developed. The 2D model run on various along-line transects is able to simulate isotopic evolutions consistent with observations and with a comparable amplitude of variability. In the model, $\delta^{18}O_p$ is mainly controlled by (1) the squall line dynamics: meso-scale subsidence in the stratiform portion of the system advects depleted water vapor downward and the horizontal flows redistribute this vapor in the low levels; and (2) the reevaporation of the rain, which moistens the low-level vapor and affects its composition.

4.4.2 What can we learn from water isotopes about squall lines?

The robust features of the evolution of $\delta^{18}O_p$ and d_p along squall lines demonstrate the strong influence of convective processes on the isotopic composition. $\delta^{18}O_p$ is particularly sensitive to both the squall line dynamics and rain reevaporation processes, and could thus provide some integrated information about the dynamics within the squall line (e.g., the vertical Lagrangian excursions of the air parcels). On the other hand, d_p is a more direct tracer of rain reevaporation, and the 2D model suggests a very robust relationship between d_p and relative humidity of the air at low levels. If incorporated into a CRM, water stable isotopes could thus serve as a tool to validate the squall line dynamics or the recycling of water through rain reevaporation.

4.4.3 Implication for the control of the composition of tropical precipitation on larger scales

One of the goals of this study was to better understand the effect of convective processes on the composition of tropical precipitation. [Risi et al., 2008a], in very different conditions (single column model over ocean) suggested that the effect of condensation processes was relatively small compared to the effect of two other processes, namely (1) rain reevaporation, enriching the rain drops as they fall, and (2) meso-scale subsidence of higher altitude vapor, depleting the low-level vapor. The

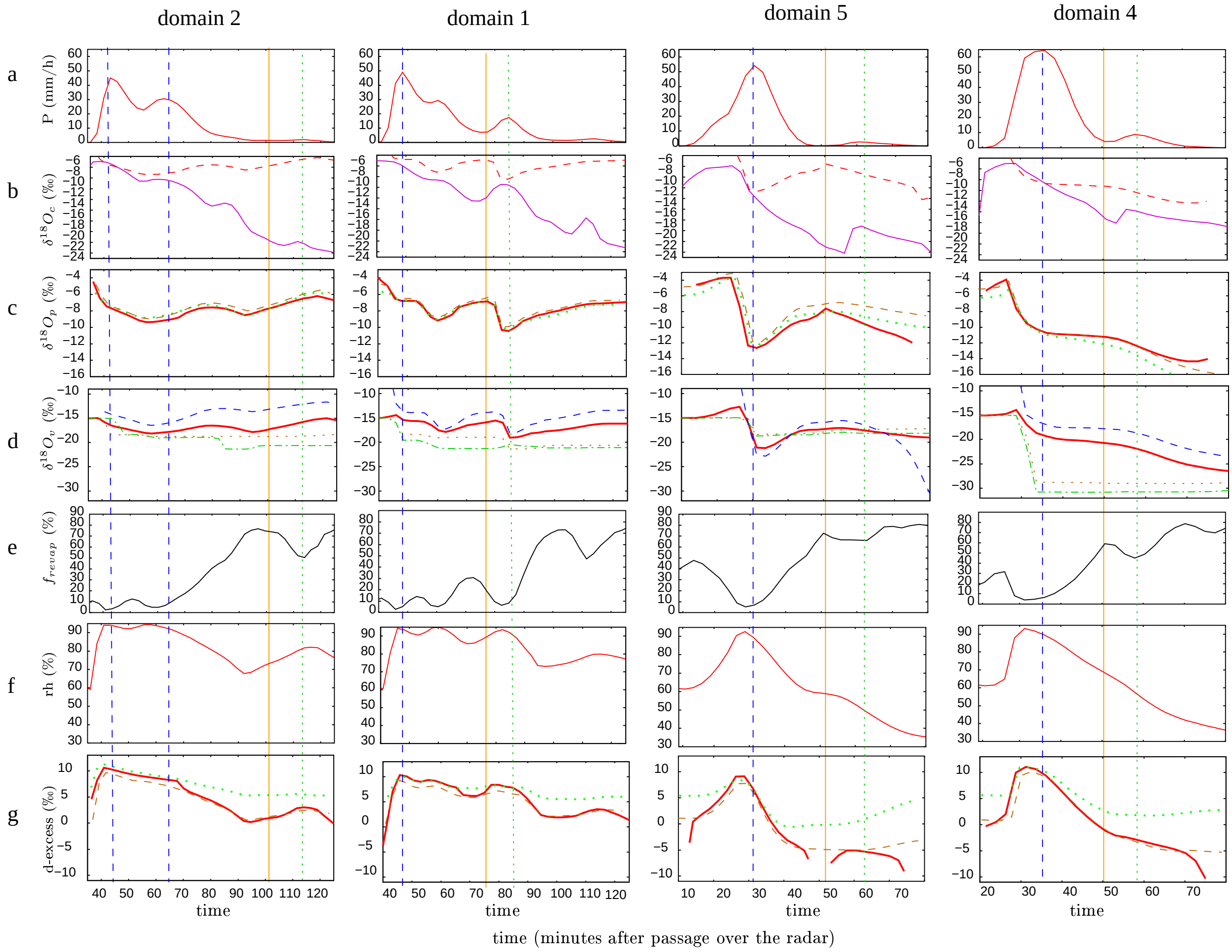

Figure 4.7: Evolution of some simulated characteristics illustrating what controls the isotopic evolution along the squall line in the model: (a) precipitation rate. (b) $\delta^{18}O$ of the condensate forming the precipitation (solid purple). The $\delta^{18}O$ of the precipitation is shown in dashed red for comparison. (c) $\delta^{18}O$ of the precipitation simulated by the 2D model (solid red) and predicted by the simple reevaporation equation 4.1 (dashed brown). The liquid in equilibrium with the lowest-level vapor is shown in dotted green. (d) $\delta^{18}O$ of the vapor at the lowest-level of the model: total vapor simulated by the model (solid red), vapor originating from rain reevaporation in the model (solid blue) and vapor advected from the different levels (solid green). The vapor predicted by a Rayleigh distillation using the maximum altitude undergone $\overline{z_{max}}$ is shown in dashed green. (e) fraction of the rain reevaporated. (f) relative humidity at lowest level. (g) d-excess of the precipitation simulated by the 2D model (solid red) and predicted by the simple reevaporation equation 4.1 (dashed brown). The liquid in equilibrium with the lowest-level vapor is shown in dotted green. As in figure 4.6, the vertical lines indicate the position of the convective cores (blue), transition zones (orange) and stratiform precipitation maxima (green).

little effect of condensation processes is confirmed in this study: as the rain drops reequilibrate with the low-level vapor, they totally "forget" the effect of condensation processes, in agreement with [Lee and Fung, 2008]. This study also confirms the strong effects of rain reevaporation (especially on d_p) and of meso-scale subsidence (particularly on $\delta^{18}O_p$). The primary control of the isotopic composition of tropical precipitation by rain reevaporation and meso-scale subsidence or convective-scale downdrafts thus seems to occur over a wide range of conditions and time and space scales.

In addition, the 2D model suggests that rain reevaporation has a significant role on vapor $\delta^{18}O$. Using global satellite data, [Worden et al., 2007] had already cited the rain reevaporation as a control for the vapor $\delta^{18}O$. However, they hypothesized that rain reevaporation depletes the vapor, whereas our study suggests that rain reevaporation tends to enrich the low-level vapor. The difference is due to (1) the strong reevaporation of the rain in our case, which invalids the approximation made in [Worden et al., 2007] that the composition of the evaporation does not depend on the reevaporated fraction of the rain, and (2) the strong depletion of the low-level vapor by meso-scale subsidence in our case (neglected in [Worden et al., 2007]). Based on our results, we would therefore rather suggest that the strong depletions of water vapor observed by [Worden et al., 2007] are related to unsaturated downdrafts and meso-scale subsidence associated with convection ([Zipser, 1977]).

The large temporal $\delta^{18}O_p$ variations along squall lines (up to 5 ‰ in the 6 and 22 August squall lines) are almost the same order of magnitude as the intra-seasonal variations of the event -averaged isotopic composition after the onset, with $\delta^{18}O_p$ ranging from -1.5 ‰ to -7.5 ‰ ([Risi et al., 2008b]). This raises the question of the role of individual squall line dynamics in controlling the $\delta^{18}O_p$ at the intra-seasonal scale. However, no correlation was found between $\delta^{18}O_p$ and the rainfall amount or the type of system at the scale of individual events: $\delta^{18}O_p$ rather seems to record a large-scale, low-frequency signal of intra-seasonal variability. Using the 2D model, we investigated the effect of $\delta^{18}O_p$ perturbations of the vapor at different levels on the event-averaged precipitation. A $\delta^{18}O$ perturbation in the monsoon flow layer (0-3km) is almost totally (85%) imprinted in the averaged $\delta^{18}O_p$. On the contrary, perturbations at the level of the African Easterly Jet (3-6km), which are potentially larger ([Bony et al., 2008]), are only partially (15%) imprinted in the averaged $\delta^{18}O$. This is because $\delta^{18}O_p$ is mainly controlled by $\delta^{18}O$ of the low-level vapor, and the stratiform zone, affected by $\delta^{18}O$ perturbations at higher levels through subsidence, contribute little to total precipitation. We hypothesize that $\delta^{18}O_p$ integrates temporally the convective activity because convection strongly affects the $\delta^{18}O$ of the boundary layer vapor, which in turn then controls $\delta^{18}O_p$ of the following rain event. More work is needed to understand the relative impact on the isotopic composition of tropical precipitation of (1) the dynamics and convective processes in individual convective systems and (2) the impact of larger scale processes imprinted in the large-scale vapor feeding the systems at different levels.

4.4.4 Perspectives

We are aware of the limits of the 2D model, due to the simple microphysics parametrization, assuming that the squall line is stationary and neglecting the along-line wind component. In particular, *[Lafore et al., 1988, Redelsperger and Lafore, 1987]* have shown that along-line variability in the 3D wind field and transient flows substantially contribute to the moisture transport. We are not able to simulate accurately the observed evolution, although all observed evolutions are in the range of the various simulations performed. Incorporating water stable isotopes into a CRM could be a next step. The coupling of such a model with a detailed soil model would also enable a more quantitative estimate of the effect of surface evaporation on the isotopic composition at the end of squall lines.

Besides, measuring the isotopic composition simultaneously in the precipitation and in the vapor would yield invaluable information about what controls $\delta^{18}O_p$ and d_p: it would allow us to evaluate the degree of reequilibration of rain drops with the low-level vapor, which might depend on drop size ([Lee and Fung, 2008]). A similar evolution in the precipitation and vapor would confirm the good reequilibration between rain and vapor and would support that the dynamics and the modification of the vapor by reevaporation are the main control of $\delta^{18}O_p$. On the other hand, the contrary would indicate that conversely to our model, the precipitation does not reequilibrate well with the vapor, and conditions of rain reevaporation as well as condensation altitude would contribute more significantly to the observed $\delta^{18}O_p$ variations. More systematic measurements of water stable isotopes in vapor and in precipitation during field experiments focused on tropical convection, or in instrumented sites, would thus be very valuable to discriminate between these two hypotheses, and more generally to better document the evolution of rain reevaporation and mesoscale subsidence in convective systems.

Chapitre 5

Isotopes stables de l'eau et transport d'eau dans la tropopause tropicale

Les trois chapitres précédents ont étudié le lien entre convection atmosphérique et composition isotopique de la précipitation. Ce chapitre est quant à lui consacré à l'influence de la convection sur la composition isotopique de l'eau au niveau de la tropopause tropicale, où de nombreuses questions se posent concernant les processus de transport d'eau de la troposphère à la stratosphère. Pour cela, nous utilisons deux types de modèles : un modèle uni-colonne de l'atmosphère tropical (utilisé dans le chapitre 2) et le modèle de circulation générale (GCM) LMDZ dans lequel les isotopes ont été introduits (chapitre 6). La partie de ce travail basée sur le modèle uni-colonne a été publiée dans l'article [Bony et al., 2008].

5.1 Introduction

5.1.1 Questions sur le transport d'eau vers la stratosphère

L'humidité dans la basse stratosphère joue un rôle important dans le bilan radiatif terrestre et dans la chimie stratosphérique. Les facteurs contrôlant cette humidité ainsi que ses variations à l'échelle inter-annuelle, ou sa tendance récente à la hausse, sont encore débattus. L'humidité stratosphérique est faible (figure 5.1a), car l'air transporté de la haute troposphère à la basse stratosphère passe au travers de la tropopause tropicale, où la température est minimale (figure 5.1b). Toutefois, ce minimum de température moyenne n'est pas suffisant pour expliquer les faibles teneurs en eau stratosphérique (e.g. [Sherwood and Dessler, 2000, Holton and Gettelman, 2001]).

Deux mécanismes sont souvent cités pour transporter l'eau de la haute troposphère à la basse stratosphère et déshydrater l'air aux faibles teneurs observées dans la stratosphère (figure 5.1c) :

- La *convection* :
  - effet déshydratant : lorsque la convection est vigoureuse, certains panaches ascendants ont des vitesses verticales importantes et peuvent monter très haut : c'est ce qu'on appelle des *overshoots*. Ces panaches continuent de monter par inertie, même si leur point de flottabilité neutre est dépassé. Ils atteignent alors des températures plus faibles que le minimum de température moyenne, déshydratant donc plus fortement l'air.
  - effet humidifiant : d'un autre coté, la forte vitesse verticale de ces panaches leur permet de retenir une grande partie de leur condensat. Des cristaux de glace sont alors apportés dans la basse stratosphère directement par la convection, détrainés vers l'environnement et réévaporés, humidifiant la basse stratosphère ([Khaykin et al., 2009]).
- *Ascendance lente* dans la tropopause tropicale : la convection détraine de l'air et du condensat à la base de la tropopause tropicale, et cet air monte lentement (plusieurs mois) par ascendance grande échelle forcée radiativement. On appelle TTL (Tropical Tropopause Layer) la couche d'air située entre (1) le niveau de détrainement convectif maximal (ou de

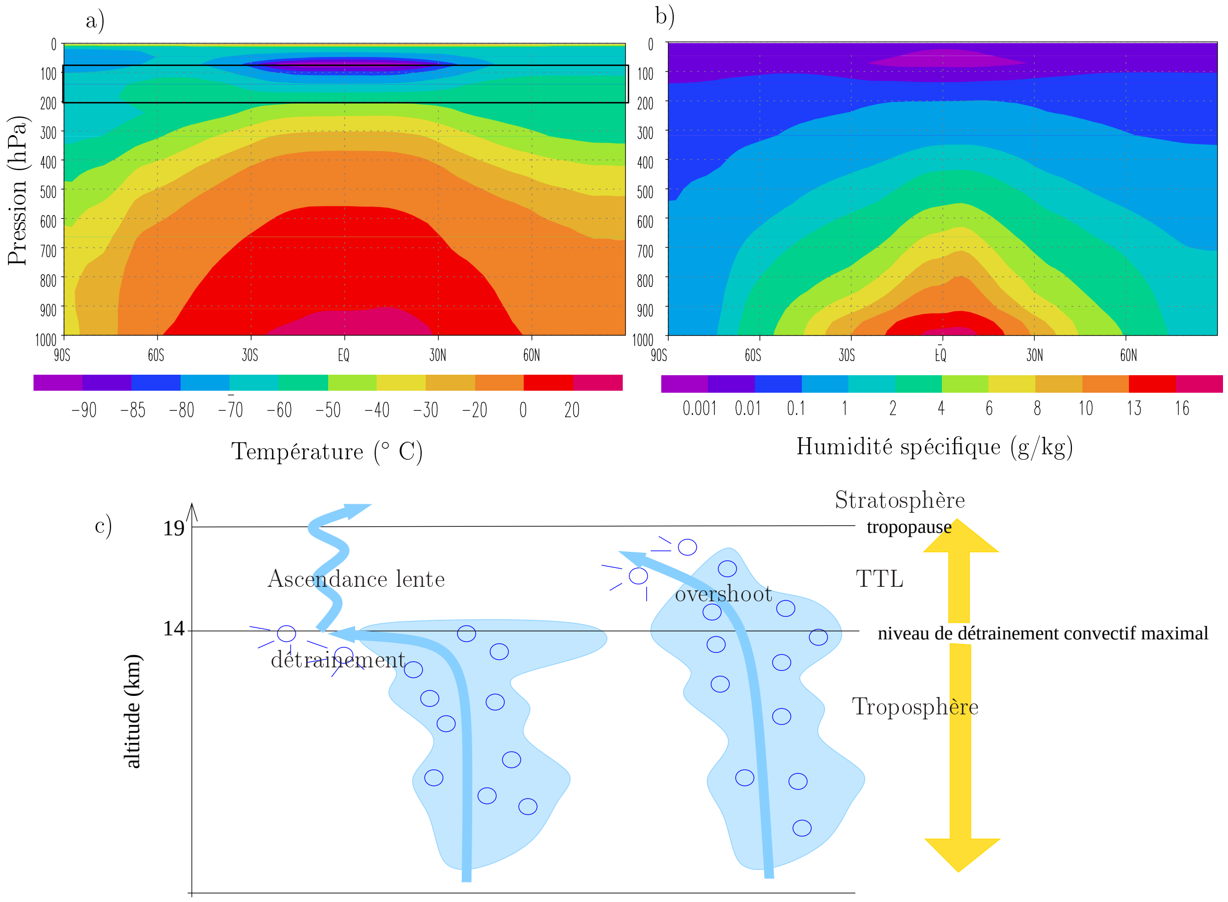

FIG. 5.1 – a) L'humidité spécifique en moyenne annuelle et zonale. b) La température en moyenne annuelle et zonale. c) Mécanisme expliquant le contrôle de l'humidité stratospérique par ascendance lente grande échelle (gauche) et par la convection (droite).

chauffage radiatif nul, selon les définitions), correspondant environ à 14km, et (2) le minimum de température, correspondant environ à 19km ([Sherwood and Dessler, 2000, Sherwood and Dessler, 2001]). Au cours de leur lent trajet, les parcelles d'air parcourent un chemin horizontal important, car les mouvements horizontaux sont de l'ordre de 10^4 plus forts que les mouvements verticaux ([Holton and Gettelman, 2001]). Ces parcelles d'air peuvent alors rencontrer des perturbations négatives de température, condenser, et être ainsi déshydratées plus fortement que par la température moyenne.

Ces différentes contributions à la déshydratation et l'humidification de la basse stratosphère sont difficiles à quantifier à grande échelle. La fréquence avec laquelle la convection pénètre la TTL, en fonction de l'altitude, est difficile à quantifer et est un sujet actif de recherche ([Folkins et al., 1999, Gettelman et al., 2002, Khaykin et al., 2009]).

5.1.2 Apport potentiel des isotopes

Dans ce contexte, la composition isotopique de l'eau dans la haute troposhère et basse stratosphère (UT-LS) est susceptible d'apporter une information. En effet, le condensat apporté directement par la convection est riche, car il a condensé majoritairement à basse altitude dans les panaches convectifs. En revanche, la déshydratation de l'air par condensation et précipitation progressive au cours d'une lente ascendance de l'air suit une distillation de Rayleigh, et la vapeur résiduelle est donc très appauvrie.

Les données isotopiques collectées in situ ([Webster and Heymsfield, 2003]) ou mesurées par satellite ([Moyer et al., 1996, Kuang et al., 2003, Nassar et al., 2007]) dans l'UT-LS montrent

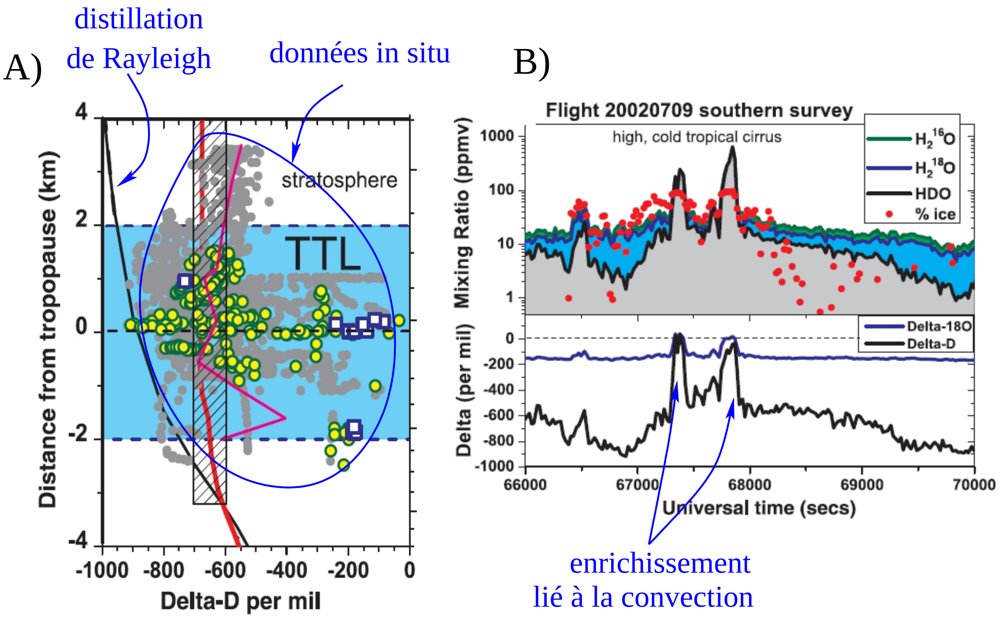

Fig. 5.2 – a) Profils isotopiques mesurés au niveau de la tropopause tropicale. b) δD mesurés in situ au cours d'un vol avion. Figures issues de [Webster and Heymsfield, 2003]

des valeurs plus enrichies qu'une distillation de Rayleigh (figure 5.2a), suggérant un apport de condensat détrainé par la convection. Elles montrent aussi une très forte variabilité spatiale, avec des valeurs plus enrichies au dessus de panaches convectifs ([Webster and Heymsfield, 2003], figure 5.2b), suggérant l'effet de la convection sur la composition isotopique de l'eau et l'humidité dans l'UT-LS.

5.1.3 Objectif et méthodes

L'interprétation des données isotopiques observées en terme de bilan d'eau nécessite tout d'abord de bien comprendre l'effet de la convection sur la composition isotopique de l'eau à ces altitudes. Jusqu'à présent, l'interprétation des observations isotopiques dans l'UT-LS a reposé sur trois types d'approches :

- Modèles microphysiques le long de rétrotrajectoires (e.g. [Dessler and Sherwood, 2003, Dessler et al., 2007]),
- Modèle de circulation générale ([Schmidt et al., 2005]),
- Modèle de simulation des gros tourbillons (Large Eddy Simulation : LES) : [Smith et al., 2006]

Ici, nous proposons d'étudier les contrôles de la composition isotopique de l'eau dans l'UT-LS en utilisant le schéma de convection d'Emanuel (section 2.2) équipé des isotopes, aussi bien dans un cadre uni-dimensionel (modèle uni-colonne utilisé dans le chapitre 2) que tri-dimensionnel (modèle de circulation général LMDZ, chapitre 6).

5.2 Processes controlling tropospheric profiles

In this section, we investigate the influence of convection on isotopic vertical profiles simulated by the single column model (SCM) described in chapter 2.

First, the vertical profiles of the isotopic composition of the environment are explored in the absence of large scale flow, representing an average over the whole tropics. We study profiles only below 100hPa, which is the level of penetration of the convection. Above, representing the Brewer-Dobson circulation would be necessary to simulate realistic humidity or isotopic profiles.

δD in the environment (δD_{env}) decreases with altitude until 175hPa, reaching a minimum value of about $-460‰$ (figure 5.3a, black curve). This depletion is due to the progressive removal of heavy isotopes through condensation and precipitation of water in convective updrafts. δD_{env} values above 700hPa are less depleted than would be predicted by a Rayleigh distillation (in which all condensate formed is isolated from the vapor, green curve on figure 5.3a), in qualitative agreement with in-situ ([Webster and Heymsfield, 2003, Hanisco et al., 2007]) and satellite ([Kuang et al., 2003]) observations. Above 175hPa, still below the tropopause, δD_{env} progressively increases with altitude (figure 5.3a, black curve). This is in qualitative agreement with isotopic profiles measured during the CR_AVE campaign (Costa Rica Aura Validation Experiment) ([Hanisco et al., 2007]). Most profiles (http://espoarchive.nasa.gov/archive/arcs/cr_ave/data/wb57/) exhibit an enrichment with altitude of the order of 100‰ above 175hPa, below the tropopause. Our model therefore reproduces the main features of the vertical profiles of water isotopes around the tropopause, at least qualitatively.

The deuterim excess in the environment (d_{env}, black curve on figure 5.3b) increases drastically with altitude, especially above 400mb (corresponding to a temperature of about -15°C). This increase is predicted by a Rayleigh distillation even without kinetic effects (figure 5.3b, red curve): as δD_{env} decreases and tends towards -1000‰, d_{env} increases and tends towards 7000‰. Although the accuracy of isotopic measurements does not allow for an accurate calculation of d, the CR_AVE data also feature a robust increase in d with altitude.

What explains this δD_{env} profile? In the free troposphere, the main source of water is the detrainment of cloud water into the environment. Therefore, the composition of the environment (black curve on figure 5.4a) tightly follows that of the total water in the adiabatic column (δD_{adiab}, green curve on 5.4a). The adiabatic column is air lifted adiabatically from the subcloud layer up to different levels, at which a fraction ϵ_p of the condensate is precipitated. In the Emanuel scheme, the adiabatic column is a significant proportion of the cloud water. We will therefore focus on understanding the profile of δD_{adiab}.

The condensate in the adiabatic column (δD_{cond} , red curve on figure 5.4a) is much more enriched at all altitudes than would predict a Rayleigh distillation (figure 5.4a). It is approximately $-80‰$ in the upper-troposphere, slightly more enriched than the mean value for ice crystals around the tropopause of $-130‰$ reported by [Webster and Heymsfield, 2003], possibly because the adiabatic condensate is more enriched than the total condensate. The condensate is very enriched because all the condensate formed in the adiabatic column is kept in adiabatic parcels as they ascend. The minimum δD_{cond} that can be achieved is that of the subcloud layer (about 80‰), and it is achieved when all the adiabatic water is in condensate form. The enrichment of total adiabatic water compared to a Rayleigh distillation is thus explained by the fact that the total adiabatic water contains enriched condensate. Above 175hPa, the condensed fraction of water steeply increases, due to the increase of condensation with altitude but a near constant precipitation efficiency above 200hPa . This leads to the increase of δD_{adiab} at this altitude.

Therefore, such a δD_{env} profile is specific of convective cases, in which updrafts are strong enough to loft condensate above its level of formation. Consequently, this confirms the potential of the isotopic composition around the tropopause to track convective vertical water transport ([Hanisco et al., 2007, Webster and Heymsfield, 2003]).

5.3 Sensitivity to convection

5.3.1 In the SCM

To better evaluate the influence of convective activity on isotopic profiles, we test here the sensitivity of the δD_{env} profiles simulated at radiative-convective equilibrium to large-scale flow. The large scale velocity profile, representing the large scale flow in our idealized model, is assumed to have a cubic shape with a maximum value at 500hPa ([Emanuel, 1991]). This maximum is hereafter noted ω. In case of ascending motions (negative ω), the convective updrafts are stronger ([Emanuel et al., 1994]), thus the convection is more intense.

We tested ω from 0hPa/day to -120hPa/day, varying correlatively with SST, following an average relationship derived from reanalysis data ([Bony et al., 2004]). Profiles for all experiments show the same features as described in the previous section (figure 5.5A): a smooth decrease of

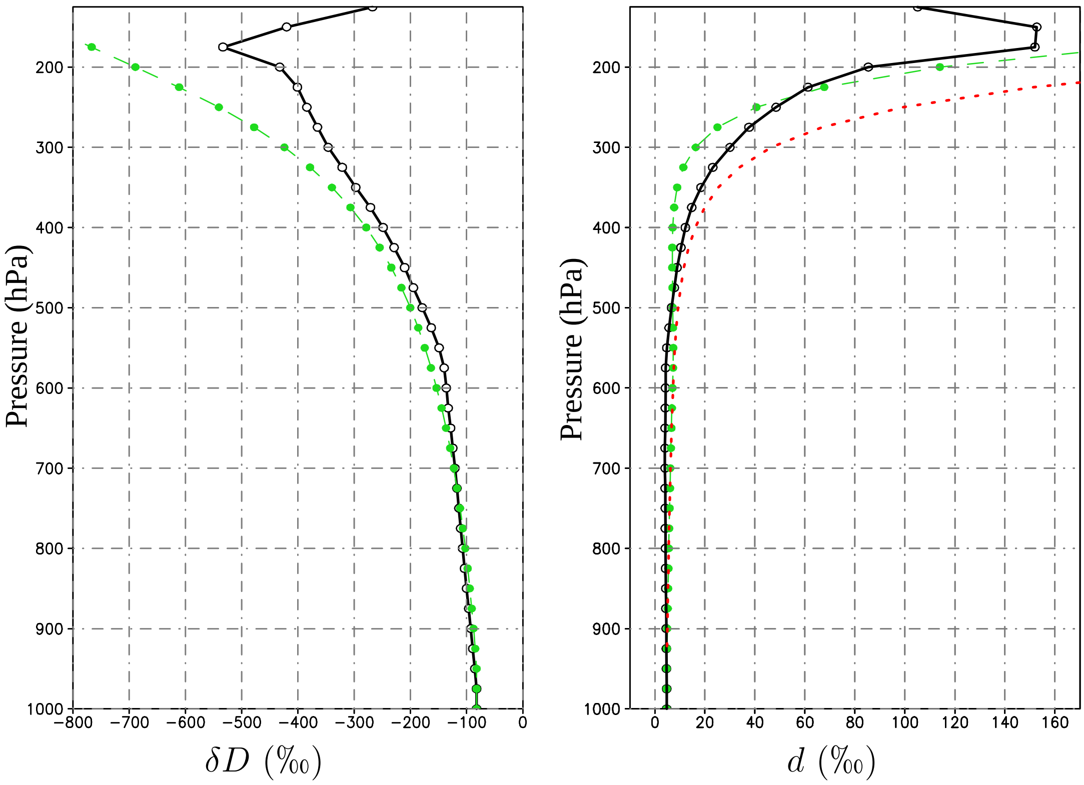

Figure 5.3: a) Profiles of δD in the environment at steady state in a SCM simulation in the absence of large scale flow, with a sea surface temperature of 29°C and a background wind speed of 5m/s. The profile predicted by the Rayleigh distillation is shown in green. b) Equilibrium profiles of d in the environment for the same conditions. The profile predicted by the Rayleigh distillation is shown in green. In red is the Rayleigh distillation profile if there were not kinetic effects during ice condensation.

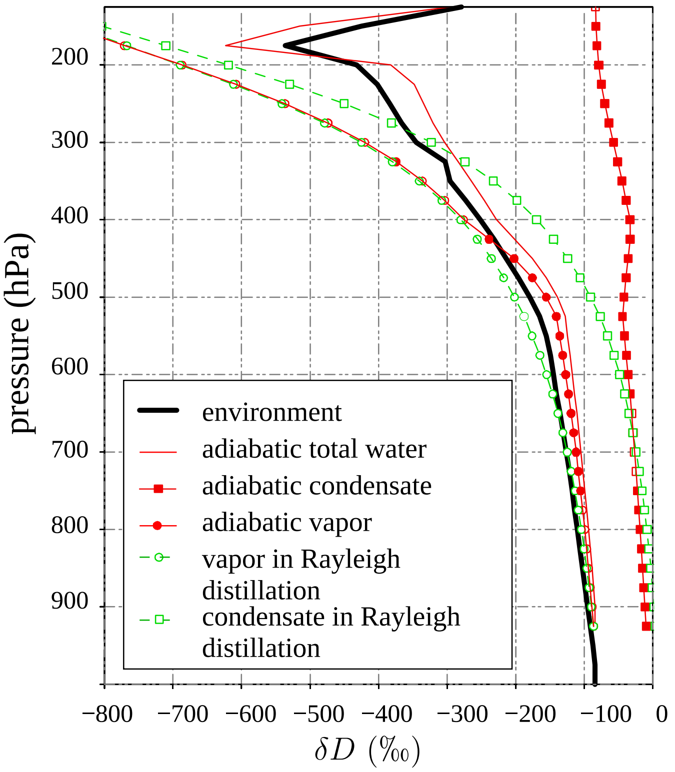

Figure 5.4: a) δD profiles in the environment (black) simulated by the SCM, in the total water of the adiabatic column (solid red) , in the condensate of the adiabatic column (red squares) and in the vapor of the adiabatic column (red circles). As a comparison, the δD in the condensate and vapor of the adiabatic column predicted by a Rayleigh distillation are shown respectively with green squares and circles.

δD_{env} with altitude until around 175hPa, and then an enrichment with altitude below the tropical tropopause. However, the similarities between these profiles in convective regime might be an artifact of the level of penetration of convective updrafts in the Emanuel parametrization, which is very high and about the same altitude (100hPa) whatever the intensity of convection.

5.3.2 In the LMDZ GCM

In the LMDZ GCM, the annual average of the isotopic profiles over the whole tropics (20S-20N) features a near constant value from 300 to 100hPa (red curve on figure 5.5B), in agreement with the ATMOS measurement ([Kuang et al., 2003]). Compared to the SCM framework, an increase in δD with altitude in the upper troposphere is observed only at locations where (and on days when) the convection is very strong (figure 5.5B). On the contrary, in areas of weak convection, the δD decreases monotonically. This confirms that the increase of δD in the upper troposphere is related to convection.

Profiles with near constant δD in the upper troposphere are obtained when averaging profiles over locations with and without convection. This may explain the constant values observed by the ATMOS measurements.

5.4 Sensitivity to model parameters

To evaluate the robustness of our results to the model representation of convection and isotopic processes, sensitivity tests to model tunable parameters are performed, in both SCM and LMDZ simulations.

Strong supersaturation in the upper tropshere has been suggested to decrease the fractionation coefficient and thus contribute to the underdepletion observed compared to the Rayleigh distillation ([Moyer et al., 1996]). However, changing the supersaturation parameter $\lambda = 0.002$ to $\lambda = 0$ (no kinetic effects) leads to changes smaller than 25‰ (figure5.6A). This is small compared to the measurement accuracy around the tropopause: approximately 50‰ for the ICOS instrument ([Hanisco et al., 2007]) or 80‰ for the ATMOS instrument ([Moyer et al., 1996]). Supersaturation is thus expected to have little influence on isotopic profiles, in agreement with [Johnson et al., 2001].

In the Emanuel scheme, the main parameters impacting the isotopic profles in the upper troposphere are those controlling the precipitation efficiency (ϵ_p), i.e the proportion of the condensate that is converted to precipitation. In particular, ϵ_p in the upper troposphere is proportional to the tunable parameter ϵ_p^{max} (i.e. the maximum value ϵ_p may reach). Small variations in the tunable parameters controlling ϵ_p leads to large variations of δD_{env}, greater than 100‰ for variations in ϵ_p that are smaller than 1%, both in the SCM and LMDZ (figure 5.6). The high sensitivity of δD_{env} profiles to precipitation efficiency confirms that isotopic measurements may constitute a valuable tool to better constrain the representation of cloud processes in large scale models. For example, in the LMDZ GCM, ϵ_p^{max} is a tunable parameter used to adjust the model mean state. While the sensitivity to ϵ_p^{max} of the vapor field is small, isotopic measurements could help constrain this parameter.

Underdepletion and enrichment of the δD_{env} under the tropopause are simulated only if the precipitation efficiency is strictly smaller that 1: if $\epsilon_p^{max} = 1$, virtually no condensate remains in the cloud and detrains into the environment, hence the highly depleted values. This shows once more that the enrichment under the tropopause can be explained by the detrainment of lofted condensate that does not precipitate before detraining ([Moyer et al., 1996, Webster and Heymsfield, 2003]).

5.5 Conclusion et perspectives

5.5.1 Summary

We have shown that convection has a specific signature on isotopic profiles around the tropopause. In particular, the underdepletion observed in the upper troposphere compared to the Rayleigh distillation and the reenrichment with altitude below the tropopause is interpreted by the lofting

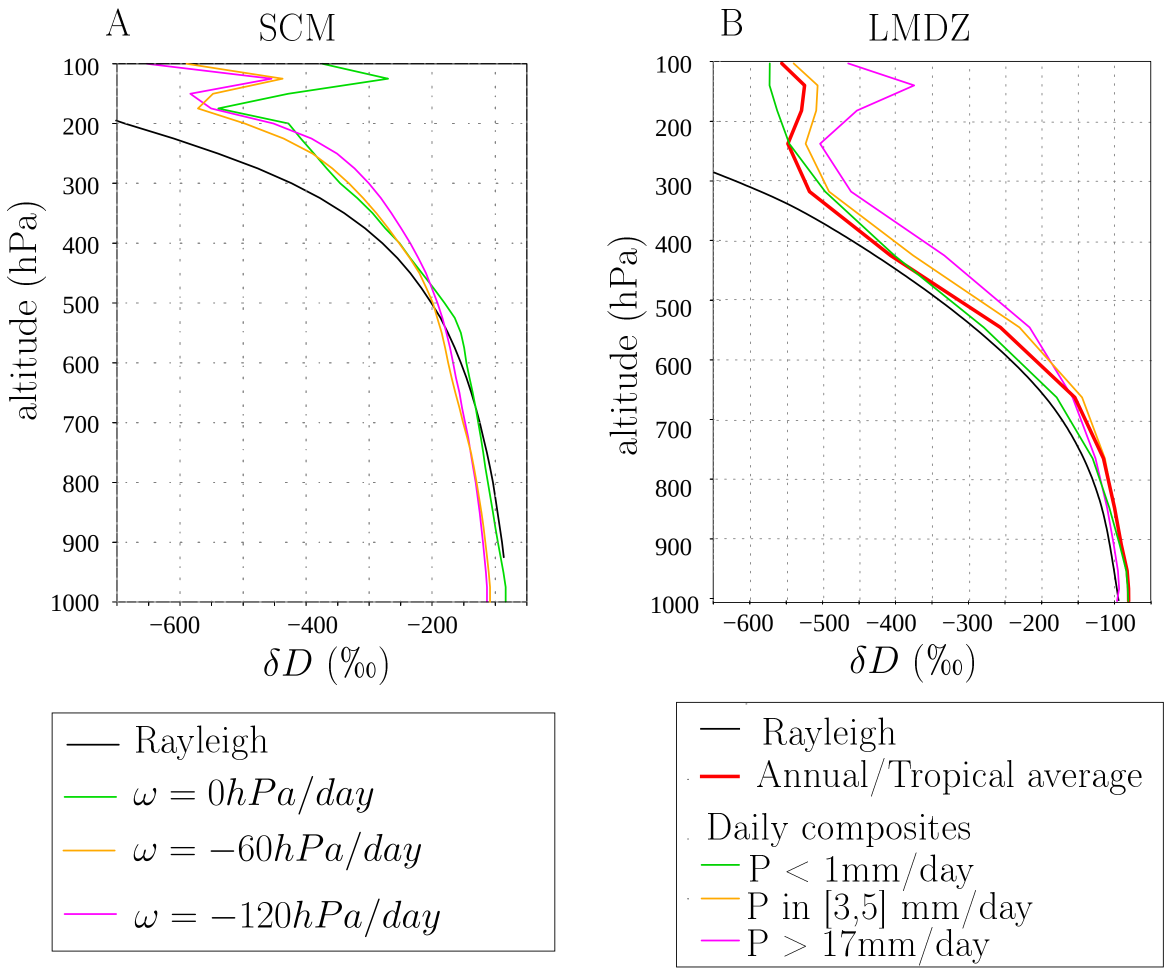

Figure 5.5: A. Profiles of δD in the environment water simulated by the SCM for different values of ω. ω was varied correlativey with SST, following an average spatial and temporal relationship at monthly scale.

B. Isotopic profiles simulated by the LMDZ GCM, composited by comvective activity measured by the precipitation rate: green: precipitation lower than 1mm/day; orange: precipitation between 3 and 5 mm/day; Magenta: precipitation higher than 17mm/day, Red: Tropical average; black: Rayleigh distillation;

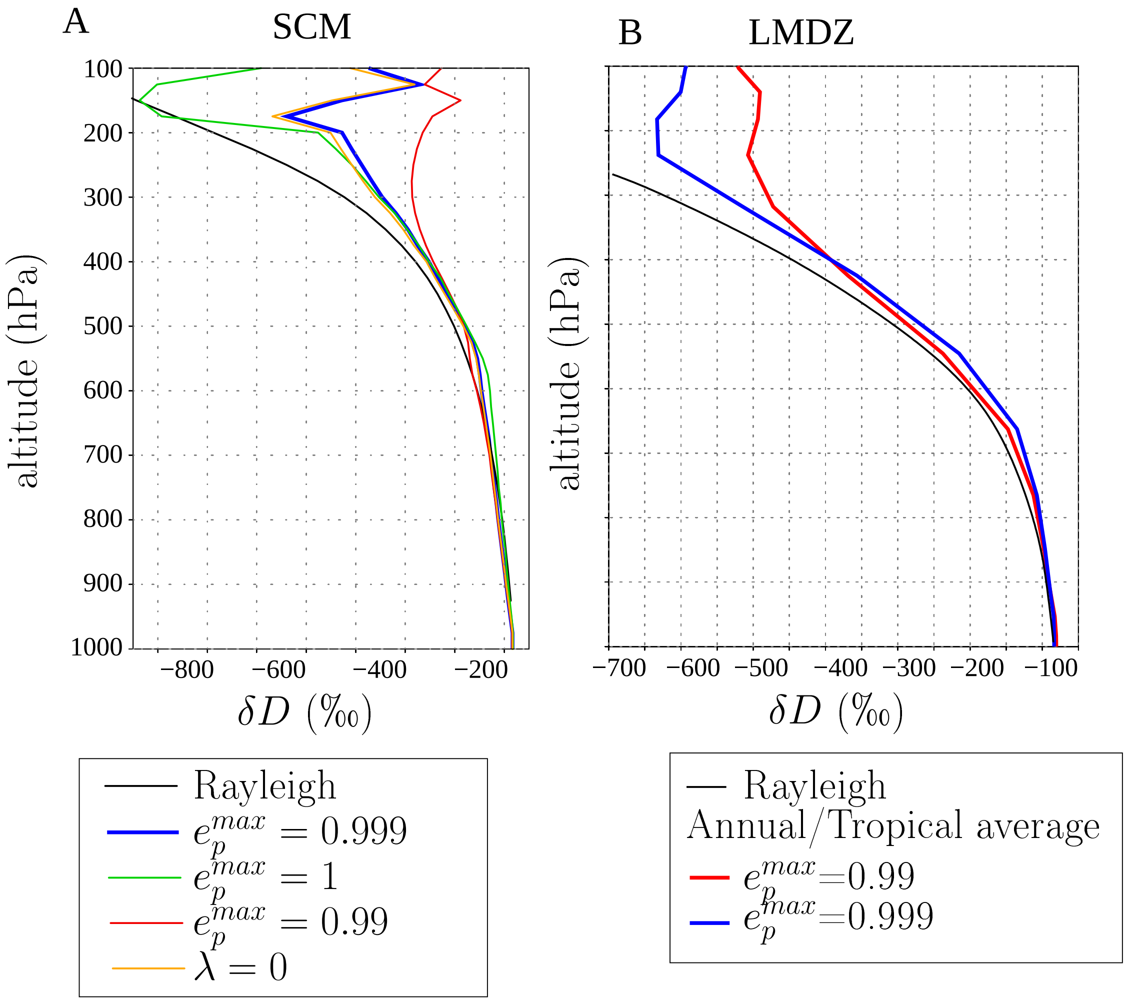

Figure 5.6: A. Isotopic profiles simulated by the SCM for different values of λ (controling supersaturation and its related kinetic effects) and of ϵ_p^{max}
B. Annual average over the whole tropics of the isotopic profiles simulated by the LMDZ GCM, for different values of ϵ_p^{max}.

of condensate by rapidly ascending drafts. The underdepletion is all the stronger as convection is stronger and as a larger proportion of the condensate is detrained rather than precipitated. This confirms the use of water isotopes as a tracer for vertical transport of water by convection from the troposphere to the stratosphere, and suggests their potential to constrain microphysical parameters in convective parametrizations.

5.5.2 Perspectives

To quantify explicitely in the GCM the proportion of water transport to the stratosphere from convection and from the slow, radiative ascent in the TTL and lower stratosphere, the water tagging functionality in LMDZ could be valuable (appendix E). For example, we could tag the condensate detrained by the convection at different levels.

The realism of the simulations in LMDZ could be improved in several ways. The stratospheric version of LMDZ ([Lott et al., 2005]) better represents the large-scale circulation in the TTL and the stratosphere (Brewer-Dobson circulation), with a finer vertical resolution. Using this version would allow a better quantification of the relative contribution of the water fluxes by convection and by the slow radiative ascent in the TTL and lower stratosphere. Using the SPARC reanalyses (Stratospheric Processes and their Role in Climate,[SPARC, 2000]) to nudge the LMDZ model would further ensure a more realistic simulation of the large-scale circulation. In addition, the chemical module of LMDZ, INCA (*[Folberth et al., 2006]*), could be used to simulate the source of enriched stratospheric water by methane oxydation ([Johnson et al., 2001]).

The stratospheric water vapor content strongly varies at the seasonal ([Mote et al., 1996]), inter-annual scales ([Randel et al., 2004]) and features increasing trends ([Oltmans et al., 2000]) that remain for the most part unexplained ([Rosenlof, 2002]). The isotopic composition of the tropical tropopause layer also feature some seasonal and inter-annual variations ([Nassar et al., 2007]) that could potentially help interpret the observed variations in water vapor content in terms of changes in water transport processes. Can water stable isotopes give additional information on what controls this variability?

Eventually, a more comprehensive vision of vertical water transport throughout the troposphere and up to the lower stratoshere by turbulence, convection and large-scale motions may potentially be gained from a combined analysis of isotopic data measured from satellites at different levels: SCIAMACHY ([Frankenberg et al., 2009]) in the boundary layer, TES around 700hPa ([Worden et al., 2007]), MIPAS ([Payne et al., 2007]) and ACE ([Nassar et al., 2007]) in the TTL and ODIN ([Urban et al., 2007]) in the stratosphere.

Conclusion de la partie

Par deux approches, modélisation numérique et observations de terrain à différentes échelles de temps, nous avons étudié l'effet des processus convectifs sur la composition isotopique de l'eau. Ces différentes études ont conduit à des résultats robustes, retrouvés dans toutes les approches :

- L'intensité de la convection a un fort impact sur la composition isotopique de l'eau, que ce soit à l'intérieur d'un système convectif, à l'échelle intra-saisonnière ou à l'échelle saisonnière.
- La convection impacte la composition isotopique de la précipitation par deux effets principaux :
  - La réévaporation des gouttes : lorsque les gouttes se réévaporent, elles s'enrichissent en isotopes lourds, d'autant plus que l'air est sec. En parallèle, les gouttes se rééquilibrent isotopiquement avec la vapeur, d'autant plus que l'air est humide.
  - Les descentes insaturées (ou subsidences méso-échelles) amènent de l'air pauvre de la moyenne troposphère vers la couche limite. La couche limite se fait ainsi appauvrir au fur et à mesure que sa vapeur se fait recycler par les descentes insaturées
- Le lien entre l'intensité de la convection et la composition isotopique de l'eau, appelé amount effect, n'est visible qu'à partir d'une échelle de temps de plusieurs jours, en particulier à partir de l'échelle intra-saisonnière. Ceci est lié au fait que la composition isotopique intègre l'activité convective sur les jours précédents, et a donc un effet intégrateur de la convection.

Les résultats de modélisation obtenus sont particulièrement sensibles à la représentation des processus isotopiques lors de la réévaporation de la pluie. Dans notre modèle, la proportion de fractionnement cinétique est contrôlée par un paramètre empirique : ϕ. Il a été ajusté à la valeur de 0.9 pour optimiser les résultats du modèle uni-colonne, mais peu de contraintes rigoureuses existe sur ce paramètres. Des jeux de données combinant à la fois composition isotopique dans la pluie et dans la vapeur, sur des sites instrumentés pour l'étude de la convection (comme les stations ARM : Atmospheric Radiation Measurement, [Stokes and Swartz, 1994]), permettraient de contraindre ce paramètre beaucoup plus rigoureusement, voire d'étudier ses éventuelles variations avec les conditions atmosphériques. Plus généralement, les mesures isotopiques dans les précipitations seraient beaucoup mieux interprétables si on disposait en parallèle de la composition de la vapeur. Ainsi, le développement de mesures vapeur par la nouvelle technologie laser (ex : instruments Picarro) et la future disponibilité des données satellitaires SCIAMACHY ([Frankenberg et al., 2009]) sont très prometteurs.

Nous avons étudié en détail l'influence des processus convectifs sur la composition isotopique de l'eau. En retour, quelles informations la composition isotopique des précipitations apporterait sur la convection et sa représentation dans les modèles ? Les études que nous avons réalisées suggèrent le potentiel des isotopes comme contrainte additionnelle de ces processus. Comment les utiliser plus concrètement, en revanche, est une perspective de travail pour l'avenir.

Nous avons vu l'importance de l'organisation de la convection sur la composition isotopique de l'eau au cours de la campagne AMMA ([Risi et al., 2008b]), en accord avec [Lawrence et al., 2004]. Dans le cadre du développement de la "nouvelle physique" du modèle LMDZ, une représentation des courants de densité et poches froides (air froid issu des subsidences convectives liées à la réévaporation de la pluie) a été introduite ([Grandpeix and Lafore, , Grandpeix et al.,]). Cette paramétrisation contient la notion de degrés d'organistion de la convection, le nombre de poches froides pouvant varier selon les conditions de l'environnement. La thèse d'Isabelle Tobin commencera d'ailleurs au LMD en automne 2009 pour étudier l'organisation de la convection à partir de cette nouvelle version d'LMDZ. Il serait intéressant de regarder si une telle paramétrisation permet de reproduire l'effet de l'organisation de la convection sur les isotopes, et d'explorer si les isotopes peuvent apporter des informations sur le degrés d'organisation de la convection et ses variations avec le climat.

Deuxième partie

Les isotopes stables de l'eau et les variations du climat

Introduction de la partie

Nous avons vu dans la partie précédente que les isotopes de l'eau étaient susceptibles d'apporter une information sur le cycle de l'eau actuel. Lors d'un changement du climat, le cycle de l'eau est modifié, et la composition isotopique des précipitations est alors affectée. Comme la précipitation est susceptible de constituter des archives (glaces, spéléothèmes...), les isotopes de l'eau peuvent être utilisés pour reconstituer les variations du climat et les réponses du cycle hydrologique associées. En particulier, la composition isotopique enregistrée dans les carottes de glaces polaires est utilisée depuis longtemps comme paléo-thermomètre ([Dansgaard, 1953]). Utiliser les isotopes pour reconstituer les variations passées du climat nécessite toutefois de bien comprendre les contrôles de la composition isotopique des précipitations, et ses variations temporelles.

Dans ce but, compte tenu de la complexité et de la diversité des processus agissant sur la composition isotopique de l'eau, nous avons introduit les isotopes de l'eau dans le *modèle de circulation générale LMDZ*. LMDZ est la composante atmosphérique du *modèle de climat de l'IPSL*. Il permet de simuler le climat actuel, mais aussi des climats passés ou des climats idéalisés, ce qui permet d'étudier *comment les variations climatiques sont enregistrées dans la composition isotopique de l'eau*. Dans un chapitre 6, nous décrivons l'implémentation des isotopes de l'eau dans LMDZ et nous évaluons les champs isotopiques simulés ainsi que leur variabilité à différentes échelles de temps : synoptique (quelques jours), inter-annuelle, climatique. Dans la section 6.4, LMDZ est utilisé pour pour aider à l'interprétation des signaux isotopiques enregistrés dans les tropiques. Ce chapitre est basé sur l'article [Risi et al., 2010b] (en révision).

Dans les archives isotopiques telles que les glaces, les compositions mesurées sont généralement l'abondance en HDO et $H_2^{18}O$. La différence de comportement entre le δD et le $\delta^{18}O$ est mesurée par le d-excess (voir chapitre introductif 1, section 1.1.2), qui apporte une information complémentaire ([Dansgaard, 1964]). Récemment, des progrès expérimentaux ([Barkan and Luz, 2005]) ont permis de mesurer en plus l'abondance en $H_2^{17}O$ avec une précision suffisante pour des applications paléoclimatiques. La différence de comportement entre le $\delta^{17}O$ ainsi mesuré et le $\delta^{18}O$ est mesurée par l'^{17}O-excess, qui est susceptible d'apporter des informations complémentaires à la fois des δ et du d-excess ([Barkan and Luz, 2007, Landais et al., 2008]). Le chapitre 7 est consacré à l'étude de ce nouveau traceur isotopique. Nous y proposons des pistes d'interprétation des signaux isotopiques en ^{17}O-excess mesurés dans la calotte de glace à Vostok ([Landais et al., 2008]). Ce chapitre est basé sur l'article [Risi et al.,] (accepté).

Chapitre 6

Les isotopes stables de l'eau dans LMDZ et applications paléoclimatiques dans les tropiques

Ce chapitre est basé sur l'article [Risi et al., 2010b] (en révision).

6.1 Introduction

Due to differences in mass and symmetry of the main isotopic forms of the water molecule ($H_2^{16}O$, HDO, $H_2^{18}O$), an isotopic fractionation occurs during phase changes depending on atmospheric conditions. As a consequence, water stable isotopes are widely used as a tracer of past climate variations and of the present day water cycle. In particular, the isotopic composition recorded in polar ice core have long been used to reconstruct past temperatures ([Dansgaard, 1953, Jouzel, 2003]). More recently, the isotopic composition recorded in low latitude ice cores ([Thompson et al., 2000, Ramirez et al., 2003]) or speleothems ([Wang et al., 2008, Cruz et al., 2005a]) have also been used to infer past temperatures ([Thompson et al., 2000]) or precipitation rates ([Hoffmann et al., 2003]).

However, processes that control the water isotopic composition are numerous and complex. For the Greenland ice cores for example, using the spatial slope as a surrogate for the temporal slope to evaluate past local temperature changes leads to a large uncertainty of a factor of 2 ([Jouzel, 1999, Jouzel, 2003]). This could be due to a change in air mass origins ([Werner et al., 2001]) or in precipitation seasonality ([Krinner et al., 1997b, Krinner and Werner, 2003]), or to a dampening of isotopic changes by ocean evaporation ([Lee et al., 2008]). At low latitudes, the paleoclimatic interpretation of isotopic records is even less quantitative. Most of the tropical precipitation arises from convective processes, which strongly affect the isotopic composition of both vapor and precipitation ([Lawrence et al., 2004, Bony et al., 2008, Risi et al., 2008a, Risi et al., 2008b]). While the earliest interpretation of Andean ice cores had linked isotopes to temperatures ([Thompson et al., 2000]), more recent studies have stressed the importance of the precipitation intensity upstream the air mass trajectories ([Hoffmann, 2003, Vimeux et al., 2005]). As a consequence, while Rayleigh distillation models (representing the loss of heavier isotopes during condensation and precipitation) are useful to study at first order the evolution of air masses as they are transported from a moisture source region to higher latitudes ([Ciais and Jouzel, 1994]), more complex models are necessary to take into account the numerous processes affecting the isotopic composition of precipitation.

Atmospheric general circulation models (GCM) are now frequently used for isotopic studies. They represent the three dimensional transport of air masses and isotopes as well as large-scale condensation and atmospheric convection, albeit in a parametrized way. Since the pioneering work of [Joussaume et al., 1984], water isotopes have been implemented in at least a semi-dozen GCM:

GISS ([Jouzel et al., 1987, Schmidt et al., 2007]), ECHAM ([Hoffmann et al., 1998]), MUGCM ([Noone and Simmonds, 2002b]), GENESIS ([Mathieu et al., 2002]), CAM ([Lee et al., 2007]), GSM ([Yoshimura et al., 2008]), Hadley GCM ([Tindall et al., 2009]) as well as in regional models (REMO: [Sturm et al., 2005]). They have been used, for example, to better understand how the climatic signal is recorded by isotopes in ice cores, at the inter-annual to decadal time scales ([Vuille et al., 2003, Vuille and Werner, 2005] and at paleo time scales ([Werner et al., 2001]).

In this paper, we present the implementation of water stable isotopes in the LMDZ4 model (whose isotopic version is hereafter named LMDZ-iso). The LMDZ4 model is the GCM developed at the Laboratoire de Météorogie Dynamique (LMD) ([Hourdin et al., 2006]). It is the atmospheric component of the Institut Pierre Simon Laplace (IPSL) ocean-land-atmosphere coupled model ([Marti et al., 2005]) that participated in CMIP3 ([Meehl et al., 2007]). Its dynamical and physical packages have completely changed since the pioneering work of [Joussaume et al., 1984]. An interesting particularity of this GCM now is the possibility to use stretched grids ([Hourdin et al., 2006]), allowing studies at both global and regional scales (e.g. [Krinner et al., 1997a]).

The first goal of this paper is to evaluate the simulation of water stable isotopes by LMDZ-iso at different time scales. We evaluate the present-day isotopic spatial and seasonal distribution and the isotopic variability at time scales ranging from synoptic to inter-annual. For this purpose, we have performed an AMIP (Atmospheric Model Inter-comparison Project, [Gates, 1992]) simulation forced by monthly observed sea surface temperatures (SST) from 1979 to 2007. To evaluate the isotopic simulation in a more rigorous way, we have also performed an AMIP simulation over the same period with the large-scale atmospheric dynamics nudged by meteorological reanalyses. Since a particular effort have been invested in the representation of the droplet reevaporation in the model ([Bony et al., 2008]), we pay a particular attention on evaluating the equilibrium between droplets and water vapor using simultaneous vapor and precipitation data available at some stations. We also pay a lot of attention to evaluating the d-excess, which is sensitive to kinetic fractionation notably during rain reevaporation. Finally, we evaluate the isotopic distribution for two past climates for which isotopic data are available: Last Glacial Maximum (21 000 years ago, 21 ka) and Mid-Holocene (6 ka).

The second goal is to use LMDZ-iso to investigate the controls of the isotopic composition of precipitation in the tropics, where the paleoclimatic interpretation is the most uncertain. In particular, what are the relative influence of temperature and precipitation changes on the isotopic composition of tropical precipitation? How useful may $\delta^{18}O$ records be for reconstructing past local precipitation changes in the tropics?

In section 6.2.1, we describe the LMDZ4 model, the implementation of water stable isotopes and the various simulations performed. In section 6.3, we evaluate the simulation of the isotopic composition for the present-day climatology, synoptic variability, inter-annual variability and past-climates. In section 6.4, we use LMDZ-iso to explore what paleoclimatic information is recorded in tropical isotopic records. We conclude and give perspectives in section 6.5.

6.2 Model and simulation description

In this section we briefly describe the LMDZ4 GCM, the implementation of water stable isotopes and the different simulations performed.

6.2.1 The LMDZ4 GCM

The dynamical equations are discretized in a latitude-longitude grid, with a standard resolution of 2.5×3.75° and 19 vertical levels. Water in its vapor and condensed forms are advected by the Van Leer advection scheme ([Van Leer, 1977]), which is a monotonic second order finite volume scheme. The physical package is described in detail in [Hourdin et al., 2006]. It includes in particular the Emanuel convective parametrization ([Emanuel, 1991, Grandpeix et al., 2004]) coupled to the [Bony and Emanuel, 2001] cloud scheme. Each grid cell is divided into four sub-surfaces: ocean, land, ice-sheet and sea-ice. Land surface is represented as a simple bucket model, and land surface evaporation is calculated as a single flux: no distinction is made between transpiration, bare soil evaporation or evaporation of intercepted water by the canopy.

6.2.2 Isotopic processes

The implementation of water stable isotopes in LMDZ is described in appendix D.3.

Water isotopic species ($H_2^{16}O$, $H_2^{18}O$ and HDO) are transported and mixed passively by the large-scale advection and various air mass fluxes. In the Van Leer advection scheme, it is assumed that the water content advected from one box to the next is a linear combination of the water contents in the two grid boxes involved. For numerical reasons, we assume similarly that the isotopic ratio of the water advected from one box to the next (rather than the isotopic content) is a linear combination of the isotopic ratios in the two grid boxes involved (appendix D.3.2).

Equilibrium fractionation coefficients between vapor and liquid water or ice are calculated after [Merlivat and Nief, 1967], [Majoube, 1971a] and [Majoube, 1971b]. We take into account kinetic effects during the evaporation from the sea surface following [Merlivat and Jouzel, 1979] and during snow formation following [Jouzel and Merlivat, 1984], with the supersaturation parameter λ set to 0.004 to optimize the simulation of d-excess over Antarctica (section 6.3.1).

Given the simplicity of the land surface parametrization in LMDZ4, no information is available about the fraction of the evapo-transpiration flux arising from fractionating evaporation (e.g. evaporation of bare soil, [Barnes and Allison, 1988]). We thus assume no fractionation during the evapo-transpiration over land, as done in most other GCM (e.g. [Hoffmann et al., 1998, Lee et al., 2007]). The coupling with the more detailed land surface scheme ORCHIDEE ([Ducoudré et al., 1993, Rosnay and Polcher, 1998, Krinner et al., 2005]) will be reported in a subsequent paper.

The implementation of water stable isotopes in the convective scheme has been extensively described in [Bony et al., 2008] (appendix D.1). We pay a particular attention to the representation of the reevaporation and diffusive exchanges as the rain falls, which is significantly different compared to other GCMs. While the proportion of the drop that reequilibrates isotopically is prescribed in many GCMs (e.g. [Hoffmann et al., 1998]), here the relative proportion of evaporative enrichment and diffusive equilibration is calculated explicitly following [Stewart, 1975]. In addition, the model takes into account the evolution of the compositions of both the rain and the surrounding vapor as the rain drops reevaporate ([Bony et al., 2008], appendix D.2).

6.2.3 Simulations

AMIP simulations

A first 1979-2007 simulation has been performed following the Atmospheric Model Intercomparison Project (AMIP) protocol ([Gates, 1992]), using monthly and inter-annually varying SST and sea-ice, and a CO_2 value of 348 ppm. We let a spin-up time of 17 months before January 1979. This simulation is named “free”. Another simulation, named “nudged”, uses the same protocol, but was nudged by the 3-D horizontal winds from ERA-40 reanalyses ([Uppala et al., 2005]) until 2002 and operational analyzes thereafter. The simulated wind fields are relaxed towards the reanalyzed winds with a time constant τ=1h, so that each component of the horizontal wind field u verifies the following differential equation:

$$\frac{\partial u}{\partial t} = \sum_{i=1}^{n} U_i + \frac{u_{obs} - u}{\tau}$$

where u_{obs} is the reanalysis wind and U_i are the temporal tendencies of each of the n dynamical and physical packages in the model.

Sensitivity tests

Sensitivity tests to tunable parameters in the physical or isotopic parametrization have been performed on 3-year simulations with climatological SST, with a spin up of 17 months. The sensitivities to parameters discussed in this paper are much larger than the inter-annual variability, justifying shorter simulations that are computationally less expensive than the AMIP 1979-2007 simulations.

Additional 3-year simulations have been performed using the same protocol, but with uniform SST perturbations (as suggested by [Cess and Potter, 1988]): $-4K$, $-2K$ and $+2K$. The sea ice distribution is not modified consistently with the SST in these simulations, but we restrict their analysis to tropical regions in this paper.

Past climate simulations

As suggested by the Paleoclimate Model Intercomparison Project (PMIP) project ([Joussaume and Taylor, 1995, Braconnot et al., 2007]) and as in other isotopic modeling studies (e.g. [Jouzel et al., 2000]), we perform past climate simulations for two periods: the Last Glacial Maximum (LGM, 21 ka) and the Mid-Holocene (MH, 6 ka). For both these periods, a large amount of data is available for model evaluation. These simulations are 3 year long, with a spin up of 17 months.

A first LGM simulation was performed following a protocol similar to PMIP1 ([Joussaume and Taylor, 1995]), using the [CLIMAP, 1981] SST and sea-ice, a CO_2 concentration of 180ppm, orbital parameters following [Berger, 1978]. Contrary to the PMIP1 protocol, we use the [Peltier, 1994] ICE-5G ice-sheet reconstruction (as in [Lee et al., 2008] and PMIP2: [Braconnot et al., 2007]), which differs from the ICE-4G reconstruction ([Peltier, 1994], used in [Joussaume and Jouzel, 1993, Jouzel et al., 2000]) in the spatial extent and height of northern hemisphere ice-sheets. Except for the different ice-sheet topography, our simulation is similar to that performed by [Joussaume and Jouzel, 1993, Jouzel et al., 2000, Werner et al., 2001].

The MH simulations were performed following the PMIP1 protocol, as in [Jouzel et al., 2000]. The only changes compared to present day are the orbital configuration ([Berger, 1978]) and atmospheric gas concentrations (CO_2 concentration of 280ppm).

The LGM and MH simulations are compared to the free AMIP simulation, considered as a reference for present day (PD).

The warm tropical SSTs and the extensive sea-ice of the CLIMAP reconstruction have been questioned (e.g. [Waelbroeck and co authors, 2008]). Therefore, as in [Lee et al., 2008], we perform an additional simulation using the SST and sea-ice simulated by a coupled model (here the IPSL model, [Marti et al., 2005]) for LGM conditions. We use here the climatological SST from an LGM simulation performed under the PMIP2 protocol ([Braconnot et al., 2007], with LGM orbital configuration and a CO_2 concentration of 185 ppm), averaged over 50 years. However, significant SST biases in the IPSL model are common to all climate conditions, including LGM and PD. Therefore, the direct comparison between SSTs simulated for LGM by the IPSL model ($T_{LGM/IPSL}$) and SSTs observed at PD (T_{PD}) is misleading : SST biases in the IPSL model could be confused with LGM−PD signals. To circumvent this problem, we use the SSTs from an IPSL model pre-industrial simulation (PI) simulation, performed following the PMIP2 protocol (with present-day orbital configuration and a CO_2 concentration of 280ppm). We force our additional LGM simulation with $T'_{LGM/IPSL} = T_{LGM/IPSL} - T_{PI} + T_{PD}$. This way, the biases in the IPSL model common to both the LGM and PI simulations are cancelled out. We can thus compare our LGM isotopic simulations from both CLIMAP and IPSL SSTs in a consistent way.

6.3 Evaluation and sensitivity tests

The present day climate simulated by LMDZ4 has been extensively evaluated in [Hourdin et al., 2006]. The mean annual temperature and precipitation maps in the nudged simulation are given in figure 6.1 for reference. We focus here on the isotopic simulation. First, we examine the isotopic spatial and seasonal distribution, then its variability at synoptic to inter-annual time scales in the present day climate, and finally we evaluate isotopic variations associated with past climates.

We present an evaluation of $\delta^{18}O$, expressed in ‰, defined as

$$\delta = \left(\frac{R_{sample}}{R_{SMOW}} - 1 \right) \cdot 1000$$

where R_{sample} and R_{SMOW} are the ratio of HDO or $H_2^{18}O$ over $H_2^{16}O$ in the sample and the Standard Mean Ocean Water (SMOW) reference respectively. At first order, variations in δD follow the same patterns as $\delta^{18}O$ but are 8 times larger. The deviation to this behavior is quantified by the deuterium excess: $d = \delta D - 8 \cdot \delta^{18}O$ ([Dansgaard, 1964]). This second order parameter is known to be more difficult to simulate by GCMs ([Lee et al., 2007, Mathieu et al., 2002]). We thus present an evaluation of this parameter as well, which is expected to provide stronger constraints on the simulated hydrological and isotopic processes.

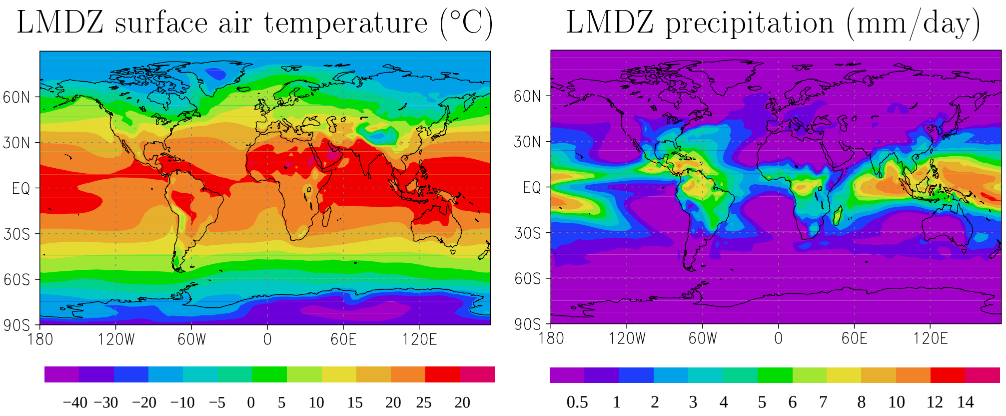

Figure 6.1: Annual mean temperature (left) and precipitation (right) in the LMDZ-iso nudged simulation.

6.3.1 Evaluation of the spatial and seasonal distributions

We use in this section the whole AMIP simulations averaged over the period 1979-2007 to produce average seasonal cycles. We compare the spatial distribution and seasonal cycle with the GNIP (Global Network for Isotopes in Precipitation) data ([Rozanski et al., 1993]), to which we add data from Antarctica (compiled by [Masson-Delmotte et al., 2008]) and Greenland (compiled by [Masson-Delmotte et al., 2005]).

Annual mean spatial distribution of isotopes in precipitation

The spatial distribution of annual mean $\delta^{18}O$ in precipitation ($\delta^{18}O_p$) is well simulated in the model, featuring the well known "effects" ([Rozanski et al., 1993]): enhanced depletion with decreasing temperature ("temperature effect"), increasing altitude ("altitude effect") or continentality ("continental effect") or precipitation intensity ("amount effect") (figure 6.2). The $\delta^{18}O$ over central Greenland and Antarctica is however overestimated, due to an overestimated temperature over Antarctica (minimum annual temperature over Antarctica of -42°C in nudged LMDZ-iso and -60°C in [Masson-Delmotte et al., 2008]). This warm bias is frequent in GCMs ([Masson-Delmotte et al., 2006]) and is worsened when nudging the model with meteorological reanalyses. The temperature effect in Antarctica is however relatively well reproduced, with a spatial slope of $0.73‰/K$ (r=0.95) in the data and $0.65‰/K$ in the model (r=0.97) over the temperature range simulated by LMDZ-iso (figure 6.3).

The deuterium excess in precipitation (d_p) is of the right order of magnitude over most regions except on tropical continents (simulated d_p too high by up to 10‰ over equatorial Africa and northern South America). LMDZ-iso reproduces the d minimum over high latitude oceans ([Uemura et al., 2008]) and features a relationship with δD consistent with observations over Antarctica (figure 6.3 and 6.4). LMDZ-iso also captures the d_p maximum over the Middle East, as was also the case in other GCMs ([Hoffmann et al., 1998, Schmidt et al., 2007]). LMDZ-iso simulates the spatial distribution reasonably well compared to other GCMs: [Yoshimura et al., 2008] reports spatial correlations between 0.39 and 0.52 between observed and simulated annual d_p values in 4 isotopic GCMs; LMDZ-iso value is 0.45. However, d_p is slightly underestimated by LMDZ-iso at high latitudes, in particular over North-western America, the arctic ocean and central Antarctica. It is slightly overestimated in convective regions of tropical South America and Africa. Regional patterns in d_p over the tropics differ strongly among the models, in particular over continents. The GISS fully coupled model ([Schmidt et al., 2007]) and the ECHAM atmospheric GCM ([Hoffmann et al., 1998]) for example do not show higher d_p values over South America than over the surrounding oceans, contrary to LMDZ-iso and GNIP. The difference seems unrelated to the representation of fractionating evaporation at the land surface, which is absent in both LMDZ-iso and ECHAM. Instead, it might reveal different simulated response of d_p to convective activity, which is known to differ between continents and oceans ([Nesbitt and Zipser, 2003, Liu and Zipser, 2005]).

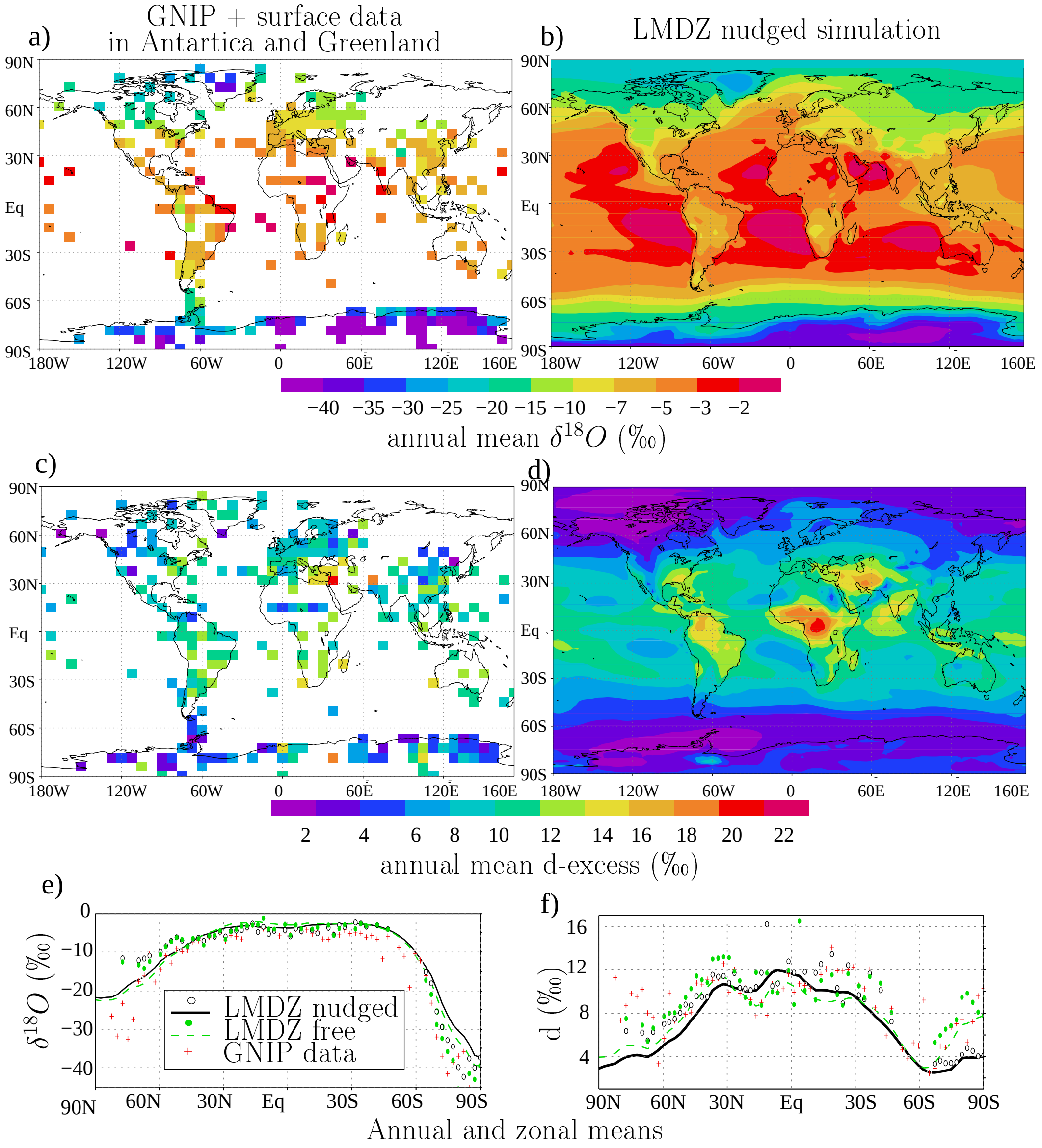

Figure 6.2: Annual mean $\delta^{18}O$ (a, b) and d-excess (c, d) in precipitation, in the data (a, c) and the LMDZ-iso nudged simulation (b, d). The data are the GNIP data ([Rozanski et al., 1993]), the Antarctica data from [Masson-Delmotte et al., 2008] and Greenland surface data ([Masson-Delmotte et al., 2005]) The data is gridded over a coarse 7.5×6.5° grid for visualization purpose. The simulation is the nudged simulation averaged over the 1979-2007 period. (e) and (f): zonal means of the annual averages of $\delta^{18}O$ (e) and d-excess (f), in red for the data, black for the nudged simulation and green for the free simulation. The lines are zonal averages for LMDZ-iso simulations, and the points are the values at data stations.

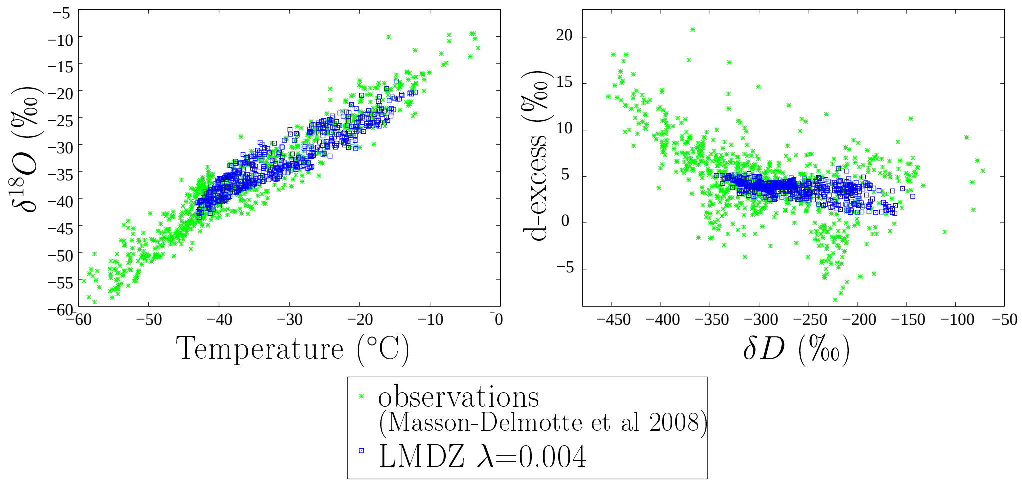

Figure 6.3: Annual mean δD as a function of annual mean air temperature at first level (left) and annual mean d-excess as a function of annual mean δD (right) in precipitation, in the data from [Masson-Delmotte et al., 2008] (green) and the LMDZ-iso nudged simulation (blue).

Name	latitude	longitude	region	active years	vapor sampling
Reykjavik	64.13	-21.93	Northern Atlantic	1961-2001	-
Vienna	48.25	16.37	Central Europe	1961-2001	2001-2003, weekly sampling
Manaus	-3.12	-60.02	Central Amazon	1966-1990	1978-1980, monthly sampling
Apia	-13.8	-171.78	Western Tropical Pacific	1962-1977	-
Ankara	39.95	32.88	Eastern Mediterranean	1963-2001	2001-2002, sub-weekly sampling
Bangkok	13.73	100.50	South East Asia	1968-2001	-

Table 6.1: Name, location and active years of the GNIP stations chosen to assess seasonal cycles and inter-annual variability of the isotopic composition of the precipitation. The last column gives the frequency and active years of the vapor sampling on some of these stations.

The parameter λ, controlling kinetic effects during snow formation, is known to have a strong impact on the d of snowfall in Antarctica ([Jouzel and Merlivat, 1984, Schmidt et al., 2005]). Typical values for λ are 0.002 (e.g. [Landais et al., 2008]), 0.003 (e.g. [Hoffmann et al., 1998, Noone and Simmonds, 2002b]) or 0.004 (e.g. [Schmidt et al., 2007, Vimeux et al., 2001, Stenni et al., 2001]). In LMDZ-iso, setting λ to 0.002 leads to very strong d_p values over central Antarctica (up to 28‰), whereas setting λ to 0.004 gives results more consistent with the data (figure 6.4).

Seasonal cycles of isotopes in precipitation

Figure 6.5 compares the observed and simulated seasonal cycles of temperature, precipitation, $\delta^{18}O_p$ and d_p over 5 GNIP stations representative of various climatic conditions (table 6.1): Reykjavik (Northern Atlantic), Vienna (Central Europe), Manaus (Amazon), Apia (Western tropical Pacific) and Ankara (Eastern Mediterranean). The seasonal cycles of $\delta^{18}O_p$ are generally well reproduced by LMDZ-iso, especially in the nudged simulation.

On the other hand, the seasonal cycles of d_p are unequally reproduced for the different stations. The performance of LMDZ-iso in simulating the seasonal cycle of d_p is in line with the other GCMs: [Yoshimura et al., 2008] reports a correlations between 0.05 and 0.62 between observed and simulated mean JJA-DJF d_p values in 4 isotopic GCMs; the LMDZ-iso value is 0.52. At high latitudes, LMDZ-iso simulates everywhere d_p in anti-phase with $\delta^{18}O_p$, in agreement with the

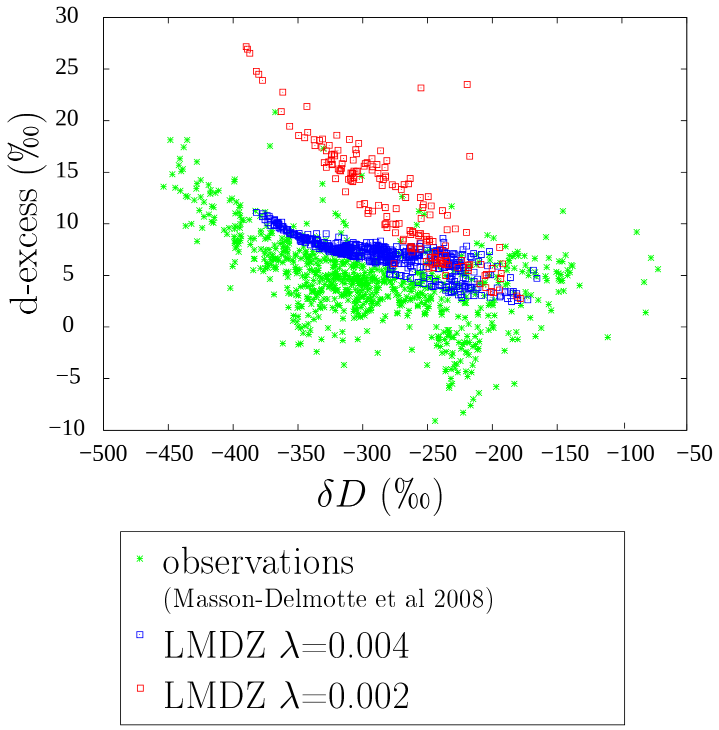

Figure 6.4: Annual mean d-excess as a function of annual mean δD (right) in precipitation in Antarctica, in the data from [Masson-Delmotte et al., 2008] (green) and in LMDZ-iso free simulations (blue and green). In blue, the supersaturation λ was set to its standard value of 0.004, whereas in red, it was set to 0.002.

Reykjavik data (figure 6.5) or inland Antarctica ([Fujita and Abe, 2006], not shown). But LMDZ-iso is not able to reproduce the phase shift of a few months observed between $\delta^{18}O_p$ and d_p in some stations of coastal Antarctica or Greenland ([Johnsen et al., 1989, Ciais et al., 1995, Delmotte et al., 2000]). Over the Mediterranean region, LMDZ-iso simulates an almost flat seasonal cycle of d_p, at odds with the lower d_p observed in summer in Turkey (Ankara figure 6.5) or in Israel ([Angert et al., 2008], not shown). Over the Amazon, LMDZ-iso is able to simulate the maximum of d_p observed during the dry season (e.g. Manaus figure 6.5). During the dry season, simulated d_p values increase with continentality as one goes inland, in agreement with observations ([Salati et al., 1979, Gat and Matsui, 1991], Vimeux et al in prep). These features have been interpreted as the effect of fractionating continental recycling (e.g. evaporation from lakes, bare soil: [Salati et al., 1979, Gat and Matsui, 1991, Henderson-Sellers et al., 2001]). It is thus surprising that LMDZ-iso is able to simulate these features without fractionation during evapo-transpiration from land. Processes controlling the seasonal cycle of d_p in South America in LMDZ-iso seem more related to rain-vapor equilibration processes. The reasons for d_p South American cycles in LMDZ-iso, and whether they are the same as in nature, will be investigated in the future (preliminary analysis in appendix F.3).

The amount effect (which refers to the decrease of $\delta^{18}O_p$ with increasing precipitation that is observed in the tropics) is well reproduced by LMDZ-iso (figure 6.6): over the 9 oceanic tropical stations used in [Bony et al., 2008], the amount effect is -0.5‰$/mm.day$ in LMDZ-iso compared to -0.7 ‰$/mm.day$ in the data. The Single Column Model (SCM) of [Bony et al., 2008] (chapter 2), which shares a very similar version of the Emanuel convective parametrization and the same isotopic representation of droplet evaporation, simulates too depleted a precipitation in humid conditions and too strong an amount effect (figure 6.6, blue). [Bony et al., 2008] hypothesized that this bias could be due to the very simple framework of the SCM, in which horizontal isotopic gradients were neglected. Figure 6.6 confirms this hypothesis: in nature as in LMDZ-iso, the

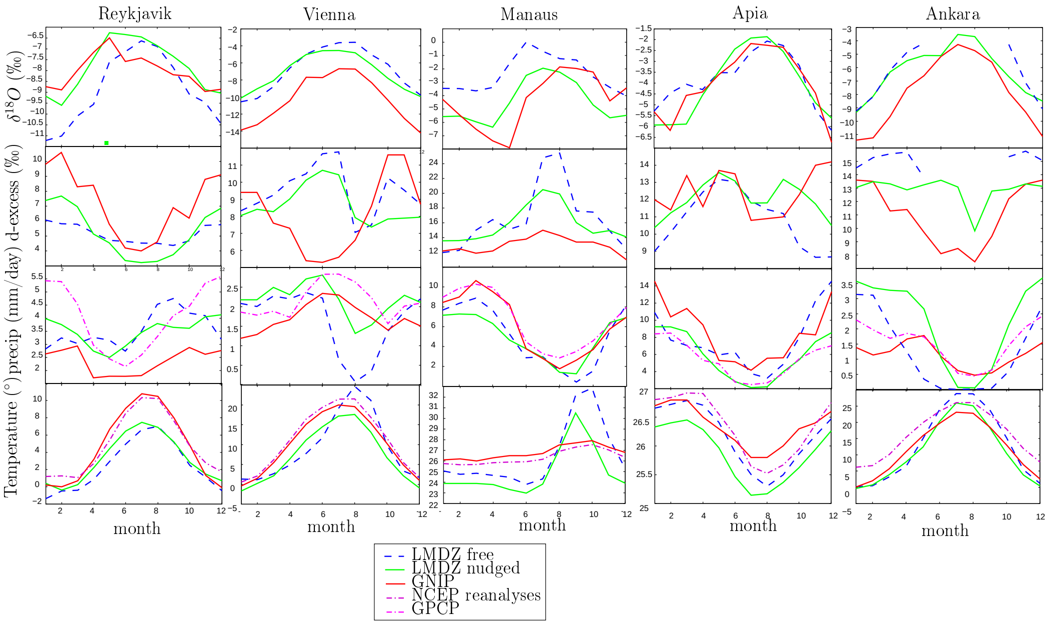

Figure 6.5: Monthly $\delta^{18}O$ and d-excess in precipitation, precipitation and temperature over Reykjavik, Vienna, Manaus and Apia, for the GNIP data (red), the LMDZ-iso nudged (green) and free simulations (blue), as well as NCEP ([Kalnay et al., 1996]) temperatures and GPCP ([Huffman et al., 1997]) precipitation (pink). Monthly averages are calculated over the 1979-2007 period for LMDZ-iso, NCEP and GPCP, and over the years available for GNIP (table 6.1). For LMDZ-iso, we plot the value of the grid box containing the station.

horizontal moisture advections of air masses of different isotopic composition in LMDZ-iso thus act to dampen the amount effect.

Evaluation of the vapor-precipitation equilibrium

A large uncertainty in the representation of water stable isotopes in GCMs is the representation of isotopic exchanges between vapor and rain droplets as the rain falls and partially reevaporates ([Lee and Fung, 2008]). The ECHAM GCM, for example, assumes that a constant fraction of the droplet reequilibrates with the vapor, depending on the cloud type ([Hoffmann et al., 1998]). Here, we calculate explicitly the relative effect of evaporation and equilibration, but we still rely on a tunable parameter ϕ, controlling the relative humidity at the droplet contact, and thus the intensity of kinetic effects: the relative humidity at the droplet contact is parametrized as $\phi + (1 - \phi) \cdot h$, where h is the relative humidity of the vapor reservoir in which droplets reevaporate. Results are very sensitive to this parameter, especially in dry regions where the reevaporation is strong and kinetic effects are crucial: the stronger the kinetic effects, the more the rain gets enriched by evaporation for a given reevaporated fraction ([Bony et al., 2008]). This parameter was set to 0.9 in [Bony et al., 2008]. When setting ϕ to 0 (i.e. reducing the relative humidity at the droplet contact), then the amount effect becomes much stronger and the d_p much lower in dry regions (figure 6.7). In LMDZ-iso as in the SCM, the optimal value for ϕ is 0.9.

As an evaluation of the representation of isotopic processes during evaporation, we compare the degree of equilibration between the vapor and the precipitation at a few stations: Vienna, Manaus and Ankara, where low-level vapor isotopic compositions are available from the GNIP database on http://nds121.iaea.org/wiser/ (table 6.1, figure 6.8). We average both the precipitation and the vapor on all the years available both for the model (1979-2007) and the data (table 6.1) to yield monthly averages. Caution is necessary for 2 sources of uncertainties in the model-data comparison, in addition to possible uncertainties in the data itself. First, vapor samples were not collected every day and might thus not be representative of monthly averages, given the significant variability observed in the vapor at the daily time scale (e.g. [Angert et al., 2008]). However, the

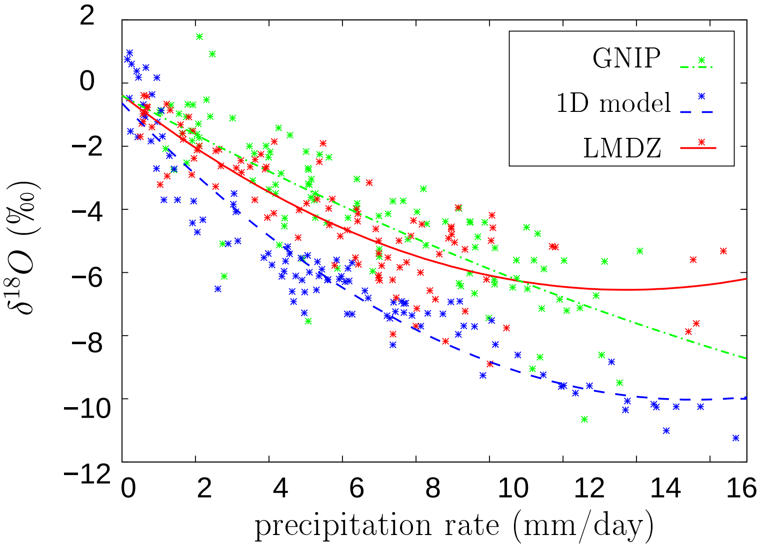

Figure 6.6: Monthly $\delta^{18}O$ in precipitation as a function of precipitation rate for the 9 ocean tropical GNIP stations selected in [Bony et al., 2008], for the GNIP data in red, the LMDZ-iso nudged simulation in green and the single column model of [Bony et al., 2008] in blue. Curves are second order polynomial fits.

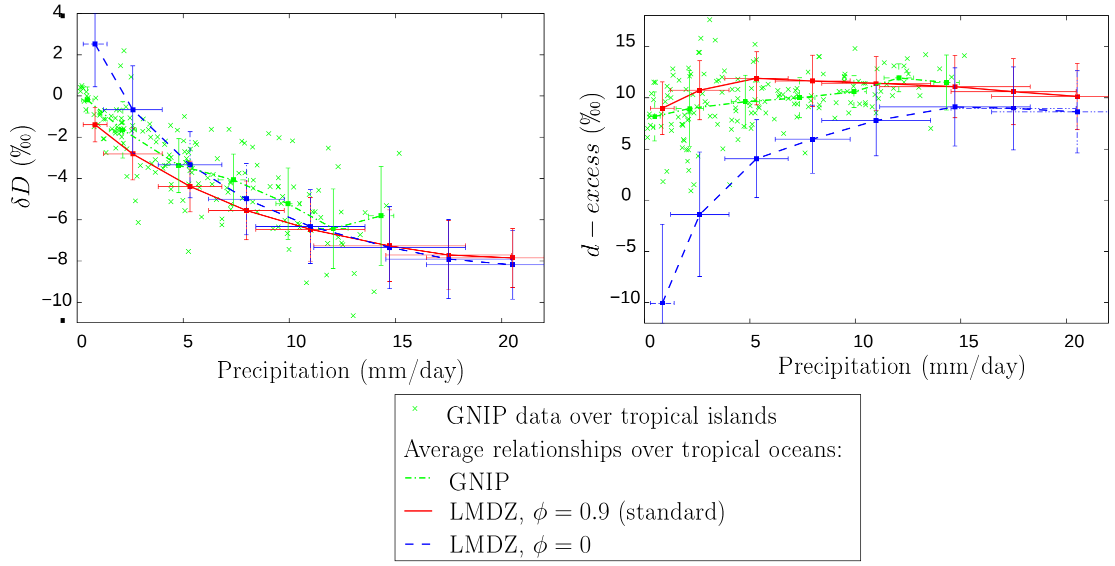

Figure 6.7: Average relationship between precipitation rate and $\delta^{18}O$ (left) and d-excess (right) of tropical oceanic precipitation, at the monthly scale, for GNIP data (green), and 3-year LMDZ-iso simulations with ϕ set to 0.9 (red) and to 0 (blue). Error bars indicate the standard deviation in each precipitation bin.

relatively smooth seasonal cycles (figure 6.8) suggest that this data is suitable for a first evaluation of rain-vapor disequilibrium (figure 6.8). Second, the precipitation and the vapor samples are not necessarily from the same years. The inter-annual variability in LMDZ-iso at the 3 stations is of the order of 1‰ for $\delta^{18}O_v$ and d_v (where $\delta^{18}O_v$ and d_v are the $\delta^{18}O$ and d of the vapor), 2‰ for $\delta^{18}O_p$ and up to 3‰ for d_p. We will thus focus on variations in composition exceeding both the standard deviation of measurements within a month for the vapor data (figure 6.8) and the typical inter-annual varability.

In the data over all stations , the rain is more enriched than the low level vapor ($\delta^{18}O_p - \delta^{18}O_v$ ranges from +7 to +20‰), but over Vienna and Manaus the rain is more depleted (by up to 6 ‰) than would be expected if the rain was in complete equilibrium with the vapor. This might suggest that the rain, which formed at higher altitude from depleted vapor, reequilibrates only partially. Over Ankara during the dry summer, on the other hand, the rain is more enriched (by about 2 ‰) than expected from total diffusive equilibration. This suggests some significant evaporative enrichment in dry air. These features are qualitatively well reproduced by LMDZ-iso.

The d_p observed over Vienna and Ankara is lower than in the vapor and lower than would be expected from equilibrium with the vapor (4 up to 19 ‰ lower). This low d_p could arise from the evaporation of the rain drops as they fall ([Dansgaard, 1964]). LMDZ-iso strongly underestimates this disequilibrium. It underestimates d in the vapor (d_v), whereas d_p is of the right order of magnitude. This mismatch could arise from (1) a problem in the representation of the kinetic effects during rain evaporation and isotopic exchanges or (2) difficulties in comparing surface vapor samples with an average over a GCM layer (about 20hPa or 200m) if some surface processes have an influence restricted to the first few meters above the surface. This calls for more vapor measurements to better constrain and evaluate the representation of isotopic processes during rain fall.

6.3.2 Evaluation of the isotopic variability at the synoptic scale

In this section, we evaluate the ability of the nudged simulation to simulate the variability at the daily and weekly scale. Unless the model is nudged, the model generates its own weather variability uncorrelated to observations, restricting the evaluation to statistics ([Hoffmann et al., 1998, Noone and Simmonds, 2002b]). Nudging with reanalyzed winds enables a more rigorous evaluation of the isotopic variability at the synoptic scale ([Yoshimura et al., 2008]). Here, we present an evaluation using unpublished daily data of both vapor and precipitation collected at the surface at the station of Saclay (near Paris, France, 48.73N, 2.17E) from September 1982 to September 1984. Vapor was collected by continuous sampling on a daily basis (except during week-ends for which the sampling period covers about 3 days). A cryogenic trap was used, and samples were analyzed for $\delta^{18}O$ and δD with an overall accuracy of ±0.15‰ and ±1‰ respectively.

The model reproduces the temperature evolution very well (figure 6.9a), especially in winter, when the variability is mainly controlled by large-scale synoptic disturbances. The correlation between observed and modeled daily temperatures is 0.84 in winter and 0.51 in summer. Consistently, the daily variability of $\delta^{18}O_v$ is well captured, especially in winter: the correlation between observed and modeled daily $\delta^{18}O_v$ is 0.65 in winter and 0.46 in summer. However, the temporal slope of $\delta^{18}O_v$ vs temperature at the daily scale in winter is underestimated by the model (0.2‰/K in LMDZ-iso and 0.6‰/K in the data). For example, while LMDZ-iso simulates accurately the strong negative temperature and precipitation anomaly during the first three weeks of February 1983, the corresponding anomaly in $\delta^{18}O_v$ is underestimated by a factor of 2. The mismatch could be due to an insufficient distillation of air masses due to a misrepresentation either of the water cycle along the air mass trajectories, or of the trajectories themselves, since LMDZ-iso is not able to simulate the observed 10% decrease in relative humidity during the same period (not shown). This low $\delta^{18}O_v$ event was also underestimated in a nudged simulation by the regional model REMO-iso ([Sturm, 2005]), suggesting that this underestimation is a robust bias in models.

The isotopic reequilibration between precipitation and vapor is relatively well reproduced by LMDZ-iso, with the $\delta^{18}O_p$ most frequently 12‰ higher than the vapor in LMDZ-iso and 10‰ in the data.

Although the model satisfactorily simulates the frequency distribution and seasonal variability of d_p, it poorly simulates its synoptic variability (correlation of 0.14 between data and model in

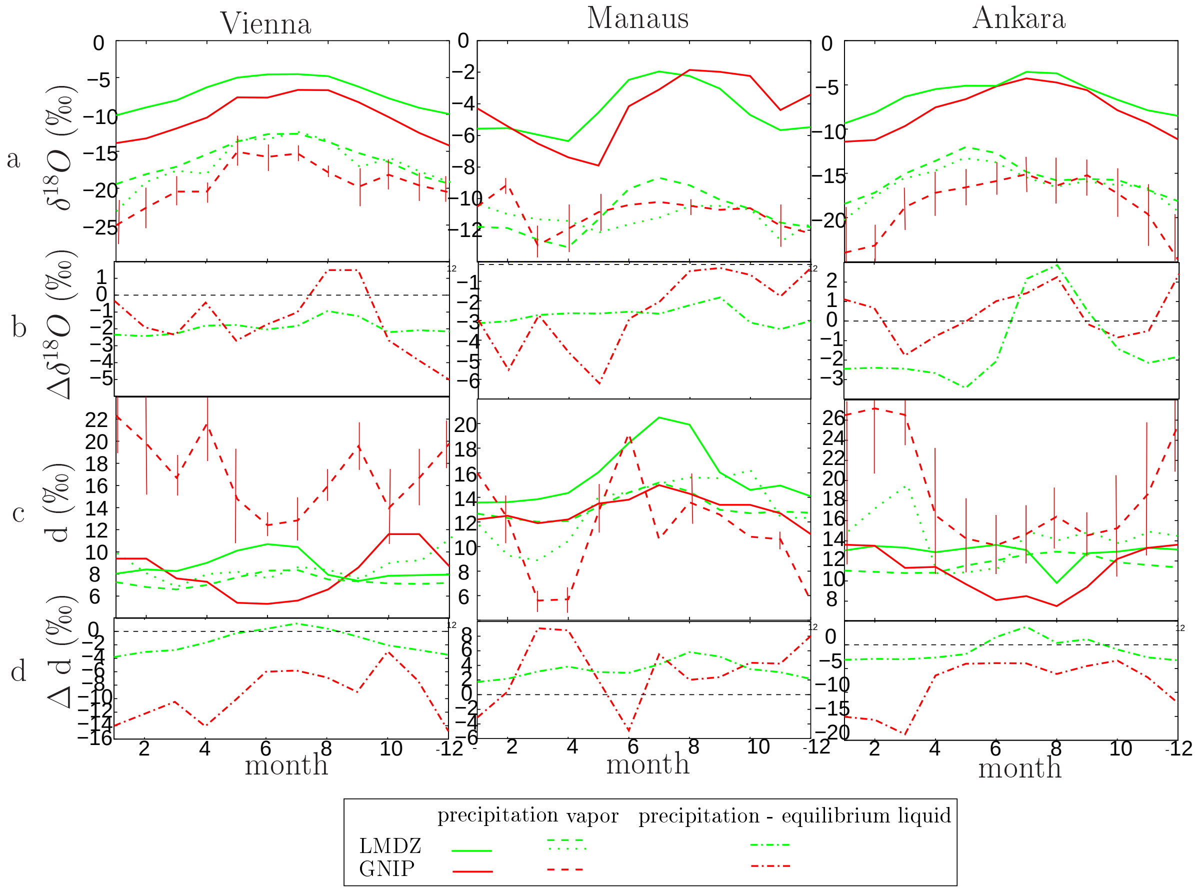

Figure 6.8: a) Monthly $\delta^{18}O$ in precipitation (solid) and vapor at the lowest level (dashed) over Vienna, Manaus, Ankara, for the GNIP-vapor data (red) and the LMDZ-iso nudged simulation (green). The dotted green curves show the LMDZ results collocalized with the date of the GNIP vapor measurements, whereas the dashed line show the monthly means. b) Difference between $\delta^{18}O$ in precipitation and the $\delta^{18}O$ of a liquid that would be in equilibrium with the vapor, for the GNIP-vapor data (red) and the LMDZ-iso nudged simulation (green). For LMDZ, the monthly means were used. c) same as a but for d-excess. d) same as b but for d-excess. The error bars for the GNIP vapor data correspond to the standard devation for the different measurements available for a given month.

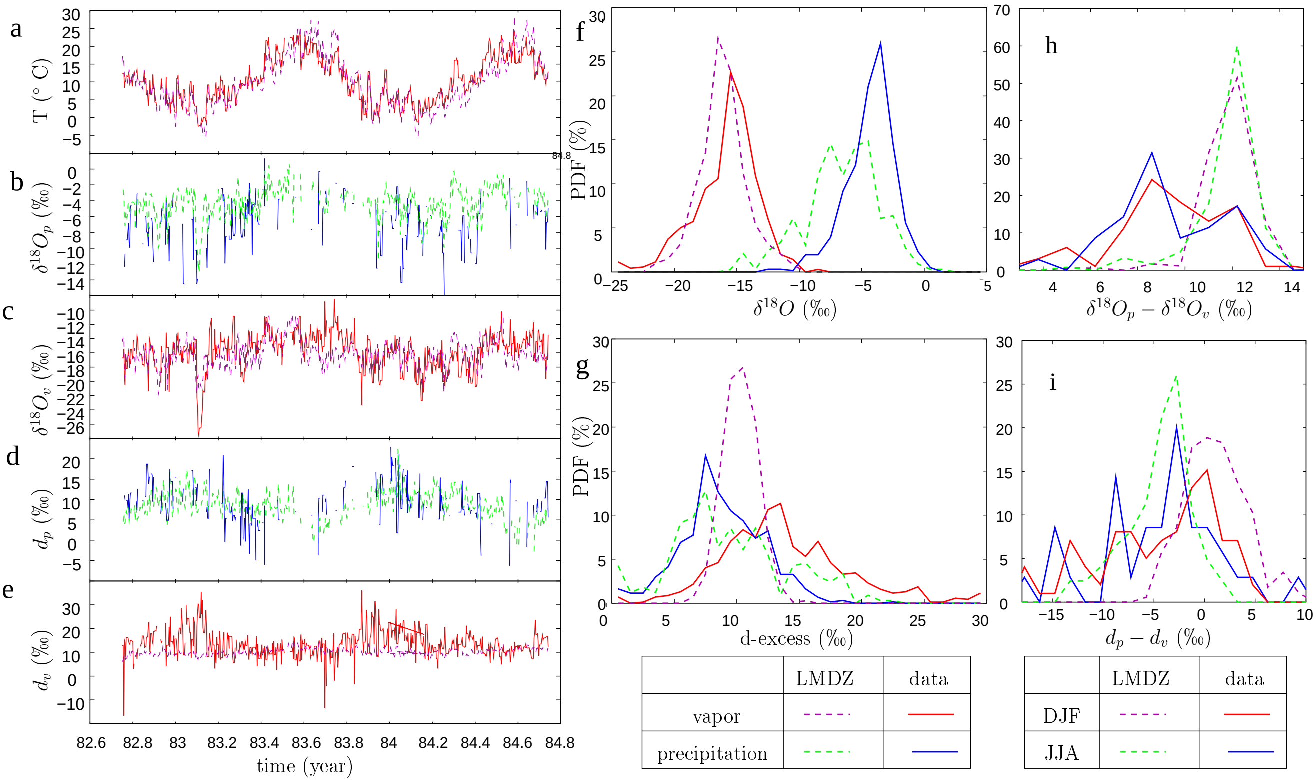

Figure 6.9: Comparison of the synoptic variability of water isotopes simulated by LMDZ-iso with that observed at the surface in Sacly (near Paris, france, 48.73N; 2.17E) from September 1982 to September 1984. Left: daily evolution of temperature (a), $\delta^{18}O_p$ (b), $\delta^{18}O_v$ (c), d_p, (d), d_v (e). Middle: probability density function of the daily $\delta^{18}O$ (f) and d (g) for all months, in both vapor and precipitation. Right: probability density function of the daily difference between $\delta^{18}O$ in the precipitation and the vapor (h) and between d in the precipitation and the vapor (i). Observed temperatures are in purple , measured $\delta^{18}O_v$ and d_v are in dashed purple; $\delta^{18}O_p$ and d_p are in dashed green; LMDZ-iso $\delta^{18}O$ is in solid red and d is in solid blue.

winter). The reequilibration between precipitation and vapor for d is well reproduced, with d most frequently 2‰ lower in average in precipitation than in the vapor in LMDZ-iso and about 5‰ lower in the data. This difference between d_p and d_v is strongly sensitive to parameter ϕ controlling kinetic effects during rain reevaporation: if ϕ is set to 0 (not shown), the simulated d_p is about 8‰ lower than d_v.

The model completely misses the observed variability in d_v, simulating a nearly constant d_v of 10‰ all year long. d_v may be more sensitive to local processes not captured by the model. The correct simulation of d_p is however surprising, suggesting that a good representation of the variability of d_v is not necessary to correctly simulate the variability of d_p. We speculate that some processes at short spatial scales near the surface influence d_v in the data, but these processes have no impact on the observed precipitation and are not represented in the lowest layer of LMDZ-iso, which is quite thick (20 hPa or 200 m).

LMDZ-iso, when nudged by reanalyses, can thus satisfactorily simulate the day-to-day variability in temperature that are related to large-scale atmospheric disturbances, and the associated $\delta^{18}O$ variability in vapor and precipitation (at least qualitatively). At the synoptic scale, as is the case at the seasonal scale, the variability in d is more difficult to simulate. d_v is even more difficult to simulate than d_p, possibly due to a mismatch between the scale of in-situ measurements and the scale of atmospheric phenomena that can be simulated by a GCM, as was already pointed for the seasonal scale (section 6.3.1). Measurements of d_v within the bulk of the boundary layer or at the top of a mat would be more comparable to LMDZ-iso simulations.

6.3.3 Evaluation of the isotopic variability at the inter-annual scale

Water isotopes have been shown to record inter-annual to decadal variability of the precipitation in the tropics ([Hoffmann, 2003, Ramirez et al., 2003]) and modes of variability in the extra-tropics such as the North Atlantic Oscillation ([Baldini et al., 2008, Sodemann et al., 2008]) or the Southern Annular Mode ([Noone and Simmonds, 2002a]). To evaluate whether LMDZ-iso could be used in the future to study such issues, we evaluate the representation of the isotopic variability at the inter-annual scale.

The simulation nudged by reanalyzed winds simulates better than the free simulation the inter-annual variability in temperature, precipitation and isotopes, as can be shown by time series (figure 6.10) over Vienna and Bangkok. These two stations were chosen for their long records and contrasting climate (as in [Yoshimura et al., 2008]) The improvement is particularly strong in mid-latitudes. For example, the correlation is 0.80 between model and data monthly anomalies of temperatures (filtered with a 6-month running mean) over Vienna in the nudged simulation compared to 0.05 in the free simulation. Consistently, the variability of $\delta^{18}O_p$ is strongly improved at this station (0.66 compared to 0.26). The simulated variability of precipitation is also improved (0.51 compared to 0.09). On the other hand, in the tropics, the variability in temperature, precipitation and $\delta^{18}O_p$ is not much improved, consistently with the results of [Yoshimura et al., 2008]: correlations between model and data $\delta^{18}O_p$ are of 0.52 and 0.58 for the nudged and free simulations respectively. Since tropical SSTs exert a dominant control on the tropical inter-annual variability, this variability is already well captured by LMDZ-iso just by forcing with observed SST, and the nudging provides little added value. In all simulations, the simulated d_p variability is completely different from the observed variability (correlations of -0.02 and -0.14 over Vienna and Bangkok in the nudged simulations). Also, the inter-annual variability of d_p is strongly underestimated by LMDZ-iso, as was the case at the synoptic scale.

LMDZ-iso overestimates the correlations of $\delta^{18}O_p$ with both the temperature and the precipitation amount (figure 6.11), as pointed by [Tindall et al., 2009] for the Hadley model, possibly due to the different spatial scale of simulations and measurements. LMDZ-iso simulates an inter-annual slope of $\delta^{18}O$-vs temperature ranging from 0.3 to 0.8 ‰/K in high latitudes, of the same order of magnitude as those derived from the GNIP data (figure 6.11). In the tropics, the simulated amount effect is about -0.5 ‰/(mm/day), also comparable with GNIP data ([Rozanski et al., 1993]).

Therefore, LMDZ-iso, when forced by observed SST and nudged by reanalyzed winds, simulates relatively well the inter-annual variability in $\delta^{18}O_p$, though it has more difficulties in simulating d_p.

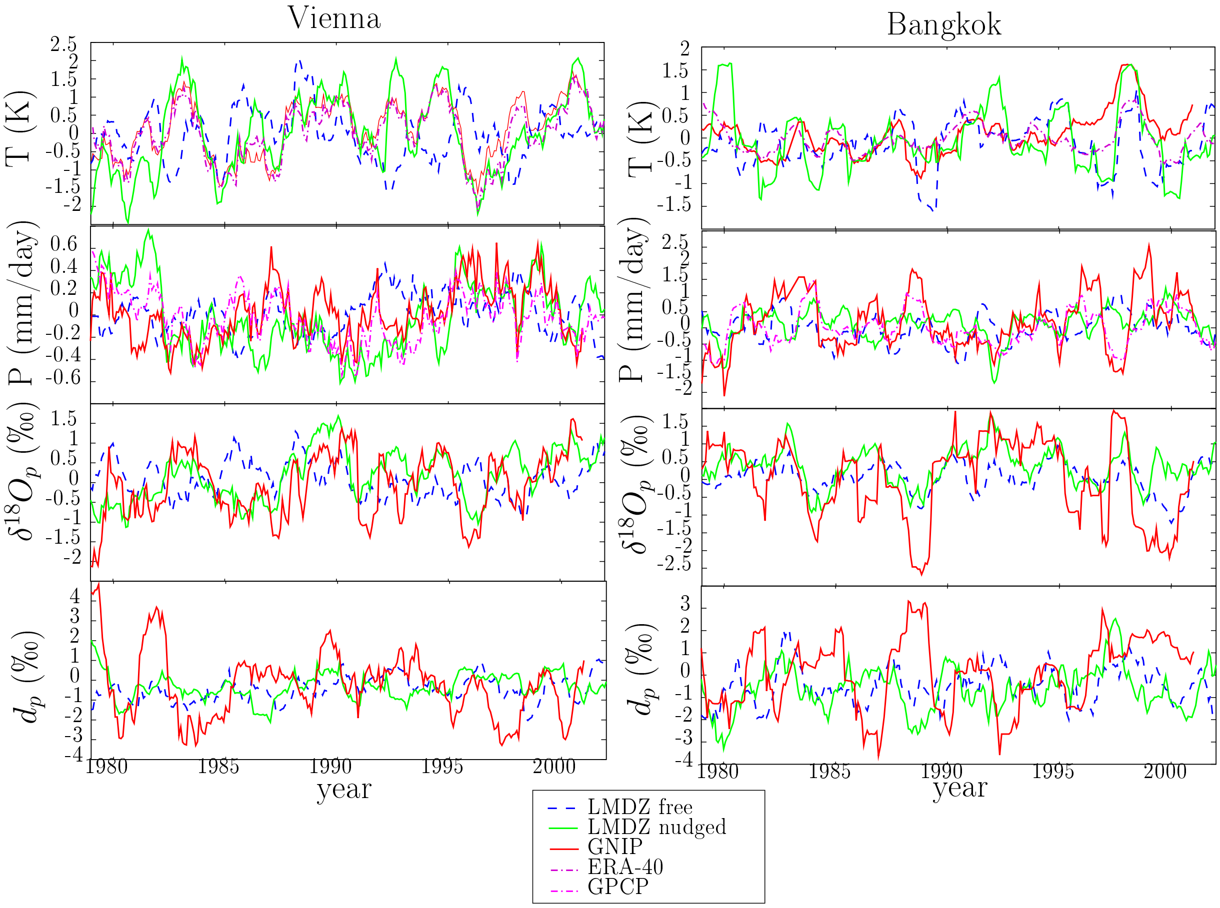

Figure 6.10: Monthly inter-annual anomaly of air temperature, precipitation rate, $\delta^{18}O$ and d-excess in precipitation over the Vienna and Bangkok GNIP stations, comparing GNIP data and the LMDZ-iso nudged simulation.

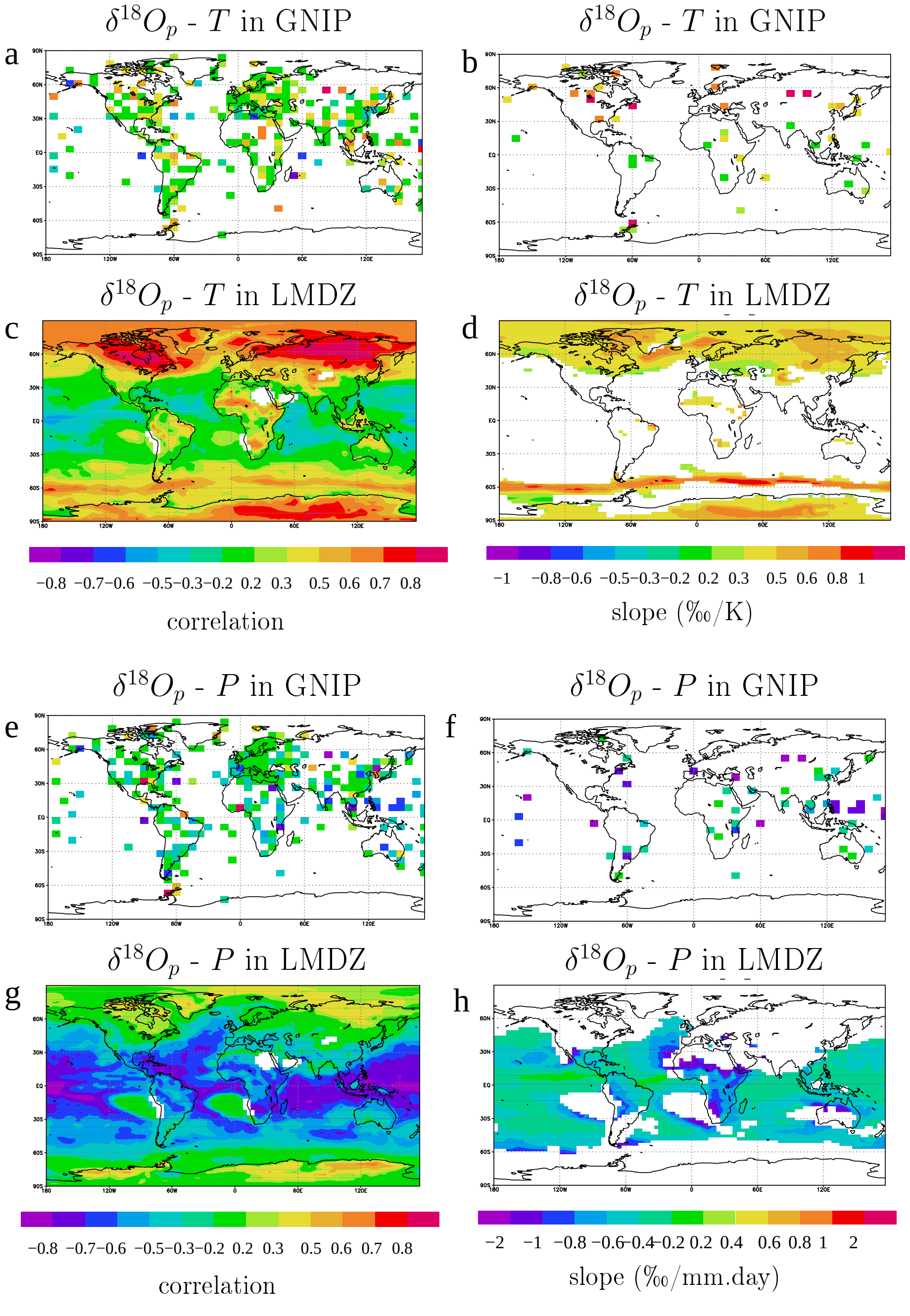

Figure 6.11: Correlation coefficients (left) and slopes (right) of the inter-annual relationship between monthly anomalies (seasonal cycle subtracted) of $\delta^{18}O$ in precipitation and temperature (a-d) and precipitation rate (e-h). Time series of monthly anomalies were applied a 6-month running mean before performing the linear regression. The regression is performed for the GNIP data (a,b,e,f) and the nudged 1979-2007 LMDZ-iso simulation (c,d,g,h). White zones correspond to correlations lower than 0.4 in absolute value.

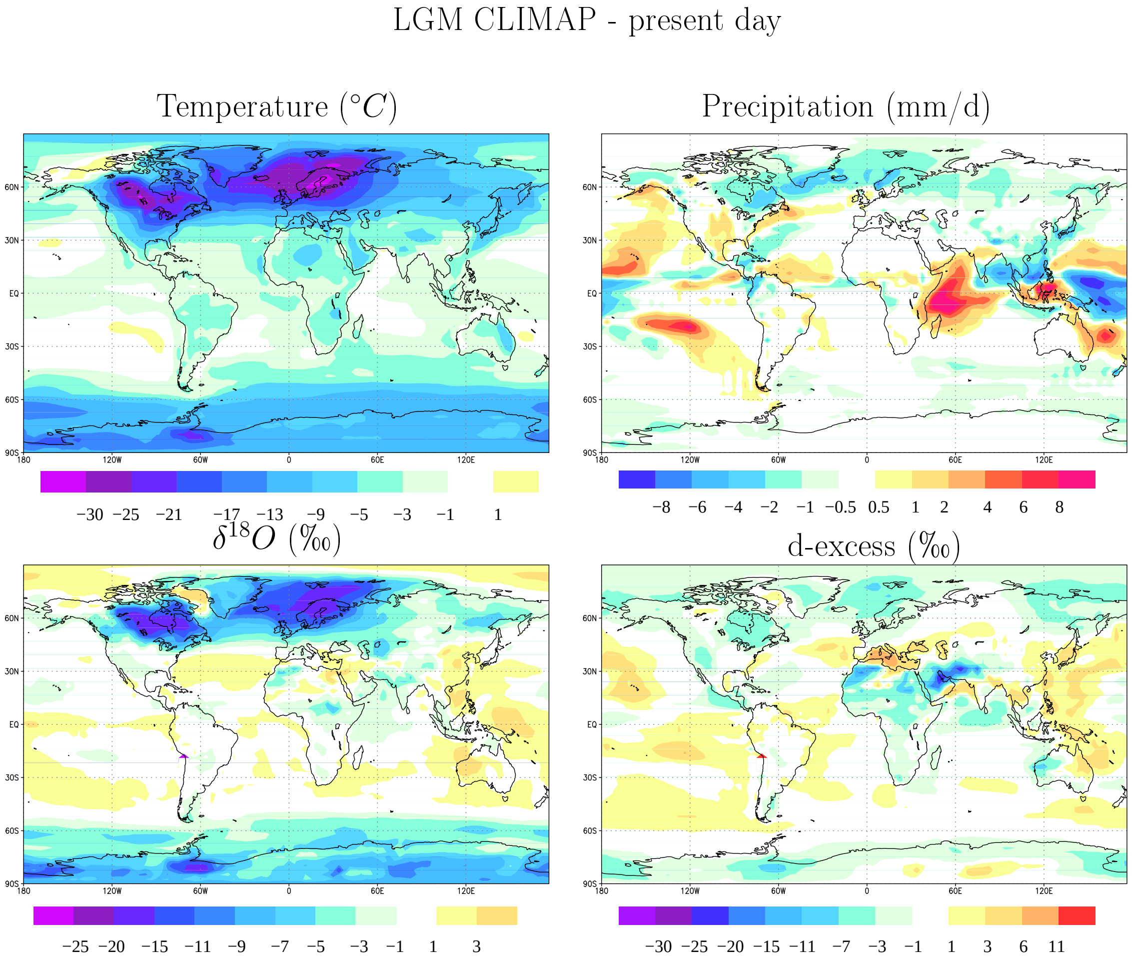

Figure 6.12: Annual average change between LGM and present-day for temperature (upper left), precipitation (upper right), $\delta^{18}O$ (lower left) and d-excess (lower right). The LGM simulation used the CLIMAP SST ([CLIMAP, 1981]).

6.3.4 Evaluation of isotopic variations at climatic scales

We have seen that LMDZ-iso reproduces reasonably well the present-day climate and its variability from the synoptic, regional scale to the inter-annual, large scale. In this section, we evaluate the capacity of LMDZ-iso to simulate the isotopic changes associated with two past climates (described in section 6.2.3): the Last Glacial Maximum (LGM) and the Mid-Holocene (MH).

The Last Glacial Maximum

Comparing the model results to the data for the LGM is not straightforward. In the case of South American speleothems, for example, the minimum $\delta^{18}O$ values are about -4.5‰ at about 18 000 years before present (18 ka) ([Cruz et al., 2006]), but values around 21 ka are about -3‰, same as in present day ([Cruz et al., 2005b]). Here, we consider that the LGM value corresponds to the minimum $\delta^{18}O$ values between 17 and 21 ka, or take the LGM values given by the author. Dating uncertainty could explain the different LGM dates. However, if the minimum $\delta^{18}O$ actually does not occur at the same time at all places (as suggested by some studies: [Smith et al., 2005, Sylvestre, 2009]), the combination of the LGM data is impossible to simulate with a time slice simulation ([Farrera et al., 1999, Pinot et al., 1999]), adding an additional source of discrepancy between the model and data.

Figure 6.12 and 6.13 show the changes between LGM and present-day (PD) simulated by LMDZ-iso when forced at LGM by CLIMAP or IPSL SSTs respectively. Forced by CLIMAP

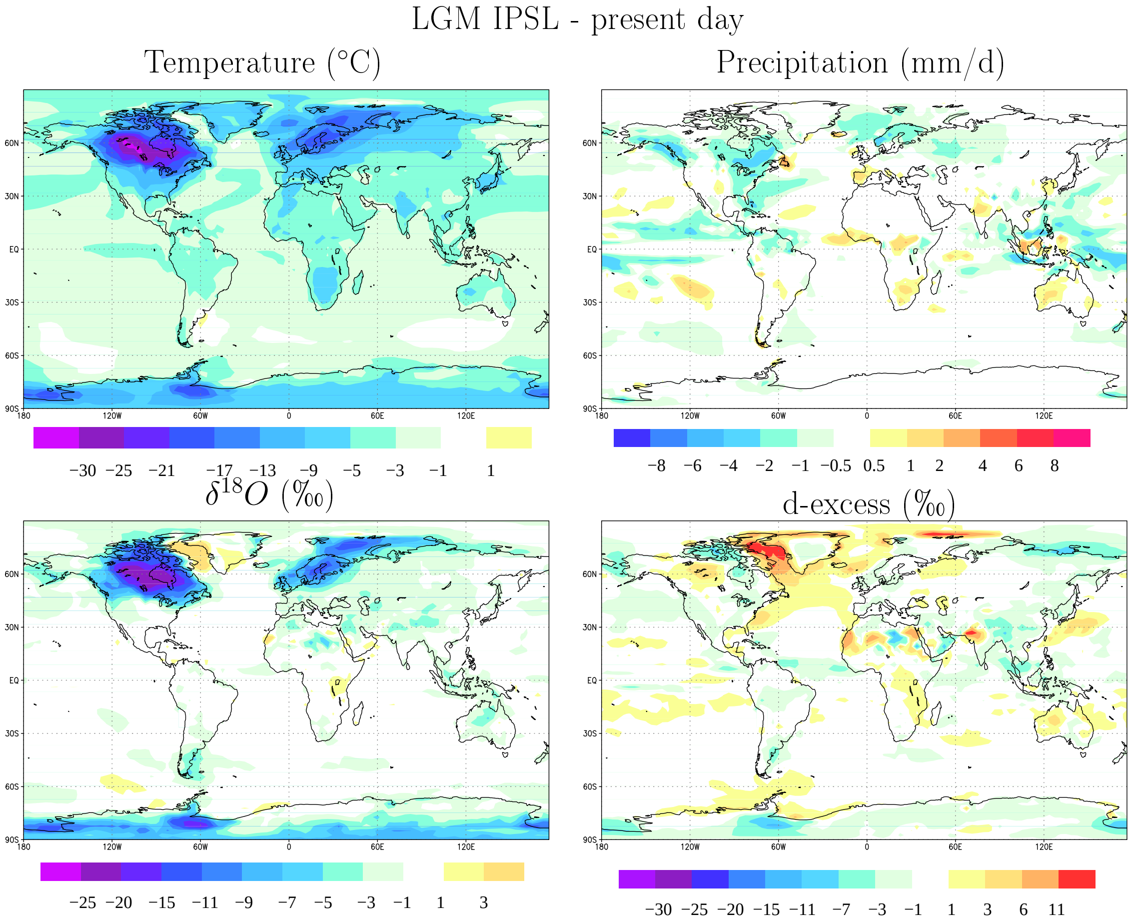

Figure 6.13: Same as for fig 6.12 but for the LGM simulations using the SSTs from an LGM simulation with the coupled IPSL model. The set-up of this simulation is detailed in section 6.2.3.

SSTs, LMDZ-iso simulates well the depletion in $\delta^{18}O_p$ over mid and high latitudes during the LGM, except in Northeastern America and over part of the Arctic where a slight enrichment is simulated. Forced by IPSL SSTs, which are up to 10K warmer than CLIMAP SSTs over high latitude oceans, LMDZ-iso is able to simulate the depletion observed in ice cores in Antarctica, but not in Greenland.

The relevance of spatial slopes for reconstructing paleo-temperatures at high latitudes has extensively been discussed ([Jouzel et al., 2003, Lee et al., 2008]). In Greenland, the temporal temperature$-\delta^{18}O_p$ slope between LGM and PD (0.3‰/K: [White et al., 1997]) has been suggested to be half the spatial slope (0.67‰/K), possibly due to colder source temperatures ([Boyle, 1997]) at LGM or to changes in the seasonality of precipitation ([Krinner and Werner, 2003, Werner et al., 2000]). This leads to an underestimation by a factor of two of temperature changes based on $\delta^{18}O_p$. In Antarctica, on the other hand, studies suggest the temporal and spatial slope are similar with a margin of ±20% ([Jouzel et al., 2003, Krinner and Werner, 2003]), leading to reconstructions of past temperature changes with an error lower than 2°C. This is supported by simulation with the GISS and ECHAM GCMs forced by CLIMAP SSTs: they simulate temporal slopes between LGM and PD in Eastern Antarctica of the order of 0.7‰/K and 0.6‰/K respectively ([Jouzel et al., 2003]) compared to a spatial slope of the order of 0.75‰/K. On the other hand, the CAM model, when forced by SSTs simulated by a coupled model, simulates temporal slopes half smaller than the spatial slopes in the same region ([Lee et al., 2008]). We compare here these results with those from LMDZ-iso forced by the CLIMAP and IPSL LGM SSTs. In Greenland, LMDZ-iso, simulates a temporal slope between LGM and PD of about 0.4‰/K over Greenland, half the spatial slope of 0.8 ‰/K, consistently with earlier studies and all other GCMs ([Jouzel et al., 2000]). In Antarctica, LMDZ-iso forced by the CLIMAP SSTs simulates temporal slopes in Vostok of 0.8‰/K, virtually equal to the spatial slope in this region. The simulated temporal slopes are within 20% of the spatial slope over most locations in Eastern Antarctica, consistently with the GISS and ECHAM simulations reported by [Jouzel et al., 2003]. On the other hand, when forced by IPSL LGM SSTs, the temporal slopes are most frequently around 0.5‰/K, i.e. 40% lower than the spatial slope. This is in closer agreement with [Lee et al., 2008], who also used simulated SSTs. This suggests that the controls of $\delta^{18}O_p$ over Antarctica, and thus the accuracy of reconstructions based on present-day spatial slopes, strongly depend on the pattern of SST change. If the change in SST features a strong equator-pole gradient as in CLIMAP, then the spatial slope can be applied to past temperature reconstructions within 20% accuracy. On the other hand, if the SST change has a lower equator to pole gradient, as simulated by the IPSL or CAM coupled models ([Lee et al., 2008]), then using the spatial slope for temperature reconstruction leads to an underestimation of past temperature changes (by about 40% in the LMDZ-iso simulation forced by IPSL SSTs). At this stage we are more confident in reconstructed than in simulated paleo SSTs, as large SST pole-equator gradients are confirmed by the recently published MARGO data ([Waelbroeck and co authors, 2008]). Our results thus rather supports the current use of PD spatial slope to interpret isotopic profiles recovered in central Antarctica.

In the tropics, LMDZ-iso simulates little isotopic changes and fails to simulate the depletions ranging from −1.5‰ to −6.3‰ inferred from tropical ice cores and South American speleothems (table 6.2). Even when using SSTs from the IPSL coupled model, which are about -2.9K colder than PD in the tropics, the decrease in $\delta^{18}O_p$ is small (less than 2‰). Temperature does not seem to have any significant effect on tropical $\delta^{18}O_p$ in LMDZ-iso, at any time scale. The failure to simulate lower $\delta^{18}O_p$ in South America is common to other GCMs ([Werner et al., 2001, Jouzel et al., 2000]). However, it is not clear whether the depletions measured in available records (table 6.2) are representative at the scale of the entire tropics.

Another typical failure of isotopic GCMs for the LGM is their inability to simulate the lower d_p measured in ice cores at high latitudes during LGM ([Werner et al., 2001]), or more generally to simulate $\delta^{18}O$ and d variations of the same sign on climatic time scales ([Noone, 2008]). However, LMDZ-iso does simulate a lower d_p over most of Greenland (e.g. Summit: −3.5‰ compared to −3‰ in observations, table 6.2), and over most of Antarctica except in central East Antarctica. In the simulation using coupled SSTs, the Antarctic d_p during the LGM is lower than present-day by -4‰, in even better agreement with the data. The reason for this behavior of d_p will be the subject of future investigations.

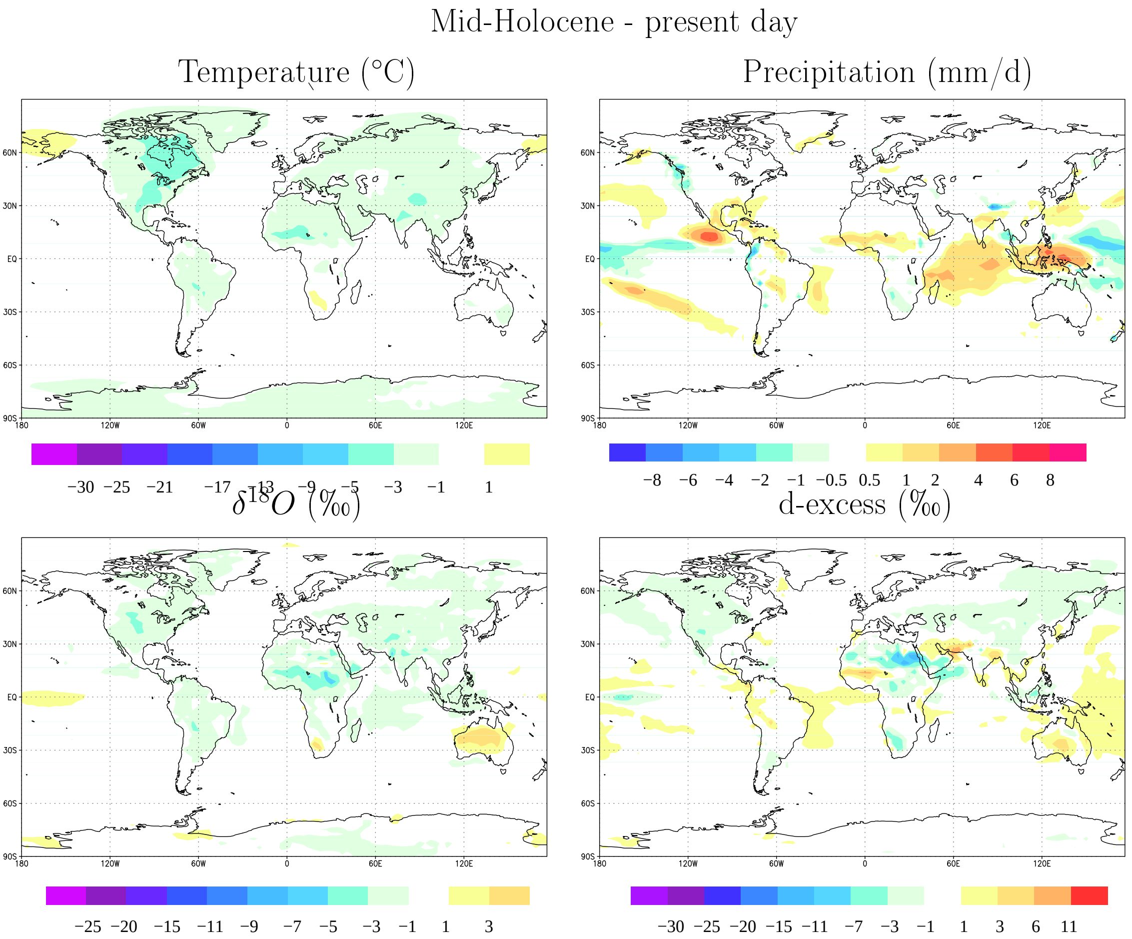

Figure 6.14: Same as for fig 6.12 but for Mid-Holocene minus present-day.

To conclude about the LGM simulations, LMDZ-iso simulates realistic LGM depletions at high latitudes but, like other GCMs, misses the more depleted values measured for LGM at low latitudes. Its main specificity is the simulation of a lower d_p in most high latitude regions, in agreement with the data.

Mid-Holocene

In agreement with simulations from the GISS and ECHAM models ([Jouzel et al., 2000]), and in agreement with measurements (table 6.3) the isotopic changes between MH and PD are very small in most regions. Exceptions are found however over the Sahel, in the Middle East, in Central Asia and in the Western US, where a depletion of the order of 5‰ is simulated (Figure 6.14).

The monsoon regions are relatively well represented in the LMDZ-iso model, though the precipitation amounts are slightly underestimated in summer ([Hourdin et al., 2006]). During the Mid-Holocene, the Indian and African monsoons are enhanced in LMDZ-iso (up to +3mm/day in annual average), in agreement with other PMIP models ([Joussaume et al., 1999]). As a result, the precipitation downstream of these regions of enhanced precipitation is more depleted (up to −8‰ in the Northern Sahel and Tibet), consistently with the amount effect. The corresponding $P - \delta^{18}O_p$ slopes are much higher than at the inter-annual or seasonal scales. For example, when averaging the Western African monsoon precipitation over the 20°W-30°E; 10°N-20°N region ([Joussaume and Taylor, 1995]) and for the July to September months (JJAS), the MH-PD $\delta^{18}O_p$ change ($\Delta\delta^{18}O_p$) is -2.0‰ for a +1.1mm/day precipitation change (ΔP), leading to a climatic slope ($\Delta\delta^{18}O_p/\Delta P$) for JJAS of -1.7‰/mm.day (much higher than the seasonal or inter-annual slope of about -0.5‰/mm.day, figure 6.11). This climatic slope is even higher when consider-

station and data type	latitude	longitude	reference	$\Delta\delta^{18}O$ obs	Δd obs	$\Delta\delta^{18}O$ LMDZ-iso	Δd LMDZ-iso
GRIP ice core (Greenland)	72.60	-38.5	[GRIP members, 1993] cited in [Lee et al., 2008]	-7	-3	-8.2 +1.9	-3.5 -2.7
Camp Century ice core (Greenland)	77.17	-61.1	[Johnsen et al., 1972] cited in [Jouzel et al., 1994]	-12.9		-8.4 +6.5	-1.8 +9.2
Renland ice core (Greenland)	72	-25	[Johnsen et al., 1992] cited in [Jouzel et al., 1994]	-5		-13.6 -4.8	-5.2 -0.5
NGRIP ice core (Greenland)	75.10	-42.32	[NGRIP members, 2004] cited in [Lee et al., 2008]	-8		-10.4 -2.5	-3.25 -4.7
England	53	-2	[Bath, 1983] cited in [Joussaume and Jouzel, 1993]	-1.2		-7.5 -5.2	-1.0 -1.0
Byrd ice core (Antarctica)	-80.2	-119.5	[Johnsen et al., 1972] cited in [Lee et al., 2008]	-8		-7.4 -10.1	-1.8 +0.1
Dome C ice core (Antarctica)	-74.7	124.2	[Lorius et al., 1979] cited in [Jouzel et al., 1994]	-5.4		-13.9 -1.3	-0.4 -1.2
Dome B ice core (Antarctica)	-77.8	94.9	[Vaikmae et al., 1993] cited in [Jouzel et al., 1994]	-5		-9.1 -4.1	+5.0 -1.6
Vostok ice core (Antarctica)	-78.45	106.85	[Lorius et al., 1985] cited in [Werner et al., 2001]	-3 to -5	-2	-11.4 -8.7	+3.6 -2.2
Taylor Dome (Antarctica)	-77.8	71.6	[Grootes et al., 2001] cited in [Lee et al., 2008]	-3		-6.3 -8.0	-0.7 -2.3
Stampriet aquifer (Namibia)	-25	18	[Stute and Talma, 1998] cited in [Gasse, 2000]	+1.5		-2.1 +2.0	-2.2 -6.1
Huascaran ice core (South America)	-9.11	-77.61	[Thompson et al., 1995]	-6.3	-4	+1.3 -0.3	+1.3 -0.3
Sajama ice core (South America)	-18.10	-68.97	[Thompson et al., 1998]	-5.4		-1.3 -1.3	-0.8 +0.9
Illimani ice core (South America)	-16.62	-67.77	[Ramirez et al., 2003]	-6	-4	-0.2 0.2	-1.6 -1.3
Botuvera cave (South America)	-27.2	-49.02	[Cruz et al., 2005b]	-1.5		-0.2 -1.2	0.4 0.2
Santana cave (South America)	-24.52	-48.72	[Cruz et al., 2006]	-1.5		+2.2 0.0	-1.0 +0.4
Salar de Uyuni (South America)	-20	-68	[Fritz et al., 2003]	-4		+0.7 +0.2	-0.3 -0.1
Guliya ice core (Tibet)	35.28	81.48	[Thompson et al., 1997] cited in [Thompson et al., 2000]	-5.4		-1.7 -3.4	-1.7 -3.4
Dunde ice core (Tibet)	38	96	[Thompson et al., 1989]	-2		-2.1 -2.3	-0.5 -1.5
Sanbao and Hulu caves (China)	31.67	110.43	[Wang et al., 2008]	+1.5		+2.3 -0.4	+2.7 -2.3

Table 6.2: Data used for comparison with the LGM simulation: name (column 1) and location (columns 2 and 3) of the data stations, reference for the data (column 4), and LGM-PD difference in $\delta^{18}O$ and d-excess measured in records (columns 5 and 6) and simulated by LMDZ (columns 7 and 8). We consider as LGM what the author considers as LGM or otherwise take the period of minimum $\delta^{18}O$ in the record between 17ka and 21ka. We take an approximate average value over 2ka. We take as present day the value averaged over the last 2ka. $\delta^{18}O$ differences in carbonates expressed as PDB were converted in SMOW using $\Delta\delta_{SMOW} \simeq 1.03 \cdot \Delta\delta_{PDB}$ ([Coplen, 1988]). Corresponding values for LMDZ-iso are given for the CLIMAP SST - PD SST (first line) and for the IPSL LGM SST - PI (second line, see section 6.2.3 for simulation set-up).

Name	latitude	longitude	reference	$\Delta\delta^{18}O$ obs	Δd obs	$\Delta\delta^{18}O$ LMDZ-iso	Δd LMDZ-iso
GRIP ice core (Greenland)	72.35	-38.30	[GRIP members, 1993] cited in [Masson-Delmotte et al., 2005]	+0.5	-0.2	-1.3	-0.4
North GRIP ice core (Greenland)	75.10	42.32	[Masson-Delmotte et al., 2005]	+0.7	-0.5	-0.7	+0.8
Vostok ice core (Antarctica)	-78.45	106.85	[Lorius et al., 1985] cited in [Thompson et al., 2000]	-0.2		-3.8	0.3
Byrd ice core (Antarctica)	-80.2	-119.5	[Johnsen et al., 1972] cited in [Thompson et al., 2000]	+1		-0.6	-0.6
Huascaran ice core (South America)	-9.11	-77.61	[Thompson et al., 1995]	0		-0.7	0.6
Sajama ice core (South America)	-18.10	-68.97	[Thompson et al., 1998]	0		-1.7	+0.2
Illimani ice core (South America)	-16.62	-67.77	[Ramirez et al., 2003]	+0.2		-0.6	-1.4
Botuvera cave (South America)	-27.2	-49.02	[Cruz et al., 2005b]	+0.5		-1.4	+0.5
Santana cave (South America)	-24.52	-48.72	[Cruz et al., 2005b]	+1		-1.3	0
Guliaa ice core (Tibet)	35.28	81.48	[Thompson et al., 2000]	-2.5		-1	-0.3
Sanbao and Hulu caves (China)	31.67	110.43	[Wang et al., 2008]	-1.8		-0.6	-0.1

Table 6.3: Data used for comparison with the MH simulation: name (column 1) and location (columns 2 and 3) of the data stations, reference for the data (column 4), and MH-present day difference in $\delta^{18}O$ and d-excess measured (columns 5 and 6) and simulated by LMDZ-iso (columns 7 and 8). We take as MH the value at 6±ka and for present day the values averaged over the last 2ka. $\delta^{18}O$ differences in carbonates expressed as PDB we converted in SMOW using $\Delta\delta_{SMOW} \simeq 1.03 \cdot \Delta\delta_{PDB}$ ([Coplen, 1988]).

ing annual averages (−5‰/mm.day). This shows that reconstructions of past precipitation based on present-day calibration at the seasonal or inter-annual scale are to be taken with caution as discussed further in section 6.4.2.

6.4 Climatic information recorded by water isotopes in the tropics

The precipitation amount dominates the isotopic composition of the tropical precipitation at intra-seasonal ([Yoshimura et al., 2003, Sturm et al., 2007b, Risi et al., 2008b]), seasonal ([Dansgaard, 1964, Rozanski et al., 1993]) and inter-annual scales ([Rozanski et al., 1993, Vuille and Werner, 2005]). At longer time scales, the interpretation of isotopic records from tropical ice cores has been the subject of debate. [Thompson et al., 2000] have shown that tropical records from ice cores in South America and Tibet share common $\delta^{18}O$ patterns during the last 25 ka, with most depleted values during the LGM (by 4 to 6‰) and an increase during the deglaciation. The temporal evolution is also qualitatively similar to higher latitude records in Greenland and Antarctica ([Thompson et al., 2000]). This could suggest a large scale control of the isotopic signal, which was first interpreted as temperature variations ([Thompson et al., 2000]). However, given that the main process controlling low latitude $\delta^{18}O$ variations at present day is the precipitation amount, these

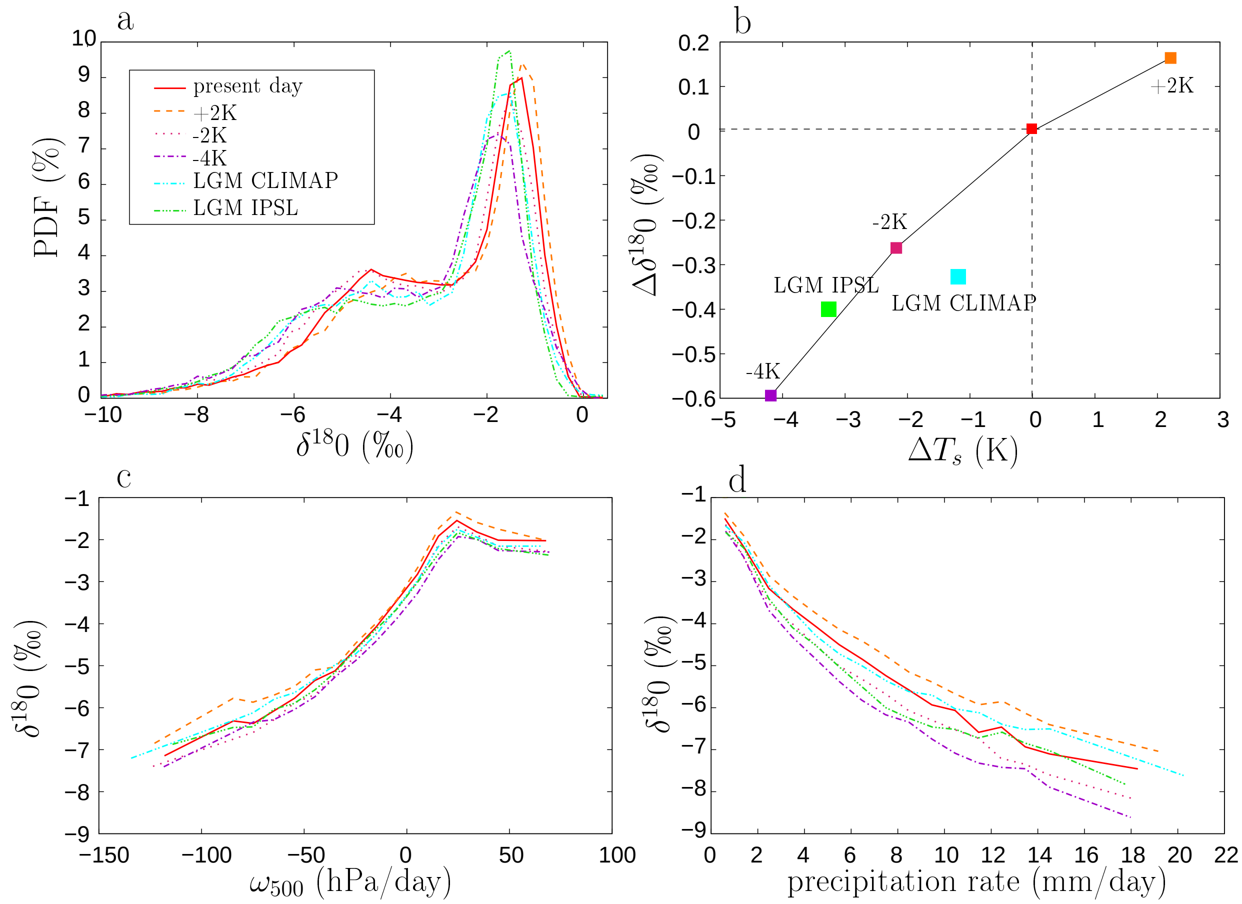

Figure 6.15: a) Frequency distribution of the $\delta^{18}O$ of precipitation over the tropics (-30°S-30°N), for the different simulations: present day (red), idealized simulation of uniform SST changes and for the two LGM simulations. b) Annually and tropically average change in $\delta^{18}O_p$ (compared to present day), as a function of the annually and tropically averaged change in sea surface temperature. c) $\delta^{18}O_p$ over tropical oceans as a function of the large-scale vertical velocity at 500hPa ω. d) same as c) but as a function of the precipitation rate P.

variations have subsequently been interpreted as wetter conditions upstream of ice cores ([Vimeux et al., 2009]).

Given the ability of LMDZ-iso to reproduce the main features of the observed water isotopic distributions, we now use it to investigate issues related to the interpretation of isotopic records as proxies for past changes in temperature and precipitation. First, we quantify the relative impact of changes in precipitation and large-scale temperature changes on $\delta^{18}O_p$ (section 6.4.1). We then evaluate the robustness of reconstructions of past precipitation based on water stable isotopes (section 6.4.2).

6.4.1 How much do global temperature changes impact tropical $\delta^{18}O_p$?

A global temperature change is likely to imprint $\delta^{18}O_p$ over the whole planet. However, if the change in surface temperature is not spatially uniform, the large-scale circulation will also change, which will lead to substantial changes in precipitation. Regional changes in $\delta^{18}O$ are thus expected to result both from background temperature and regional circulation changes.

To identify a possible effect of mean temperature on $\delta^{18}O_p$, we perform simulations with uniform changes of SST (-4K, -2K, +2K). Uniform changes in SST result in uniform shifts in the $\delta^{18}O_p$ probability distribution in the tropics (figure 6.15a), by about 0.1‰/K. The probability distributions of $\delta^{18}O$ in the vapor and in the evaporation are equally shifted (not shown), suggesting that this small sensitivity to mean SST is mainly due to a change in fractionation during evaporation at the sea surface (a sensitivity of 0.08‰/K is predicted by the [Merlivat and Jouzel, 1979] simple closure assumption). The sensitivity to SST is the same for all uniform SST change experiments (figure 6.15b) and consistent with the SCM results of [Bony et al., 2008]. The LGM simulations are also associated with a decrease in mean $\delta^{18}O_p$. Figure 6.15c plots $\delta^{18}O_p$ as a function of the large-scale vertical velocity at 500hPa, considered as a proxy for dynamical regimes (e.g. large-scale ascent or subsidence: [Bony et al., 2004]): the sensitivity to SST is nearly uniform for all dynamical regimes (figure 6.15d). Therefore, in our GCM, the sensitivity of $0.1‰/K$ is robust for all types of climate changes and dynamical regimes.

This sensitivity of $\delta^{18}O_p$ to mean SST is smaller than the sensitivity to local temperature measured at high latitudes: temperature$-\delta^{18}O_p$ slopes at high latitudes are about 0.4‰/K at the seasonal scale ([van Ommen and Morgan, 1997, Ekaykin and Lipenkov, 2008]) and range from 0.3 to 1‰/K at the inter-annual scales (figure 6.11). Therefore, the sensitivity of $\delta^{18}O_p$ to mean SST in the tropics simulated by LMDZ cannot explain by itself the strong depletion in $\delta^{18}O_p$ measured in the tropics for the LGM. Then, how to interpret the unability of GCMs to reproduce the depletion measured locally in most tropical records? If this is a large-scale mismatch due to an underestimate of the sensitivity of $\delta^{18}O_p$ to mean SST in the tropics, il might reveal a misrepresentation by GCMs of some hydrological or isotopic processes in the tropics. Alternatively, it might be a regional mismatch due to the coarse spatial resolution of GCMs over mountainous regions from where most of the LGM tropical isotopic records originate. A better spatial coverage of $\delta^{18}O$ data at LGM would help understand whether this mismatch is a large-scale or regional feature.

While changes in mean tropical SST has little impact on $\delta^{18}O_p$, the precipitation amount appears to be the dominant control on $\delta^{18}O_p$ in the Tropics (figure 6.15d) . Following the framework of [Bony et al., 2004], precipitation variations can be decomposed into two components: (1) a dynamical component, due to changes in the large-scale atmospheric circulation associated with changes in the SST distribution, and (2) a thermodynamical component, related to the change in the mean tropical precipitation with mean tropical SST (about 2%/K, [Held and Soden, 2006]). In LMDZ-iso, a uniform increase in SST leads to both a thermodynamic increase in precipitation and a slight increase in $\delta^{18}O_p$ (figure 6.15a), leading to an apparent $P - \delta^{18}O_p$ relationship opposite to the amount effect. $\delta^{18}O_p$ thus responds only to the dynamical component of the precipitation change, in agreement with a previous SCM study ([Bony et al., 2008]). Therefore, the tropical $\delta^{18}O_p$ records mainly regional changes in precipitation related to changes in the large-scale circulation, rather than changes in mean temperature or precipitation at the tropical scale.

6.4.2 How much can we consider water isotopes in tropical precipitation as a good proxy for local precipitation rate?

In LMDZ-iso, the tropical $\delta^{18}O_p$ records mainly dynamical changes in precipitation. General circulation models simulate precipitation responses to climate change that are very model dependent, in particular in monsoon regions (e.g. [Held et al., 2005]). As the tropical $\delta^{18}O_p$ is closely related to the precipitation amount, the ability of GCMs to reproduce past $\delta^{18}O_p$ changes might help to assess, indirectly, the ability of GCMs to simulate the precipitation response to a global climate change. A pre-requisite for this approach, however, is that past local precipitation changes can, indeed, be accurately inferred from water stable isotopic records. Here, we examine this issue through a "perfect model" experiment, using the CLIMAP LGM and PD simulations: we reconstruct the LGM-PD change in precipitation ($\Delta P_{reconst}$, fig 6.16b) from the LGM-PD $\delta^{18}O_p$ change simulated by LMDZ-iso ($\Delta\delta^{18}O_{sim}$, fig 6.12c), and compare this reconstruction with the precipitation change actually simulated by LMDZ-iso (ΔP_{sim}, fig 6.16a).

To do so, we first calculate at each grid point the slope of the linear regression (s) of the annual mean $\delta^{18}O_p$ vs annual mean P simulated at the inter-annual scale by LMDZ-iso. We use annual mean values since the temporal resolution of paleo records is infrequently higher than the year. Then, we reconstruct the precipitation change as $\Delta P_{reconst} = \frac{1}{s} \cdot \Delta\delta^{18}O$, when the coefficient of the linear regression is lower than -0.25, an arbitrary negative cutoff, which ensures that P is indeed a significant control on $\delta^{18}O_p$. Performances of the reconstructions increase as the cutoff decreases, but the relative performances of the different reconstruction methods are insensitive to the choice of the cutoff.

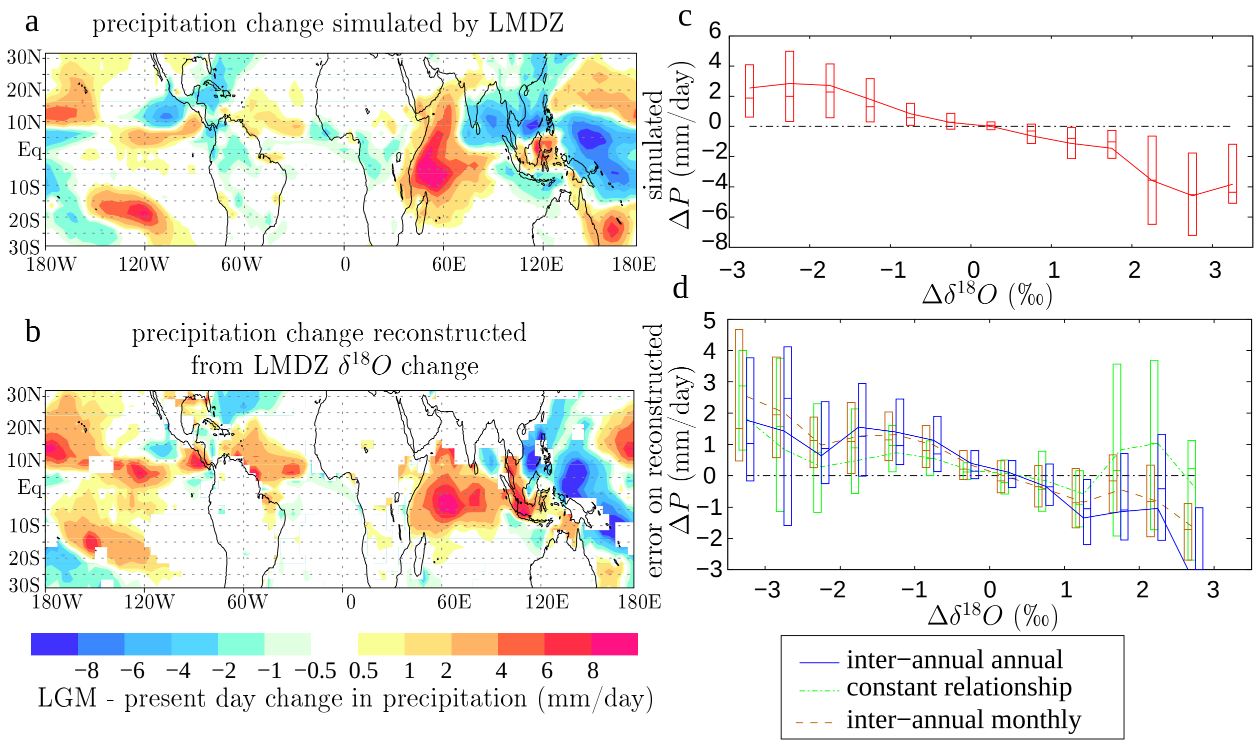

Figure 6.16: a) LGM - present day change in P simulated by LMDZ-iso. b) LGM - present day change in P reconstructed from the inter-annual $\delta^{18}O_p - P$ slope simulated by LMDZ-iso. Areas where the correlation coefficient is higher than -0.25 are let in white. c) Annually averaged precipitation change between LGM and PD as a function of the annually averaged change in $\delta^{18}O_p$ simulated by LMDZ-iso, over all tropical locations. The curve shows the average while the bars show the median and quartiles. d) Error in the reconstructed precipitation change (reconstructed minus simulated by LMDZ-iso) as a function of change in $\delta^{18}O_p$, for different methods: blue: local slope between annual mean precipitation and annual mean $\delta^{18}O$; dashed green; constant relationship of -0.7‰/(mm/day); local slope between monthly anomalies of $\delta^{18}O_p$ and precipitation, applied on monthly values.

The reconstructed precipitation pattern compares well with the pattern actually simulated by the model (figure 6.16 a and b): the spatial correlation between $\Delta P_{reconst}$ and ΔP_{sim} is 0.61 (table 6.4). The larger the precipitation changes, the better the reconstruction (figure 6.16d, blue), such as over the Indian ocean. Where $|\delta^{18}O_p|$ changes are larger than 2‰, 93% of the location have $\Delta P_{reconst}$ of the right sign, and 35% of the locations have a reconstructed ΔP relative error (calculated as$(\Delta P_{reconst} - \Delta P_{sim})\,/\Delta P_{sim})$ smaller than 50% (table 6.4). These probabilities decrease to 75% and 28% respectively when considering all locations (table 6.4). ΔP reconstructions are thus more robust when $\delta^{18}O_p$ variations are larger and thus when the signal to noise ratio is higher. Consistently, reconstructing changes in precipitation is less successful for the Mid-Holocene, for the LGM with IPSL SST and for uniform SST change experiments, because these simulations show small dynamical changes of precipitation and small $\delta^{18}O_p$ variations. The probability that the relative error in reconstructed ΔP be smaller than 50% at locations where $|\delta^{18}O_p|$ changes are larger than 2‰ is only 23% for the LGM with IPSL SSTs and 17% for the MH (table 6.4).

The reconstruction is also the best where the correlation between annual mean $\delta^{18}O_p$ and P is the most negative. For example, the spatial correlation between $\Delta P_{reconst}$ and ΔP_{sim} rises from 0.61 to 0.68 (table 6.4) when we choose a cutoff of -0.7 compared to -0.25: where the local P is the main control on $\delta^{18}O_p$ at the inter-annual scale, it is also the case at the climatic scale. Consequently, changes over land are generally not well captured by the reconstruction, as expected from the lower local correlation there: $\delta^{18}O_p$ in South America, in particular, has been shown to depend more on upstream precipitation ([Vimeux et al., 2005]).

The reconstruction overestimates the magnitude of precipitation changes (figure 6.16d, blue): this means that the $\delta^{18}O_p - P$ slope at the climatic scale is larger in absolute value than the annual slope used in the reconstruction, as was already pointed out for the Mid-Holocene simulation (section 6.3).

To test the importance of a local calibration, we reconstructed the LGM-PD ΔP for the CLIMAP simulation using the same slope at all grid points (figure 6.16d, green). The slope yielding, on average, the minimum reconstruction error is -0.7‰/(mm/day), which is significantly stronger than the inter-annual slope (ranging from -0.3 to -0.6‰/mm.day). Using a local calibration compared to a constant slope slightly improves the spatial correlation between ΔP_{sim} and $\Delta P_{reconst}$ (from 0.58 to 0.61: table 6.4). However, since the inter-annual slopes are generally lower than the climatic slopes, using a constant slope of -0.7‰/(mm/day) slightly reduces the reconstruction errors (figure 6.16d, green).

When taking into account the thermodynamic effect of mean SST on $\delta^{18}O_p$ (0.1‰/K) and on precipitation (2%/K), the reconstructed LGM-PD ΔP is uniformly lower by 0.5mm/day. Therefore, this thermodynamical effect explains part of the overestimate of the reconstructed LGM precipitation.

So far, we have discussed reconstructions performed at the annual mean scale, i.e. neglecting the seasonal cycle, essentially because monthly $\delta^{18}O_p$ is not available from long term records. However, the tropical precipitation experiences strong seasonal variations, so that the isotopic records at the annual scale record preferentially the $\Delta\delta^{18}O_p$, and thus the ΔP, during the wet season. Using annual mean $\delta^{18}O_p$ values to reconstruct the annual mean ΔP thus constitutes a likely source of errors in the reconstruction. We gave an illustrative example of this source of error in section 6.3.4, showing that over West Africa the climatic slope between PD and MH was 3 times larger when calculated with annual averages than with wet season (JJAS) averages, thus leading to an overestimation of $\Delta P_{reconst}$ of a factor of 3 just by neglecting the seasonal variability. To quantify more systematically this source of error, we reconstruct monthly ΔP using simulated monthly $\Delta\delta^{18}O_p$ and the slope calculated on present-day monthly inter-annual anomalies (figure 6.16d, brown). In this case the reconstruction is significantly improved for positive LGM-PD changes. For the LGM CLIMAP simulation, the probability that the reconstructed ΔP relative error is smaller than 50% rises to 42% (compared to 35%) when considering seasonal information when not (table 6.4). The uncertainty in the reconstruction due to the seasonality of the precipitation is the largest for the MH simulation: the probability that the reconstructed ΔP relative error is smaller than 50% rises to 33% (compared to 17%) when considering seasonal information when not (table 6.4). This is consistent with the strong changes in precipitation seasonality for the MH, with the precipitation increase occurring mainly during the wet season in monsoon regions.

Past climate	Reconst- -ruction method	cut-off	Spatial corre- -lation	Probability right sign $\|\Delta\delta^{18}O_p\| > 2‰$	Probability error<50% $\|\Delta\delta^{18}O_p\| > 2‰$	Probability right sign all locations	Probability error<50% all locations
LGM CLIMAP	annual	-0.25	0.61	93	35	75	25
LGM CLIMAP	constant	-0.25	0.56	91	32	73	25
LGM CLIMAP	monthly	-0.25	0.72	94	42	63	17
LGM CLIMAP	monthly	-0.7	0.68	96	47	73	28
LGM IPSL	annual	-0.25	0.33	84	26	66	17
MH	annual	-0.25	0.61	87	17	69	17
MH	monthly	-0.25	0.60	94	33	74	25

Table 6.4: Performance of the reconstruction of past changes in precipitation (ΔP) using the present day inter-annual slope $P - \delta^{18}O_p$ slope, in the "perfect model" experiments described in section 6.4.2. We reconstruct ΔP between a past climate (column 1) and present day, using different methods (column 2): slope of annual mean $\delta^{18}O_p$ vs annual mean P ("annual"), constant slope of -0.7‰/(mm/d) ("constant"), slope of monthly anomalies of $\delta^{18}O_p$ vs P applied on monthly $\Delta\delta^{18}O_p$ values ("monthly"). Column 4 gives the spatial correlation between the simulated and reconstructed ΔP . Columns 5 and 7 give the probablity that the reconstructed ΔP is of the right sign, for locations where $|\Delta\delta^{18}O_p| > 2‰$ and for all locations respectively. Columns 6 and 8 give the probability that the reconstructed ΔP is within 50% of the simulated ΔP, for locations where $|\Delta\delta^{18}O_p| > 2‰$ and for all locations respectively. All correlations and probabilities are calculated only on locations where the inter-annual correlation is lower than an arbitrary cutoff (column 3).

To conclude, using the PD inter-annual $\delta^{18}O_p - P$ slope to reconstruct past precipitation changes yields good results qualitatively: the spatial patterns of ΔP are well reconstructed, especially for past climates involving large circulation changes. Where measured changes of $\delta^{18}O_p$ are high (>2‰), it is very likely that the reconstructed ΔP has the right sign (93%): this means that inter-annual and climatic controls on $\delta^{18}O_p$ are similar. Quantitatively however, the reconstructed errors are high and most likely above 50%. The magnitude of the reconstructed ΔP is generally overestimated. Considering the seasonal cycle of P and $\delta^{18}O_p$ both for the calibration and reconstruction would improve the reconstructions quantitatively, in particular for past climates associated with strong changes in precipitation seasonality (e.g. MH).

6.5 Conclusion and perspectives

6.5.1 Evaluation of LMDZ-iso

We present the implementation of water stable isotopes in the LMDZ-iso GCM, and evaluate the present day isotopic distribution simulated at different time scales: synoptic, seasonal and inter-annual, as well as for past climate changes. LMDZ-iso forced by observed SSTs reproduces the annual mean and the seasonal distribution of $\delta^{18}O_p$ reasonably well, as well as its inter-annual variability in the tropics. Nudging the model winds by atmospheric reanalyzes improves the simulation of the inter-annual and synoptic variability of temperature and $\delta^{18}O$ at middle latitudes.

Deuterium excess is known to be a more difficult parameter to simulate ([Mathieu et al., 2002]). Despite some discrepancies over tropical continents, LMDZ-iso is able to correctly simulate the average d-excess values as well as the zonal gradient. LMDZ-iso is not able to reproduce the observed variability of d-excess *in the vapor*, neither at synoptic nor at inter-annual scales, producing near constant values all year long and for all years in some regions.

Numerous sensitivity tests were performed on both isotopic and non-isotopic parameters of the model. The precipitation composition is most sensitive to two parameters controlling kinetic effects: λ, involved in the parametrization of the supersaturation during snow formation ([Jouzel and Merlivat, 1984]), and ϕ, involved in the parametrization of the relative humidity at the droplet contact ([Bony et al., 2008]). These representations of kinetic effects are thus a large source of uncertainties in isotopic modeling. More measurements are certainly needed to better constrain these processes. In particular, the degree of equilibration of the rain drops with the vapor can be parametrized in many ways (e.g. [Stewart, 1975, Hoffmann et al., 1998, Mathieu et al., 2002, Lee and Fung, 2008, Bony et al., 2008]), and is difficult to evaluate due to the scarcity of isotopic measurements in the vapor. It would thus be extremely useful to have simultaneous measurements of precipitation and vapor at the same stations to evaluate the representation of isotopic processes during rain reevaporation in models. New technology (e.g. *[Gupta et al., 2009]*) now facilitates measurements in the vapor and will certainly offer new evaluation possibilities.

LMDZ-iso simulates LGM isotopic compositions similar to other GCMs, with relatively realistic depletions at high latitudes and a near constant $\delta^{18}O$ in the tropics. However, contrary to other GCMs, LMDZ-iso is able to reproduce the measured decrease of d-excess over most polar regions during the LGM.

6.5.2 Interpretation of paleoclimatic proxies

At high latitudes, based on a LGM simulation with LMDZ-iso forced by the CLIMAP SST reconstruction, we show that using the present-day spatial slope to reconstruct past temperatures leads to an underestimation of a factor of 2 in Greenland, but is more adequate in Antarctica, in agreement with previous studies ([Jouzel et al., 2000, Jouzel et al., 2003]). However, the accuracy of this reconstruction in Antarctica strongly depends on the equator-pole SST gradients of the reconstructed past climate. If the equator-pole at LGM was weaker than reconstructed by CLIMAP, then past temperature reconstructions in Antarctica would be underestimated, in agreement with [Lee et al., 2008].

In the tropics changes in $\delta^{18}O_p$ may result from global scale changes in SSTs, and/or from regional precipitation changes associated with changes in SSTs that are not spatially uniform. We found that changes in mean tropical SSTs have relatively little impact on $\delta^{18}O_p$ (0.1‰/K) and cannot explain the large changes in $\delta^{18}O_p$ recorded in few tropical locations for the LGM. On the other hand, large changes in $\delta^{18}O_p$ are more likely related to precipitation changes associated with a reorganization of SST patterns.

We thus examine the ability of $\delta^{18}O_p$ records to reconstruct past local precipitation changes in the tropics. Our analysis suggests that past regional precipitation changes can be reconstructed from $\delta^{18}O_p$ records, but only in cases where the signal to noise ratio for $\delta^{18}O_p$ is the largest. The use of a $\delta^{18}O - P$ slope calibrated locally from present day annual data seems adequate to reconstruct at least qualitatively the broad pattern and signs of precipitation changes. However, this overestimates the magnitude of precipitation changes. Considering the seasonal cycle of precipitation and $\delta^{18}O_p$ for both the calibration and reconstruction would improve considerably the reconstruction quantitatively. Over continents however, the sensitivity of $\delta^{18}O_p$ to upstream precipitation rather than local precipitation makes reconstructions of past precipitation at the regional scale more adequate ([Vimeux et al., 2005]).

6.5.3 Perspectives

LMDZ-iso, like other GCMs, does not simulate the large isotopic depletion measured in tropical ice cores, questioning whether all processes affecting $\delta^{18}O_p$ in the tropics are well represented. Tropical ice cores are located in mountainous regions, characterized by a complex topography which can only be resolved with high resolution modeling ([Sturm et al., 2005]). Part of the difficulty in simulating the ice core isotopic data at LGM could be due to the coarse resolution of GCMs (here 2.75 x 3.5°). In the future, we plan to use the stretched grid functionality of LMDZ-iso (e.g. [Krinner et al., 1997a]) to run zoomed simulations for present-day and for LGM over low latitude mountain regions such as the Andes and Tibet, to better simulate the relationship between isotopes and climate and explore climatic controls on low latitude ice core isotopic composition (appendix G).

Air parcels supplying precipitation to ice core regions usually travel several days over continental regions (the Amazon for the Andes, India for Tibet), over which continental recycling of precipitation occurs. The proportion of precipitation recycled to the atmosphere or lost by runoff has been shown to control continental gradients in $\delta^{18}O$ ([Rozanski et al., 1993]) and its variation could affect the ice core composition ([Pierrehumbert, 1999]). Moreover, processes by which precipitation is recycled (transpiration or evaporation from open water or soil) are suggested to strongly affect d-excess gradients over the Amazon ([Salati et al., 1979, Gat and Matsui, 1991, Henderson-Sellers et al., 2004]) and thus possibly the Andean ice core d-excess. Despite the potentially strong impact of land surface processes on the isotopic distribution, in LMDZ-iso as in most other GCMs, we have assumed no fractionation when recycling precipitation over land, due to the simplicity of the land surface model. Coupling atmospheric models with more sophisticated land surface models ([Aleinov and Schmidt, 2006, Yoshimura et al., 2006]) would enable a more accurate representation of isotopic fractionation over land. Water stable isotopes have been implemented in ORCHIDEE, the land surface component of the IPSL model, and LMDZ-OR-iso coupled simulations are reported in chapter 8.

Finally, further global evaluations of our GCM will be carried out in the future by comparing its simulations with the newly available global isotopic data measured by satellite, in particular the TES (Tropospheric Emission Spectrometer, [Worden et al., 2007]) and SCIAMACHY (Scanning Imaging Absorption Spectrometer for Atmospheric Cartography, [Frankenberg et al., 2009]) data.

Chapitre 7

L'^{17}O-excess, un traceur nouveau des variations passées du climat : étude avec des modèles simples

Si au premier ordre les δ varient de manière similaire, la différence de comportement entre l'HDO et l'$H_2^{18}O$, mesurée par le d-excess, apporte des informations complémentaires ([Dansgaard, 1964]). Tandis que les abondances en HDO et $H_2^{18}O$ (δD et $\delta^{18}O$ respectivement) sont mesurés depuis longtemps dans les eaux météoriques, la mesure de l'abondance en $H_2^{17}O$ ($\delta^{17}O$) à des précisions suffisantes pour des applications paléoclimatologique n'a été développée que très recemment ([Barkan and Luz, 2005]). Ceci permet de calculer l'^{17}O-excess, qui mesure la différence de comportement entre l'$H_2^{17}O$ et l'$H_2^{18}O$. Mesurée en permeg, sa définition est analogue à celle du d-excess (annexe C.4.1, figure 7.1a).

Jusqu'à présent, les données d'^{17}O-excess disponibles sont encore eparses. Aux pôles, l'^{17}O-excess ne montre pas de tendances significatives en fonction de la température ([Landais et al., 2008]), suggérant que les informations qu'il porte sont à la fois différentes des δ et du d-excess. L'^{17}O-excess mesuré dans la carotte de Vostok ([Landais et al., 2008]) montre des fortes variations glaciaires-interglaciaires, avec en particulier une augmentation de 20 permeg lors des déglaciations (figure 7.1b).

Dans ce chapitre, nous tentons d'interpréter les causes de ces variations. Pour simuler à la fois (1) l'effet des conditions d'évaporation et de la convection dans les zones sources et (2) l'effet des processus lors du transport des zones sources vers Vostok, nous utilisons la combinaison de deux modèles simples, comme illustré sur la figure 7.2 : le modèle uni-colonne d'atmosphère tropicale (SCM, [Bony et al., 2008], décrit dans le chapitre 2) et un modèle de distillation de Rayleigh (MCIM, [Ciais and Jouzel, 1994]). Compte tenu du faible nombre de données d'^{17}O-excess disponibles pour le moment, et de la difficulté du GCM LMDZ à simuler des valeurs réalistes d'^{17}O-excess sur l'Antarctique (annexe D.3.4), ce travail avec des modèles simples permet une première exploration de plusieurs processus non pris en compte jusqu'à présent, même si ces modèles très simples ne permettent pas de prendre en compte tous les processus pouvant potentiellement affecter l'^{17}O-excess.

Ce chapitre est basé sur l'article [Risi et al.,] (soumis).

7.1 Introduction

Stable isotopic measurements of water ($\delta^{18}O$ and δD) have been performed for more than 50 years ([Dansgaard, 1953, Epstein and Mayeda, 1953, Craig, 1961]) with the aim to improve our understanding of the water cycle and its links to climate. At first order, variations of $\delta^{18}O$ and δD are mainly due to the difference in saturation vapor pressures between the light and heavy isotopes, leading to an equilibrium fractionation. In addition, the larger diffusivity of light isotopes with respect to the heavy ones results in a kinetic fractionation, involved in evaporation and in snowflakes

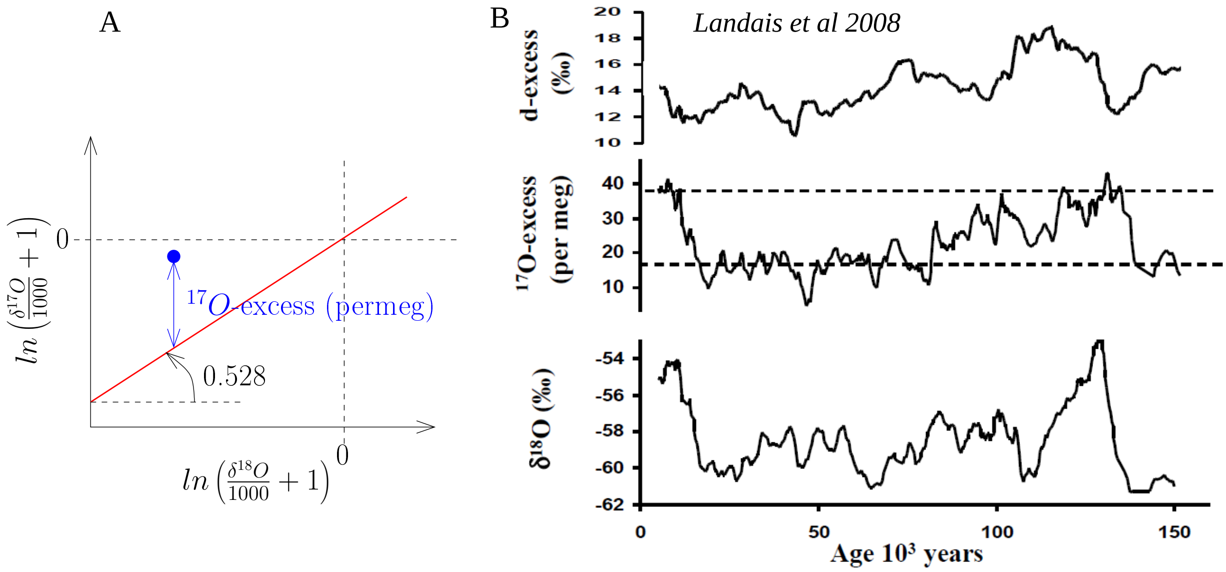

FIG. 7.1 – A : illustration de la défintion de l'^{17}O-excess. B : l'évolution de l'^{17}O-excess au cours des ? dernière années (d'après [Landais et al., 2008]).

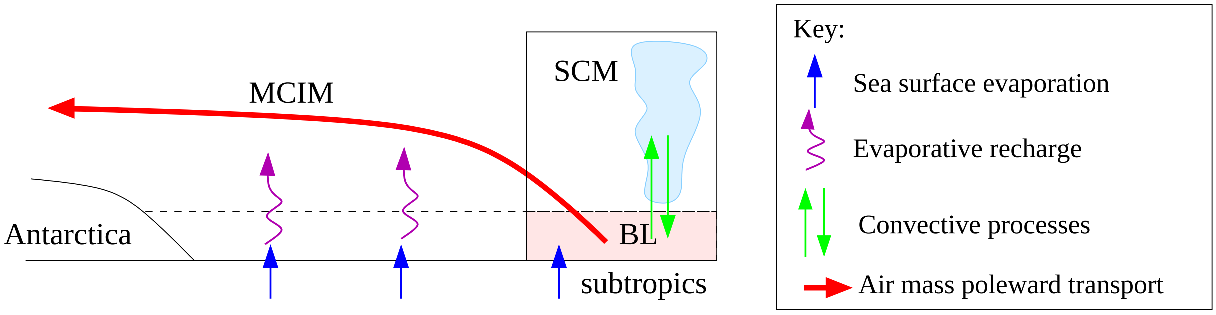

FIG. 7.2 – Schematic picture showing the processes that we take into account in our approach : the main source of the vapor is assumed to be the subtropics, in which the composition of the vapor is simulated by a single colum, model. The the MCIM simulates the transport from the subtropics to Antarctica. We test the sensitivity to the addition of evaporative recharge along the way.

formation. Since these kinetic effects have a larger influence on $\delta^{18}O$ than on δD ([Merlivat and Nief, 1967, Merlivat, 1978]), there is an added value in combining $\delta^{18}O$ and δD measurements.

This second order effect is measured by d-excess=$\delta D - 8 \cdot \delta^{18}O$ ([Dansgaard, 1964]). The d-excess in oceanic water vapor is a tracer of evaporative conditions (sea surface temperature, surface relative humidity, wind speed) and air-sea interaction (e.g. [Merlivat and Jouzel, 1979, Gat, 1996]). In particular, d-excess in water vapor over the ocean increases when humidity over the evaporative ocean decreases, which led [Jouzel et al., 1982] to interpret isotopic records in polar ice as a tracer of past humidity changes. However, numerous fractionation processes take place along the transport of air masses from the evaporative to the polar regions, so that d-excess in ice is also influenced by the moisture source and condensation temperatures, and by the isotopic composition of seawater ([Petit et al., 1991, Vimeux, 1999, Stenni et al., 2001, Schmidt et al., 2007]). For instance, modeling studies have shown that the effect of relative humidity changes in evaporative regions on polar d-excess could be overwhelmed by the effect of sea surface temperature changes at evaporation ([Vimeux, 1999]). Therefore, d-excess is now often interpreted as a tracer of the source temperature ([Vimeux, 1999, Stenni et al., 2001]).

Recent experimental developments have made it possible to accurately measure $H_2^{17}O$ abundance and to define a new isotopic tracer in the water cycle, ^{17}O-excess ([Barkan and Luz, 2007, Landais et al., 2008]), expressed in permeg (10^{-3}‰):

$$^{17}O\text{-excess} = 10^6 \cdot \left(\ln\left(\frac{\delta^{17}O}{1000}+1\right) - 0.528 \cdot \ln\left(\frac{\delta^{18}O}{1000}+1\right)\right)$$

with the δ notation defined as:

$$\delta = \left(\frac{R_{sample}}{R_{SMOW}} - 1\right) \cdot 1000$$

where R_{sample} and R_{SMOW} are the molar ratio of the heavy to light isotopes in the sample and in the SMOW standard ([Dansgaard, 1964]). Note that ^{17}O-excess and d-excess have slightly different definitions: d-excess is defined in a linear scale and ^{17}O-excess in a logarithm scale (see [Luz and Barkan, 2005] for the advantage of the logarithm scale).

As δD and $\delta^{18}O$, $\delta^{17}O$ and $\delta^{18}O$ show different sensitivities to equilibrium and kinetic fractionation processes so that ^{17}O-excess, as d-excess, has the potential to bring additional information on climate conditions and the hydrological cycle.

^{17}O-excess and d-excess do not show similar spatial distributions and are thus expected to be complementary ([Landais et al., 2008]). While d-excess in precipitation features a strong poleward gradient over Antarctica ([Dahe et al., 1994, Masson-Delmotte et al., 2008]), so far ^{17}O-excess has shown constant values in present-day Antarctic surface snow ([Landais et al., 2008]). Because of these different behaviors, it has been suggested using simple isotopic modeling that ice ^{17}O-excess was a more direct tracer of the evaporative regions than ice d-excess ([Landais et al., 2008]).

A record of ^{17}O-excess over the last 150 kyears has been obtained from the Vostok ice core (East-Antarctica, 78°S, 106°E). The most prominent features are the significant increases of ^{17}O-excess by 20 permeg during the last two deglaciations ([Landais et al., 2008]). Using a Rayleigh-type distillation model initialized by the traditional closure assumption (i.e. assuming that the vapor originates from surface evaporation only: [Merlivat and Jouzel, 1979]), [Landais et al., 2008] suggested that the large increase in ice ^{17}O-excess recorded in the Vostok ice core over the last deglaciation was due to a decrease of *relative humidity at the surface* (rh_s) by 10 to 20% over the source regions. However, both theoretical considerations ([Schneider et al., 2009]) and General Circulation Models (GCMs) suggest very small changes of the *near-surface air relative humidity* (rh_a) over oceanic regions from LGM to present day ([Bush and Philander, 1999]) or in the context of future climate change ([Bony et al., 2006]). If rh_s and rh_a vary in concert, which is assumed in studies interpreting water isotopes in polar ice cores using simple models ([Vimeux et al., 2001, Stenni et al., 2001]), GCMs simulations contradict the interpretation of ^{17}O-excess as a tracer of rh_s.

The goal of this article is thus to explore various processes that might explain the observed glacial-interglacial ^{17}O-excess shift, both at the source and during the poleward transport. To this aim, we use a single column model for tropical or subtropical source regions and a Rayleigh distillation model for the effect along the air mass trajectory, as described and justified in section

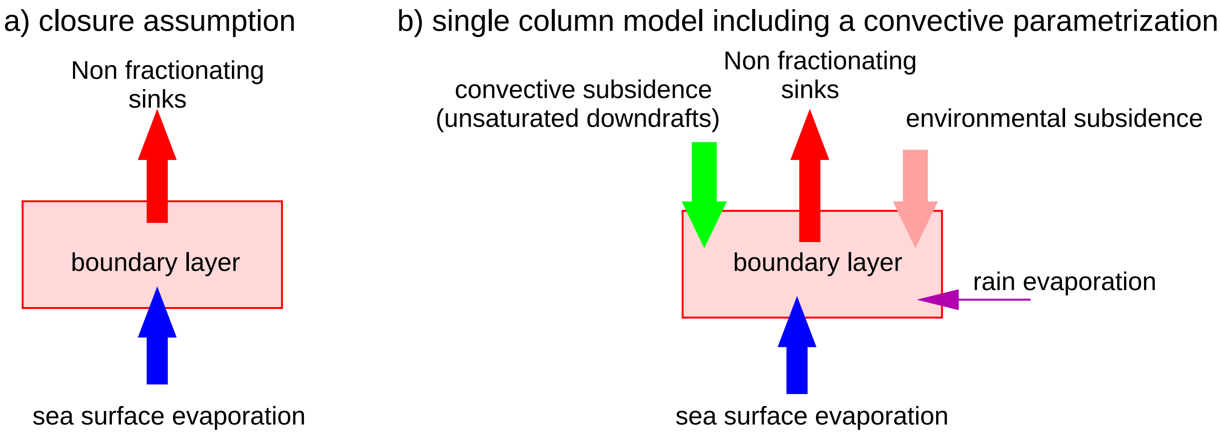

Figure 7.3: Scheme illustrating the moisture balance of the boundary layer: (a) in the closure assumption ([Merlivat and Jouzel, 1979]); (b) in the single column model. Whereas the BL vapor in the closure assumption only originates from sea-surface evaporation, the BL vapor in the single-column model receives water vapor from: (1) sea-surface evaporation (blue); (2) vapor just above the BL, entering the BL through subsiding motions (magenta); (3) unsaturated downdrafts, driven by the rain evaporation (green); (4) rain reevaporation (purple). In both models the sinks of the BL vapor do not fractionate (e.g. updrafts).

7.2 and illustrated in figure 7.2. We explore the effect of source conditions on ^{17}O-excess of the moisture source in section 7.3 and possible modifications of ^{17}O-excess between the source and Vostok in section 7.4. We discuss paleoclimatic implications in section 7.5.

7.2 Method

Atmospheric General Circulation Models (GCMs) incorporating water stable isotopes seem the ideal tool to understand the isotopic composition of worldwide water vapor and precipitation. However, GCMs still have difficulties to simulate surface temperature and snowfall amount over inland Antarctica ([Masson-Delmotte et al., 2008]). Moreover, they have difficulties to simulate d-excess glacial-interglacial variations of the right sign over high latitudes (e.g. [Werner et al., 2001]). This difficulty could arise from either deficiencies in representing isotopic processes such as kinetic effects, or from a poor simulation of some LGM climatic properties influencing d-excess, such as surface conditions at the evaporative source. In both cases, these deficiencies reduce the confidence in using GCMs to interpret d-excess or ^{17}O-excess glacial-interglacial variations in polar ice cores. Consequently, quantitative interpretations of variations in ice d-excess are still mainly based on simple Rayleigh distillation models (e.g. [Johnsen et al., 1989, Ciais and Jouzel, 1994, Ciais et al., 1995, Kavanaugh and Cuffey, 2003, Stenni et al., 2001, Masson-Delmotte et al., 2005]). Finally, results from GCMs including $H_2^{17}O$ have not, to our knowledge, been published yet.

To explore processes at work during the transport of air masses from the source regions to the poles, we thus use a Rayleigh type distillation model: MCIM (Mixed Cloud Isotopic Model, [Ciais and Jouzel, 1994]). This model permits to quantify the water isotopic fractionation along the air mass trajectory as well as to explore the effect of evaporative recharge over mid and high latitude oceans (section 7.4.2).

To represent the influence of source regions on water isotopic composition, most Rayleigh distillation models are initialized by the isotopic composition R_{BL} of an air parcel originating from the planetary boundary layer (BL), and the influences of changing climatic conditions on this isotopic composition are estimated through the so-called closure assumption ([Merlivat and Jouzel, 1979], appendix H.5.2):

$$R_{BL} = \frac{R_{oce}}{\alpha_{eq} \cdot (\alpha_K + rh_s \cdot (1 - \alpha_K))} \tag{7.1}$$

with α_{eq} and α_K the equilibrium and kinetic fractionation coefficients, R_{oce} the isotopic ratios of the ocean surface and rh_s the relative humidity *at the surface*, i.e. the relative humidity of near surface air at the temperature of the ocean surface T_s:

$$rh_s = rh_a \cdot \frac{q_{sat}\left(T_a\right)}{q_{sat}\left(T_s\right)} \tag{7.2}$$

where q_{sat} is the specific humidity at saturation and rh_a and T_a are the relative humidity and temperature of the near-surface air respectively.

The closure assumption relies on the hypothesis that the only source of vapor in the BL is from the surface evaporation (figure 7.3a). However, progress in tropical meteorology, in our understanding of the physical processes that control the distribution of water stable isotopes in the atmosphere, and in isotopic modeling, makes the applicability of the closure assumption increasingly questionable (e.g. [Jouzel and Koster, 1996, Delmotte et al., 2000]). Besides, in the tropics the BL air is not only influenced by sea-surface evaporation but also by convective activity and the large-scale atmospheric circulation (e.g. [Raymond, 1995]). Observations show that convective processes substantially affect the isotopic composition of the BL vapor ([Lawrence et al., 2004]). Large scale-subsidence and boundary layer mixing can also be important in dry regions ([Angert et al., 2008]). These reasons may explain why GCMs predict $\delta^{18}O$ (d-excess, respectively) values that can differ from the closure assumption predictions by 3‰ (2‰, respectively) in the tropics and by up to 6‰ (8‰, respectively) in mid-latitudes ([Jouzel and Koster, 1996])

Therefore, to explore the impact on ^{17}O-excess of a broader range of processes than in [Landais et al., 2008], we use, instead of the closure assumption, a Single Column Model (SCM) whose physics package incorporates the essential controls of water vapor and water stable isotopes in the tropics and Subtropics ([Bony and Emanuel, 2001]). In particular, the SCM includes the Emanuel convective parametrization ([Emanuel, 1991]), which represents in detail some convective processes such as rain reevaporation and allows for a detailed representation of the isotopic fractionation during these processes ([Bony et al., 2008], chapter 2). The representation by this SCM of cumulus convection and of isotopic processes has been carefully evaluated using tropical data ([Bony and Emanuel, 2001, Bony et al., 2008]). As illustrated in figure 7.3b, in contrast with the closure assumption, the SCM simulates the effect of both large-scale and convective subsidence on the isotopic composition of the BL.

According to GCM studies ([Delaygue et al., 2000, Werner et al., 2001]), about 15% of the East Antarctic precipitation originates from moisture evaporated in the tropics, 30% from the subtropics (30-40°S) and 50% from mid and high latitude oceans. The SCM permits to explore the influence of processes (convective processes and large-scale motions in particular) occurring over the tropics and the subtropics. The 50% of the Vostok precipitation that originates from evaporation in mid and high latitude can be considered as evaporative recharge of air masses during their poleward transport ([Hendricks et al., 2000, Noone, 2008]). In this paper, we take this recharge into account by adding it to the Rayleigh distillation model. Therefore, the combined analysis of the SCM and MCIM models allows us to consider the main processes that are likely to affect the isotopic composition of the polar snowfall: conditions at the evaporative source (surface conditions, convection), Rayleigh distillation and evaporative recharge over mid and high latitudes. Note that the condensation in frontal clouds is represented in a simple and implicit way by the Rayleigh distillation of MCIM. This latter does not allow to represent the impact, on the isotopic composition of the water transported poleward, of changes that might occur in the physical or microphysical properties of frontal cloud systems during climate change.

7.3 Single-column simulation of the isotopic composition of the vapor evaporated from the tropics and subtropics

The Single Column model and its isotopic implementation were extensively described in [Bony and Emanuel, 2001] and [Bony et al., 2008] (chapter 2, appendix D.1). Each of our SCM simulation represents the steady state of the atmosphere in radiative-convective equilibrium, determined by the boundary conditions: surface temperature and wind speed, large-scale profile of vertical velocity, radiation, CO_2. The model is run over tropical and subtropical oceanic conditions.

For example, for a wind speed of 5 m/s, sea surface temperature of 25°C and no large scale ascent or descent (corresponding to average tropical conditions), the precipitation rate is about 3.6 mm/day and the simulated isotopic composition of the BL vapor is -12.9‰ , 14.7‰ and 20 permeg for $\delta^{18}O$, d-excess and ^{17}O-excess respectively. These values compare well with measurements over tropical ocean: $\delta^{18}O \simeq$-10‰ to -13‰ ([Lawrence et al., 2004]). Very few data are available for d-excess and ^{17}O-excess in tropical oceanic vapor. For comparison, unpublished results over the Amazon are in the ranges of 10-20‰ for d-excess and 15-20 permeg for ^{17}O-excess.

Compared to the closure assumption, the SCM yields $\delta^{18}O$ 2.3‰ lower, d-excess 1.3 ‰ higher and ^{17}O-excess 3 permeg higher (Table 7.1), in agreement with GCM outputs ([Jouzel and Koster, 1996]). In the SCM, this is due to the admixture into the BL of depleted and high d-excess vapor by the unsaturated downdraft (figure 7.3). Therefore, considering convective downdrafts in the SCM leads, in regions of significant convection, to a significant modification of the BL composition compared to the closure assumption.

7.3.1 Sensitivity to boundary conditions

To investigate what controls the BL composition in the SCM, we perform sensitivity tests to large scale boundary conditions: sea surface temperature (SST), surface wind speed and large scale vertical velocity (controlling the convective intensity). Note that the surface relative humidity (rh_s) is not a boundary condition in the model, but rather a prognostic variable that depends mainly on the surface wind speed and on the large-scale convective activity.

All sensitivity tests are performed around a control simulation corresponding to subtropical/tropical conditions (45% of the moisture source according to GCMs), with an SST of 25°C, surface wind speed of 5m/s and a large-scale descent of 15hPa/day at 500 hPa. We vary the boundary conditions of the SCM within a range for which the neglect of horizontal advections constitutes a reasonable approximation: SST from 21 to 24°C, wind speed from 2 to 6.5m/s and vertical velocity from -90 to +30hPa/day. These conditions correspond to dynamical regimes for which the neglect of horizontal advections in the SCM constitutes a reasonable approximation.

Note that we test independently the sensitivity to SST, surface wind and large-scale velocity to better isolate their effects, though in nature these variables vary in concert ([Sobel and Bretherton, 2000, Bony et al., 2004]).

Sensitivity to SST

We test SST variations of up to 4°C, which is an upper-bound of SST glacial-interglacial variations at low latitudes ([Harrison, 2000, Barrows and Juggins, 2005, Waelbroeck and co authors, 2008]). The sensitivity to SST simulated by the SCM is of 0.08 ‰/K for $\delta^{18}O$ and 0.3‰/K in d-excess (figure 7.6a, red solid and table 7.1). This sensitivity is predicted by the closure assumption (figure 7.6a, dotted green) and is due mainly to the variation of fractionation coefficients with temperature.

The BL ^{17}O-excess is not expected to change with temperature ([Barkan and Luz, 2005]). Indeed, $\frac{ln(^{17}\alpha_{eq})}{ln(^{18}\alpha_{eq})}$ remains equal to 0.529 for temperature variations between 10 and 40°C (with $^{17}\alpha_{eq}$ and $^{18}\alpha_{eq}$ the fractionation coefficients at liquid-vapor equilibrium for $H_2^{17}O/H_2^{16}O$ and $H_2^{18}O/H_2^{16}O$). The 7 permeg increase in ^{17}O-excess from 21°C to 25°C (figure 7.6a) is only due to the 3% decrease in rh_s (driving a 3 permeg increase in ^{17}O-excess) and the 1 mm/day increase in precipitation (driving a 4 permeg increase in ^{17}O-excess). These sensitivities to rh_s and precipitation will be explained in the next sections.

Sensitivity to surface wind speed

We vary the surface wind speed V_s along a range of values typically found over tropical oceans from 2 to 6.5m/s. We only test values in the smooth regime below 7m/s (where the kinetic fractionation is constant), since 95% of the ocean surface is in this regime ([Eriksson and Bolin, 1964]). Besides, V_s greater than 7m/s would imply a large change in the kinetic fractionation coefficient at the transition between smooth and rough regime ([Merlivat and Jouzel, 1979]), whose physical significance over the ocean remains unclear.

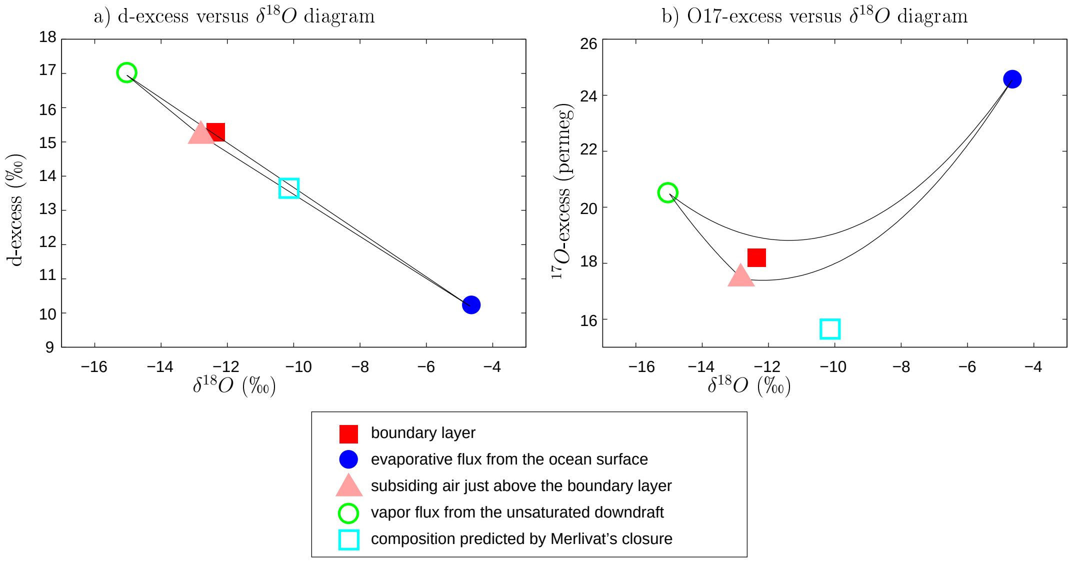

Figure 7.4: Isotopic composition of the BL simulated by the model (red filled square) in a $\delta^{18}O$ versus d-excess (a) and ^{17}O-excess diagrams (b). The composition of the unsaturated downdraft vapor mass flux into the boundary layer, the evaporative flux from the ocean and the subsiding environment just above the boundary layer are shown respectively with green empty circles, blue filled circles and magenta triangles. Mixing lines (lines representing the ensemble of possible mixtures between two samples) are in black. The isotopic composition of the boundary layer predicted by closure assumption for the simulated surface conditions is shown with cyan empty squares.

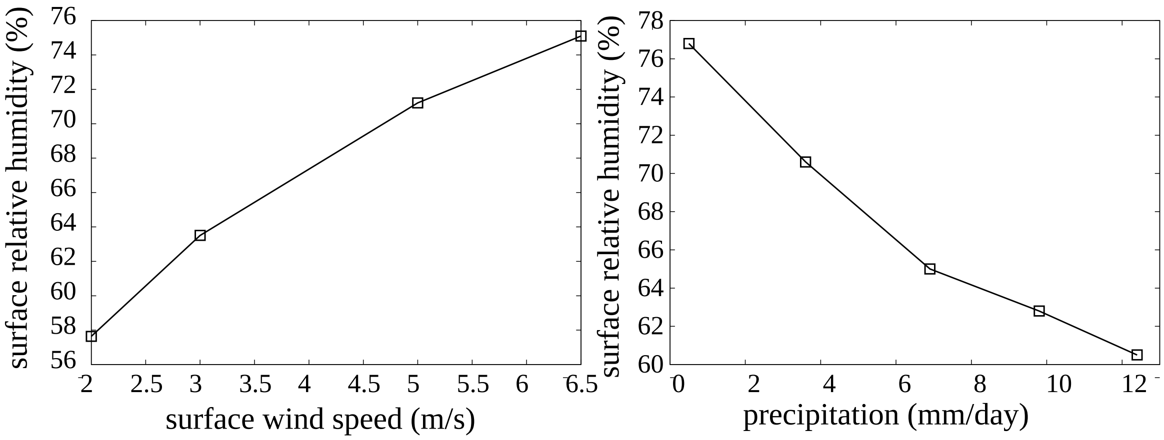

Figure 7.5: Sensitivity of surface relative humidity rh_s to surface wind speed V_s (a) and precipitation (b) in the SCM simulations. In figure (a), SST=25°C, ω_{max}=15hPa/day and V_s is varied from 2 to 6.5 m/s. In figure (b), SST=25°C, V_s=5m/s and ω_{max} is varied from -90 to 30hPa/day.

As V_s increases, $\delta^{18}O$ increases (0.9 ‰/(m/s)) and both d-excess and ^{17}O-excess decrease (-2.4‰/(m/s) and -4.4 permeg/(m/s) respectively: figure 7.6b, solid red). The sensitivity of the isotopic composition to V_s is mainly explained by coincident rh_s variations: when V_s increases, surface evaporation is enhanced, the water content in the BL increases and rh_s increases, by about 4.6%/(m/s) (figure 7.5b). To quantify the effect of rh_s, we performed the same simulations but with rh_s artificially fixed constant at 70% in the calculation of the isotopic composition of the evaporation flux. Without the coincident variations in rh_s, the sensitivity of the isotopic composition to V_s becomes very small (figure 7.5b, dotted green), confirming that the underlying factor explaining this sensitivity is rh_s.

Sensitivity to convective intensity

Convective intensity is modulated in the SCM by prescribing a large scale ascent or descent within the troposphere, and measured by the precipitation rate P.

BL vapor $\delta^{18}O$ decreases by about 0.4 ‰/(mm/day) as convective intensity increases (figure 7.6d), consistent with the well known tropical amount effect observed in the precipitation ([Dansgaard, 1964, Rozanski et al., 1993]). This compares well with the measurements of [Lawrence et al., 2004] over tropical ocean ranging from -10 ‰ in quiescent weather to below -20‰ after intense convective systems. Meanwhile, d-excess increases by about 0.6 ‰/(mm/day) as convective intensity increases (figure 7.6c, solid red).

Convective processes decrease $\delta^{18}O$ and increase d-excess in the BL vapor mainly through convective mixing bringing down depleted and high d-excess vapor ([Risi et al., 2008a]). However, as for the sensitivity to V_s, part of the sensitivity of d-excess to convection is explained by coincident rh_s variations: convection dries the BL in the model, owing to stronger upward transport of humidity by convective fluxes. Sensitivity tests to convective intensity in which rh_s is artificially held constant at 70% in the calculation of the composition of the surface evaporation (figure 7.6c, dashed blue) show that the effect of rh_s contributes for 55% to the sensitivity to convection. This explains why the closure assumption partly predicts the effect of rh_s on the BL d-excess, despite its neglect of convective processes (figure 7.6c, dashed blue).

^{17}O-excess increases with increasing convective activity by about 0.8 permeg/(mm/day) as precipitation increases from 4mm/day to 12mm/day (figure 7.6c). For these precipitation rates, the increase in ^{17}O-excess is mainly due to the decrease in rh_s: without coincident rh_s variations, the BL ^{17}O-excess varies by less than 0.1 permeg/(mm/day) (dotted green). The sensitivity of ^{17}O-excess to convective activity is higher for low precipitation rate: 4 permeg/(mm/day) for precipitation rates lower than 4mm/day. Variations in rh_s account for 40% of this sensitivity for these precipitation rates.

7.3.2 Main drivers of ^{17}O-excess changes in the source regions

The previous experiments have revealed that convective processes and changes in rh_s were the two main processes underlying the sensitivities of ^{17}O-excess to boundary conditions.

To calculate an upper bound for the impact of convective processes on ^{17}O-excess, we assume that the precipitation rate varies from 1 mm/day at LGM to 4 mm/day at Early Holocene (EH) in tropical and subtropical regions contributing to 50% of the Vostok precipitation. This is an extreme assumption since (1) GCMs rarely simulate larger precipitation changes, even regionally ([Braconnot et al., 2007]), (2) tropical and subtropical regions are not expected to contribute more than 50% to the Vostok precipitation ([Delaygue et al., 2000]) and (3) the sensitivity to convection is maximum at low precipitation rates. Excluding the effect of coincident rh_s variations, this would lead to a change of only 4 permeg in the Vostok precipitation, thus explaining 20% of the observed ^{17}O-excess change. Convection is therefore a minor influence on ice ^{17}O-excess.

Sensitivity experiments to V_s and convection have revealed the large influence of rh_s on ^{17}O-excess. By comparing the sensitivity to V_s with and without fixed rh_s (figure 7.6d, solid pink), we estimate the sensitivity of ^{17}O-excess to rh_s to -1.0 permeg/%. Similarly, the $\delta^{18}O$ and d-excess sensitivities to rh_s are 0.2‰/% and -0.5‰/%.

These sensitivities to rh_s are roughly linear (figure 7.6d). and consistent both with the closure assumption (dotted green) and with the sensitivities deduced from the response to convection

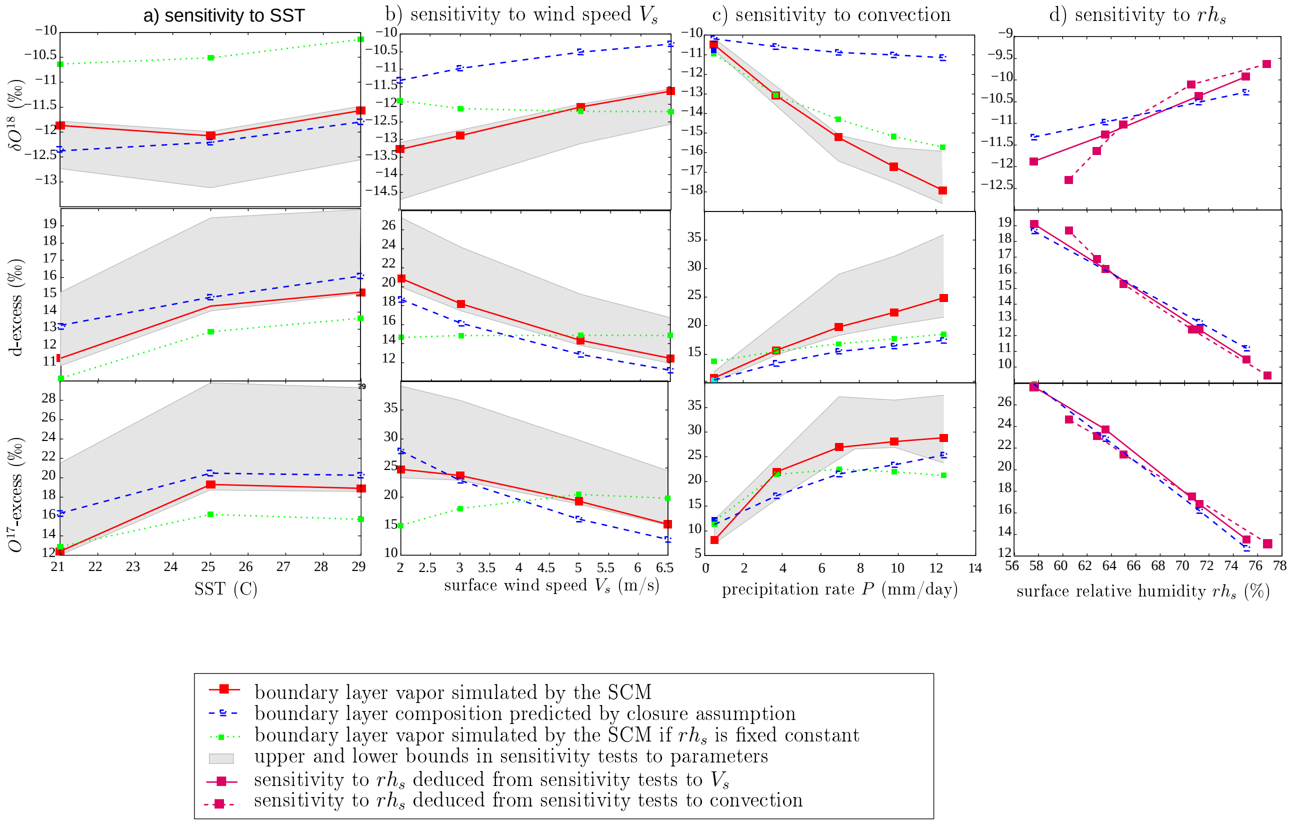

Figure 7.6: (a) to (c): Thick red: sensitivity of boundary layer $\delta^{18}O$, d-excess and ^{17}O-excess to: (a) sea surface temperature (SST); (b) surface wind speed;(c) convective intensity, measured here as precipitation rate. Dashed blue: sensitivity predicted by closure assumption for the same SST and the same relative humidity at the surface. Dotted green: sensitivity simulated by the model when the relative humidity at the surface is held artificially constant at 70% in the calculation of the composition of surface evaporation, highlighting the direct effect of convective processes on the BL composition (section 7.3.1 and 7.3.1). The gray shading represents the envelop of the simulated boundary layer compositions ($\delta^{18}O$, d-excess and ^{17}O-excess) when model parameters related to unsaturated downdraft are varied by ±20% and when parameter ϕ is varied from 0 to 0.9.
d) Sensitivity to rh_s deduced from the sensitivity tests to V_s (solid pink) and convective activity (dashed pink): the simulations with "constant" rh_s have been subtracted to the standard simulations. Also shown is the closure assumption (dashed blue).

Table 7.1: (next page) First 3 columns: boundary conditions imposed to the SCM: surface wind speed V_s , sea surface temperature SST and large-scale circulation (ω_{max} is the maximum vertical velocity of the large scale ascent profile; this maximum occurs at 500hPa; negative values indicates large scale ascent).
Column 4 to 12: precipitation rate P, isotopic composition of the boundary layer (BL) ($\delta^{18}O$, d-excess d and ^{17}O-excess), isotopic composition of the BL if it was predicted by the closure assumption ([Merlivat and Jouzel, 1979]), relative humidity of the air at the lowest level rh_a and relative humidity at the surface rh_s, simulated at equilibrium by the single column model. The humidity rh_s is calculated using equation H.13. The control simulation described in 4.1 is highlighted in bold.
Last 3 columns: isotopic composition of the ice simulated by the MCIM (see section 5.1) for the different initial conditions given in the previous columns.

(dashed pink), supporting the robustness of these sensitivity to rh_s. We thus suggest that these sensitivities to rh_s are robust and can be applied in extratropical conditions as well, as suggested also by d-excess observations over mid and high latitude Southern Ocean ([Uemura et al., 2008]).

Taking into account uncertainties in the ^{17}O-excess sensitivity to rh_s (supplementary material section 2), a 12 to 22% decrease in rh_s from LGM to EH may explain the 20 permeg change in BL ^{17}O-excess, a conclusion similar to [Landais et al., 2008].

7.4 Poleward transport processes

To understand how ^{17}O -excess variations in the source regions are transmitted to d-excess and ^{17}O-excess in the polar regions, we initialize the MCIM with the BL isotopic composition simulated by the SCM (previous section) and simulate the isotopic composition of the snowfall over the Vostok station (-55°C, 3500 m above sea level: [Petit et al., 1999]). Table 7.1 displays $\delta^{18}O$, d-excess and ^{17}O-excess simulated in the ice at the Vostok location. The $\delta^{18}O$, d-excess and ^{17}O-excess simulated by the model (respectively -54.2‰, 17.5‰ and 40 permeg) compare reasonably well with the measurements in Vostok for the present-day (about -55‰, 16 ‰ and 40 permeg respectively for annual averages). Nevertheless, an accurate simulation of the Vostok snowfall composition is not expected given the idealized framework of both the SCM and MCIM. We thus focus here on the sensitivity to climatic conditions rather than the absolute value of the isotopic composition.

7.4.1 Effect of pure Rayleigh distillation

The sensitivities of d-excess and ^{17}O-excess in the source BL to source conditions is also visible in the polar snowfall isotopic composition (Table 7.1). For example, when increasing rh_s from 69 to 81%, d-excess and ^{17}O-excess decrease both in the source BL and in the polar snowfall. However, distillation processes induce a dampening of the initial vapor d-excess anomaly: while ^{17}O-excess decreases by 10 permeg both in the source vapor and in the snowfall, d-excess decreases by 8.4‰ in the source vapor and only by 6.6‰ in the surface snow. Here are two reasons for these different behaviors of d-excess and ^{17}O-excess along the distillation process.

(1) A change in $\delta^{18}O$ of the source vapor influences d-excess in the snowfall even if the source d-excess remains constant (e.g. [Delaygue, 2000, Cuffey and Vimeux, 2001, Werner et al., 2001, Vimeux et al., 2002, Jouzel, 2003]). On the contrary, ^{17}O-excess is not affected by such a change in $\delta^{18}O$ of the source region (table 7.2, two last lines), due to the different definitions of d-excess (linear) and ^{17}O-excess (logarithm) (appendix H.5.4).

(2) d-excess is influenced by air temperature while ^{17}O-excess is almost insensitive to temperature along the distillation (table 7.2, first three lines), due to different evolutions of the equilibrium fractionation coefficients with temperature. Indeed, while $\frac{ln(^{17}\alpha_{eq})}{ln(^{18}\alpha_{eq})}$ remains equal to 0.529 for temperature increasing from $0°C$ to $20°C$, $\frac{^{D}\alpha_{eq}-1}{^{18}\alpha_{eq}-1}$ varies between 9.6 and 8.7 ($^{D}\alpha_{eq}$ being the fractionation coefficient at liquid-vapor equilibrium for $HD^{16}O/H_2^{16}O$). Note that a similar dependency on temperature is observed for $\delta D/\delta^{18}O$ if we consider the evolution of $\frac{ln(^{D}\alpha_{eq})}{ln(^{18}\alpha_{eq})}$ (9.1

0	1	2	3	4	5	6	7	8	9	10	11	12	13	14	15
sensi- -tivity test	V_s (m/s)	SST (°C)	ω_{max} (hPa /day)	P (mm) /day	$\delta^{18}O$ in BL (‰)	d in BL (‰)	^{17}O-excess in BL (permeg)	$\delta^{18}O$ if closure (‰)	d if closure (‰)	^{17}O-excess if closure (permeg)	rh_a (%)	rh_s (%)	$\delta^{18}O$ in ice (‰)	d in ice (‰)	^{17}O-excess in ice (permeg)
control	**5**	**25**	**15**	**1.4**	**-12.1**	**14.4**	**19.3**	**-10.5**	**12.9**	**16.2**	**78.8**	**71.2**	**-54.2**	**15**	**42**
SST	5	21	15	2.3	-11.9	11.3	12.4	-10.7	10.2	12.9	80.7	74.6	-51.9	8.3	34
SST	5	29	15	2.6	-11.6	15.2	18.9	-10.1	13.6	16.0	79.9	72.1	-53.3	17.5	40
V_s	2	25	15	1.3	-13.3	20.9	24.8	-11.3	18.7	27.9	69.3	57.6	-53.4	20.2	49
V_s	3	25	15	1.7	-12.9	18.2	23.7	-11.0	16.1	22.9	73.2	63.5	-53.5	19.1	48
V_s	6.5	25	15	2.6	-11.6	12.5	15.3	-10.3	11.2	12.7	80.7	75.1	-53.0	13.6	39
ω_{max}	5	25	30	0.5	-10.5	10.9	8.2	-10.2	10.5	11.31	81.8	76.8	-52.9	8.3	31
ω_{max}	5	25	0	3.6	-12.9	14.7	19.8	-10.6	13.4	17.2	77.7	70.6	-53.3	15.7	44
ω_{max}	5	25	-30	6.9	-15.2	19.8	27.0	-10.9	15.5	21.5	73.8	65.0	-54.9	21.7	50
ω_{max}	5	25	-60	9.8	-16.7	22.3	28.1	-11.0	16.4	23.4	71.9	62.8	-56.1	27.2	52
ω_{max}	5	25	-90	12.4	-17.9	24.9	28.9	-11.1	17.4	25.4	70.0	60.5	-56.8	31.5	53

T_{source} (°C)	T_{site} (inversion) (°C)	vapor $\delta^{18}O$ (‰)	ice $\delta^{18}O$ (‰)	ice d-excess (‰)	ice ^{17}O-excess (‰)
26	-35	-13	-55.6	27.5	42
24	-35	-13	-54.5	24.5	42
28	-35	-13	-56.8	30.6	43
26	-38	-13	-59.6	35	43
26	-32	-13	-51.6	21	42
26	-35	-10	-52.7	20	42
26	-35	-16	-58.5	35	42

Table 7.2: Isotopic composition of the ice simulated for different source and site temperature and different $\delta^{18}O$ of the boundary layer. In the boundary layer, d-excess=15‰ and ^{17}O-excess=20 permeg.

at 0°C and 8.4 at 20°C) and the same behavior holds for vapor-solid fractionation. Therefore, the near-surface temperature in the moisture source regions influences the polar snowfall d-excess ([Petit et al., 1991, Vimeux et al., 2002]) but not ^{17}O-excess.

Consequently, the ^{17}O-excess variations of the BL vapor in the source region are perfectly preserved in the polar precipitation (table 7.2). On the contrary, the polar d-excess is sensitive to the initial and final temperatures of the distillation (table 7.2), and thus only partially reflects the d-excess signal from the source region.

7.4.2 Effect of evaporative recharge

Classical Rayleigh distillation models assume that air parcels are isolated. However, in nature, air masses are partially recharged through surface evaporation: for example, [Trenberth, 1998] estimated a recycling ratio (proportion of the moisture originating from the local evaporation versus horizontal advection) from 10 to 20% at the 1000km scale over subtropical and mid-latitude oceans. The isotopic composition of Antarctic snowfall is affected by the evaporative recharge ([Kavanaugh and Cuffey, 2003, Lee et al., 2008]) and the competition between mixing of surface evaporated water through the BL and poleward advection of moisture ([Noone, 2008]). Evaporative recharge is expected to affect even more strongly ^{17}O-excess than $\delta^{18}O$ or d-excess because mixing lines are curved in a logarithmic plot (figure 7.7a), so that ^{17}O-excess is not preserved during mixing.

To quantify the effect of evaporative recharge through the mixing of air masses with contrasted $\delta^{18}O$, we perform an idealized sensitivity experiment. We start a distillation of the initial vapor ($\delta^{18}O$=-12 ‰, d-excess=15‰, ^{17}O-excess=18 permeg) until the vapor reaches a 2‰ $\delta^{18}O$ depletion. Then, we recharge 10% of the vapor by an evaporative source, corresponding to the composition of the evaporation flux simulated by the SCM in the control simulation :$\delta^{18}O$=-5‰ (consistent with [Lee et al., 2007]), d-excess=10‰, ^{17}O-excess=25 permeg (figure 7.4). The same distillation – recharge steps are repeated again until the precipitation $\delta^{18}O$ corresponds to the $\delta^{18}O$ measured at the coast of Antarctica. Then, the parcel is distilled without recharge until reaching the Vostok station. This experiment is roughly equivalent to a recycling ratio of 20% at the 1000km scale (consistent with [Trenberth, 1998]), until 70°S in latitude. Compared to an isolated parcel, ^{17}O-excess in Vostok snowfall is lower by 14 permeg, due to the curvature of the mixing lines (figure 7.7). The Vostok snowfall d-excess is just slightly reduced by 4‰ due to the admixture of lower d-excess vapor by surface evaporation.

Note that recycling in this test is artificial and does not accurately represent the complexity of recharge processes. The previous test estimated an upper bound of the effect by mixing the distilled air mass with a very contrasted $\delta^{18}O$. If the vapor was recharged with a less contrasted vapor ($\delta^{18}O$=-12‰ instead of -5‰, e.g. recharge by vertical mixing with the BL: [Noone, 2008]), the Vostok ^{17}O-excess would be lower by 10 permeg instead of 14 permeg. The recycling ratio used is also an upper bound, since air masses in mid and high latitudes are not transported poleward directly in contact with the ocean surface ([Noone, 2008]).

Finally, we find a maximum sensitivity of ^{17}O-excess to the evaporative recycling ratio of -0.7 to -0.5 permeg/%. A decrease of the recycling ratio from LGM to EH by 30% to 40% (i.e. recycling ratio from 40-60% to 10-20%) would thus be required to explain by itself the 20 permeg ^{17}O-excess increase. For the LGM to present-day change, PMIP2 models ([Braconnot et al., 2007]) simulate a slight decrease (smaller than 5%) of the recycling ratio between 20°S and 60°S from LGM to present day. This process is thus not likely to contribute to more than 20% to the observed ^{17}O-excess increase from LGM to EH.

Effect of $\delta^{18}O$ seasonality in Antarctica

Due to the curvature of the mixing lines in the log-log diagram, the annually averaged ^{17}O-excess in precipitation depends on the amplitude of the $\delta^{18}O$ seasonal cycle (figure 7.7b): if the seasonal amplitude of $\delta^{18}O$ in snowfall increases, then the annually averaged ^{17}O-excess decreases. As an example, we assume that at present day, 40% of the Vostok snow accumulation occurs from October to March with a $\delta^{18}O$ of -50‰ and that the remaining 60% of the accumulation occurs from April to September with a $\delta^{18}O$ of -60‰ (values of the same magnitude as reported in [Ekaykin, 2003]). For simplicity, we assume a constant ^{17}O-excess in the snowfall all over the year. If the seasonal amplitude of $\delta^{18}O$ in Vostok snowfall increases from 10‰ today to 20‰ during the LGM, then the annual ^{17}O-excess in Antarctica snowfall decreases by 10 permeg (figure 7.7b). Since mixing lines are linear when dealing with d-excess, this last effect does not affect the d-excess.

No data describing $\delta^{18}O$ seasonality in Antarctica is available during the LGM. Some isotopic GCM show either no change ([Jouzel et al., 1994]) or a small change (20% in simulations presented in [Jouzel et al., 2007a]) in the seasonal cycle in Eastern Antarctica between the LGM and today. PMIP2 models simulate a decrease of the seasonal amplitude of temperature from LGM to present-day, ranging from about 0 to 6°C over Antarctica depending on models. We thus propose here a rough estimate based on temperature seasonality derived from GCM simulations of the LGM, and applying the modern seasonal slope of $\frac{d\delta^{18}O}{dT} \sim 0.4‰/K$ ([Ekaykin and Lipenkov, 2008]). As an upper bound for this effect, considering a decreased seasonal amplitude of 6°C from LGM to EH, the $\delta^{18}O$ seasonal amplitude in polar snowfall would decrease by 2.4‰ from LGM to EH. The consequence is a small increase of snowfall ^{17}O-excess of about 2.4 permeg from LGM to EH.

Given these results, the variation in the seasonality of $\delta^{18}O$ is thus unlikely to contribute for more than 15% to the observed ^{17}O-excess shift.

7.5 Paleoclimatic implications

In the two previous sections, we have explored different processes affecting the source ^{17}O-excess, its evolution along air mass distillation and the impact of precipitation seasonality. While convective changes, recharge and seasonality may account for part of the ^{17}O-excess shift between the LGM and EH, these influences, even combined, are not likely account for more than 50% of the shift. On the other hand, a higher rh_s at LGM by 12 to 20%, would explain the observed shift (as in [Landais et al., 2008]). This is an upper bound, neglecting the role of the aforementioned processes that have a secondary impact. We discuss here the realism of an extreme 20% change in rh_s and its implications for LGM temperature reconstructions using stable water isotopes in ice cores. s

7.5.1 Realism of a higher rh_s over evaporative regions during the LGM

As mentioned in the introduction, GCMs outputs do not produce significant changes of rh_a between the LGM and the present-day ([Bush and Philander, 1999]) thus questioning the interpretation of the ^{17}O-excess shift. However, variations in rh_s are not equal to variations in rh_a. rh_s differs from rh_a owing to the difference between the air and surface temperatures (thermodynamic disequilibrium) ([Angert et al., 2008, Pfahl and Wernli, 2008]). By differentiating equation H.13 as a function of rh_a, T_s and $T_s - T_a$, and quantifying the different terms for rh_a ranging from 60 to 80%, T_s from 0 to 15°C (conditions over mid-latitude oceans, which are important sources of the Vostok precipitation) and $T_s - T_a$ from -3 to 3°C, we express the variations of rh_s as:

$$\Delta rh_s = (1.0 \pm 0.2) \cdot \Delta rh_a - (2 \pm 11) \cdot 10^{-2} \cdot \Delta T_s - (4.7 \pm 0.7) \cdot \Delta (T_s - T_a) \quad (7.3)$$

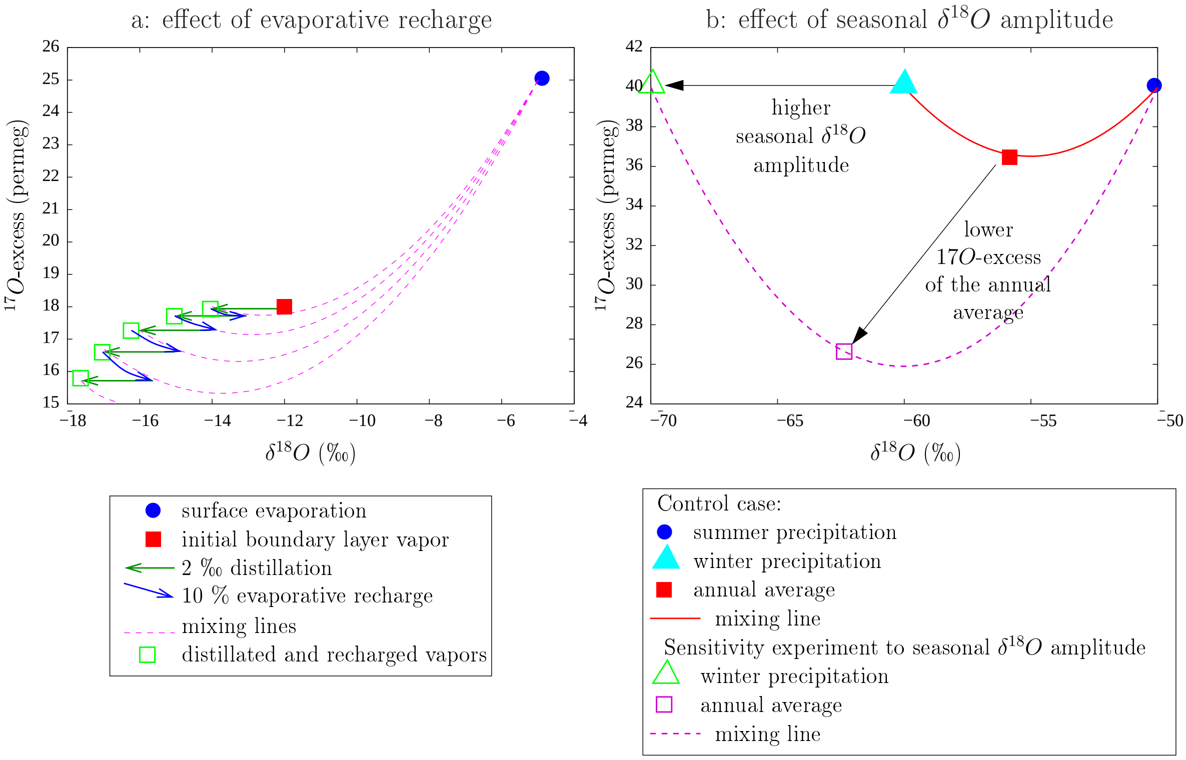

Figure 7.7: Schemes illustrating the effect of (a) the evaporative recharge of air masses along their poleward transport and (b) the seasonal amplitude of snow $\delta^{18}O$ over Antarctica. Both effects are due to the curvature of the mixing lines in the ^{17}O-excess vs $\delta^{18}O$ diagram, because of the logarithmic definition of ^{17}O-excess. (a) In an idealized sensitivity experiment to evaporative recharge described in section 7.4.2, an initial boundary layer vapor (filled red square) undergoes successive distillation and recharge steps by a surface evaporation flux (blue circle). Both the initial vapor and surface evaporation have the composition illustrated on figure 7.4. As the distillation depletes the vapor without significantly changing its ^{17}O-excess, evaporative recharge decreases ^{17}O-excess due to the curvature of the mixing lines. (b) In an idealized sensitivity experiment, we assume that at the present day, 40% of the Vostok snow accumulation occurs from October to Mars with a $\delta^{18}O$ of -50‰ and that the remaining 60% of the accumulation occurs from April to September with a $\delta^{18}O$ of -60‰ (values of the same magnitude as reported in [Ekaykin, 2003]). If the amplitude of the $\delta^{18}O$ seasonal cycle in Antarctic snow is increased from 10‰ to 20‰, then the annual ^{17}O-excess of the snow decreases by about 10 permeg, due to the curvature of the mixing line.

Variations in rh_s can thus arise either from a variation of rh_a of the same order of magnitude (first term on the right hand side) or a variation in the thermodynamical disequilibrium between the sea surface and the near-surface air $T_s - T_a$ (third term). The second term is negligible (ΔT_s of $10°C$ yields rh_s variations lower than 1%).

A first possibility to explain the rh_s decrease from LGM to EH is a decrease of rh_a over the source region. This can be obtained through a general rh_a decrease over the Indian and Southern ocean or through a shift of the location of the moisture sources toward regions of lower relative humidity. On the one hand, PMIP2 simulations show variations lower than 3% between 20°S and 60°S. Moreover, GCMs simulate a poleward shift of the source regions from LGM to EH ([Delaygue et al., 2000, Werner et al., 2001]), which is not consistent with a decrease in rh_a from LGM to EH, since rh_a increases polewards ([Vimeux et al., 2001]).

On the other hand, [Jouzel et al., 1982] argued that a higher rh_a during the LGM could be consistent with higher wind speeds over the ocean during this period, as suggested by highest aerosol and sea salt content measured in Antarctic ice ([Petit et al., 1981, Petit et al., 1999]). In addition, global warming during the deglaciation are associated with a change in the intensity, frequency and latitudinal position of the storm tracks ([Laîne et al., 2008, Toggweiler et al., 2006]) and with a southward shift of the Inter-tropical convergence zone during the LGM ([Chiang and Bitz, 2005, Kang et al., 2008]). Such large reorganizations could also affect the latitudinal distribution of relative humidity at low-levels.

A second possibility to explain the variations of rh_s is a change in the thermodynamical disequilibrium between the sea surface and the near-surface air in the source regions (equation 7.3). For example, the 20% higher rh_s during the LGM could be explained by a $4°C$ lower $T_s - T_a$ (i.e. T_s increase from LGM to EH $4°C$ more strongly than T_a). However, LGM simulations with coupled ocean-atmosphere models conducted in PMIP2 ([Braconnot et al., 2007]) do not show such a disequilibrium. They rather simulate a slightly lower rh_s (decrease of 3% in average between 30°S and 60°S) during the LGM.

There is thus a mismatch between the 20% change in rh_s suggested by the ^{17}O-excess shift in polar ice and the small variations in rh_s simulated by GCMs.

7.5.2 Implications of relative humidity changes on LGM temperatures reconstructions

If true, a large change in surface relative humidity at the source may have strong consequences for the classical interpretation of ice $\delta^{18}O$ and d-excess as indicators of site and source temperatures T_{site} and T_{source} ([Vimeux et al., 2002, Jouzel et al., 2007b, Masson-Delmotte et al., 2005, Stenni et al., 2001]). Indeed, $\delta^{18}O$ and d-excess in polar snowfall also depend on the variations in rh_s in the source regions. Until now, variations in rh_s were assumed to equal variations in rh_a, and variations in rh_a were either neglected or assumed to vary with T_{source} by -0.38%/°C ([Vimeux et al., 2002]). This slope was obtained from spatial correlation between SST (between 7°C and 24°C) and rh_a from GCM outputs for present-day simulations ([Vimeux et al., 2002]). However, these assumptions are questionable: (1) rh_s can vary even though rh_a is constant and (2) seasonal correlations between SST and rh_a in NCEP data ([Kalnay et al., 1996]) show weak values and variations in sign, questioning whether the slope given by [Vimeux et al., 2002] is robust and holds in time (especially between glacial and interglacial periods). Therefore, changes in rh_s might have been underestimated in previous studies.

In the light of the rh_s variations suggested by the ^{17}O-excess record, we thus reconsider the previous temperature reconstructions in Vostok over the deglaciation based on $\delta^{18}O$ and d-excess records alone. To do so, we perform an inversion of the $\delta^{18}O$ and d-excess ice core data at LGM to retrieve simultaneously T_{site} and T_{source}. The system of equations for $\delta^{18}O$ and d-excess in ice are derived from MCIM simulations initialized by the SCM (table 7.1), assuming linear relationships:

$$\Delta\delta^{18}O_{corr\,SW} = -0.30 \cdot \Delta T_{source} + 1.0 \cdot \Delta T_{site} + 0.02 \cdot \Delta rh_s \tag{7.4}$$

$$\Delta d_{corr\,SW} = 1.50 \cdot \Delta T_{source} - 1.1 \cdot \Delta T_{site} - 0.38 \cdot \Delta rh_s \tag{7.5}$$

Δrh_s (%)	ΔT_{site} (°C)	ΔT_{source} (°C)
-20	+7.8	+1.3
-10	+8.5	+4.4
0	+9.2	+7.4

Table 7.3: Variations of site (T_{site}) and source (T_{source}) temperatures deduced from the inversion of $\delta^{18}O$ and d-excess changes at Vostok over the last deglaciation, assuming different rh_s variations. The Δ sign refers to Early Holocene minus Last Glacial Maximum.

where $\Delta\delta^{18}O_{corr\,SW}$ and $\Delta d_{corr\,SW}$ are the variations of $\delta^{18}O$ and d-excess in the Vostok ice from LGM to EH, corrected by the -1 ‰ change in seawater $\delta^{18}O$ from LGM to EH: $\Delta\delta^{18}O_{corr\,SW}$=+7‰ and $\Delta d_{corr\,SW}$=+1 ‰ ([Jouzel, 2003]).

The coefficients for the sensitivity of Vostok $\Delta\delta^{18}O$ and Δd to ΔT_{source} and ΔT_{site} given with a 20% uncertainty and are similar to those obtained by [Vimeux et al., 2002] except for (1) $\frac{\partial d}{\partial rh_s}$: -0.15‰/% in [Vimeux et al., 2001] and -0.38‰/% in this study, and (2) $\frac{\partial d}{\partial T_{site}}$: -0.5‰$/K$ in [Vimeux et al., 2002] and -1.1‰$/K$ in this study, due to a different tuning of the MCIM (mainly supersaturation parametrization) based on the additional constraint from ^{17}O-excess ([Landais et al., 2008])

Doing the extreme assumption that the increase in ^{17}O-excess from LGM to EH should be attributed to a decrease in rh_s only, we have Δrh_s =-20% and obtain $\Delta T_{site} = +7.8°C$ and $\Delta T_{source} = +1.4°C$ from LGM to EH. Such a variation of T_{site} over the deglaciation is in fair agreement with the results of [Jouzel et al., 2003] and the ΔT_{source} is realistic compared to the available estimates of LGM oceanic temperature ([Barrows and Juggins, 2005, Sarnthein et al., 2003, Waelbroeck and co authors, 2008]). Surprisingly, we find similar values as in [Vimeux et al., 2002] despite different tunings of the MCIM, because the stronger dependency of d-excess to T_{site} in our model is counterbalanced by the strong effect of rh_s.

Taking into account the change in rh_s has a strong influence on the reconstruction of T_{source} (table 7.3): for example, assuming a constant rh_s from LGM to EH yields T_{site} and T_{source} changes of +7.4°C and +9.2°C respectively. The reconstruction of ΔT_{source} is twice more sensitive to the assumed Δrh_s than ΔT_{site}. Estimating the past rh_s variations through ^{17}O-excess measurements would thus have a strong impact on past temperature reconstructions, strengthening the added value of ^{17}O-excess measurements.

This calculation contains many uncertainties: tuning of the MCIM, linearity assumption, uncertainties related to the SCM, uncertainties in the exact change of rh_s if part of the change should be attributed to convective changes, to the evaporative recharge, to the seasonal cycle or to other processes not considered here.

To estimate the uncertainties related to the linearity assumption and the neglect of convection in our simplified equations (e.g. equations 7.4 and 7.5), we performed experiments using rh_s, T_{source} and T_{site} variations given in table 7.3. To do so, for each Δrh_s scenario, we perform simulations of the isotopic composition of the Vostok ice for the LGM and EH by the SCM and MCIM (table 7.4). The inputs of the SCM and MCIM are such that the change of rh_s, T_{source} and T_{site} between EH and LGM (columns 9, 10 and 12 of table 7.4) are almost identical to those in table 7.3. Changes in rh_s are obtained in the SCM either by varying V_s or ω (column 3 of table 7.4), or both simultaneously when ω variations only are not sufficient to explain rh_s variations. We take EH conditions from the control simulation (except when the change in rh_s was impossible to simulate through reasonable V_s or ω variations), but we focus on the EH-LGM differences rather than on the absolute values. Simulations show that whatever the method to vary rh_s in the SCM, be it through an extreme variation of V_s or of convective activity, the simulated EH-LGM change in ^{17}O-excess (in permeg) corresponds to the change in rh_s (in %), with an error of 2 permeg maximum (column 18 of table 7.4). Taking a slope of 1 permeg/% and neglecting the effect of convective processes on ^{17}O-excess are thus very robust assumptions. Simulated changes in $\delta^{18}O$ and d-excess in ice are similar to observations with maximum errors of 1.5 and 1.1‰ respectively (columns 16 and 17 of table 7.4). This translates into uncertainties of 2.2 and 2.4°C respectively on the reconstruction of ΔT_{site} and ΔT_{source}.

Table 7.4: (next page) Simulations to estimate the uncertainties related to the linearity assumption and the neglect of convection when inferring T_{site}, T_{source} and rh_s from $\delta^{18}O$, d-excess and ^{17}O-excess in the Vostok ice.
We simulate the Vostok ice composition for both the EH and the LGM (column 4) corresponding to the scenarii of change in rh_s (Δrh_s, column 2), in sea surface temperature of the source (ΔT_{so}, column 10) and in the polar temperature (ΔT_{si}, column 12). For each scenario, we vary rh_s in the SCM by two methods (column 3): wind speed (V_s) or large-scale vertical velocity at 500hPa (ω), or both simultaneously when ω variations alone are not sufficient to explain Δrh_s (simulations 3 and 4). For each scenario and method of rh_s variation, we perform two simulations, one for EH and one for LGM (column 4), so that the Δrh_s is a close as possible to the Δrh_s scenario. The inputs of the SCM (sea surface temperature T_{so}, V_s and ω) used to achieve the Δrh_s scenario are listed in colums 5, 6 and 7 respectively. The rh_s simulated by the SCM as well as the Δrh_s between EH and LGM are listed in columns 8 and 9. The outputs of the SCM are then used as input for the MCIM, together with the polar temperature (T_{si}, column 11). The Vostok ice composition ($\delta^{18}O$, d-excess and ^{17}O-excess) simulated by the MCIM is given in columns 13, 14 and 15 respectively, and the corresponding EH-LGM variations for each scenario and method of rh_s variation are given in columns 16, 17 and 18 respectively. These simulated variations are to be compared with the observed +7‰ , +1‰ and +20 permeg for Vostok ice $\delta^{18}O$, d-excess and ^{17}O-excess respectively. Note that we focus here on the EH-LGM differences, rather than on the absolute values.

To estimate the uncertainties related to the models, we perform sensitivity tests with the SCM and the MCIM. We vary tunable parameters in the SCM (supplementary material section 2) and in the MCIM (within ranges of values for which the modeled evolutions of ^{17}O-excess and d-excess in Antarctica still agree with the data). In the highest deviation from the inversion presented above, obtained by an extreme tuning of the SCM, the reconstruction of T_{site} is virtually unchanged (-0.2°C) whereas the reconstruction of T_{source} is more affected (-1.9°C).

Therefore, when considering the uncertainties mentionned above, the maximum uncertainty ranges for T_{site} and T_{source} are of the order of $2°C$ and $4°C$ respectively. However, the major source of uncertainty in this reconstruction remains the estimated change in rh_s, if other factors than rh_s contribute to the observed ^{17}O-excess shift (table 7.3): 0.4°C for ΔT_{site} and 9°C for ΔT_{source}.

7.6 Conclusion

7.6.1 Summary

We explore various processes, both at the evaporative source and during the poleward transport, that could explain the +20 permeg increase over the last deglaciation.

Using a Single Column Model (SCM) over tropical and subtropical oceans, we show that the ^{17}O-excess of the low level vapor is affected mainly by the relative humidity at the surface, rh_s, with a sensitivity of -1.0 permeg/%. This sensitivity is robust and similar to that predicted by the closure assumption, so that it can likely be extended to all latitudes. Given this sensitivity, a 12 to 22% increase in rh_s would be necessary to explain the +20 permeg increase over the last deglaciation. Changes in rain rates over tropical or subtropical sources, conversely, are not likely to contribute to more than a few permeg to the shift.

Using a Rayleigh type distillation model, we show that the amplitude of ^{17}O-excess variations in the moisture source regions is well recorded in the ^{17}O-excess of the polar precipitation, while they are damped in d-excess. The ^{17}O-excess in polar snowfall can also be influenced by evaporative recharge and by the amplitude of the $\delta^{18}O$ seasonal cycle at the precipitation site, but the contribution of these effects to the observed ^{17}O-excess shift is expected to remain secondary (at most 35% of the shift).

Among the different processes considered in this study (changes in convective activity, SST or relative humidity at source regions, in evaporative discharge over mid-to-high latitude oceans, in the seasonal cycle of Antarctica precipitation), only one can explain the large magnitude (+20 permeg)

1	2	3	4	5	6	7	8	9	10	11	12	13	14	15	16	17	18
n°	Δrh_s scenario	method	age	T_{so} (°C)	V_s (m/s)	ω (hPa/d)	rh_s (%)	Δrh_s (%)	ΔT_{so} (°C)	T_{si} (°C)	ΔT_{si} (°C)	$\delta^{18}O_i$ (‰)	d_i (‰)	$^{17}O_i$ (permeg)	$\Delta\delta^{18}O_i$ (‰)	Δd_i (‰)	$\Delta^{17}O_i$ (permeg)
1	-20	V_s	EH	29	2	0	56.0	-20.3	1.3	-55	7.8	-55.96	23.1	57	5.61	-0.1	20
2			LGM	27.7	6.9	0	76.3			-62.8		-61.57	23.2	37			
3		ω and V_s	EH	29	4.5	-90	61.2	-19.3	1.3	-55	7.8	-56.01	22.9	52	5.84	1.7	20
4			LGM	27.7	6.5	30	80.5			-62.8		-61.85	21.2	32			
5	-10	V_s	EH	29	3.6	15	65.6	-10.3	4.4	-55	8.5	-55.64	18.0	47	5.96	1.7	10
6			LGM	24.6	6.9	15	75.9			-63.5		-61.60	16.3	37			
7		ω	EH	29	5	-45	66.2	-10.3	4.4	-55	8.5	-54.88	21.0	47	6.60	1.8	10
8			LGM	24.6	5	30	76.5			-63.5		-61.48	19.2	37			
control	0	V_s	EH	29	5	15	72.5	0.2	7.4	-55	9.2	-54.2	15	42	7.66	0.7	2
9			LGM	21.6	4.5	15	72.3			-64.2		-61.86	14.3	40			
control		ω	EH	29	5	15	72.5	0.4	7.4	-55	9.2	-54.2	15	42	7.95	0.8	2
10			LGM	21.6	5	13	72.1			-64.2		-62.15	14.2	40			

of the ^{17}O-excess shift observed in Antarctica over the deglaciation: the decrease of the surface relative humidity (rh_s) by 8-20% from LGM to present (in agreement with [Landais et al., 2008]). This might arise either through a decrease of the surface-air relative humidity (rh_a), or through an increase of the thermodynamical disequilibrium between the surface and the near-surface air as the global mean temperature increases.

The fact that current GCMs do not simulate any large change in rh_s during the LGM raises questions. This mismatch could have a link with the inability of current isotopic GCMs to simulate the observed increase of d-excess from LGM to EH over polar regions ([Werner et al., 2001]): if GCMs simulated a higher rh_s during the LGM, they would more likely simulate a lower d-excess, closer to observations.

Such a large change in rh_s strengthens the interest of ^{17}O-excess to provide more accurate reconstructions of source and site temperatures than from the combination of $\delta^{18}O$ and d-excess only. The assumption that rh_s changes are either negligible or linearly related to temperature ([Vimeux et al., 2001, Stenni et al., 2001]) can be relaxed. Using ^{17}O-excess measurements to constrain the change in rh_s yields a LGM source temperature about 1.4°C lower than at EH, and a Vostok temperature 7.8°C lower. Both these estimates are consistent with previous studies ([Vimeux et al., 2001]), but owing to compensating effects. These estimates are particularly sensitive to the reconstructed change in rh_s.

7.6.2 Perspectives

While we explore the influence of different climate conditions both at the evaporative source and during the poleward transport, our approach is still incomplete. First, we considered only one evaporative source and one trajectory, whereas the polar snowfall originates from different sources through various trajectories (e.g. [Helsen et al., 2006]). Given the sensitivity of ^{17}O-excess to mixing of contrasted $\delta^{18}O$ moisture, the heterogeneity of the sources could have an impact on the polar ^{17}O-excess. Second, the SCM was run for subtropical conditions, whereas middle and high latitudes are also important sources of vapor for Antarctica snowfall ([Delaygue et al., 2000, Werner et al., 2001]). Whereas the sensitivity of the isotopic composition of low-level vapor to surface relative humidity can be applied to all latitudes ([Jouzel et al., 1982, Landais et al., 2008]), the sensitivity to tropical convective processes is more difficult to generalize to extra-tropical latitudes. In addition, some effects controlling the ice ^{17}O-excess in middle and high latitudes might have been ignored. For example, 3D large-scale advections or changes in cloud dynamics and microphysics in frontal systems ([Gedzelman and Arnold, 1994]) might play an important role. The type of water transport (diffusive or advective: [Hendricks et al., 2000, Kavanaugh and Cuffey, 2003]) might also affect the ^{17}O-excess, since diffusive transport would involve some mixing, which decreases the ^{17}O-excess due to the non-linearity of the mixing curves in the logarithmic diagram (figure 7.4). GCM simulations with isotopic capabilities including $H_2^{17}O$ (appendix D.3.4) would be necessary to explore these processes and thus to better understand what information is recorded in snowfall ^{17}O-excess.

Conclusion de la partie

Au cours de cette thèse, nous avons implémenté les isotopes stables de l'eau dans le GCM LMDZ (chapitre 6). LMDZ-iso simule la distribution spatiale et temporelle (aux échelles journalière à inter-annuelle, climats passés) de la composition isotopique de l'eau des précipitations de manière satisfaisante. Ses performances se comparent bien aux autres GCMs isotopiques existant déjà.

Ce chapitre a été consacré à l'enregistrement des changements climatiques par la composition isotopique des précipitations. Nous présentons ci-dessous quelques pistes de réflexion et perspectives concernant les variations isotopiques entre le LGM et l'actuel, simulées par LMDZ-iso et les autres GCMs, ou mesurées dans l'^{17}O-excess. Puis nous présentons quelques perspectives concernant l'utilisation du modèle LMDZ-iso pour l'étude du cycle de l'eau actuel.

1 Le LGM et ses mystères isotopiques

1 Les variations de $\delta^{18}O$ dans les tropiques entre le LGM et l'actuel

LMDZ-iso partage avec les autres GCMs des défauts communs. En particulier, il n'arrive pas à simuler les $\delta^{18}O$ plus faibles dans les précipitations (de l'ordre de 5‰) observés au LGM sur les glaciers tropicaux ([Jouzel et al., 2000]). Pourquoi les GCMs n'arrivent-ils pas à reproduire ces faibles $\delta^{18}O$? La cause de cette difficulté dépend de la réponse à deux autres questions, qui sont très liées :

1. les faibles $\delta^{18}O$ au LGM sont-ils contrôlés par la température ([Thompson et al., 2000]), ou par la précipitation ([Hoffmann, 2003, Hoffmann et al., 2003, Vimeux et al., 2005]), ou par un autre processus ?
2. Les faibles $\delta^{18}O$ au LGM constituent-ils un signal global ou régional ?

La cause la plus probable d'un changement à l'échelle globale de $\delta^{18}O$ serait une réponse au changement de température globale. En effet, s'il s'agissait de changement de précipitations, ils seraient probablement régionaux, car les forts changements de précipitation dans les tropiques sont généralement associés à une réorganisation de la circulation atmosphérique. La similitude entre les évolutions isotopiques aux cours des quelques centaines de milliers d'années des différentes carottes tropicales et polaires suggère une réponse à un changement à l'échelle globale.

Toutefois, la température ne semble pas affecter la composition isotopique dans le climat actuel, et les GCMs simulent une sensibilité à la température globale très faible (0.1‰/°C, chapitre 6). Cette sensibilité est-elle si faible dans la réalité ? Si les faibles $\delta^{18}O$ observés constituent un signal en température globale, alors cela suggère la difficulté des GCMs à simuler cette sensibilité du $\delta^{18}O$ à la température globale. Si au contraire il s'agit d'un signal régional, cela semble indiquer des difficultés des GCMs dans les régions de montagne (où sont situées la plupart des données), ou des difficultés à simuler le changement de précipitation au LGM. Des simulations avec LMDZ-iso zoomé sur l'Amérique du Sud (annexe G) au LGM sont prévues, et permettront de vérifier si une meilleure représentation de l'orographie dans les Andes permet de simuler des $\delta^{18}O$ plus bas. Plus généralement, seule une meilleure couverture spatiale des données isotopiques au LGM dans les tropiques permettra de mieux connaître l'échelle spatiale des changements isotopiques au LGM.

2 Les variations de d-excess aux pôles entre le LGM et l'actuel

Si LMDZ-iso présente des défauts communs à tous les autres GCMs, il présente aussi quelques caractéristiques uniques. En particulier, il simule un d-excess plus bas au LGM qu'à l'actuel aux hautes latitudes, en accord avec les mesures et contrairement aux autres GCMs ([Werner et al., 2001]). Jusqu'à présent, les GCMs aux hautes latitudes avaient beaucoup de difficultés à simuler des variations de δ et de d-excess dans le même sens ([Werner et al., 2001, Noone, 2008]). Dans le futur, nous étudierons les raisons pour lesquelles LMDZ-iso prédit une baisse du d-excess en accord avec les données. Ceci aidera plus généralement à mieux comprendre les processus contrôlant le d-excess (annexe F).

3 L'^{17}O-excess et ses variations entre le LGM et l'actuel

Les variations observées de composition isotopique entre l'actuel et le LGM sont décidemment bien mystérieuses. Nous avons vu que la difficulté des GCMs à simuler au LGM un $\delta^{18}O$ plus bas dans les tropiques et un d-excess plus bas aux pôles posait de nombreuses questions quant à l'interprétation de ces signaux. De même, les variations d'^{17}O-excess mesurées récemment dans la carotte de Vostok ([Landais et al., 2008]) posent des questions. Parmi tous les processus explorés dans le chapitre 7, aucun n'est suffisant pour expliquer l'^{17}O-excess plus faible de 20 permeg au LGM, si ce n'est une humidité relative plus haute au LGM de l'ordre de 10 à 20%. Or aucun GCM ne simule une telle variation d'humidité relative entre le LGM et l'actuel ([Bush and Philander, 1999]), et les possibilités théoriques de variation de l'humidité relative près de la surface sont fortement limitées par des contraintes énergétiques ([Held and Brian J Soden, 2000]).

Dans le futur, plus de données seront nécessaires pour mieux comprendre les contrôles de l'^{17}O-excess. De nombreuses mesures sont en cours au LSCE par Amaelle Landais. Notamment, des mesures sont réalisées en région tropicale, ce qui permettra une meilleure couverture spatiale. L'analyse des échantillons collectés pendant la campagne AMMA (chapitres 3 et 4) apporteront aussi de nombreuses informations sur la sensibilité de ce traceur aux processus convectifs.

L'analyse de ces données pourra être complémentée de l'analyse de simulations avec LMDZ-iso incluant l'$H_2^{17}O$. Un effort sera réalisé pour surmonter les difficultés actuelles de simulation de l'^{17}O-excess dans LMDZ-iso (annexe D.3.4).

2 LMDZ-iso et les applications pour l'étude du cycle de l'eau actuel

Pour l'instant, nous nous avons utilisé LMDZ-iso essentiellement pour des applications paléoclimatiques. Mais de plus en plus, les GCMs isotopiques sont utilisés pour l'étude du cycle de l'eau actuel (e.g. [Schmidt et al., 2005, Wright et al., 2009]). Cette perspective sera développée dans le futur, notamment grâce au traçage de l'eau et de ses isotopes (water tagging) dans LMDZ-iso. De nombreuses options de traçage (décrites en annexe E) permettent de tracer non seulement les zones géographiques d'évaporation (e.g. [Delaygue et al., 2000, Werner et al., 2001, Noone and Simmonds, 2002a, Vuille et al., 2003]), mais aussi de nombreuses étapes du cycle hydrologique.

Troisième partie

Les isotopes de l'eau et les processus à la surface continentale

Introduction de la partie

Sur les continents tropicaux, la composition isotopique de la précipitation semble affectée par les interactions avec la surface continentale ([Gat and Matsui, 1991, Rozanski et al., 1993]). Mieux comprendre ces processus a un intérêt paléoclimatologique, puisque la majorité des archives tropicales de précipitations sont continentales (glaciers, spéléothèmes). Cela a aussi un intérêt en retour pour l'hydrologie de surface, où les isotopes de l'eau ont déjà été utilisés pour mieux contraindre certains processes à l'échelle locale (e.g. [Moreira et al., 1997, Brunel et al., 1997, Millet et al., 1997]). Toutefois, le potentiel des isotopes a encore été relativement peu exploité pour l'hydrologie de surface à grande échelle ([Fekete et al., 2006]). Dans cette partie, nous étudions donc l'influence des processus hydrologiques à la surface continentale sur la composition isotopique de l'eau. Pour cela, nous avons implémenté les isotopes de l'eau dans le modèle d'hydrologie continentale ORCHIDEE, dont les simulations sont exploitées dans le chapitre 8.

1 Processus isotopiques à la surface continentale

Un fractionnement isotopique est associé lors de l'évaporation de l'eau liquide, du fait de fractionnements à la fois à l'équilibre (annexe B.1) et cinétiques (annexe B.3) ([Craig and Gordon, 1965]). Ainsi, l'eau évaporée d'un sol nu est plus pauvre que l'eau du sol, et l'eau transpirée par la végétation est plus pauvre que l'eau des feuilles. La composition isotopique de l'eau évapotranspirée par rapport à l'eau arrivant sur la surface continentale par précipitation dépend de la façon dont l'évapo-transpiration se fait (figure .8a) :

- *transpiration par la végétation* : aux échelles supérieures à journalière, il n'y a pas de fractionnement isotopique entre l'eau du sol et transpirée. En effet, il n'y a pas de fractionnement au niveau des racines ([Washburn and Smith, 1934, Barnes and Allison, 1988]). Même s'il existe un fractionnement isotopique au niveau des feuilles, le réservoir d'eau dans la plante est faible par rapport au flux d'eau la traversant en une journée. En conséquence, l'état stationnaire pour la plante est rapidement atteint : en quelques heures ([Cuntz et al., 2007]), les feuilles s'enrichissent de telle façon que la composition isotopique entrante par les racines est alors égale à celle sortante par les feuille.
- *évaporation de l'eau du sol nu* (*ou de l'eau interceptée par la canopée*) : dans ce cas, il y a un fractionnement isotopique entre l'évaporation et l'eau du sol nu. Si la réévaporation n'est pas totale, et si une partie de l'eau du sol en train de s'évaporer est perdue par drainage, alors la composition isotopique de l'évaporation fractionnante est plus pauvre que celle de la précipitation, et a un d-excess plus fort à cause du fractionnement cinétique (figure .8b).

La proportion de la précipitation recyclée par évapo-transpiration vers l'atmosphère, ainsi que la partition de l'évapo-transpiration entre transpiration et évaporation du sol nu, ont un impact sur les distributions isotopiques à l'échelle continentale. Les données isotopiques dans les précipitations du réseau GNIP montrent une perte progressive d'isotopes lourds par précipitation le long des trajectoires des masses d'air sur les continents ([Rozanski et al., 1993], figure .8c). Ce gradient continental est plus faible dans les régions où une proportion plus forte de la précipitation est recyclée vers l'atmosphère, comme en Amazonie ([Rozanski et al., 1993]). En parallèle, le d-excess augmente le long des trajectoires sur les continents, en particulier en Amazonie ([Salati et al., 1979, Gat and Matsui, 1991], figure .8c). Ce gradient y a été interprété comme l'effet d'un recyclage de l'eau par l'évaporation fractionnante de l'eau du sol, des lacs, ou interceptée par la canopée (figure .8).

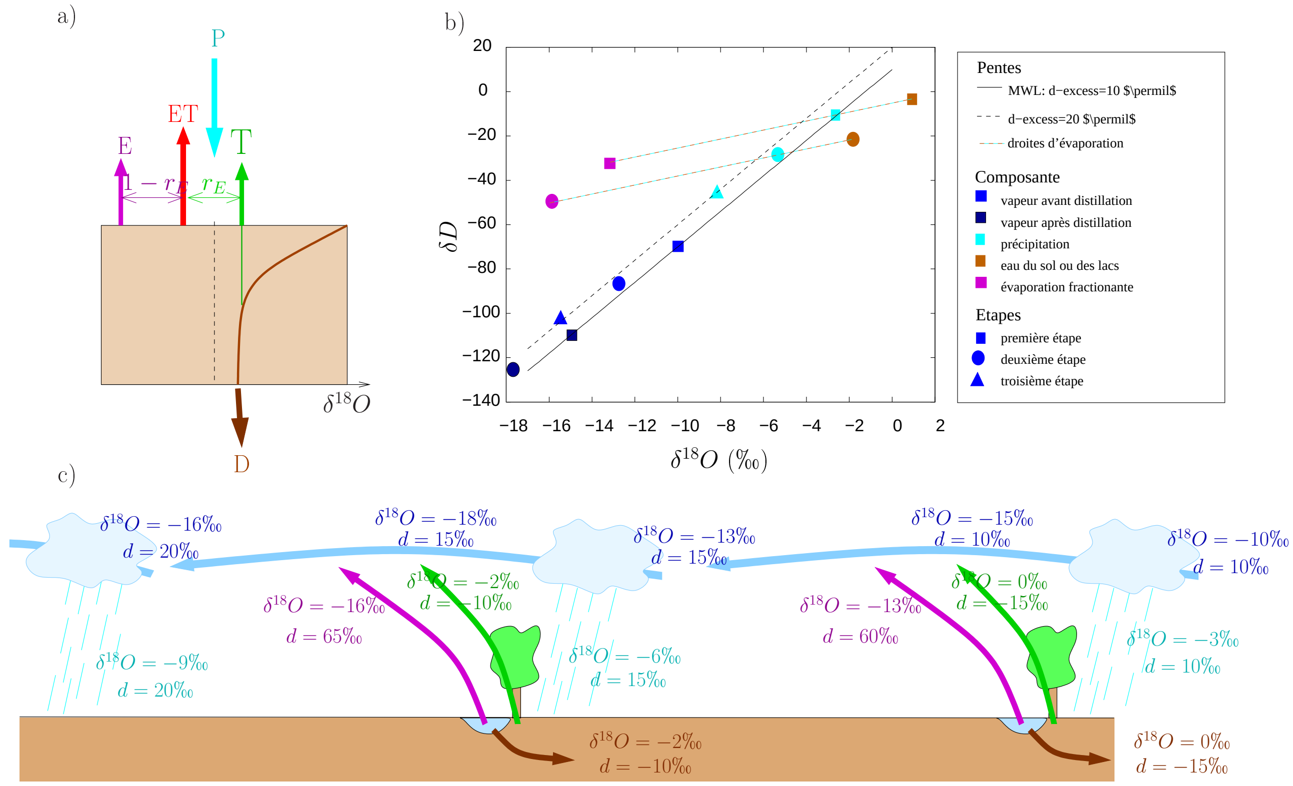

Fig. .8 – a) Schéma illustrant les fractionnements isotopiques en jeu au niveau du sol et de la végétation. La précipitation P (cyan) s'infiltre dans le sol. L'évaporation du sol nu E est associée à un fractionnement, tendant à enrichir le sol en surface. La transpiration T, elle, ne fractionne pas. Si du drainage (D) prélève de l'eau du sol qui a été enrichie, alors il y a une perte nette d'eau riche et l'évapotranspration totale (ET) est plus pauvre que la précipitation.
b) Diagramme δD-$\delta^{18}O$ montrant l'évolution de la composition isotopique des précipitations au cours du recyclage continental. On présente ici 3 étapes idéalisées de distillation puis recyclage d'une masse d'air, schématisées en (c). Au cours de chaque étape, la vapeur (bleu) est distillée jusqu'à perdre 40% de son eau sous forme de précipitation (cyan), donnant une vapeur résiduelle plus pauvre (carré bleu foncé). Cette précipitation s'infiltre dans le sol. Par évaporation fractionnante (carré violet), le sol s'enrichit. On suppose que cette eau du sol enrichie (carré marron) est drainée sans fractionnement (50%), transpirée par la végétation sans fractionnement (25%) ou évaporée directement par le sol nu (25%). La vapeur résiduelle (carré bleu foncé) est alors mélangée à la transpiration et à l'évaporation fractionnante, donnant une nouvelle vapeur (rond bleu). Et ainsi de suite.
c) schéma illustratif du recyclage continetal correspondant à la figure b, et montrant des valeurs numériques. Dans ce cas idéalisé, la précipitation s'appauvrit de 6‰ et son d-excess augmente de 10‰ par recyclage fractionnant.

2 Motivations pour étudier l'effet des processus à la surface continentale sur la composition isotopique de l'eau

Les motivations pour étudier le lien entre composition isotopique de l'eau et processus à la surface continentale sont les suivantes.

1 Interprétation paléoclimatique des signaux isotopiques en région continentale

Comprendre l'impact du recyclage continental sur la composition isotopique de la précipitation est crucial pour espérer interpréter quantitativement les archives isotopiques continentales, telles les glaciers andins. Par exemple, tandis que le $\delta^{18}O$ des glaciers andins est souvent interprété comme enregistrant des changements de précipitation sur l'Amazonie ([Hoffmann, 2003, Vimeux et al., 2005]), [Pierrehumbert, 1999] a montré qu'un changement dans la fraction de précipitation perdue par ruissellement pouvait expliquer le signal observé lors de la dernière déglaciation dans les carottes andines.

2 Réserve d'eau du sol et constantes de temps de l'amount effect

Nous avons vu dans la section 3.3.3 que le $\delta^{18}O$ des précipitations collectées à Niamey enregistrait une moyenne de l'activité convective au cours de 9 derniers jours. Le sol a-t-il un rôle dans cette mémoire ? Si oui, le $\delta^{18}O$ peut-il être utilisé pour évaluer des temps de résidence de l'eau dans le sol et les constantes de temps des intéractions surface-atmosphère ?

3 Bilans d'eau en région continentale

Le recyclage de l'eau par les continents est difficile à quantifier à l'échelle continentale : quelle est la proportion de précipitation recyclée vers l'atmosphère ou perdue par ruissellement ou drainage ? Quelle est la proportion de la précipitation qui s'est évaporée localement sur le continent ([Gong and Eltahir, 1996, Burde and Zangvil, 2001]) ? Quelle est la proportion de l'évaporation continentale qui se fait sous forme de transpiration ou d'évaporation directe du sol ? Comment ces proportions varient-elles dans le cadre du changement climatique ([Gedney et al., 2006, Piao et al., 2007]), ou de la déforestation ([Henderson-Sellers et al., 2001, McGuffie and Henderson-Sellers, 2004]) ?

Les isotopes de l'eau pourraient s'avérer utile pour mieux contraindre le bilan d'eau ([Gat, 1996, Henderson-Sellers et al., 2004]), du fait des compositions isotopiques différentes de la transpiration, de l'évaporation du sol nu et du ruissellement ou du drainage.

Par exemple, le contraste de composition entre eau transpirée et eau évaporée du sol nu peut être utilisé pour estimer la partition de l'évapo-transpiration entre ces deux flux ([Moreira et al., 1997, Yepez et al., 2003, Williams et al., 2004]). Soit R_E, R_T et R_{ET} les compositions isotopiques de l'évaporation du sol nu, de la transpiration et de l'évapo-transpiration totale, et r_E la proportion d'évapo-transpiration par évaporation directe. On a :

$$R_{ET} = r_E \cdot R_E + (1 - r_E) \cdot R_T$$

Connaissant, R_E, R_{ET} et R_T, on peut donc déduire r_E. Jusqu'à présent, la plupart des études utilisant les isotopes pour étudier le bilan d'eau à la surface sont restées limitées à petite échelle (ex : échelle du champs sur quelques heures ou jours, avec des applications agronomiques ([Brunel et al., 1997, Moreira et al., 1997, Yepez et al., 2003, Williams et al., 2004]). Pour estimer r_E, la composition isotopique de l'eau du sol, des tiges (environ égale à R_T) et de la vapeur d'eau à différentes altitudes (permettant de déduire R_{ET}) sont mesurés. R_E est calculé théoriquement d'après les propriétés atmosphériques et la composition isotopique du sol d'après la formule de [Craig and Gordon, 1965].

A l'échelle du continent, ces applications ont encore été peu explorées ([Fekete et al., 2006]). Quantifier la partition de l'évapo-transpiration entre différents flux évaporatoires et ruissellement ou drainage serait pourtant très utile pour mieux contraindre la représentation des surfaces continentales dans les modèles de climat. Le gradient de d-excess observé en Amazonie dans les précipitations, par exemple, a déjà été exploité pour estimer la proportion du recyclage continental se faisant par évaporation fractionnante ([Salati et al., 1979, Gat and Matsui, 1991]).

4 Contrainte des paramétrisations d'hydrologie continentale

Les paramétrisations de l'hydrologie continentale sont une source importante de dispersion dans les modèles, aussi bien dans leur simulation du cycle saisonnier ([Koster and Milly, 1996]), de la variabilité inter-annuelle ([Koster and Suarez, 1999]) ou synoptique à intra-saisonnière ([Koster et al., 2006]). Les isotopes peuvent-ils aider à mieux contraindre ces paramétrisations ([Henderson-Sellers, 2006]) ?

3 Approche

Etudier l'effet de l'hydrologie continentale sur les isotopes nécessite une représentation détaillée des différents processus de surface : évaporation du sol nu, extraction racinaire, transpiration, ruissellement, drainage, interception de la précipitation par la canopée... Pour cela, l'approche naturelle est d'implémenter les isotopes de l'eau dans un modèle de surface continental ([Yoshimura et al., 2006, Aleinov and Schmidt, 2006]).

Pour mieux comprendre l'effet de la surface continentale sur les isotopes et explorer leur potentiel pour étudier des problématiques d'hydrologie continentale, nous introduisons donc les isotopes de l'eau dans le modèle de surface continentale ORCHIDEE. Le chapitre suivant, basé sur un article en préparartion, présente les résultats de simulations offline et couplées avec le modèle atmosphérique LMDZ. Il s'agit d'un travail encore en progrès.

Chapitre 8

Les isotopes de l'eau dans ORCHIDEE : applications à l'étude des processus hydrologiques continentaux

8.1 Introduction

Due to isotopic fractionation during phase changes, the different isotopologues ($H_2^{16}O$, HDO, $H_2^{18}O$) are useful tracers of the water cycle (e.g. [Gat, 1996, Worden et al., 2007, Noone, 2009]). Over land, the intensity of the continental recycling of precipitation back to the atmosphere through evapo-transpiration affects the spatial distribution of water stable isotopes in precipitation ([Rozanski et al., 1993]) and in water vapor ([Brown et al., 2008, Frankenberg et al., 2009]). Temporal variations in continental recycling may also affect isotopic records in ice cores ([Pierrehumbert, 1999]). In addition, the way precipitation is recycled (i.e. through transpiration, evaporation of bare soils, open water bodies or water intercepted by the canopy), affects the spatial ([Gat and Matsui, 1991]) and seasonal (Vimeux et al, in prep) distributions of the precipitation isotopic composition. In turn, it has been suggested that measurements of water isotopes could help constrain water fluxes over land ([Gat, 1996, Henderson-Sellers et al., 2004]) and their response to climate or land use change ([Henderson-Sellers et al., 2001]), as well as the representation of land processes in large-scale models ([Henderson-Sellers, 2006]).

At the local scale, measurements of water stable isotopes in the different water pools of the soil-vegetation-atmosphere continuum have been used to infer water fluxes or pathways. For example, field measurements in soils, plants and/or vapor at different heights have been successfully used to estimate the fraction of total evapo-transpiration due to transpiration ([Moreira et al., 1997, Yepez et al., 2003, Williams et al., 2004]), plant source water depth ([Brunel et al., 1997]) or evaporation loss from lakes ([Gibson, 2002, Gibson and Edwards, 2002]). At the regional scale, most studies have made used of the relatively good spatial coverage of isotopic measurements in precipitation to infer terms of the water budget very difficult to quantify otherwise, such as the proportion of regional evapo-transpiration arising from transpiration ([Gat and Matsui, 1991]).

The goal of this modeling study is to evaluate the potential of water stable isotopes in constraining terms of the water budget at large spatial (>100km) and temporal (>1 yr) scales, and to identify the measurements that would be most needed for this type of application.

So far, water isotopes have been implemented in several land surface models (LSMs), from sophisticated, multilayer models to better understand isotopic fractionation during soil evaporation and soil water vertical movements at the local scale ([Braud et al., 2005, Melayah et al., 1996]), to larger-scale water balance models to explore hydrological applications at the continental scale ([Fekete et al., 2006]). The inter-comparison of several isotopic LSMs has also shed light on the potential of water isotopes to identify biases in LSMs and to better constrain LSM parameterizations

([Henderson-Sellers, 2006]). The coupling of such isotope-enabled LSMs and general circulation models (GCM, [Aleinov and Schmidt, 2006]) or simpler atmospheric models ([Yoshimura et al., 2003]) has shown the impact of isotopic processes at the land surface on the global distribution of the precipitation isotopic composition. The implementation of water stable isotopes in LSMs is also required to simulate the ^{18}O content of atmospheric CO_2, which has applications in quantifying and partitioning land-atmosphere carbon exchanges into vegetation and soil respiration components ([Riley et al., 2002, Cuntz et al., 2003, Wingate et al., 2009]).

Water stable isotopes have already been implemented and validated in LMDZ, the atmospheric component of the IPSL climate model ([Risi et al., 2010b]). In this study, we implemented water stable isotopes in ORCHIDEE (ORganizing Carbon and Hydrology In Dynamic EcosytEms, [Ducoudré et al., 1993, Krinner et al., 2005]), the land surface component of the Institut Pierre-Simon Laplace (IPSL) climate model ([Marti et al., 2005]). While the evaluation of isotope-enabled LSMs has long been limited by the lack of data (e.g. [Aleinov and Schmidt, 2006, Yoshimura et al., 2006]), a considerable effort has been invested in the recent years to collect and compile isotopic data in the different water pools of the land-atmosphere system, offering unprecedented evaluation opportunities. In this context we bring together several datasets:

(1) isotopic data in the precipitation with a relatively good spatial coverage from the GNIP database (Global Network for isotopes in Precipitation, [Rozanski et al., 1993]) to evaluate the main processes in the coupled mode;

(2) isotopic data in soils, stems, leaves and vapor from the MIBA database (Moisture and Isotopes in the Biosphere and Atmosphere, e.g. [Twining et al., 2006, Knohl et al., 2007, Hemming et al., 2007], available on the IAEA web site:

http://www-naweb.iaea.org/napc/ih/MIBA/IHS_MIBA_results.html), and from additional individual campaigns, to evaluate isotopic processes in the soil and vegetation; and

(3) isotopic data in rivers from the GNIR database (Global Network for isotopes in Rivers, [Vitvar et al., 2006, Vitvar et al., 2007]) to evaluate continental processes integrated at the scale of large watersheds.

Following common practice ([Craig, 1961]), we express isotopic ratios in the different water pools in ‰ using the "delta" notation:

$$\delta = \left(\frac{R_{sample}}{R_{SMOW}} - 1 \right) \cdot 1000$$

where R_{sample} and R_{SMOW} are the isotopic ratio ($HDO/H_2^{16}O$ or $H_2^{18}O/H_2^{16}O$) of the sample and of the Standard Mean Ocean Water (SMOW) respectively ([Craig, 1961]). At first order, variations in δD follow the same patterns as $\delta^{18}O$ but are 8 times larger. Deviation from this behavior is quantified by the deuterium excess: $d = \delta D - 8 \cdot \delta^{18}O$ ([Dansgaard, 1964]). This second order parameter provides additional information on hydrological processes ([Dansgaard, 1964, Gat, 1996, Gat, 2000]), and is known to be more difficult to simulate by GCMs ([Mathieu et al., 2002]). We will present an evaluation of deuterium excess when data is available.

Hereafter, we note $\delta^{18}O_p$, $\delta^{18}O_v$, $\delta^{18}O_s$, $\delta^{18}O_{stem}$, $\delta^{18}O_{leaf}$, $\delta^{18}O_{river}$ and $\delta^{18}O_{ET}$ the $\delta^{18}O$ of the precipitation, atmospheric vapor, soil, stem, leaf, rivers and evapo-transpiration water respectively. The same subscripts apply for d.

In the following, we first describe the isotopic versions of the ORCHIDEE and LMDZ models and the simulations set-up (section 8.2), then evaluate the representation of isotopic processes in the models (section 8.3). We then use coupled land-atmosphere simulations to evaluate the potential of water isotopes to quantify terms of the hydrological cycle over land (section 8.4.2) We then summarize our main conclusions and present perspectives for future work (section 8.5).

8.2 Model and simulation description

The ORCHIDEE and LMDZ4 models are respectively the LSM and atmospheric GCM of the IPSL climate model ([Marti et al., 2005]) that participated in CMIP3 ([Meehl et al., 2007]). We call LMDZ-iso, ORCHIDEE-iso and LMDZ-OR-iso the isotope-enabled versions of the LMDZ, ORCHIDEE and coupled LMDZ-ORCHIDEE models, respectively.

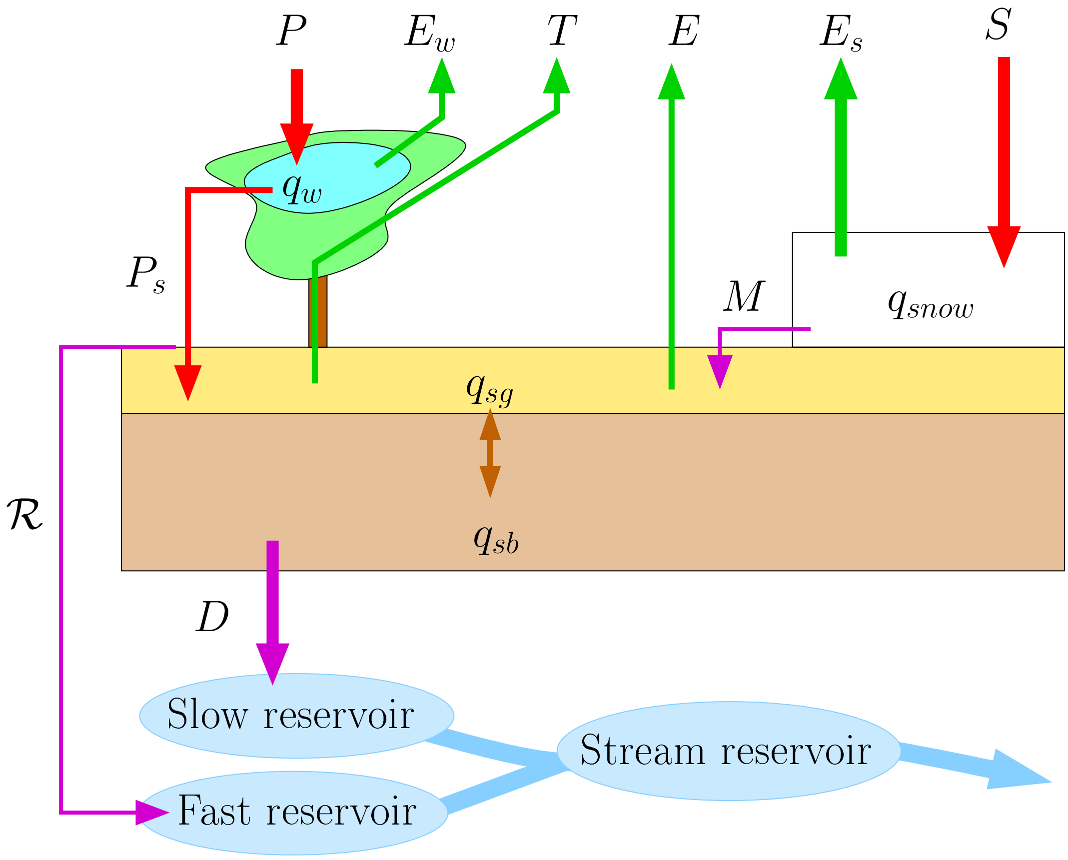

Figure 8.1: Water fluxes and pools represented in the ORCHIDEE LSM. Water pools are the soil water in the superficial (q_{sg}) and bottom (q_{sb}) layers, the water intercepted by the canopy (q_w) and the snow pack (q_{snow}). Fluxes onto the land surface are the total rain (P) and snow (S), and possibly dew or frost. As some rain is intercepted by the canopy, only throughfall rain (P_s) arrives at the soil surface. Evaporation fluxes are the evaporation of intercepted water (E_w), transpiration by the vegetation (T), bare soil evaporation (E) and snow sublimation (E_s). Snow melt may be transferred from the snow pack to the soil (M). Water from rainfall, melt (and possibly dew) exceeding the soil capacity is converted to surface runoff ($\mathcal{R}$) and drainage (D). The routing model then transfers surface runoff and drainage to streams.

8.2.1 The ORCHIDEE-iso model

Physical parametrizations

The ORCHIDEE model merges three separate modules:

(1) SECHIBA simulates land-atmosphere water and energy exchanges ([Ducoudré et al., 1993, De Rosnay, 1999]);

(2) STOMATE simulates vegetation phenology and biochemical transfers ([Krinner et al., 1997b]); and

(3) LPJ ([Sitch, 2003]) simulates the dynamic evolution of the vegetation. We implemented water stable isotopes in the first module, and use prescribed land cover maps so that the two other modules could be de-activated.

Up to 13 land cover types can coexist within each grid box: bare soil (no vegetation), deciduous or evergreen forests, C3 and C4 grasslands, spread over the boreal, temperate and tropical regions. Water fluxes and pool sizes are computed independently for each vegetation type. The bare soil fraction f_{bare} is calculated as:

$$f_{bare} = \sum_{j=1}^{n_{veget}} \max\left(1 - 2 \cdot LAI_j \cdot f_j, 0\right) \tag{8.1}$$

where LAI_j is the LAI of the vegetation type $j \in [1, n_{veget}]$ and f_j the maximum proportion of the grid box covered by vegetation type j. Alternatively, f_{bare} can be calculated as ([d'Orgeval, 2006]):

$$f_{bare} = \sum_{j=1}^{n_{veget}} e^{-k \cdot LAI_j \cdot f_j} \tag{8.2}$$

where k is a tunable parameter.

The different water fluxes and pools represented in the ORCHIDEE LSM are illustrate in figure 8.1. The water in the 2m deep soil is divided into a superficial and a bottom reservoir ([Choisnel, 1977, Choisnel et al., 1995]). Within each grid point, the bare soil and the different vegetation types share the same bottom layer.

Evapo-transpiration is partitioned into bare soil evaporation (E), vegetation transpiration (T), evaporation of water intercepted by the canopy (E_w) and snow sublimation (E_s). The transpiration rate is limited during plant water stress, calculated as a function of the soil water content and an exponential root profile whose characteristics are prescribed for each vegetation type ([Rosnay and Polcher, 1998]). Fluxes onto the soil surface are throughfall rain (i.e. rain that is not intercepted by the vegetation: P_s), snow melt (M), throughfall dew and frost. Fluxes out of the soil are transpiration, bare soil evaporation, surface runoff ($\mathcal{R}$) and drainage (D). Surface runoff and drainage occur when the soil water content exceeds the soil holding capacity, corresponding to 300mm water. In this case, the excess water is partitioned into 95% drainage and 5% surface runoff ([Ngo-Duc, 2005]).

Snow is represented by a single layer reservoir. Water input into this reservoir is snow precipitation, and outputs are snow sublimation and melt.

A water routing model describes the water movements from soil to the coastlines ([Polcher, 2003]). Surface runoff and drainage are stored in fast and slow reservoirs respectively, with residence times of 3 and 25 days respectively. The contents of these reservoirs are progressively poured into a stream reservoir, with a residence time of 0.24 days. Streams are finally routed to the coastline, according to a map of large watersheds.

Implementation of water stable isotopes

The implementation of water stable isotopes ($H_2^{16}O$, $H_2^{18}O$, HDO, $H_2^{17}O$) in the ORCHIDEE model is described in detail in appendix D.4. In brief, water isotopes are passively advected between the different reservoirs by non-fractionating water fluxes. We calculate the fractionation during evaporation at the soil surface and at the surface of intercepted water using the [Craig and Gordon, 1965] equation. We neglect the fractionation and diffusion associated with the vapor phase in the soil ([Melayah et al., 1996]). In the simulations described here, we assume that transpiration does not fractionate and diagnose the composition of leaf water assuming a stationary state. We neglect the effect of water storage in the leaves and the dffusion between leaf water and xylem (Peclet effect, [Ogée et al., 2007], appendix D.4.4). We assume that the surface runoff has the composition of the excess inflow into the soil (i.e. precpitation or snow melt), and that the drainage has the composition of the soil water. We assume that the isotopic composition is homogeneous vertically. However, we implemented a representation of the isotopic vertical distribution in the soil for the purpose of sensitivity tests to the homogeneity assumption.

8.2.2 The LMDZ-iso model

The LMDZ4 model ([Hourdin et al., 2006]) is a grid point GCM with a standard resolution of 2.5° in latitude, 3.75° in longitude and 19 vertical levels. Each grid cell is divided into four subsurfaces: land (treated by ORCHIDEE), ocean, ice-sheet and sea-ice. The model includes the Emanuel convective parameterization ([Emanuel, 1991, Grandpeix et al., 2004]) coupled to the [Bony and Emanuel, 2001] cloud scheme. Turbulent transport in the planetary boundary layer is treated as a diffusion process and a dry convective adjustment prevents unstable profiles. Water in its vapor and condensed forms are advected by the [Van Leer, 1977] advection scheme. All parameterizations, including ORCHIDEE, are called every 30 min.

The implementation of water stable isotopes and the validation of isotopic simulations in a stand-alone mode have been presented in [Risi et al., 2010b] (chapter 6). The implementation is similar to other GCMs (e.g. [Joussaume et al., 1984, Jouzel et al., 1987, Schmidt et al., 2007, Hoffmann et al., 1998, Noone and Simmonds, 2002b, Mathieu et al., 2002, Lee et al., 2007, Yoshimura et al., 2008, Tindall et al., 2009]), except it uses a more sophisticated representation of isotopic processes during re-evaporation of raindrops ([Bony et al., 2008]). LMDZ-iso reproduces satisfactorily the spatial and seasonal variations of the isotopic composition in precipitation ([Risi et al., 2010b]).

8.2.3 Simulations set-up

Coupled simulations

For coupled simulations, we nudged the 3D horizontal wind field by ECMWF reanalyses ([Uppala et al., 2005]), to ensure a more realistic simulation of the large-scale atmospheric circulation. Also, to make sure that the water balance is closed at the annual scale, we performed iteratively 10 times the 2006 year. We chose the 2006 year arbitrarily and keep the inter-annual variability in land surface processes for future work. We also performed additional simulations for 2002 and 2005 to compare with data from intensive field campaigns.

Offline simulations

We performed offline simulations on two forest sites where water isotope and meteorological data was available: the Bray in Southern France and Yatir in Israel. On both sites, we forced the model using meteorological measurements and monthly data of isotopic composition in precipitation and water vapor.

The Bray site (44.70°N 00.77°W) is an even-aged Maritime pine forest with C3 grass understorey ([Stella et al., 2009]). In 2007, samples in precipitation, soil surface, needles, twigs and atmospheric vapor were collected each month for oxygen isotope analysis following the MIBA protocol ([Hemming et al., 2007, Wingate et al., 2010]). We assume the land surface is covered by 65% of temperate needle evergreen, 28% C3 grass and 7% bare soil. This bare soil fraction was chosen to better simulate profiles of isotopic enrichment in the soil. We ran the model iteratively three times over 2007 and analyse only the last iteration.

The Yatir site (31.33°N, 35.0°E) is a semi-arid Aleppo pine forest ([Yaseef et al., 2009]). In 2004-2005, samples in soil at different depth, stems and needles were collected following the MIBA protocol (N. Raz-Yaseef, unpublished data). Vapor was collected daily at the nearby Rehovot site (31.9°N, 34.65E), [Angert et al., 2008]), and precipitation data is available from a nearby GNIP station: Bet Dagan (32°N, 34.82°E). We assume the land surface is covered by 66% of temperate needle evergreen (shaded fraction: [Raz-Yaseed et al., 2010]) and 44% bare soil. We ran the model iteratively four times over 2004 and then over the full 2004-2005 period that we analyse.

Sensitivity tests to hydrological parameterizations

Sensitivity tests to the hydrological or isotopic parameterizations were conducted in both offline (OL) and coupled (CO) modes (table 8.1).

To test the sensitivity of the model to the fraction of bare soil in the coupled simulation, we perform an additional coupled simulation ("CO.bare") with f_{bare} calculated following equation 8.2 with $k = 0.05$. This leads to a higher fraction of bare soil over most regions, and a higher proportion of evapo-transpiration occurring as bare soil evaporation by 20 to 40% (figure 8.2 a and b).

We also test the sensitivity to the partitioning between surface runoff and drainage: in an additional coupled simulation ("CO.runoff""), all the excess water leaves the soil as surface runoff only. Because we assume that surface runoff has the isotopic composition of the input water (rain, snow melt or dew) whereas drainage has the composition of the soil water, the partitioning between surface runoff and drainage is expected to have a strong impact on the soil water isotope budget.

To be consistent with CMIP3 simulations, coupled simulations were performed without canopy interception. In an additional coupled simulation ("CO.canop"), canopy interception was activated. In this test, a large proportion (up to 80%) of the evapo-transpiration arises from evaporation of intercepted water (figure 8.2c), thus constituting an extreme sensitivity test compared to observed evaporation losses of the order of 10 to 30% ([Shuttleworth, 1988, Ubarana, 1996, Jackson, 2000]).

River discharge has been shown to be sensitive to time constants in the routing scheme ([Guimberteau et al., 2008]). To test the sensitivity of the isotopic composition of rivers to these time constants, we performed a coupled simulation ("CO.slow") where the time constant of the slow reservoir was increased from 25 days to 75 days .

Sensitivity tests to isotopic parameterizations

The formulation used to compute kinetic isotope fractionation during bare soil evaporation contains a parameter n whose values ranges from 0 to 1 depending on the flow regime over the soil surface (equation B.4 of appendix B.3.1). It equals 0.67 in the control simulation (laminar flow). In two additional simulations ("CO.n1" and "CO.n0.5"), this parameter was set to 1 (molecular flow) and 0.5 (turbulent flow). These two values correspond to dry and saturated soil respectively ([Mathieu and Bariac, 1996]).

In the control simulation, soil water is assumed to have an homogeneous isotopic composition. In reality soil water usually exhibits strong vertical isotopic variations ([Mathieu and Bariac, 1996, Gazis and Geng, 2004, Wingate et al., 2009]). These variations are affected by the soil water effective diffusivity, that critically depends on soil water content θ_l and soil tortuosity τ (appendix D.4.2), and on rainfall infiltration type ([Gazis and Geng, 2004]). We thus performed three additional kinds of simulations with soil isotopic profiles (appendix D.4.5): simulations ".profile" and ".diff" both use piston-like infiltration, with $\theta_l \cdot \tau$=0.1 and 0.01 respectively; simulation ".infiltr" uses preferential pathways of infiltration with $\theta_l \cdot \tau$=0.1.

At the leaf level, non steady state effects or mixing could occur during isotopic enrichment (appendix D.4.4), violating some assumptions made in our standard simulation. To evaluate the influence of these two effects on the leaf water composition, we performed an additional simulation ("CO.peclet") where these two effects are accounted for.

Finally, to quantify the effect of isotopic fractionation during land surface evaporation on the isotopic composition of the different water pools, we performed additional coupled simulations without isotopic fractionation during land surface evaporation ("CO.nofrac"). The composition of the evaporation from bare soil then equals that of the soil water, and the composition of the evaporation from canopy interception equals that of the intercepted water.

8.3 Evaluation of the representation of isotopic processes in the land surface

Evaluating the representation of isotopic processes at the land surface requires measurements in different water pools of the land-atmosphere system. First, we evaluate the simulated global isotopic distribution of precipitation using the GNIP database (section 8.3.1), which has the best spatial coverage of in-situ measurements to date. However, at first order the isotopic distribution in the different components of the land surface generally reflect that in the precipitation (e.g. [Kendall and Coplen, 2001] for rivers). Therefore, comparing the isotopic composition in simultaneous samples of precipitation, atmospheric vapor, soil water and vegetation provides a much stronger constraint on the representation of isotopic fractionation processes. We thus use two MIBA stations where data for these different water pools are available (section 8.3.2). To evaluate isotopic processes in leaves, we use simultaneous data of leaves, stems and vapor on the two MIBA stations and from two isolated campaigns (section 8.3.3). Finally, we use the isotopic composition in rivers from the GNIR database to evaluate in an integrated way hydrological and isotopic processes at the scale of large watersheds (section 8.3.4).

name	offline/ coupled	inter ception	bare soil fraction	soil isotopic profiles	$\theta_l \cdot \tau$	infil tration	drainage fraction (%)	kinetic fractionation exponent	slow reservoir time constant (day)	isotopic fractionation	non-stationary state and Peclet effect in leaves
OL.ctrl	OL	yes	depends on site	no	-	-	95	0.67	-	yes	no
CO.ctrl	CO	no	eq. 8.1	no	-	-	95	0.67	25	yes	no
CO.canop	CO	yes	eq. 8.1	no	-	-	95	0.67	25	yes	no
CO.bare	CO	no	eq. 8.2 $k = 0.05$	no	-	-	95	0.67	25	yes	no
CO.runoff	CO	no	eq. 8.1	no	-	-	0	0.67	25	yes	no
CO.slow	CO	no	eq. 8.1	no	-	-	95	0.67	75	yes	no
CO.n0.5	CO	yes	eq. 8.2 $k = 1$	no	-	-	95	0.5	25	yes	no
CO.n1	CO	no	eq. 8.1 $k = 1$	no	-	-	95	1	25	yes	no
OL.profile	OL	yes	depends on site	yes	0.1	piston	95	0.67	-	yes	no
CO.profile	CO	no	eq. 8.1	yes	0.1	piston	95	0.67	25	yes	no
OL.diff	OL	yes	depends on site	yes	0.01	piston	95	0.67		yes	no
OL.infiltr	OL	yes	depends on site	yes	0.1	pref. path.	95	0.67	-	yes	no
CO.ctrl. nofrac	CO	no	eq. 8.1	no	-	-	95	0.67	25	no	no
CO.canop. nofrac	CO	yes	eq. 8.1	no	-	-	95	0.67	25	no	no
CO.bare. nofrac	CO	no	eq. 8.2 $k = 0.05$	no	-	-	95	0.67	25	no	no
CO.leaf	CO	no	eq. 8.1	no	-	-	95	0.67	25	no	yes

Table 8.1: Summary of the different simulations performed with ORCHIDEE. The first two simulations are the control simulations. The next four simulations are sensitivity test to hydrological properties, and the remaining simulations are sensitivity tests to the isotopic representation.

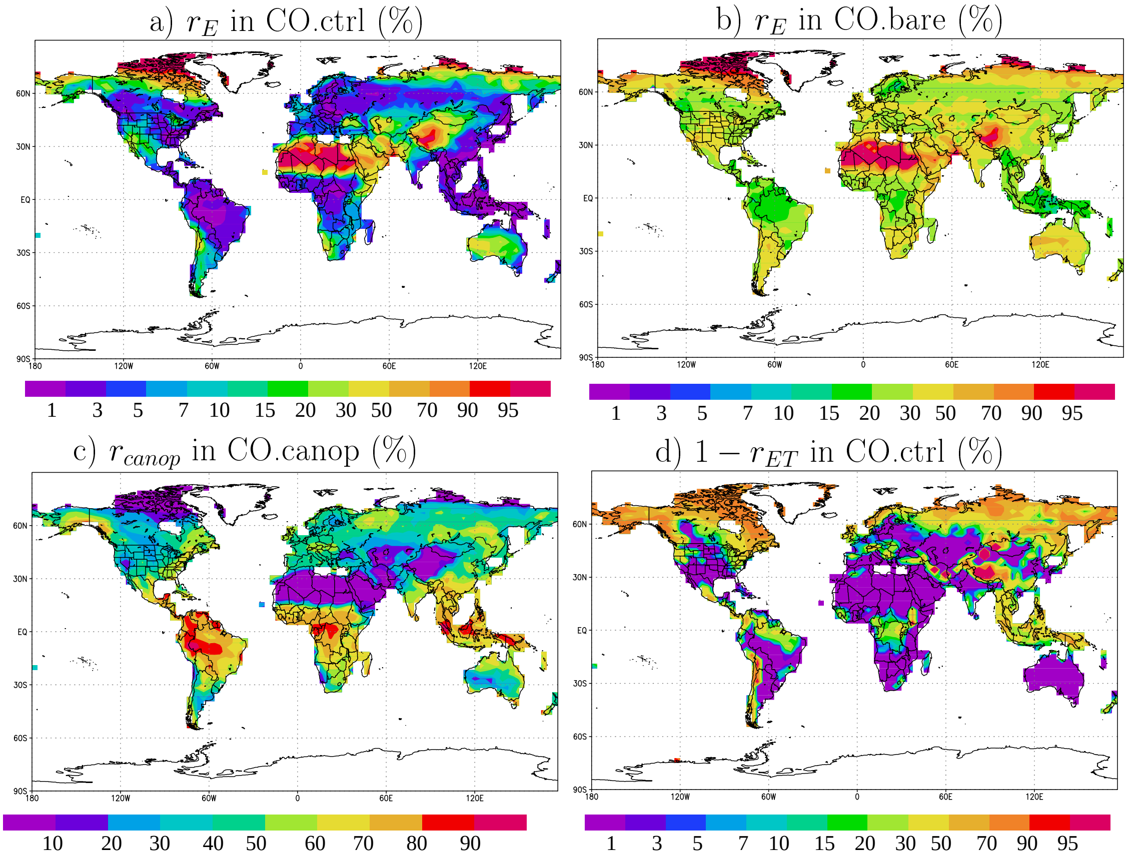
a) r_E in CO.ctrl (%)

b) r_E in CO.bare (%)

c) r_{canop} in CO.canop (%)

d) $1-r_{ET}$ in CO.ctrl (%)

Figure 8.2: a) proportion of liquid evapo-transpiration arising from bare soil evaporation rather than transpiration ($r_E = \frac{E}{E+T}$) in the CO.ctrl simulation (notations defined in figure 8.1). b) same as a but for the CO.bare simulation, in which the fraction of bare soil is increased. c) proportion of liquid evapo-transpiration arising from the evaporation of water intercepted by the canopy ($r_{canop} = \frac{E_w}{E+T+E_w}$) in the CO.canop simulation. d) proportion of the soil water that is lost through drainage rather than evapo-transpiration ($1-r_{ET} = \frac{D}{P_s+M-R}$) in the CO.ctrl simulation.

8.3.1 Global distribution of isotopes in precipitation

Evaluation of the model against GNIP data

The simulated distributions of annual mean $\delta^{18}O_p$ and d_p simulated by LMDZ-OR-iso in the CO.ctrl simulation (figure 8.3a and b) are similar to those simulated by the LMDZ-iso model alone ([Risi et al., 2010b], not shown), with a spatial correlation between the two simulations of 0.98 and 0.88 for $\delta^{18}O_p$ and d_p respectively. As was the case in LMDZ-iso, the main features of the spatial distribution of $\delta^{18}O_p$ and d_p are well captured by LMDZ-OR-iso. d_p is overestimated over Western and Southern Africa and Brazil, by up to 10‰. This bias was already present in the LMDZ-iso model alone, but is amplified here by about 2‰ when fractionation at the land surface is present.

Effect of isotopic fractionation at the soil surface

Simulated $\delta^{18}O_p$ and d_p with and without fractionation at the land surface (figure 8.3e and f) are very similar, indicating isotopic processes in the atmosphere exert the main controls on the isotopic composition of precipitation, while processes at the land surface have a second order effect (consistent with [Yoshimura et al., 2006, Aleinov and Schmidt, 2006]).

However, taking into account fractionation at the land surface leads to a better agreement with the GNIP data over Canada, where $\delta^{18}O_p$ was overestimated by about 4‰ without fractionation at the land surface. Indeed, the simulated precipitation in CO.ctrl is slightly more depleted (by up to 1.5‰) than in CO.ctrl.nofrac over these regions. The effect of land surface fractionation is most important in these boreal and continental regions because (1) the fraction of bare soil evaporation is maximal (figure 8.2a) leading to more depleted evapo-transpiration, (2) a significant proportion of soil water is lost by drainage (figure 8.2d) leading to larger loss of evaporatively enriched soil water and thus more depleted evapo-transpiration and (3) a larger proportion of the moisture in continental regions has been recycled by the land surface.

Also, d_p is up to 5‰ higher in boreal and continental regions when fractionation during soil evaporation is accounted for (figure 8.3b), consistent with a higher d of fractionating evaporation over continents ([Gat and Matsui, 1991]). This is in better agreement with the GNIP data in high latitudes, where d_p was underestimated by 4 to 7‰ in CO.ctrl.nofrac.

Finally, the sensitivity of the isotopic composition of precipitation to the formulation of the kinetic fractionation is very small. When varying n over the extreme range from 0.5 to 1 in equation B.4 (appendix B.3.1), significant changes in $\delta^{18}O$ and d are restricted to areas where bare soil covers more than 70% and never exceed 2‰ for $\delta^{18}O$ and 7‰ for d-excess.

Effect of isotopic fractionation during evaporation of canopy-intercepted water

Accounting for fractionation during evaporation of canopy-intercepted rainfall leads to a decrease in $\delta^{18}O_p$ by up to 1.5‰ and an increase in d_p by up to 3‰ (figure 8.3g and h) over wide regions of Eurasia, Northern America, Southern Africa and the Amazon, with a maximum over North-eastern Asia. This strong isotopic effect is probably an upper bound, given the high proportion of interception in CO.canop (50% of total evapo-transpiration over Europe and Siberia, up to 80% of over the Amazon and the Congo basin, figure 8.2c).

To summarize, the isotopic fractionation associated with bare soil evaporation has a significant impact on the isotopic composition of precipitation over northern continental regions (in particular for d_p) whereas fractionation associated with the evaporation of canopy-intercepted water may have a more significant impact over tropical forests. This confirms the sensitivity of the continental effect (the increased depletion as one goes inland) to the fraction of water recycled by transpiration ([Gat and Matsui, 1991]), and suggests the potential of water isotopes to constrain these components in the water cycle.

8.3.2 Evaluation of fractionation in the soil

To evaluate fractionation in the soil, we select two stations from the MIBA database with data in precipitation, vapor, plants and soil for at least a full seasonal cycle. We first evaluate the seasonal cycles of the different water pools over these two sites, then soil isotopic profiles.

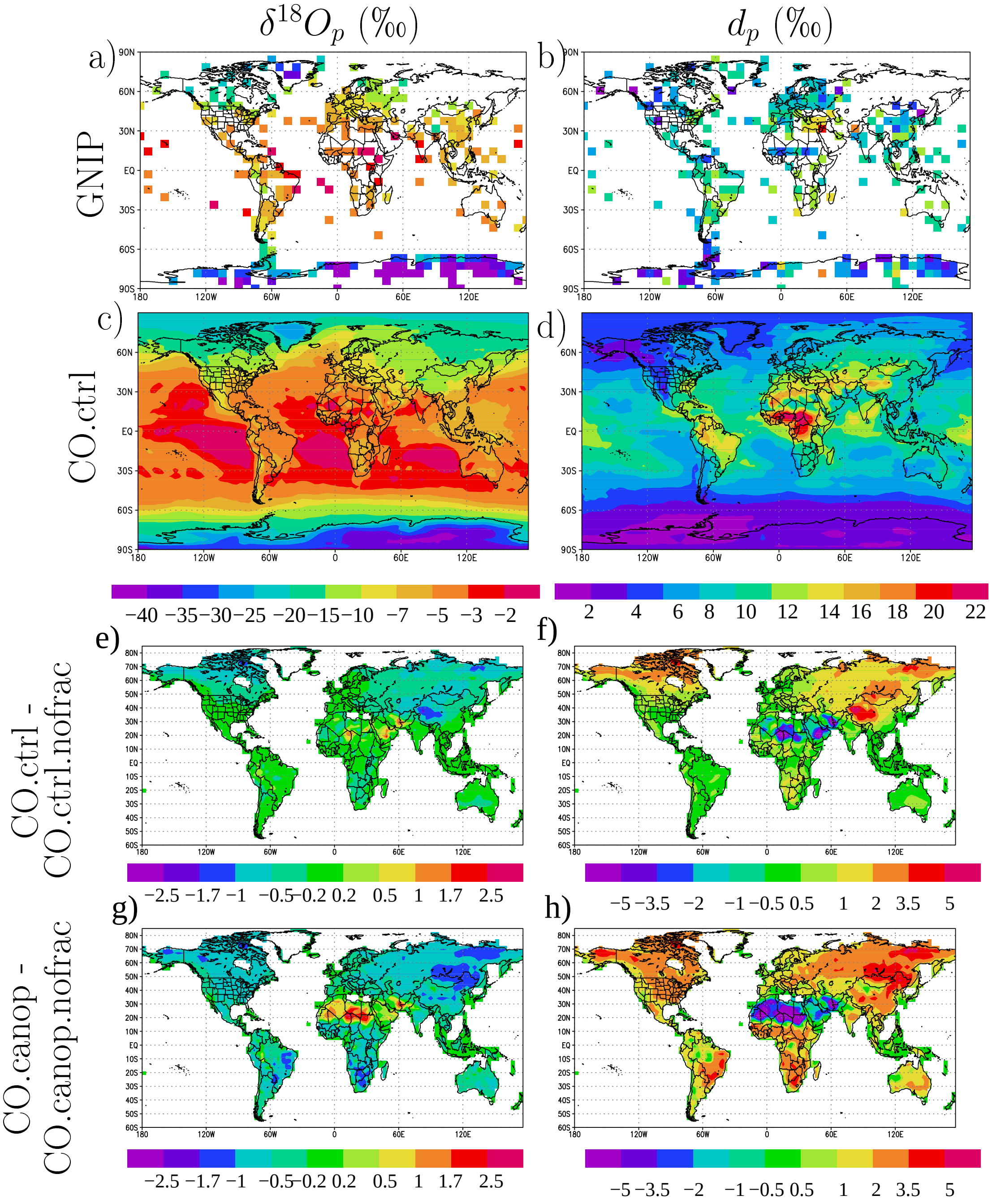

Figure 8.3: a) Annual mean $\delta^{18}O_p$ from GNIP ([Rozanski et al., 1993]), Antarctica ([Masson-Delmotte et al., 2008]) and Greenland ([Masson-Delmotte et al., 2005]) data. The data is gridded over a coarse 7.5×6.5° grid for visualization purpose. b) Same as a) but for annual mean d_p. c) Annual mean $\delta^{18}O_p$ simulated by LMDZ in the CO.ctrl simulation. d) same as c) but for annual mean d_p. e) Annual mean $\delta^{18}O_p$ in the CO.ctrl simulation minus annual mean $\delta^{18}O_p$ in the CO.ctrl.nofrac simulation (CO.ctrl−CO.ctrl.nofrac), showing the effect of isotopic fractionation at the soil surface on $\delta^{18}O_p$. f) Same as e) but for d_p. g) CO.canop−CO.canop.nofrac showing the effect of isotopic fractionation at the soil surface and associated with the evaporation of water intercepted by the canopy. .

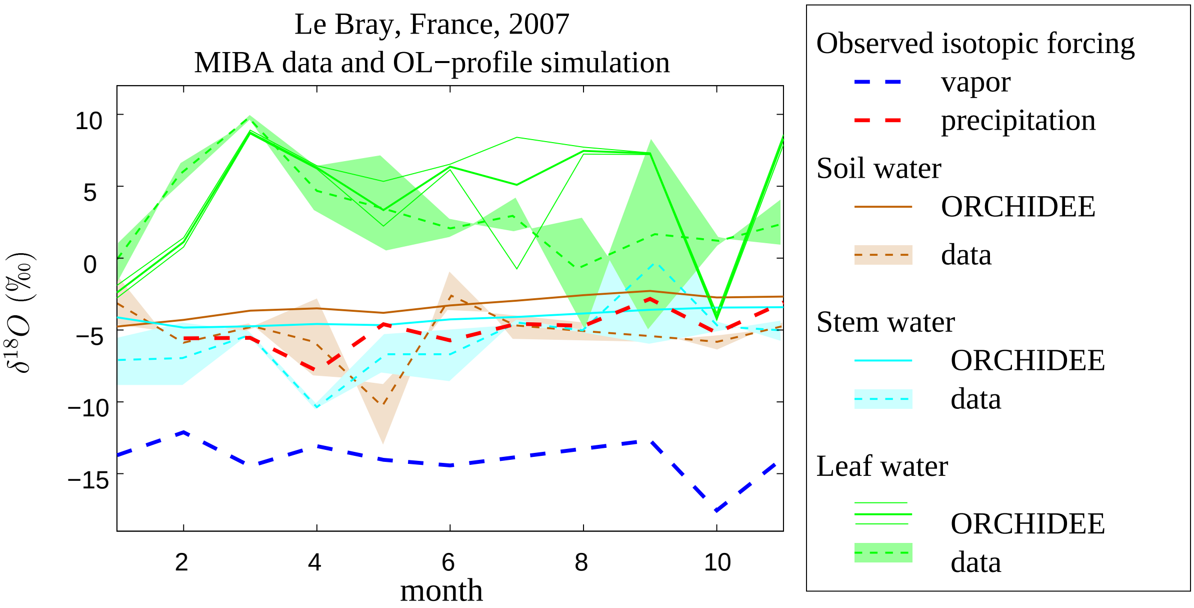

Figure 8.4: $\delta^{18}O$ of the surface soil (brown), twigs (cyan), leaves (green) simulated by ORCHIDEE-iso in the OL-profile simulation (solid) and observed once a month in 2007 on the Bray site (dashed). For observations, the dashed line gives the average values of two measurements for the same day, and the envelope shows the maximum and minimum values. For ORCHIDEE, leaf water values are sampled at the same time as data. The solid thick green line is the average value of $\delta^{18}O_{leaf}$ during the sampling period, and the thin lines are maximum and minimum values during the 1-hour sampling period, over which simulated $\delta^{18}O_{leaf}$ exhibits a strong diurnal cycle. Other values vary very slowly in the model and are given as monthly averages. We assume that the twig water in ORCHIDEE has the composition of the transpiration flux. Observed $\delta^{18}O$ in precipitation (red) and vapor (blue) used as forcing are also shown.

Seasonal cycles over MIBA sites

At the Bray site, the measured seasonal cycle of total evapo-transpiration ([Stella et al., 2009]) is very well captured by ORCHIDEE (r=0.98 for monthly values), with simulated and observed annual mean evapo-transpiration rates of 2.4mm/d and 2.0mm/d respectively. The OL-profile simulation with ORCHIDEE-iso produces similar values of $\delta^{18}O_s$ and $\delta^{18}O_{stem}$ with little seasonal variations over the year, in agreement with the data (figure 8.4). The observed values exhibit larger variability, which could be due to local processes or spatial heterogeneity that are not captured by the model.

At the Yatir site, ORCHIDEE captures the seasonal cycle of evapo-transpiration moderately well (r=0.64 for monthly values), but it overestimates by about 15% the proportion of radiative energy dissipated as latent heat versus sensible heat (not shown). ORCHIDEE also underestimates the proportion of bare soil evaporation to total evapo-transpiration: less than 10% in LMDZ versus 38% observed ([Yaseef et al., 2009]). The observed soil water, stem water and precipitation $\delta^{18}O$ have similar values although in summer soil water is more enriched due to evaporative enrichment. The stem water corresponds well with the most depleted values of the soil. These seasonal variations are reproduced by OL.diff. The observed $\delta^{18}O$ difference between the top and bottom of the soil column is about 5 to 10 ‰ , llustrating a strong surface enrichment of the soil. These vertical variations are slightly underestimated by the model with $\delta^{18}O$ differences between the top and bottom of the profile ranging from 2 to 7 ‰.

Evaluation of soil profiles

We first compare the OL.profile simulation for 2007 to measured isotopic profiles collected on the Bray site between 1994, 1997 and 2008 (figure 8.6). Comparison between model and data contains

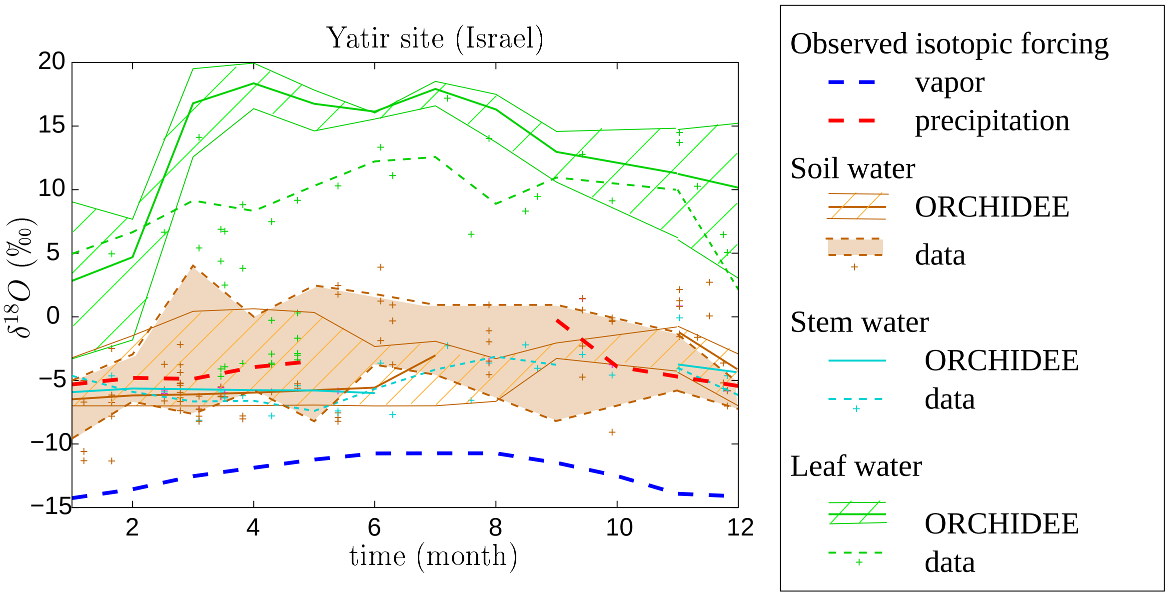

Figure 8.5: $\delta^{18}O$ of the soil (brown), stems (cyan), leaves (green), precipitation (red) and vapor (blue) simulated by LMDZ-ORCHIDEE-iso in the OL-diff simulation (solid) and observed at the Yatir site (markers for individual measurements, dashed for monthly averages of these measurements). We assume that the stem water in ORCHIDEE has the composition of the transpiration flux. For the ORCHIDEE soil water, the heavy line is the total water and the thin lines are the maximum and minimum $\delta^{18}O$ throughout the soil column, in monthly average. Brown dashed lines are the maximum and minimum $\delta^{18}O$ measured between the surface and 50cm deep. All monthly averages for ORCHIDEE are calculated by sampling the soil, stems and leaves at the same time as the data. The solid thick green line is the average value of $\delta^{18}O_{leaf}$ during the sampling period, and the thin lines are maximum and minimum values during the sampling period, over which simulated $\delta^{18}O_{leaf}$ exhibits a strong diurnal cycle.

many sources of mismatches, including local processes and heterogeneity in the soil not captured by the model, and inter-annual variability. However, the goal here is to evaluate the key robust features observed in the data. Nearly all the data feature an isotopic enrichment at the soil surface especially during July, August and September. The isotopic enrichment is maximum in August with a 2‰ enrichment from 1m to the surface, likely due to surface evaporation ([Mathieu and Bariac, 1996]). Then, by the end of September 1994, the surface becomes depleted, likely due to the input of depleted rainfall, while previously enriched water remains between 20 and 60 cm below the ground, suggesting an infiltration through piston-flow ([Gazis and Geng, 2004]). In 2007, only the top 20 cm of the soil was sampled, but the features observed in the profiles collected during the 90's are still apparent. On the average the 2007 profiles are around 3‰ more enriched, and the surface depletion in fall occurs two months later (in November) and is restricted to a shallower layer. ORCHIDEE-iso predicts but underestimates the isotopic enrichment in summer (in August, the model predicts 1‰ enrichment compared to 2‰ in the observed profiles during the 90's). The model also captures the surface depletion observed in fall, as well as the imprint of the previous summer enrichment at depth. However, the simulated surface depletion in December lags the data by at least one month (September or November in the data).

At the Yatir site, observed profiles exhibit a strong isotopic enrichment from deep to shallow soil layers in March to June (up to 10‰), and a depletion at the surface from July to December, with a maximum $\delta^{18}O$ at about 10 cm below the surface (figure 8.7). As for Le Bray site, the model captures but underestimates the isotopic enrichment in spring and summer (simulated enrichment accross the profile of 7‰). This discrepancy could be the result of the underestimation of bare soil evaporation. In addition, the model is unable to simulate the observed surface depletion and inversion in late summer and fall. This depletion could be due to back diffusion of depleted vapor in dry soils ([Barnes and Allison, 1983, Allison et al., 1983, Mathieu and Bariac, 1996, Braud et al., 2009]), a process not represented in ORCHIDEE-iso but likely significant in this region. Alternatively, this depletion may be due to contamination of the samples with atmospheric vapor when the soil humidity is very low.

Sensitivity tests to parameters controling soil water isotopic vertical variations

We performed sensitivity tests on the Bray site. The simulated profiles are quite sensitive to vertical water fluxes in the soil (figure 8.8a): when $\theta_l \cdot \tau$ is decreased by a factor 10 in OL.diff compared to OL.profile, the soil is more depleted at depth by 0.7‰ (figure 8.8a) and the isotopic gradient in summer is steeper (0.4‰ steeper from soil bottom to top), because the enriched soil water diffuses slower through the soil column.

Simulated profiles are also sensitive to the way rainfall infiltrates the soil. When precipitation is added only to the top layer (piston-flow, OL.profile) the summer enrichment is reduced by mixing of the surface soil water with rainfall, and the summer enrichment propagates more easily to lower layers during fall and winter. Conversely, when rainfall is evenly spread throughout the soil column (a crude representation of preferential pathway infiltration, OL.infiltr), the surface enrichment is slightly more pronounced and the deep soil water is more depleted by up to 0.8‰ in winter (figure 8.8a). However, only the piston-like infiltration may explain the quick surface depletion observed in fall (figure 8.8a): the observed surface depletion occurs in February only with preferential pathways, compared to December in the piston-like in infiltration. This suggests that observed isotopic profiles could help constrain infiltration processes in nature ([Gazis and Geng, 2004]) and their representation in multi-layer models.

At the seasonal scale, the average composition of the soil water is not strongly affected by water diffusion and infiltration processes (figure 8.8b): the $\delta^{18}O$ of the soil surface water is only 1‰ more enriched in summer and 1‰ more depleted in winter when considering vertical profiles.

8.3.3 Evaluation of fractionation in the leaves

The isotopic composition of leaf water has been the subject of many observational and numerical modeling studies (e.g. [Farquhar and Cernusak, 2005, Cuntz et al., 2007, Ogée et al., 2007, Wingate et al., 2010]). Predicting the composition of leaf water has applications for predicting

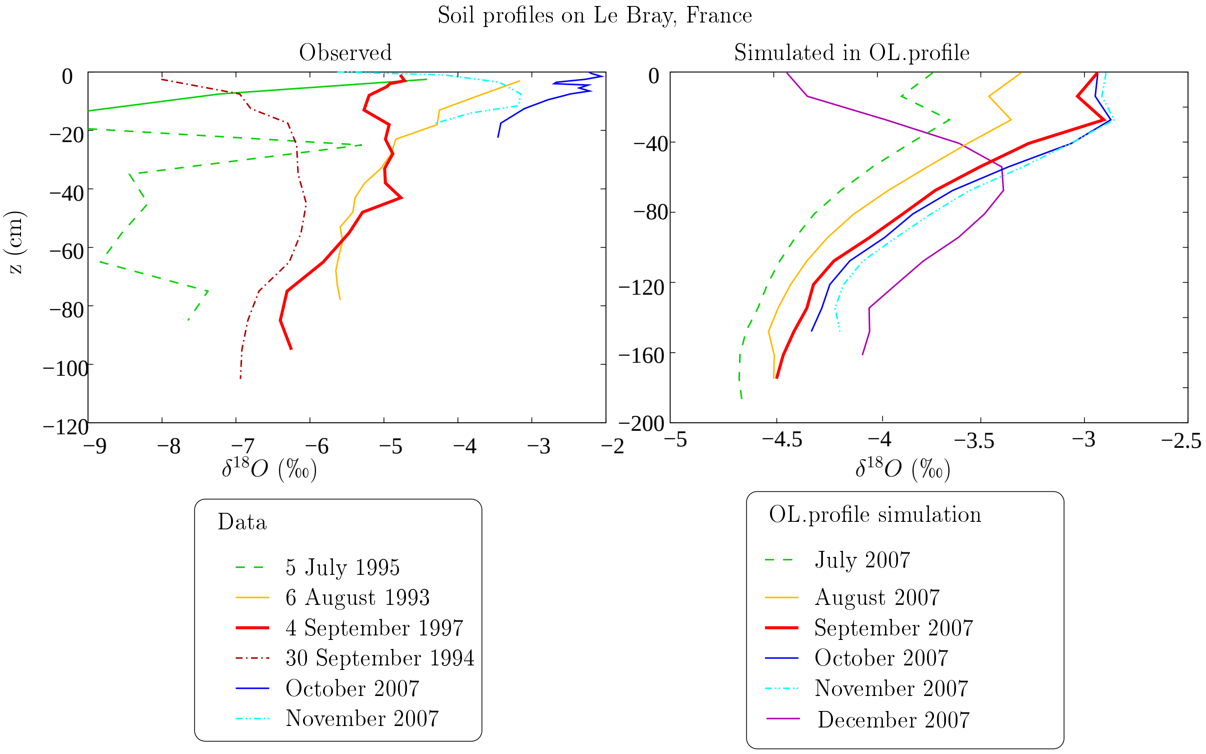

Figure 8.6: a) Vertical profiles of soil $\delta^{18}O$ measured (a) and modelled by ORCHIDEE-iso using the OL.profile simulation (b) on the Bray site. Note that the representation of the soil water content is very rudimentary in the Choisnel bucket model, preventing any quantitative comparison of measured and simulated soil depth.

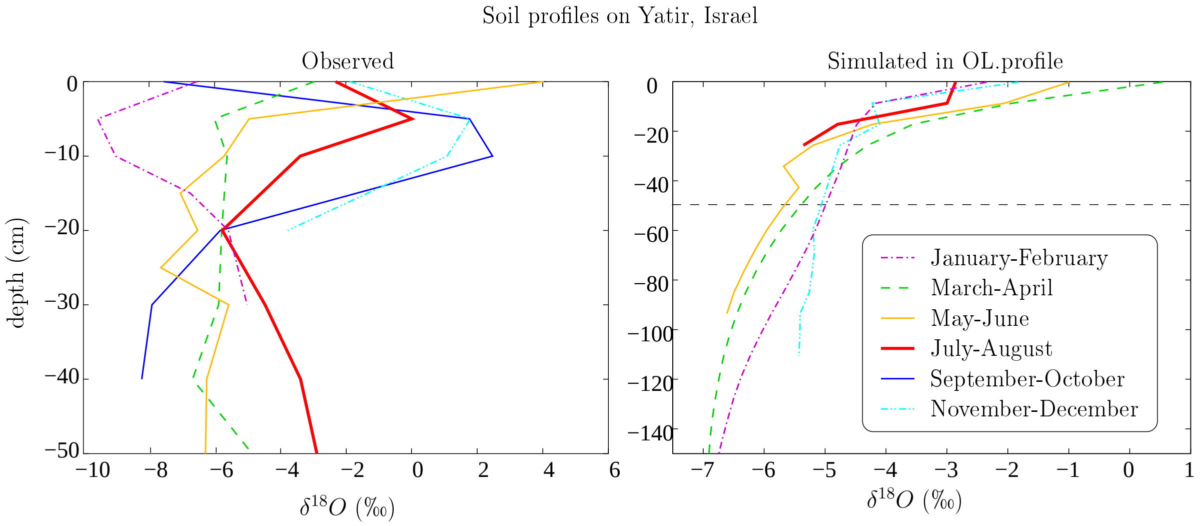

Figure 8.7: a) Vertical profiles of soil $\delta^{18}O$ measured (a) and modelled by ORCHIDEE-iso using the OL.diff simulation on the Yatir site. Note that the representation of the soil water content is very rudimentary in the Choisnel bucket model, preventing any quantitative comparison of measured and simulated soil depth. Model outputs are sampled at the same time as the data.

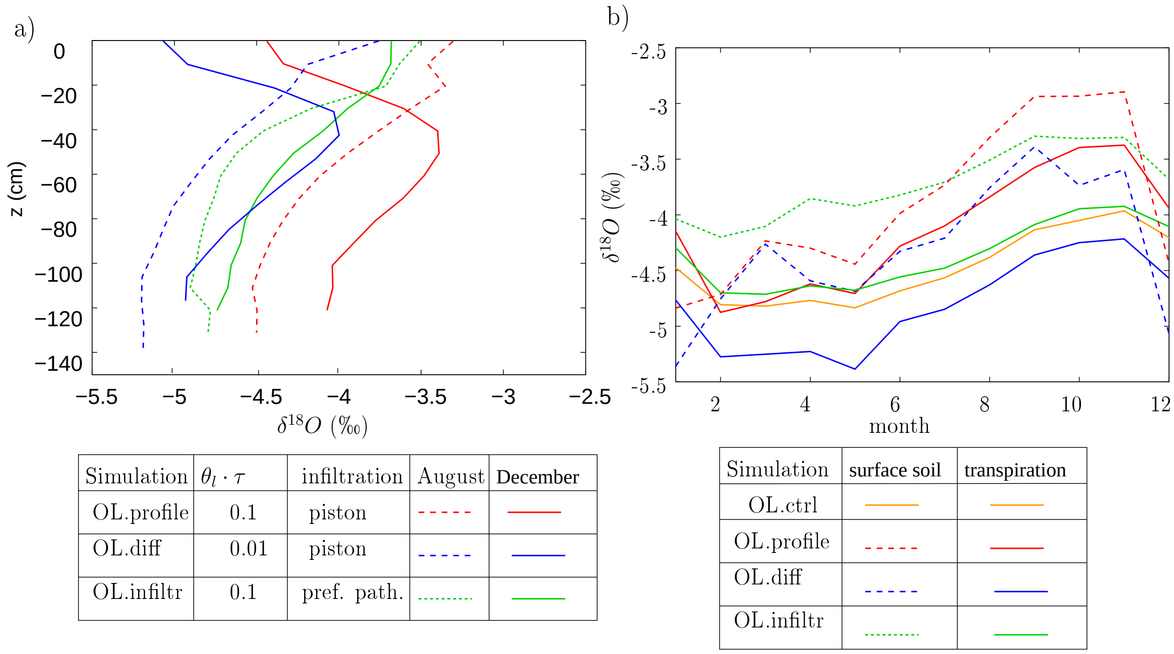

Figure 8.8: a) Sensitivity of isotopic profiles to the representation isotopic profiles in the soil: isotopic profiles simulated in July (dashed) and December (solid) for the OL.profile (red), OL.diff (blue) and OL.infiltr (green) simulations. b) Sensitivity of seasonal variations in surface soil water (solid) and transpiration (dashed) $\delta^{18}O$: OL.ctrl (orange), OL.profile (red), OL.diff (blue) and OL.infiltr (green). For the simulation without soil profiles, soil and transpiration water are virtually equal.

(1) the isotopic composition of atmospheric CO_2, which may be used to partition CO_2 fluxes into respiration from the vegetation and the soil ([Yakir and Wang, 1996, Yakir et al., 2000]),

(2) the isotopic composition of atmospheric O_2, which may be used to infer biological productivity ([Bender et al., 1994, Blunier et al., 2002]),

(3) the isotopic composition of cellulose, which constitutes valuable paleo-climatological archives ([Danny and Loader, 2004]).

To check whether LMDZ-OR-iso could be used in the future for such applications, we evaluate $\delta^{18}O_{leaf}$ at the seasonal and diurnal scales.

Evaluation at the seasonal scale

At both the Yatir and the Bray sites, $\delta^{18}O_{leaf}$ exhibits large variations of about 10‰ over the season (figures 8.4 and 8.5). At the Bray site, the simulated and observed seasonal variations of $\delta^{18}O_{leaf}$ share some common features, such as the increase from January to March followed by a decrease until May. However, the model likely overestimates $\delta^{18}O_{leaf}$ by up to 8‰ from June to August, although there is a large uncertainty in the model-data comparison due to the uncertainty on sampling time. This overestimate could also be due to neglecting diffusion in leaves or non-steady state effects.

At Yatir, in winter, $\delta^{18}O_{leaf} - \delta^{18}O_{stem}$ is about 10‰ in both model and data. In summer, when the air is drier, it is of 15‰ in the data and more than 20‰ in the model. As at the Bray site, the overestimation of summer $\delta^{18}O_{leaf}$ could be due to neglecting diffusion in leaves or non-steady state effects. In addition, in arid regions, leaves may close stomata during the most stressfull periods of the day and thus retain the depleted isotopic signal associated with the moister conditions of the morning ([Yakir and Yechieli, 1995, Gat et al., 2007]).

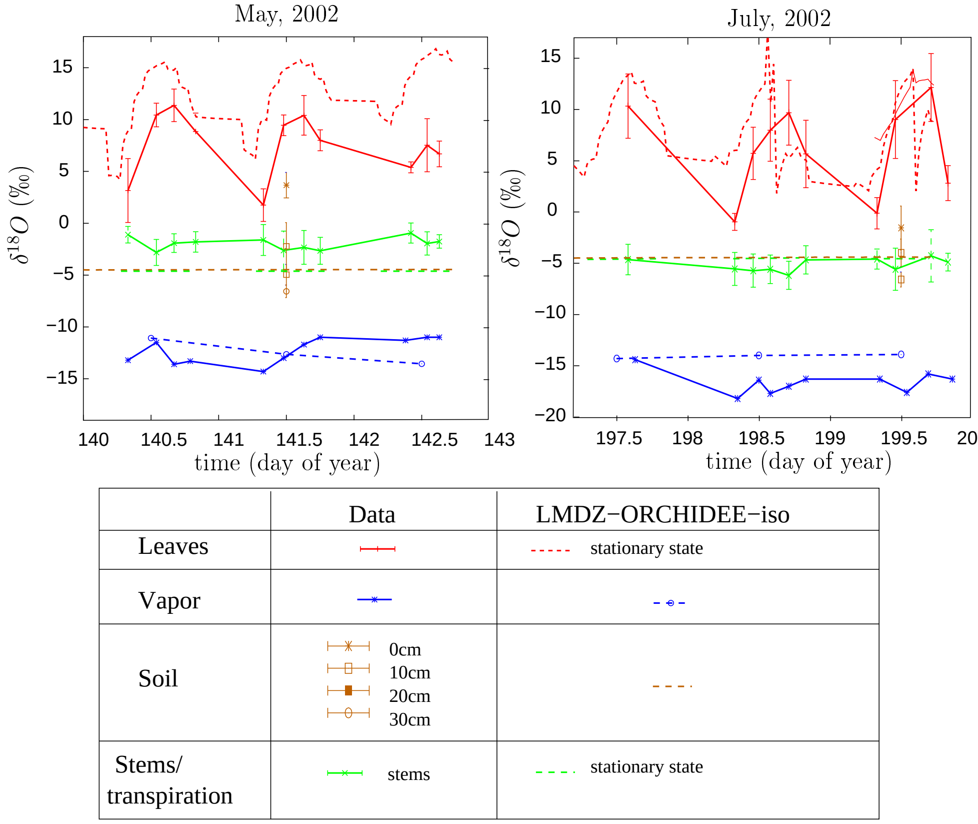

Figure 8.9: $\delta^{18}O$ of vapor, grass leaves, soil and stems measured during two series of 3 diurnal cycles in May and July 2002 over the plains of Kansas ([Lai et al., 2006b]) and simulated by LMDZ-OR-iso for the same year in the grid box containing the observation site.

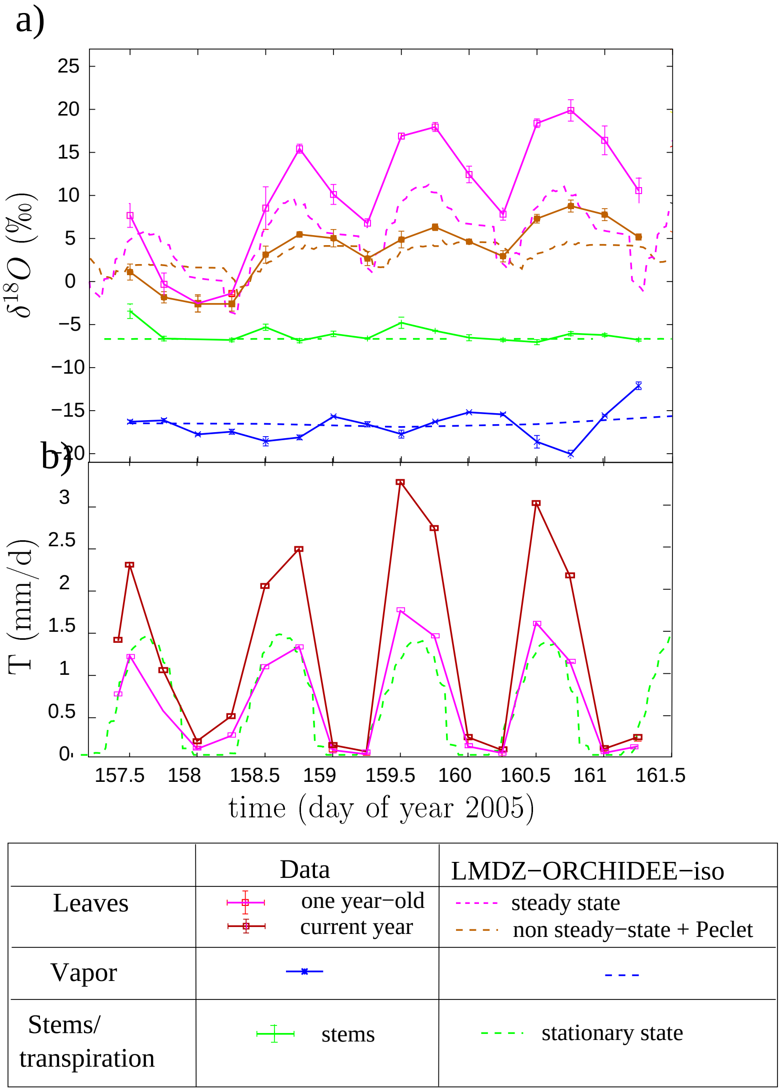

Figure 8.10: a) $\delta^{18}O$ of vapor (blue), pine leaves (pink and red) and stems (green) measured during four diurnal cycles in June 2005 in Hartheim, Germany ([Barnard et al., 2007]) and simulated by LMDZ-OR-iso for the same year in the grid box containing the observation site. Simulated values are dashed, observed values solid. Two kinds of leaves were sampled during this campaign: one-year-old leaves (solid pink) and current-year leaves (solid brown). Two leaf water diagnostics were computed for in LMDZ-OR: stationary state at the evaporative site (dashed red, equation D.4) or non-stationary state in the lamina, taking into account the Peclet effect (dashed brown, equation D.8, using an effective length scale of 25mm). b) Transpiration rate measured for one year old leaves (pink) and current-year leaves (brown) and simulated by LMDZ-OR-iso (dashed green).

Evaluation at the diurnal scale

At the daily scale, $\delta^{18}O_{leaf}$ exhibit large variations that can exceed 10‰. To evaluate the representation of the diurnal cycle in $\delta^{18}O_{leaf}$, we use data from two intensive campaigns:

(1) two series of 3 diurnal cycles in May and July 2002 in a grassland prairie in Kansas (39.20°N 96.58°W , [Lai et al., 2006b]); and

(2) four diurnal cycles in June 2005 over a pine plantation in Hartheim, Germany (7.93°N, 7.60°E , [Barnard et al., 2007]).

We compare these measurements with the CO.ctrl simulation for the years 2002 and 2005 (figure 8.9 and 8.10). The simulated $\delta^{18}O_v$ and $\delta^{18}O_{stem}$ for the two campaigns are very similar to those observed (except in May 2002 in Kansas when stem water is underestimated by 2‰), allowing us to evaluate the leaf processes rigorously.

At the grassland site, LMDZ-OR-iso reproduces the phasing and the amplitude of about 10‰ observed in $\delta^{18}O_{leaf}$ over the day, despite our simple model, consistent with [Lai et al., 2006b] (figure 8.9). However, the model systematically overestimates $\delta^{18}O_{leaf}$ by about 4‰, maybe due to a bias in the simulated relative humidity or to uncertainties in the kinetic fractionation.

In Hartheim, the observed diurnal amplitude of $\delta^{18}O_{leaf}$ is weaker for current-year needles (5 to 8‰) than for 1-year-old needles (10 to 15‰). Current-year needles are also 8‰ more depleted on average. This is consistent with the longer diffusion length for current-year needles (5 cm) compared to 1-year-old needles (15cm) ([Barnard et al., 2007]) and with larger transpiration rates (figure 8.10b), both leading to a stronger Peclet effect. At steady state, the model simulates an average $\delta^{18}O_{leaf}$ closer to that of 1-year-old needles. In this case with a small Peclet effect, a steady model neglecting leaf diffusion is a reasonable approximation. The phasing of the diurnal cycle is well simulated, but the diel amplitude is underestimated by about 4‰, most likely caused by an underestimation of the simulated diel amplitude of relative humidity by 20% (not shown). Accounting for Peclet and non-steady state effects strongly reduce both the average and diel amplitude of $\delta^{18}O_{leaf}$ (CO.ctrl, dashed brown on figure 8.10a), bringing values closer to those observed in current-year needles.

To summarize, the $\delta^{18}O$ of water vapor, soil, stem, and leaf water predicted by the coupled model agree reasonably well with observations. The [Craig and Gordon, 1965]'s diagnostic for leaf water simulates the right phasing and amplitude for leaves associated with short diffusive length or low transpiration rates. However, non-steady state and diffusion effects should be taken into account in other situations.

8.3.4 Evaluation of integrated processes through river data

Comparison of simulated and observed river discharge are often used to evaluate integrated hydrological processes at the scale of GCM grid boxes (e.g. [Abdulla et al., 1996, Nijssen et al., 1997, Bosilovich et al., 1999, Oki and Sud, 1998, Ducharne et al., 2003]). Similarly, the isotopic composition of large rivers can be used as an integrative evaluation tool ([Hoffmann et al., 1998]). Indeed, the isotopic composition of rivers results from a large range of hydrological and isotopic processes:

(1) the isotopic composition of precipitation over the watershed;
(2) the proportion of precipitation that becomes surface runoff or drainage;
(3) the isotopic enrichment of soil water before drainage;
(4) the input of water by snow melt or from groundwater if any; and
(5) the residence time of water in the different reservoirs.

Annual mean $\delta^{18}O_{river}$ follows at first order the patterns observed for the isotopic composition of precipitation, and thus is well simulated by LMDZ-OR-iso (figure 8.11 a and b). The difference between the isotopic composition of precipitation and river water ($\delta^{18}O_{river} - \delta^{18}O_p$) constitute a stronger constraint. We calculate this difference using the GNIP and GNIR data at all 7.5x5.6° grid boxes where both data are available, and compare it to the model results (figure 8.11c and d). Over Europe, South America and some parts of the US, the river water is typically 1‰ to 4‰ more depleted than the precipitation. This is caused by a larger contribution of precipitation to rivers (by runoff and drainage) at those times of the year when the precipitation is the most depleted (winter in mid-latitudes, wet season in South America). In contrast, over central Asia or northern America,

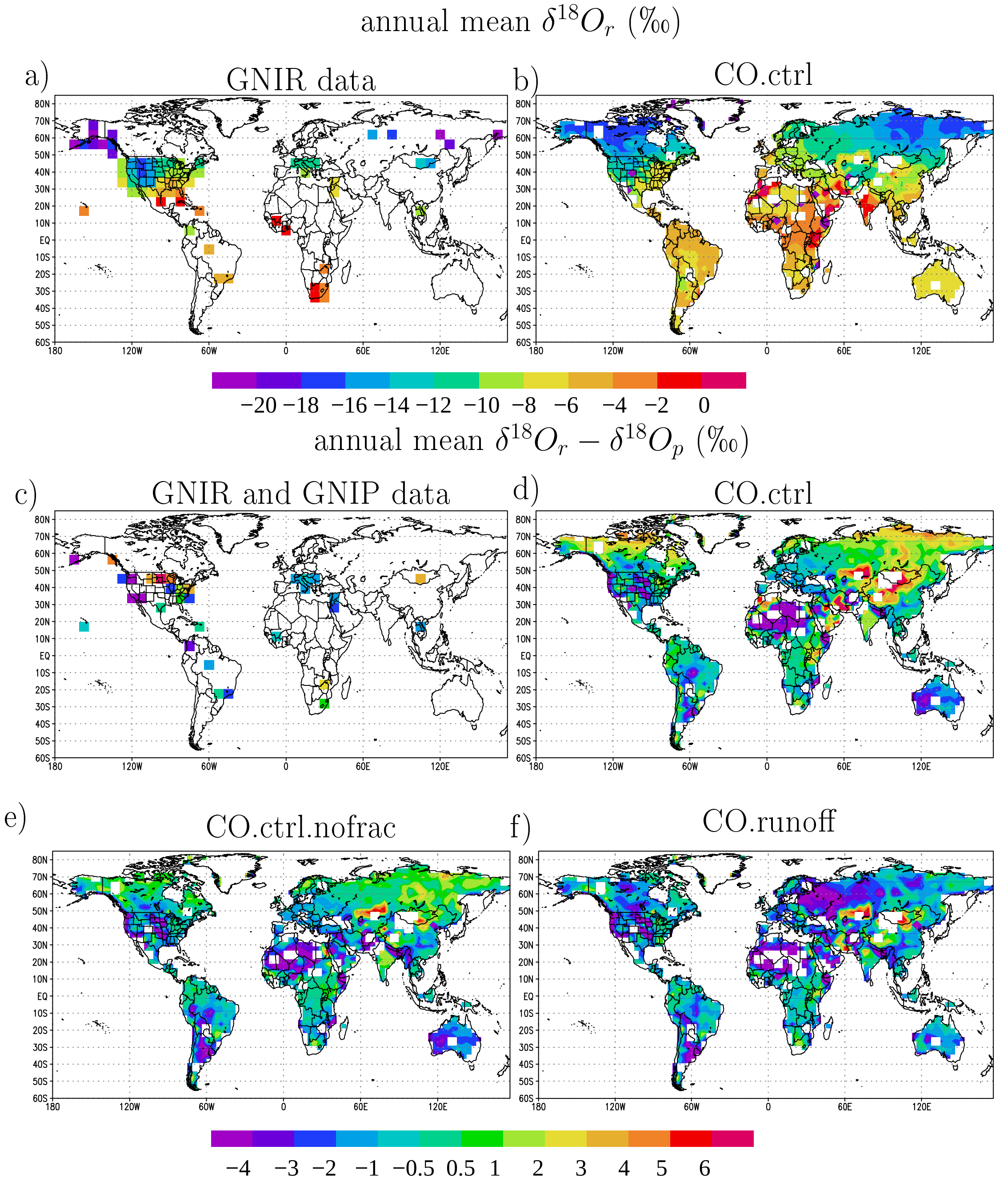

Figure 8.11: Annual mean $\delta^{18}O$ in rivers ($\delta^{18}O_{river}$) measured from the GNIR database (a) and simulated by LMDZ-OR-iso using the CO.ctrl simulation (b). c) Annual mean $\delta^{18}O_{river} - \delta^{18}O_p$ from the GNIR database. d) Simulated $\delta^{18}O_{river} - \delta^{18}O_p$ for the CO.ctrl simulation. e) same as d for the CO.nofrac simulation. f) same as d for the CO.runoff simulation

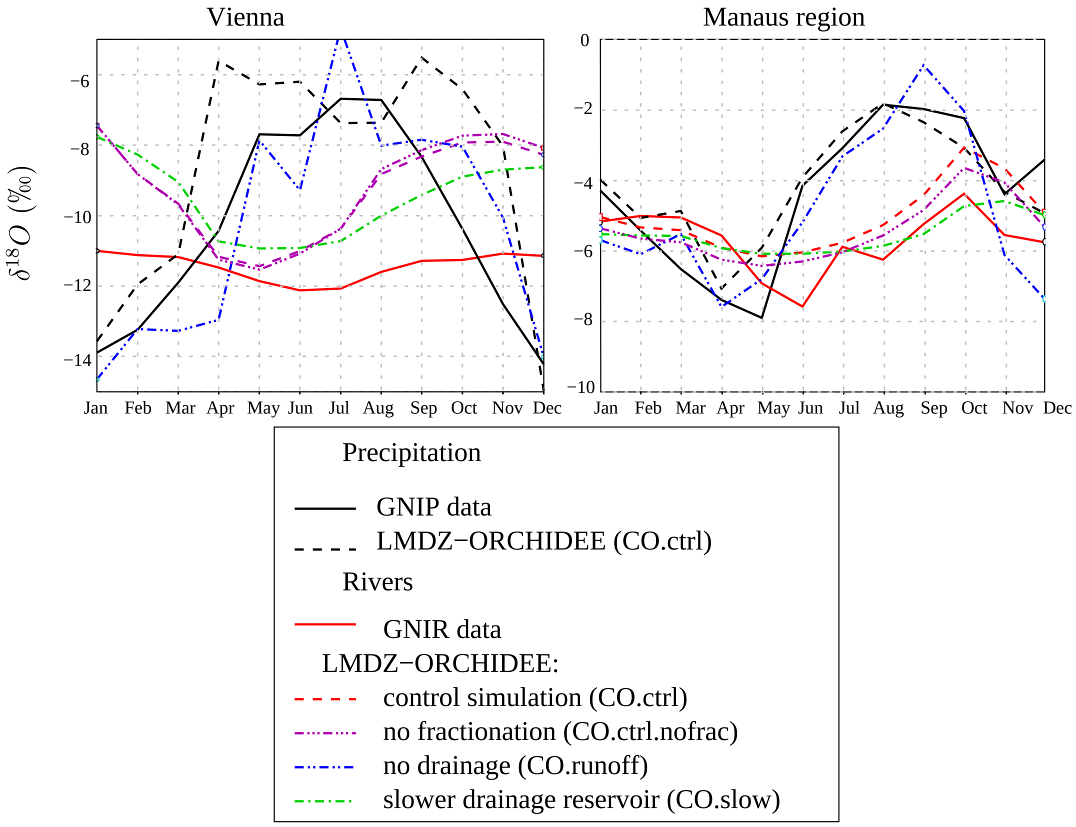

Figure 8.12: Seasonal variations in $\delta^{18}O_p$ and $\delta^{18}O_{river}$ observed (solid; GNIP and GNIR database) and modelled (dashed, see table 8.1 for the different sensitivity tests) for (a) the Danubel river in Vienna and (b) the Amazon river in the Manaus region (average over the 8°S-3°S-56°W 63°W domain).

river water is more enriched than the precipitation, possibly caused by evaporative enrichment of soil water ([Kendall and Coplen, 2001, Gibson et al., 2005]). This general pattern is captured by the model (figure 8.11d). When we prescribe no fractionation during land surface evaporation (CO.ctrl.nofrac), the model still simulates reasonably well the contrast between precipitation and river water over mid latitudes and South America, but underestimates the enrichment in rivers observed at higher latitudes and central Asia by up to 3‰ (figure 8.11e). This confirms the role of evaporative enrichment of soil water in the controlling the river composition in these regions. When assuming that all the runoff occurs as surface runoff rather than drainage (CO.runoff), river water is depleted compared to precipitation (figure 8.11f). This is caused by the fact that rivers are no more alimented by water that has been enriched during its transit through the soil, and that runoff occurs preferentially during strong precipitation events that are more depleted.

We use two well established GNIR and GNIP stations in Vienna (Danube river) and Manaus (the Amazon) to investigate seasonal variations in $\delta^{18}O_{river}$ (figure 8.12). Seasonal variations in $\delta^{18}O_{river}$ are smoother than in $\delta^{18}O_p$, and are not always in phase with $\delta^{18}O_p$ (figure 8.12). LMDZ-OR-iso simulates qualitatively well the amplitude and the phaseing observed in $\delta^{18}O_p$ and $\delta^{18}O_{river}$. This attenuation and phase shift are caused by the storage of water in the slow reservoir accumulating drainage water: if all the runoff occurred as surface runoff (cyan curve), then the seasonal cycle of $\delta^{18}O_{river}$ would be similar to that of $\delta^{18}O_p$. The simulated phase shift over Vienna is in closer agreement with the data (7 months compared to 5 months) when the time constant of the slow reservoir routing the drainage is multiplied by 2 (CO.slow simulation). On the other hand, the seasonal cycle in $\delta^{18}O_{river}$ is not sensitive to time constants in the stream and fast reservoirs (not shown), though the seasonal cycle of river discharge has been shown to be mainly sensitive to the stream time constant ([Guimberteau et al., 2008]). In our case, only the time constant of the slow reservoir, whose isotopic signature is significantly enriched by soil evaporation, has any influence.

No strong seasonal variations are observed in d_{river} over Vienna or Manaus (not shown). Measured d_{river} stays within 7‰ and 12‰ in Vienna, 7‰ and 13‰ in Manaus. This is well simulated by LMDZ: d_{river} varies between 8‰ and 12‰ in Vienna, 8‰ and 13‰ in Manaus, without any clear seasonal cycle.

Therefore, the isotopic composition of rivers allows us to evaluate in an integrated way the representation of hydrological processes (in particular the partitioning between drainage and surface runoff), the representation of isotopic processes in the soil and in the routing scheme, as well as the representation of isotopic processes in LMDZ-OR-iso. Observed $\delta^{18}O_{river} - \delta^{18}O_p$ may help constrain the ratio of surface runoff versus drainage, recognized as a key uncertainty in LSMs ([De Rosnay, 1999]). The seasonal variations in $\delta^{18}O_{river}$ can further help estimate the proportion of surface runoff versus drainage and constrain empirical time constants in the routing scheme, to which river discharge are extremely sensitive ([Guimberteau et al., 2008]).

8.4 What information about land surface processes could we learn from water isotopes?

We have shown that LMDZ-OR-iso reproduces reasonably well the isotopic processes that explain the main features of the observed spatial and seasonal isotopic distributions in the different water pools of the land-atmosphere system. We now use LMDZ-OR-iso simulations to quantify the effect of the water budget at the land surface on the isotopic composition of the soil water and evaporation fluxes (section 8.4.1), and to evaluate the potential of water isotopes to quantify terms of the hydrological cycle over land (section 8.4.2). We simplify the analysis by not considering canopy interception.

8.4.1 Influence of the soil water budget on the isotopic composition of soil water and evapo-transpiration fluxes

We describe the soil water balance with two quantities: the proportion of infiltrating water that is evapo-transpired back into the atmosphere ($r_{ET} = \frac{ET}{F_i}$, where $ET = E + T$, E is the bare soil evaporation, T the transpiration and $F_i = P + M - R$ the incoming water that infiltrates into the soil), and the proportion of this evapo-transpiration that occurs through bare soil evaporation ($r_E = \frac{E}{ET}$).

Over mid and high latitudes, where spatial variations of annually averaged r_E and r_{ET} are strongest (figure 8.2), the soil water is more enriched and displays a lower d when r_E is higher (figure 8.13). The evapo-transpiration is more depleted and displays a higher d as r_E is higher and r_{ET} is lower.

At first order, this behavior can be understood using a simple theoretical framework, as described in appendix H.6. In this framework, we assume that

(1) the soil hydrological and isotopic balance is closed;

(2) the surface runoff has the composition of the rain;

(3) the soil is homogeneous and both the drainage and the transpiration have the composition of the soil; and

(4) the evaporation of bare soil follows the [Craig and Gordon, 1965] equation, and we assume constant atmospheric conditions.

The two key parameters in this framework are r_{ET} and r_E. This framework reproduces very well the first order sensitivity of the isotopic composition of the water pools and fluxes to r_{ET} and r_E simulated by the model (figure 8.13), despite the extreme simplicity of this framework compared to LMDZ-OR-iso and despite considering a constant atmospheric forcing for all locations. As r_E increases (figure 8.13 a and c), the soil water becomes more evaporatively enriched while its d decreases. As a consequence, the bare soil evaporation also becomes more enriched and its d decreases. The total evapo-transpiration becomes more depleted and its d decreases, tending towards that of bare soil evaporation as r_E approaches 1.

The decreasing δ_{ET} as r_E increases is only visible for $r_{ET} \leq 1$. If $r_{ET} = 1$, then all incoming water is evapo-transpired. In this case, the isotopic composition of the evapo-transpiration equals that of incoming water, whatever r_E (figure 8.13 b and d). As r_{ET} decreases (figure 8.13b and d), more enriched soil water is lost as drainage, leading to a more depleted total evapo-transpiration.

To summarize, the impact of soil surface fractionation is all the strongest as r_E is high and r_{ET} is low. The impact of these two parameters on the isotopic composition of evapo-transpiration and soil water can be explained using a simple framework, and is so strong that it overwhelms the effect of both crude assumptions in the framework and the spatial and temporal variability in the atmospheric forcing. This confirms the potential of water stable isotopes to constrain r_{ET} and r_E.

8.4.2 Estimating the soil water budget from water isotopes

Can we use isotopic measurements to constrain r_{ET} and r_E? What kind of observations would be the most valuable for this purpose, and what would be the accuracy of estimating these parameters using water stable isotopes? To address these questions, we use the LMDZ-ORCHIDEE-iso model as a testbed for isotopic methods to estimate the soil water budget. To do this, we use the isotopic composition of some water pools simulated by LMDZ to estimate some terms of the water budget. We then compare these isotope-derived estimates with the value actually simulated by LMDZ, and evaluate errors on these estimates.

Estimating r_E from water isotopes in soils and evapo-transpiration

At the local scale, measurements of the isotopic composition of the soil, vapor and evapo-transpiration (inferred from vapor profiles using the Keeling plot method: [Keeling, 1961]) has been successfully used to partition evapo-transpiration into its transpiration and soil evaporation components, i.e. r_E ([Moreira et al., 1997, Yepez et al., 2003, Williams et al., 2004]). These methods assume that the composition of bare soil evaporation follows the [Craig and Gordon, 1965] equation, and that evapo-transpiration arises solely from bare soil evaporation and transpiration. Basically, these methods apply an equation relating r_E as a function of $\delta^{18}O_s$, $\delta^{18}O_{ET}$, $\delta^{18}O_v$, temperature and relative humidity (equation H.22 of appendix H.21):

$$r_E = \frac{(R_{ET} - R_s) \cdot \alpha_{eq} \cdot \alpha_K \cdot (1-h)}{R_s \cdot (1 - \alpha_{eq} \cdot \alpha_K \cdot (1-h)) - \alpha_{eq} \cdot h \cdot R_v} \tag{8.3}$$

where R is the isotopic ratio and the other variables are defined in appendix H.6.

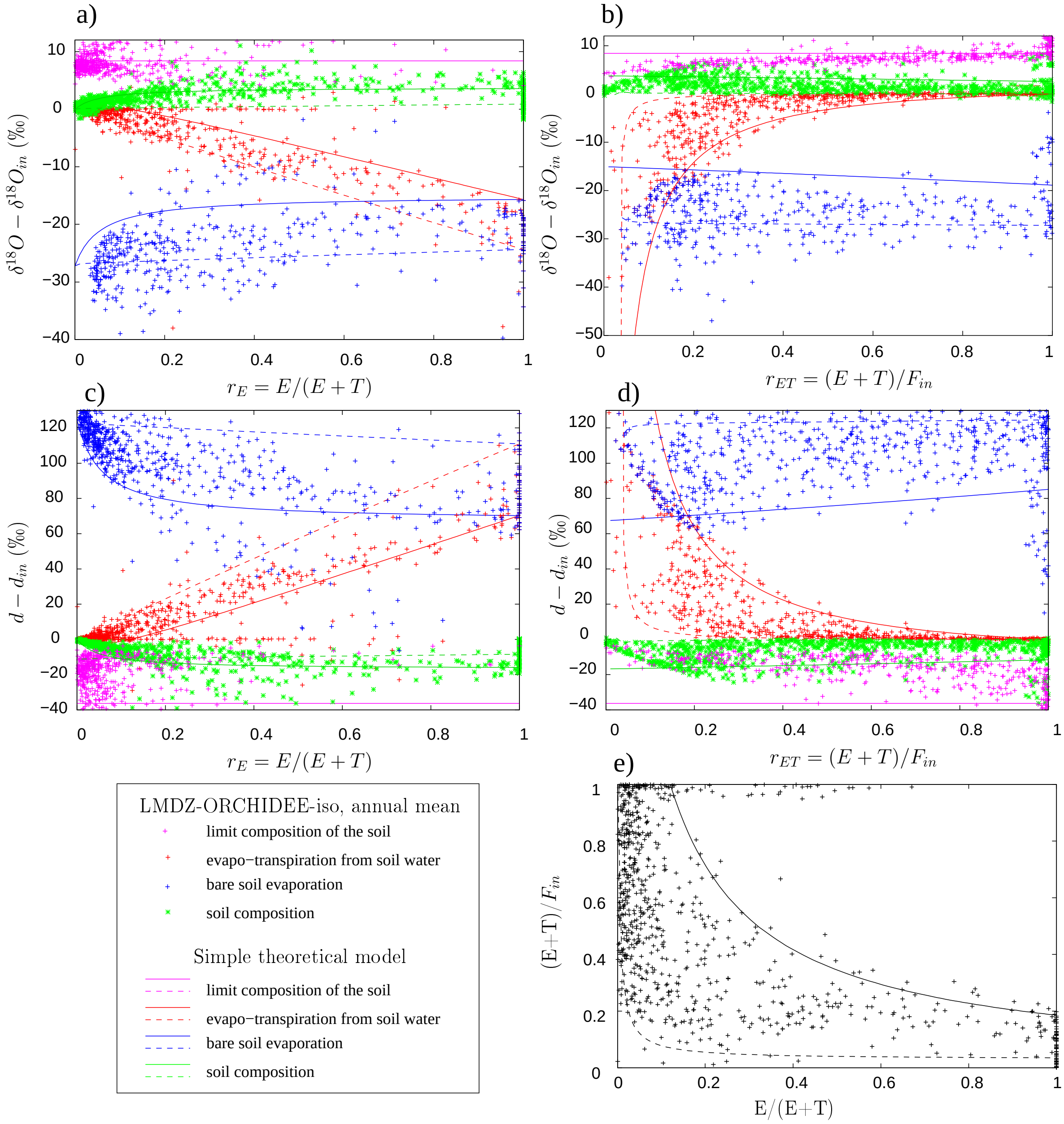

Figure 8.13: a) to d): Annual mean isotopic composition ($\delta^{18}O$, top and d, middle) of the total evapo-transpiration from soil water (δ_{E+T}, red), of the bare soil evaporation (δ_E, blue), of the soil water (δ_s, green) and of the soil water in the limit case where $r_E = r_{ET} = 1$ (δ_{slim}, magenta), minus that of the incoming water flux into the soil (δ_{in}), as a function of annual mean $r_E = \frac{E}{E+T}$ (left) and $r_{ET} = \frac{E+T}{F_{in}}$ (right). Crosses corresponds to the simulated values by LMDZ-OR-iso at each grid box at latitudes higher than 40°N. The distribution of these values in the r_{ET} vs r_E diagram is shown in e. Lines correspond to estimations by the simple theoretical model of a single bucket at stationary state (appendix H.6). Inputs to this theoretical model are an air temperature of 20°C, a relative humidity of 70%, $\delta^{18}O_p = -10‰$, $d_p = 10‰$, $\delta^{18}O_v = -15‰$ and $d_v = 15‰$. We assume two different relationships between r_{ET} and r_E (dashed and solid lines on figure e), constituting an envelope for most model points.

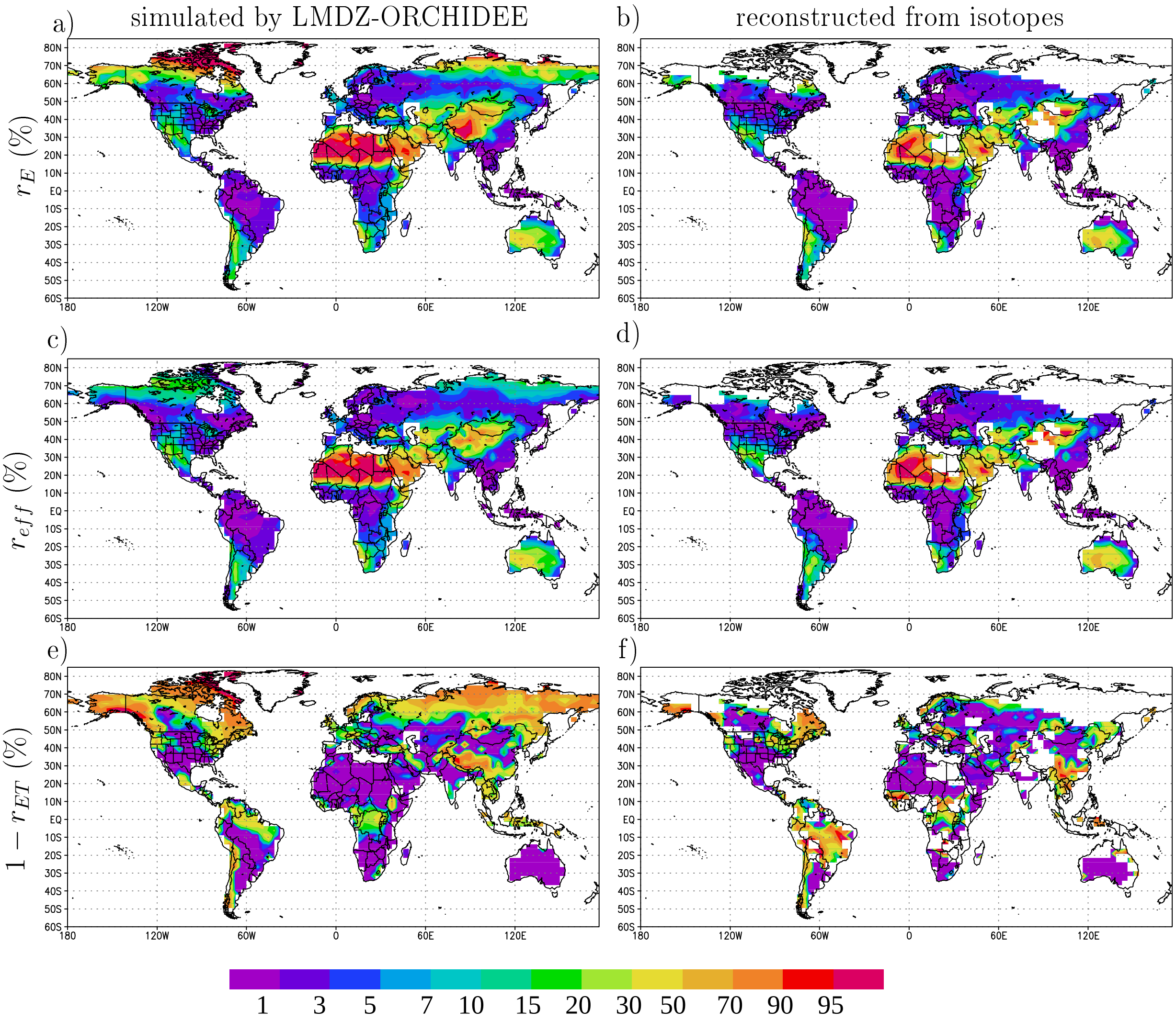

Figure 8.14: a), c) and e): annual mean r_E, $1 - r_{ET}$ and r_{eff} simulated by LMDZ-ORCHIDEE for the CO.ctrl simulation. b), d) and f): r_E, $1 - r_{ET}$ and r_{eff} reconstructed from water isotopes methods described in section 8.4.2. We perform the estimations only on grid points where the denominators in the equation are different from 0 and where the soil water contents and the water fluxes whose compositions we need are strictly positive. Grid points where estimations cannot be performed are left white.

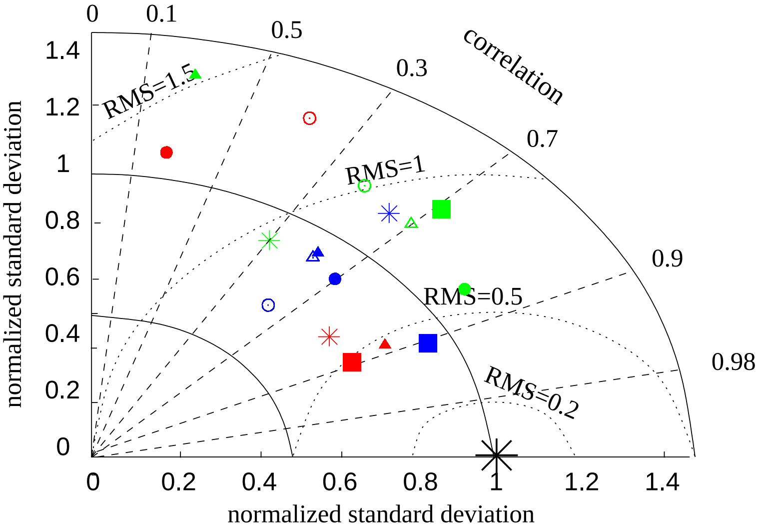

	CO.ctrl	CO.bare	CO.runoff	CO.bare−CO.ctrl	CO.runoff−CO.ctrl	CO.profile
r_E	■	●	▲	○	△	✳
r_{ET}	■	●	▲	○	△	✳
r_{eff}	■	●	▲	○	△	✳

Figure 8.15: Taylor diagram ([Taylor, 2001]) representing the performance of estimated annual mean r_E, r_{ET} and r_{eff} from water isotope methods. A perfect match between estimated and simulated values would fall on the black star. Red, green and blue: estimated maps of r_E , r_{ET} and r_{eff} respectively. Filled markers: estimation for one given simulation. Empty markers: estimation of differences between two simulations, representing for example the estimation of an hydrological change with climate.

Here, we test this method within the model at the annual scale: at each grid point where the denominator of equation 8.3 is different from zero and where evapo-transpiration and soil water content are strictly positive, we estimate the annual mean r_E using simulated annual mean $\delta^{18}O_s$, $\delta^{18}O_{ET}$, $\delta^{18}O_v$, temperature and relative humidity (figure 8.14b) and we compare it to the annual mean value of r_E simulated by LMDZ-ORCHIDEE (figure 8.14a). The spatial distribution of r_E is remarkably well estimated using this isotopic method. On average, errors are of 0.12 for the CO.ctrl simulation, corresponding to less than 50% of the standard deviation at the global scale. This method of estimating r_E is thus very robust even at the annual scale. However, it requires the measurement of $\delta^{18}O_{ET}$, which is difficult and costly.

Estimating $r_E \cdot r_{ET}$ from water isotopes in precipitation and soils

Alternatively, the product of r_E and r_{ET}, corresponding to the proportion of infiltrating water that evaporates from bare soil, may be estimated from measurements of $\delta^{18}O_s$, $\delta^{18}O_v$, $\delta^{18}O_p$, temperature and relative humidity, by inverting equation H.19 (appendix H.6):

$$r_{eff} = r_{ET} \cdot r_E = \frac{\alpha_{eq} \cdot \alpha_K \cdot (1-h) \cdot R_p - R_s}{R_s \cdot (1 - \alpha_{eq} \cdot \alpha_K \cdot (1-h)) - \alpha_{eq} \cdot h \cdot R_v}$$

In doing so, we approximate the composition of the incoming water (rain and melt water) to that of total precipitation. This equation, in addition to the assumptions necessary to estimate r_E, requires that all the assumptions listed in section 8.4.1, in particular hydrological and isotopic balance of the soil, are fulfilled.

Using this isotopic method, the spatial pattern of r_{eff} is remarkably well estimated, with maxima over the Sahara, Southern South America, Australia, central Asia, Siberia and Northern America (figure 8.14c and d). The isotope-derived spatial distribution of r_{eff} correlates well with the simulated distribution (r=0.91). Average errors are lower than 50% of the standard deviation at the global scale. This means that r_{eff} could be estimated provided that simultaneous measurements of soil, precipitation and vapor are available, which is the case at some MIBA stations.

Changes in r_{eff} associated with changes in the bare soil fraction, or with changes in the surface runoff versus drainage partitioning, are also captured well by this isotopic method (figure 8.15, open blue markers). This suggests that long term monitoring of the isotopic composition of precipitation and soil water may be useful in detecting changes in land surface hydrology.

In regions where r_{ET} is close to one, which is the case for many regions with the exception of central Asia and the Arctic (figure 8.14e), r_{eff} is a good proxy for r_E. Indeed, estimated r_{eff} correlates with the simulated r_E with a coefficient of 0.89.

Over Yatir, using annually averaged observed values ($\delta^{18}O$ of -5.1‰ and -3.7‰ in the precipitation and the surface soil respectively), we obtain r_{eff}=46%, compared to 38% observed ([Yaseef et al., 2009]). In ORCHIDEE-iso, the annually averaged surface soil $\delta^{18}O$ values are 0.8‰ lower when sampled as in the data, suggesting a sampling bias. When correcting for this bias, we obtain r_{eff}=28%. These two estimates encompass the observed r_{eff}, though a dedicated study may be necessary to estimate rigorously the soil water budget using isotopic data.

Estimating r_{ET} from water isotopes in precipitation, soils and evapo-transpiration

If r_E and r_{eff} are estimated by the two methods above, r_{ET} may be estimated as a residual:

$$r_{ET} = \frac{R_{ET} - R_s}{R_p - R_s}$$

The estimation of r_{ET} is less accurate than those of r_E or r_{eff} (figure 8.14e and f, figure 8.15), with average errors higher than the standard deviation at the global scale. Estimates of r_{ET} are the best when r_E is significantly positive: in the CO.bare simulation, average errors are two times lower than in the CO.ctrl simulation (figure 8.15).

Estimated ratio	r_E	r_E	r_E	r_E	r_{eff}	r_{eff}	r_{eff}	r_{eff}	r_{ET}	r_{ET}	r_{ET}	r_{ET}
Absolute or relative error	abs	rel	abs	rel	abs	rel	abs	rel	abs	rel	abs	rel
region where r_E...	>0.5	>0.5	<0.5	<0.5	>0.5	>0.5	<0.5	<0.5	>0.5	>0.5	<0.5	<0.5
$\Delta T = 1°C$	0.006	1	$\simeq 0$	1	0.004	1	$\simeq 0$	2	-	-	-	-
$\Delta rh = 1\%$	0.007	1	$\simeq 0$	1	0.01	2	$\simeq 0$	2	-	-	-	-
$\Delta \delta_v = 1$‰	0.03	5	0.006	7	0.02	6	0.004	13	-	-	-	-
$\Delta \delta_p = 1$‰	-	-	-	-	0.05	14	0.02	83	0.08	17	0.38	53
$\Delta \delta_s = 1$‰	0.08	13	0.04	200	0.07	25	0.04	340	0.01	8	0.09	21
$\Delta \delta_{ET} = 1$‰	0.05	7	0.02	49	-	-	-	-	0.01	3	0.24	25
$\Delta n = 0.5$	0.30	44	0.04	35	0.29	49	0.04	48	-	-	-	-
soil profiles	0.10	14	0.04	27	0.19	40	0.04	250	0.12	43	0.06	18

Table 8.2: Uncertainties in the estimation of r_E, r_{eff} and r_{ET} related to measurement errors and assumptions necessary in the simple conceptual model (equation H.19). Values give absolute (in ratio) and relative variations (in %) in estimated r_E, r_{eff} and r_{ET} when temperature T is modified by $1°C$, when relative humidity rh is modified by 1%, when $\delta^{18}O_v$, $\delta^{18}O_p$, $\delta^{18}O_s$ and $\delta^{18}O_{ET}$ are modified by 1‰ , when n in the kinetic fractionation is varied from 0.5 to 1, and when the soil $\delta^{18}O$ is not homogeneous vertically. The resulting variations in estimated are r_E, r_{eff} and r_{ET} averaged over all land grid points where the estimation could be performed, separately for grid points where r_E is higher or lower than 0.5. We write values lower than 10^{-3} as $\simeq 0$.

Uncertainty estimation related to measurement errors, kinetic fractionation and soil profiles

We performed some sensitivity tests to estimate the uncertainty of each method to errors in measured $\delta^{18}O_s$, $\delta^{18}O_v$, $\delta^{18}O_p$, temperature and relative humidity and to the kinetic fractionation formulation (table 8.2).

Estimated r_E and r_{eff} are most sensitive to errors in measured $\delta^{18}O_s$ and to the kinetic fractionation formulation, especially where r_E is high. In contrast, where r_E is lower than 0.5, an error of 1‰ on $\delta^{18}O_s$ translates into an error of only 0.04 on estimated r_E or r_{eff}. The average uncertainty associated with the kinetic fractionation factor also leads to an error of 0.04 on estimated r_E or r_{eff} (if considering that n may vary from 0.5 to 1).

On the other hand, the estimation of r_{ET} is very sensitive to measurement errors in $\delta^{18}O_{ET}$, $\delta^{18}O_s$ and $\delta^{18}O_p$, especially where r_E is small (table 8.2). This may limit the applicability of this method to arid regions only. Indeed, in regions where r_E is greater than 0.5, measurement errors of 1‰ in $\delta^{18}O_{ET}$, $\delta^{18}O_s$ and $\delta^{18}O_p$ translate into errors in estimated r_{ET} of only 0.08, 0.01 and 0.01 respectively.

All these methods assume that the soil is vertically homogeneous. To estimate the impact of this assumption in the case of vertical variations in the soil $\delta^{18}O$, we performed the same reconstruction experiments using $\delta^{18}O_s$ from the CO.profile simulation. The best reconstructions were obtained when using surface soil $\delta^{18}O$, but even in this case the quality of the reconstruction deteriorated significantly (figure 8.15). The vertical variations in soil water composition is the second largest source of uncertainty in the estimation of r_E and r_{eff} after the kinetic fractionation, and the largest source of uncertainty in the estimation of r_{ET} in regions where r_E is high (last line of table 8.2).

8.4.3 Summary

Model simulations show that r_{eff} (the product of r_E and r_{ET}) may be estimated with significant accuracy from the measurement of $\delta^{18}O$ in the soil water, precipitation and vapor only. If measurements of $\delta^{18}O_{ET}$ are also available, r_E can be estimated with significant accuracy, and r_{ET} may be estimated in regions where r_E is sufficiently large (especially northern latitudes and mountane regions). However, uncertainties in the kinetic fractionation and vertical $\delta^{18}O$ variations in soil water are significant sources of error. Moreover, the estimates of accuracy we provide in our study are likely optimistic. Indeed, the controls on the isotopic composition of the soil water in LMDZ are over-simplified compared to reality. Only the few processes that we understand and that we can represent at the scale of a GCM grid box are represented. In reality, various processes not taken into account here, together with spatial heterogeneity, may lead to additional estimation errors.

8.5 Conclusion

8.5.1 Model evaluation

We have implemented water stable isotopes into the land surface model ORCHIDEE and the atmospheric general circulation model LMDZ. The coupled LMDZ-OR-iso model reproduces reasonably well the main features of the seasonal and spatial distribution of the isotopes in precipitation, with a comparable accuracy to other GCMs. Annual mean isotopic composition of the soil, stem and leaf water simulated on two MIBA sites (Le Bray in France and Yatir in Israel) generally agree with the measurements. Taking into account non-steady-state and diffusion effects in leave imroves the simulation of diel isotopic variations in leaf water at some locations. Simulated soil profiles feature a surface isotopic enrichment in summer consistent with observations. In the future, the implementation of water isotopes in a more recent version of SECHIBA using a multi-layer soil model ([Rosnay and Polcher, 1998, De Rosnay, 1999]) will allow us to better compare the simulated soil water composition with data at different depths.

In the future, this evaluation work should be extended to other sites where multiple isotopic measurements are available. More generally, to evaluate the representation of isotopic processes in LSMs coupled to GCMs, it would be extremely valuable to collect systematic, simultaneous and collocated measurements of the isotopic composition in the different water pools of the land-atmosphere system. We expect that more comprehensive evaluation of isotopic LSMs will be possible in the future with the development of databases such as MIBA.

8.5.2 The potential of water isotopes to constrain land surface parameterizations

Comparing the isotopic composition of river and rain water at the annual and seasonal scales may give some information about the partitioning of rainfall into surface runoff and drainage, and about the residence times of water in the different reservoirs of the routing scheme. The value of water isotopes to partition peaks in river discharge into recent rainfall and soil water had already been shown at the local scale ([Wels et al., 1991, Millet et al., 1997, Weiler et al., 2003]). This kind of studies could be extended with the purpose of parameterization development and evaluation.

Soil water isotopic profiles are sensitive to vertical water transfers in the soil, which are key in the development of multi-layer soil models ([De Rosnay, 1999]).

The isotopic enrichment of the soil water relatively to the rain is very sensitive to the partitioning of the infiltrated rain into evapo-transpiration and drainage (r_{ET}), and to the partitioning of evapo-transpiration into transpiration and fractionating evaporation (r_E). The way models represent the partitioning of these fluxes is a major source of dispersion between different LSMs ([Koster and Milly, 1996]), but these fluxes are difficult to estimate directly at the regional scale. This strengthens the interest of water isotope approaches to estimate the partitioning of these fluxes.

Overall, the isotopic composition of different water pools of the land surface are strongly sensitive to some parameterized processes, confirming the potential of isotopes to help constrain parameterization of land surface processes ([Henderson-Sellers, 2006]).

8.5.3 The potential of water isotopes to constrain land surface water budgets

We used coupled land-atmosphere simulations as a testbed for methods to estimate terms of the water budget over continental regions from water stable isotopes. These experiments show that the partitioning of rainfall into bare soil evaporation ($r_{eff} = r_{ET} \cdot r_E$) could be inferred from the isotopic composition of soil water, precipitation and vapor. This highlights the interest in more measurements of these water pools simultaneous at the same site. Estimating r_E and r_{ET} separately would require in addition the isotopic composition of evapo-transpired water (e.g. [Moreira et al., 1997]).

8.5.4 Perspectives

Several studies have shown that coloring (tagging) the different water and isotopes molecules according to their origin (e.g. [Delaygue et al., 2000, Noone and Simmonds, 2002a, Yoshimura et al., 2004]) constitute a powerful diagnostic tool. This could be used to quantify the proportion of vapor arising from the evaporation of bare soil, of canopy-intercepted water or from transpiration. In the future, we plan to use this tool to better understand how these different evaporation fluxes affect the isotopic composition of the vapor and of the subsequent precipitation. This would help evaluate what we can learn about the water cycle using stable isotope approaches. For example, isotopic methods based on spatial gradients in precipitation have been used to estimate the proportion of evapo-transpiration occurring as transpiration ([Gat and Matsui, 1991]). What is the accuracy of such methods? This depends on how contrasted the isotopic signature of the rain arising from the different land surface fluxes are, and this could be diagnosed through water tagging.

For all water isotope applications in the water cycle, the isotopic composition of water vapor is key, since it determines the isotopic composition of the fractionating evaporation fluxes. In addition, the isotopic distribution in the vapor may yield some information about continental recycling and land surface water budget with more accuracy than in the precipitation alone (as was done in [Gat and Matsui, 1991]). Indeed, the vapor can be sampled continuously, and it is a more direct tracer of water origin and air mass history, whereas complex processes affect the rain composition as it falls ([Bony et al., 2008, Lee and Fung, 2008, Risi et al., 2010a]). So far, measuring water isotopes in the vapor has been difficult and costly, but recent measurement of the boundary layer vapor isotopic composition from space at the global scale ([Frankenberg et al., 2009]) and in-situ using new laser spectrometry ([Gupta et al., 2009]) will open many new perspectives. In the future, we plan to explore what we can learn from this new data about land-atmosphere interactions.

Conclusion de la partie

Les isotopes stables de l'eau ont été implémentés dans le modèle de circulation générale LMDZ (chapitre 6) et dans le modèle de surface continentale ORCHIDEE (chapitre 8). La version isotopique de modèle couplé continent-atmosphère (LMDZ-OR-iso) simule relativement bien la distribution spatiale, saisonnière et diurne des principales composantes du système continent-atmosphère. Toutefois, le travail d'évaluation du modèle est actuellement limité par le nombre de données disponibles sur des stations où sont échantillonnées simultanément les différentes composantes du système continent-atmosphère (précipitation, vapeur, sol, tiges, feuilles, rivières). Le travail d'évaluation mériterait d'être approfondi lorsque plus de données isotopiques simultanées et collocalisées des différentes composantes seront disponibles avec une couverture spatiale et saisonnière plus complète. Le développement actuel du réseau MIBA est en cela très prometteur.

Les tests de sensibilité effectués confirment l'intérêt potentiel des isotopes de l'eau pour mieux contraindre certains aspects des paramétrisations hydrologiques. Aussi, par le biais d'expériences "modèle parfait", dans lesquelles nous reconstituons des termes du bilan d'eau par des mesures isotopiques dans le monde du modèle, nous avons montré que des mesures de composition isotopique dans la précipitation, la vapeur et le sol simultanément pouvaient aider à contraindre la partition de la précipitation en évaporation du sol nu, transpiration et drainage. Ce travail d'évaluation du potentiel des isotopes pour contraindre les bilans d'eau sera prolongé par l'évaluation des méthodes basées sur l'étude des gradients spatiaux de composition isotopique de la précipitation ([Gat and Matsui, 1991]). Ce type de méthode est plus facilement applicable du point de vue de la disponibilité des données.

Dans le cadre de l'exploration du potentiel des isotopes pour la contrainte des échanges continents-atmosphère à une échelle plus régionale, nous prévoyons de tirer profit de simulations utilisant le water tagging dans LMDZ (annexe E). Cela permettra de diagnostiquer dans LMDZ-OR-iso la proportion de la vapeur issue des différents flux d'évaporation (la transpiration, l'évaporation de l'eau interceptée par la canopée, l'évaporation du sol nu, l'évaporation océanique) et la composition caractéristique de ces flux. Cela permettra d'évaluer dans quelle mesure la signature isotopique de la vapeur de différentes origines peut renseigner sur les différents termes du bilan d'eau.

Nous prévoyons aussi d'implémenter le water tagging dans ORCHIDEE. Ceci constituera un diagnostique puissant des transferts d'eau à la surface continentale dans ORCHIDEE et des interactions surface-atmosphère dans LMDZ-ORCHIDEE. Il permettra d'explorer des questions scientifiques variées liées aux changements actuels et futurs en ressources en eau, telles que :

(1) les variations du débit des fleuves

(2) et l'impact de l'irrigation.

Concernant l'exemple 1, le water tagging dans ORCHIDEE permettra de quantifier les contributions au débit d'un fleuve de la précipitation de différentes saisons d'une part, et de la fonte des neiges d'autre part. Ceci pourra être très utile dans le cadre de la détection-attribution des changements observés des débits des fleuves. ([Milly et al., 2005]), et de l'étude des causes de dispersion des modèles dans la prévision de ces changements.

Concernant l'exemple 2, on s'attend à ce que l'irrigation ait un impact sur le cycle de l'eau des régions fortements irriguées ([Adegoke et al., 2002, Douglas et al., 2006]). Une paramétrisation de l'irrigation a d'ailleurs été implémentée dans le but d'étudier cet impact([de Rosnay et al., 2003]). Taguer l'irrigation permettrait de diagnostiquer quelle est la part de l'évaporation et de la précipitation provenant de l'irrigation, et donc quantifier son impact sur le cycle de l'eau dans LMDZ-ORCHIDEE.

Dans ces deux exemples, les signatures isotopiques des eaux de différentes origines seront-elles suffisamment contrastée pour pouvoir évaluer des termes du cycle de l'eau et leurs variations temporelles ? En quoi les isotopes peuvent-ils permettre d'évaluer le comportement du modèle par rapport à des observations ? Ce sont des questions auxquelles nous souhaitons nous intéresser dans le futur.

Enfin, une grande quantité de données isotopiques a été collectée dans les lacs, eaux souterraines, rivières, sources et marécages, dans le cadre du réseau IGLASS (Isotopes in Groundwater, Lakes, Springs and Streams, [Aggarwal et al., 2007]) sous l'égide de l'IAEA. L'utilisation de ces données pourrait être intéressante à la fois dans le cadre de l'évaluation de modèles et de l'exploration du potentiel des isotopes de l'eau pour contraindre les bilans d'eau.

Chapitre 9

Conclusion générale et perspectives

9.1 Conclusion

Le principal but de cette thèse était de mieux évaluer le potentiel des isotopes pour déduire des informations sur le cycle hydrologique actuel et ses variations passées, et mieux contraindre sa représentation dans les modèles. Pour cela, une première étape a été la compréhension des processus contrôlant la distribution spatiale et temporelle de la composition isotopique de l'eau.

Dans les tropiques, la composition isotopique de la vapeur des basses couches et de la précipitation est fortement affectée par l'activité convective ([Lawrence et al., 2004]). Une anticorrelation est observée sur les stations tropicales entre precipitation et δ (amount effect, [Rozanski et al., 1993]). Dans cette thèse, l'effet des processus convectifs sur la composition isotopique de l'eau a été étudiée en utilisant des modèles numériques isotopiques de différents degrés de complexité (modèle uni-colonne, modèle de ligne de grains, GCM) et des données de la campagne AMMA (partie I). Les différentes approches ont toutes montré la forte influence de la convection sur la composition isotopique de la précipitation, par le biais de deux types de processus : (1) la réévaporation des gouttes de pluies lors de leur chute et (2) la subsidence convective associée à la réévaporation de ces gouttes. Ces deux processus expliquent en majeure partie l'amount effect observé à l'échelle saisonnière, ainsi que les variations de composition isotopique (à la fois δ et d-excess) de la précipitation observées aux échelles intra-saisonnières et intra-évènement. D'autre part, la composition isotopique dans la haute troposphère est fortement influencée par le transport de condensat par les acendances convectives (section 5).

En domaine continental, où la majeure partie des archives paléo-climatiques existent, la composition isotopique de la précipitation est aussi affectée par les interactions entre surface continentale et atmosphère. L'effet des processus à la surface continentale sur la composition isotopique de la précipitations et des différents réservoirs d'eau continentaux a été étudié grâce au modèle de surface continentale ORCHIDEE couplé au GCM LMDZ (partie III). La composition de l'eau des différents reservoirs dépend de la partition de la précipitation entre ruissellement de surface, drainage, transpiration par la végétation et évaporation de sol nu et de l'eau interceptée par la canopée, ainsi que des constantes de temps des transferts d'eau au travers du sol et jusqu'aux rivières.

En retour, la composition isotopique peut être utilisée pour mieux contraindre certains termes du bilan d'eau ou certains processus convectifs ou hydrologiques actuels ou passés, et pour mieux évaluer leur représentation dans les modèles. Le tableau 9.1 résume les différentes applications des isotopes stables de l'eau étudiées ou discutées au cours de cette thèse.

Mesures isotopiques	ce qu'on pourrait en déduire ou évaluer dans les modèles	chapitre correspondant ou article
Contrôles de l'humidité atmosphérique		
δ dans l'UT-LS	contribution de la convection au transport d'eau dans l'UT-LS ; efficicacité de precipitation dans les ascendances convectives	[Webster and Heymsfield, 2003], chapitre 5
δ_v dans les zones sèches	intensité de la subsidence grande échelle	[Frankenberg et al., 2009], annexe E.2.3
δ_v dans les tropiques	effet de la réévaporation de la précipitation sur l'humidification de l'atmosphère	[Worden et al., 2007], annexe E.2.2
d_v dans les tropiques	effet de la réévaporation de la précipitation sur l'humidification de l'atmosphère	annexe E.2.2
Convection atmosphérique		
$\delta_p - \delta_v$ (δ_p si δ_v varie peu)	taux de réévaporation des gouttes de pluies ; taux de rééquilibration isotopique des gouttes avec la vapeur lors de leur chute	chapitres 2, 3 et 4
d_p	humidité relative lors de la réévaporation des gouttes	chapitre 4
^{17}O-excess$_p$	humidité relative lors de la réévaporation des gouttes	*[Landais et al.,]* en préparation
variations de δ_v ou δ_p au cours d'un système convectif	intensité des descentes insaturées ou des subsidences méso-échelles associées au systèmes convectifs	chapitres 2 et 4
δ_p aux échelles intra-saisonnières	variabilité intra-saisonnière de l'activité convective en conditions humides ; degrés d'organisation et intensité des systèmes convectifs en conditions sèches	chapitre 3
Hydrologie continentale		
δ_v, δ_s, δ_{ET} et humidité relative	proportion de l'évapo-transpiration sous forme d'évaporation du sol nu (r_E)	[Moreira et al., 1997], chapitre 8
δ_v, δ_s, δ_p et humidité relative	proportion de la précipitation retrournée à l'atmosphère sous forme d'évaporation du sol nu (r_{eff})	chapitre 8
δ_{river} et δ_p	r_E ; proportion de l'excédent d'eau sous forme de ruissellement de surface ou de drainage	chapitre 8
cycles saisonniers de δ_{river}	proportion de l'excédent d'eau sous forme de ruissellement de surface ou drainage ; temps de résidence de l'eau dans différents réservoirs	[Weiler et al., 2003], chapitre 8
profils isotopiques dans les sols	mouvements verticaux d'eau dans les sols (diffusion, infltration)	[Gazis and Geng, 2004], chapitre 8
δ_{stem}, δ_s	profil d'extraction racinaire	[Brunel et al., 1997]
gradients de δ_v	taux de recyclage continental	[Brown et al., 2008]
gradients de d_v ou d_p	r_E à l'échelle régionale	[Gat and Matsui, 1991], annexe F.3
Climats passés		
archives de δ_p dans les tropiques	variations climatiques de la précipitation et de l'activité convective	[Hoffmann, 2003], chapitre 6
archives de δ_p aux pôles	variations climatiques de la température polaire	chapitre 6
archives de δ_p et d_p aux pôles	variations climatiques de la température de surface des régions sources (régions dont l'évaporation est source de précipitation polaire)	[Stenni et al., 2001], chapitre 7
archives ^{17}O-excess aux pôles	variations climatiques de l'humidité relative à la surface des régions sources	chapitre 7

Tab. 9.1 – Tableau résumant les différentes applications possibles des isotopes stables de l'eau pour l'étude du cycle de l'eau et des climats passés, et pour leur évaluation dans les modèles. Pour chaque application, on donne un exemple de publication ou le chapitre de thèse où cette application est discutée.

9.2 Perspectives

9.2.1 Nouvelles possibilités offertes par la disponibilité de nouvelles données

A plusieurs reprises dans cette thèse, la disponibilité de certaines données isotopiques supplémentaires aurait permis de mieux comprendre certains processus isotopiques et de mieux évaluer leur représentation dans les modèles. Tandis que les données isotopiques dans les précipitations sont relativement répendues depuis plusieurs décennies, en particulier grâce au réseau GNIP maintenu par l'IAEA ([Rozanski et al., 1993]), mais aussi grâce à certaines campagnes (comme lors d'AMMA pendant cette thèse), la disponibilité de plus de données dans la vapeur et à la surface continentale dans le futur offrira de nouvelles possibilités.

Données de vapeur

Des données isotopiques dans la vapeur seraient particulièrement utiles pour mieux comprendre le signal isotopique dans les précipitation, comme on a pu le voir dans le cadre de la campagne AMMA (chapitres 3 et 4). En effet, la composition isotopique de la précipitation δ_p peut être considérée comme la somme de deux composantes : $\delta_p = \delta_v + (\delta_p - \delta_v)$. Le premier terme correspond à la composition de la vapeur, et le deuxième au désequilibre de la précipitation avec la vapeur lors de la chute. δ_v affecte δ_p à la fois parce que la précipitation se forme par condensation de cette vapeur, et parce que la précipitation se rééquilibre avec cette vapeur lors de sa chute. Un premier pas pour comprendre les signaux dans la précipitation est donc de comprendre les signaux dans la vapeur. Ces signaux sont potentiellement plus simples à comprendre, car la vapeur est contrôlée par des processus de plus grande échelle. Dans le cadre d'AMMA par exemple, des données de vapeur auraient permis de comprendre si les variations observées étaient liées à l'effet grande échelle des processus convectifs sur la vapeur, ou au contraire à des effets locaux de rééquilibration plus ou moins poussée de la précipitation avec la vapeur (chapitre 3, [Risi et al., 2008b]).

Avoir des données de vapeur permettrait aussi de mieux comprendre d'éventuels biais dans les modèles : si une évolution isotopique est mal reproduite, est-ce à cause d'une mauvaise représentation de processus grande échelle affectant la vapeur, ou une mauvaise représentation de la réévaporation de la précipitation, ou une mauvaise représentation de la rééquilibration isotopique entre gouttes et vapeur ?

Enfin, nous avons vu au cours des différents chapitres qu'une incertitude majeure dans les modèles était la représentation de la réévaporation des gouttes et de leur rééquilibration avec la vapeur ([Lee and Fung, 2008, Bony et al., 2008, Risi et al., 2010a, Risi et al., 2010b]). Disposer de données de vapeur en même temps que de données de précipitation permettrait de mieux contraindre cette représentation dans les modèles.

Les données de vapeur ont jusqu'à présent été limitées par la difficulté de l'échantillonage. Mais le développement de nouvelles méthodes de mesures de la vapeur, moins coûteuses et laborieuses, changera sans doute la donne dans les années à venir ([Helliker and Noone, 2009]). En particulier, l'arrivée sur le marché d'instruments Picarros, appareils mesurant automatiquement et continuement la composition isotopique de la vapeur par technologie laser, est très prometteuse. Cela permettra d'aquérir plus facilement de longues séries de données de composition dans la vapeur, à haute fréquence. L'installation de Picarros est prévue sur le site instrumenté du SIRTA à Palaiseau, à Niamey, en Bolivie et en Amazonie, dans le cadre de projets en collaboration entre le LMD et le LSCE et de la thèse de Guillaume Tremoy (2009-2012).

En outre, des données collectées par satellite, offrant une couverture globale, deviennent disponibles. Elle permettront notamment une évaluation globale des GCMs isotopiques. En particulier, les données SCIAMACHY ([Frankenberg et al., 2009]) documentent la composition isotopique dans les basses couches, les données TES aux alentours de 700 hPa ([Worden et al., 2007, Brown et al., 2008]), les données IASI dans la basse à moyenne troposphère ([Herbin et al., 2009]).

Données de surface continentale

Dans le cadre de l'évaluation de la représentation des isotopes de l'eau dans un modèle de surface continentale tel qu'ORCHIDEE, la distribution de la composition isotopique dans chaque reservoir individuellement est peu contraignante : que ce soit dans le sol, les tiges, les feuilles ou les rivières, la composition isotopique au premier ordre ressemble à celle de la précipitation (e.g. [Kendall and Coplen, 2001]). Ce sont les différences de composition entre ces différents réservoirs qui sont susceptibles d'apporter une contrainte sur la performance des modèles, mais aussi des informations sur le cycle de l'eau (chapitre 8). Par exemple, la différence de composition entre précipitation et sol peut apporter des informations sur l'évaporation fractionnante des sols, et vérifier si ces processus sont bien représentés dans les modèles. La différence de composition entre précipitation et rivières apporte une information additionnelle sur les processus de ruissellement et de drainage. A l'avenir, le développement de la collecte systématique de données collocalisées et simultanées de la composition isotopique dans différents réservoirs du système continent-atmosphère, sur de nombreuses stations (ce que l'on peut espérer dans le cadre du projet MIBA, e.g. [Twining et al., 2006]) permettra d'évaluer les LSMs isotopiques de manière plus complète et rigoureuse qu'actuellement.

9.2.2 L'utilisation des isotopes stables de l'eau pour l'étude du cycle de l'eau actuel

De plus en plus d'études présentent les isotopes stables de l'eau comme un outil prometteur de l'étude du cycle de l'eau (e.g. [Worden et al., 2007, Noone, 2009]). Cela necessite dans un premier temps une bonne compréhension du contrôle de la compositon isotopique de l'eau. Le coloriage de l'eau et de ses isotopes (water tagging) dans un modèle atmosphérique est pour cela un outil diagnostique extrêmement puissant (e.g. [Noone and Simmonds, 2002a, Bosilovich and Schubert, 2002, Yoshimura et al., 2004, Galewsky et al., 2005]). Le water tagging peut permettre de tracer non seulement l'origine de l'eau, mais aussi différent processus de transport d'eau ainsi que ses changements de phase (annexe E.1). Dans le futur, nous prévoyons de mieux exploiter les différentes possibilités du water tagging dans le GCM LMDZ. De plus, l'implémentation du water tagging dans le schéma de surface continentale ORCHDEE permettra le suivi des eaux de différentes origines au travers des différents réservoirs d'eau continentaux. Par exemple, le diagnostique de l'origine de l'eau des rivières pourra avoir des aplications pour la détéction-attribution des changements observés de débits des fleuves. Enfin, l'utilisation du water tagging dans le modèle couplé LMDZ-ORCHIDEE constituera un diagnostique des processus d'échange continents-atmosphère et de ses variations temporelles. Si les compositions isotopiques des eaux de différentes origines sont suffisamment contrastée, la composition isotopique de différents reservoirs du système continent-atmosphère pourra aider à estimer des termes du cycle hydrologique et évaluer leur simulation dans les modèles.

De manière concrète et quantitative, que peuvent permettre d'estimer les isotopes stables de l'eau, et avec quelle précision ? Quel est la robustesse des estimations quantitative réalisées grâce aux isotopes dans certaines études ? Par exemple, 20-40% de l'eau recyclée par évaporation fractionnante en Amazonie ([Gat and Matsui, 1991]), 20-50% de réévaporation des gouttes dans les nuages convectifs ([Worden et al., 2007]) ? Des éléments de réponse peuvent être apportés par des expériences de type “modèle parfait” réalisées avec GCMs isotopiques. Ces expériences consistent en estimer grâce à la composition isotopique simulée une variable climatique ou une composante du cycle hydrologique, puis comparer cette estimation à ce qui est vraiment simulé par le modèle (exemples en sections 6.4 et 8.4.2). Ces expériences permettront d'évaluer la robustesse et la précision des reconstructions basées sur les isotopes. Plus généralement, elles peuvent aider à mettre au point des *méthodes observationnelles* basées sur les isotopes pour estimer certains termes du cycle de l'eau. Par exemple, quelles variables isotopiques (et à quelles échelles de temps) seraient idéales pour contraindre tel ou tel processsus ?

Enfin, les isotopes stables de l'eau peuvent-ils aider à mieux contraindre les paramétrisations physiques des modèles de climat ? Comment les paramétrizations physiques affectent-elles conjointement la simulation du cycle de l'eau et la composition isotopique de l'eau ? Des réponses à cette question pourront être apportées par le projet d'intercomparaison des GCMs isotopiques SWING (Stable water Isotopes intercomparison Group, http ://www.bgc-jena.mpg.de/projects/SWING/). Peut-on mettre au point de *tests observationnels* basés sur les isotopes pour évaluer la représentation du cycle de l'eau dans les modèles ?

9.2.3 L'utilisation des isotopes de l'eau en paléo-climatologie

Les projections climatiques pour les prochaines décennies simulées par les GCMs sont très modèle-dépendantes. Par exemple, les réponses au changement climatique en terme de précipitation sont dispersées dans les régions de mousson (ex : [Held et al., 2005]). La capacité des GCMs à reproduire les changements isotopiques passés pourrait, indirectement, permettre d'évaluer leur capacité à simuler la réponse du cycle hydrologique aux changements climatiques.

L'introduction des isotopes stables de l'eau dans des modèles couplés ocean-atmosphère permet la simulation d'autres proxies que la simple composition isotopique de la précipitation : exemple : le $\delta^{18}O$ de l'eau de mer enregistré dans les carbonates ([Roche et al., 2004, LeGrande and Schmidt, 2008, LeGrande and Schmidt, 2009]), les coraux ([Tindall et al., 2009]). Ces simulations couplées permettent de plus de tenir compte de l'effet des variations de $\delta^{18}O$ à la surface de l'océan ([LeGrande and Schmidt, 2006]). Des simulations couplées atmosphère-continents permettraient de plus la simulation du $\delta^{18}O$ de la cellulose, proxy aussi très utilisé en paléo-climatologie ([Danny and Loader, 2004]). Ainsi, de nombreuses études paléo-climatiques pourront être réalisées à partir de la version isotopique du modèle couplé de l'IPSL ([Marti et al., 2005]), lorsque celle-ci sera développée. Les isotopes ont été introduits au cours de cette thèse dans la composante atmosphérique (LMDZ) et de surface continentale (ORCHIDEE). Ils avaient déjà été introduits dans le modèle d'océan OPA (Didier Roche, pers. comm.). Il ne reste donc plus qu'à finaliser le couplage pour obtenir un modèle couplé contenant les isotopes dans toutes ses composantes.

9.2.4 L'^{17}O-excess

L'^{17}O-excess apporte une information complémentaire à la fois au d-excess et aux δ ([Landais et al., 2008], chapitre 7), ce qui en fait un traceur très prometteur. Toutefois, la mesure de ce paramètre avec une précision suffisante n'a été possible que très récemment ([Barkan and Luz, 2005]), et sa distribution spatio-temporelle ainsi que ses contrôles sont encore très mal connus. Dans les années à venir, de nombreux progrès sont à espérer concernant la compréhension des processus contrôlant de ce paramètre. De nombreuses mesures sont en effet réalisées au LSCE par Amaelle Landais, notamment en domaine tropical ([Landais et al.,] en préparation), qui permettront de documenter les variations spatio-temporelles de l'^{17}O-excess. D'autre part, la simulation de l'^{17}O-excess dans les GCMs, si validées par comparaison aux mesures, permettra de mieux comprendre les contrôles de ce paramètre. En retour, quel est le potentiel de l'^{17}O-excess pour l'étude du cycle de l'eau et des climats passés ?

Annexe A

Acronymes et notations courantes

Acronymes

Acronyme	Signification
AEJ	African Easterly Jet
AMIP	Atmospheric Model Inter-comparison Project ([Gates, 1992])
AMMA	Analyse Multidisciplinaire de la Mousson Africaine ([Janicot et al., 2008]) `http ://database.amma-international.org/`
ARM	Atmospheric Radiation Measurement ([Stokes and Swartz, 1994]), gérant des sites instrumentés aux Etats-Unis et dans le monde. `http ://www.arm.gov/sites/`
BL	Boundary layer
CLIMAP	Reconstructions saisonnières de la température de surface au dernier maximum glaciaire ([CLIMAP, 1981])
CMAP	Climate Prediction Center Merged Analysis of Precipitation = reconstruction des précipitations basées sur des satellites, pluviomètres et sorties de modèles ([Xie and Arkin, 1997]) `http ://www.cpc.noaa.gov/products/global_precip/html/wpage.cmap.html`
CRM	Cloud Resolving Model = modèle haute résolution (quelques km à quelques centaines de m) résolvant explicitement les mouvements convectifs
DJF	Decembre Janvier Février
ECMWF	European Center for Medium-range Weather Forcasting. Produit des réanalyses météorologiques ([Uppala et al., 2005])
GCM	General Circulation Model
GNIP	Global Network for Isotopes in Precipitation `http ://www-naweb.iaea.org/napc/ih/GNIP/IHS_GNIP.html`
GNIR	Global Network for Isotopes in Rivers `http ://www-naweb.iaea.org/napc/ih/IHS_resources_GNIR2.html`
GPCP	Global Precpitation Product=reconstruction des précipitations basées sur des satellites, pluviomètres et sorties de modèles ([Huffman et al., 1997]) `http ://precip.gsfc.nasa.gov/`
IASI	Infrared Atmospheric Sounding Interferometer, mesurant par satellite le δD de la vapeur de la basse et moyenne troposphère ([Herbin et al., 2009])
IAEA	International Agency for Atomic Energy
IPSL	Institut Pierre Simon Laplace= Institut dont fait partie le LMD et développant un modèle couplé de climat
JJA	Juin Juillet Aout
LAI	Leaf Area Index : surface of leaf per area unit.
LES	Large Eddy Simulation = simulation très haute résolution (quelques centaines à dizaines de m) résovant les gros tourbillons
LGM	Last Glacial Maximum)dernier maximum glaciaire

Acronyme	Signification
LMDZ	Laboratoire de Météorologie Dynamique-Zoom=modèle de circulation général atmosphérique dévoloppé au LMD, composante atmosphérique du modèle de l'IPSL, comportant une fonction zoom ([Hourdin et al., 2006]) `http ://lmdz.lmd.jussieu.fr/`
LMDZ-iso	version isotopique d'LMDZ
LMDZ-OR-iso	version isotopique du modèle couplé LMDZ-ORCHIDEE
LPJ	Lund-Postdam-Jena=modèle de végétation dynamique d'ORCHIDEE ([Sitch, 2003])
LSM	Land Surface Model
MIBA	Moisture Isotopes in the Biosphere and Atmosphere Meteoric Water Line = droite des eaux météoriques = droite formée par les précipitations dans le diagramme $\delta^{18}O$-δD
MWL	Meteoric Water Line = droite des eaux météoriques = droite formée par les précipitations dans le diagramme $\delta^{18}O$-δD
MH	Mid-Holocène
NCEP	National Center for Environmental Prediction. Produit des réanalyses météorologiques ([Kalnay et al., 1996]) `http ://www.esrl.noaa.gov/psd/data/gridded/data.ncep.reanalysis.html`
NOAA	National Oceanic and Atmospheric Administration. Fournissent des jeux de données telles l'OLR
OLR	Outgoing Longwave Radiation données de la NOAA disponibles sur http ://www.esrl.noaa.gov/psd/data/gridded/data.interp_OLR.html
ORCHIDEE	ORganizing Carbon and Hydrology In Dynamic EcosystEms=modèle de surface continentale de l'IPSL ([Krinner et al., 2005]) `http ://orchidee.ipsl.jussieu.fr/`
ORCHIDEE-iso	version isotopique d'ORCHIDEE
PD	present-day
PI	pre-industrial
PMIP	Paleoclimate Model Inter-comparison Project ([Joussaume and Taylor, 1995, Braconnot et al., 2007])
RH	Relative Humidity
SCIAMACHY	Scanning Imaging Absorption Spectrometer for Atmospheric Cartography, mesurant par satellite le δD de la vapeur intégrée verticalement ([Frankenberg et al., 2009])
SECHIBA	Schématisation des EChanges Hydriques a l'Interface entre la Biosphère et l'Atmosphère=composante hydrologique d'ORCHIDEE ([Ducoudré et al., 1993])
SL	Sub-cloud layer
SST	Sea surface temperature
STOMATE	Saclay Toulouse Orsay Model for the Analysis of Terrestrial Ecosystems=composante biologique d'ORCHIDEE ([Krinner et al., 2005])
SWING	Stable Water Isotope Inter-comparison Group `http ://www.bgc-jena.mpg.de/bgc-synthesis/projects/SWING/`
TES	Tropospheric Emission Spectrometer, mesurant par satellite le δD de la vapeur vers 700hPa ([Worden et al., 2007]).
TTL	Tropical Tropopause Layer
TOGA-COARE	Tropical Ocean Global Atmosphere Couple Ocean-Atmosphere Response Experiment
UT-LS	Upper Tropspere-Lower Stratosphere

Notations

Notation	Signification
$\delta^{18}O$	abondance en $H_2^{18}O$ en ‰
d	d-excess=deuterium excess en ‰
R	rapport isotopique
R_v, R_p, R_e, R_l, R_c	rapports isotopiques dans la vapeur des basses couches, la précipitation, la réévaporation des gouttes, le liquide, le condensat. Ces indices peuvent aussi s'appliquer au $\delta^{18}O$ ou au d.
R_E, R_T, R_{ET}	rapports isotopiques dans l'évaporation de surface, la transpiration, l'évapo-transpiration
R_s, R_{stem}, R_{leaf}, R_{river}	rapports isotopiques dans le sol, les tiges, les feuilles et les rivières.
α_{eq}, α_K, α_{eff}	coefficients de fractionnement isotopique, à l'équilibre, cinétique, total
T	température ou constante de temps, selon le contexte
T_a, T_s	température de l'air, température de surface
P	taux de précipitation (mm/jour)
q, q_l, q_s	humidité spécifique (kg/kg), teneur en liquide, humidité spécifique à saturation
rh_a, rh_s	humidité relative de l'air, humidité relative normalisée à la température de surface.
ϵ_p	efficacité de précipitation
ϕ	paramètre ajustable dans la représentation des processus isotopiques lors de la réévaporation des gouttes (annexe D.2)
f	fraction résiduelle d'une vapeur en train de condenser, ou d'une goutte en train de se réévaporée.
T, E, ET, M, $\mathcal{R}$, D	Taux de transpiration, d'évaporation du sol nu, d'évapo-transpiration, de fonte de la neige, de ruissellement et de drainage
r_E, r_{ET}, r_{eff}	fraction de l'évapo-transpiration sous forme d'évaporation de sol nu, fraction de l'eau infiltrée dans le sol retournée vers l'atmosphère par évapo-transpiration, fraction de l'eau infiltrée dans le sol retournée vers l'atmosphère par évaporation du sol nu
τ	constante de temps

Annexe B

Fractionnements à l'équilibre et cinétique

Dans cette section, nous rappelons la formulation des coefficients de fractionnement à l'équilibre et cinétique pour l'HDO, l'$H_2^{18}O$ et l'$H_2^{17}O$.

B.1 Fractionnement à l'équilibre

Les fractionnements à l'équilibre pour les changements de phase liquide/vapeur ont été déterminés expérimentalement par [Majoube, 1971b]

$$\alpha_{H_2^{18}O,l/v} = exp(\frac{1137.}{(273.15+T)^2} - \frac{0.4156}{273.15+T} - 2.0667E-3)$$

$$\alpha_{DO,l/v} = exp(\frac{24844.}{(273.15+T)^2} - \frac{76.248}{273.15+T} - 52.612E-3)$$

Les coefficients de fractionnements à l'équilibre pour les changements de phase glace/vapeur ont été mesurés expérimentalement entre 0 et -40°C par [Majoube, 1971a, Merlivat and Nief, 1967] :

$$\alpha_{H_2^{18}O,l/v} = exp(\frac{11.839}{273.15+T} - 0.028244)$$

$$\alpha_{H_2^{18}O,l/v} = exp(\frac{16288.}{273.15+T} - 0.0934)$$

La figure B.1 illustre la variation de ces coefficients de fractionnement avec la température.

Les coefficients de fractionnement pour l'$H_2^{17}O$ sont exprimés en fonction des coefficients de fractionnements pour l'$H_2^{18}O$ ([Barkan and Luz, 2005, Barkan and Luz, 2007]) :

$$\alpha_{H_2^{17}O} = \left(\alpha_{H_2^{18}O}\right)^{0.528}$$

B.2 Fractionnement cinétique lors de la formation des cristaux de glace

Lors de la formation des cristaux de glace, un fractionnement cinétique a été introduit par [Jouzel and Merlivat, 1984] pour tenir compte du fait que la condensation en glace est hors équilibre et pour simuler les données de d-excess observées en Antarctique : le coefficient de fractionnement effectif est fonction du coefficient de fractionnement à l'équilibre, α_{ice}^{eq} et de la sur-saturation S autour des cristaux de glace :

$$\alpha_{ice}^{eff} = \frac{\alpha_{ice}^{eq} \cdot S}{1 + \alpha_{ice}^{eq}(S-1) \cdot D/D_i}$$

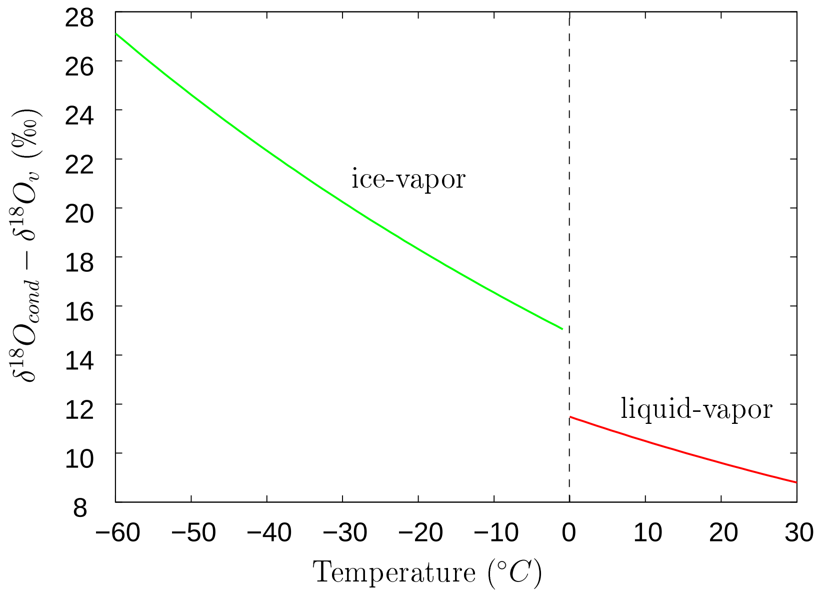

FIG. B.1 – Illustration de la variation des coefficients de fractionnement avec la température : différence entre le $\delta^{18}O$ d'une vapeur à -20‰ et le $\delta^{18}O$ du liquide ou de la glace à l'équilibre avec cette vapeur. Par exemple, à 30°C, le liquide est 9‰ plus riche que la vapeur avec laquelle il s'équilibre, tandis qu'à -40°C, la glace est 22‰ plus riche que cette vapeur.

D et D_i sont les diffusivités de l'eau normale et de l'isotope respectivement, mesurées par [Merlivat, 1978]. S est paramétrisée en fonction de la température T ([Jouzel and Merlivat, 1984]) :

$$S_i = 1 - \lambda \cdot T$$

avec λ un paramètre ajusté pour optimiser la simulation du d-excess en Antarctique (de 0.002 à 0.004 selon les études).

B.3 Fractionnement cinétique lors de l'évaporation d'un liquide

B.3.1 La composition du flux d'évaporation

La composition du flux d'évaporation d'une surface d'eau liquide est donnée par la formule de [Craig and Gordon, 1965], que nous démontrons ici de manière très simplifiée.

Considérons l'évaporation à la surface d'une eau liquide de composition R_l et de température T_s dans une atmosphère d'humidité spécifique q_v et de composition R_v.

Le taux d'évaporation E pour l'eau normale est de la forme :

$$E = p \cdot (q_s(T_s) - q_v)$$

avec p une fonction croissante de la diffusivité moléculaire de l'eau dans la vapeur et de la vitesse du vent, et $q_s(T_s)$ l'humidité spécifique à saturation à la température de la surface T_s.

De même, le taux d'évaporation E_i pour les isotopes est de la forme :

$$E_i = p_i \cdot (q_{si}(T_s) - q_{vi})$$

Avec

$$q_{vi} = R_v \cdot q_v$$

et par définition du coefficient de fractionnement à l'équilibre liquide/vapeur α_{eq} :

$$q_{si}(T_s) = q_s(T_s) \cdot \frac{R_l}{\alpha_{eq}}$$

La composition du flux d'évporation est donc :

$$R_e = \frac{E_i}{E} = \frac{p_i}{p} \cdot \frac{q_s(T_s) \cdot \frac{R_l}{\alpha_{eq}} - R_v \cdot q_v}{q_s(T_s) - q_v}$$

Soit h l'humidité relative de l'air rapportée à la tempéarture de la surface :

$$h = \frac{q_v}{q_s(T_s)}$$

On obtient alors

$$R_e = \frac{p_i}{p} \cdot \frac{\frac{R_l}{\alpha_{eq}} - h \cdot R_v}{1 - h}$$

On peut alors définir, par analogie au coefficient à l'équilibre, le coefficient cinétique α_K par

$$\alpha_K = \frac{p}{p_i} \tag{B.1}$$

On obtient alors la formule de l'évaporation de [Craig and Gordon, 1965] :

$$R_e = \frac{1}{\alpha_K} \cdot \frac{\frac{R_l}{\alpha_{eq}} - h \cdot R_v}{1 - h} \tag{B.2}$$

Développement limité Dans la littérature, il est courant d'effectuer un développement limité au premier ordre de cette équation, en supposant que $\alpha_{eq} = 1 + \epsilon_{eq} \simeq 1$, $\alpha_K = 1 + \epsilon_K \simeq 1$, et en utilisant la définition de la notation δ : $R = \frac{\delta}{1000} + 1 \simeq 1$. On obtiens alors :

$$\delta_e = \frac{\delta_l - h \cdot \delta_v - \epsilon_{eq} - \epsilon_K}{1 - h}$$

B.3.2 Formulation du coefficient de fractionnement cinétique

Le coefficient de fractionnement cinétique (équation B.1) est le rapport de la diffusivité de l'eau normale par celle de l'isotope. Les diffusivités se décomposent en deux diffusivités : turbulente et moléculaire. La diffusivité turbulente p_t , est liée aux mouvement convectifs près de la surface, et est donc la même pour l'eau normale et les isotopes. En revanche, les diffusivités moléculaires p_m des différentes molécules d'eau dans la vapeur varient selon le type de molécule. On a :

$$\frac{p_{mi}}{p_m} = \left(\frac{D_i}{D}\right)^n$$

avec n un coefficient qui vaut 0.5 pour un régime turbulent, 0.67 pour un régime laminaire et 1 pour un régime stagnant ([Brutsaert, 1975]).

Notons

$$\theta = \frac{p_m}{p}$$

θ tend vers 1 si le vent est très faible et que la diffusivité moléculaire est beaucoup plus grande que la diffusivité turbulente. θ tend vers 0 au contraire quand le vent est très fort et que le transport d'eau est majoritairement turbulent.

On obtient alors :

$$\alpha_K = \frac{1}{1 - \theta + \theta \cdot \left(\frac{D_i}{D}\right)^n} \tag{B.3}$$

Cas de l'évaporation océanique Sur océan, la diffusivité turbulente est toujours importante. Le rapport θ peut se calculer en fonction de la vitesse du vent. [Merlivat and Jouzel, 1979] ont établi expérimentalement des relations entre coefficient de fractionnement cinétique et vent de surface. Par exemple, pour des vents inférieurs à 7m/s, $\epsilon_K \simeq 6‰$ pour l'$H_2^{18}O$.

Cas de l'évaporation d'une petite étendue d'eau Sur une petite étendue d'eau, par vent faible, la diffusivité turbulente devient négligeable par rapport à la diffusivité moléculaire. On obtient alors, pour $\theta = 1$,

$$\alpha_K = \left(\frac{D}{D_i}\right)^n$$

C'est la formulation utilisée par [Stewart, 1975] pour l'évaporation des gouttes, avec n=0.58.

Cas de l'évaporation d'un sol Pour l'évaporation d'un sol, [Mathieu and Bariac, 1996] suppose que l'équation B.3 revient à une équation du type [Stewart, 1975] en introduisant un exposant n'_k.

$$\alpha_K = \left(\frac{D}{D_i}\right)^{n'_k} \tag{B.4}$$

n'_K vaut 0.5 pour un sol saturé en eau (diffusivité turbulente non négligeable), et tend vers 1 pour un sol très sec (la diffusivité moléculaire domine).

Par exemple, de manière explicite ou non, [Yepez et al., 2003, Lai et al., 2006a, Tsujimura et al., 2007] utilisent cette formulation avec $n'_K = 1$, [Moreira et al., 1997] avec $n'_K = 0.67$, [Williams et al., 2004] avec $n'_K = 0.5$ pour les sols irrigués, tandis que [Mathieu and Bariac, 1996] utilisent une relation empirique entre n'_K et l'humidité du sol.

Annexe C

Evolutions de la composition isotopique lors de quelques transformations

C.1 Distillation de Rayleigh

C.1.1 Condensation avec perte immédiate du condensat

La composition d'une vapeur qui condense progressivement et perd son condensat immédiatement par précipitation suit ce qu'on appelle une distillation de Rayleigh. Soit une masse initiale m_{v0} de vapeur de composition R_{v0}. Au cours de sa distillation, on note sa masse résiduelle d'eau et d'isotopes m_v et x_v, et son rapport isotopique $R_v = \frac{x_v}{m_v}$.

La variation de rapport isotopique R_v au cours d'un incrément de condensation est :

$$dR_v = \frac{dm_v}{m_v} \cdot \left(\frac{dx_v}{dm_v} - R_v \right) = \frac{dm_v}{m_v} \cdot (R_c - R_v)$$

Cet incrément de condensation de composition R_c se forme en équilibre avec la vapeur :

$$R_c = \alpha \cdot R_v$$

avec α le coefficient de fractionnement effectif, comprenant le fractionnement à l'équilibre et éventuellement un fractionnement cinétique (annexes B.2 et B.3.1).

Donc

$$\frac{dR_v}{R_v} = \frac{dm_v}{m_v} \cdot (\alpha - 1)$$

En notant $f = \frac{m_v}{m_{v0}}$ la fraction de vapeur résiduelle, on obtient donc par intégration :

$$R_v = R_{v0} \cdot f^{\alpha - 1} \tag{C.1}$$

C.1.2 Evaporation dans un air sec : une distillation de Rayleigh "inverse"

Soit une masse m_{l0} de liquide de composition R_{l0} qui se réévapore progressivement. On suppose que l'air environnement est très sec et que la vapeur évaporée ne s'accumule pas autour de la goutte. Au cours de la réévaporation de la goutte, on note sa masse résiduelle d'eau $m_l = f \cdot m_{l0}$, sa masse résiduelle d'isotopes x_l, et son rapport isotopique $R_l = \frac{x_l}{m_l}$.

Comme précédemment, la variation de rapport isotopique R_l au cours d'un incrément d'évaporation est :

$$dR_l = \frac{dm_l}{m_l} \cdot (R_e - R_l)$$

La composition de l'incrément d'évaporation R_e est donnée par l'équation de [Craig and Gordon, 1965] (équation B.2). Dans le cas une atmosphère sèche ($h = 0$), on a :

$$R_e = \frac{R_l}{\alpha}$$

avec $\alpha = \alpha_{eq} \cdot \alpha_K$ le coefficient de fractionnement effectif, comprenant le fractionnement à l'équilibre α_{eq} et cinétique α_K.

Donc

$$\frac{dR_l}{R_l} = \frac{dm_l}{m_l} \cdot (\alpha - 1)$$

Ceci s'intègre en :

$$R_l = R_{l0} \cdot f^{\frac{1}{\alpha}-1}$$

C.1.3 Pentes dans le diagramme $\delta D - \delta^{18}O$ lors d'une distillation de Rayleigh

Nous avons vu qu'au premier ordre, les données de précipitations s'alignent autour de la droite des eaux météoriques $\delta D = 8 \cdot \delta^{18}O + 10‰$ (figure 1.3). Nous étudions ici la pente de la trajectoire d'une distillation dans le diagramme $\delta D - \delta^{18}O$.

La distillation de Rayleigh (équation C.1) s'écrit en notation δ sous la forme :

$$\delta_v + 1000 = (\delta_{v0} + 1000) \cdot f^{\alpha - 1} \tag{C.2}$$

Lors d'un petit incrément de fraction condensée df, la variation de la composition de la vapeur $\delta = \left(\frac{R}{R_{SMOW}} - 1\right) \cdot 1000$ se calcule en dérivant l'équation C.2 :

$$d\delta_v = (\delta_{v0} + 1000) \cdot (\alpha - 1) \cdot f^{\alpha - 2} \cdot df$$

La pente dans le diagramme $\delta D - \delta^{18}O$ est donc :

$$\frac{d\delta D_v}{d\delta^{18}O_v} = \frac{(\delta D_{v0} + 1000) \cdot (\alpha_{HDO} - 1) \cdot f^{\alpha_{HDO} - 2} \cdot df}{(\delta^{18}O_{v0} + 1000) \cdot \left(\alpha_{H_2^{18}O} - 1\right) \cdot f^{\alpha_{H_2^{18}O} - 2} \cdot df}$$

Ce qui donne après simplifications et utilisation de l'équation C.2 :

$$\frac{d\delta D_v}{d\delta^{18}O_v} = \frac{\delta D_v + 1000}{\delta^{18}O_v + 1000} \cdot \frac{\alpha_{HDO} - 1}{\alpha_{H_2^{18}O} - 1} \tag{C.3}$$

Pente lors de la condensation d'un liquide Le facteur $\frac{\alpha_{HDO}-1}{\alpha_{H_2^{18}O}-1}$ augmente légèrement avec la température, de 8.7 à 20°C à 11.1 à -30°C. En parallèle, la vapeur est d'autant plus appauvrie que la température est faible, par distillation de Rayleigh. Le facteur $\frac{\delta D_v+1000}{\delta^{18}O_v+1000}$ diminue donc avec la température, de 0.91 quand $\delta D_v \simeq -100‰$ (dans les tropiques) à 0.73 quand $\delta D_v \simeq -300‰$ (près des pôles). Il en résulte que la pente $\frac{d\delta D_v}{d\delta^{18}O_v}$ reste proche de 8. Ceci explique les pentes de 8 observées lorsque les différentes données diffèrent par une intensité de distillation. Le fait que cette pente soit relativement constante avec la température est un hasard, lié au fait que les évolutions opposées avec la température de chacun des deux facteurs de C.3 se compensent.

Pente lors de l'évaporation dans un air sec Dans le cas de l'évaporation dans un air sec (section C.1.2), le coefficient de fractionnement est $\alpha = \alpha_{eq} \cdot \alpha_K$. En prenant par exemple la formulation de [Stewart, 1975], pour laquelle $\alpha_K = (D/D')^n$, on obtient, pour une température de 20°C, $n = 0.58$ (évaporation d'une goutte) et des δ proches de 0, une pente de l'ordre de 3.6. Les pentes sont donc beaucoup plus faibles lors de l'évaporation.

C.2 Condensation à l'équilibre

Soit une masse initiale m_{v0} de vapeur de composition R_{v0}. On suppose cette fois qu'au cours de la condensation, le condensat formé reste dans le système et s'équilibre au fur et à mesure avec la vapeur : à tout moment,

$$R_l = \alpha \cdot R_v$$

avec α le coeffcient de fractionnement à l'équilibre, R_l et R_v les compositions du liquide et de la vapeur au fur et à mesure de la condensation.

La conservation des isotopes donne :

$$m_{v0} \cdot R_{v0} = m_v \cdot R_v + (m_{v0} - m_v) \cdot R_l$$

avec $m_v = f \cdot m_{v0}$ la masse de vapeur résiduelle.

Après réarangements, on déduit que :

$$R_v = \frac{R_{v0}}{f + \alpha \cdot (1 - f)}$$

C.3 Réévaporation d'un liquide

We consider the evaporation of a mass m_{l0} of liquid of composition R_{l0} into an air containing a mass m_{v0} of vapor of composition R_{v0}. The liquid can be the sea, a lake, soil water or raindrops. We consider the liquid and the vapor as a closed system.

As the reevaporation proceeds, we note m_l, m_v, R_l and R_v the liquid mass, vapor mass, liquid composition and vapor composition. We note f the remaining fraction in the liquid:

$$f = \frac{m_l}{m_{l0}}$$

C.3.1 Evolution of the liquid and vapor composition if the vapor composition varies little

We assume here that R_v varies little during the evaporation process (first order approximation for the vapor).

When considering the evaporation of a small water reservoir, R_l is affected by the evaporation process:

$$dR_l = \frac{dm_l}{m_l} \cdot \left(\frac{dx_l}{dm_l} - R_l \right) = \frac{dm_l}{m_l} \cdot (R_e - R_l)$$

where x_l is the isotopic equivalent of m_l.

Replacing R_e by its expression from equation B.2, we obtain:

$$dR_l = \beta \cdot (R_l - \gamma \cdot R_v) \cdot \frac{dm_l}{m_l} \tag{C.4}$$

where β and γ were defined by [Stewart, 1975]:

$$\beta = \frac{1 - \alpha_{eq} \cdot \alpha_K \cdot (1 - h)}{\alpha_{eq} \cdot \alpha_K \cdot (1 - h)}$$

$$\gamma = \frac{\alpha_{eq} \cdot h}{1 - \alpha_{eq} \cdot \alpha_K \cdot (1 - h)}$$

Integration of equation C.4 yields ([Stewart, 1975]):

$$R_l = R_{l0} \cdot f^{\beta} + \gamma \cdot R_{v0} \cdot \left(1 - f^{\beta}\right) \tag{C.5}$$

In the limit case where $h = 0$ (dry air), R_l follows an inverse Rayleigh distillation ($R_l = R_{l0} \cdot f^\beta$, appendix C.1.2). In the limit case where $h \rightarrow 1$ (saturated air), then the droplet reequilibrates with the surrounding vapor: $R_l \rightarrow \alpha_{eq} \cdot R_v$.

We can use a mass conservation equation to deduce the average value of the evaporation over the evaporation process, $\overline{R_e}$: isotopes in the initial liquid are redistributed into the final liquid and the evaporation:

$$m_{l0} \cdot R_{l0} = m_l \cdot R_l + (m_{l0} - m_l) \cdot \overline{R_e}$$

So by replacing R_l by its expression from equation C.5:

$$\overline{R_e} = \frac{R_{l0} \cdot \left(1 - f^{\beta+1}\right) - \gamma \cdot R_v \cdot f \cdot \left(1 - f^\beta\right)}{1 - f} \tag{C.6}$$

Similarily for the vapor, the mass conservation equation for total water is

$$m_{l0} + m_{v0} = m_l + m_v$$

and for isotopes:

$$m_{l0} \cdot R_{l0} + m_{v0} \cdot R_{v0} = m_l \cdot R_l + m_v \cdot R_v$$

So by replacing R_l by its expression from equation C.5:

$$R_v = \frac{R_{v0} \cdot \left(M - \gamma \cdot f \cdot \left(1 - f^\beta\right) + R_{l0} \cdot \left(1 - f^{\beta+1}\right)\right)}{M + 1 - f} \tag{C.7}$$

where M is the initial ratio of vapor mass to liquid mass:

$$M = \frac{m_{v0}}{m_{l0}}$$

If equation C.7 yields a composition significantly different from R_{v0}, then the first order approximation for the vapor is not valid. In this case the evolution of R_v during the evaporation process can be taken into account as detailed below.

C.3.2 Evolution of the liquid and vapor composition if both compositions vary

If R_v is affected by the reevaporation process,

$$dR_v = \frac{dm_v}{m_v} \cdot \left(\frac{dx_v}{dm_v} - R_v\right) = \frac{dm_v}{m_v} \cdot (R_e - R_v)$$

with x_v the isotopic equivalent of m_v.

Replacing R_e by its expression from equation B.2, we obtain:

$$dR_v = \frac{dm_l}{m_{l0} \cdot (M + 1 - f)} \cdot (-R_l \cdot (1 + \beta) + R_v \cdot (1 + \beta \cdot \gamma)) \tag{C.8}$$

Equations C.4 and C.8 constitute a system of two coupled differential equations.

The solution of this sytem is ([Bony et al., 2008]):

$$R_l = f^\beta \cdot g^{-\beta \cdot \gamma} \cdot \left(R_{l0} \cdot \left(1 + \gamma \cdot \beta \cdot \frac{J}{M \cdot m_{l0}}\right) + R_{v0} \cdot \gamma \cdot \beta \cdot \frac{J}{m_{l0}}\right) \tag{C.9}$$

$$R_v = R_{v0} \cdot g^{-1} \left(1 - f^{\beta+1} \cdot g^{-\beta \cdot \gamma} \cdot \gamma \cdot \beta \cdot \frac{J}{M \cdot m_{l0}}\right) + R_{l0} \cdot g^{-1} \cdot \frac{1}{M} \cdot \left(1 - f^{\beta+1} \cdot g^{-\beta \cdot \gamma} \cdot \left(1 + \gamma \cdot \beta \cdot \frac{J}{M \cdot m_{l0}}\right)\right) \tag{C.10}$$

with g the fractional increase of the vapor during the reevaporation process:

$$g = \frac{M+1-f}{M}$$

and

$$J = \int_{m}^{m_0} g^{\beta\cdot\gamma-1} \cdot f^{-(1+\beta)} \cdot dm_*$$

(Note that in the notations of [Bony et al., 2008], $\frac{q_{p0}}{A} = M \cdot m_{l0}$).

C.4 Evolution du d-excess et de l'^{17}O-excess pendant quelques transformations

C.4.1 Comparaison des définitions

Au premier ordre, δD varie 8 fois plus que le $\delta^{18}O$, et le $\delta^{17}O$ 0.528 fois plus. Les excess sont des paramètres de second ordre permettant de mesurer l'écart par rapport à ce comportement de premier ordre (figure C.1).

Ainsi, on définit le d-excess par :

$$d = \delta D - 8 \cdot \delta^{18}O$$

exprimé en ‰.

L'^{17}O-excess est défini légèrement différemment :

$$^{17}O\text{-excess} = 10^6 \cdot \left(\ln\left(\frac{\delta^{17}O}{1000}+1\right) - 0.528 \cdot \ln\left(\frac{\delta^{18}O}{1000}+1\right)\right)$$

exprimé en permeg.

Toutefois, pour des valeurs de δ proches de 0‰ (proches de celles de l'océan), un développement limité de premier ordre conduit à :

$$^{17}O\text{-excess} \simeq 10^3 \cdot \left(\delta^{17}O - 0.528 \cdot \delta^{18}O\right)$$

Les définitions du d-excess et de l'^{17}O-excess sont donc très similaires pour des valeurs de δ proches de 0‰. Les différences entre les définitions sont :

- les valeurs d'^{17}O-excess étant très petites, on les exprime en permeg, tandis que d est exprimé en ‰.
- le d-excess est défini linéairement alors que l'^{17}O-excess est défini logarithmiquement, ce qui conduit à des différences significatives pour des δ appauvris.

C.4.2 Distillation de Rayleigh

L'avantage de la définition logarithmique de l'^{17}O-excess est que l'^{17}O-excess de la vapeur est conservé au cours d'une distillation de Rayleigh.

^{17}O-excess

Par définition de l'^{17}O-excess.

$$^{17}O\text{-excess} = 10^6 \cdot \left(\ln\left(R_{H_2^{17}O}\right) - 0.528 \cdot \ln\left(R_{H_2^{18}O}\right)\right)$$

Si les rapports isotopiques sont issus d'une distillation de Rayleigh, alors :

$$R_x = R_{x,0} \cdot f^{\alpha_x - 1}$$

où x peut remplacer aussi bien $H_2^{17}O$, $H_2^{18}O$, HDO.

Donc

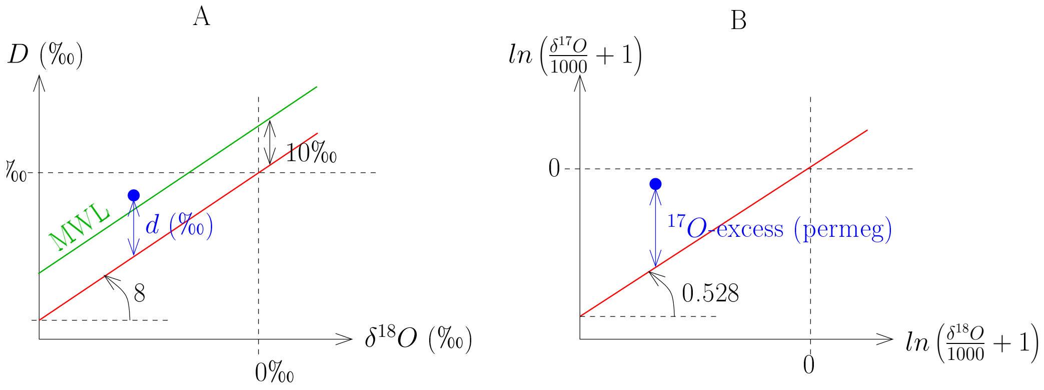

FIG. C.1 – A : représentation graphique de la définition du d-excess. B : représentation graphique de la définition de l'^{17}O-excess.

$$^{17}O\text{-excess} = 10^6 \cdot \left(\ln\left(R_{H_2^{17}O,0} \cdot f^{\alpha-1}\right) - 0.528 \cdot \ln\left(R_{H_2^{18}O,0} \cdot f^{\alpha-1}\right)\right)$$

Ce qui se simplifie en :

$$^{17}O\text{-excess} = {}^{17}O\text{-excess}_0 + 10^6 \cdot \ln(f) \cdot \left(\alpha_{H_2^{18}O} - 1\right) \cdot \left(\frac{\alpha_{H_2^{17}O} - 1}{\alpha_{H_2^{18}O} - 1} - 0.528\right) \tag{C.11}$$

Or par définition des fractionnements pour l'$H_2^{17}O$ et $H_2^{18}O$,

$$\alpha_{H_2^{17}O} = \left(\alpha_{H_2^{18}O}\right)^{0.529}$$

Un développement limité à l'ordre 1 donne donc :

$$\frac{\alpha_{H_2^{17}O} - 1}{\alpha_{H_2^{18}O} - 1} = 0.529$$

Comme $\alpha_{H_2^{18}O} - 1 \simeq 1$ et $0.529 \simeq 0.528$, le terme de droite est petit par rapport à ^{17}O-excess$_0$. Par exemple : pour $f = 0.9$, le terme de droite est de l'ordre de -1 permeg, à comparer à 20 à 40 permeg pour ^{17}O-excess$_0$.

d-excess

Variations selon les coefficients de fractionnement Par approximation de premier ordre du type $\delta D \simeq \ln(\delta D + 1)$, valable pour des δD proches de 0‰, on obtient une équation pour le d-excess similaire à l'équation C.11 :

$$d \simeq d_0 + 10^3 \cdot \ln(f) \cdot \left(\alpha_{H_2^{18}O} - 1\right) \cdot \left(\frac{\alpha_{HDO} - 1}{\alpha_{H_2^{18}O} - 1} - 8\right) \tag{C.12}$$

Le facteur $\frac{\alpha_{HDO}-1}{\alpha_{H_2^{18}O}-1}$ varie avec la température. Il vaut ainsi 8.7 à 0°C et 9.6 à 20°C. De même, la fraction résiduelle f varie au cours de la distillation. Ceci induit donc des variations du d-excess au cours de la distillation.

Variations "mathématiques" Le raisonnement précédent s'appuie sur un développement limité à l'ordre 1, et ne s'applique donc que pour des valeurs de δD proches de 0‰. Quand la distillation de Rayleigh est plus aboutie, le d-excess est significativement différent de C.12 et devient beaucoup plus élevé. Ainsi, dans le cas extrême où $\delta D \rightarrow 0$‰ et $\delta^{18}O \rightarrow 0$‰, $d \rightarrow +7000$‰.

Annexe D

Implémentation des isotopes stables de l'eau dans les modèles

Les isotopes sont introduits dans tous les modèles par l'ajout de nouvelles variables qui sont les équivalents isotopiques des variables représentant l'eau "normale". Ces nouvelles variables sont des tableaux contenant comme dimension additionnelle les différents isotopes. $H_2^{16}O$, $H_2^{17}O$, $H_2^{18}O$, HDO, HTO sont possibles, selon le choix de l'utilisateur.

Les isotopes sont advectés passivement par les différents flux de masse, mais subissent un fractionnement lors des changements de phase.

D.1 Isotopes dans le schéma de convection d'Emanuel

Cette annexe est basée sur une section de l'article [Bony et al., 2008].

Water stable isotopes ($H_2^{18}O$, HDO, $H_2^{17}O$) are passively transported along convective mass fluxes like "normal" water ($H_2^{16}O$), but are subject to fractionation whenever a phase change occurs. Equilibrium coefficients between vapor and liquid water or ice are calculated following [Majoube, 1971b] and [Majoube, 1971a, Merlivat and Nief, 1967]. Note that laboratory measurements from which these equations were inferred have been performed for temperatures higher than -40°C only. Therefore, there might be some uncertainty in the value of these coefficients at colder temperatures, such as those found in the upper troposphere (temperatures as low as -90°C may be simulated around the tropopause).

Condensation in convective updrafts When air parcels originating from the SL are lifted to a level i between cloud base and the level of neutral boyancy, condensate forms. Owing to the rapid ascension of air by convective updrafts, the characteristic time for parcel lifting (a few seconds) is much smaller than the characteristic time for precipitation processes (a few minutes or tens of minutes) ([Emanuel, 1997]). Consequently, it is assumed that all condensate formed between the SL and i remains inside the parcel until the end of the condensation process. Only then is a fraction of the total accumulated condensate precipitated.

When vapor condensates in the liquid form (at temperature higher than T_{melt}=0°C) , isotopic equilibrium is assumed between droplets and the residual vapor. Thus the isotopic ratios in vapor and liquid are respectively given by:

$$R_v = \frac{R_v^0}{\alpha_{liq}^{eq} - f_v \cdot (\alpha_{liq}^{eq} - 1)}$$

$$R_l = \alpha_{liq}^{eq} \cdot R_v$$

where R_v and R_l are the isotopic ratios in the vapor and liquid during the condensation process, R_v^0 is the initial isotopic ration in the vapor, α_{liq}^{eq} is the fractionation coefficient between vapor and liquid water and f_v is the residual fraction of vapor.

When vapor condensates in the frozen form (at temperatures lower than T_{ice}=-15°C), ice crystals are assumed to get isotopically isolated from the residual vapor ([Jouzel and Merlivat, 1984]), and thus a Rayleigh distillation is assumed: the vapor isotopic ratio is given by:

$$R_v = R_v^0 \cdot (f_v)^{\alpha_{ice}^{eff}-1}$$

where α_{ice}^{eff} is the fractionation coefficient between ice and vapor including a kinetic effect due to ice condensation in a sursaturated environment, as described by [Jouzel and Merlivat, 1984] (appendix B.2).

The isotopic ratio in ice is inferred from the water mass conservation, since all previously condensed water is conserved:

$$R_{ice} = \frac{R_v^0 - f_v \cdot R_v}{1 - f_v}$$

Between the two temperatures T_{melt}=0°C and T_{ice}=-15°C, liquid and solid phases coexist and the isotopic composition of the total condensate is assumed to be a linear combination of the isotopic composition in the liquid and solid phases.

Reevaporation of precipitation Le traitement de la réévaporation de la précipitation est détaillé dans l'annexe D.2.

D.2 Isotopes lors de la réévaporation de la pluie

The representation of isotopic species during reevaporation and diffusive exchanges was already described in detail in [Bony et al., 2008] and is only briefly summarized here.

We take the kinetic fractionation formulation from [Stewart, 1975]:

$$\alpha_K = \left(\frac{D'}{D}\right)^n \tag{D.1}$$

with n an exponent depending on the drop size: $n = 0.56$ for radii of 1.5mm and $n = 0.59$ for radii of 0.7mm ([Stewart, 1975]). We choose n=0.58. For n=0.58, $\epsilon_K \simeq 16‰$ for $\delta^{18}O$ and 14‰ for δD.

We use equation B.2 to calculate the composition of the reevaporation flux. In models, h can be the average relative humidity in the grid box or in the compartment in which the evaporation takes place (e.g. unsaturated downdraft in [Bony et al., 2008]). We note h_{box} this humidity.

However, in the case of the reevaporation of raindrops, using directly h_{box} in equation B.2 leads to too strong kinetic fractionation ([Bony et al., 2008]). In reality, the relative humidity h is expected to be higher than h_{box}, due to (1) the reevaporation of the raindrops humidifying its surroundings and (2) colder raindrops than the surrounding air. We thus use in [Bony et al., 2008] and [Risi et al., 2010a] an effective relative humidty h_{eff}, parametrized as:

$$h_{eff} = \phi + (1 - \phi) \cdot h_{box}$$

with ϕ a tunable parameter. ϕ was set to 0.9 in [Bony et al., 2008] to optimize the simulation of the amount effect and d-excess. Sensitivity to this parameter in the 2D model is discussed in section 4.3.4.

We consider the evolution of both the raindrop and vapor compositions, as explained in appendix C.3.2.

D.3 Isotopes dans LMDZ

D.3.1 Principe général de l'implémentation

Pour chaque variable représentant de l'eau, on ajoute une variable équivalente isotopique : par exemple, si une variable s'appelle q(ip1jmp1,llm,nqmx), on définit xt(ntraciso,ip1jmp1,llm,nqmx).

Cette variable contient à la fois les isotopes classiques et les isotopes liés au water tagging (chapitre E).

La plupart du temps, les isotopes sont traités exactement comme l'eau. Il y a 3 types de cas où les calculs isotopiques diffèrent de l'eau :

1. fractionnements isotopiques (annexe B.1).
2. advection des traceurs par la dynamique (annexe D.3.2)
3. cas "délicats", où de simples transports ou mélanges peuvent donner lieu à des fractionnements non physiques et/ou à des valeurs aberrantes de composition isotopiques annexe D.3.3).

D.3.2 Advection de l'eau par la dynamique

Water isotopes are advected passively during the large-scale water advection. However, for numerical reasons, the advection of water isotopes can be problematic in some schemes (e.g. [Joussaume, 1989, Mathieu et al., 2002]). We present here the Van Leer advection scheme ([Van Leer, 1977]) used in LMDZ-iso, explain the possible problem of isotopic advection and how we handle it. To simplify, we consider in the following a uni-dimensional advection along the x axis, with a westerly wind (figure D.1).

The Van Leer advection scheme

The Van Leer scheme ([Van Leer, 1977]) used in LMDZ is a finite volume advection scheme, conserving water mass. In the grid box i, m'_i , the total air mass at time $t+\Delta t$, is function of the total air mass at time t and the air mass fluxes on the left and right border, $U_{i-1/2}$ and $U_{i+1/2}$ respectively:

$$m'_i = m_i + U_{i-1/2} - U_{i+1/2}$$

Similarly, the averaged specific humidity in grid box i at time $t+\Delta t$, q'_i, is function of the specific humidity at time t and the water flux on the left and right border,$F_{i-1/2}$ and $F_{i+1/2}$.

$$q'_i = \frac{q_i \cdot m_i + F_{i-1/2} - F_{i+1/2}}{m'_i}$$

Water fluxes (for example $F_{i-1/2}$) are calculated as the product of the air mass flux ($U_{i-1/2}$) and the specific humidity of the advected air ($q_{\breve{i-1/2}}$):

$$F_{i-1/2} = U_{i-1/2} \cdot q_{\breve{i-1/2}}$$

In the Van Leer scheme, $q_{\breve{i-1/2}}$ is interpolated between the averaged specific humidity of the adjacent boxes, so that $q_{\breve{i-1/2}}$ is a function of (q_i, q_{i+1}, q_{i-1}).

As long as $q_{\breve{i-1/2}}$ is intermediate between q_i and q_{i-1}, the monotony of the scheme is ensured: q'_i remains intermediate between q_i and q_{i-1} ([Van Leer, 1977, Hourdin, 2005]).

Implementation of water isotopes in the Van Leer scheme

As for water, the isotopic equivalent of specific humidity, X, is advected in finite volume:

$$X'_i = \frac{X_i \cdot m_i + G_{i-1/2} - G_{i+1/2}}{m'_i}$$

with $G_{i-1/2}$ and $G_{i+1/2}$ the isotope fluxes at the left and right boundaries. The isotope mass is thus conserved during advection. The isotope flux at the left boundary, $G_{i-1/2}$, is calculated as the product $U_{i-1/2}$ and the isotopic content of the advected air $X_{\breve{i-1/2}}$:

$$G_{i-1/2} = U_{i-1/2} \cdot X_{\breve{i-1/2}}$$

In a purely Lagrangian framework, transport should simultaneously conserve the water, the isotopic content and the isotopic ratio $R = X/q$: indeed, it can be shown that if X follows the

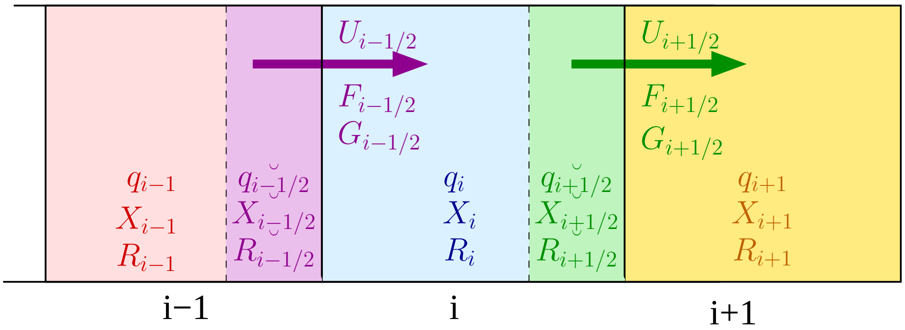

Figure D.1: Illustration of the advection of water isotopes by the Van Leer scheme.

same conservation equation as q of the form $\frac{\partial q}{\partial t} + u \cdot \frac{\partial q}{\partial x} = 0$, then R also follows the same conservation equation.

In the Van Leer scheme, however, due to the discretization, X and R cannot follow simultaneously the same equations as q. A choice has thus to be made regarding how to handle the transport of water isotopes.

If X were to be treated exactly like water, $X_{i\breve{-}1/2}$ should be interpolated between the adjacent grid boxes, so that $X_{i\breve{-}1/2}$ is a function of (X_i, X_{i+1}, X_{i-1}). Then the monotony of the transport would be ensured for q and X. However, the monotony would not be ensured for R, due to the non-linearity of R as a function of X and q. In particular, it could happen that the isotopic ratio after advection, R'_i, becomes either larger or smaller than the ratios in both adjacent grid boxes. Spurious variations of the isotopic ratio could thus appear.

Problems arising from representing the isotopic mixing ratio exactly like the water mixing ratio are justified physically: isotopes are not transported independently from the water, but inside water.

Therefore, to ensure that isotopes are not transported without water, we calculate $X_{i\breve{-}1/2}$ as the product of the advected water content $q_{i\breve{-}1/2}$ and the isotopic ratio of this advected water $R_{i\breve{-}1/2}$:

$$X_{i\breve{-}1/2} = q_{i\breve{-}1/2} \cdot R_{i\breve{-}1/2}$$

To ensure the monotony of the isotopic ratio, $R_{i\breve{-}1/2}$ is interpolated between the adjacent boxes, so that $R_{i\breve{-}1/2}$ is a function of (R_i, R_{i+1}, R_{i-1}).

This representation of the isotopic transport ensures both the conservation of the mass of water isotopes (finite volume scheme) and the monotony of the isotopic ratio.

D.3.3 Cas "délicats"

La plupart du temps, on utilise des opérations similaires à l'eau normale.

Par exemple, si pour l'eau normale q est incrémentée de dq :

q'=q+dq

Alors de même pour les isotopes :

X'=X+dX

Mais il existe certains cas délicats où calquer exactement les calculs isotopiques sur l'eau normale poserait des problèmes. C'est le cas quand il y a des eaux négatives.

Exemple de problème d'eau négative on considère l'ajout de l'eau de pluie dans l'eau du sol :

qsol'=qsol+P*dt

Si qsol>=0, alors l'équivalent isotopiques est :

Xsol'=Xsol+PX*dt

Mais cela induirait des fractionnements isotopiques non physiques si qsol<0. Par exemple, si :

qsol= -1mm

δ_{sol}= -500‰
P= 2mm
δ_P= -50‰.

On obtiendrait alors dans ce cas qsol'= 1mm et $\delta'_{sol} = \frac{-500\cdot(-1)+2\cdot(-50)}{-1+2} = +400$‰, ce qui est aberrant

Dans le cas où qsol<0, on calcule alors Xsol' par :
Xsol'=qsol'*PX/P
avec PX l'équivalent isotopique de P.

Ceci évite les fractionnements non physiques. Toutefois, la masse n'est pas conservée dans ce cas.

Quand il y a des eaux négatives, un choix doit généralement être fait entre conservation de la masse ou valeurs raisonnables des isotopes. Une alternative est d'empêcher le modèle de simuler des eaux négatives.

D.3.4 L'$H_2^{17}O$ dans LMDZ et les problèmes associés

Dans LMDZ, l'implémentation de l'$H_2^{17}O$ s'est révélée problématique. A bout de quelques itérations, l'^{17}O-excess chute à des valeurs anormalement basses aux hautes latitudes, allant jusqu'à -10 permeg en Antarctique (au lieu de 30 à 40 permeg). Cette diminution a lieu même lorsque les paramétrisations physiques sont débranchées, c'est-à-dire quand seules la dynamique et l'advection des traceurs fonctionnent. La diminution anormale de l'^{17}O-excess a lieu dans l'advection des traceurs, et a pu être reproduite offline dans des cas idéalisés 1D. Cette diminution apparaît lorsqu'on advecte l'eau et ses isotopes au travers de gradients de $\delta^{18}O$. En effet, comme expliqué au chapitre 7, la définition de l'^{17}O-excess étant logarithmique, le mélange de deux eaux de $\delta^{18}O$ différents peut donner une eau d' ^{17}O-excess plus bas que le minimum des ^{17}O-excess initiaux. Comme l'advection des traceurs dans le schéma de [Van Leer, 1977] se fait par mélange de proche en proche entre les cases successives, l'^{17}O-excess diminue donc lors de l'advection. Les valeurs simulées d'^{17}O-excess trop basses aux hautes latitudes dans LMDZ sont peut-être liées à une advection trop diffusive par ce schéma.

Ce problème n'a pas encore été résolu à ce jour (automne 2009) dans LMDZ.

D.4 Isotopes dans ORCHIDEE

D.4.1 Bilan d'eau du sol

Les isotopes ont été implémenté dans le module d'hydrologie continental d'ORCHIDEE : SECHIBA. Dans la version du modèle utilisée ici, le sol est représenté par le modèle de deux couches de Choisnel ([Choisnel, 1977, Choisnel et al., 1995]).

Les flux entrant et sortant du sol sont indiqués sur la figure D.2 :

$$q_l(t) = q_l(t-dt) + dt \cdot (P - E + M - \mathcal{R} - D)$$

avec $q_l(t)$ la hauteur d'eau dans le sol au temps t, dt le pas de temps d'ORCHIDEE (=30 minutes), P, E, M, $\mathcal{R}$ et D respectivement la précipitation liquide, l'évaporation (ou rosée si $E < 0$), la fonte de la neige, le ruissellement et le drainage.

Chacun des 13 types de végétation, dont le sol nu, a son propre sol.

Ce bilan d'eau "normale" n'est jamais modifié par les isotopes et le traitement des isotopes est toujours cohérent avec celui de l'eau normale.

Les flux d'eau normale comme des isotopes sont traités séquentiellement. Par exemple, on fait d'abord entrer dans le sol les flux entrants. Puis ensuite seulement on évapore une partie de l'eau du sol.

Deux traitements du sol sont possibles :

1. on assimile le sol à un seau d'eau homogène de composition uniforme. Les deux buckets de Choisnel sont "raccordés" pour éviter les discontinuités de composition isotopique lors de la reconnection ou séparation des buckets et éviter que les variations de hauteur du réservoir de

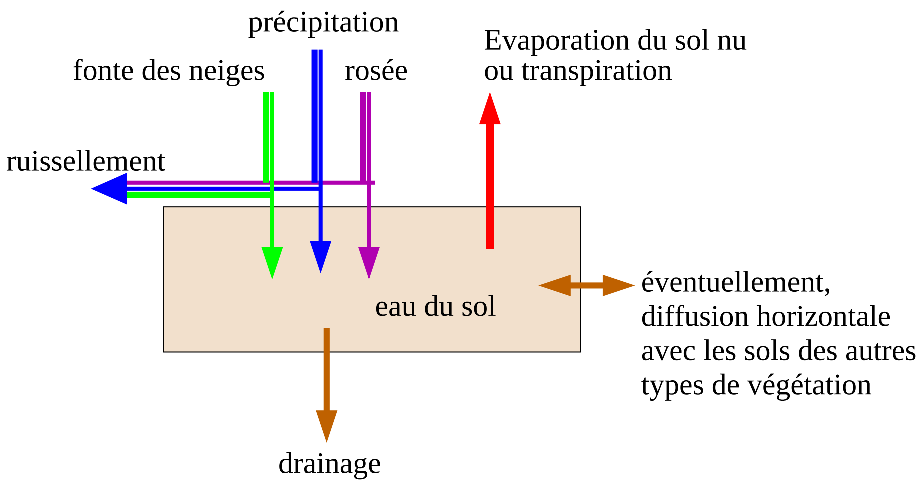

FIG. D.2 – bilan d'eau du sol dans le module hydrologique de SECHIBA.

surface aient un effet artificiel sur la composition isotopique des flux évaporés. Ce “raccordage” des deux couches n'est “vu” que par les isotopes.

2. on représente la distribution verticale des isotopes dans le sol. Pour cela, on ajoute une discrétisation verticale pour la composition isotopique. De nouveau, cette discrétisation verticale n'est “vue” que par les isotopes.

D.4.2 Evaporation du sol nu

Les flux d'eau entrant dans le sol (pluie, rosée, fonte des neiges) sont ajoutés au sol lors d'une étape précédente. Ci dessous, on explique la formule utilisée pour le fractionnement associé à l'évaporation du sol nu (D.3).

On assimile le sol à un seau contenant de l'eau de composition isotopique homogène. On néglige la vapeur du sol. On veut calculer le flux évaporatoire isotopique x_E connaissant le flux évaporatoire E, l'état du sol et l'état de l'atmosphère au-dessus.

Craig et Gordon A l'interface entre le sol et l'atmosphère, le rapport isotopique du flux évaporatoire $R_E(t) = \frac{x_E}{E}(t)$ est donné par la formule de Craig et Gordon ([Craig and Gordon, 1965], equation B.2) :

$$R_E(t) = \frac{R_l(t) - \alpha_{eq} \cdot h \cdot R_v(t)}{\alpha_K \cdot \alpha_{eq} \cdot (1-h)} \tag{D.2}$$

avec $R_l(t)$ le rapport isotopique de l'eau du sol “concernée” par l'évaporation, $R_v(t)$ et h le rapport isotopique et l'humidité relative de l'atmosphère au-dessus du sol, α_{eq} et α_K les coefficients de fractionnement à l'équilibre et cinétique.

Si on considère que le réservoir de vapeur dans la couche limite est très grand devant l'évaporation $E \cdot \Delta t$, alors on peut supposer que $R_v(t)$ est constante et égale à R_{v0} (approximation de premier ordre pour la vapeur). En revanche, on considère l'évolution de R_l au cours de l'évaporation pendant un pas de temps, et on utilise donc les équations C.5 et C.6

avec

$$f = \frac{q_l}{q_{l0}}$$

où q_{l0} est la quantité initiale d'eau dans le sol et q_l la quantité d'eau résiduelle.

Approximation pour q_{l0} Physiquement, q_{l0} représente la hauteur d'eau du sol affectée isotopiquement par l'évaporation. Elle dépend de la diffusion des isotopes dans l'eau du sol : considérons par exemple ces deux cas extrêmes :

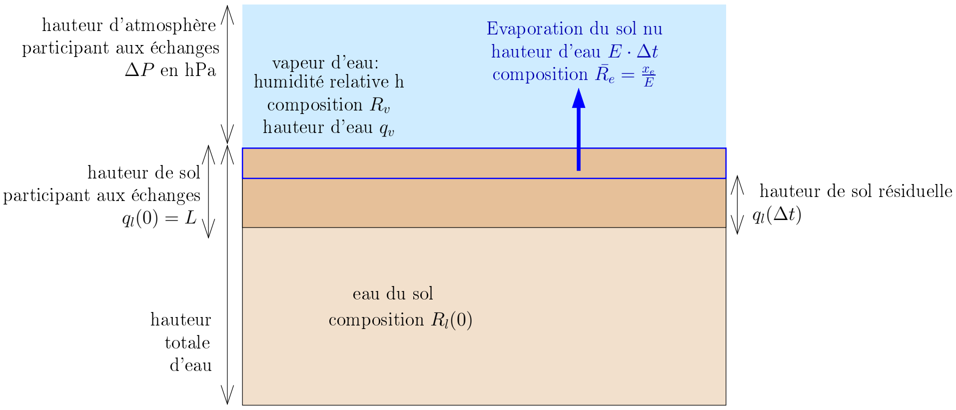

Fig. D.3 – Principe et notations pour le traitement de l'évaporation du sol nu.

1. Si les isotopes diffusent infiniment bien, alors toute l'eau du sol est bien brassée. $q_l(0)$ réprésente alors la hauteur totale initiale d'eau du sol. Mais si on utilise cette approximation dans les modèles, on obtient des valeurs aberrantes de composition d'évaporation dans certains cas (h près de 1).
2. Si au contraire, les isotopes ne diffusaient pas du tout, alors $q_l(0)$ serait égale à la hauteur d'eau prélévée par évaporation : $E \cdot dt$. On n'aurait alors aucun fractionnement lors de l'évaporation. De manière similaire, la sublimation de la glace n'est pas associé à un fractionnement, car les diffusivités dans la glace sont très faibles.

La longueur caractéristique de la diffusion pendant le pas de temps Δt est $L = \sqrt{K_D \cdot \Delta t}$, avec K_D la diffusivité des isotopes dans l'eau du sol. Ici, on fait donc l'approximation que $q_{l0} = L$**.**

On calcule K_D d'après [Braud et al., 2005], en négligeant le terme de dispersion :

$$K_D = D_i^l \cdot \tau \cdot \theta_l \tag{D.3}$$

avec D_i^l la diffusivité moléculaire de l'isotope dans l'eau, τ la tortuosité du sol et θ_l le contenu volumétrique d'eau liquide. Pour faire simple, on prend $D_i^l = 2.5 \cdot 10^{-9}\, m^2/s$ pour tous les isotopes quelque soit la température et $\tau \cdot \theta_l$ est un paramètre ajustable, pris par défaut à 0.1 (ordre de grandeur dans [Braud et al., 2005]). L est de l'ordre de 0.7mm pour $\Delta t = 30min$.

Comparaison aux traitement dans les autres modèles :

- [Melayah et al., 1996] utilisent des pas de temps très petits (moins d'une minute) et une discrétisation verticale très fine près du sol (<1mm). Cela leur permet d'utiliser l'approximation à l'ordre 0 de la formule de Craig et Gordon. Mais dans notre cas, le pas de temps est long (30 minutes), d'où la nécessité de considérer les variations de $R_l(t)$ au cours du pas de temps.
- Ce traitement est cohérent avec la façon dont on traite la réévaporation des gouttes dans le schéma de convection dans LMDZ ([Bony et al., 2008]), à part qu'on fait ici l'approximation de premier ordre pour la vapeur.

Cas particulier pour h=1 Quand h=1, l'équation C.6 ne s'applique pas ([Stewart, 1975]). On suppose alors que le sol subit une rééquilibration partielle avec la vapeur au dessus, par échanges diffusifs. La composition du flux isotopique d'évaporation, noté x_e, est calculée par un bilan de masse en supposant que la partie supérieure du sol (hauteur L) s'équilibre isotopiquement avec une quantité q_v de vapeur au dessus (vapeur contenue dans une couche d'épaisseur ΔP d'atmosphère, au choix de l'utilisateur) :

$$x_E = \frac{L \cdot q_v \cdot (R_{l0} - \alpha_{eq} \cdot R_{v0}) + E \cdot \Delta t \cdot (L \cdot R_{l0} + \alpha_{eq} \cdot R_{v0} \cdot q_v)}{q_v + E \cdot \Delta t + (L - E \cdot \Delta t) \cdot \alpha_{eq}}$$

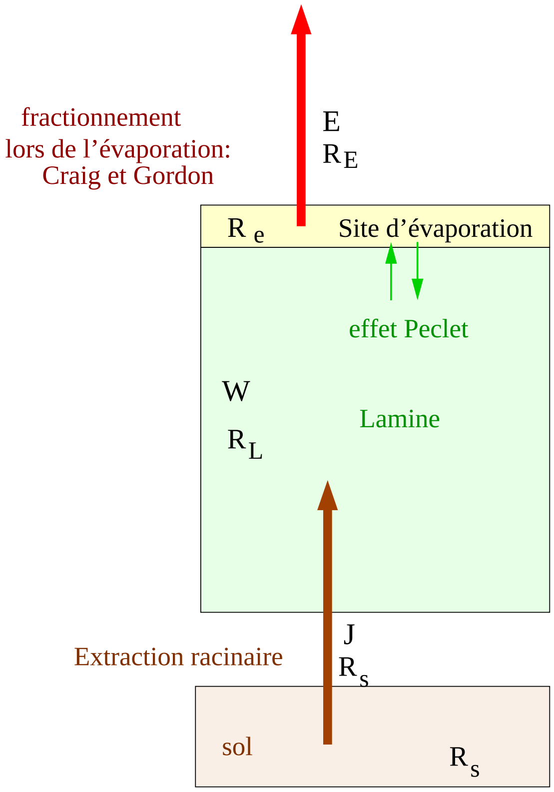

FIG. D.4 – Principe et notations pour le traitement de la transpiration.

D.4.3 Ruissellement et drainage

Dans le modèle de Choisnel de SECHIBA, ruissellement et drainage sont produits lorsque la hauteur d'eau du sol dépasse une hauteur d'eau maximale. Ce débordement est partitionné par défaut en 5% de ruissellement, et 95% de drainage. On suppose que le ruissellement de surface a la même composition que les flux entrant dans le sol (précipitation, fonte de la neige, rosée) qui le font déborder, et que le drainage a la composition du sol total.

D.4.4 La transpiration et l'eau des feuilles

La transpiration peut-être traité en régime stationnaire ou non stationnaire. On s'appuie surtout sur l'article [Farquhar and Cernusak, 2005], dont on utilise des notations similaires (figure D.4). La figure D.5 résume les différentes façon de traiter l'eau des feuilles implémentées dans ORCHIDEE, et les approximations sous-jacentes.

En régime stationnaire

On suppose que la végétation n'a aucune capacité de stockage de l'eau. Tout ce qui est exrait des racines est instantanément transpiré. La composition du flux transpiratoire (R_E) est donc la même que celle du sol (R_s).

Comme expliqué dans [Cuntz et al., 2007], la composition des feuilles au site d'évaporation R_e peut avoir un intéret pour la composition du CO_2 et de l'O_2. Au contraire, c'est la composition de la lamine R_L qui impacte la composition de la cellulose, d'intérêt paléoclimatologique. Ici, comme la feuille a une capacité nulle de stockage, on suppose $R_L = R_e$. La composition isotopique des feuille est diagnostiquée d'après l'équation de Craig et Gordon ([Craig and Gordon, 1965]) :

$$R_e = R_e^{RP} = \alpha_{eq}\alpha_K(1-h)R_{sol} + \alpha_{eq}h \cdot R_v \tag{D.4}$$

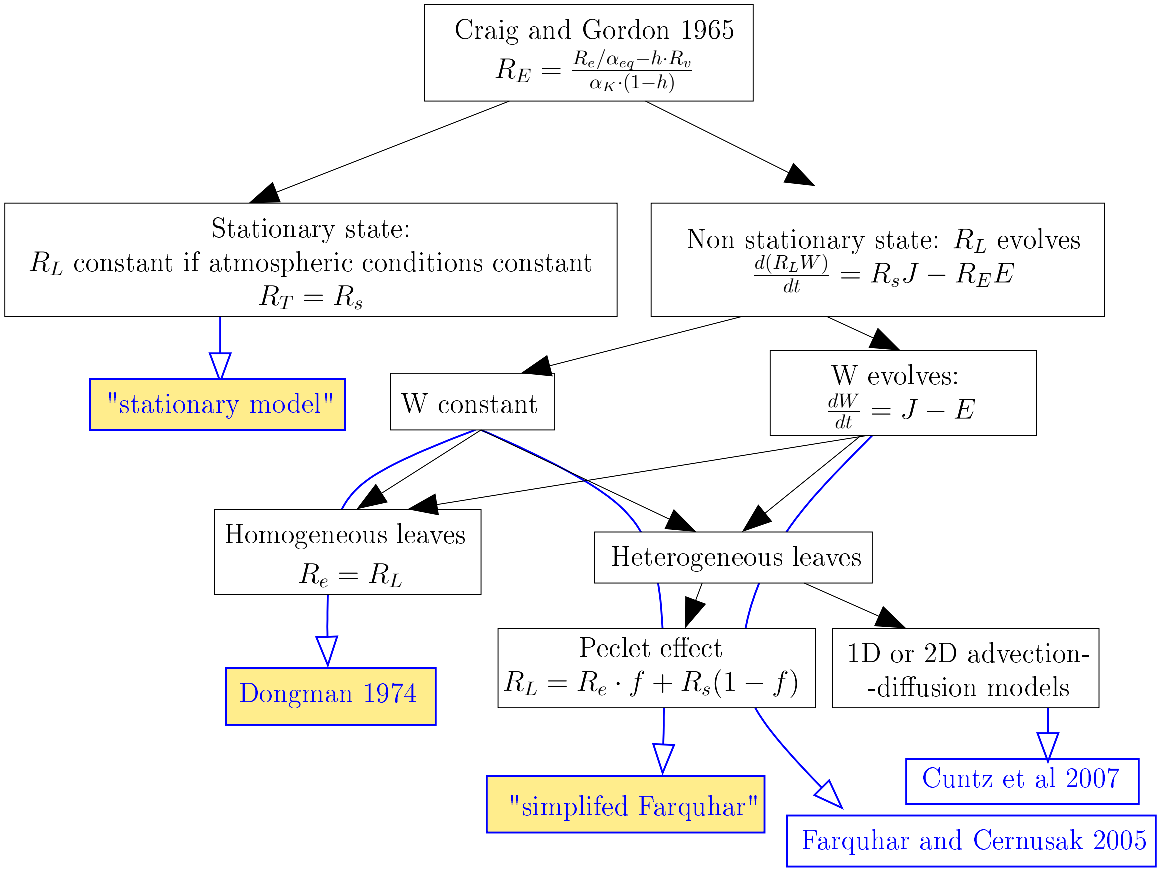

FIG. D.5 – Différentes façons de traiter l'eau des feuilles dans les modèles de surface continentales (rectangles bleus), selon différentes hypothèses (rectangles noirs). Les trois façons implémentées dans ORCHIDEE sont coloriées en jaune. Les notations ont été définies dans la figure D.4

Le régime stationnaire est suffisant pour étudier ce qui se passe à l'échelle supérieure à la journée. Pour étudier le cycle diurne, au contraire, le régime stationnaire n'est pas suffisant ([Cuntz et al., 2007]).

En régime non stationnaire

En régime non stationnaire, on prend en compte la capacité de stockage en eau de la végétation ($W > 0$). La composition de l'eau extraite du sol par les racine est toujours la même que celle du sol (R_s), mais la composition de l'eau transpirée n'est pas nécessairement égale à celle extraite ($R_s \neq R_E$).

La conservation de la masse et des isotopes donne :

$$\frac{dW}{dt} = J - E \tag{D.5}$$

$$\frac{d\left(R_L W\right)}{dt} = R_s \cdot J - R_E \cdot E \tag{D.6}$$

E est le flux d'évaporation en $E\ kg/s/m^2$ de feuilles et W le contenu en eau des feuilles par unité de surface de feuilles en kg/m^2.

On fait ici l'approximation, contrairement à [Farquhar and Cernusak, 2005] mais comme [Dongmann et al., 1974], que le contenu en eau de la feuille W est constant. On a donc :

$$\frac{dR_L}{dt} = \frac{E}{W} \cdot \left(R_s - R_E\right) \tag{D.7}$$

Pour déduire l'évolution de R_L, R_e et la composition du flux d'évaporation $R_E = \frac{x_E}{E}$, deux degrés de complexité ont été programés : formule de [Dongmann et al., 1974] et formule de [Farquhar and Cernusak, 2005] simplifiée.

Formule de [Dongmann et al., 1974] On suppose ici que la composition de la feuille est homogène : $R_L = R_e$.

L'équation D.7 couplée à l'équation de Craig et Gordon (D.4) donne :

$$\frac{dR_L}{dt} = \frac{E}{W \cdot \alpha_{eq} \cdot \alpha_K \cdot (1-h)} \left(R_e^{RP} - R_L\right) = \frac{R_e^{RP} - R_L}{\tau}$$

avec τ le temps d'équilibration :

$$\tau = \frac{W \cdot \alpha_{eq} \cdot \alpha_K \cdot (1-h)}{E}$$

Comme dans [Dongmann et al., 1974], on utilise le fait que $\alpha_{eq} \cdot \alpha_K \sim 1$. D'autre part, E est une fonction de h de la forme $E = c \cdot (1-h)$, avec c la conductance totale. On a alors une formule plus simple pour τ et applicable quelque soit h :

$$\tau = \frac{W}{c}$$

Dans ORCHIDEE, on suppose $W = 0.36\, kg/m^2$ (même ordre de grandeur que dans [Farquhar and Cernusak, 2005]).

Au temps t, la nouvelle composition de la feuille est, si on néglige les variations de température, d'humidité et de composition de la vapeur et du sol au cours du pas de temps Δt :

$$R_L(t) = R_L(t-\Delta t) \cdot e^{-dt/\tau} + R_e^{RP}(t) \cdot \left(1 - e^{-\Delta t/\tau}\right)$$

La composition du flux d'évaporation est alors calculée de manière à conserver la masse d'eau et d'isotopes dans la feuille :

$$x_E = E \cdot R_s + \left(R_L(t) - R_L(t-\Delta t)\right) \cdot \frac{W}{\Delta t} \tag{D.8}$$

Formule de [Farquhar and Cernusak, 2005] simplifiée Ici, on prend en compte les variations spatiales de composition dans la feuille entre le site d'évaporation et la lamine. $R_L \neq R_e$. Cette différence de composition est traitée par l'équation "Peclet" :

$$R_L = R_e \cdot f + R_s(1-f) \tag{D.9}$$

avec

$$f = \frac{1-e^{-P}}{P}$$

et P le paramètre de Peclet (défini de manière similaire à [Cuntz et al., 2007]) :

$$P = \frac{E \cdot L_{eff} \cdot e_{eff}}{W \cdot D^i}$$

avec L_{eff} la longeur efficace de la diffusion dans la feuille, e_{eff} l'épaisseur moyenne des feuilles et D^i la diffusivité de l'isotopes i dans l'eau liquide. On prend dans ORCHIDEE $L_{eff} = e_{eff} = 8$ mm, valeurs empiriques cohérentes avec [Cuntz et al., 2007] et [Cuntz et al., 2007, Barnard et al., 2007].

La combinaison des équations D.7, et D.9) permet d'obtenir la composition de la lamine :

$$R_L(t) = R_L(t-dt) \cdot e^{-dt/\tau} + R_L^{RP}(t) \cdot \left(1 - e^{-dt/\tau}\right)$$

avec

$$R_L^{RP} = R_e^{RP} \cdot f + R_s(1-f)$$

et

$$\tau = \frac{W \cdot \alpha_K \cdot \alpha_{eq} \cdot f}{c}$$

La composition au site d'évaporation $R_e(t)$ est déduite par l'équation de Peclet (equation D.9). La composition du flux d'évaporation est enfin calculée de manière à conserver la masse dans la feuille (equation D.8).

Ceci est un cas particulier (W constant) de [Farquhar and Cernusak, 2005].

D.4.5 Prise en compte de la distribution verticale des isotopes dans le sol

Le but est de représenter de manière simple la distribution verticale des isotopes dans le sol, de façon a évaluer l'impact de la prise en compte des profils isotopiques sur la composition des flux d'évaporation, transpiration et de ruissellement. Le but ici n'est pas de reconstruire un modèle multi-couche de sol.

Discrétisation verticale

L'eau du sol est discrétisée en n couches (figure D.6a).

- La première couche a pour epaisseur L, avec $L = \sqrt{K_D \cdot dt} \sim 0.7mm$ (épaisseur caractéristique de la diffusion), pour faciliter le traitement de l'évaporation du sol nu détaillé dans la section D.4.2
- Les autres couches ont pour épaisseur $l = L \cdot r$. Le paramètre r est au choix de l'utilisateur (r=30 par défaut, donc l=21mm par défaut).
- La dernière couche a une épaisseur variable comprise entre l et $2 \cdot l$ afin que la hauteur totale d'eau dans le sol soit égale à la somme des hauteur des couches.

La hauteur d'eau maximale dans le sol dans le modèle de Choisnel est 30m (dans un sol de 2m). Si le sol est plein, il y a donc n=16 couches par défaut.

A chaque fois que de l'eau est ajoutée ou retranchée dans le sol, la discrétisation du sol est recalculée tout en conservant la masse d'isotopes et le profil isotopique, comme indiquée sur la figure D.6b dans l'exemple d'un ajout de précipitation par le haut du profil.

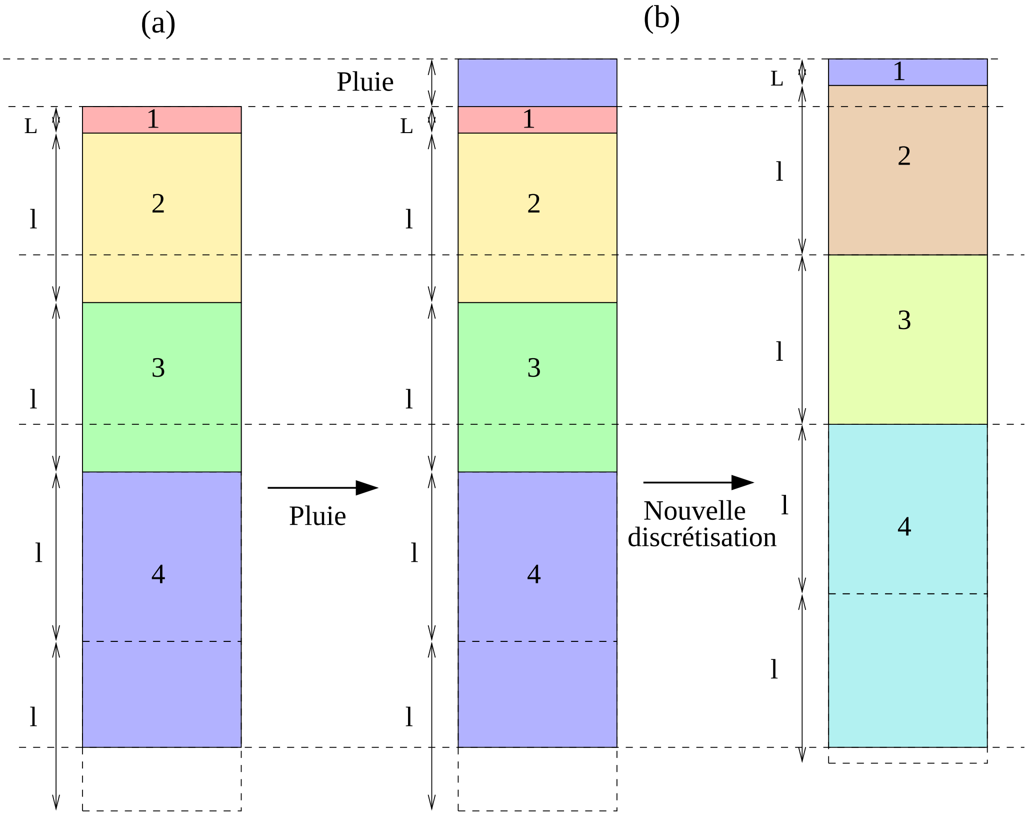

Fig. D.6 – Discrétisation verticale de l'eau du sol pour représenter le profil isotopique : (a) principe de la discrétisation. (b) Exemple du calcul de la nouvelle discrétisation en cas d'ajout de pluie par le haut du sol. Les couleurs réprésentent schématiquement la composition isotopique.

Evaporation et transpiration

L'évaporation du sol nu est traitée comme expliqué dans le cas du sol homogène, sauf qu'elle ne concerne que la première couche (ou les premières couches si l'évaporation dépasse la hauteur de la première couche).

Pour la transpiration, on suppose un profil d'extraction racinaire exponentiel, cohérent avec la façon dont sont calculés les stress hydriques dans l'hydrologie de Choisnel : la proportion d'eau transpirée par la ième couche délimitée par z_{i-1} en eau et z_i en bas par rapport à la transpiration totale est, pour $i > 1$:

$$\frac{T_i}{\sum_{i=1}^{n} T_i} = \frac{\int_{z_{i-1}}^{z_i} e^{-h \cdot z}}{\int_{z_1}^{z_n} e^{-h \cdot z}}$$

où h est une constante propre à chaque type de végétation et déjà présente dans ORCHIDEE. On suppose que la première couche ne contribue pas à la transpiration ([De Rosnay, 1999]).

Infiltration, ruissellement, drainage

- Plusieurs types d'infiltration sont possibles ([Gazis and Geng, 2004]) :
  - "piston" : on ajoute l'eau au dessus de l'eau déjà présente, ce qui décale toutes les couches vers le bas.
  - infiltration préférentielle au travers de pores ou fractures : on distribue uniformément la précipitation dans toutes les couches.
- Le ruissellement a la composition des flux entrant.
- Le drainage a la composition des couches les plus profondes.

Diffusion verticale entre les couches

A chaque itération, on effectue de la diffusion verticale entre les couches.

Soit $\theta_l(t,z)$ la teneur en eau du sol et K_d la diffusivité. L'équation de diffusion s'écrit :

$$\frac{\partial \theta_l}{dt} = -\frac{\partial F_\theta}{\partial z} \tag{D.10}$$

avec F_θ le flux d'eau diffusif :

$$F_\theta = -K_d \frac{\partial \theta_l}{\partial z} \tag{D.11}$$

avec K_d une constante de diffusion.

Soit $X_l(t,z)$ la teneur isotopique du sol : $X_l = \theta_l \cdot R_l$, avec R_l le rapport isotopique dans le sol. X_l vérifie aussi l'équation de diffusion D.10.

Dans le modèle, on suppose que

1. θ_l est constante quel que soit les conditions et la profondeur (grosse approximation),
2. K_d est aussi une constante, donnée par l'équation D.3.

Alors on obtient :

$$\frac{\partial R_l}{dt} = -\frac{\partial F_R}{\partial z} \tag{D.12}$$

avec

$$F_R = -K_d \frac{\partial R_l}{\partial z} \tag{D.13}$$

L'équation D.12 représente l'effet de la diffusion générée par les gradients isotopiques, en supposant que la teneur en eau dans le sol est uniforme. Seuls les isotopes sont transportés par la diffusion dans ce modèle. Cette approximation aura pour effet de sur-estimer la diffusion dans les couches supérieures (où θ_l dans la nature est plus faible) et de la sous-estimer dans les couches inférieures.

Dans le modèle, pour chaque couche i de 1 à $n-1$, on calcule le flux de diffusion $F_{i/i+1}$ entre la couche i et $i+1$ par (discétisation de D.13) :

$$F_{i/i+1} = -K_d \cdot \frac{R_{i+1} - R_i}{\left(l_i + l_{i+1}\right)/2}$$

On calcule alors la nouvelle composition des couches i et $i+1$ (discrétisation de D.12) :

$$R_i(t) = R_i(t - dt) + dt \cdot \frac{F_{i/i+1}}{l_i}$$

$$R_{i+1}(t) = R_{i+1}(t - dt) - dt \cdot \frac{F_{i/i+1}}{l_{i+1}}$$

Annexe E

Traçage de l'eau et des espèces isotopiques (water tagging)

Le traçage de l'eau est un diagnostic consistant en colorier ("Colored Moisture Analysis", [Yoshimura et al., 2004]) les molécules d'eau de différentes couleurs selon une certaine convention de coloriage. De même, on peut colorier les molécules d'isotopes. Ainsi, il est possible de diagnostiquer à tout moment dans LMDZ la proportion des différentes couleurs dans une eau, et la composition isotopique des eaux de différentes couleurs.

Le traçage de l'eau a été introduit dans de nombreux GCMs isotopiques afin d'étudier la composition isotopique de l'eau selon l'origine de cette eau ([Joussaume et al., 1984, Koster et al., 1986, Koster et al., 1992, Cole et al., 1999, Delaygue et al., 2000, Werner et al., 2001, Noone and Simmonds, 2002a, Vuille et al., 2003, Yoshimura et al., 2004, Frankenberg et al., 2009]). Dans ces cas, les molécules sont coloriées selon l'origine évaporatoire des molécules d'eau : continent, ou différents bassins océaniques. De la même façon mais indépendamment des isotopes, cette même technique a été utilisée par [Bosilovich and Schubert, 2002] pour quantifier le recyclage continental. Cette technique a par la suite été étendue au traçage d'autres processus que seulement la région d'évaporation. [Galewsky et al., 2005] a utilisé cette technique pour tracer la latitude et l'altitude de dernière saturation, afin de vérifier le lien entre température de dernière saturation et humidité relative. Enfin, [Wright et al., 2009] a utilisé une technique légèrement différente permettant de tracer la vapeur issue de l'évaporation du condensat nuageux et des précipitations.

Au cours de cette thèse, nous avons introduit le traçage de l'eau et des espèces isotopiques (water tagging) dans deux modèles : le modèle de lignes de grains ([Risi et al., 2010a]) et LMDZ. Nous avons largement étendu les types de processus marqués : en plus de la possibilité de tracer les zones géographiques ou types de surface d'évaporation comme le plus souvent décit dans la littérature, nous pouvons aussi tracer la température minimale atteinte (correspondant approximativement à la température de dernière saturation), tracer la réévaporation de la précipitation, tracer des zones tri-dimensionnelles par lesquelles l'eau est passée, tracer l'eau de certaines composantes de paramétrisations physiques telles que les descentes insaturées... Les possibilités de traçage sont infinies, et l'architecture informatique des traceurs permet l'implémentation facile de n'importe quelle nouvelle convention de coloriage. Nous ne sommes limités que par notre imagination !

La section E.1 présente quelques caracteristiques générales de l'implémentation du water tagging. La section E.2 présente différentes options de traçage utilisée dans LMDZ et leur résultats.

E.1 Quelques principes généraux d'implémentation du water tagging

Numériquement, il s'agit d'ajouter des traceurs passifs se comportant comme l'eau "normale" , ou comme les isotopes "normaux", chacun correspondant à une couleur. Dans le modèle de lignes de grains comme dans LMDZ, ces différents traçeurs sont implémentés comme les isotopes de l'eau. Il y a pour chaque simulation $n_{iso} \times (n_{trac} + 1)$ "traceurs d'eau" en tout : il y a tout d'abord n_{iso}

isotopes "normaux", dont l'$H_2^{16}O$ correspondant à l'eau "normale". Et pour chacune de ces espèces isotopiques, il y a en plus n_{trac} traceurs correspondant chacun à une couleur.

Lors des changements de phase, les fractionnements sont les mêmes pour toutes les molécules d'une espèce isotopique donnée quelque soit leur couleur. D'autre part, la probabilité de condenser ou de s'évaporer est la même pour toutes les molécules d'$H_2^{16}O$ quelque soit leur couleur. Par exemple, si une vapeur avec de l'eau de différente couleurs $j \in [1, n_{trac}]$ condense avec une fraction résiduelle f selon une distillation de Rayleigh, alors le rapport isotopique de la vapeur résiduelle pour l'isotope i est donnée par :

$$R_{i,j} = \frac{x_{i,j}}{x_{eau,j}} = R^0_{i,j} \cdot f^{\alpha_i - 1}$$

avec $x_{i,j}$ la quantité d'isotope i colorié en j, $x_{eau,j}$ la quantité d'$H_2^{16}O$ colorié en j, $R^0_{i,j}$ le rapport isotopique initial de l'eau coloriée en j, et α_i le coefficient de fractionnement pour l'isotope i.

Lors de l'évaporation des gouttes, des échanges diffusifs ont lieu entre la pluie et la vapeur. On suppose alors que chaque molécule de pluie, quelque soit sa couleur, se rééquilibre partiellement avec la vapeur totale. Ainsi, si la rééquilibration avec la vapeur est totale lors de la chute de la goutte, alors chaque couleur de la goutte aura la même composition, en équilibre avec la vapeur totale. Cela représente le fait que dans la nature, si la rééquilibration est forte, la goutte prendra une composition dépendant de la vapeur avec laquelle elle s'équilibre, en perdant toute information isotopique donnée par son origine.

E.2 Différentes options de taggage dans LMDZ et quelques résultats

E.2.1 Tagging evaporative zones or types

Tagging oceanic basins

As in [Joussaume et al., 1984, Koster et al., 1992, Cole et al., 1999, Delaygue et al., 2000, Werner et al., 2001, Noone and Simmonds, 2002a, Vuille et al., 2003, Yoshimura et al., 2004], the tagging of different oceaninc regions has been introduced. Results from this tagging option have been used, for example, to evaluate the relative contributions of evaporation over the Atlantic Ocean, the Mediterranean sea and the Indian Ocean for the precipitation over Niamey (table 3.2 in section 3.5).

Continental recycling

The tagging of continental evaporation has also been introduced, to quantify the continental recycling. Numerous methods exist to quantify continental recycling (e.g. [Trenberth, 1998, Burde and Zangvil, 2001, Brubaker et al., 2001]), but water tagging is the method that provides the best consistency with the model physics ([Bosilovich and Schubert, 2002, Yoshimura et al., 2004]). Results obtained at the global scale are consistent with those of [Yoshimura et al., 2004] (figure E.1a).

In LMDZ-iso, land evaporation (assumed not to fractionate), enriches the low level vapor (figure E.1b) and increase its d-excess (figure E.1c) : land evaporation is in average richer by 4‰ and with a d-excess higher by 4‰ than the low level vapor. The enriching power of continental recycling depends on the relative composition of the precipitation (which is the source of evapo-transpired water) and the low-level vapor. Over oceans, the vapor originating from land evaporation is more depleted than the total vapor, due to more remote an origin and thus more intense a distillation.

Types of land-surface evaporation

When LMDZ is coupled with the land-surface model ORCHIDEE, it is possible to tag the different types of continental evapo-transpiration : transpiration, bare soil evaporation, evaporation of water intercepted by the canopy. Such simulations are currently in progress.

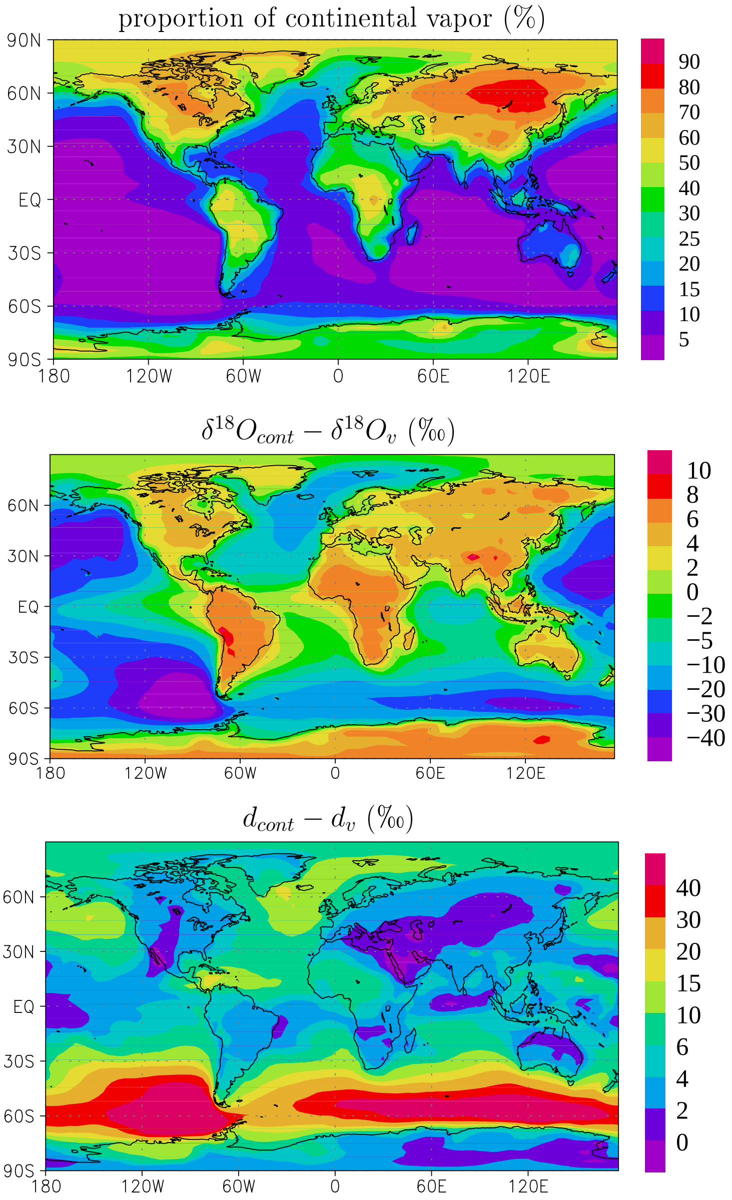

FIG. E.1 – a) proportion of the lowest level vapor (lowest 130m) originating from continental evaporation. b) same as a but for the zonal averages and as a function of altitude. c) Difference between the $\delta^{18}O$ of the vapor originating from continental evaporation ($\delta^{18}O_{cont}$) and the $\delta^{18}O$ of the total vapor at lowest level ($\delta^{18}O_v$). d) same for d-excess.

E.2.2 Tagging water from precipitation reevaporation

Processes controlling the relative humidity in the tropical and subtropical atmosphere are still debated, while their understanding is crucial to quantify climatic feedbacks related to water vapor. Relative humidity can be controlled by large-scale transport : when an air mass subsides, it conserves the specific humidity it has aquired the last time it has saturated (last saturation analysis : [Sherwood, 1996, Pierrhumbert and Roca, 1998]). Cloud microphysics, such as precipitation reevaporation, can also play a role ([Sun and Lindzen, 1993]). The isotopic composition of the vapor may help to quantify some terms of the water budgets ([Worden et al., 2007, Noone, 2009]).

In this tagging mode, as soon as a rain drop or snow flake evaporates, the evaporated water takes the "reevaporation" tag. This tag is lost when precipitation reaches the surface. This tagging mode allows us to quantify the contribution of precipitation reevaporation to the water vapor budget, and to the spatial and temporal variability of relative humidity.

The proportion of low-level water vapor originating from precipitation reevaporation is maximum in convective regions (figure E.2a). In the Pacific warm pool, more than 35% of the low-level vapor originates from precipitation reevaporation : precipitation reevaporation thus contributes significantly to the water budget. This vapor is then transported upward and poleward by the atmospheric circulation, and accumulates in the upper troposphere and over polar regions (figure E.2b). In Antarctica, more than 45% of the low-level vapor originates from precipitation reevaporation that occurs mainly in the tropics.

Water vapor originating from precipitation reevaporation is more depleted than the total vapor (-4 to -6‰ in convective regions, figure E.2c). This is in agreement with [Worden et al., 2007], who attempted quantifying the proportion of vapor originating from rain reevaporation by assuming that rain reevaporation depletes the total vapor. In a modelling study of the squall line isotopic composition in the Sahel, we found on the contrary that rain reevaporation rather enriches the vapor ([Risi et al., 2010a], chapter 4). This is the case when the reevaporated fraction of the rain is very large, but this case seldomly happens in LMDZ.

Rain reevaporation tends to increase the vapor d-excess : it is 8 to 15‰ higher in convective regions (figure E.2d). Using the d-excess of the vapor (d_v) to infer the proportion of vapor originating from rain reevaporation (r_{rev}) in the tropics (figure E.3) would yield better results than using $\delta^{18}O$ (as in [Worden et al., 2007]) : if assuming that d_{rev} and d_{res} (the d-excess of the precipitation reevaporation and of the residual vapor respectively) are constant, then r_{rev} can be infered from d_v by $r_{rev} = \frac{d_v - d_{res}}{d_{rev} - d_{rev}}$. Using $d_{rev} = 35‰$ and $d_{res} = 5‰$, the inferred r_{rev} (figure E.3b) compares reasonably well with the simulated r_{rev} (figure E.3a), with a spatial correlation between the two maps of 0.61 and absolute and relative error within ±15% and ±100% respectively. The corresponding reconstructions with $\delta^{18}O_v$ would yield a spatial correlation of 0.48 only and absolute and relative errors within ±40% and ±150% respectively. D-excess in vapor could thus be used to evaluate the moistening effect of rain reevaporation on the atmospheric humidity.

E.2.3 Tagging minimum temperature

Last saturation analysis has been successful in reproducing the first order spatial distribution of relative humidity in the atmosphere ([Sherwood, 1996, Pierrhumbert and Roca, 1998]). Last saturation temperature is expected to control both the relative humidity and the isotopic composition, following a Rayleigh distillation. To check to what extent the joint humidity and isotopic distribution can be explained by last saturation, and to assess the potential of isotopes to quantify the dehydrating effect of subsidence, we implemented a tagging option in which we tag the minimum temperature undergone by the vapor along its trajectory.

This tagging option was already described and used in the squall line model (chapter 4, appendix H.3), except that in a GCM temperature varies both vertically and horizontally. A similar tagging option was implemented in an idealized GCM by [Galewsky et al., 2005], but the latitude and altitude of the last saturation was tagged rather than directly the last saturation temperature.

As an example, we applied this tagging option over West Africa. In the Sahara, the subsiding branch of the Hadley cell strongly depletes the atmospheric water vapor in winter : the low-level δD_v measured from space by SCIAMACHY is up to 80‰ lower in DJF than JJA ([Frankenberg et al., 2009]). LMDZ-iso reproduces this behavior well, though the winter depletion is underestimated by 20‰ compared to SCIAMACHY (not shown). In LMDZ-iso, the last saturation temperature, as

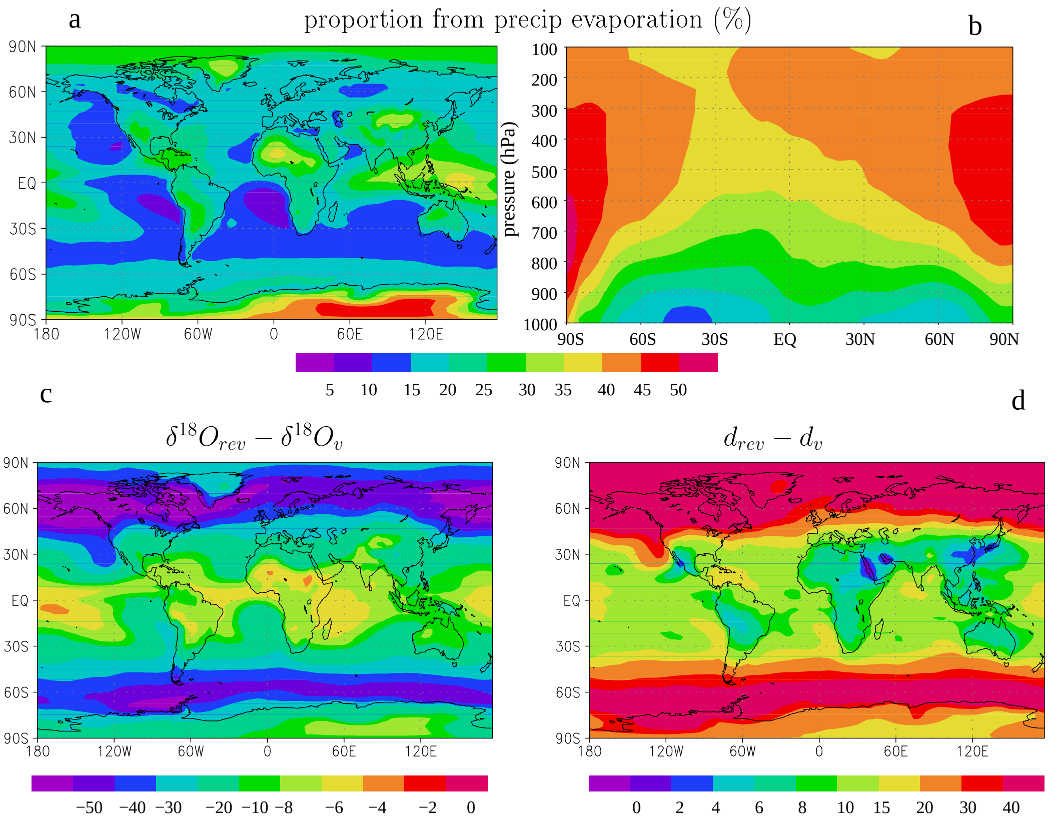

FIG. E.2 – a) Proportion of the lowest level vapor (lowest 130m) originating from precipitation reevaporation. b) Difference between the $\delta^{18}O$ of the vapor originating from precipitation reevaporation ($\delta^{18}O_{rev}$) and the $\delta^{18}O$ of the total vapor at lowest level ($\delta^{18}O_v$). c) same for d-excess.

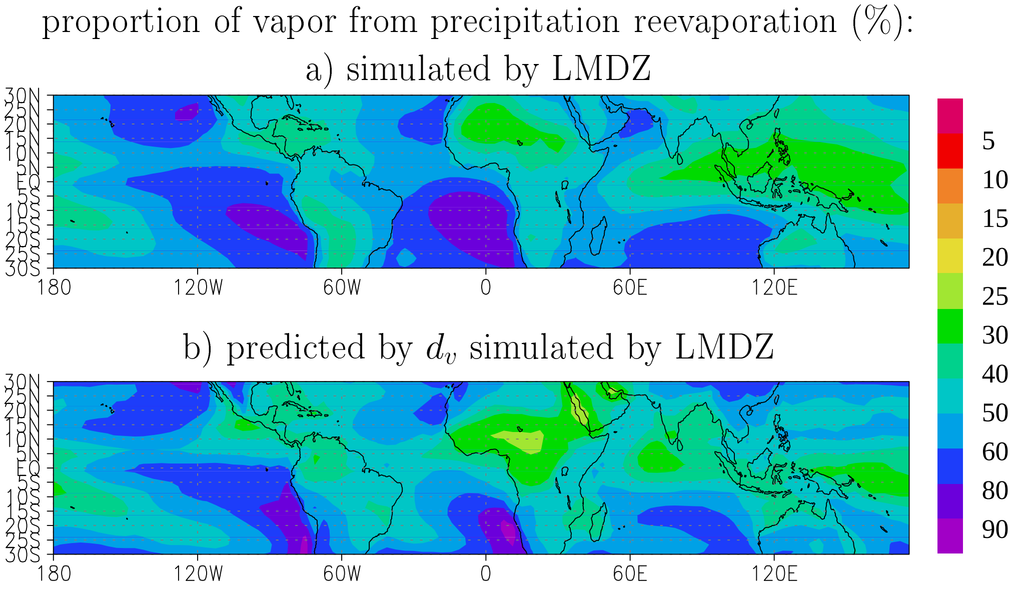

FIG. E.3 – Proportion of the lowest level vapor (lowest 130m) originating from precipitation reevaporation : a) simulated by LMDZ and b) inferred from d_v simulated by LMDZ using equation $r_{rev} = \frac{d_v - d_{res}}{d_{rev} - d_{rev}}$ (see text for details).

diagnosed from our tagging experiment, and δD_v at the lowest level show very similar spatial and seasonal variations (figure E.4). This confirms that last saturation temperature strongly controls at first order the spatial and seasonal variations of δD of low level vapor in LMDZ-iso.

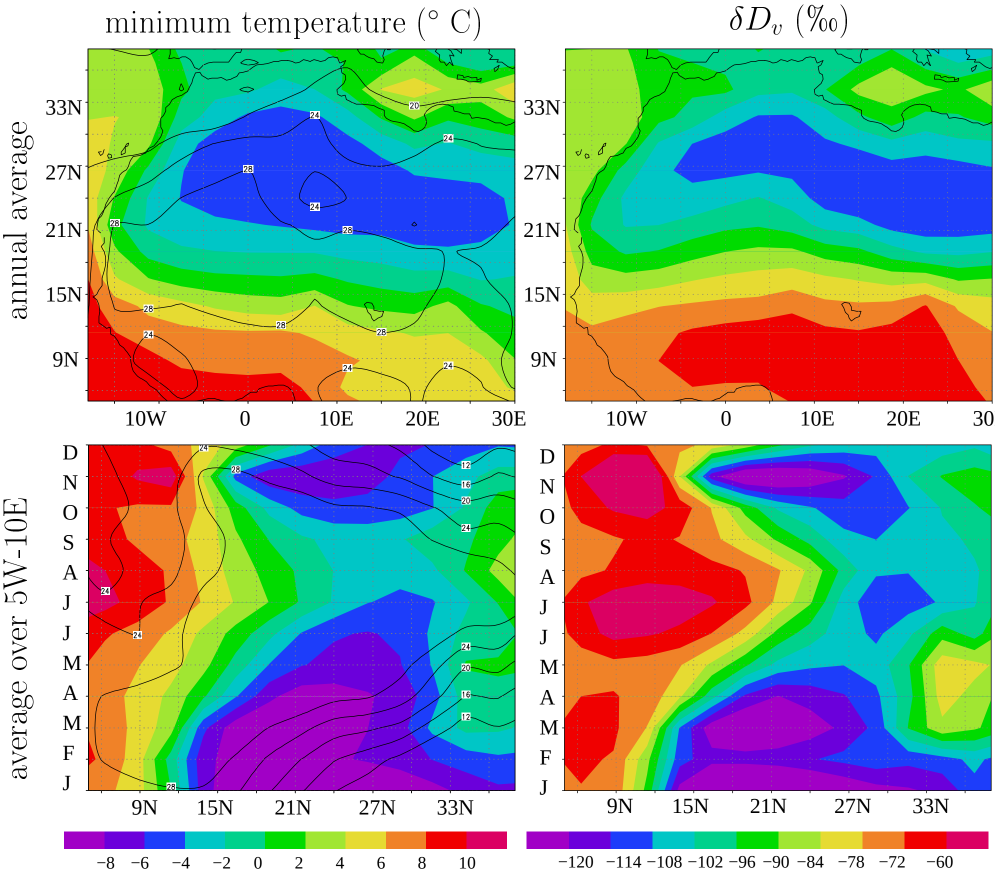

Fig. E.4 – Relationship between the low-level vapor δD and subsidence in LMDZ-iso over West and North Africa : a) annual mean minimum temperature undergone by water molecules since evaporation from the surface, averaged over all water molecules. Contours are the surface air temperature in $^\circ C$. b) annual mean δD of the low-level vapor. c) Same as a) but for the seasonal cycles as a function of latitude, averaged over 5W-10E. d) Same as b) but for the seasonal cycles as a function of latitude, averaged over 5W-10E.

E.2.4 Tagging 3D zones

As soon as a water molecule enters into a pre-defined zone, it takes the color of this zone. It then looses it only when it enters into a zone of another color, or if it precipitates. An example of this tagging functionality is described in section 3.5 to analyze the origin of Sahelian vapor (table 3.3).

E.2.5 Tagging unsaturated downdrafts

Based on a single column modelling study ([Risi et al., 2008a]) and on isotopic observations at the squall line scale ([Risi et al., 2010a]), we argued in chapter I that convective subsidence plays an crucial role in the isotopic response of the vapor and precipitation to variations in convective activity : convective downdrafts add depleted and high d-excess vapor into the low level vapor. In this tagging mode, we tag the vapor that go through unsaturated downdrafts in the Emanuel convective scheme. The tag is lost when precipitation reaches the surface.

As expected, the proportion of lowest-level water vapor having been through an unsaturated downdraft is the highest in convective regions (up to 80% in the Pacific warm pool). This vapor is more depleted (-2 to -4‰ in convective regions) and has a higher d-excess than the total vapor (4 to 6‰ in convective regions) . This mode of tagging is used in section 3.5 to investigate the controls of intra-seasonal variability in $\delta^{18}O$ over West Africa.

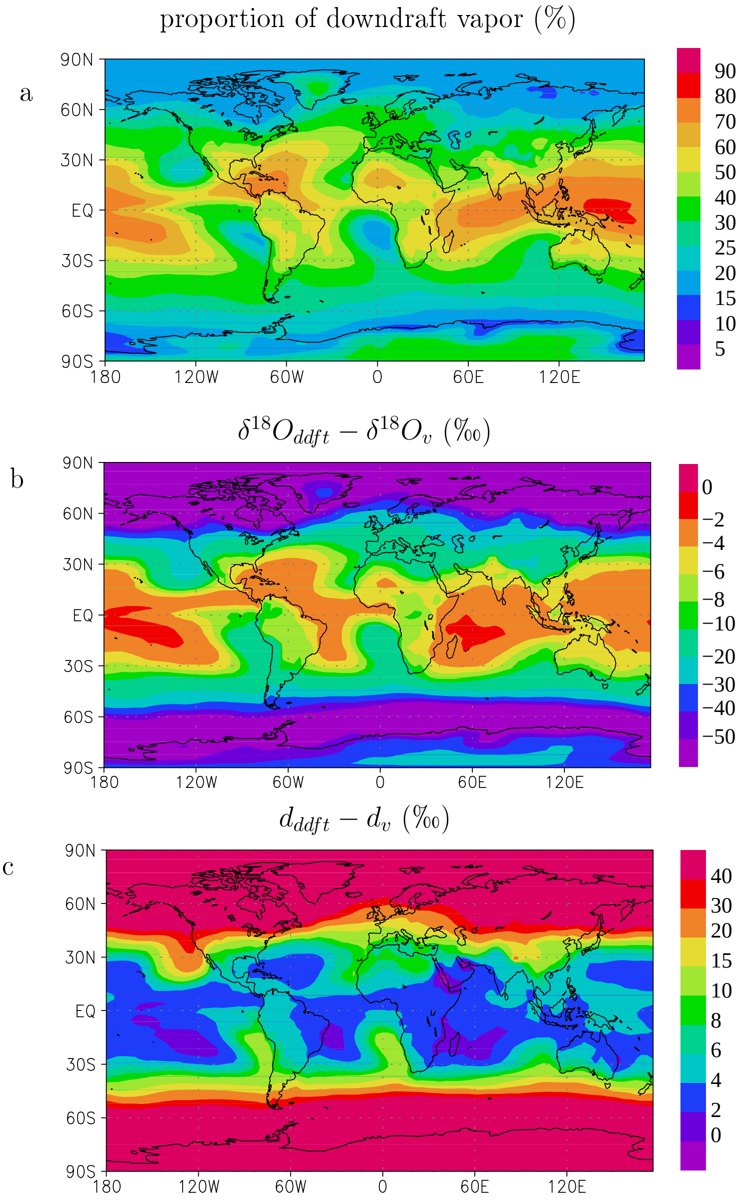

FIG. E.5 – a) proportion of the lowest level vapor (lowest 130m) having been through an unsaturated downdraft. b) Difference between the $\delta^{18}O$ of the vapor having been through an unsaturated downdraft ($\delta^{18}O_{ddft}$) and the $\delta^{18}O$ of the total vapor at lowest level ($\delta^{18}O_v$). c) same for d-excess.

Annexe F

Contrôles du d-excess dans LMDZ-iso

Deuterium excess, as a second parameter, is usually a more difficult parameter to simulate by GCMs than δD or $\delta^{18}O$. Some GCMs struggle to have the right average value ([Mathieu et al., 2002]) and its results ar not published for all GCMs ([Lee et al., 2007]). Besides, most GCMs have difficulties simulating the observed lower LGM d-excess in Greenland and Antarctica, and rather simulate higher values ([Werner et al., 2001]).

A number of processes can affect d-excess, making it a complicated parameter to interpret. It has been shown to be particularly sensitive to surface evaporative conditions ([Merlivat and Jouzel, 1979]), in particular sea surface temperature (SST) and relative humidity rh_s . The sensitivity to these parameters have been evidenced both theoretically using a simple model ([Merlivat and Jouzel, 1979]) and in some vapor data ([Uemura et al., 2008]): 0.38‰/° for SST and by -0.43‰/% for rh_s (section 1.1). It can then be affected by the distillation of air masses ([Jouzel and Merlivat, 1984]), generally increasing as the Rayleigh distillation proceeds, depending on kinetic fractionation during snow formation. It is affected by convective activity ([Bony et al., 2008]), and by fractionation during evaporation of bare soil or vegetation-intercepted water over land (chapter 8).

We have shown that LMDZ simulates relatively well the spatial and seasonal distribution of d-excess, and simulates the LGM change of the right sign (section 6.3.4). We investigate in this appendix what control the spatial and seasonal distribution of d-excess, as well as its lower LGM value. In section F.1, we evaluate the contribution of variations of d-excess in the vapor to d-excess in the precipitation. We then quantify the contributions from surface evaporative conditions (SST and rh_s) to zonal and temporal d-excess variations (sectionF.2). In section F.3, we investigate the causes of the seasonal cycle of d-excess simulated in South America.

F.1 Contributions of variations of d-excess in the vapor to those in the precipitation

Variations of d-excess in precipitation (d_p) may be due to

1. large-scale processes (evaporative conditions, distillation along the air mass): in this case, the variations of d_p reflects those in the low-level vapor (d_v).
2. local processes related to precipitation processes: condensation altitude, reevaporation and diffusive exchanges as the rain falls. In this case, variations in d_p reflects those in $d_p - d_v$.

Zonal variations in d_p closely follow variations in d_v (figure F.1a, black lines), especially in the tropics and lower mid-latitudes, where the rain equilibrates efficiently with the low-level vapor. In these regions, large-scale controls on d_v dominate. Exceptions ar found in the subtropics, where the air is dry: rain reevaporation account for a decrease of d_p of 1‰ compared to d_v in zonal average (figure F.1b, purple). In high latitudes, where the snow does not reequilibrate with the low-level vapor, d_p and d_v are decoupled: d_p rather reflects the composition of the vapor at the altitude of condensation.

At the seasonal scale, LMDZ-iso simulates a maximum d_p in winter over mid and high latitudes, and a maximum d_p during the rain season in the tropics. Such seasonal cycle are observed in the precipitation at many GNIP stations ([Risi et al., 2010b]). Large-scale controls on d_v dominate seasonal variations of d_p in the tropics, while they contribute only partly to seasonal variations of d_p in mid and high latitudes (figure F.1c, black lines).

At LGM (here using the IPSL SSTs, section 6.3) compared to present day (PD), LMDZ-iso simulates lower d-excess in both the vapor and precipitation over most mid and high latitude regions (poleward of 40°) (dashed black on figure F.2b). This is consistent with observed precipitation with lower d-excess at LGM in Antarctica and Greenland. The zonal pattern of d_p difference equatorward of 60° reflects that of d_v, suggesting the role of large scale processes such as evaporative conditions. Changes in d_p and d_v are decoupled at very high latitudes. In particular, d_p is 5‰ in average lower at LGM than at PD at 80°S, while d_v is virtually unchanged. Therefore, the reason for the lower d_p at LGM at extreme southern latitudes in LMDZ-iso is rather related to changes in local condensation processes, or changes in the vertical gradient of d_v.

In the next section, we investigate what controls d_v, focusing on the effect of evaporative conditions.

F.2 Effect of evaporative conditions (SST and rh_s)

To quantify the contributions of SST and rh_s in controlling the spatial and seasonal variations in d_v, we perform 3 kinds of LMDZ simulations:

1. a control simulation
2. a simulation in which we set rh_s to 60% everywhere when calculating the composition of the water evaporated from the ocean.
3. a simulation in which we set rh_s to 60% and SST to 20°C everywhere when calculating the composition of the water evaporated from the ocean.

The difference between experiment 2 and 1 yields the effect of rh_s variations at evaporation. The difference between experiment 3 and 2 yields the effect of SST variations at evaporation. This protocol was used in [Risi et al.,]. Note that rh_s and SST remain the same as in the control simulation for all other calculations than the composition of the water evaporated from the ocean.

F.2.1 Spatial distribution

Results from the different simulations are shown on figure F.1.

At first order, the d_v maximum over tropical regions and minimum over mid-latitude oceans is due to the sensitivity of d-excess of evaporation to the SST. Zonal variations in SST of about 30°C from the equator to 60°S induce zonal variations of d_v of 6‰. The marked minimum simulated around 60°S is also partly due to a minimum in rh_s : the increase of rh_s from 65% at 30°S to 80% at 60°S leads to a decrease of d_v by 3‰.

The effect of SST and rh_s on the zonal distribution of d_v are reasonably well predicted if taking sensitivities of d_v to local SST and rh_s of 0.12‰/°C and -0.15‰/% respectively (blue curve on figure F.1). This confirms the importance of SST and rh_s in controlling d-excess locally, in agreement with [Uemura et al., 2008]. These slopes are however 3 times lower than predicted by the [Merlivat and Jouzel, 1979] closure assumption (0.38‰/°C and -0.43‰/%), probably because the controls of d_v are not exclusively local, so that the predicted sensitivity to local SST and rh_s are smoothed out.

When both SST and rh_s are held constant during evaporation, the zonal distribution of d_v features:

- a maximum over the equator, possibly due to the effect of convection in the ITCZ on d_v as expected from [Risi et al., 2008a].

- an increase of d_v over Antarctica, due to the effect of the distillation of air masses with little recycling.

F.2.2 Seasonal cycles

When rh_s is held constant during evaporation, the seasonal cycle in mid and high latitudes disappears. The effect of SST, on the other hand, is very small. This shows that in LMDZ, the seasonal cycles of d_v over mid and high latitudes are due to rh_s variations. However, this effect is not local: applying local sensitivities to rh_s and SST to reconstruct the d-excess seasonal yields very different results.

When both SST and rh_s are held constant during evaporation, the maximum d_v during the rainy season persists: this is likely due to the effect of convection on d-excess, as observed for example over West Africa ([Risi et al., 2008b]). Over Antarctica, the higher d_v during winter also persists, and is likely due to the more intense distillation in winter.

F.2.3 LGM change

The lower d_p at LGM measured in ice cores has been suggested to be related to moister evaporative conditions at the source ([Jouzel et al., 1982]) or a lower SST at the source (e.g. [Vimeux et al., 2002, Stenni et al., 2001]). The zonal pattern of the LGM - PD d_v difference (black on figure F.2) indeed reflects the pattern due to changes in SST and rh_s conditions (green dashed): for instance, the 3‰ lower d_v around 40°S is due for 1.5‰ to the 4°C lower SST and the 4% higher rh_s at LGM. However, even when holding these evaporative conditions constant (soild green), d_v is between -1 and -4‰ lower at LGM than at PD: the globally mean lower d_v is not explained by changes in SST and rh_s, but by other processes.

F.2.4 Summary

In LMDZ-iso, variations in d_p reflect those d_v in the tropics, indicating the influence of large-scale processes. In mid and high altitudes, both large-scale processes and local condensation and precipitation processes paly a role. Evaporative conditions (SST and rh_s) are the main controls on the zonal and seasonal distribution in d_v, except at very high latitudes where distillation processes dominate, and in the ITCZ where convective processes play a significant role. Variations in evaporative conditions between the LGM and PD may explain ±1‰ changes in d-excess regionally, but other processes, such as changes in condensation altitude or in the vertical isotopic distribution, are responsible for the lower d_p at high latitudes.

F.3 Seasonal cycles of d-excess over South America

In tropical South America, the d-excess in precipitation (d_p) increases inland along the air trajectories. This increase has been interpreted as the result of the input of vapor from fractionating evaporation (i.e. evaporation from bare sol, lakes or water intercepted by the canopy) ([Gat and Matsui, 1991]). On this basis, longitudinal gradients in d_p have been used to quantify the proportion of evapo-transpiration from bare soil or open water bodies versus transpiration ([Gat and Matsui, 1991]). The increase of d_p inland is the strongest during the dry season. A stronger d_p by about 10‰ during the dry season has indeed been measured in the Andes (F. Vimeux, pers. comm.). This suggests a higher proportion of bare soil evaporation during the dry season ([Henderson-Sellers et al., 2004]).

Using water isotopes to quantify the relative contributions of evapo-transpiration has been successfully applied at the local scale through measurments of $\delta^{18}O$ in the different components of the soil-vegetation-atmosphere system ([Yepez et al., 2003, Williams et al., 2004]). On the contrary, at the continental scale, the tentative quantifications based on water isotopes have so far relied on observed gradients in d_p ([Gat and Matsui, 1991, Henderson-Sellers et al., 2004]). However, this requires that the observed d_p distribution is totally caused by fractionating evaporation, an assumption that is a priori difficult to check.

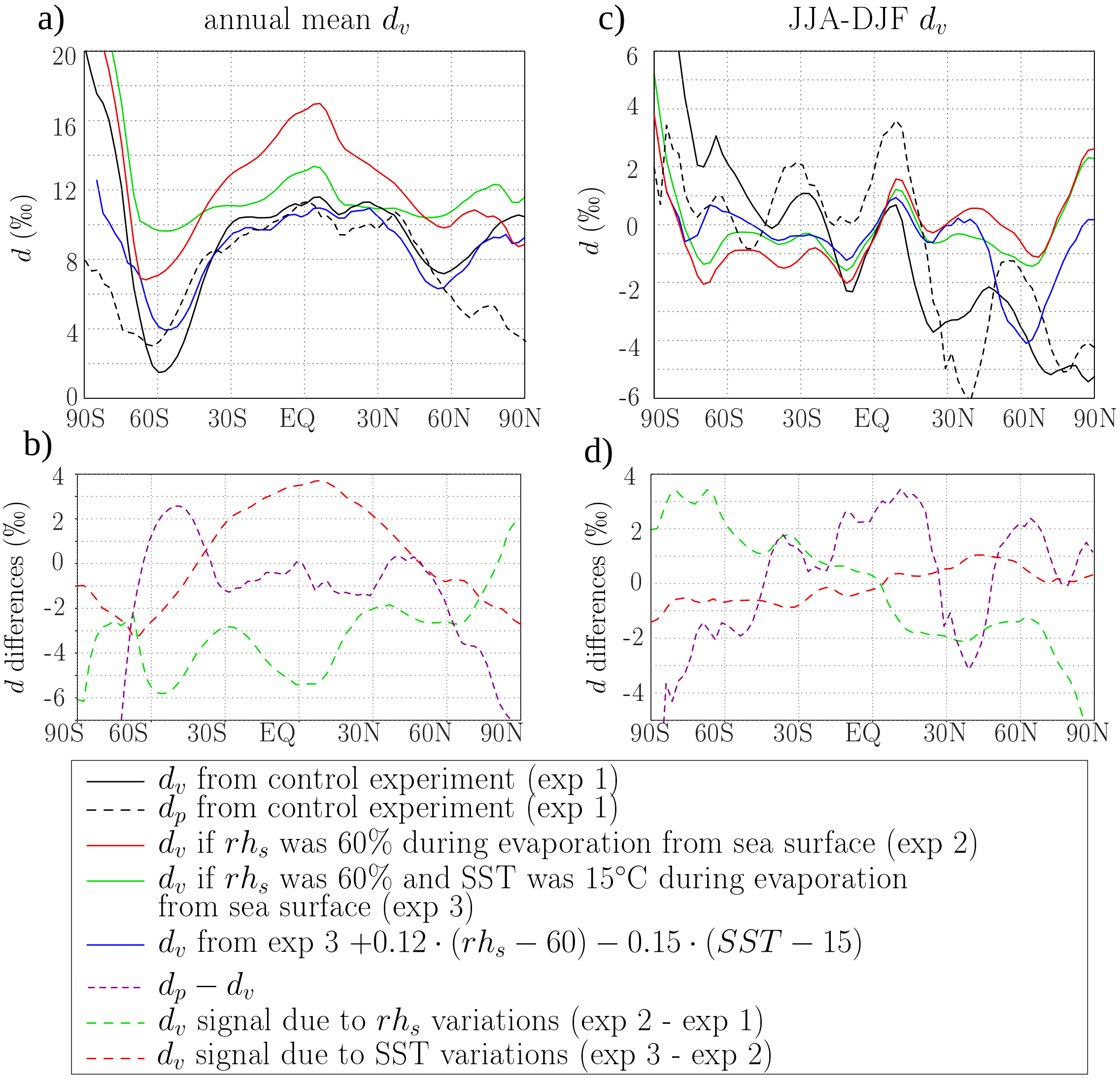

Figure F.1: Controls on the zonal and seasonal distribution of d_p in LMDZ: a) Zonal and annual average of d_p (dashed black) and d_v (solid black) simulated by LMDZ in the control experiment. Zonal and annual average in d_v simulated in experiment 2 (rh_s held constant during the calculation of the composition of the surface evaporation flux, red) and in experiment 3 (both SST and rh_s are held constant, green). Blue: d_v calculated as the sum of the green curve and $0.12 \cdot (rh_s - 60) - 0.15 \cdot (SST - 15)$. b) Zonal and annual average of the difference of d_v in experiment 3 and 2 (dashed red) and experiment 2 and 1 (dashed green), representing the contributions of variations in SST and rh_s respectively. c) same as a, but for zonal averages of JJA-DJM d-excess values. d) same as b) but for zonal averages of JJA-DJM d-excess values.

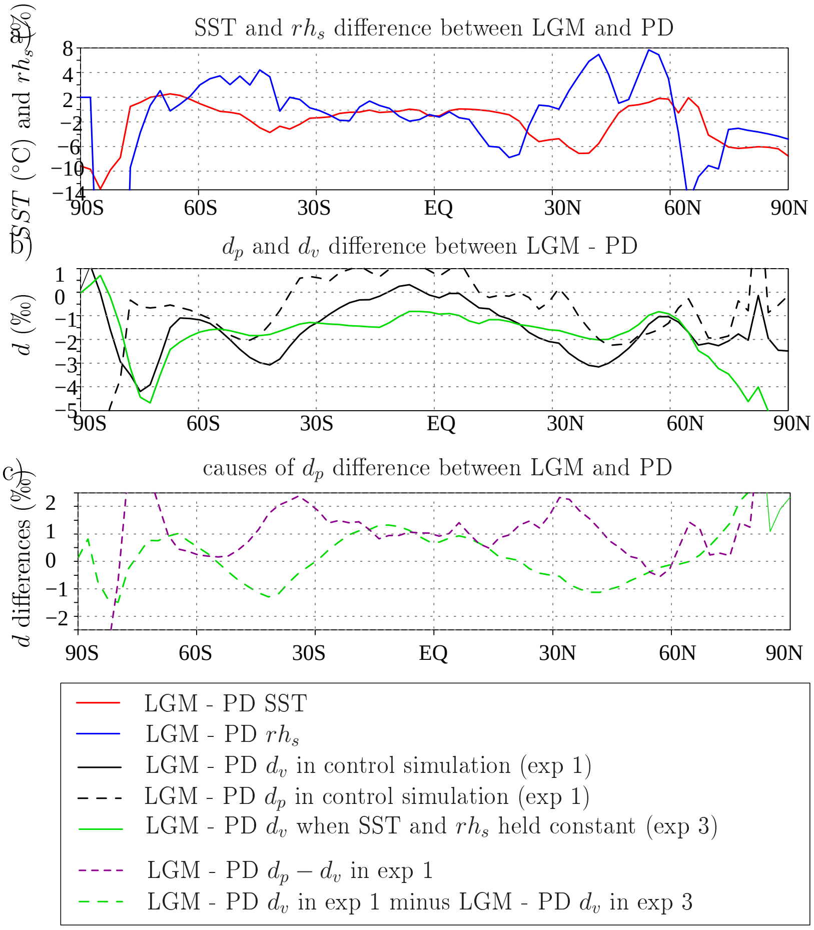

Figure F.2: a) change in SST and rh_s between LGM and PD. b) change in d_p (dashed black), d_v (solid black) between LGM and PD in the control simulation. Change in d_v simulated in experiment 3 (SST and rh_s held constant in the calculation of the isotopic composition of the surface evaporation flux) is in green. c) Dashed purple: contribution of local precipitation processes ($d_p - d_v$, purple) on the LGM-PD change in d_p. Dashed green: contribution of the change in evaporative conditions (SST and rh_s) on the LGM-PD change in d_v.

LMDZ-iso is able to simulate the increase of d_p inland, and this simulated increase is the strongest during the dry season (figure F.3b), consistently with the available data. The simulated d_p in the eastern Amazon is up to 15‰ higher during the dry season that the wet season. This is surprising, as land evaporation is assumed not to fractionate in LMDZ-iso. This paradox was also noticed in REMO-iso simulations (F. Vimeux, pers. comm.). This suggests that other processes than fractionating evaporation may lead to the spatial and seasonal distribution of d_p in South America. We thus investigate below what processes explain the simulated d_p distribution in LMDZ-iso.

The seasonal distribution of d-excess in the vapor (d_v) in the eastern Amazon is quite similar to the one in d_p, but dampened by a factor of about 5 (figure F.3c) and slightly lagged. On the other hand, the distribution of $d_p - d_v$, representing the disequilibrium between the rain and vapor as rain falls, is virtually the same as d_p (figure F.3d). This suggests that the reason for the seasonal and longitudinal distribution of d_p is rain-vapor disequilibrium rather than processes affecting the vapor. This rules out the effect of land surface evaporation, which would affect the vapor as much as the precipitation. This is confirmed by a simulation in which the isotopic composition is fixed constant (not shown), erasing the seasonal cycle in d_p. The d-excess of the vapor originating from land surface evaporation (d_{cont}, diagnosed using water tagging as described in appendix E.2.1) features a seasonal cycle of the same order of magnitude as d_p, but slightly lagged. This is consistent with this vapor originating from previous precipitation, and explains the dampened seasonal cycle in d_v. Land surface evaporation thus amplifies the seasonal cycle of d_p in the eastern Amazon in LMDZ-iso, but is not the main reason.

To conclude, LMDZ-iso simulates a longitudinal and seasonal distribution of d_p consistent with the data, but without fractionating evaporation. This contradicts the common thinking that d_p in this region is controlled by fractionating recycling ([Gat and Matsui, 1991, Henderson-Sellers et al., 2004]). In LMDZ-iso, the distribution of d_p is rather due to processes affecting the rain-vapor disequilibrium, such as rain reevaporation. More data would be necessary to check if the processes at play in LMDZ are realistic. In particular, measurements of the isotopic composition both in the precipitation and in the vapor along a East-West transect and at the seasonal scale would be very valuable to quantify the effect of rain-vapor disequilibrium, and more generally to better understand what processes explain the distribution of d_p in tropical South America.

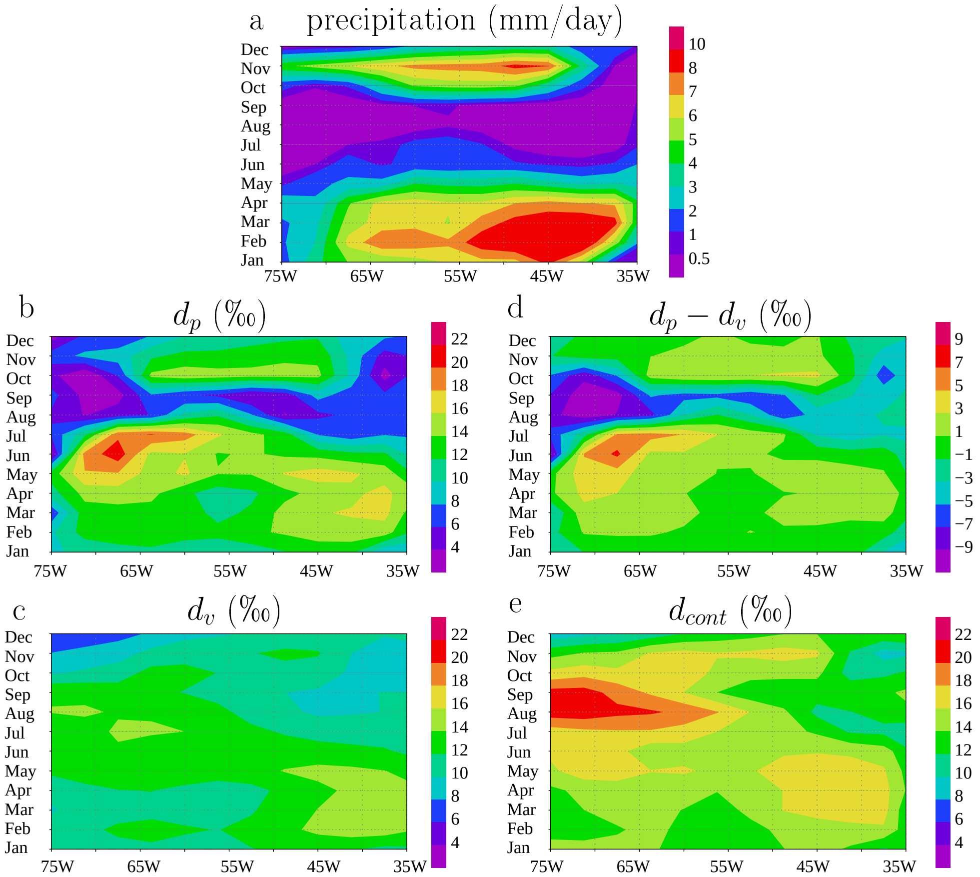

Figure F.3: Longitude-time diagrams averaged between 4°S and 10°S of latitude showing the seasonal cycles over tropical South America of: a) precipitation rate, b) d-excess in the precipitation (d_p), c) d-excess in the lowest level vapor (d_v), d) disequilibrium between the precipitation and the vapor ($d_p - d_v$) and e) d-excess in the vapor originating from land surface evaporation.

Annexe G

Simulations zoomées avec LMDZ

G.1 Motivations générales

La majorité des simulations avec le GCM LMDZ au cours de cette thèse a été réalisés avec une résolution standard assez grossière: 2.5°×3.75°, ce qui correspond à des mailles d'environ 270km par 400 km dans les tropiques. Si cette résolution grossière permet de reproduire de manière assez satisfaisante les variations isotopiques observées à grande échelle (chapitre 6, [Risi et al., 2010b]), une résolution plus fine faciliterait la comparaison aux données dans les régions de forte hétérogénéité spatiale, comme c'est le cas par exemple en région montagneuse. Dans la résolution standard du modèle LMDZ, les Andes ne culminent qu'à 4000 m seulement au lieu de 7000 m dans la réalité. Une meilleure résolution permet en outre une meilleure représentation de l'orographie, et donc de son effet sur le climat.

Un avantage du GCM LMDZ est de pouvoir rafiner la grille ("zoomer") sur une certaine région (e.g. [Krinner et al., 1997a, Coindreau et al., 2007]). Nous présentons l'utilisation de cette fonctionalité sur l'Amérique du Sud, puis des projets de zoom sur d'autres régions.

G.2 Simulation zoomée sur l'Amérique du Sud

G.2.1 Motivations spécifiques à l'Amérique du Sud

De nombreux forages ont été réalisés en Amérique du Sud (e.g. [Thompson et al., 1995, Thompson et al., 2000, Ramirez et al., 2003, Vimeux et al., 2008], revus dans [Vimeux et al., 2009]), des Andes Tropicales (Chimborazo: 1°30'S) à la Patagonie (San Valentin: 46°35'S). Des enregistrements isotopiques y sont disponibles montrant des variations aux échelles décennales (e.g. [Hoffmann et al., 2003]) à climatiques ([Thompson et al., 2000]). Cette région présente donc un fort intérêt paléo-climatologique, mais la topographie andine est particulièrement mal représentée dans la simulation standard. Des simulations à fine résolution sont donc susceptibles d'apporter une valeur ajoutée pour l'étude des contrôles isotoques sur cette région ([Sturm et al., 2007a, Sturm et al., 2007b]).

G.2.2 Configuration de la simulation

Le zoom a été configuré pour que la résolution soit de l'ordre de 60 km sur l'Amérique du Sud, permettant aux Andes de culminer à 6600m (figure G.1). La résolution est relativement constante sur toute l'Amérique du Sud, ce qui permettra d'analyser les contrôles isotopiques sur les régions de forage de l'Amérique du Sud tropicale à la Patagonie. LMDZ est guidé par les vents des réanlayses ECMWF. Ainsi, la circulation atmosphérique aux bords du zoom est fortement contrainte par les réanalyses, ce qui lui permet d'être réaliste malgré la très faible résolution à l'exterieur du zoom. La simulation réalisée couvre la période 1998 à 2001, au cours de la quelle des données à l'événement ont été collectées à différentes altitudes le long de la vallée du Zongo ([Vimeux et al., 2005]), à la limite entre les Andes et le bassin amazonien.

G.2.3 Principaux avantages et inconvénients du zoom

L'analyse de cette simulation a fait l'objet du stage de Master de Guillaume Trémoy co-encadré avec Françoise Vimeux. En bref, la simulation zoomée présente des caractéristiques similaires à la simulation non zoomée. La distribution spatiale et saisonnière des compositions isotopiques ($\delta^{18}O$ et d-excess) dans les précipitations est simulée de manière satisfaisante dans la simulation zoomée ([Tremoy, 2009]) . Par rapport à la simulation non zoomée, les avantages de la simulation zoomée sont:

- l'amélioration de la simulation de la précipitation, qui est plus forte que dans la résolution standard (figure G.2b) (figure G.2c). Une augmentation de la précipitation avec une résolution plus fine est fréquente (F. Hourdin, pers. comm.);
- la possibilité d'analyser statistiquement la relation entre isotopes et altitude (figure G.2c, [Sturm et al., 2007a]);
- la simulation satisfaisante des principales variations observées à l'échelle journalière dans la vallée du Zongo ([Tremoy, 2009]).

Toutefois:

- le zoom aggrave la sur-estimation des précipitation sur le sommet des Andes et la sous-estimation au pied des Andes (figure G.2c). La sur-estimation des précipitations sur les reliefs est un problème fréquent dans les GCMs ([Sturm et al., 2007a]). En conséquence, la distillation des masses d'air au cours de leur ascension des Andes ne se fait pas de la même façon dans LMDZ et dans la réalité, induisant une erreur systématique dans la relation entre isotope et altitude (figure G.2d). Ceci incite à la prudence lors des futures exploitations de ces simulations sur les Andes elles-mêmes.
- le zoom a un cout numérique important. La grille choisie est de 144×142 points et le pas de temps d'intégration de la dynamique de 36s (par rapport à 96×71 et 1 min dans la résolution standard), ce qui multiplie environ par 3 le temps d'execution.

G.3 Autres zooms

D'autres zooms sont prévus, en particulier sur le Tibet où des forages ont aussi été réalisés ([Thompson et al., 1989]), et où des données de précipitation sont collectées à l'événement (travail de thèse de Gao Jing encadrée par V. Masson-Delmotte, [Gao et al.,] en préparation).

Résolution standard

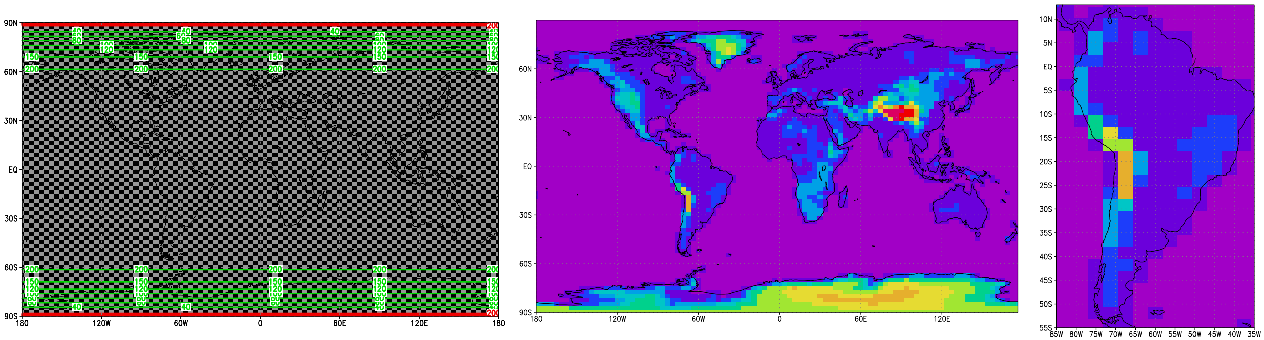

Zoom sur l'Amérique du Sud

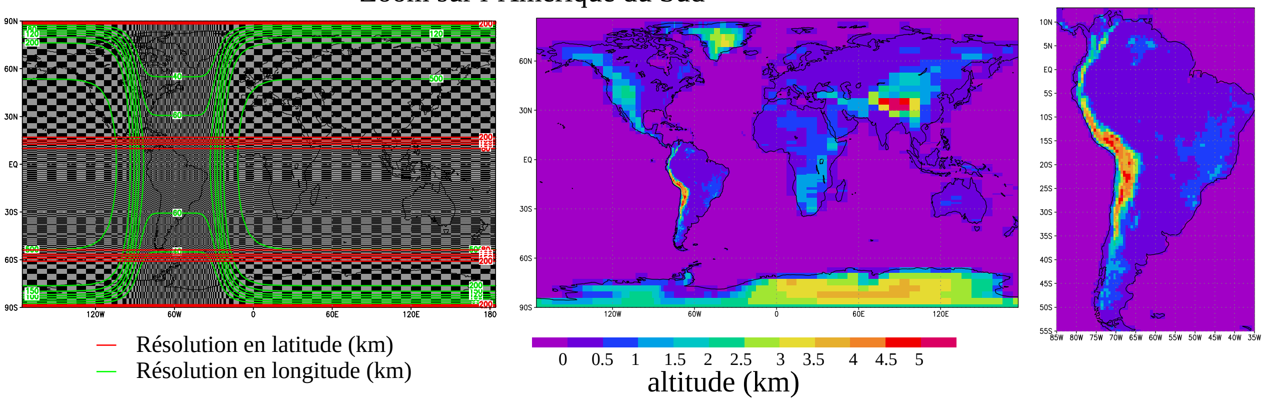

Figure G.1: Haut: grille pour la résolution standard 2.5°×3.75° de LMDZ (gauche), et topographie représentée dans cette résolution standard à l'échelle globale (milieu) et sur l'Amérique du Sud (droite). Bas: même chose pour la grille zoomée sur l'Amérique du Sud.

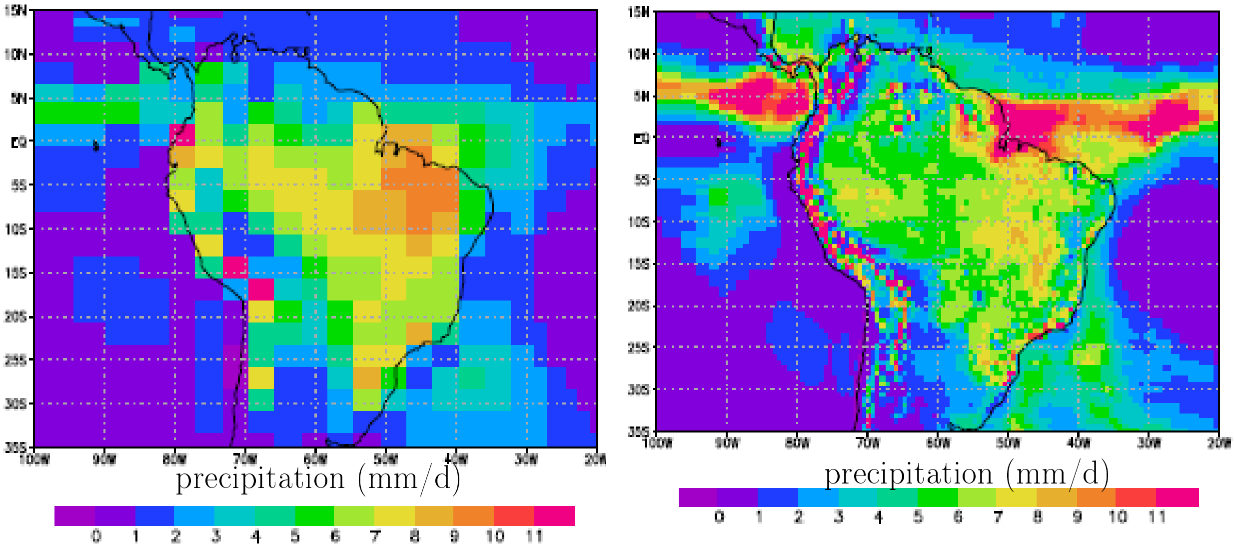
a) precipitation, standard resolution

b) precipitation, zoom

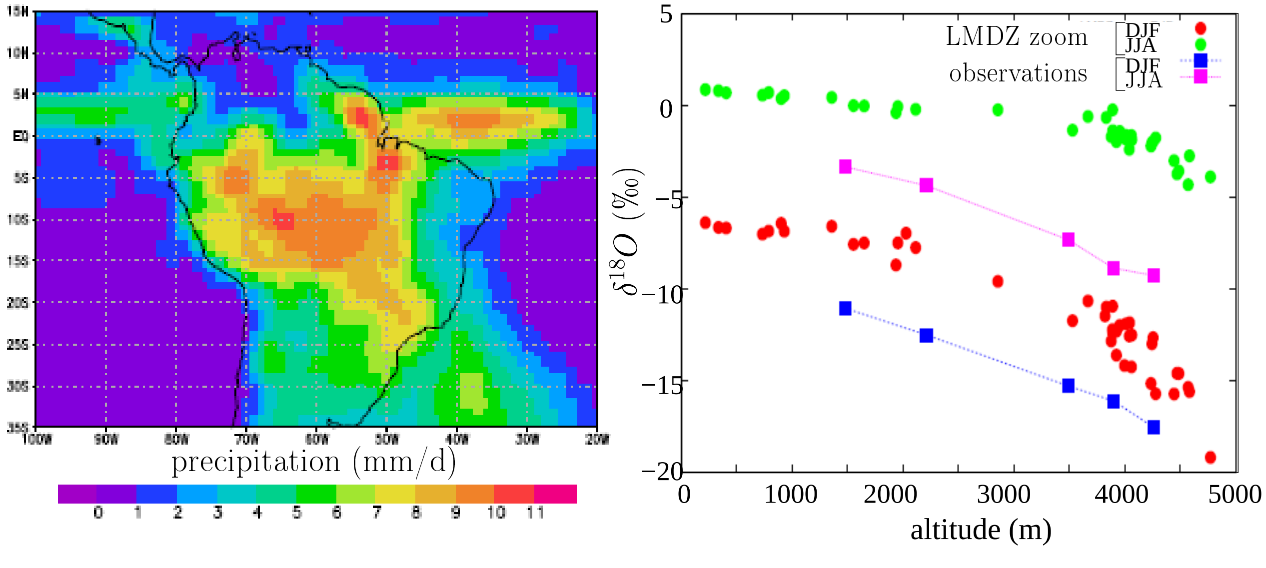
c) precipitation, CMAP observations

d) altitude-$\delta^{18}O$ relationship

Figure G.2: a) Taux de précipitation moyen sur la saison de mousson (DJF) simulé par LMDZ dans sa résolution standard. b) idem pour la simulation zoomée. c) idem pour les observations CMAP (CPC Merged Analysis of Precipitation, [Xie and Arkin, 1997]). d) $\delta^{18}O$ des précipitations en fonction de l'altitude, observé le long de la vallée du Zongo ([Vimeux et al., 2005], bleu et rose) et simulé par LMDZ sur les points de grilles autour de la vallée du Zongo. Adapté d'après Guillaume Trémoy ([Tremoy, 2009]).

Annexe H

Annexes des différents chapitres

H.1 Decomposition of the amount effect

The analysis method described here provides a general framework for quantifying the effect of different processes on the control of the isotopic composition of precipitation.

To unravel the different processes responsible for the amount effect, $\frac{d\,\delta D_p}{d\,P}$ is split into a sum of contributions from different processes.

H.1.1 Chasles's relationship

First, we use Chasles's relationship to split the isotopic composition of the precipitation δD_p into that of the SL feeding the convective system, the effect of processes converting this vapor into condensate that precipitates, and the effect of processes converting this condensate into precipitation:

$$\delta D_p = \delta D_{SL} + (\delta D_{dtr} - \delta D_{SL}) + (\delta D_p - \delta D_{dtr}) \tag{H.1}$$

where δD_{SL} is the composition of the environment in the subcloud layer (the lowest 50 hPa in which the adiabatic updraft originates, hereafter named SL); δD_{dtr} is the average composition of the condensate that precipitates at all altitudes. Therefore, the first term represents the composition of low level vapor feeding the convective system. The second term represents the modifications of the isotopic composition of water during the ascent, from low level vapor to precipitating condensate. These modifications are related to processes such as fractionation during condensation or entrainement of environmnental air. The last term represents the modification of the isotopic composition of the precipitating water during its fall down to the surface.

To isolate the different contributions from different processes on the amount effect, that is, on $\frac{d\,\delta D_p}{d\,P}$, equation H.1 is differentiated:

$$d\,\delta D_p = d\,\delta D_{SL} + d\,(\delta D_{dtr} - \delta D_{SL}) + d\,(\delta D_p - \delta D_{dtr}) \tag{H.2}$$

H.1.2 Decomposition of the subcloud-layer vapor

At steady state, the isotopic composition of the SL vapor is determined by the composition of the different sources of vapor into the SL. We thus decompose the $d\,\delta D_{SL}$ component by calculating the water budget in the subcloud layer. Water inputs are the following (figure 2.7):

- Evaporation from the ocean surface. The water input flux is referred to as F^q_{surf} and its composition as δD_{surf}.
- Input of already depleted water vapor from the unsaturated downdraft. The water input flux is referred to as F^q_{vp} and its composition as δD_{vp}.
- Input of environmental moisture from above through the environmental subsidence. This environmental subsidence is due on the one hand to the compensation of convective ascending

fluxes, and on the other hand to large scale subsidence when the large scale vertical motion is subsident. The water input flux is referred to as F^q_{subs} and its composition as δD_{subs}.

- Input from rain reevaporation within the subcloud layer. The water input flux is referred to as F^q_{revap} and its composition as δD_{revap}.
- Input of low-level moisture through horizontal advection. The water input flux is referred to as F^q_{LS} and its composition as δD_{LS}.

The only output of SL vapor is the ascent in convective updrafts. Since there is no fractionation associated with this output (i.e. no condensation below cloud base, homogeneous composition in the SL), at steady state, the composition of the vapor in the subcloud layer is the weighted mean of the composition of all these inputs:

$$\delta D^{eq}_{SL} = r_{surf} \cdot \delta D_{surf} + r_{vp} \cdot \delta D_{vp} + r_{subs} \cdot \delta D_{subs} + r_{revap} \cdot \delta D_{revap} + r_{LS} \cdot \delta D_{LS} \tag{H.3}$$

where r_{surf}, r_{vp}, r_{subs}, r_{revap} and r_{LS} are the proportions of vapor in the subcloud layer originating from each process, at steady state ($r_{surf} + r_{vp} + r_{subs} + r_{revap} + r_{LS} = 1$). For example,

$$r_{surf} = \frac{F^q_{surf}}{F^q_{surf} + F^q_{vp} + F^q_{subs} + F^q_{revap} + F^q_{LS}}$$

Since the compositions of water in convective drafts and in the environment all depends on the composition of the SL vapor (a shift in the SL composition would be propagated in all convective drafts), we write all the compositions in reference to δD^{eq}_{SL}, to better isolate the influence of the different convective processes. Equation H.3 therefore yields:

$$\begin{aligned} \delta D^{eq}_{SL} = \delta D_{surf} + r'_{vp} \cdot (\delta D_{vp} - \delta D^{eq}_{SL}) + r'_{subs} \cdot (\delta D_{subs} - \delta D^{eq}_{SL}) \\ + r'_{revap} \cdot (\delta D_{revap} - \delta D^{eq}_{SL}) + r'_{LS} \cdot (\delta D_{LS} - \delta D^{eq}_{SL}) \end{aligned} \tag{H.4}$$

where $r'_{vp} = \frac{r_{vp}}{r_{surf}}$, and other r' coefficients are defined similarly.

It appears now more clearly that δD^{eq}_{SL} is equal to the composition of the surface evaporation, plus modifications by other water fluxes. Equation H.4 can be compared with the traditional closure assumption ([Merlivat and Jouzel, 1979]), in which water fluxes other than surface evaporation are neglected and thus $\delta D^{eq}_{SL} = \delta D_{surf}$.

Finally, equation H.4 is differenciated to yield the contributions from different processes:

$$\begin{gathered} d\delta D^{eq}_{SL} = d\delta D_{surf} \\ + r'_{vp} \cdot d\left(\delta D_{vp} - \delta D^{eq}_{SL}\right) + r'_{revap} \cdot d\left(\delta D_{revap} - \delta D^{eq}_{SL}\right) \\ + r'_{subs} \cdot d\left(\delta D_{subs} - \delta D^{eq}_{SL}\right) + r'_{LS} \cdot d\left(\delta D_{LS} - \delta D^{eq}_{SL}\right) \\ + dr'_{vp} \cdot \left(\delta D_{vp} - \delta D^{eq}_{SL}\right) + dr'_{subs} \cdot \left(\delta D_{subs} - \delta D^{eq}_{SL}\right) \\ + dr'_{revap} \cdot \left(\delta D_{revap} - \delta D^{eq}_{SL}\right) + dr'_{LS} \cdot \left(\delta D_{LS} - \delta D^{eq}_{SL}\right) \end{gathered} \tag{H.5}$$

H.1.3 Summary of this decomposition

To summarize, the $d\,\delta D_p$ signal is decomposed into 5 contributions:

$$\frac{d\,\delta D_p}{d\,P} = \frac{d\,\delta D_{surf}}{d\,P} + c_{ascend} + c_{unsat} + c_{recycling} + c_{env} \tag{H.6}$$

1. $\frac{d\,\delta D_{surf}}{d\,P}$ is the contribution due to the composition of the evaporative flux from the ocean: $d\delta D_{surf}$. It is represented in orange on figures 2.8 and 2.12.
2. c_{ascend} is the contribution due to condensation and precipitation processes in the ascending drafts: $\delta D_{dtr} - \delta D_{SL}$, with the effect of the composition of the entrained environment substracted. It is represented in magenta on figures 2.8 and 2.12.

3. c_{unsat} is the contribution due to all processes during the fall of the rain, including the direct effect of reevaporation and diffusive exchange on the falling precipitation composition ($\delta D_{precip} - \delta D_{dtr}$), and the effect of the composition of the vapor in the unsaturated downdraft on the composition of the SL vapor ($r'_{vp} \cdot d\,(\delta D_{vp} - \delta D^{eq}_{SL}) + r'_{revap} \cdot d\,(\delta D_{revap} - \delta D^{eq}_{SL})$, with the effect of the composition of the entrained environment substracted. This is represented in green on figures 2.8 and 2.12.

4. $c_{recycling}$ is the contribution due to the origin of the SL vapor: $dr'_{vp} \cdot (\delta D_{vp} - \delta D^{eq}_{SL}) + dr'_{subs} \cdot (\delta D_{subs} - \delta D^{eq}_{SL}) + dr'_{revap} \cdot (\delta D_{revap} - \delta D^{eq}_{SL}) + dr'_{LS} \cdot (\delta D_{LS} - \delta D^{eq}_{SL})$. This depends on the proportion of vapor originating from the surface evaporation or from the convective fluxes, but not directly on their isotopic composition. It is represented in cyan on figures 2.8 and 2.12.

5. c_{env} is the contribution due to the composition of the environment relatively to that of the subcloud layer vapor: $r'_{subs} \cdot d\left(\delta D_{subs} - \delta D^{eq}_{SL}\right) + r'_{LS} \cdot d\,(\delta D_{LS} - \delta D^{eq}_{SL})$. We also add the effect of the composition of the environment entrained into convective drafts. This contribution thus gathers the effects of the composition of the environment through entrainment into ascending drafts and unsaturated downdrafts, and through environmental subsidence. It mainly represents the effect of the vertical gradient of the isotopic composition in the environment. It is represented in dark blue on figures 2.8 and 2.12.

H.1.4 Diagnostic of these contributions

Each contributing term in equations H.2 and H.5 is diagnosed from the model.

In section 2.6.3, the amount effect and its contributions are calculated by comparing two equilibrium simulations simulating different precipitation rates. For example, if simulations (1) and (2) simulate different precipitation rates around P, we calculate:

$$\frac{d\,\delta D_p}{dP}(P) = \frac{\delta D_p(2) - \delta D_p(1)}{P(2) - P(1)}$$

The amount effect and its contributions are shown as a function of precipitation rate on figure 2.8.

In section 2.7, the variability of δD_p and its contributions are calculated as a function of time t every 6 hours by comparing variables at time t to the mean values over the simulation. For example, at each time t,

$$d\,\delta D_p(t) = \delta D_p(t) - \delta \bar{D}_p$$

The evolution of $d\,\delta D_p(t)$ simulated by the model as well as $d\,\delta D_p(t)$ reconstructed by summing all the different contributions are shown on figure 2.11. The spectral analysis of each contribution is performed on figure 2.12.

H.2 Time scale of maximum correlation between δD_p and averaged precipitation

The goal here is to calculate the time scale of maximum correlation, τ_m^{max} , between $\delta D_p(t)$ and the average of the precipitation rate over the τ_m previous days: $\bar{P}(t) = \int_{t-\tau_m}^{t} P(t)dt$. As an idealized example, we assume that precipitation $P(t)$ is a sinusoid of period τ_p: $P(t) = P_0 \cdot \cos(\frac{2\pi}{\tau_p})$ (in nature, precipitation signals are more complex). We further assume that the response of δD_p to $P(t)$ is given by the following differential equation:

$$\frac{d\delta D_p}{dt} = S \cdot P(t) - \frac{\delta D_p}{T} \tag{H.7}$$

equation

The correlation is maximal when δD_p and $\bar{P}$ are in phase.

$$\bar{P}(t) = \int_{t-\tau_m}^{t} P(t)dt = \frac{P_0 \cdot \tau_p}{\pi} \cdot \sin(\frac{\pi \tau_m}{\tau_p}) \cdot \cos(\frac{2\pi}{\tau_p}(t - \frac{\tau_m}{2})) \tag{H.8}$$

equation

$\bar{P}$ is thus delayed by $\frac{\tau_m}{2}$ compared to P.

The differential equation is solved in the frequency domain, with $P(t) = \Re(P_0 \cdot e^{i\omega t})$ and $\delta D_p(t) = \Re(\delta \hat{D}_p \cdot e^{i\omega t})$, where $\omega = \frac{2\pi}{\tau_p}$ is the frequency of both P and δD_p:

$$i\omega \delta \hat{D}_p = S \cdot P_0 - \frac{\delta \hat{D}_p}{T} \tag{H.9}$$

Thus:

$$\delta \hat{D}_p = S \cdot P_0 \frac{1}{\frac{1}{T} + i\omega} = S \cdot P_0 \frac{1}{\sqrt{\frac{1}{T^2} + \omega^2}} e^{i \cdot \arctan(\omega \cdot T)} \tag{H.10}$$

Thus δD_p is shifted by $\frac{1}{\omega} \cdot \arctan(\omega \cdot T)$ compared to $P(t)$.

Therefore, δD_p and $\bar{P}$ are in phase when

$$\tau_m = \frac{\tau_P}{\pi} \cdot \arctan(\frac{2\pi T}{\tau_P}) \tag{H.11}$$

Note that in nature, the relationship between T and τ_m is complexified by the continuous spectrum of variability frequencies.

H.3 Water tagging in the 2D squall line

Tracking the origin of water and isotopes has been implemented in several isotopic general circulation models ([Cole et al., 1999, Delaygue et al., 2000, Werner et al., 2001, Noone and Simmonds, 2002a]) to determine the geographic origin of water vapor. Here, we use the same tracking concept, but for tracking altitude and reevaporation. We define n altitude layers, and refer to the summit and middle of the layer $j \in [1, n]$ as z_s^j and z_m^j . We consider $n = 4$ layers: 0-2km, 2-4km, 4-6km, >6km. We also define $n + 1$ two-dimensional fields X_v^j corresponding to vapor tracers: n fields for tracking the n altitude layers, and one field to track reevaporation. At each time and in each grid box, the sum of these tracers is equal to that of the total vapor content q_v:

$$\sum\nolimits_{j=1}^{n+1} X_v^j = q_v$$

so that the vapor can be exactly decomposed into the $n+1$ origins. Similarly, additional tracor fields are defined for the condensate and the precipitation q_c and q_p, as well as for all the isotopic species in vapor, condensate and precipitation.

In the initial state, we assume that all the vapor originates from the lowest layer: $X_v^j = 0$ for $j \in [2, n + 1]$ and $X_v^1 = q_v$. Then, during the simulation, all tracers are advected passively like "normal" water and isotopes, and behave similarly during phase changes. However, after advection, the following operation is done so that tracers trace the maximum altitude encountered: in each grid point (let z be the altitude of the grid point), for each of the tracor layers $j \in [1, n - 1]$, if both $X_v^j > 0$ and $z > z_s^j$, then the content of X_v^j is transfered to X_v^{j+1}. Besides, to track the water originating from rain reevaporation, all the rain that reevaporates, whatever its origin, is transfered to X_v^{n+1}. One can thus estimate, in each grid point, the fraction of the vapor that has originated from rain reevaporation r_e:

$$r_e = \frac{X_v^{n+1}}{q_v}$$

Approximating the average altitude of the tracers in each layer by the altitude of the middle of the layer, z_m^j, we can also estimate the maximum altitude encountered by the vapor in average, $\overline{z_{max}}$:

$$\overline{z_{max}} = \frac{\sum_{j=1}^{n} \left(X_v^j \cdot z_m^j \right)}{\sum_{j=1}^{n} X_v^j}.$$

Note that the estimate of $\overline{z_{max}}$ bears uncertainties due to the heterogeneous distribution of the tracers in each altitude layer. The uncertainty is half the thickness of the layers, that is, 1km.

H.4 Surface evaporation in the 2D transport and microphysics model

To estimate the effect of surface evaporation on the rain isotopic composition, we calculate the evaporation from the surface E as

$$E = \lambda \cdot EP$$

with EP the potential evaporation and λ a parameter depending on the sol property. We assume that the soil becomes quicky saturated as rain falls: $\lambda = 1$ when q_{sol}>10mm and $\lambda = \frac{q_{sol}}{10}$ otherwise. The soil water q_{sol} at grid point i is the integral of the precipitation that has fallen since the beginning of the line substracted by the evaporation:

$$q_{sol}(i) = \sum_{j=1}^{i} (P(j) - E(j)) \cdot \frac{\Delta x}{u_{SL}}$$

with P the precipitation rate, u_{SL} the advection speed of the squall line and Δx the horizontal resolution of the model.

We calculate potential evaporation using a Penman-like equation ([Penman, 1948], used for Niger in [Wallace and Holwill, 1997]):

$$EP = \frac{R_n - G}{L_v} \frac{\Delta}{\Delta + \gamma} + \rho \cdot \frac{1}{r} \cdot (q_s(T_a) - q_a) \cdot \frac{\gamma}{\Delta + \gamma}$$

with $\Delta = \frac{L_v \cdot q_s(T_a)}{R_d \cdot T_a^2}$, $\gamma = \frac{c_p}{L_v}$, $\frac{1}{r} = C_d \cdot u$, L_v the latent heat of vaporisation, q_s the specific humiidty at saturation, R_d the perfect gas constant, T_a and q_a the air temperature and specific humidity in the lowest layer (0-500m), c_p and ρ the heat capacity and volumetric mass of air, u the wind speed, c_d a drag coeficient set to $1.2 \cdot 10^{-3}$, R_n the net radiation and G the heat flux to the soil.

We neglect vegetation, which is very sparse in Niamey.

We then add this evaporated water directly into the lowest layer of the model, neglecting the effect of turbulence on vapor transport. This approximation is justified because most of the evaporation is expected in the stratiform zone, which is subsident.

For isotopes, we calculate that the soil composition as the weigted mean of the precipitation that has fallen since the beginning of the line. We use the [Craig and Gordon, 1965] equation to calculate the composition of the surface evaporation. We consider the soil water during a squall line as open water and calculate the kinetic fractionation following [Merlivat and Jouzel, 1979].

There is a large uncertainty on the calculation of the net radiation term $R_n - G$. During the night, R_n is sligthly negative in the Sahel ($\simeq -20W/m^2$: [Wallace and Holwill, 1997, Guichard et al., 2008]). At midday in August under precipitation events, an upper bound for R_n is of the order of $400W/m^2$ (F. Guichard, pers. comm.). Assuming $G \simeq 0.4 \cdot R_n$ ([Wallace and Holwill, 1997]), an upper bound for $R_n - G$ is thus $250W/m^2$. We tested these different values for $R_n - G$.

H.5 Appendix and supplementary material of “Understanding the ^{17}O-excess glacial-interglacial variations in Vostok precipitation”

H.5.1 The distillation model MCIM

To model the evolution of the isotopic composition of air masses from the source region to the poles as well as the composition of the Vostok snowfall, we use the Mixed Cloud Isotopic Model

(MCIM: [Ciais and Jouzel, 1994]) adapted for the calculation of ice ^{17}O-excess ([Landais et al., 2008]), with the same fractionation coefficients as in the SCM.

The MCIM is an extension of Lagrangian models based on a Rayleigh distillation ([Merlivat and Jouzel, 1979, Jouzel and Merlivat, 1984]). It describes the isotopic processes at each phase transition and thus the isotopic composition of (1) the condensed phase (liquid water or solid ice) and (2) the water vapor at each step from the oceanic source region to the precipitation site on the ice sheet. During liquid precipitation, only equilibrium fractionation occurs. Then, kinetic fractionation is taken into account for snowflakes formation. Depending on the temperature, the MCIM allows for a zone of mixed clouds, where liquid droplets and ice crystal can coexist. In this zone, the Bergeron-Findeisen process associated with significant kinetic fractionation effects is considered (details in [Ciais and Jouzel, 1994]). As for the SCM, the relative proportion of equilibrium vs. kinetic fractionation is controlled by the supersaturation .

The transport path of the water mass is described in term of temperature and pressure. The air parcel is transported in saturated (or supersaturated in polar regions) conditions from the source region to the precipitation site, hence implying continuous fractionation. In nature, air parcels are transported mainly in unsaturated conditions and most of the saturation occurs during the last day of transport ([Helsen et al., 2006]). However, since the depletion associated with the distillation depends mainly on the initial and final temperatures, considering transport in saturated conditions has little impact on the results (less than 2‰ for $\delta^{18}O$, and negligible for d-excess: [Helsen et al., 2006]).

The model receives as main inputs (1) the temperature and pressure of the source region as well as the isotopic composition of the initial water vapor and (2) the temperature and pressure at the precipitation site.

The MCIM includes several tunable parameters ([Ciais and Jouzel, 1994]) such as the dependence of supersaturation on temperature, the fraction of condensate remaining in clouds. We performed numerous sensitivity experiments to tune these parameters and kept only those enabling a reproduction of the $\delta^{18}O$, d-excess and ^{17}O-excess on the Antarctic transect ([Landais et al., 2008]). Note that the same dependency of supersaturation with temperature has been taken for the MCIM and the SCM. For the other tunable parameters, we choose values very similar to those used in previous studies ([Ciais and Jouzel, 1994, Vimeux et al., 2001, Stenni et al., 2001]). Other parameters have however been tested (section 7.5).

H.5.2 Closure assumption

Most Rayleigh distillation models are initialized by the isotopic composition of an air parcel originating from the planetary boundary layer (BL). The influences of changing climatic conditions on this isotopic composition are estimated through the so-called closure assumption ([Merlivat and Jouzel, 1979]). In this assumption, the only source of vapor in the BL is the evaporation from the sea surface. The composition R_E of this evaporation is given by the [Craig and Gordon, 1965] equation:

$$R_E = \frac{1}{\alpha_K} \cdot \frac{R_{oce}/\alpha_{eq} - rh_s \cdot R_{BL}}{1 - rh_s} \tag{H.12}$$

with α_K the kinetic fractionation coefficient, α_{eq} the liquid vapor equilibrium fractionation coefficient and R_{oce} the isotopic ratios of the ocean surface. The relative humidity *at the surface*, rh_s is the relative humidity of near surface air at the temperature of the ocean surface T_s:

$$rh_s = rh_a \cdot \frac{q_{sat}(T_a)}{q_{sat}(T_s)} \tag{H.13}$$

where q_{sat} is the specific humidity at saturation and rh_a and T_a are the relative humidity and temperature of the near-surface air respectively.

If the only source of vapor in the BL is the surface evaporation and if the sinks of vapor from the BL do not fractionate (i.e. have the composition of the BL), then in a stationary state the composition of the BL R_{BL} is equal to the composition of the surface evaporation R_E. Equaling R_{BL} and R_E yields the composition of the BL ([Merlivat and Jouzel, 1979]):

$$R_{BL} = \frac{R_{oce}}{\alpha_{eq} \cdot (\alpha_K + rh_s \cdot (1 - \alpha_K))} \tag{H.14}$$

Previous studies interpreting water stable isotopes in ice cores from simple distillation models implicitly assumed that rh_s and rh_a were identical ([Vimeux et al., 2001]). However, we emphasize here that in nature, rh_s differs from rh_a owing to the difference between the air and surface temperatures (thermodynamic disequilibrium) ([Angert et al., 2008, Pfahl and Wernli, 2008]). By linearizing equation H.13, we obtain:

$$rh_s \simeq rh_a \cdot \left(1 - \frac{\partial \ln\left(q_{sat}\left(T_s\right)\right)}{\partial T_s} \cdot (T_s - T_a)\right) \tag{H.15}$$

For T_s ranging from 0 to 30°C:

$$rh_s \simeq rh_a \cdot \left(1 - (6.5 \pm 0.7) \cdot 10^{-2} \cdot (T_s - T_a)\right) \tag{H.16}$$

For example, if rh_a is 70% and $T_s - T_a$ is 2°C, then rh_s is 61%.

H.5.3 Uncertainties on the sensitivities of the BL composition to rh_s to SCM parameters

The SCM includes some tunable parameters, e.g. in the parametrization of the supersaturation as a function of temperature (equation A1 of the article’s appendix), or in the microphysical parameters used in the representation of unsaturated downdrafts. Sensitivity tests are performed to test the robustness of our results with respect to these parameters (envelopes on figure 4 of the article) .

The sensitivity of the SCM to kinetic effects during ice condensation is negligible: varying parameter λ in equation A1 from 0 (no kinetic effects) to 0.004 or μ from 1 to 1.05 (the maximum value in [Ciais et al., 1995]) results in variations in $\delta^{18}O$ d-excess and ^{17}O-excess of the BL vapor lower than 0.01 ‰, 0.05‰ and 0.4 permeg respectively.

As in [Bony et al., 2008], we also performed sensitivity tests to tunable parameters controlling the reevaporation rate of the precipitation and downdraft properties ([Emanuel, 1991]) by varying these parameters by ±20%. In addition, we varied the isotopic parameter ϕ (controlling the relative humidity at the droplets contact in equation A2 of the article’s appendix, set to 0.9 in the control simulation) from 0 to 0.9, which is an extreme variation. These parameter variations mainly results in shifts in BL $\delta^{18}O$, d-excess and ^{17}O-excess, but the sensitivities to convective processes and rh_s remain of the same order of magnitude (figure 4). In particular, the slope of the BL ^{17}O-excess versus rh_s among all tests varies from -0.9 permeg/% to -1.6 permeg/%. Similarly, $\left(\frac{\partial d_{BL}}{\partial rh_s}\right)_P$ varies from -0.5 to -0.8‰/%.

The dependence of the BL composition to rh_s and convective activity is thus sensitive to the representation of rain reevaporation in the convective scheme and of the associated isotopic fractionation. The fact that the convective parameters have been rigorously optimized and evaluated ([Emanuel and Zivkovic-Rothman, 1999]) and the representation of isotopic fractionation during evaporation has been evaluated ([Bony et al., 2008]) constitutes currently the best guarantee that the sensitivities derived from the SCM are of the right order of magnitude.

H.5.4 Sensitivity of d-excess and ^{17}O-excess in ice to $\delta^{18}O$ of the source vapor

The goal here is to show that whereas d-excess in ice depends on the $\delta^{18}O$ of the source vapor, ^{17}O-excess is independent of this variable.

In a Rayleigh model describing the isotopic behavior of an air mass from the first vapor above the ocean to the final precipitation site, the isotopic ratio in precipitation (here $^{18}R_{ice}$) can be written:

$$^{18}R_{ice} =^{18} F \cdot^{18} R_{vap}$$

where ${}^{18}R_{vap}$ is the isotopic ratio in the initial vapor and ${}^{18}F$ is a function of climatological parameters and fractionation coefficients for the system $H_2^{18}O/H_2^{16}O$. Differentiating this equation for variations in ${}^{18}R_{vap}$ yields:

$$\Delta^{18}R_{ice} = {}^{18}F \cdot \Delta^{18}R_{vap}$$

or, in δ notation:

$$\Delta\delta^{18}O_{ice} = {}^{18}F \cdot \Delta\delta^{18}O_{vap}$$

When applied to d-excess ($\Delta d_{ice} = \Delta\delta D_{ice} - 8 \cdot \Delta\delta^{18}O_{ice}$), this yields:

$$\Delta d_{ice} =^{D} F \cdot \Delta d_{vap} + 8 \cdot ({}^{D}F - {}^{18}F) \cdot \Delta\delta^{18}O_{vap}$$

Hence the dependency of d-excess in ice on $\Delta\delta^{18}O_{vap}$.
When applied to ${}^{17}O$-excess, this yields:

$$\Delta^{17}O\text{-excess}_{ice} = \frac{\Delta^{17}R_{ice}}{{}^{17}R_{ice}} - 0.528 \cdot \frac{\Delta^{18}R_{ice}}{{}^{18}R_{ice}} = \frac{\Delta^{17}R_{vap}}{{}^{17}R_{vap}} - 0.528 \cdot \frac{\Delta^{18}R_{vap}}{{}^{18}R_{vap}} = \Delta^{17}O\text{-excess}_{vap}$$

Hence ice ${}^{17}O$-excess does not depend on $\Delta\delta^{18}O_{vap}$.

H.6 A simple framework to understand the effect of fractionation at the soil surface

To better understand how the isotopic fractionation at the soil surface impacts the composition of different water pools in the soil-vegetation-atmosphere system, and explore how in turns the isotopic composition may add a constrain on the water cycle over continents, we derive here a very simple theoretical framework.

First, we assume that the soil is at stationary state. This is a reasonable assumption over sufficiently long time periods (at least a year). The water balance writes:

$$F_{in} = P + M = E + T + D + \mathcal{R} \tag{H.17}$$

where P is the precipitation, M the snow melt, $\mathcal{R}$ the surface runoff, F_{in} the incoming water at the soil surface, E the bare soil evaporation, T the transpiration and D the drainage. We note $ET = E + T$ the total evapo-transpiration from the soil. Similarly, the isotopic balance writes:

$$F_{in} \cdot R_{in} = E \cdot R_E + T \cdot R_T + D \cdot R_D + \mathcal{R} \cdot R_R \tag{H.18}$$

where R_{in}, R_E, R_T, R_D and $R_{\mathcal{R}}$ are the isotopic ratios of the incoming water at the soil surface, the bare soil evaporation, the transpiration , the drainage and surface runoff.

We assume that the surface runoff has the composition of the incoming water: $R_{\mathcal{R}} = R_{in}$, neglecting the temporal covariation between $\mathcal{R}$ and R_{in}. We further assume that the soil composition is uniform, and that the drainage and transpiration have the same composition of the bulk soil R_s: $R_T = R_D = R_s$. In doing so, we neglect spatial isotopic variations in the soil and the temporal covariations between R_s and D on the one hand and R_s and T one the other hand.

The aforementioned hypotheses, injected in equation H.18 and combined with equation H.17, lead to:

$$R_{in} = r_E \cdot r_{ET} \cdot R_E + (1 - r_E \cdot r_{ET})\, R_s$$

with $r_E = \frac{E}{ET}$ and $r_{ET} = \frac{ET}{F_i}$, where $F_i = F_{in} - \mathcal{R}$ is the water that infiltrates into the soil.

Eventually, we assume that R_E follows the [Craig and Gordon, 1965] equation (equation B.2), with atmospheric conditions assumed constant over the long study period. Combined with the previous equation, we deduce that:

$$R_s = \frac{r_E \cdot r_{ET} \cdot R_{slim} + (1 - r_E \cdot r_{ET}) \cdot \alpha_{eq} \cdot \alpha_K \cdot (1-h) \cdot R_{in}}{r_E \cdot r_{ET} + (1 - r_E \cdot r_{ET}) \cdot \alpha_{eq} \cdot \alpha_K \cdot (1-h)} \tag{H.19}$$

where α_{eq}, α_K, h and R_v were defined in appendix B.3, and R_{slim} is the isotopic ratio of the soil in the limiting case where $r_E = 1$ and $r_{ET} = 1$:

$$R_{slim} = \alpha_{eq} \cdot (\alpha_K \cdot (1-h) \cdot R_{in} + h \cdot R_v) \tag{H.20}$$

The isotopic compositon of the evapo-transiration flux from the soil is the weighted average of R_E and $R_T = R_s$:

$$R_{ET} = r_E \cdot R_E + (1 - r_E) \cdot R_s \tag{H.21}$$

Using the [Craig and Gordon, 1965] equation to relate R_E to R_s and R_v, we obtain:

$$R_{ET} = \frac{R_s \cdot (r_E + (1 - r_E) \cdot \alpha_{eq} \cdot \alpha_K \cdot (1-h)) - r_E \cdot \alpha_{eq} \cdot h \cdot R_v}{\alpha_{eq} \cdot \alpha_K \cdot (1-h)} \tag{H.22}$$

Annexe I

Listes des articles liées à la thèse

1. *S. Bony, C. Risi and F. Vimeux*, 2008. Influence of convective processes on the isotopic composition ($\delta^{18}O$ and δD) of precipitation and water vapor in the tropics : 1. Radiative-convective equilibrium and Tropical Ocean-Global Atmosphere-Coupled Ocean-Atmosphere Response Experiment (TOGA-COARE) simulations, ***Journal of Geophysical Research****, vol 113, doi : 10.1029/2008JD009943*
2. *C. Risi, S. Bony and F. Vimeux*, 2008. Influence of convective processes on the isotopic composition ($\delta^{18}O$ and δD) of precipitation and water vapor in the tropics : 2. Physical interpretation of the amount effect, ***Journal of Geophysical Research****, vol 35, doi :10.1029/2008GL035920*
3. *C. Risi, S. Bony, F. Vimeux, L. Descroix, B. Ibrahim, E. Lebreton, I. Mamadou and B. Sultan*, 2009. What controls the isotopic composition of the African monsoon precipitation ? Insights from event-based precipitation collected during the 2006 AMMA field campaign, ***Geophysical Research Letters****, vol 35, doi : 10.1029/2008JD009942*
4. *C. Risi, S. Bony, F. Vimeux, M. Chong and L. Descroix.* Evolution of the water stable isotopic composition of the rain sampled along Sahelian squall lines, *in press in* ***Quarterly Journal of the Royal Meteorological Society***
5. *C. Risi, A. Landais, S. Bony, V. Masson-Delmotte, J. Jouzel and F. Vimeux.* Modeling the ^{17}O-excess and d-excess variations in Antarctic precipitation and its moisture source, *accepted by* ***Journal of Geophysical Research***
6. *C. Risi, S. Bony, F. Vimeux and Jean Jouzel.* Water stable isotopes in the LMDZ4 General Circulation Model : model evaluation for present day and past climates and applications to climatic interpretation of tropical isotopic records, *in revision for* ***Journal of Geophysical Research***
7. *C. Risi, S. Bony, J. Ogée, T. Bariac and co-auhors.* What can we learn from water stable isotopes about land surface processes ? Investigation with an isotopic version of the ORCHIDEE land surface model, *in preparation for* ***Journal of Geophysical Research***

Bibliographie

[Abdulla et al., 1996] Abdulla, F. A., Lettenmaier, D. P., Wood, E. F., and Smith, J. A. (1996). Application of a macroscale hydrological model to estimate the water balance of the Arkansas-Red River Basin. *J. Geophys. Res.*, 101 :7449–7459.

[Adegoke et al., 2002] Adegoke, J. O., Pielke, R. A., Eastman, J., Majhmood, R., and Hubbard, K. G. (2002). Impact of Irrigation on Midsummer Surface Fluxes and Temperature under Dry Synoptic Conditions : A Regional Atmospheric Model Study of the U.S. High Plains. *Mon. Wea. Rev.*, 131 :556–564.

[Aggarwal et al., 2007] Aggarwal, P. K., Alduchov, O., Araguás, L. A., Dogramaci, S., Katzlberger, G., Kriz, K., Kulkarni, K. M., Kurttas, T., and Newman, B. D. (2007). New capabilities for studies using isotopes in the water cycle. *Eos*, 88 (49) :537 ?538.

[Aleinov and Schmidt, 2006] Aleinov, I. and Schmidt, G. A. (2006). Water isotopes in the GISS ModelE land surface scheme. *Global and Planet. Change*, 51 :108–120.

[Allison et al., 1983] Allison, G. B., Barnes, C. J., and Hughes, M. W. (1983). The distribution of deuterium and oxygen 18 in dry soils : II. Experimental. *J. Hydrol.*, 64 :377–397.

[Angert et al., 2008] Angert, A., Lee, J.-E., and Yakir, D. (2008). Seasonal variations in the isotopic composition of near-surface water vapour in the eastern Mediterranean. *Tellus*, 60 (4) :674–684.

[Baldini et al., 2008] Baldini, L. M., McDermott, F., Foley, A. M., , and Baldini, J. U. L. (2008). Spatial variability in the European winter precipitation d18O-NAO relationship : Implications for reconstructing NAO-mode climate variability in the Holocene. *Geophys. Res. Lett.*, 35 :L04709, doi :10.1029/2007GL032027.

[Barkan and Luz, 2005] Barkan, E. and Luz, B. (2005). High precision measurements of 17O/16O and 18O/16O ratios in H2O. *Rapid Commun Mass Spectrom.*, 19 :3737 – 3742.

[Barkan and Luz, 2007] Barkan, E. and Luz, B. (2007). Diffusivity fractionations of H216O/H217O and H216O/H218O in air and their implications for isotope hydrology. *Rapid Commun Mass Spectrom.*, 21 :2999–3005.

[Barnard et al., 2007] Barnard, R. L., Salmon, Y., Kodama, N., Sörgel, K., Holst, J., Rennenberg, H., Gessler, A., and Buchmann, N. (2007). Evaporative enrichment and time lags between d18O of leaf water and organic pools in a pine stand. *Plant, Cell and Environment*, 30 :539–550.

[Barnes and Allison, 1988] Barnes, C. and Allison, G. (1988). Tracing of water movement in the unsaturated zone using stable isotopes of hydrogen and oxygen. *J. Hydrol*, 100 :143–176.

[Barnes and Allison, 1983] Barnes, C. J. and Allison, G. B. (1983). The distribution of deuterium and oxygen 18 in dry soils : I. Theory. *J. Hydrol.*, 60 :141–156.

[Barras and Simmonds, 2009] Barras, V. and Simmonds, I. (2009). Observation and modelling of stable water isotopes as diagnostics of rainfall dynamics over southeastern Australia. *J. Geophys. Res., accepted.*

[Barrows and Juggins, 2005] Barrows, T. and Juggins, S. (2005). Sea-surface temperatures around the Australian margin and Indian Ocean during the last glacial maximum. *Quaternary Science Reviews*, 24 :1017 :1047.

[Bath, 1983] Bath, A. H. (1983). Stable isotopic evidence for paleo-recharge conditions of groundwater. *in Paleoclimates and Paleowaters : A Collection of Environmental Isotope Studies*, Internat. At. Energy Agency, Vienna :169–168.

[Bender et al., 1994] Bender, M., Sowers, T., and Labeyrie, L. (1994). The Dole Effect and Its Variations During the Last 130,000 Years as Measured in the Vostok Ice Core. *Glob. Biogeochem. Cycles*, 8 (3) :363 ?376.

[Berger, 1978] Berger, A. (1978). Long-Term Variations of Caloric Solar Radiation Resulting from the Earth's Orbital Elements. *Quatern. Res.*, 9 :139–167.

[Blunier et al., 2002] Blunier, T., Barnett, B., Bender, M. L., , and Hendricks, M. B. (2002). Biological oxygen productivity during the last 60,000 years from triple oxygen isotope measurements. *Glob. Biogeochem. Cycles*, 16 (3) :DOI 10.1029/2001GB001460.

[Bony et al., 2006] Bony, S., Colman, R., Kattsov, V.M.and Allan, R., Bretherton, C., Dufresne, J.-L., Hall, A., Hallegatte, S., Holland, M., Ingram, W., Randall, D., Soden, D., Tselioudis, G., and Webb, M. (2006). How well do we understand and evaluate climate change feedback processes ? *J. Climate*, 19 :3445–3482.

[Bony et al., 2004] Bony, S., Dufresne, J.-L., Le Treut, H., Morcrette, J.-J., and Senior, C. (2004). On dynamic and thermodynamic components of cloud changes. *Climate Dynamics*, 22 :71–86.

[Bony and Emanuel, 2001] Bony, S. and Emanuel, K. A. (2001). A Parameterization of the Cloudiness Associated with Cumulus Convection ; Evaluation Using TOGA COARE Data. *J. Atmos. Sci.*, 58 :3158–3183.

[Bony et al., 2008] Bony, S., Risi, C., and Vimeux, F. (2008). Influence of convective processes on the isotopic composition (deltaO18 and deltaD) of precipitation and water vapor in the Tropics. Part 1 : Radiative-convective equilibrium and TOGA-COARE simulations. *J. Geophys. Res.*, 113 :D19305, doi :10.1029/2008JD009942.

[Bosilovich and Schubert, 2002] Bosilovich, M. G. and Schubert, S. D. (2002). Water vapor tracers as diagnostics of the regional hydrologic cycle. *J. Hydrometeor.*, 3 :149–165.

[Bosilovich et al., 1999] Bosilovich, M. G., Yang, R., and Houser, P. R. (1999). River basin hydroloy in a global offline land-surface model. *J. Geophys. Res.*, 104 :19661–19673.

[Boyle, 1997] Boyle, E. A. (1997). Cool Tropical Temperatures Shift the Global ?18O-T Relationship : An Explanation for the Ice Core 18O - Borehole Thermometry Conflict ? *Geophys. Res. Lett.*, 24 :273–276.

[Braconnot et al., 2007] Braconnot, P., Otto-Bliesner, B., Harrison, S., Joussaume, S., Peterschmitt, J.-Y., Abe-Ouchi, A., Crucifix, M. ansd Driesschaert, E., Fichefet, T., Hewitt, C. D., Kageyama, M., Kitoh, A. aand Laîné, A., Loutre, M.-F., Marti, O., Merkel, U., Ramstein, G., Valdes, P., Weber, S. L., Yu, Y., , and Zhao, Y. (2007). Results of PMIP2 coupled simulations of the Mid-Holocene and Last Glacial Maximum - Part 1 : experiments and large-scale features. *Climate of the Past*, 3 :261–277.

[Braud et al., 2005] Braud, I., Bariac, T., Gaudet, J.-P., and Vauclin, M. (2005). SiSPAT-Isotope, a coupled heat, water and stable isotope (HDO and H218O) transport model for bare soil. Part I. Model description and first verifications. *J. Hydrol.*, 309 :301–320.

[Braud et al., 2009] Braud, I., Biron, P., Bariac, T., Richard, P., Canale, L., Gaudet, J., and Vauclin, M. (2009). Isotopic composition of bare soil evaporated water vapor. Part I : RUBIC IV experimental setup and results. *J. Hydrol.*, 369 :1–16.

[Broecker, 1997] Broecker, W. S. (1997). Mountain glaciers : Recorders of atmospheric water vapor content ? *Global Biogeochemical Cycles*, 11 :589–598.

[Brown et al., 2008] Brown, D., Worden, J., and Noone, D. (2008). Comparison of atmospheric hydrology over convective contnental regions using water vapor isotope measurements from space. *J. Geophys. Res.*, 113.

[Brubaker et al., 2001] Brubaker, K. L., Dirmeyer, P. A., Sudradjat, A., Levy, B. S., and Bernal, F. (2001). A 36-yr climatological description of the evaporative sources of warm-season precipitation in the Mississippi River basin. *J. Hydrometeor.*, 2 :537–557.

[Brunel et al., 1997] Brunel, J., Walker, G., Dighton, J., and Montenya, B. (1997). Use of stable isotopes of water to determine the origin of water used by the vegetation and to partition evapotranspiration. A case study from HAPEX-Sahel. *J. Hydrol*, 188-189 :466–481.

[Brutsaert, 1975] Brutsaert, W. A. (1975). Theory for local evaporation (or heat transfer) from rough and smooth surfaces at ground level. *Water Resour. Res.*, 11 :543–550.

[Burde and Zangvil, 2001] Burde, G. I. and Zangvil, A. (2001). The Estimation of Regional Precipitation Recycling. Part I : Review of Recycling Models. *J. Clim.*, 14 :2497–2508.

[Bush and Philander, 1999] Bush, A. B. and Philander, S. G. H. (1999). The climate of the last glacial maximum : results from a coupled atmosphere-ocean general circulation model. *J. Geophys. Res.*, 24 :509–525.

[Caniaux et al., 1994] Caniaux, G., Redelsperger, J.-L., and Lafore, J.-P. (1994). A numerical study of the stratiform region of a fast mooving squall line. part 1 : general description and water and heat budgets. *J. Atm. Sci*, 51 :2046–2074.

[Celle-Jeanton et al., 2004] Celle-Jeanton, H., Gonfiantini, R., Travia, Y., and Solc, B. (2004). Oxygen-18 variations of rainwater during precipitation : application of the Rayleigh model to selected rainfalls in Southern France. *J. Hydrol.*, 289 :165–177.

[Cess and Potter, 1988] Cess, R. D. and Potter, G. L. (1988). A methodology for understanding and intercomparing atmospheric climate feedback processes in general circulation models. *J. Geophys. Res.*, 97 (7) :8305–8314.

[Chalon et al., 1988] Chalon, J.-P., Jaubert, G., Lafore, J.-P., and Roux, F. (1988). The West African Squall Line Observed on 23 June 1981 during COPT 81 : Mesoscale Structure and Transports. *J. of Atmos. Sci.*, 45 :2744–2763.

[Chiang and Bitz, 2005] Chiang, J. C. H. and Bitz, C. M. (2005). Influence of high latitude ice cover on the marine Intertropical Convergence Zone. *Clim. Dyn.*, 25 :477–496.

[Choisnel, 1977] Choisnel, E. (1977). Le bilan d'énergie et hydrique du sol. *La Météorologie*, 6 (11) :103–133.

[Choisnel et al., 1995] Choisnel, E., Jourdain, S. V., and Jaquart, C. J. (1995). Climatological evaluation of some fluxes of the surface energy and soil water balances over France. *Annales Geophysicae*, 13 :666–674.

[Chong, 2009] Chong, M. (2009). The 11 August 2006 squall line system as observed from MIT Doppler radar during the AMMA SOP. *Quart. J. R. Meteor. soc.*, this volume.

[Chong and Hauser, 1990] Chong, M. and Hauser, D. (1990). A tropical squall line observed during the COPT81 experiment in West Africa : Part III : heat and moisture budgets. *Mon. Wea. Rev.*, 118 :1696–1706.

[Ciais et al., 1996] Ciais, P., Denning, A. S., Tans, P. P., Berry, J. A., Randall, D. A., Collatz, G. J., Sellers, P. J., White, J. W. C., Trolier, M., Meijer, H. A. J., Francey, R. J., Monfray, P., and Heimann, M. (1996). A three-dimensional synthesis study of ?18O in atmospheric CO2 1. Surface fluxes . *J. Geophys. Res.*, 102(D5) :5857 ?5872.

[Ciais and Jouzel, 1994] Ciais, P. and Jouzel, J. (1994). Deuterium and oxygen 18 in precipitation : isotopic model, including cloud processes. *J. Geophys. Res.*, 99 :16,793–16,803.

[Ciais et al., 1995] Ciais, P., White, W., Jouzel, J., and Petit, J. (1995). The origin of present-day Antarctic precipitation from surface snow deuterium excess data. *J. Geophys. Res.*, 100 :18917–18927.

[CLIMAP, 1981] CLIMAP (1981). Seasonal reconstructions of the Earth's surface at the last glacial maximum. *Geol. Soc. Am.*

[Coindreau et al., 2007] Coindreau, O., Hourdin, F., Haeffelin, M., Mathieu, A., and Rio, C. (2007). Assessment of physical parameterizations using a global climate model with stretchable grid and nudging. *Mon. Wea. Rev.*, 135 :1474.

[Cole et al., 1999] Cole, J. E., Rind, D., Webb, R. S., Jouzel, J., and Healy, R. (1999). Climatic controls on interannual variability of precipitation delta18O : Simulated influence of temperature, precipitation amount, and vapor source region. *J. Geophys. Res.*, 104 :14223–14236.

[Coplen, 1988] Coplen, T. (1988). Normalization of oxygen and hydrogen isotope data. *Chem. Geol.*, 72 :44 :293–297.

[Craig, 1961] Craig, H. (1961). Isotopic variations in meteoric waters. *Science*, 133 :1702–1703.

[Craig and Gordon, 1965] Craig, H. and Gordon, L. I. (1965). Deuterium and oxygen-18 variations in the ocean and marine atmosphere. *Stable Isotope in Oceanographic Studies and Paleotemperatures.*

[Criss, 1999] Criss, R. E. (1999). *Principles of stable isotope distribution.* Oxford University Press.

[Cruz et al., 2006] Cruz, F. W., Burns, S. J., Karmann, I., Sharp, W., and Vuille, M. (2006). Reconstruction of regional atmospheric circulation features during the late Pleistocene in subtropical Brazil from oxygen isotope composition of speleothems. *Earth Planet. Sci. Lett.*, 248(1-2) :495–507, doi :10.1016/j.epsl.2006.06.019.

[Cruz et al., 2005a] Cruz, F. W., Burns, S. J., Karmann, I., Sharp, W. D., Vuille, M., Cardoso, A. O., Ferrari, J. A., Dias, P. L. S., and Viana, O. J. (2005a). Insolation-driven changes in atmospheric circulation over the past 116,000 years in subtropical Brazil. *Nature*, 434 :63–66.

[Cruz et al., 2005b] Cruz, F. W., Karmann, I., Viana Jr, O., Burns, J. A., Ferrari, M., Vuille, M., Sial, A. N., and Moreira, M. Z. (2005b). Stable isotope study of cave percolation waters in subtropical Brazil : implications for paleoclimate inferences from speleothems. *Chem. Geol.*, 220 :245–262.

[Cuffey and Vimeux, 2001] Cuffey, K. and Vimeux, F. (2001). Covariation of carbon dioxide and temperature from the Vostok ice core after deuterium-excess correction. *Nature*, 412 :523–7.

[Cuntz et al., 2003] Cuntz, M., Ciais, Hoffmann, G., and Knorr, W. (2003). A comprehensive global three-dimensional model of D18O in atmospheric CO2 : 1. Validation of surface processes. *J. Geophys. Res.*, 108 :doi :10.1029/2002JD003153.

[Cuntz et al., 2007] Cuntz, M., Ogee, J., Farquhar, G., Peylin, P., and Cernuzak, L. (2007). Modelling advection and diffusion of water isotopologues in leaves. *Plant, cell and environment*, 30 :892–909.

[Dahe et al., 1994] Dahe, Q., Petit, J. R., Jouzel, J., and Stievenard, M. (1994). Distribution of stable isotopes in surface snow along the route of the 1990 International Trans-Antarctica Expedition. *Journal of Glaciology*, 40 :107–118.

[Danny and Loader, 2004] Danny, M. and Loader, N. (2004). Stable isotopes in tree rings. *Quat. Sci. Rev.*, 23 :771–801.

[Dansgaard, 1964] Dansgaard (1964). Stable isotopes in precipitation. *Tellus*, 16 :436–468.

[Dansgaard, 1953] Dansgaard, W. (1953). The abundance of 18O in atmospheric water and water vapour. *Tellus*, 5 :461–469.

[De Rosnay, 1999] De Rosnay, P. (1999). *Représentation de l'interaction sol-végétation-atmosphère dans le Modèle de Circulation Générale du Laboratoire de Météorologie Dynamique.* PhD thesis, Université de Paris 06.

[de Rosnay et al., 2003] de Rosnay, P., Polcher, J., Laval, K., , and Sabre, M. (2003). Integrated parameterization of irrigation in the land surface model ORCHIDEE. Validation over Indian Peninsula. *Geophys. Res. Lett.*, 30 (19) :1986, doi :10.1029/2003GL018024.

[Delaygue, 2000] Delaygue, G. (2000). *Relations entre surface océanique et composition isotopique des précipitations antarctiques : simulations pour différents climats.* PhD thesis, Université d'Aix-Marseille III.

[Delaygue et al., 2000] Delaygue, G., Masson, V., Jouzel, J., Koster, R. D., and Healy, R. J. (2000). The origin of Antarctic precipitation : A modelling approach. *Tellus*, 52B :19–36.

[Delmotte et al., 2000] Delmotte, M., Masson, V., Jouzel, J., and Morgan, V. (2000). A seasonal deuterium excess signal at Law Dome, coastal eastern Antarctica : A southern ocean signature. *J. Geophys. Res.*, 105 :7187–7197.

[Dessler et al., 2007] Dessler, A. E., Hanisco, T., and Fueglistaler, S. (2007). Effects of ice lofing on H2O18 and HDO in the tropical tropopause layer. *J. Geophys. Res.*, 112.

[Dessler and Sherwood, 2003] Dessler, A. E. and Sherwood, S. C. (2003). A model of HDO in the tropical tropopause layer. *Atmos. Chem. Phys.*, 3 :2173–2181.

[Dongmann et al., 1974] Dongmann, G., Nurnberg, H., Forstel, H., and Wagener, K. (1974). On the enrichment of H2018 in the leaves of transpiring plants. *Rad. and Environm. Biophys.*, 11 :41–52.

[d'Orgeval, 2006] d'Orgeval, T. (2006). *Impact du changement climatique sur le cycle de l'eau en Afrique de l'Ouest : Modélisation et incertitudes.* PhD thesis, Université Paris 6.

[Douglas et al., 2006] Douglas, D., Niyogi, D., Frolking, S., Yeluripati, J., Sr., R. P., Niyogi, N., Vörösmarty, C., and Mohanty, U. (2006). Changes in moisture and energy fluxes due to agricultural land use and irrigation in the indian monsoon belt. *Geophy. Res. Lett.*, 33 :L14403.

[Ducharne et al., 2003] Ducharne, A., Golazb, C., Leblois, E., Lavala, K., Polcher, J., Ledoux, E., and de Marsily, G. (2003). Development of a high resolution runoff routing model, calibration and application to assess runoff from the LMD GCM. *J. Hydrol.*, 280 :207–228.

[Ducoudré et al., 1993] Ducoudré, N., Laval, K., and Perrier, A. (1993). SECHIBA, a new set of parametrizations of the hydrological exchanges at the land-atmosphere interface within the LMD atmospheric general circulation model. *J. Clim.*, 6 :248–273.

[Ekaykin, 2003] Ekaykin, A. (2003). *Meteorological regime of central Antarctic and its role in the formation of isotope composition of snow thickness.* PhD thesis, University Grenoble 1-Joseph Fourier.

[Ekaykin and Lipenkov, 2008] Ekaykin, A. A. and Lipenkov, V. Y. (2008). Formation of the ice core isotope composition. *The 2nd International Workshop on Physics of Ice Core Records (PICR-2).*

[Emanuel, 1997] Emanuel, K. (1997). *The Physics and Parametrization of Moist Convective Atmospheric Convection.* Springer Netherlands.

[Emanuel et al., 1994] Emanuel, K., Neelin, D., and Bretherton, C. (1994). On large-scale circulations in convecting atmospheres. *Quaterly Journal of the Royal Meteorological Society*, 120 :1111–1143.

[Emanuel, 1991] Emanuel, K. A. (1991). A Scheme for Representing Cumulus Convection in Large-Scale Models. *J. Atmos. Sci.*, 48 :2313–2329.

[Emanuel and Zivkovic-Rothman, 1999] Emanuel, K. A. and Zivkovic-Rothman, M. (1999). Development and Evaluation of a Convection Scheme for Use in Climate Models. *J. Atmos. Sci.*, 56 :1766–1782.

[Epstein and Mayeda, 1953] Epstein, S. and Mayeda, T. (1953). Variations of O18 content of waters from natural sources. *Geochimica et Cosmochimica Acta*, 4 :213–224.

[Eriksson and Bolin, 1964] Eriksson, E. and Bolin, B. (1964). Oxygen-18, deuterium and tritium in natural waters and their relations to the global circulation of water. *Proceedings of second conference on radiative fallout from nuclear weapon tests*, pages 675–686.

[Farquhar and Cernusak, 2005] Farquhar, G. and Cernusak, L. (2005). On the isotopic composition of leaf water in the non-steady state. *Functional Plant Biology*, 32 :293–303.

[Farrera et al., 1999] Farrera, I., Harrison, S. P., Prentice, I. C., Ramstein, G., Guiot, J., Bartlein, P. J., Bonnefille, R., Bush, M., Cramer, W., von Grafenstein, U., Holmgren, K., Hoohiemstra, H., Hope, G., Jolly, D., Lauritzen, S.-E., Ono, Y., Pinot, S., Stute, M., and Yu, G. (1999). Tropical climates at the Last Glacial Maximum : a new synthesis of terrestrial palaeoclimate data. I. Vegetation, lake-levels and geochemistry. *Clim. Dyn.*, 15 :823–856.

[Fekete et al., 2006] Fekete, B., Gibson, J., Aggarwal, P., and Vorosmarty, C. J. (2006). Application of isotope tracers in continental scale hydrological modeling. *J. Hydrol.*, 330 :444–456.

[Fleitmann et al., 2007] Fleitmann, D., Burns, S., Mangini, A., Mudelsee, M., Kramers, J., Villa, I., Neff, U., Al-Subbary, A. A., Buettner, A., Hppler, D., and Matter, A. (2007). Holocene ITCZ and Indian monsoon dynamics recorded in stalagmites from Oman and Yemen (Socotra). *Quat. Sci. Rev.*, 16 :170–188.

[Folberth et al., 2006] Folberth, A., Hauglustaine, D. A., Lathière, J., and Brocheton, F. (2006). Interactive chemistry in the Laboratoire de Météorologie Dynamique general circulation model : model description and impact analysis of biogenic hydrocarbons on tropospheric chemistry. *Atmos. Chem. Phys.*, 6 (8) :2273–2319.

[Folkins et al., 1999] Folkins, I., Loewenstein, M., Podolske, J., Oltmans, S. J., and Proffitt, M. (1999). A barrier to vertical mixing at 14 km in the tropics : Evidence from ozonesondes and aircraft measurements. *J. Geophys. Res.*, 104(18) :22095–22102.

[Fouquart and Bonnel, 1980] Fouquart, Y. and Bonnel, B. (1980). Computation of solar heating of the Earth's atmosphere : a new parameterization. *Beitr. Phys. Atmos.*, 53 :35–62.

[Frankenberg et al., 2009] Frankenberg, C., Yoshimura, K., Warneke, T., Aben, I., Butz, A., Deutscher, N., Griffith, D., Hase, F., Notholt, J., Schneider, M., Schrijver, H., and Röckmann, T. (2009). Dynamic processes governing lower-tropospheric hdo/h20 ratios as observed from space and ground. *Science*, 325 :1374–1377.

[Fritz et al., 2003] Fritz, S., Baker, P., Lowenstein, T. K., Seltzer, G. O., Rigsby, C. A., Dwyer, G. S., Tapia, P. M., Arnold, K. K., Ku, t.-L., and Luo, S. (2003). Hydrologic variation during the last 170,000 years in the southern hemisphere tropics of South America. *Quat. Res.*, 61 :95–104.

[Fudeyasu et al., 2008] Fudeyasu, H., Ichiyanagi, K., Sugimoto, A., Yoshimura, K., Ueta, A., Yamanaka, M. D., , and Ozawa, K. (2008). Isotope ratios of precipitation and water vapor observed in Typhoon Shanshan. *J. Geophys. Res.*, 113 :D12113, doi :10.1029/2007JD009313.

[Fujita and Abe, 2006] Fujita, K. and Abe, O. (2006). Stable isotopes in daily precipitation at Dome Fuji, East Antarctica. *Geophys. Res. Lett.*, 33 :L18503, doi :10.1029/2006GL026936.

[Galewsky et al., 2005] Galewsky, J., Sobel, A., and Held, I. (2005). Diagnosis of subtropical humidity dynamics using tracers of last saturation. *J. Atm. Sci.*, 62 (9) :3353–3367.

[Gao et al.,] Gao, J., Masson-Delmotte, V., Yao, T., Risi, C., Hoffmann, G., and Tian, L. Precipitation water stable isotopes in the south Tibetan Plateau : observations and modelling. *in preparation*.

[Gasse, 2000] Gasse, F. (2000). Hydrological changes in the African tropics since the Last Glacial Maximum. *Quat. Sci. Rev.*, 19 :189–211.

[Gat, 2000] Gat, J. (2000). Atmospheric water balance-the isotopic perspective. *Hydrol. Processes*, 14 :1357–1369.

[Gat, 1996] Gat, J. R. (1996). Oxygen and hydrogen isotopes in the hydrologic cycle. *Annual Review of Earth and Planetary Sciences*, 24 :225–262.

[Gat and Matsui, 1991] Gat, J. R. and Matsui, E. (1991). Atmospheric water balance in the Amazon basin : An isotopic evapotranspiration model. *J. Geophys. Res.*, 96 :13179–13188.

[Gat et al., 2007] Gat, J. R., Yakir, D., Goodfriend, G., Fritz, P., Trimborn, P., Lipp, J., Gev, I., Adar, E., and Waisel, Y. (2007). Stable isotope composition of water in desert plants. *Plant Soil*, 298 :31–45, doi :10.1007/s11104–007–9321–6.

[Gates, 1992] Gates, W. L. (1992). AMIP : The Atmospheric Model Intercomparison Project. *Bull. Am. Meteor. Soc.*, 73 :1962–1970.

[Gazis and Geng, 2004] Gazis, C. and Geng, X. (2004). A stable isotope study of soil water : evidence for mixing and preferential flow paths. *Geoderma*, 119 :97–111.

[Gedney et al., 2006] Gedney, N., Cox, P. M., Betts, R. A., Boucher, O., Hutingford, c., and Stott, P. A. (2006). Detection of a direct carbon dioxide effect in continental river runoff records. *Nature*, 16.

[Gedzelman et al., 2003] Gedzelman, S., Lawrence, J., Gamache, J., Black, M., Hindman, E., Black, R., Dunion, J., Willoughby, H., and Zhang, X. (2003). Probing hurricanes with stable isotopes of rain and water vapor. *Mon. Wea. Rev.*, 131 :112–1127.

[Gedzelman and Arnold, 1994] Gedzelman, S. D. and Arnold, R. (1994). Modeling the isotopic composition of precipitation. *J. Geophys. Res.*, 99 :10455–10472.

[Gettelman et al., 2002] Gettelman, A., Salby, M. L., and Sassi, F. (2002). Distribution and influence of convection in the tropical tropopause region. *J. Geophys. Res.*, 107.

[Gibson, 2002] Gibson, J. (2002). Short-term evaporation and water budget comparisons in shallow Arctic lakes using non-steady isotope mass balance. *J. Hydrol.*, 264 :242–261.

[Gibson and Edwards, 2002] Gibson, J. J. and Edwards, T. W. D. (2002). Regional water balance trends and evaporation-transpiration partitioning from a stable isotope survey of lakes in northern Canada. *Glob. Biogeochem. Cycles*, 16 :1026, 10.1029/2001GB001839.

[Gibson et al., 2005] Gibson, J. J., Edwards, T. W. D., Birks, S. J., Amour, N. A. S., Buhay, W. M., McEachern, P., Wolfe, B. B., and Peters1, D. L. (2005). Progress in isotope tracer hydrology in Canada. *Hydrol. Processes*, 19 :303–327.

[Gonfiantini et al., 2001] Gonfiantini, R., Roche, M.-A., Olivry, J.-C., Fontes, J.-C., and Zuppi, G. M. (2001). The altitude effect on the isotopic composition of tropical rains. *Chem. Geol.*, 181 :147–167.

[Gong and Eltahir, 1996] Gong, C. and Eltahir, E. (1996). Sources of moisture for rainfall in West Africa. *Water Resources Res.*, 10 :3115–3121.

[Grandpeix and Lafore,] Grandpeix, J.-Y. and Lafore, J.-P. A density current parameterization coupled with Emanuel's convection scheme. Part I : The models. *J. Atm. Sci.*, in press.

[Grandpeix et al.,] Grandpeix, J.-Y., Lafore, J.-P., and Cheruy, F. A density current parameterization coupled with Emanuel's convection scheme Part II : 1D simulations. *J. Atm. Sci.*, in press.

[Grandpeix et al., 2004] Grandpeix, J. Y., Phillips, V., and Tailleux, R. (2004). Improved mixing representation in Emanuel's convection scheme. *Quarterly Journal of the Royal Meteorological Society*, 130 :3207–3222.

[GRIP members, 1993] GRIP members (1993). Climate instability during the last interglacial period recorded in the GRIP ice core. *Nature*, 364 :203–207.

[Grootes et al., 2001] Grootes, P. M., Steig, E. J., Stuiver, M., Waddington, E. D., and Morse, D. L. (2001). The Taylor Dome Antarctic 18O record and globally synchronous change in climate. *Quat. Res.,*, 56 :289–298.

[Guichard et al., 2008] Guichard, F., Kergoat, L., Mougin, E., Timouk, F., Baup, F., Hiernaux, P., and Lavenu, F. (2008). Surface thermodynamics and radiative budget in the sahelian gourma : Seasonal and diurnal cycles. *J. Hydrol.*, page doi :10.1016/j.jhydrol.2008.09.007.

[Guimberteau et al., 2008] Guimberteau, M., Laval, K., Perrier, A., and Polcher, J. (2008). Streamflow Simulations by the Land Surface Model ORCHIDEE Over the Mississippi River Basin : Impact of Resolution and Data Source on the Model. In *American Geophysical Union, Fall Meeting.*

[Gupta et al., 2009] Gupta, P., Noone, D., Galewsky, J., Sweeney, C., , and Vaughn, B. H. (2009). Demonstration of high-precision continuous measurements of water vapor isotopologues in laboratory and remote field deployments using wavelength-scanned cavity ring-down spectroscopy (WS-CRDS) technology. *Rapid Commun. Mass Spectrom.*, 23 :2534–2542.

[Hall and Peyrillé, 2006] Hall, N. and Peyrillé, P. (2006). Dynamics of the West African monsoon. *J. Phys. IV France*, 139 :81–99.

[Hanisco et al., 2007] Hanisco, T., Moyer, E., Weinstock, E., St Claire, J. M., Sayres, D. S., Smith, J. B., Lockwood, R., Anderson, J. G., Dessler, A. E., Keutsh, F. N., Spackman, J. R., Read, W. G., and Bui, T. P. (2007). Observations of deep convective influence on stratospheric water vapor and its isotopic composition. *Geophysical research letters*, 34.

[Harrison, 2000] Harrison (2000). Palaeoenvironmental data sets and model evaluation in PMIP. In Braconnot, P., editor, *Paleoclimate Modelling Intercomparison Project (PMIP)*, volume WMO/TD-No. 1007, pages pp. 9–25.

[Hauser et al., 1988] Hauser, D., Roux, F., and Amayenc, P. (1988). Comparison of two methods for the retrieval of thermodynamic and microphysical variables from Doppler radar measurements : application to the case of a tropical squall line. *J. Atm. Sci.*, 45 :1285 ?1303.

[Held and Brian J Soden, 2000] Held, I. M. and Brian J Soden, B. J. (2000). Water vapor feedback and global warming. *Annu. Rev. Energy Environ.*, 25 :441–475.

[Held et al., 2005] Held, I. M., Delworth, T. L., Findell, K. L., and Knutson, T. R. (2005). Simulation of Sahel drought in the 20th and 21st centuries. *PNAS*, 102 :17891–17896, doi : 10.1073/pnas.0509057102.

[Held and Soden, 2006] Held, I. M. and Soden, B. J. (2006). Robust responses of the hydrological cycle to global warming. *J. Clim.*, 19 :5686–5699.

[Helliker and Noone, 2009] Helliker, B. and Noone, D. (2009). *Novel approaches to monitoring of water vapor isotope ratios : Plants, satellites and lasers,*. Springer.

[Helsen et al., 2007] Helsen, M. M., van de Wal, R. S. W., and van den Broeke, M. R. (2007). The isotopic composition of present-day Antarctic snow in a Lagrangian atmospheric simulation. *J. Clim.*, 20 :739–756.

[Helsen et al., 2006] Helsen, M. M., van de Wal, R. S. W., van den Broeke, M. R. ; Masson-Delmotte, V., Meijer, H. A. J., Scheele, M. P., and Werner, M. (2006). Modeling the isotopic composition of Antarctic snow using backward trajectories : Simulation of snow pit records. *J. Geophys. Res.*, 111.

[Hemming et al., 2007] Hemming, D., Griffiths, H., Loader, A., Robertson, I., Wingate, L., and Yakir, D. (2007). The moisture isotopes in biosphere and atmosphere network (miba) : initial results from the uk. *Eos Trans. AGU*, 88 (52).

[Henderson-Sellers, 2006] Henderson-Sellers, A. (2006). Improving land-surface parameterization schemes using stable water isotopes : Introducing the 'iPILPS' initiative. *Glob. Planet. Change*, 51 :3–24.

[Henderson-Sellers et al., 2004] Henderson-Sellers, A., McGuffie, K., Noone, D., and Irannejad, P. (2004). Using Stable Water Isotopes to Evaluate Basin-Scale Simulations of Surface Water Budgets. *J. Hydromet.*, 5 :805–822.

[Henderson-Sellers et al., 2001] Henderson-Sellers, A., McGuffie, K., and Zhang, H. (2001). Stable Isotopes as Validation Tools for Global Climate Model Predictions of the Impact of Amazonian Deforestation. *J. Clim*, 15 :2664–2677.

[Hendricks et al., 2000] Hendricks, M., DePaolo, D., and Cohen, R. (2000). Space and time variation of deltaO18 and deltaD in precipitation : can paelotemperatures be estimated from ice cores ? *Glob. Geochem. Cycles*, 14 :851–861.

[Herbin et al., 2009] Herbin, H., Hurtmans, D., Clerbaux, C., Clarisse, L., and Coheur, P.-F. (2009). H216O and HDO measurements with IASI/MetOp. *Atmos. Chem. Phys. Discuss.*, 9 :92679290.

[Hoffmann, 2003] Hoffmann, G. (2003). Taking the pulse of the tropical water cycle. *Science*, 301 :776–777.

[Hoffmann et al., 2003] Hoffmann, G., Ramirez, E., Taupin, J., Francou, B., Ribstein, P., Delmas, R., Dürr, H., Gallaire, R., Simôes, J., Schotterer, U., Stievenard, M., and Werner, M. (2003). Coherent isotope history of Andean ice cores over the last century. *Geophys. Res. Lett.*, 30 :1179.

[Hoffmann et al., 1998] Hoffmann, G., Werner, M., and Heimann, M. (1998). Water isotope module of the ECHAM atmospheric general circulation model : A study on timescales from days to several years. *J. Geophys. Res.*, 103 :16871–16896.

[Holton and Gettelman, 2001] Holton, J. R. and Gettelman, A. (2001). Horizontal transport and the dehydration of the stratosphere. *Geophys. Res. Lett.*, 28(14) :2799–2802.

[Hourdin, 2005] Hourdin, F. (2005). Représentation du transport direct et inverse dans les modèles globaux de climat et étude des couplages entre composition et dynamique atmosphérique sur Titan. Habilitation à Diriger des Recherches.

[Hourdin et al., 2006] Hourdin, F., Musat, I., Bony, S., Braconnot, P., Codron, F., Dufresne, J.-L., Fairhead, L., Filiberti, M.-A., Friedlingstein, P., Grandpeix, J.-Y., Krinner, G., Levan, P., Li, Z.-X., and Lott, F. (2006). The LMDZ4 general circulation model : climate performance and sensitivity to parametrized physics with emphasis on tropical convection. *Clim. Dyn.*, 27 :787–813.

[Houze, 1977] Houze, R. A. (1977). Structure and dynamics of a tropical squall line system. *Mon. Wea. Rev.*, 105 :1540–1567.

[Huffman et al., 1997] Huffman, G. J., Arkin, P., and Janowiak, J. (1997). The Global Precipitation Climatology Project (GPCP) combined precipitation dataset. *Bull. Am. Meteor. Soc.*, 78 :5–20.

[Jackson, 2000] Jackson, N. (2000). Measured and modelled rainfall interception loss from an agroforestry system in Kenya. *Agricultural and Forest Meteorology*, 100 :323–336.

[Janicot et al., 2008] Janicot, S., Thorncroft, D., Ali, A., Asencio, N., and coauthors (2008). Large-scale overview of the summer monsoon over West and Central Africa during the AMMA field experiment in 2006. *Ann. Geophys.*, 26 :2569–2595.

[Johnsen et al., 1992] Johnsen, S., Clausen, H., Dansgaard, W., Gundestrup, N., Hansson, M., Jonsson, P., Steffensen, J., and Sveinbjörnsdottir, A. (1992). A "deep" ice core from East Greenland. *Meddelelser om Gronland, Geoscience*, 29 :1–22.

[Johnsen et al., 1972] Johnsen, S., Dansgaard, W., Clausen, H., and Langway, J. C. (1972). Oxygen isotope profiles through the Antarctic and Greenland ice sheets. *Nature*, 235 :429–434.

[Johnsen et al., 1989] Johnsen, S., Dansgaard, W., and White, J. (1989). Origin of Arctic precipitation under present and glacial conditions. *Tellus*, 41B :452–458.

[Johnson et al., 2001] Johnson, D. G., Jucks, K. W., Traub, W. A., and Chance, K. V. (2001). Isotopic composition of stratospheric water vapor : Implications for transport. *Journal of Geophysical research*, 106 :12219–12226.

[Johnson et al., 2001] Johnson, D. G., Jucks, K. W., Traub, W. A., and Chance, K. V. (2001). Isotopic measurements of startospheric water vapor : measurements and photochemistry. *J. Geophys. Res.*, 106 :12211–12217.

[Joussaume, 1989] Joussaume, S. (1989). *Simulations du climat du dernier maximum glaciaire à l'aide d'un modèle de circulation générale de l'atmosphère incluant une modélisation du cycle des isotopes de l'eau et des poussières d'origine désertique.* PhD thesis, Univ. of Paris VI, Paris, France.

[Joussaume and Jouzel, 1993] Joussaume, S. and Jouzel, J. (1993). Paleoclimatic tracers : An investigation using an atmospheric general circulation model under ice age conditions. 2. water isotopes. *J. Geophys. Res.*, 98 :2807–2830.

[Joussaume et al., 1984] Joussaume, S., Jouzel, J., and Sadourny, R. (1984). A general circulation model of water isotope cycles in the atmosphere. *Nature*, 311 :24–29.

[Joussaume and Taylor, 1995] Joussaume, S. and Taylor, K. E. (1995). Status of the paleoclimate modeling intercomparison project. In *Proceedings of the first international AMIP scientific conference, WCRP-92, Monterey, USA, 425-430.*

[Joussaume et al., 1999] Joussaume, S., Taylor, K. E., Braconnot, P., Mitchell, J. F. B., Kutzbach, J. E., Harrison, S. P., Prentice, I. C., Broccoli, A. J., Abe-Ouchi, A., Bartlein, P. J., Bonfils, C., Dong, B., Guiot, J., Herterich, K., Hewitt, C. D., Jolly, D., and co athors (1999). Monsoon Changes for 6000 Years Ago : Results of 18 Simulations from the Paleoclimate Modeling Intercomparison Project (PMIP). *Geophys. Res. Lett.*, 26(7) :859 ?862.

[Jouzel, 1999] Jouzel, J. (1999). Calibrating the isotopic paleothermometer. *Science*, 286 :910–911.

[Jouzel, 2003] Jouzel, J. (2003). Water Stable Isotopes : Atmospheric Composition and Applications in Polar Ice Core Studies. *Treatise on Geochemistry*, 4 :213–243.

[Jouzel et al., 2000] Jouzel, J., Hoffmann, G., Koster, R. D., and Masson, V. (2000). Water isotopes in precipitation : data/model comparison for present-day and past climates. *Quat. Sci. Rev.*, 19 :363–379.

[Jouzel et al., 1994] Jouzel, J., Koster, R., Suozzo, R., and Russel, G. L. (1994). Stable water isotope behavior during the last glacial maximum : a general circulation model analysis. *J. Geophys. Res.*, 99 :25791–25801.

[Jouzel et al., 1991] Jouzel, J., Koster, R., Suozzo, R., Russell, G., White, J., and Broecker, W. (1991). Simulations of the HDO and H2O-18 atmospheric cycles using the NASA GISS general circulation model : Sensitivity experiments for present-day conditions. *J. Geophys. Res.*, 96 :7495–7507.

[Jouzel and Koster, 1996] Jouzel, J. and Koster, R. D. (1996). A reconsideration of the initial conditions used for stable water isotope models. *J. Geophys. Res.*, 101 :22933–22938.

[Jouzel et al., 1987] Jouzel, J., Koster, R. D., Suozzo, R. J., Russel, G. L., White, J. W. C., and Broecker, W. S. (1987). Simulations of the HDO and H2O18 atmospheric cycles using the NASA GISS General Circulation Model : The seaosnal cycle for present day conditions. *J. Geophys. Res.*, 92 :14,739–14,760.

[Jouzel et al., 2007a] Jouzel, J., Masson-Delmotte, V., Cattani, O., Dreyfus, G., Falourd, S., Hoffmann, G., Minster, B., Nouet, J., Barnola, J. M., Chappellaz, J., Fischer, H., Gallet, J. C., Johnsen, S., Leuenberger, M., Loulergue, L., Luethi, D., Oerter, H., Parrenin, F., Raisbeck, G., Raynaud, D., Schilt, A., Schwander, J., Selmo, E., Souchez, R., Spahni, R., Stauffer, B., Steffensen, J. P., Stenni, B., Stocker, T. F., Tison, J. L., Werner, M., and Wolff, E. W. (2007a). Orbital and Millennial Antarctic Climate Variability over the Past 800,000 Years. *Science*, 317 (5839) :DOI : 10.1126/science.1141038.

[Jouzel and Merlivat, 1984] Jouzel, J. and Merlivat, L. (1984). Deuterium and oxygen 18 in precipitation : modeling of the isotopic effects during snow formation. *J. Geophys. Res.*, 89 :11 :749.

[Jouzel et al., 1982] Jouzel, J., Merlivat, L., and Lorius, C. (1982). Deuterium excess in an East Antarctic ice core suggests higher relative humidity at the oceanic surface during the last glacial maximum. *Nature*, 299 :688–691.

[Jouzel et al., 2007b] Jouzel, J., Stiévenard, M., Johnsen, S., Landais, A., Masson-Delmotte, V., Sveinbjornsdottir, A., Vimeux, F., von Grafenstein, U., and White, J. (2007b). The GRIP deuterium-excess record. *Quat. Sci. Rev.*, 26 :1–17.

[Jouzel et al., 2003] Jouzel, J., Vimeux, F., Caillon, N., Delaygue, G., Hoffmann, G., Masson-Delmotte, V., and Parrenin, F. (2003). Magnitude of isotope/temperature scaling for interpretation of central Antarctic ice cores. *J. Geophys. Res.*, 108 :4361.

[Kalnay et al., 1996] Kalnay, E., Kanamitsu, M., Kistler, R., Collins, W., Deaven, D., Gandin, L., Iredell, M., Saha, S., White, G., Woollen, J., Zhu, Y., Leetmaa, A., Reynolds, B., Chelliah, M., Ebisuzaki, W., Higgins, W., Janowiak, J., Mo, K. C., Ropelewski, C., Wang, J., Jenne, R., and Joseph, D. (1996). The NCEP/NCAR 40-year reanalysis project. *Bull. Amer. Meteor. Soc.*, 77 :437–470.

[Kang et al., 2008] Kang, S., Held, I., Frierson, D., and Zhao, M. (2008). The response of the ITCZ to extratropical thermal forcings : idealized slab ocean experiments with a GCM. *J. Clim.*, 21 :3521–3532.

[Kavanaugh and Cuffey, 2003] Kavanaugh, J. L. and Cuffey, K. M. (2003). Space and time variation of deltaO18 and deltaD in Antarctic precipitation revisited. *Global Biogeochem. Cycles*, 17.

[Keeling, 1961] Keeling, C. (1961). The concentration and isotopic abundances of carbon dioxide and marine air. *Geochim. Cosmochim. Acta*, 24 :277–298.

[Kendall and Coplen, 2001] Kendall, C. and Coplen, T. B. (2001). Distribution of oxygen-18 and deuterium in river waters across the United States. *Hydrol. Processes*, 15 :1363–1393.

[Kessler, 1969] Kessler, E. (1969). On the distribution and continuity of water substance in atmospheric circulation. *Meteor. Monogr.*, 32 :84.

[Khaykin et al., 2009] Khaykin, S., Pommereau, J.-P., Korshunov, L., , V. Yushkov and, J. N., , N. L. T. C., Garnier, A., Lukyanovand, A., and E.Williams (2009). Hydration of the lower stratosphere by ice crystal geysers over land convective systems. *Atmos. Chem. Phys.*, 9 :2275 ?2287.

[Knohl et al., 2007] Knohl, A., Tu, K. P., Boukili, V., Brooks, P. D., Mambelli, S., Riley, W. J., and Dawson, T. E. (2007). MIBA-US : Temporal and Spatial Variation of Water Isotopes in Terrestrial Ecosystems Across the United States. *Eos Trans. AGU*, 88 (52).

[Koster et al., 1986] Koster, R., Jouzel, J., Suozzo, R., Russell, G., Broecker, W., Rind, D., and Eagleson, P. (1986). Global sources of local precipitation as determined by the NASA/GISS GCM. *Geophy. Res. Lett.*, 13 (2) :121–124, DOI :10.1029/GL013i002p00121.

[Koster et al., 2006] Koster, R. D., Guo, Z., Dirmeyer, P., and coauthors (2006). GLACE : The Global LandAtmosphere Coupling Experiment. Part I : Overview. *J. Hydromet.*, 7 :590–610.

[Koster et al., 1992] Koster, R. D., Jouzel, J., Suozzo, R. J., and Russell, G. L. (1992). Origin of July Antarctic precipitation and its influence on deuterium content : a GCM analysis. *Clim. Dyn.*, 7 :195203.

[Koster and Milly, 1996] Koster, R. D. and Milly, P. C. D. (1996). The Interplay between Transpiration and Runoff Formulations in Land Surface Schemes Used with Atmospheric Models. *J. Clim.*, 10 :1578–1591.

[Koster and Suarez, 1999] Koster, R. D. and Suarez, M. J. (1999). A simple framework for examining the interannual variability of land surface moisture fluxes. *J. Clim.*, 12 :1911–1917.

[Krinner et al., 1997a] Krinner, G., Genthon, C., Li, Z.-X., and Van, P. L. (1997a). Studies of the Antarctic climate with a stretched-grid general circulation model. *J. Geophys. Res*, 102 :13,731–13,745.

[Krinner et al., 1997b] Krinner, G., Genton, C., and Jouzel, J. (1997b). GCM analysis of local influences on ice core delta signals. *Geophys. Res. Lett*, 24 :2825–2828.

[Krinner et al., 2005] Krinner, G., Viovy, N., de Noblet-Ducoudre, N., Ogee, J., Polcher, J., Friedlingstein, P., Ciais, P., Sitch, S., and Prentice, I. C. (2005). A dynamic global vegetation model for studies of the coupled atmosphere-biosphere system. *Glob. Biogeochem. Cycles*, 19.

[Krinner and Werner, 2003] Krinner, G. and Werner, M. (2003). Impact of precipitation seasonality changes on isotopic signals in polar ice cores : a multi-model analysis. *Earth Planet. Sci. Lett.*, 216 :525–538.

[Kuang et al., 2003] Kuang, Z., Toon, G., Wennberg, P., and Yung, Y. L. (2003). Measured HDO/H2O ratios across the tropical tropopause. *Geophysical Research Letters*, 30 :25–1.

[Lafore et al., 1988] Lafore, J.-P., Redelsperger, J.-L., and Jaubert, G. (1988). Comparison between a tree-dimensional simulation and doppler radar data of a tropical squall line : transports of mass, momentum, heat and moisture. *J. Atm. Sci.*, 45 :3483–3500.

[Lai et al., 2006a] Lai, C.-T., Ehleringer, J., Bond, B., and U, K. P. (2006a). Contributions of evaporation, isotopic non-steady state transpiration, and atmospheric mixing on the deltaO18 of water vapor in Pacific Northwest coniferous forests. *Plant, Cell and Environment*, 29(1) :77–94.

[Lai et al., 2006b] Lai, C.-T., Riley, W., Owensby, C., Ham, J., Schauer, A., and Ehleringer, J. R. (2006b). Seasonal and interannual variations of carbon and oxygen isotopes of respired CO2 in a tallgrass prairie : Measurements and modeling results from 3 years with contrasting water availability. *J. Geophys. Res.*, 111 :D08S06,doi :10.1029/2005JD006436.

[Landais et al., 2008] Landais, A., Barkan, E., and Luz, B. (2008). Record of deltaO18 and O17-excess in ice from Vostock Antarctica during the last 150,000 years. *Geophys. Res. Let.*, 35.

[Landais et al.,] Landais, A., Risi, C., and co authors. The triple isotopic composition of oxygen in water as a tracer for the African monsoon. *in preparation.*

[Lawrence and Gedzelman, 2003] Lawrence, J. and Gedzelman, S. (2003). Tropical ice core isotopes : Do they reflect changes in storm activity ? *Geophys. Res. Lett.*, 30 :44–1.

[Lawrence and Gedzelman, 1996] Lawrence, J. R. and Gedzelman, S. D. (1996). Low stable isotope ratios of tropical cyclone rains. *Geophys. Res. Lett.*, 23 :527–530.

[Lawrence et al., 2004] Lawrence, J. R., Gedzelman, S. D., Dexheimer, D., Cho, H.-K., Carrie, G. D., Gasparini, R., Anderson, C. R., Bowman, K. P., and Biggerstaff, M. I. (2004). Stable isotopic composition of water vapor in the tropics. *J. Geophys. Res.*, 109 :D06115, doi :10.1029/2003JD004046.

[Laîne et al., 2008] Laîne, A., Kageyama, M., Salas-Mélia, D., Voldoire, A., Rivière, G., Ramstein, G., Planton, S., Tyteca, S., and Peterschmitt, J.-Y. (2008). Northern hemisphere storm tracks during the last glacial maximum in the PMIP2 ocean-atmosphere coupled models : energetic study, seasonal cycle, precipitation. *Clim. Dyn.*

[Lee and Fung, 2008] Lee, J.-E. and Fung, I. (2008). "Amount effect" of water isotopes and quantitative analysis of post-condensation processes. *Hydrological Processes*, 22 (1) :1–8.

[Lee et al., 2007] Lee, J.-E., Fung, I., DePaolo, D., and Fennig, C. C. (2007). Analysis of the global distribution of water isotopes using the NCAR atmospheric general circulation model. *J. Geophys. Res.*, 112 :D16306, doi :10.1029/2006JD007657.

[Lee et al., 2008] Lee, J.-E., Fung, I., DePaolo, D. J., and Otto-Bliesner, B. (2008). Water isotopes during the Last Glacial Maximum : New general circulation model calculations. *J. Geophys. Res.*, 113.

[LeGrande and Schmidt, 2006] LeGrande, A. N. and Schmidt, G. A. (2006). Global gridded data set of the oxygen isotopic composition in seawater. *Geophys. Res. Lett.*, 33 :L12604, doi :10.1029/2006GL026011.

[LeGrande and Schmidt, 2008] LeGrande, A. N. and Schmidt, G. A. (2008). Ensemble, Water-Isotope Enabled, Coupled General Circulation Modeling Insights into the 8.2-kyr Event. *Paleoceanography*, 23.

[LeGrande and Schmidt, 2009] LeGrande, A. N. and Schmidt, G. A. (2009). Sources of Holocene variability of oxygen isotopes in paleoclimate archives. *Clim. Past*, 5 :441455.

[Liebmann and Smith, 1996] Liebmann, B. and Smith, C. (1996). Description of a complete (interpolated) outgoing longwave radiation dataset. *Bull. Amer. Meteor. Soc.*, 77 :1275–1277.

[Liebminger et al., 2006] Liebminger, A., Haberhauer, G., Papesch, W., and Heiss, G. (2006). Correlation of the isotopic composition in precipitation with local conditions in alpine regions. *J. Geophys. Res.*, 111 :5104.

[Liu and Zipser, 2005] Liu, C. and Zipser, E. J. (2005). Global distribution of convection penetrating the tropical tropopause. *J. Geophys. Res.*, 110 :doi :10.1029/2005JD006063.

[Lorius et al., 1985] Lorius, C., Jouzel, J., Ritz, C., Merlivat, L., Barkov, N. I., Korotkevitch, Y. S., and Kotlyakov, V. M. (1985). A 150,000-year climate record from Antarctic ice. *Nature*, 316 :591–596.

[Lorius et al., 1979] Lorius, C., Merlivat, L., Jouzel, J., and Pourchet, M. (1979). A 30,000 yr isotope climatic record from Antarctic ice. *Nature*, 280 :644–648.

[Lott et al., 2005] Lott, F., Fairhead, L., Hourdin, F., and Levan, P. (2005). The stratospheric version of LMDz : dynamical climatologies, arctic oscillation, and impact on the surface climate . *Clim. Dyn.*, 25 :DOI : 10.1007/s00382–005–0064–x.

[Luz and Barkan, 2005] Luz, B. and Barkan, E. (2005). The isotopic ratios 17O/16O and 18O/16O in molecular oxygen and their significance in bio-geochemistry. *Geochem. Cosmochim. Acta.*, 69 :1099–1110.

[Majoube, 1971a] Majoube, M. (1971a). Fractionnement en O18 entre la glace et la vapeur d'eau. *Journal de Chimie Physique*, 68 :625–636.

[Majoube, 1971b] Majoube, M. (1971b). Fractionnement en Oxygène 18 et en Deutérium entre l'eau et sa vapeur. *Journal de Chimie Physique*, 10 :1423–1436.

[Marti et al., 2005] Marti, O., Braconnot, P., Bellier, J., Benshila, R., Bony, S., Brockmann, P., Cdule, P., Caubel, A., Denvil, S., Dufresne, J.-L., Fairhead, L., Filiberti, M.-A., Foujols, M.-A., Fichefer, T., Friedlingstein, P., Grandpeix, J.-Y., Hourdin, F., Krinner, G., Lévy, C., Madec, G., Musat, I., de Noblet, N., Polcher, J., and Tanlandier, C. (2005). The new IPSL climate system model : IPSL-CM4. Technical report, IPSL.

[Masson-Delmotte et al., 2008] Masson-Delmotte, V., Hou, S., Ekaykin, A., Jouzel, J., Aristarain, A., Bernardo, R. T., D.Bromwhich, Cattani, O., Delmotte, M., Falourd, S., Frezzotti, M., Gallée, H., Genoni, L., Isaksson, E., Landais, A., Helsen, M., Hoffmann, G., Lopez, J., Morgan, V., Motoyama, H., Noone, D., Oerter, H., Petit, J., Royer, A., Uemura, R., Schmidt, G., Schlosser, E., Simões, J., Steig, E., Stenni, B., Stievenard, M., van den Broeke, M., van de Wal, R., van den Berg, W.-J., Vimeux, F., and White, J. (2008). A review of Antarctic surface snow isotopic composition : observations, atmospheric circulation and isotopic modelling. *J. Climate*, 21 :3359–3387.

[Masson-Delmotte et al., 2006] Masson-Delmotte, V., Kageyama, M., Braconnot, P., Charbit, S., Krinner, G., Ritz, C., Guilyardi, E., Jouzel, J., A.-O. A., Crucifix, M., Gladstone, R., Hewitt, C.D., K.-A. L., A.N., Marti, O., Merkel, U., Motoi, T., Ohgaito, R., Otto-Bliesner, B., Peltier, W., Ross, I., Valdes, P., Vettoretti, G., Weber, S., Wolk, F., and Yu, Y. (2006). Past and future polar amplification of climate change : Climate model intercomparisons and ice-core constraints. *Clim. Dynam.*, 26 :513–529.

[Masson-Delmotte et al., 2005] Masson-Delmotte, V., Landais, A., Stievenard, M., Cattani, O., Falourd, S., Jouzel, J., Johnsen, S. J., Dahl-Jensen, D., Sveinsbjornsdottir, A., White, J. W. C., Popp, T., and Fischer, H. (2005). Holocene climatic changes in Greenland : Different deuterium excess signals at Greenland Ice Core Project (GRIP) and NorthGRIP. *J. Geophys. Res.*, 110.

[Mathieu and Bariac, 1996] Mathieu, R. and Bariac, T. (1996). A numerical model for the simulation of stable isotope profiles in drying soils. *J. Geophys. Res.*, 101 (D7) :12685–12696.

[Mathieu et al., 2002] Mathieu, R., Pollard, D., Cole, J., White, J. W. C., Webb, R. S., and Thompson, S. L. (2002). Simulation of stable water isotope variations by the GENESIS GCM for modern conditions. *J. Geophys. Res.*, 107.

[McGuffie and Henderson-Sellers, 2004] McGuffie, K. and Henderson-Sellers, A. (2004). Stable water isotope characterization of human and natural impacts on land-atmosphere exchanges in the Amazon Basin. *J. Geophys. Res.*, 109 :17104.

[Meehl et al., 2007] Meehl, G. A., Covey, K., Delworth, T., Latif, M., McAvaney, B., Mitchell, J. F. B., Stouffer, R. J., and Taylor, K. (2007). The WCRP CMIP3 multimodel dataset : A new era in climate change research. *Bull. Am. Meteor. Soc.*, 7 :1383–1394.

[Melayah et al., 1996] Melayah, A., Bruckler, L., and Bariac, T. (1996). Modeling the transport of water stable isotopes in unsaturated soils under natural conditions 1. theory. *water resources res.*, 32 :2047–2054.

[Merlivat, 1978] Merlivat, L. (1978). Molecular diffusivities of H2O16, HDO16, and H2O18 in gases. *J.Chem. Phys.*, 69 :2864–2871.

[Merlivat and Jouzel, 1979] Merlivat, L. and Jouzel, J. (1979). Global climatic interpretation of the Deuterium-Oxygen 18 relationship for precipitation. *J. Geophys. Res.*, 84 :5029–5332.

[Merlivat and Nief, 1967] Merlivat, L. and Nief, G. (1967). Fractionnement isotopique lors des changements d'états solide-vapeur et liquide-vapeur de l'eau à des températures inférieures à 0C. *Tellus*, 19 :122–127.

[Millet et al., 1997] Millet, A., Bariac, T., Ladouche, B., Mathieu, R., Grimaldi, C., Grimaldi, M., Hubert, P., Molicova, H., Bruckler, L., Valles, V a, d. B. P., Brunet, Y., and Boulègue, J. (1997). Influence of deforestation on the hydrological behavior of small tropical watersheds. *Revue des Sciences de l'eau*, 1 :61–84.

[Milly et al., 2005] Milly, P. C. D., Dunne, K. A., and Vecchia, A. V. (2005). Global pattern of trends in streamflow and water availability in a changing climate. *Nature*, 17.

[Morcrette, 1991] Morcrette, J.-J. (1991). Radiation and cloud radiative properties in the European Centre for Medium-range Weather Forecasts forecasting system. *J. Geophys. Res.*, 96 :9121–0132.

[Moreira et al., 1997] Moreira, M., Sternberg, L., Martinelli, L., Victoria, R., Barbosa, E., Bonates, C., and Nepstad, D. (1997). Contribution of transpiration to forest ambient vapor based on isotopic measurements. *Global Change Biol.*, 3 :439–450.

[Mote et al., 1996] Mote, P. W., Rosenlof, K. H., Holton, J. R., Harwood, R. S., and Waters, J. W. (1996). An atmospheric tape recorder : The imprint of tropical tropopause temperatures on stratospheric water vapor. *J. Geophys. Res.*, 101 :3989 ?4006.

[Mounier and Janicot, 2004] Mounier, F. and Janicot, S. (2004). Evidence of two independent modes of convection at intraseasonal timescale in the west african summer monsoon. *Geophys. Res. Lett.*, 31.

[Moyer et al., 1996] Moyer, E. J., Irion, F. W., Yung, Y. L., and Gunson, M. R. (1996). ATMOS stratospheric deuterated water and implications for troposphere-stratosphere transport. *Geophys. Res. Lett.*, 23 :2385–2388.

[Nassar et al., 2007] Nassar, R., Bernath, P. F., Boone, C. D., Gettelman, A., McLeod, S. D., and Rinsland, C. P. (2007). Variability in HDO/H2O abundance ratio in the Tropical Tropopause Layer. *J. Geophys. Res.*, 112 (D21) :doi :10.1029/2007JD008417.

[Nesbitt and Zipser, 2003] Nesbitt, S. W. and Zipser, E. J. (2003). The diurnal cycle of rainfall and convective intensity according to three years of TRMM measurements. *J. Clim.*, 16(10) :1456–1475.

[Ngo-Duc, 2005] Ngo-Duc, T. (2005). *Modélisation des bilans hydrologiques continentaux : variabilité interannuelle et tendances. Comparaison aux observations.* PhD thesis, Université Pierre et Marie Curie.

[NGRIP members, 2004] NGRIP members (2004). High-resolution record of Northern Hemisphere climate extending into the last interglacial period. *Nature*, 431 :147–151.

[Nijssen et al., 1997] Nijssen, B., Lettenmaier, D. P., Xu Liang, S., Wetzel, W., and Wood, E. F. (1997). Streamflow simulation for continental-scale river basins. *Water Resour. Res.*, 33 :711–724.

[Noone, 2008] Noone, D. (2008). The influence of midlatitude and tropical overturning circulation on the isotopic composition of atmospheric water vapor and Antarctic precipitation. *J. Geophys. Res.*, 113.

[Noone, 2009] Noone, D. (2009). An isotopic evaluation of the factors controlling low humidity air in the troposphere. *J. Clim.*, submitted.

[Noone and Simmonds, 2002a] Noone, D. and Simmonds, I. (2002a). Annular variations in moisture transport mechanisms and the abundance of deltaO18 in Antarctic snow. *J. Geophys. Res.*, 107 :4742, doi : 4710.1029/2002JD002262.

[Noone and Simmonds, 2002b] Noone, D. and Simmonds, I. (2002b). Associations between delta18O of Water and Climate Parameters in a Simulation of Atmospheric Circulation for 1979-95. *J. Climate*, 15 :3150–3169.

[Nuret et al., 2008] Nuret, M., Lafore, J.-P., Guichard, F., Redelsperger, J.-L., Bock, O., Augusti-Panareda, A., and N'Gamini, J.-B. (2008). Correction of humidity bias for Vaisala RS80-A sondes during the AMMA 2006 Observing Period. *J. Atmos. Oceanic Technol.*, 25 :2152–2158.

[Ogée et al., 2007] Ogée, J., Cuntz, M., Peylin, P., and Bariac, T. (2007). Non-steady-state, non-uniform transpiration rate and leaf anatomy effects on the progressive stable isotope enrichment of leaf water along monocot leaves. *Plant, Cell and Environment*, 30 :367–387.

[Oki and Sud, 1998] Oki, T. and Sud, Y. C. (1998). Design of Total Runoff Integrating Pathways (TRIP) - A Global River Channel Network. *Earth Interactions*, 2 :1–36.

[Oltmans et al., 2000] Oltmans, S. J., Volmel, H., Hofmann, D. J., Rosenlof, K., and Kley, D. (2000). The increase in stratospheric water vapor from balloon borne frostpoint hygrometer measurements at Washington, D. C. and Boulder, Colorado. *Geophys. Res. Lett.*, 27 :3453 ?3456.

[Payne et al., 2007] Payne, V. H., Noone, D., Dudhia, A., Piccolo, C., and Grainger, R. G. (2007). Global satellite measurements of HDO and implications for understanding the transport of water vapour into the stratosphere. *Quart. J. R. Meteor. soc.*, 133 :1459–1741.

[Peltier, 1994] Peltier, W. R. (1994). Ice age paleotopography. *Science*, 265 :195–201.

[Penman, 1948] Penman, H. L. (1948). Natural evaporation from open water, bare soil and grass. *Proceedings of the Royal Society of London. Series A*, 193 :120–145.

[Petit et al., 1981] Petit, J., Briat, M., and Royer, A. (1981). Ice age aerosol content from east Antarctic ice cores samples and past wind strength. *Nature*, 293 :391–394.

[Petit et al., 1999] Petit, J. R., Jouzel, J., Raynaud, D., Barkov, N. I., Barnola, J.-M., Basile, I., Bender, M., Chappellaz, J., Davs, M., Delaygue, G., Delmotte, M., Kotlyakov, V. M., Legrand, M., Lipenkov, V. Y., Lorius, C., Pépin, L., Ritz, C., Saltzman, E., and Stievnard, M. (1999). 420,000 years of climate and atmopheric history revealed by the Vostok deep Antarctic ice core. *Nature*, 399 :429–436.

[Petit et al., 1991] Petit, J. R., White, J. W. C., Young, N. W., Jouzel, J., and Korotkevich, Y. S. (1991). Deuterium excess in recent Antarctic snow. *J. Geophys. Res.*, 96 :5113–5122.

[Pfahl and Wernli, 2008] Pfahl, S. and Wernli, H. (2008). Air parcel trajectory analysis of stable isotopes in water vapor in the eastern Mediterranean. *J. Geophys. Res.*, 113.

[Piao et al., 2007] Piao, S., Friedlingstein, P., Ciais, p., de Noblet-Ducoudré, N., Labat, D., and Zaehle, S. (2007). Changes in climate and land use have a larger direct impact than rising CO2 on global river runoff trends. *PNAS*, 104 :15242–15247.

[Pierrehumbert, 1999] Pierrehumbert, R. T. (1999). Huascaran delta18O as an indicator of tropical climate during the Last Glacial Maximum. *Geophys. Res. Lett.*, 26 :1345–1348.

[Pierrhumbert and Roca, 1998] Pierrhumbert, R. T. and Roca, R. (1998). Evidence for control of atlantic subtropical humidity by large scale advection. *Geophys. Res. Lett.*, 25 :4537–4540.

[Pinot et al., 1999] Pinot, S., Ramstein, G., Harrison, S. P., Prentice, I. C., Guiot, J., Stute, M., and Joussaume, S. (1999). Tropical paleoclimates at the Last Glacial Maximum : comparison of Paleoclimate Modeling Intercomparison Project (PMIP) simulations and paleodata. *Clim. Dyn.*, 15 :857–874.

[Polcher, 2003] Polcher, J. (2003). Les processus de surface à l'échelle globale et leurs interactions avec l'atmosphère. In *Thèse d'habilitation à diriger des recherches, Université Paris 6*.

[Ramirez et al., 2003] Ramirez, E., Hoffmann, G., Taupin, J. D., Francou, B., Ribstein, P., Caillon, N., Ferron, F. A., Landais, A., Petit, J. R., Pouyaud, B., Schotterer, U., Simoes, J. C., and Stievenard, M. (2003). A new Andean deep ice core from Nevado Illimani (6350 m), Bolivia. *Earth and Planetary Science Letters*, 212 :337–350.

[Randel et al., 2004] Randel, W. J., Wu, F., Oltmans, S., Rosenlof, K., and Nedoluha, G. E. (2004). Interannual changes of stratospheric water vapor and correlations with tropical tropopause temperatures. *J. Atm. Sci.*, 61 :2133–2148.

[Raymond, 1995] Raymond, D. (1995). Regulation of moist convection over the west pacific warm pool. *J. Atmos. Sci.*, 52 :3945–3959.

[Raz-Yaseed et al., 2010] Raz-Yaseed, N., Rotenberg, E., and Yakir, D. (2010). Spatial variations in shading and their effects on water flux partitioning in an open canopy semi-arid pine forest. *Agric. Forest Meteorol.*, pages in press, doi :10.1016/j.agrformet.2010.01.010.

[Redelsperger and Lafore, 1987] Redelsperger, J.-L. and Lafore, J.-P. (1987). A three dimensional simulation of a tropical squall line : convective organisation and thermodynamic vertical transport. *J. Atm. Sci.*, 47 :1334–1356.

[Redelsperger et al., 2006] Redelsperger, J.-L., Thorncroft, C., Arona, D., Lebel, T., Parker, D., and Polcher, J. (2006). African monsoon multidisciplinary analysis : An international research project and field campaign. *Bull. Am. Meteor. Soc.*, 87 :1739–1746.

[Reynolds et al., 2002] Reynolds, R. W., Rayner, N. A., Smith, T. M., Stokes, D. C., and Wang, W. (2002). An improved in situ and satellite sst analysis fo climate. *J. Climate*, 15 :1609–1625.

[Riley et al., 2002] Riley, W. J., Still, J., Torn, M. S., and Berry, J. A. (2002). A mechanistic model of H218O and C18OO fluxes between ecosystems and the atmosphere : Model description and sensitivity analyses. *Global Biogeochem. Cycles*, 16 (4) :1095, doi :10.1029/2002GB001878.

[Rindsberger et al., 1990] Rindsberger, M., Jaffe, S., Rahamim, S., and Gat, R. (1990). Patterns of the isotopic composition of precipitation in time and space : data from the israeli storm water collection program. *Tellus*, 42 :263–271.

[Risi et al., 2008a] Risi, C., Bony, S., and Vimeux, F. (2008a). Influence of convective processes on the isotopic composition (O18 and D) of precipitation and water vapor in the Tropics : Part 2 : Physical interpretation of the amount effect. *J. Geophys. Res.*, 113 :D19306, doi :10.1029/2008JD009943.

[Risi et al., 2010a] Risi, C., Bony, S., Vimeux, F., Chong, M., and Descroix, L. (2010a). Evolution of the water stable isotopic composition of the rain sampled along Sahelian squall lines. *Quart. J. Roy. Meteor. Soc.*, 136 (S1) :227 – 242.

[Risi et al., 2008b] Risi, C., Bony, S., Vimeux, F., Descroix, L., Ibrahim, B., Lebreton, E., Mamadou, I., and Sultan, B. (2008b). What controls the isotopic composition of the African monsoon precipitation ? Insights from event-based precipitation collected during the 2006 AMMA campaign. *Geophys. Res. Lett.*, 35 :doi :10.1029/2008GL035920.

[Risi et al., 2010b] Risi, C., Bony, S., Vimeux, F., and Jouzel, J. (2010b). Water stable isotopes in the LMDZ4 General Circulation Model : model evaluation for present day and past climates and applications to climatic interpretation of tropical isotopic records. *J. Geophys. Res.*, in press :doi :10.1029/2009JD013255.

[Risi et al.,] Risi, C., Landais, A., Bony, S., Masson-Delmotte, V., Jouzel, J., and Vimeux, F. Modeling the 17O-excess and d-excess variations in Antarctic precipitation and its moisture source. *submitted for J. Geophys. Res.*

[Roche et al., 2004] Roche, D., Paillard, D., and Cortijo, E. (2004). Constraints on the duration and freshwater release of Heinrich event 4 through isotope modelling. *Nature*, 432 :379–382.

[Rosenlof, 2002] Rosenlof, K. (2002). Transport changes inferred from HALOE water and methane measurements. *J. Meteor. Soc. Japan*, 80 :831–848.

[Rosnay and Polcher, 1998] Rosnay, P. D. and Polcher, J. (1998). Modelling root water uptake in a complex land surface scheme coupled to a GCM. *Hydrol. Earth Sci.*, 2 :239–255.

[Rozanski et al., 1993] Rozanski, K., Araguas-Araguas, L., and Gonfiantini, R. (1993). Isotopic patterns in modern global precipitation. *Geophys. Monogr. Seri., AGU*, Climate Change in Continental Isotopic records.

[Salati et al., 1979] Salati, E., Dall'Olio, A., Matsui, E., and Gat, J. (1979). Recycling of water in the Amazon basin : An isotopic study. *Water Resources Research*, 15 :1250–1258.

[Sarnthein et al., 2003] Sarnthein, M., Gersonde, R., Niebler, S., Pflaumann, U., Spielhagen, R., Thiede, J., Wefer, G., and Weinelt, M. (2003). Overview of Glacial Atlantic Ocean Mapping (GLAMAP 2000). *Paleoceanography*, 18 :1030.

[Schmidt et al., 2005] Schmidt, G., Hoffmann, G., Shindell, D., and Hu, Y. (2005). Modelling atmospheric stable water isotopes and the potential for constraining cloud processes and stratosphere-troposphere water exchange. *J. Geophys. Res.*, 110 :D21314, doi :10.1029/2005JD005790.

[Schmidt et al., 2007] Schmidt, G., LeGrande, A., and Hoffmann, G. (2007). Water isotope expressions of intrinsic and forced variability in a coupled ocean-atmosphere model. *J. Geophys. Res.*, 112.

[Schneider et al., 2009] Schneider, T., O'Gorman, P., and Levine, X. (2009). Water vapor and the dynamics of climate changes. *Rev. Geophys.*

[Sherwood and Dessler, 2001] Sherwood, S. and Dessler, A. (2001). A model for transport across the tropical tropopause. *J. Atmos. Sci.*, 58 :765–779.

[Sherwood, 1996] Sherwood, S. C. (1996). Maintenance of the free tropospheric tropical water vapor distribution. part II : simulation of large-scale advection. *J. Clim.*, 11 :2919–2934.

[Sherwood and Dessler, 2000] Sherwood, S. C. and Dessler, A. E. (2000). On the control of stratospheric humidity. *Geophys. Res. Lett.*, 27 :2513–2516.

[Sherwood and Wahrlich, 1999] Sherwood, S. C. and Wahrlich, R. (1999). Observed evolution of tropical deep convective events and their environment. *Mon. Wea. Rev.*, 127 :1777–1795.

[Shuttleworth, 1988] Shuttleworth, W. (1988). Evaporation from amazonian rainforest. *Proc. R. Soc. Lond.*, 233 :321–348.

[Sitch, 2003] Sitch, S. e. a. (2003). Evaluation of ecosystem dynamics, plant geography and terrestrial carbon cycling in the LPJ dynamic vegetation model. *Global Change Biol.*, 9 :161–185.

[Smith et al., 2006] Smith, J. A., Ackerman, A. S., Jensen, E. J., and Toon, O. B. (2006). Role of deep convection in establishing the isotopic composition of water vapor in the tropical transition layer. *Geophys. Res. Lett.*, 33 :6812.

[Smith et al., 2005] Smith, J. A., Seltzer, G. O., Farber, D. L., Rodbell, D. T., and Finkel, R. C. (2005). Early Local Last Glacial Maximum in the Tropical Andes. *Science*, 308 :678–681.

[Sobel and Bretherton, 2000] Sobel, A. H. and Bretherton, C. S. (2000). Modeling tropical precipitation in a single column. *J. Climate*, 13 :4378–43–92.

[Sodemann et al., 2008] Sodemann, H., Masson-Delmotte, V., Schwierz, C., Vinther, B. M., and Wernli, H. (2008). Interannual variability of Greenland winter precipitation sources : 2. Effects of North Atlantic Oscillation variability on stable isotopes in precipitation. *J. Geophys. Res.*, 113 :D12, doi :10.1029/2007JD009416.

[SPARC, 2000] SPARC (2000). Assessment of water vapor in the upper stratosphere and lower stratosphere, stratospheric processes and their role in climate. *Rep. WMO/TD-1043*.

[Stella et al., 2009] Stella, P., Lamaud, E., Brunet, Y., Bonnefond, J.-M., Loustau, D., , and Irvine, M. (2009). Simultaneous measurements of CO2 and water exchanges over three agroecosystems in South-West France. *Biogeosciences Discuss.*, 6 :2489–2522.

[Stenni et al., 2001] Stenni, B., Masson-Delmotte, V., Johnsen, S., Jouzel, J., Longinelli, A., Monnin, E., Röthlisberger, R., and Selmo, E. (2001). An oceanic cold reversal during the last deglaciation. *Science*, 293 :2074–2077.

[Stewart, 1975] Stewart, M. K. (1975). Stable isotope fractionation due to evaporation and isotopic exchange of falling waterdrops : Applications to atmospheric processes and evaporation of lakes. *J. Geophys. Res.*, 80 :1133–1146.

[Stokes and Swartz, 1994] Stokes, G. M. and Swartz, S. E. (1994). The Atmospheric Radiation Measurement (ARM) Program : Programmatic background and design of the cloud and radiation testbed. *Bull. Amer. Meteor. Soc.*, 75 :1201–1221.

[Sturm et al., 2007a] Sturm, C., Hoffmann, G., and barbel Langmann (2007a). Simulation of the Stable Water Isotopes in Precipitation over South America : Comparing Regional to Global Circulation Models. *J. Clim.*, 20 :3730–3750.

[Sturm et al., 2007b] Sturm, C., Vimeux, F., and Krinner, H. (2007b). Intraseasonal variability in South America recorded in stable water isotopes. *J. Geophys. Res.*, 112.

[Sturm, 2005] Sturm, K. (2005). *Regional atmospheric modelling of the stable water isotope cycle.* PhD thesis, Université Joseph Fourier.

[Sturm et al., 2005] Sturm, K., Hoffmann, G., Langmann, B., and Stichler, W. (2005). Simulation of 18O in precipitation by the regional circulation model REMOiso. *Hydrological Processes*, 19 :3425–3444.

[Stute and Talma, 1998] Stute, M. and Talma, S. (1998). Glacial temperature and moisture transport regimes reconstructed from noble gas and deltaO18, Stampriet aquifer, Namibia. In *Isotope Techniques in the Study of Past and Current Environmental Changes in the Hydrosphere and the Atmosphere. Proceedings of Vienna Symposium 1997, IAEA, Vienna, SM- 349/53, pp. 307-328.*

[Sultan and Janicot, 2003] Sultan, B. and Janicot, S. (2003). The West African Monsoon Dynamics. Part II : The 'Preonset' and 'Onset' of the Summer Monsoon. *J. Climate*, 16 :3407–3427.

[Sultan et al., 2003] Sultan, B., Janicot, S., and Diedhiou, A. (2003). The West African Monsoon Dynamics. Part I : Documentation of Intraseasonal Variability. *J. Climate*, 16 :3389–3406.

[Sun and Lindzen, 1993] Sun, D.-Z. and Lindzen, R. S. (1993). Distribution of tropical tropospheric water vapor. *J. Atm. Sci.*, 50 (12) :1643–1660.

[Sylvestre, 2009] Sylvestre, F. (2009). Moisture pattern during the Last Glacial Maximum in South America. *F. Vimeux et al. (eds.), Past Climate Variability in South America and Surrounding Regions, Developments in Paleoenvironmental Research 14*, 14 :3–27.

[Taupin et al., 2000] Taupin, J., Coudrain-Ribstein, A., Gallaire, R., Zuppi, G. M., and Filly, A. (2000). Rainfall characteristics in Western Africa : regional scale and influence of irrigated areas. *J. Geophys. Res.*, 105 :11,911–11,924.

[Taupin and Gallaire, 1998] Taupin, J.-D. and Gallaire, R. (1998). Variabilité isotopique à I'échelle infra-événement de quelques épisodes pluvieux dans la région de Niamey, Niger. *C.R. Acad. des Sciences*, 326 :493–498.

[Taupin et al., 1997] Taupin, J.-D., Gallaire, R., and Arnaud, Y. (1997). Analyses isotopiques et chimiques des précipitations sahélienne de la région de Niamey au Niger : implications climatologiques. *Hydrochemistry*, 244.

[Taylor, 2001] Taylor, K. E. (2001). Summarizing multiple aspects of model performance in a single diagram. *J. Geophys. Res.*, 106 :7183–7192.

[Thompson et al., 1989] Thompson, L., Mosley-Thompson, L., Davis, M., Bolzan, J., Yao, T., Gundestrup, N., Wu, X., Klein, L., and Xie, Z. (1989). Holocene-late Pleistocene climatic ice core records from Quinghai-Tibetan Plateau. *Science*, 246 :474–477.

[Thompson et al., 1997] Thompson, L., Yao, T., Davis, M., Henderson, K., Mosley-Thompson, E., Lin, P.-N., Beer, J., Synal, H.-A., Cole-Dai, J., and Bolzan, J. (1997). Tropical climate instability : the last glacial cycle from a Qinghai- Tibetan ice core. *Science*, 276 :1821 ?1825.

[Thompson et al., 1998] Thompson, L. G., Davis, M. E., Mosley-Thompson, E., Sowers, T. A., Henderson, K. A., Zagorodnov, V. S., Lin, P.-N., Mikhalenko, V. N., Campen, R. K., Bolzan, J. F., Cole-Dai, J., and Francou, B. (1998). A 25,000-year tropical climate history from Bolivian ice cores. *Science*, 282 :1858–1864.

[Thompson et al., 1995] Thompson, L. G., Mosley-Thompson, E., Davis, M. E., Lin, P.-N., Henderson, K. A., Cole-Dai, J., Bolzan, J. F., and b. Liu, K. (1995). Late Glacial Stage and Holocene Tropical Ice Core Records from Huascarán, Peru. *Science*, 269 :46 – 50, DOI : 10.1126/science.269.5220.46.

[Thompson et al., 2000] Thompson, L. G., Mosley-Thompson, E., and Henderson, K. A. (2000). Ice-core paleoclimate records in Tropical South America since the Last Glacial Maximum. *J. Quat. Sci.*, 15 :1579–1600.

[Tindall et al., 2009] Tindall, J. C., Valdes, P., and Sime, L. C. (2009). Stable water isotopes in HadCM3 : Isotopic signature of El Nino-Southern Oscillation and the tropical amount effect. *J. Geopys. Res.*, 114 :D04111, doi :04110.01029/02008JD010825.

[Toggweiler et al., 2006] Toggweiler, J. R., Russell, J. L., and Carson, S. R. (2006). Midlatitude westerlies, atmospheric CO2, and climate change during the ice ages. *Paleoceanography*, 21.

[Tremoy, 2009] Tremoy, G. (2009). Etude de la composition isotopique des précipitations en Amérique du Sud tropicale à l'aide du modèle LMDZ-iso : amélioration de l'interprétation climatique des carottes de glace andines. Master's thesis, Université Paul Sabatier.

[Trenberth, 1998] Trenberth, K. (1998). Atmospheric moisture recycling : role of advection and local evaporation. *J. Clim.*, 12 :1368–1381.

[Tsujimura et al., 2007] Tsujimura, M., Sasaki, L., Yamanaka, T., Sugimoto, A., Li, S.-G., Matsushima, D., Kotani, A., and Saandar, M. (2007). Vertical distribution of stable isotopic composition in atmospheric water vapor and subsurface water in grassland and forest sites, eastern Mongolia. *J. Hydrol.*, 333 :35–46.

[Twining et al., 2006] Twining, J., Stone, D., Tadros, C., Henderson-Sellers, A., and A, W. (2006). Moisture Isotopes in the Biosphere and Atmosphere (MIBA) in Australia : A priori estimates and preliminary observations of stable water isotopes in soil, plant and vapour for the Tumbarumba Field Campaign. *Global and Planetary Change*, 51 :59–72.

[Ubarana, 1996] Ubarana, V. N. (1996). *Observations and modelling of rainfall interception at two experimental sites in Amazonia*. Amazonian deforestation and climate.

[Uemura et al., 2008] Uemura, R., Matsui, Y., Yoshimura, K., Motoyama, H., and Yoshida, N. (2008). Evidence of deuterium-excess in water vapour as an indicator of ocean surface conditions. *J. Geophys. Res.*, 113 :doi :10.1029/2008JD010209.

[Uppala et al., 2005] Uppala, S., Kallberg, P., Simmons, A., Andrae, U., da Costa Bechtold, V., Fiorino, M., Gibson, J., Haseler, J., Hernandez, A., Kelly, G., Li, X., Onogi, K., Saarinen, S., Sokka, N., Allan, R., Andersson, E., Arpe, K., Balmaseda, M., Beljaars, A., van de Berg, L., Bidlot, J., Bormann, N., Caires, S., Chevallier, F., Dethof, A., Dragosavac, M., Fisher, M., Fuentes, M., Hagemann, S., Holm, E., Hoskins, B., Isaksen, L., Janssen, P., Jenne, R., McNally, A., Mahfouf, J.-F., Morcrette, J.-J., Rayner, N., Saunders, R., Simon, P., Sterl, A., Trenberth, K., Untch, A., Vasiljevic, D., Viterbo, P., and Woollen, J. (2005). The ERA-40 re-analysis. *Quart. J. Roy. Meteor. Soc.*, 131 :2961–3012.

[Urban et al., 2007] Urban, J., Lautié, N., Murtagh, D., Erikson, P., Kasai, Y., Loßow, Dupuy, E., de la Noë, J., Frisk, U., Oldberg, M., Le Flochmoën, E., and Ricuaud, P. (2007). Global observations of middle atmospheric water vapour by the Odin satellite : An overview . *Planet. Space Sci.*, 55 (9) :1093–1102.

[Vaikmae et al., 1993] Vaikmae, R., Jouzel, J., Petit, J. R., and Stievenard, M. (1993). A new Antarctic climate record from Dome B ice core. *paper presented at the Isotopic Technique in the Study of Past and Current Environmental changes in the Hydrosphere and Atmosphere*, Int. At. Energy Agency, Vienna.

[Van Leer, 1977] Van Leer, B. (1977). Towards the ultimate conservative difference scheme : IV. a new approach to numerical convection. *J. Computational Phys.*, 23 :276–299.

[van Ommen and Morgan, 1997] van Ommen, T. D. and Morgan, T. (1997). Calibrating the ice core paleothermometer using seasonality. *J. Geophys. Res.*, 102 :9351–9357.

[Vimeux, 1999] Vimeux, F. (1999). *Variations de l'Excès en Deutérium en Antarctique au cours des 400 00 dernières années : implications climatiques*. PhD thesis, Université Paris VI.

[Vimeux et al., 2002] Vimeux, F., Cuffey, K., and Jouzel, J. (2002). New insights into Southern Hemisphere temperature changes from Vostok ice cores using deuterium excess correction. *Earth Planet. Sci. Lett.*, 203 :829–843.

[Vimeux et al., 2008] Vimeux, F., de Angelis, M., Ginot, P., Magand, O., Casassa, G., B. Pouyaud, S., Falourd, , and Johnsen, S. (2008). A promising location in Patagonia for paleoclimate and paleoenvironmental reconstructions revealed by a shallow firn core from Monte San Valentin (Northern Patagonia Icefield, Chile) Ž. *J. Geophys. Res.,*, 113.

[Vimeux et al., 2005] Vimeux, F., Gallaire, R., Bony, S., Hoffmann, G., and Chiang, J. C. H. (2005). What are the climate controls on deltaD in precipitation in the Zongo Valley (Bolivia) ? Implications for the Illimani ice core interpretation. *Earth Planet. Sci. Lett.*, 240 :205–220.

[Vimeux et al., 2004] Vimeux, F., Gallaire, R., Sturm, K., Hoffmann, G., and Ramirez, E. (2004). Deuterium Excess in Bolivian Precipitation : From Short-term Station Data to ice Core Records. *AGU Fall Meeting Abstracts*, pages B1028+.

[Vimeux et al., 2009] Vimeux, F., Ginot, P., Schwikowski, M., Vuille, M., Hoffmann, G., Thompson, L. G., and Schotterer, U. (2009). Climate variability during the last 1000 years inferred from Andean ice cores : A review of methodology and recent results. *Palaeogeogr. Palaeoclimatol. Palaeoecol.*, 281 (3-4) :doi :10.1016/j.palaeo.2008.03.054.

[Vimeux et al., 2001] Vimeux, F., Masson, V., Delaygue, G., Jouzel, J., Petit, J. R., and Stievenard, M. (2001). A 420,000 year deuterium excess record from East Antarctica : Information on past changes in the origin of precipitation at Vostok. *J. Geophys. Res.*, 106 :31,863–31,873.

[Vitvar et al., 2006] Vitvar, T., Aggarwal, P., and Herczeg, A. (2006). Towards a global network for monitoring isotopes in rivers. *Geophys. Res. Abstracts, EGU*, 8.

[Vitvar et al., 2007] Vitvar, T., Aggarwal, P. K., and Herczeg, A. L. (2007). Global network is launched to monitor isotopes in rivers. *Eos Trans. AGU*, 88 (33) :doi :10.1029/2007EO330001.

[Vuille et al., 2003] Vuille, M., Bradley, R. S., Werner, M., Healy, R., and Keimig, F. (2003). Modeling delta18O in precipitation over the tropical Americas : 1. Interannual variability and climatic controls. *J. Geophys. Res.*, 108 :1–1.

[Vuille and Werner, 2005] Vuille, M. and Werner, M. (2005). Stable isotopes in precipitation recording South American summer monsoon and ENSO variability : observations and model results. *Climate Dynamics*, 25 :401–413.

[Waelbroeck and co authors, 2008] Waelbroeck, C. and co authors (2008). Constraints on the magnitude and patterns of ocean cooling at the Last Glacial Maximum. *NGS, submitted.*

[Wallace and Holwill, 1997] Wallace, J. and Holwill, C. (1997). Soil evaporation from tiger-bush in south-west niger. *J. Hydrol.*, 188-189 :426–442.

[Wang et al., 2008] Wang, Y., Cheng, H., Edwards, L., Kong, X., Shao, X., Chen, S., Wu, J., Jiang, X., Wang, X., and An, Z. (2008). Millennial- and orbital-scale changes in the East Asian monsoon over the past 224,000 years. *Nature*, 451 :1090–1093.

[Washburn and Smith, 1934] Washburn, E. and Smith, E. (1934). The isotopie fractionation of water by physiologieal processes. *Science*, 79 :188–189.

[Webster and Heymsfield, 2003] Webster, C. R. and Heymsfield, A. J. (2003). Water Isotope Ratios D/H, 18O/16O, 17O/16O in and out of Clouds Map Dehydration Pathways. *Science*, 302 :1742–1746.

[Weiler et al., 2003] Weiler, M., McGlynn, B. L., McGuire, K. J., and McDonnell, J. J. (2003). How does rainfall become runoff ? A combined tracer and runoff transfer function approach. *Water Resources Research*, 39.

[Wels et al., 1991] Wels, C., Cornett, J., and Lazerte, B. D. (1991). Hydrograph separation : a comparison of geochmical and isotopic tracers. *J. Hydrol.*, 122 :253–274.

[Werner et al., 2001] Werner, M., Heimann, M., and Hoffmann, G. (2001). Isotopic composition and origin of polar precipitation in present and glacial climate simulations. *Tellus*, 53B :53–71.

[Werner et al., 2000] Werner, M., Mikolajewicz, U., Heimann, M., and Hoffmann, G. (2000). Borehole versus isotope temperatures on Greenland : Seasonality does matter. *Geophys. Res. Lett.*, 27 (5) :723–726.

[White et al., 1997] White, J. W. C., Barlow, L. K., Fisher, D., Grootes, P., Jouzel, J., Johnsen, S. J., Stuiver, M., and Clausen, H. (1997). The climate signal in the stable isotopes of snow from Summit, Greenland : Results of comparisons with modern climate observations. *J. Geophys. Res.*, 102 :26,425–26,439.

[Williams et al., 2004] Williams, D. G., Cable, W., Hultine, K., and co authorso (2004). Evapotranspiration components determined by stable isotope, sap flow and eddy covariance techniques. *Agricult. Forest. Meteor.*, 125 :241–258.

[Williams et al., 1992] Williams, E., Rutledge, S. A., Geotis, S. G., Renno, N., Rsmussen, E., and Rickenbach, T. (1992). A radar and electrical study of Tropical "hot towers". *J. Atm. Sci.*, 49 :1386–1395.

[Wingate et al., 2010] Wingate, L., Ogee, J., Burlett, R., and Bosc, A. (2010). Strong seasonal disequilibrium measured between the oxygen isotope signals of leaf and soil co2 exchange. *Glob. Change Biology*, pages doi : 10.1111/j.1365–2486.2010.02186.x.

[Wingate et al., 2009] Wingate, L., Ogée, J., Cuntz, M., Genty, B., andUlli Seibtf, I. R., Yakir, D., Maseyk, K., Pendallh, E. G., Barbouri, M. M., Mortazavij, B., Burlett, R., Peylin, P., Miller, J., Mencuccini, M., Shimn, J. H., Hunti, J., , and Gracea, J. (2009). The impact of soil microorganisms on the global budget of deltao18 in atmospheric co2. *PNAS*, page doi : 10.1073/pnas.0905210106.

[Worden et al., 2007] Worden, J., Noone, D., and Bowman, K. (2007). Importance of rain evaporation and continental convection in the tropical water cycle. *Nature*, 445 :528–532.

[Wright et al., 2009] Wright, J. S., Sobel, A. H., and Schmidt, G. A. (2009). The influence of condensate evaporation on water vapor and its stable isotopes in a GCM. *Geophys. Res. Lett.*

[Xie and Arkin, 1997] Xie, P. and Arkin, P. (1997). Global precipitation : A 17-year monthly analysis based on gauge observations, satellite estimates, and numerical model outputs. *Bull. Amer. Meteor. Soc.*, 78 :2539 – 2558.

[Xu and Emanuel, 1989] Xu, K.-M. and Emanuel, K. (1989). Is the Tropical Atmosphere conditionally unstable ? *Mon. Weath. Rev.*, 117 :1471–1479.

[Yakir et al., 2000] Yakir, D., da Silveira, L., and Sternberg, L. (2000). The use of stable isotopes to study ecosystem gas exchange. *Oecologia*, 123 :297–311.

[Yakir and Wang, 1996] Yakir, D. and Wang, X.-F. (1996). Fluxe of co2 and water between terrestrial vegetation and the atmosphere estimated from isotope measurements. *Nature*, 380 :515–517.

[Yakir and Yechieli, 1995] Yakir, D. and Yechieli, Y. (1995). Plant invasion of newly exposed hypersaline Dead Sea shore. *Nature*, 374 :803–805.

[Yaseef et al., 2009] Yaseef, N. R., Yakir, D., Rotenberg, E., Schiller, G., and Cohen, S. (2009). Ecohydrology of a semi-arid forest : partitionning among water balance components and its implications for predicted precipitation changes. *Ecohydrolohy*, page 10.1002/eco.65.

[Yepez et al., 2003] Yepez, E., Williams, S., Scott, R., and Lin, G. (2003). Partitioning overstory and understory evapotranspiration in a semiarid savanna woodland from the isotopic composition of water vapor. *Agricultural and Forest Meteorology*, 119 :53–68.

[Yoshimura et al., 2008] Yoshimura, K., Kanamitsu, M., Noone, D., and Oki, T. (2008). Historical isotope simulation using reanalysis atmospheric data. *J. Geophys. Res.*, 113 :D19108, doi :10.1029/2008JD010074.

[Yoshimura et al., 2006] Yoshimura, K., Miyazaki, S., Kanae, S., and Oki, T. (2006). Iso-MATSIRO, a land surface model that incorporates stable water isotopes. *Glob. Planet. Change*, 51 :90–107.

[Yoshimura et al., 2003] Yoshimura, K., Oki, T., Ohte, N., and Kanae, S. (2003). A quantitative analysis of short-term O18 variability with a Rayleigh-type isotope circulation model. *J. Geophys. Res.*, 108 :D20, 4647, doi :10.1029/2003JD003477.

[Yoshimura et al., 2004] Yoshimura, K., Oki, T., Ohte, N., and Kanae, S. (2004). Colored moisture analysis estimates of variations in 1998 asian monsoon water sources. *J. Meteor. Soc. Japan*, 82 :1315–1329.

[Zahiri, 2007] Zahiri, E.-P. (2007). *Cycle de l'eau des systèmes convectifs Ouest-Africains : preparation à l'exploitation des mesures radar Xport dans AMMA par simulations.* PhD thesis, Université Paul Sabatier - Toulouse III.

[Zipser, 1977] Zipser, E. (1977). Mesoscale and convective scale downdrafts as distinct components of squall-line structure. *Mon. Wea. Rev.*, 105 :1568–1589.